Reconstruction of Holocene climate change using image analysis of laminated sediments

Michael James Green

Department of Earth Sciences, University College London

Thesis submitted for the degree of Doctor of Philosophy

July 2004

ProQuest LLC
789 East Eisenhower Parkway
P.O. Box 1346
Ann Arbor, MI 48106-1346

Acknowledgements

I would like to thank:

Juergen Thurow and Kevin Pickering, my supervisors. Sandra Nederbragt, for support during the first NIOZ trip. Ian Bailey, for constant support, assistance, and advice. Dan Herron, for advice on time-series analysis.

Rienk Smittenberg and NIOZ, for making the Drammensfjord cores available and for sharing data from these cores, and for assistance during the digital imaging. Daniel Ariztegui, for assistance with the Lake St Moritz imaging and for contributing useful data from Lake St Moritz. Elisabeth Alve, for assistance with the Drammensfjord varve mechanism. The Geological Survey of Finland, for the images of varved sediment used to illustrate image analysis techniques.

James Scourse and Rick Battarbee, for many useful comments and corrections.

My parents and Kate Halladay, for their constant support.

This research was funded by NERC Studentship GT04/99/ES/175.

Abstract

Concern about anthropogenic climate change has created an urgent need for pre-instrumental climate data. Reliable instrumental data only extend back to c. AD 1850, so pre-instrumental proxy data are essential to allow the study of climate variability on decadal, centennial and millennial timescales. Laminated sediment cores can potentially supply annual-resolution palaeoclimate proxy data.

Techniques have been developed to allow the application of high-resolution digital image analysis to annually-laminated Holocene sediment cores from two basins: Drammensfjord, Norway, and Lake St Moritz, Switzerland. Core chronologies have been produced by integrating digital-image-based varve counting, radiocarbon dating, and other independent chronological data. Image processing techniques have then been used to measure sediment greyvalue, which can be linked to sediment composition, and lamination thicknesses, which can be linked to changes in sediment accumulation. These data have been converted to evenly-sampled time-series, and have then been analysed using spectral analysis and comparisons with instrumental climate data in order to interpret the climatic influences that they record.

The Drammensfjord record indicates that the onset of anoxia in Drammensfjord occurred at c. AD 1000. The thicknesses of the grey varve sublayers are a proxy for the magnitude of the annual spring flood. A significant increase in the frequency of large spring floods in c. AD 1470 may be linked to the onset of the Little Ice Age. There is no signal of the North Atlantic Oscillation in the Drammensfjord varves. Spectral analysis reveals "solar" periodicities in the varve data, but a solar explanation is unconvincing.

The Lake St Moritz record indicates only a weak correlation between varve thickness and temperature. Sediment greyvalue is closely linked to sediment total organic carbon content, allowing a high-resolution proxy record to be produced. Spectral analysis of this indicates a red noise spectrum with possible significant periodicities at c. 2,870, 250, and 113 years, but interpretation of these is difficult because of the multiple climatic, anthropogenic and lake-ontogenetic influences on the record.

Contents

Chapter 1: Introduction and Aims

1.1 Introduction to climate change

Climate change is the subject of much concern [e.g. 1-5]: in the words of the Intergovernmental Panel on Climate Change (IPCC), "the Earth's climate system has demonstrably changed on both global and regional scales since the pre-industrial era, with some of these changes attributable to human activities" [6]. Consider the following annual global mean surface air temperature data from the University of East Anglia (UEA) Climatic Research Unit [7]. They incorporate both land and sea surface temperature measurements, and are expressed as anomalies from the mean of 1961-1990.

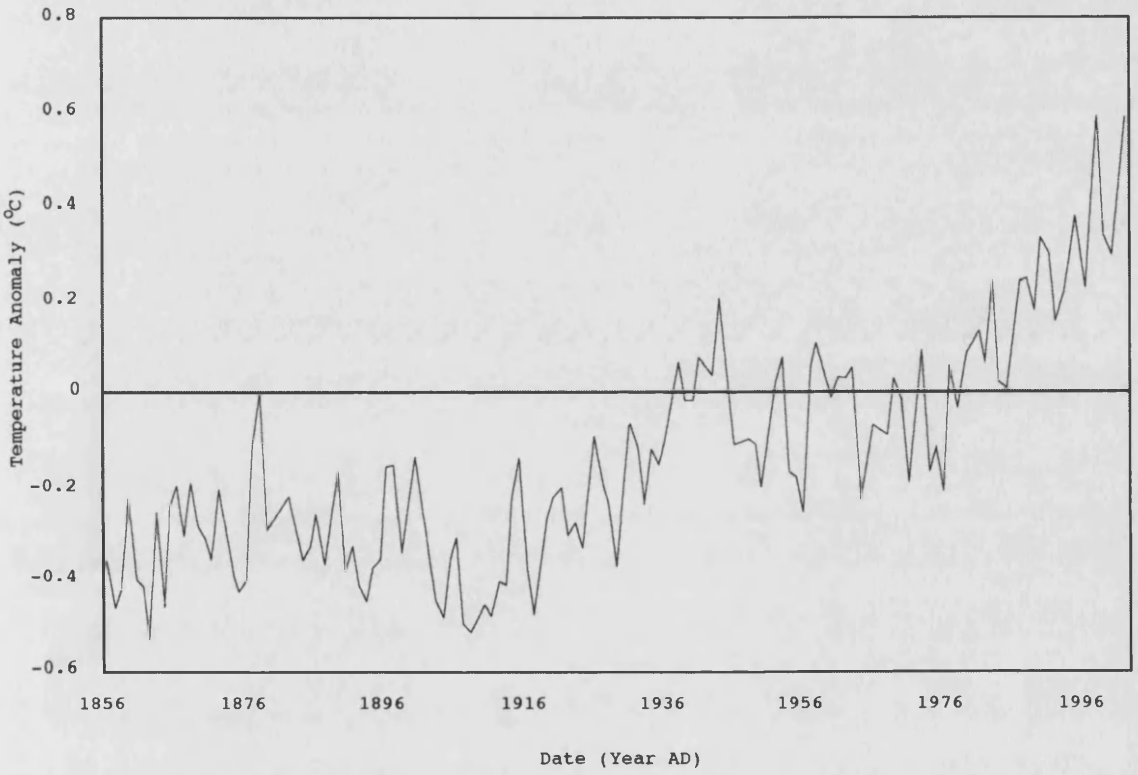

Figure 1.1: University of East Anglia Climatic Research Unit annual global mean surface temperature data for 1856-2002. Data taken from [7].

The overall pattern is a temperature increase of 0.6 ± 0.2°C since 1900, with the temperature rise concentrated in two intervals, 1910 to 1945 and 1976 to the present [6]. It is "very likely" - a 90-99% chance, in the IPCC's terminology - that the 1990s were the warmest decade, and 1998 the warmest year, since 1861 [6]. However, it is important to draw a distinction between these factual data and their interpretation, which is more controversial. Attributing this "global warming" or any other observed climate change to the activities of mankind is an uncertain process, for several reasons.

First, the Earth's climate is naturally variable: any anthropogenic changes that do occur will be superimposed on a constantly-changing background. Second, little is known about the mechanisms of this natural climate change, especially over timescales longer than a few decades, because of a lack of observational data: few instrumental

records are as long as the temperature record above, for example. And thirdly, the different components of the climate system interact, producing a complex and unpredictable network of feedbacks incorporating the atmosphere, hydrosphere, cryosphere, land surface, and biosphere [6]. Anthropogenic perturbation of any of these components will affect the others, and may become manifest as enhanced or diminished aspects of natural variability rather than a separate anthropogenic "fingerprint".

So, there is a need to separate and quantify, where possible, the different causes of climate change. By restricting the scope of enquiry to certain of these, perhaps operating over specified geographical areas and/or within specified intervals of time, the task of understanding variability in the global climate system can be made manageable.

1.2 Causes of climate change

Natural climate change can be categorised using a division between external and internal forcing factors, as used by the IPCC [6]. External forcing factors originate outside the network of climate components listed in section 1.1; internal forcing factors originate within this network. A summary of these is given below, followed by a summary of anthropogenic forcing factors.

1.2.1 External climate forcing factors

Changes in the Earth's orbit around the Sun affect the amount and distribution of incoming solar energy, resulting in "Milankovitch cycles" of c. 100,000, 41,000 and 23,000 years, among others, which are widely accepted as driving Quaternary ice ages [8,9]. Within both glacials and interglacials, there is evidence for millennial and centennial-scale climate variability, though this is poorly understood. Evidence for this comes primarily from the Greenland ice cores [10]. During the last glacial, and probably during earlier glacials [11], a series of millennial-scale temperature oscillations occurred, called Dansgaard-Oeschger events [12]; these are bundled into longer "Bond cycles" [13] lasting 10-15 ka, each of which culminates in a massive discharge of icebergs into the North Atlantic - a "Heinrich event" [14] - followed by rapid warming.

These cycles may result from the interaction of major ice sheets with the ocean's temperature and salinity, disrupting its thermohaline circulation [13]; if so, this would be an internal climate forcing factor. However, millennial-scale climate variability also occurs during interglacials, including the Holocene, which was previously thought to be extremely stable [e.g. 12]. Various strands of evidence indicate one or more millennial-scale climate cycles [e.g. 15,16], one of which may be a continuation of the millennial cyclicity seen during the last glacial [17], although much smaller in amplitude. This suggests that there is an underlying external forcing factor which is not dependent on the presence of large ice sheets: perhaps solar forcing, which is supported by evidence from cosmogenic nuclides [18]. The Sun may also play a role in centennial-scale climate cyclicity seen in the Greenland ice cores and other records [e.g. 19].

Solar cycles also occur at decadal scales: the c. 88-year Gleissberg sunspot cycle, the 22-year Hale double sunspot cycle, and the 11-year Schwabe sunspot cycle, among others [20]. The three cycles named can all be tracked by changes in the occurrence of sunspots; other cycles which are not visible in this way are also likely to exist, especially over decadal and centennial timescales [20]. The effect of solar cycles on climate is controversial: radiative changes alone are far too small to affect the climate significantly, except via an unknown amplification mechanism, possibly involving cloud formation [21]. The changing length of the 11-year Schwabe cycle has been invoked to explain the warming seen over the last century [21]; however, this has been described as the "double miracle hypothesis" [22] since it must simultaneously support an unknown amplification mechanism for solar influence on climate, and denigrate any role for increasing atmospheric CO_2, which has a well-understood warming influence. Furthermore, after 1970, the solar data no longer agree with the observed climate warming [23]. A better explanation for 20th century warming is provided by combining modelled influences of greenhouse gases, solar variability, and volcanic dust [6].

The latter is classed as an external forcing factor, since volcanic eruptions are not influenced by feedback from other parts of the climate system (though it may be possible for glacial ice-loading to inhibit eruptions in some locations [24]). Volcanic dust in the atmosphere promotes cooling by screening out solar radiation, both directly and via the formation of sulphate aerosols and other cloud condensation nuclei [25]. This cooling is short-lived, but may be sufficient to flip the global climate system into a different state if it were to occur at a critical moment [e.g. 26].

1.2.2 Internal climate forcing factors

Internal climate forcing factors are less tangible than external ones because there is no clear distinction between their causes and effects. A perturbation in one component of the climate system will propagate into the others, which may in turn feed back into the original component, setting up a loop internal to the climate system.

Most prominent among these is ENSO, the El Niño Southern Oscillation [27], which is a linked oscillation in atmospheric pressure and sea surface temperature over the Pacific Ocean. ENSO is pseudoperiodic, with oscillations between El Niño and La Niña states producing a broad spectral peak between wavelengths of 2 and 10 years. In places, ENSO has a greater influence on some aspects of climate than the annual cycle: along the west coast of South America, for example, precipitation tends to come and go with the ENSO cycle, rather than with the seasons [28]. A system of climate teleconnections [29] also links El Niño events to droughts in central Africa, forest fires in Indonesia [30], and some failures of the Indian monsoon [31]. This wide impact is reflected in the record global temperatures seen in 1998, which were partly caused by a strong El Niño event [6].

However, ENSO is unusual in the magnitude and areal extent of its influence. Less prominent modes of internal climate variability include the Pacific Decadal

Oscillation (PDO), the Quasi-Biennial Oscillation (QBO), and the North Atlantic Oscillation (NAO). The latter is regionally significant: it strongly affects winter climate in Europe [32]. Evidence from climate models [33], and from the "Great Salinity Anomaly" of the 1960s and 1970s [34], demonstrates how decadal variability in the NAO is coupled to changes in circulation in the North Atlantic, though this variability has no spectral peak comparable to that of ENSO. Tree-ring records suggest a possible 70-year cycle [35] but even this is non-stationary; it is only apparent after AD 1850. The NAO is better considered [36] as the most robust member of a set of "annular modes", so-called because they describe zonal coherence in atmospheric conditions; these arise internally in the climate system and exhibit little temporal cyclicity unless forced by external factors [37].

Internal climate variability on timescales of less than a year is perhaps a contradiction in terms: changes in the state of the atmosphere over weeks or months generally qualify as "weather" rather than "climate", though the distinction is necessarily imprecise. Sub-annual variability is also mostly too brief to be recorded by geological and biological agents such as sedimentation and tree growth. Furthermore, although there are some reasonably periodic signals in sub-annual climate, such as the 30-60 day Madden-Julian Oscillation [38], the weather itself is unpredictable beyond a few days in the future, owing to its chaotic nature [39].

This unpredictability also applies across longer timescales of climate change, such that random or pseudoperiodic oscillations of climate are much commoner than the precise, astronomical cyclicity seen in the Milankovitch bands. This makes any climate signal much harder to distinguish from the inevitable background noise of the climate, whether internal or from random external forcings like volcanic eruptions [40,41]. In addition, external and internal climate variability interact, affecting each other in a complex system of feedbacks. For example, solar forcing may affect ENSO and the NAO [42]. Climate variability is evidently complex, even without any anthropogenic contributions.

1.2.3 Anthropogenic climate forcing factors

Modern man affects virtually all aspects of the global environment [43], having transformed up to half the global land surface [44], and appropriating up to 55% of terrestrial net primary productivity [45]. Climate is unlikely to be an exception: it is hard to see how we can possibly transfer six billion tons of carbon per year from fossil fuels into the atmosphere without causing a change in the climate [46].

Atmospheric CO_2 concentration has been directly measured since 1957; earlier measurements are available from bubbles trapped in Antarctic ice. These show that the CO_2 concentration has risen from c. 280 parts per million (ppm) in 1800 to 367 ppm in 1999, and is increasing at 0.4% per year [6]. This increase is a result of anthropogenic CO_2 emissions, mostly from burning fossil fuels, as revealed by a concomitant decline in atmospheric O_2 concentration, and by the isotopic signature of the carbon. Land-use change, especially deforestation, is also a significant anthropogenic source of CO_2 [6].

However, the atmospheric CO_2 concentration is only increasing at about half the rate of fossil fuel CO_2 emissions, because of CO_2 sinks removing CO_2 from the atmosphere. For example, it can dissolve in seawater or be taken up by plant growth. Detailed knowledge of the carbon cycle, including the fate of atmospheric CO_2, is currently incomplete, making it difficult to predict how CO_2 concentrations will behave in the future. But even with efforts to reduce emissions, and perhaps also active sequestration of atmospheric CO_2 [47], its concentration is likely to level off at between 500 and 1,000 ppm [6]. Compared to the fluxes involved in the global carbon cycle, this is a tiny change: the ocean would still contain c. 50 times as much carbon as the atmosphere, for example. However, this change could still significantly perturb the global climate system [6].

Increased atmospheric concentrations of CO_2, and of other anthropogenic "greenhouse gases" such as methane and synthetic CFCs, serve to retain more heat within the atmosphere. This "greenhouse effect" and its anthropogenic enhancement are well-understood [6]: it arises, in short, because greenhouse gases are transparent to shortwave radiation from the Sun, which passes through the atmosphere and warms the Earth, but absorb re-emitted longwave (infrared) radiation from the Earth, warming the atmosphere.

However, anthropogenic forcing of climate is not limited to greenhouse gas emissions. Other anthropogenic forcing factors exist, including some which cause the climate to cool. For example, aerosols - liquid or solid particles suspended in the atmosphere - have a short-lived net cooling effect, since they scatter radiation and promote cloud formation [6]. Anthropogenic aerosols include sulphate particles, released by burning fossil fuels, and soil dust, released by land-use change. Aerosols can also come from natural sources, such as volcanoes, but records from the Greenland ice cores show a distinct anthropogenic signature [6]. Antarctic ice does not show this signature, since industrial aerosol pollution is concentrated in the Northern Hemisphere. The extent to which future global warming is likely to be mitigated by aerosol-based cooling is uncertain [6].

The rise in global surface temperature described in section 1.1 has not occurred in isolation from the other components of the climate system: the IPCC's Third Assessment Report documents a swathe of related climate changes [6]. Warmer temperatures have affected the cryosphere, resulting in less sea-ice, less snow cover, iceshelf collapse, and glacial recession. The hydrological cycle has become more energetic: the warmer atmosphere can contain more water vapour, leading to an increase in cloud cover and extreme precipitation events. Sea-level has risen 1-2mm/year during the 20th century, owing to both ice melting and thermal expansion of seawater. In addition to these direct effects, it is probable that a warmer Earth has influenced the magnitude of El Niño events and other forms of natural climate variability [e.g. 48].

The uncertainties involved in characterising these effects of mankind on natural variability, in attributing any given climate change to a natural or anthropogenic cause, and in understanding natural climate variability in itself, can be addressed by

improving our knowledge of how climate change occurs. This requires better records of past climate change.

Computer models may also help, although their ability to reproduce observed climate change is limited [49] by the need to parameterise "sub-grid" features such as cloud formation, snow melt, and river discharge, and by the need to add or remove energy to keep them from drifting into unrealistic states: so-called "flux correction". These problems may be overcome in the future by more powerful computers, but the problem will still remain that the quality of modelled results is limited by the quality of the data against which the models are calibrated. Again, the requirement is for better records of past climate change.

1.3 Instrumental and proxy records of climate change

The best information concerning past climate change comes directly from the instrumental record. However, there are several limitations on its quality, namely its limited geographical coverage, its inhomogeneity, and most severely, its limited time coverage. It is these limitations which necessitate the use of natural "proxy" climate records.

1.3.1 Limited geographical coverage of the instrumental record

Many "global" instrumental climate records have greatly improved their geographical coverage over time. For example, the UEA Climatic Research Unit global mean surface temperature record [7], described in section 1.1, begins in 1856; however, the percentage of global coverage given with the data shows that in 1856, only c. 15% of the globe was covered by recording stations, rising to c. 80% at the present day. Many parts of the globe - Antarctica, for example - have no instrumental climate records earlier than the 1950s [50]. The terrestrial coverage of the instrumental climate record is limited, especially for long records and remote regions.

Similarly, the record of sea surface temperatures (SSTs) is a major component of the UEA temperature data; agreement between the land and sea records, which are independent, is a significant reassurance that the data are reliable [6]. Modern SST measurements are made by satellites, giving global coverage [51]; before the 1970s, however, they come mostly from shipboard measurements, and until the early 20th century, virtually all ship routes were confined to the Atlantic Ocean [52].

1.3.2 Inhomogeneity of the instrumental record

A homogeneous climate record is unaffected by any changes other than those of the specific climate elements themselves [53]. This is an abstract ideal, and a realistic aim can only be to remove or reduce inhomogeneity in climate records as far as possible.

Temperature records are particularly vulnerable to inhomogeneity. A key example here is the method of early sea surface temperature measurement from ships, since this both affects crucially important data and shows that minor procedural details can be critical. SSTs used to be measured by lowering a bucket over the side of the ship,

filling it, letting it settle, then immediately taking the temperature. The type of bucket - specifically, whether it was made of wood or canvas - determined its thermal properties, and thereby the temperature reading; later readings were made from engine intakes [54]. These apparently innocuous changes have introduced inhomogeneity into the SST record, suggesting warming where there is none.

Land temperatures, too, can cause difficulties. The urban heat island effect is well-documented, with London, for example, being up to 5°C warmer than the surrounding countryside on calm nights [55]; in general, built-up areas slow wind speeds and reflect heat, such that urbanisation over the 20th century is expected to create an apparent warming trend. The global temperature records used by the IPCC can be corrected for this, by comparing urban and rural records, and the difficulties introduced are not significant [6]. However, it is not easy to move a weather station should its climate become affected by new buildings - several years of parallel operation of both sites are required [50] - so it may be necessary to reduce the geographical coverage of a climate record by missing out certain stations in order to preserve its homogeneity.

1.3.3 Limited time coverage of the instrumental record

Obviously, the instrumental climate record is insufficiently long to show millennial and centennial-scale climate change, even though the climate is known to change on these timescales. A further limitation affects the study of cyclicity. It may appear that a 150-year climate record can reveal cycles up to 150 years in length, but to get a statistically reliable result, as a rule of thumb, there should be at least four full cycles in the time-series, giving a maximum period of n/4, where n is the number of data points [56]. This means that only climate cycles up to about 40 years in length can be properly studied using the instrumental climate record.

Wunsch [57] uses the North Atlantic Oscillation (NAO) as an example of "unusual" behaviour which could simply result from a random process operating over a long enough interval. The NAO has been almost continuously locked into its positive phase for the past 26 years, with possible consequences for the interpretation of the global warming pattern seen since 1976. However, decadal cyclicity of this kind is poorly understood because the instrumental record is too short, even at 150 years, to reveal whether a 26-year positive phase in the NAO is unusual.

Similarly, in the Pacific Ocean, there is an Interdecadal Pacific Oscillation (IPO), whose behaviour has been linked to the two-phase 20th century warming pattern, with its warming phases in 1910-1946 and after 1976 [6]. However, instrumental climate records are too short to explore this relationship. Other longer cycles, e.g. the c. 88-year Gleissberg solar cycle, could also be significant; long records of sunspot observations show the cycle as the envelope of the 11-year Schwabe sunspot cycle [58], but instrumental climate records are not long enough to demonstrate that it has any significant climatic effect.

Finally, there are also isolated events in climate history which may have recurrence times that are so long that they have not yet featured in the instrumental record. For

example, devastating multi-decadal droughts in the American dust bowl [59] may recur every few centuries, but there are no instrumental records of their passing because none have occurred in the last 150 years.

1.3.4 Proxy climate records and the importance of chronological control

Natural climate records exist as climate proxies. A proxy [60] is a variable which has a close relationship with a second, unobservable "target" parameter. The value of the target parameter is inferred from the value of the proxy variable using a transform equation, which is established via a set of paired data points used for calibration. The quality of the proxy is the accuracy with which the transform equation correctly predicts the target parameter. Inevitably, the correlation between the two is imperfect, and other more or less independent parameters also influence the proxy. The pervasive influence of climate on the geology and biology of the Earth means that there are many thousands of possible climate proxies [61].

Some proxy-based climate records extend back thousands or even millions of years into the past. However, unless the resulting climatic data can be placed within a time framework, the record will be meaningless: all it can reveal is that the climate was different at some times than at others. For sophisticated climate proxies, which preserve detailed information on past climates, the quality of the reconstruction is limited by the quality of the available chronology. This is exemplified by the confirmation of the Milankovitch hypothesis of glaciations [62].

The occurrence of glacial periods in the past had been suspected since Agassiz's "Discourse of Neuchatêl" in the 1840s, and possibly earlier [62]. In 1875, James Croll developed the astronomical theory that would later be fully explored by Milankovitch. But the paper that finally confirmed the Milankovitch hypothesis in 1976 [63] depended as much upon the chronology as upon the climate proxy that it used. Spectral analysis of the oxygen isotope record of deep-sea sediment showed clear Milankovitch frequencies, but this analysis could only be carried out because the core material could be dated using the last geomagnetic reversal, the Brunhes-Matuyama boundary at c. 700,000 BP. Only a sediment record that included this chronological point of reference could have confirmed the hypothesis [62].

Now, even before any accurate dating methods were available, it was known that there had been several glacial cycles in the past, each overprinting the record of the previous one to some extent [62]. But climatic changes on shorter timescales, from "human" timescales of 1-50 years up to centennial and millennial timescales, are more subtle than the waxing and waning of ice sheets. Without precise dating techniques, the climatic history of the Holocene on interannual to millennial timescales, as recorded by proxy variables, cannot be properly reconstructed.

Climatic proxy variables in the geological record can be dated by many different techniques. For data from the last few tens of thousands of years, including the Holocene, the most common technique is radiocarbon dating [64]. This is based on the predictable rate of atomic decay of carbon-14: it has a half-life of c. 5,730±40

years. The range of radiocarbon dating is clearly adequate for reconstructing climate change beyond the instrumental climate record. But is the resolution good enough?

The resolution depends on the exact method used, as well as on the nature of the sample being dated, and its age. High-precision methods applied to large enough samples can give a resolution as low as ±12 years (one standard deviation) [65], though this is unusual: 50-100 years is a typical resolution. As is discussed in later chapters, complications resulting from differing carbon sources can greatly reduce the accuracy of radiocarbon dates, even if the isotopic counts are precise. So, radiocarbon dating in isolation is really only useful for reconstructing climate variability on timescales in excess of several hundred years.

A range of other dating techniques can be used alongside or instead of radiocarbon, such as uranium series dating, fission track dating, and age-equivalent stratigraphic techniques such as palaeomagnetic correlation and tephrochronology [61]. But no other technique, whether radiometric or otherwise, can significantly improve the maximal chronological resolution of radiocarbon dating, except in very recent records (e.g. caesium-137, which has only ever been formed by nuclear weapons testing, can date sediment deposited since 1945) [61].

For this reason, annual-resolution natural climate records, which are described in the next section, have an important role to play in reconstructing year-to-year past climate change: their intrinsic chronology allows the restriction in dating precision imposed by the limits of radiocarbon and other techniques to be overcome. Nonetheless, whilst their chronological significance is obvious, understanding the climate proxies which they contain, and resolving climatic from non-climatic influences on these proxies, is not a simple task.

1.3.5 Annual-resolution natural climate records

There are four kinds of annual-resolution natural climate records: tree rings, ice core layers, faunal growth rings, and annually-laminated sediments. All arise because of a sensitivity to climate of some kind. And because Earth's climate is dominated by the annual cycle, there is a very strong annual signal in these natural records.

So, the fact that one can count the rings of a tree and determine its age is a simple consequence of the cyclic variability of climate on an annual scale. One corollary of this is that many tropical trees produce faint or non-existent growth rings because of a lack of climate seasonality [66]. In contrast, in the arid southwest of the USA, where trees get almost all of their water from precipitation, a year without rain may result in a missing ring, and a year with two distinct rainy seasons may produce a double ring [67].

Because these records are sensitive to the annual cycle, they are also sensitive to longer-term climate change. The processes of calibration may be difficult, and in some cases the exact nature of the climate elements involved may be obscure, but any climatically-influenced records which exist as series of annual data points are valuable in extending the instrumental climate record further back in time.

Tree rings are the best-known annual-resolution record; their seasonal associations are well-known, and Leonardo Da Vinci supposedly first suggested a link between precipitation and ring width. The limitations of tree rings are that individual records are only as long as the lifetime of the particular tree, and are vulnerable to inhomogeneities caused by local environmental changes, such as the tree falling over or being attacked by disease. Master chronologies can be constructed to avoid these limitations, but these are no longer records from particular climatic settings, and this introduces additional problems [68]. Furthermore, records can only come from the right kind of tree ("sensitive" to climate change rather than "complacent") and from the right kind of location (where the tree is growth-limited by a particular climate element).

Ice cores are expensive and difficult to obtain, store and process: a small number have been extensively studied. Ice core drilling sites are obviously restricted to a few places on the globe, but they are valuable because usually no other climate records are available from these locations. Annual layers in the ice are sometimes visible to the human eye, either through finer, denser snow accumulating in winter [69], or through annual dust layers, as seen in the Quelccaya icecap, Peru [70]. Annual layers can also be detected using oxygen isotopes, electrical conductivity, and other properties, which allow the counting of 110,000 annual layers in the Greenland GISP2 core, for example [71].

Many animals with hard parts produce annual growth bands; by analogy with dendrochronology, their study has been called "sclerochronology". Such carbonate skeletons record oxygen isotope concentrations and other climate proxy data with an annual resolution. Short records are available from some vertebrate bones and teeth, and fish otoliths, for example. These records generally only contain a "snapshot" of a few years in the distant past. Longer, absolutely-dated annual records can be obtained from bivalve shells and from corals. The bivalve *Arctica islandica*, the ocean quahog, for example, can live for over 200 years, giving proxy climate records from the North Atlantic over the last few centuries [72]. Care is necessary in the palaeoclimatic interpretation of bivalve growth bands [73]. Similarly, corals from the Great Barrier Reef, the Galapagos [74], and other locations, exhibit annual growth bands formed over many centuries. Again, care needs to be taken with "vital effects": changes in proxy variables which are not caused by changes in climate, such as the effects of changing coral growth rate [75].

Finally, annually-laminated sediments also preserve annual-resolution climate records. These fall into two categories. The first category is speleothem - reprecipitated carbonate - which is studied using similar techniques to sclerochronology (above), although it is technically a sedimentary rock. For example, under the right conditions, oxygen isotope concentrations in annual speleothem growth bands can record surface temperature variations [e.g. 76]. However, such records are limited to karstic limestone regions. The second category is varved sediment from lakes and marine basins. Varved sediment cores are valuable because they give long climate records from

a wide variety of locations. Varves are discussed at length in the next section and throughout the rest of the thesis.

Note that a single annual resolution record can contain more than one proxy: varved sediment, for example, can record tens of different proxy variables in the same chronological framework. Such a year-by-year multi-proxy record, combined with additional data from tree rings, ice cores, faunal growth bands, and speleothem, can allow detailed reconstruction of past climate change, and by comparison with the instrumental record, can be calibrated in order to extend this record back further into the past.

1.4 Introduction to varves

1.4.1 De Geer and the Swedish glacial varves

The term "varve" was coined by the Swedish geologist Gerhard De Geer in 1910 [77], from the Swedish "varv", meaning a lap or revolution. Under the soil across most of southern Sweden, there is a layer of visually-distinct varved clay 1-10m thick which has been raised above sea-level by postglacial isostatic uplift, and which is exposed in river valleys, cuttings, and pits. As De Geer wrote [78]:

"During my very first geological fieldwork in the Stockholm region, I was struck by the marked cyclical banding of the varved clay ... so denominated from its alternating, tiny layers of fine sand and clay. From the obvious similarity with the regular, annual rings of the trees I got at once the impression that both ought to be annual deposits."

De Geer's impression was correct: the varves were annual layers. He observed that varve thicknesses were laterally consistent, allowing varve records from different sites to be correlated; and that the earliest varve in any given location lay directly above unlaminated glacial till, indicating that the onset of varve deposition commenced immediately after the retreat of the Scandinavian ice sheet from that location. De Geer reasoned that if he could correlate enough varve thickness measurements, noting the relative year of the earliest varve in many different places, he could precisely reconstruct the chronology of the retreat of the Scandinavian ice sheet during the last deglaciation. This began to retreat after the Last Glacial Maximum, then retreated much faster during the Early Holocene, melting entirely by c. 8,500 ^{14}C years BP.

The varves that De Geer measured were couplets, consisting of a pale, normally-graded sublayer, deposited following ice-melting in spring and summer, and a dark, clay-rich sublayer, which settled out of suspension during the quiet, frozen conditions in winter. The varves showed much local variation, e.g. in colour; therefore, De Geer decided only to measure varve thickness. The sediment also contained dropstones, ice-rafted debris, and ice-push structures, testament to its glacial environment of deposition; these were classic "glacial varves". The huge, undisturbed meltwater lakes that covered Scandinavia, wherein the varves were deposited, were lost when the ice sheet finally melted, leaving only a few localities where postglacial varves continued to accumulate. Counting of these postglacial varves allowed an approximate absolute

chronology to be applied to the melting of the Scandinavian ice sheet. De Geer thus produced the first accurate estimate of the length of the Holocene [78].

The Swedish glacial varves would have a further chronological significance during the development of radiocarbon dating, as described in the next section, but as a record of climate change they are not especially useful: they contain little biogenic material [79], and it is difficult to avoid inhomogeneity in the varve thickness record (which might be expected to be temperature-sensitive) because of the constantly-retreating ice margin and uneven lake bathymetry [78]. Palaeoclimate records have been extracted from Swedish glacial varves from the start of the Holocene [80], and from the unique varves of the Ångermanälven estuary where varve deposition has continued up to the present day [81], but their primary significance is as a chronological tool.

Exactly comparable glacial varves occur in North America, deposited at the margins of the Laurentide ice sheet as it retreated. De Geer's American contemporaries were familiar with the potential of varve chronologies; for example, Joseph Barrell, at Yale, wrote in 1917 [82]:

"The temperature rhythm of the seasons is now felt in all but a few parts of the Earth, and outside of the tropics enters strikingly into the nature of geological processes. Even the year, however, is too brief a space of time to find stratigraphic record except in special cases, the most notable perhaps being in the annual rhythm of clay and silt laid down on the bottoms of lakes, especially those which face glaciers and receive during the melting season an abundant supply of waste. ... The possibility of measuring the time of accumulation of strata by means of climatic rhythms has been dealt with rather fully, since notwithstanding the lack of results thus far obtained, it seems to contain large possibilities and should lie in the background of the mental vision ready to be invoked."

These possibilities could not be fully realised until the development of coring technology allowed the recovery of the many other types of varved sediment that exist [83]. Glacial varves are unusual in that isostatic uplift has exposed them at the surface: most other varves are submerged beneath lakes, fjords, or the open ocean. Widespread availability of simple lake corers [e.g. 84,85], and later, equipment that could recover cores from deeper marine basins such as the Gulf of California [86] and Saanich Inlet, Canada [87], resulted in a rapid expansion of varved sediment records and the realisation that glacial varves formed only a minor component of the totality of varved sediment.

1.4.2 Varves, non-annual laminations, and dating

Varved sediment records have always attracted debate over whether the varves are genuinely annual. The discovery of radiocarbon dating in the 1940s [88] provided a way to test this assumption for the Swedish glacial varves. Initially there were some disagreements between the varve counts and the radiocarbon dates, but these were resolved upon the discovery of "wiggles" in the atmospheric ^{14}C curve by de Vries [89]. A calibrated radiocarbon curve, derived from dendrochronology, showed several radiocarbon "plateaux" which could explain the anomalously young radiocarbon dates of some of the varves. Additional dating techniques, such as ^{210}Pb dating and the use of

historically-identifiable depositional events, were also applied to strengthen the chronology of varved sediment records.

However, controversy continued over the supposed annual nature of some sedimentary laminations, in part because of a confusion over descriptive and interpretative terminology. The tendency to call any thin sedimentary laminations "varves" parallelled the tendency to call any normally-graded deep marine clastic unit a "turbidite" [90]; just as "turbidites" like this can be produced by sandy debris flows and other mechanisms [91], so-called "varves" can be produced by depositional mechanisms which do *not* reflect the annual cycle. These are best described as "non-annual laminations", since "non-annual varves" is a contradiction in terms.

Care is necessary when describing laminations as "varves" since this implies an annual chronology. For ancient geological formations, the chronology may be uncertain: for example, the Eocene Green River Formation contains >1 million laminations which are likely to be varves [92] (despite the continuing claims of biblical literalists [93]); in contrast, the Precambrian Elatina Formation in Australia contains laminations which were once thought to be varves but are more likely to be semi-diurnal tidal deposits [94]. Numerous mechanisms have been identified which can produce non-annual laminations, from thin distal turbidites to microbial activity [90]. Thus, it is crucial to be certain that one is dealing with true varves, either by linking each component of the varve to a specific seasonal process [95], or by reconciling the results of independent dating techniques into a coherent model that fits the annual-layer assumption.

One varve is defined here as one whole year's worth of sediment: it may include separate sediment layers for spring, summer, and winter, or any more complex sequence of depositional events. The separate layers that make up one varve are always referred to as *sublayers*, to avoid any confusion.

1.4.3 Formation, preservation, and distribution of varved sediment

Varve *formation* requires seasonal heterogeneity in sediment supply. There are many ways this can occur, so there are many types of varves, found in a range of depositional environments [90]. O'Sullivan [96] identifies four main types: clastic varves (such as the Swedish glacial varves); ferrogenic varves (in which ferric and ferrous ions record an alternation between oxidising and reducing conditions, such as an alternation between pale iron hydroxide and dark iron sulphide); calcareous varves (produced by summer precipitation of calcite in carbonate lakes); and biogenic varves (produced by the sedimented remains of seasonally-growing organisms).

The latter are of interest because both of the varve sequences studied in this thesis contain significant biogenic components. Biogenic varves are generally more complex than varves produced by physical processes such as the inorganic precipitation of calcite, or deposition of clastic sediment from a river in flood [97]; for example, biogenic processes can precipitate dissolved material when it is not saturated, and the species assemblage associated with a particular season may change according to water column nutrient availability, pH, light levels, and so on. Of course, varves

which contain both biogenic and abiogenic components contain yet more information. Examples of clastic and biogenic varve components, and of how palaeoclimatic information can be extracted from them, are discussed in section 1.5.

Sediment traps reveal unambiguously how seasonal changes in sediment supply result in the deposition of varves [e.g. 98], though they are expensive and can be difficult to recover. If for any reason the heterogeneity in sediment supply is lost, then the resulting sediment will be massive, not laminated; this may have occurred at times in the Santa Barbara Basin, for example [99]. By analogy, turbidites off the west coast of Saharan Africa are genuinely deposited by turbidity currents, but they do not show characteristic normal grading, because the sediment supply - aeolian sand - is so well sorted anyway that no grading is possible [100].

Varve *preservation* is also important. Laminations in unconsolidated sediment are easily disrupted by animals such as shrimps and echinoderms burrowing and searching for food: the process of bioturbation. Intense bioturbation can homogenise sediment to a depth of tens of centimetres, removing any traces of varves. For this reason, well-preserved varves tend to occur in anoxic basins, where the absence of oxygen in the bottom water keeps out bioturbating animals. Such anoxia occurs in silled fjords and marine basins (like the Santa Barbara Basin) where deep water circulation is restricted; it also occurs in meromictic lakes, where anoxia occurs in the monimolimnion; and on some oceanic shelves where there is an oxygen minimum zone (OMZ) caused by a combination of a high flux of sedimentary organic matter and low ventilation, as found off Pakistan [101]. Varves can be preserved in all these environments.

Oxygenation ("renewal") of an anoxic basin rapidly leads to the establishment of a bioturbating fauna. It is possible in some cases to construct a bioturbation index using the varve record, and to calibrate this in terms of oxygen availability [e.g. 102]. The benthic fauna is the crucial factor: without it, there would be no bioturbation regardless of oxygen availability. The "varve paradigm" (*sensu* Anderson [95]) suggests that in the absence of bioturbation or any other form of disturbance, seasonal sedimentation patterns should be preserved (as varves) in most depositional zones on the Earth. Reference to the Precambrian sedimentary system, which is characteristically laminated, and which was deposited before the evolution of bioturbating animals in the Cambrian explosion [103], supports this notion [95].

However, anoxia and bioturbation are not the only factors which affect varve preservation. Varves can still be preserved in oxygenated environments, if there are other factors which inhibit bioturbating organisms, such as very cold, nutrient-poor, sediment-rich water [e.g. 79], or even if there is a bioturbating fauna, a varved fabric can survive if the sediment accumulation rate is fast enough to bury it before it becomes homogenised. Similarly, varves can be destroyed by factors other than bioturbation. They are especially vulnerable just after deposition, when the sediment has not yet been buried and is still unconsolidated. Here, even a slight disturbance can destroy the varves, such as wind-driven resuspension of sediment in shallow lakes, or mixing caused by lake overturn. To prevent these kinds of disturbances, lakes need

to be absolutely deep (> c.70m) or "overdeep" relative to their surface areas [96]. In some depositional environments, biogenic stabilisation of sediment may be significant; for example, there is evidence that extensive Neogene diatom mats in the Pacific Ocean preserve a seasonal fabric [104].

Varve sequences that are apparently continuous can be interrupted by any of the factors described above. Macrobioturbation may be obvious, but the continuity of the varve sequence can also be affected by microbioturbation or other minor sediment mixing which leaves no trace except for homogenising a small interval of sediment. Varves may also be missing from an apparently-continuous sequence because of erosion by turbidity currents, or slumping; the latter can result in parts of sequences being repeated [105]. Independent chronological data are important in confirming the continuity of a varve sequence, even if the annual nature of the laminations is certain.

Varve distribution, then, is determined by the co-existence of suitable conditions for varve formation *and* for varve preservation. The variety of ways in which this co-existence can occur means that the spatial distribution of varves is global. Clusters of varve locations which are apparent in the published literature - in Finland, for example - arise in part from their proximity to active researchers equipped for sampling [96]. As proxy records of climate change, varves should preferably be undisturbed by human activities; the best records for this purpose come from remote locations such as the Arctic [e.g. 106].

The distribution of varved sediment in time is similarly broad, from the Precambrian to the present day, though many records are restricted to the Holocene - the present interglacial, beginning c. 11,500 cal years BP - because they formed in postglacial lakes. At least 100 such lakes in Sweden [107], 30 in Finland [108], and many more in North America, contain varves. Anthropogenic eutrophication over the last century or so has led to anoxia and consequent varve preservation in many more lakes [e.g. 109]. Once again, the best palaeoclimate proxy records are those which have suffered minimal human disturbance; varves from the last interglacial (the Eemian) are valuable in this respect [110]. Other long varve records include those from Lake Suigetsu, Japan, which contains varves back to 45,000 years ago [111], and from the Santa Barbara Basin off California, which contains varves up to 160,000 years old [112]. Examples of palaeoclimate proxy records from varves are discussed in the next section.

1.5 Palaeoclimate information preserved in varves

This section summarises some recent research on palaeoclimate reconstruction using varved sediment. The emphasis is on varves containing biogenic and clastic components, since the varve records studied later in the thesis are of this type.

The following examples use the presence of varves to construct a high-resolution chronology for the chosen palaeoclimate proxies. In the first part, sediment is sampled from individual varves, giving an annual resolution. In the second, the varves are not all suitable for annual sampling, but they are used as the dominant chronometer, in addition to radiocarbon dates, extrapolated sediment accumulation

rates, and other dating methods, giving slightly reduced overall time resolutions of typically 5-20 years.

Research using sampling from individual varves:

- $\delta^{18}O$ in lake calcite, as a combined proxy for temperature and for isotopically distinct precipitation sources, from Fayetteville Green Lake, USA, AD 1906-1980 [113] and Baldeggersee, Switzerland, AD 1885-1993 [114].

- Charcoal particles and spruce pollen as a proxy record of forest fires from Ristijärvi, Finland, between c. 100 BC - AD 500 [115].

Research using varves as the dominant chronometer:

- Precise timing and effects of the early Holocene cooling at c. 8,200 cal years BP, which is well-known from ice core records, in two small Swedish lakes, based on pollen and magnetic susceptibility [116] and in Soppensee, Switzerland, and Schleinsee, Germany, based on tree pollen [117].

- SST reconstruction in the Santa Barbara Basin, off the coast of California, based on the U^{K}_{37} index from C_{37} alkenones during AD 1440-1940 [118].

- Lead concentrations in several varved Swedish lakes, showing the history of lead pollution in great detail, allowing it to be linked to historical developments [119].

- A palaeoseismicity record from Saanich Inlet, Canada, where large earthquakes trigger debris flows which leave recognisable deposits in the varve record. Links can be made with several historically-observed earthquakes, allowing recurrence times of large earthquakes to be quantified [120].

- Diatoms, pollen, and fungal spores from varves in Seebergsee, Switzerland: independent proxies showing the combined influences of climate change and changing land use as expressed by lake eutrophication and re-oligotrophication during the last millennium [121].

As well as indicating a chronology, the varve structures themselves contain a palaeoclimate proxy: varve thickness. Before discussing the meaning of varve thickness, its use in the correlation of varved sediment should be noted. Some extraordinary examples are known of varve thickness being laterally consistent over long distances [e.g. 122], and this property has been used for more than a century in constructing and refining the Swedish glacial varve chronology [78], which now consists of over 1,000 correlated varve thickness diagrams [123].

But what does varve thickness mean? Since each varve represents a year's worth of sediment, varves are like long sediment trap records: they record the sediment flux each year. So varve thickness is a record of sediment accumulation (once corrected for compaction, of course, if this is significant). There are many different types of

varved sediment, and so the controls on varve thickness vary from basin to basin. Varve thickness records can be classified as either calibrated or uncalibrated.

The best way to use varve thickness as a convincing palaeoclimate proxy is to have *calibrated* data: a sequence of varves that overlaps with the instrumental record, and which shows a significant correlation with measured climate variables. Such records may be simply calibrated, using a good correlation with a single variable, or there may be multiple controls on varve thickness. For example:

- The simplest use of varve thickness as a palaeoclimate proxy is in glacier-fed basins with little biogenic input, where glacial melting, controlled on a year-to-year timescale by summer temperature, is essentially the only factor controlling sediment supply. Varve thickness therefore correlates very closely with summer temperature. Good examples of calibrated records come from Baffin Island, Canada: Upper Soper Lake [124] and Donard Lake [125]. The former record shows evidence of dramatic recent anthropogenic warming, and the latter shows a warm interval during c. AD 1200-1375 followed by the "Little Ice Age", c. AD 1375-1820.

- Many varves reflect a dual sediment input. One classic example is the Santa Barbara Basin, where varves occur as distinct couplets: they comprise a terrigenous layer and a diatomaceous layer. Sediment trap studies allow the flux of these sediment components to be calibrated separately, with precipitation, primary productivity, and so on. But the overall picture is fairly simple, on a year-to-year scale, because climate variability in the Santa Barbara Basin is predominantly attributable to ENSO, which affects both the terrigenous and diatomaceous sediment flux. This control is sufficiently well understood to enable signals of El Niño events to be detected in Santa Barbara Basin varves from 160,000 years ago [126]; the sublayer thicknesses are in antiphase, such that conditions that produce a thick terrigenous layer tend to produce a thin diatomaceous layer, and vice versa.

- A similar situation exists in Saanich Inlet, Canada: again, there are two components in each varve, with separate controls on their thicknesses, although here the record is not so well calibrated. Diatomaceous layer thickness is controlled by primary productivity [127], and terrigenous layer thickness is likely to be controlled by precipitation [128], but there is no clear dominance of the whole system by ENSO, or other comparable phenomena.

Many varve records are influenced by a range of independent environmental variables, such that a single variable like temperature or precipitation only accounts for a small amount of the variability in varve thickness. In these situations, even well-calibrated records are not much use as palaeoclimate proxies, since although varve thickness is likely to be affected by climate, the different climatic variables involved cannot be untangled from the thickness time-series; further complications arise where human activities have influenced varve thickness.

- One example is Baldeggersee, Switzerland [129], where attempts to calibrate varve thickness from the last 100 years show that temperature and precipitation can only

explain one-third of the variability in varve thickness. All that can be said in general is that precipitation is more influential than temperature.

- Similarly, a comparison of varve thicknesses and instrumental data from Lake Silvaplana, Switzerland [130], shows the combined influence of summer temperature, precipitation, and length of snow cover. The calibrated data cannot be used to interpret earlier, uncalibrated varve thicknesses unambiguously in terms of palaeoclimate variables, because of these multiple influences.

- Links between precipitation, temperature, discharge, and varve thickness for the River Ångermanälven, Sweden, are dissected by Wohlfarth *et al.* [81]; the picture is complex, but precipitation during certain times of year is here the dominant control on thickness.

Most varve thickness records cannot be calibrated: some varves are too old to be calibrated against instrumental data; some areas have no instrumental records for calibration, and for those that do, the most recent varves have often been strongly affected by human activities such as land-use change. In the absence of calibration, varve thickness can still be scrutinised for recognisable climatic patterns. For example:

- Without knowing precisely what controls varve thickness, it is still possible to get an idea of general climate variability over long timescales, e.g. varves from Lake Meerfelder Maar, Germany, show a striking pattern of general climatic instability during the last glacial-to-interglacial transition [131]. It is not clear exactly which aspects of climate have influenced this record of changing varve thickness, but the changes can be precisely dated, and thereby linked to known climatic events like the Younger Dryas, to obtain a general picture of climate instability.

- Another way to deal with an uncalibrated record is to look for variability at specific frequencies in the varve thickness time-series. For example, Godsey *et al.* [132] assume that variability within certain frequency bands can be assigned to known climatic phenomena like the Quasi-Biennial Oscillation (QBO) and ENSO. Changes in the variability within these frequency bands, as seen in varves from Lake Huron during the Younger Dryas, are then assumed to represent changes in the amplitude of these climatic phenomena. But without instrumental calibration, the link seems tenuous, especially given the many other sources of variability at these frequencies which occur at the present day.

- More convincing are phenomena with well-known, relatively constant frequencies which can be specified beforehand and then searched for. The classic example here is the 11-year sunspot cycle, often with other, longer, known solar output cycles. Solar output does influence the Earth's climate, so the solar output cycles should perhaps show up in some palaeoclimate records. Do any records of varve thickness show these cycles? The complexities of frequency analysis make such claims difficult to assess. Livingstone and Hajdas [133] find a spectral peak at 10.9 years in the varves from Soppensee, Switzerland; Vos *et al.* [134] find solar

periodicities in varves from Holzmaar, Germany, but only after complex statistical processing.

- Caution is also required when assessing "significant" patterns in uncalibrated varve thicknesses because of the "file drawer problem". Scientific papers are more likely to be published if they have positive results, i.e. if they find something "significant"; studies which fail to find what they are looking for are more likely to be consigned to the "file drawer" and left unpublished [135]. So the important question is not "have any studies detected variability at solar frequencies?" but "how successful has this search been, in general?" Are the "significant" finds in the literature just type I errors, i.e. where the null hypothesis of no significant variability at the predicted frequencies is true? Unsuccessful searches for specific periodicities have been published (e.g. Young *et al.* [136], who found no evidence for an 11-year cycle in varve thicknesses from Lake Gosciaz, Poland), but they are rare.

In conclusion, then, when dealing with a varve record, varve counting is the first step since this provides an annual chronology for whichever other proxies are to be studied. Secondly, varve thickness is also important, both as a means of correlation, and in some instances as a useful palaeoclimate proxy in its own right.

1.6 Varve measurement using traditional techniques

Varve measurement techniques began with De Geer's work on the Swedish glacial varves [78]. He did not have access to modern coring equipment, so was restricted to measuring varve sequences which had been exposed either by natural erosion, or by digging of trenches and pits. Initially, he marked the varve boundaries directly onto a strip of paper held against the sediment; later, he obtained a precursor of the modern "cookie-cutter" - a thin metal box which could be pressed into soft sediment, extracting a slice through the varves - which allowed him to remove sections of the varve sequence to be measured in the laboratory, again either directly or by using a ruler. These simple methods were quite sufficient for the thick, highly-contrasting Swedish glacial varves.

De Geer produced varve thickness diagrams by cutting up the original marked strip of paper, where possible, or by otherwise plotting varve thickness as a function of varve number - that is, as a year-by-year time-series. Since his main interest was in varve correlation, he developed a standardised thickness scale which allowed him to match up similar thickness patterns in contiguous varve sections [78]. This was done "by eye", looking for cross-correlatable patterns, tied into a master chronology using thick "marker varves", produced by catastrophic drainage of ice-dammed lakes. There are remarkably few errors in De Geer's original "Swedish Varve Chronology" [137], but De Geer's lack of an objective, statistical method to measure and correlate varves led to problems with other varve sequences.

Figure 1.2: Gerhard De Geer measuring thick, clastic glacial varves in the USA [78], marking the varve boundaries directly onto a strip of paper.

De Geer attempted to correlate the Swedish varves with other varves from around the world [e.g. 138]. If reliant only on simple pattern recognition, the human eye tends to match up any small sections of a time-series that correlate, leaving the intervening sections to be explained away as "anomalies": this led De Geer into an argument based on circular reasoning. He was convinced that there was a single global climate signal preserved in varve thicknesses, even though contemporary climate observations showed this to be "out of the question" [139]. Improved techniques for measuring and correlating varves would later help to refute his theory of a global varve thickness curve.

Longer sequences from single sites would obviate the need for so many correlations, and would reduce inhomogeneity in the record, which resulted from the fact that no two sites of varve deposition were exactly the same. De Geer knew of so-called microdistal glacial varves, which were deposited far from the ice margin and were therefore millimetres rather than centimetres thick [78]. By using expanded photographs of sediment slabs containing these thin varves, he was able to generate longer sequences of varve thickness measurements from single sites, and made the incidental realisation that photographs were much more convenient to store and manipulate than sediment cores. Of course, the quality of the photographs was crucial, and this issue will recur when digital image analysis is considered.

Meanwhile, attention turned to other features besides relative varve thickness, initially as a means of correlation and later as palaeoenvironmental proxies. Whilst the technology involved is very different, the methodological approach introduced in this thesis can arguably be traced back to the work of Matti Sauramo in Finland in the 1920s [140]. He describes his approach to varve correlation thus:

"A better method must be independent of the variation of thickness of the varves, the inconstancy of which is the main source of trouble, and rely upon other characters, inherent in each individual varve or group of varves and more constant than the relative thickness. Such characters in fact exist among the physical properties of the sediments. Of course, primary properties only must be considered and not secondary ones, such as those due to weathering, or the action of ground water. Those primary properties that may serve for the purpose of connexion are: colour of the sediment in the state of natural humidity above the ground water level, coarseness of grain and hygroscopicity, plasticity, arrangement of grains of different coarseness in the varves, i.e. whether the coarser and finer materials are mixed together or arranged in separate layers, and in the latter case, whether these layers of definite coarseness of grain limit each other with sharp lines or by gradual transition."

Sauramo, quoted in Zeuner [141]

Sediment colour could only be "measured" by noting abrupt changes; later work used Munsell colour chips as a crudely objective way of measuring quantitative colour changes, though these were affected by changes in the colour perception of different human individuals. Outcrop-scale Munsell colour estimates can be used to estimate sediment composition [e.g. 142], but subtle colour changes on a varve-by-varve scale that indicate compositional change can only be measured objectively using digital image analysis (see section 1.6).

Biogenic and other non-glacial varves present a greater challenge to counting and measuring techniques because they can be very thin (typically <1mm thick) and may number in the thousands in a single sediment core. Such varves could be counted by painstakingly sticking pins into the sediment at varve boundaries, and by counting these in intervals defined by identifiable marker varves. This traditional method is still used today [e.g. 143]. The resolution of human vision is c. 0.1mm, but realistically, direct measurement of varve thickness is only possible to the nearest 1mm, so typical thin biogenic varves cannot be measured using this "pin method", only counted. Again, working from expanded photographs can help, as described by Renberg [144], for example. However, problems remain with inaccuracies arising from human error (which can only be reduced by time-consuming multiple recounts and remeasurements), and with subjectivity, i.e. variable "opinion" on what constitutes a varve or where the exact location of a varve boundary lies. These problems affect many analyses of varved sediment, and are particularly acute in varve sequences which are partially disturbed or unclear.

There is a need, then, for a measurement technique which is precise enough to count and measure very thin varves (<1mm thick), which can measure sediment colour objectively, and which can use these data to decide, on the basis of varve thickness, sediment colour changes, lateral continuity, and/or any other appropriate criteria, what does or does not constitute a varve. This would be valuable for research on varve

sequences, especially those of imperfect quality. This thesis includes some attempts to develop such a technique using digital image analysis.

1.7 Varve measurement using digital image analysis

This section is an introduction to digital image analysis and its application to varved sediment. Details of the specific methods developed and used can be found in chapter 4.

1.7.1 Introduction to digital images of varved sediment

Digital images consist of an array of discrete units, pixels, each of which is assigned a specific colour. The size of the pixels determines the resolution of the image, that is, the level of detail it can represent. However, it is important to distinguish between "real" and "interpolated" resolution. Interpolated resolution can easily be increased by reducing the pixel size and generating new pixels with intermediate colour values; this does not, unlike an increase in real resolution, increase the information content of the image.

The basis of varve measurement using digital image analysis lies in capturing a digital image of the varves, with sufficient resolution to allow the varves to be measured using information contained in the pixel array; in a sense, the digital camera is used instead of the human eye. This requires an awareness of the various biases that arise from "image processing" within the human visual system [145]. For example, we are poor at detecting gradual changes in colour, yet very good at detecting sudden changes; we are better at separating slightly different shades of pale grey than slightly different shades of dark grey. For the digital camera, these biases are absent, and the digital images it produces are objectively representative of the varved sediment - provided that the imaging conditions are suitable.

Suitable imaging conditions are important because during digital image analysis of varved sediment, the digital camera is effectively being used as a sensitive measuring device, counting photons very precisely over a high-resolution grid. This operation is easily affected by noise and distortion of various kinds, to which the human eye is not prone because of our ability to process the images we perceive.

Digital images of varved sediment should effectively have a one-dimensional information content, assuming that the varves are laterally parallel and continuous. This greatly simplifies the processes of image analysis, which can be built up using both forward and reverse modelling. The former starts from an idealised varve image (alternating black and white horizontal stripes, for example) and models the effects of adding noise; the latter starts from a real varve image and attempts to remove the noise and to simplify it to a comparable idealised image. In both cases, the effects of noise, focus, changes in illumination in space and time, and other controls on image quality need to be taken into account.

1.7.2 Previous research on digital image analysis of varves

In general terms, the outcome of research into image analysis of varved sediment should be a computer-based method for locating varve boundaries, counting and measuring the thicknesses of varves and their component sublayers, measuring sediment colour, and possibly other features such as lateral continuity, and exporting these data in a convenient format.

Drawing on similar work on tree-rings [e.g. 146], a small specialised literature has developed on the subject since c. 1990. This can be divided into two categories: general reviews of image analysis as applied to varves, and attempts to apply image analysis to specific varve records. The methodological aspects of the research carried out for this thesis were initiated by observed weaknesses in both of these categories. Again, the two themes introduced below are discussed in more detail in chapter 4.

General reviews of image analysis as applied to varved sediment, notably Cooper [147] and Saarinen and Petterson [148], emphasise the range of different image analysis processes available, but pay insufficient attention to imaging conditions. The latter are of greater importance in determining image quality; indeed, they limit the success of the image analysis, since image defect correction processes will never give as good a result as avoiding the need for them in the first place. A detailed description of the effects of changing imaging conditions on image quality would be valuable in helping others avoid potential pitfalls.

Attempts to apply image analysis to specific varve records have so far met with little success; however, this may be a result of misguided attitudes to image analysis rather than fundamental weaknesses in the techniques used. For example, Zolitschka [149] describes an early attempt at "automated" varve measurement, applying digital image analysis to varves from Fayetteville Green Lake, New York, USA, and Holzmaar, Germany. It was unsuccessful owing to insufficient resolution of the digital images and an inability to filter out noise. Both of these problems can be addressed by improving image quality and applying more sophisticated image analysis techniques. But Zolitschka's aim was specifically to *save time and effort* by using automatic varve measurement, which meant that the solutions above were not considered feasible.

Similarly, Schaaf and Thurow [150] describe a system of "digital sediment colour analysis" developed on varved sediments from the Santa Barbara Basin as a *fast and easy* method of extracting data from varved sediment cores. A one-pixel-wide linescan was extracted from the images, corrected for uneven illumination, processed to remove cracks and voids, smoothed, and analysed. In this case, spectral analysis of the data produced a definite peak at a frequency of one cycle per year, showing that the varve signal in the sediment greyscale record was significant. But attempts to apply this method to lower-quality varve records (see chapter 4) showed no such peak. The Santa Barbara Basin varves are unusual in this respect: they are so regular and well-preserved that little image processing is required.

Ideally, once a system of digital imaging hardware and processing software has been set up, such as that described by Schaaf and Thurow [150], the time and effort

expended in doing so will be more than repaid by the ability to apply the system to a large number of other varved records. But as will be noted, other varve records are mostly too noisy for a simple method like this - yet these noisy records are precisely where digital image analysis is most needed.

Thick, well-preserved varves, such the Swedish glacial varves, can be counted and measured perfectly well using traditional techniques: experienced workers will produce perfectly replicable results. In this sense, using digital image analysis is overkill: using a more complex technique for its own sake. Only with very long sequences of such varves, like those from the Santa Barbara Basin ODP Site 893 cores [150], can savings in time and effort be realised. Most varve records are shorter and less well-preserved than this, and the real test of image analysis lies in what it can do with such records.

Specifically, the value of digital image analysis lies in the fact that it can generate results that *could not have been generated any other way*, rather than in simply saving time and effort. Analysis of varves, and of high-resolution palaeoclimate data in general, is necessarily somewhat slow and painstaking. Digital image analysis can potentially perform objective, precise varve counting and measuring, and can measure sediment colour objectively at very high resolution, producing unique, high-quality data which should be valuable in varve-based palaeoclimate reconstruction, especially for varve records of imperfect quality.

1.8 Time-series analysis of varve-derived data

By their nature, data from varved sediment are drawn from one site at many different times, and not vice versa - however useful the latter would be in palaeoclimate reconstruction! In other words, they form time-series. Simple techniques of time-series analysis, such as correlation with other records, are widely used in palaeoclimate research; more complex and powerful techniques, such as spectral analysis, are less well-known but can be applied to varve-derived data with relative ease because of its annual resolution. For example, one data point per varve is equivalent to one data point per year, producing an evenly-sampled time-series. Spectral analysis can detect signals in these data by looking for temporal patterns that repeat in a predictable way; in particular, it can separate such periodic signals from background noise even though they may be apparently undetectable in a plot of the original time-series.

However, seeking to understand complex, noisy time-series such as those derived from palaeoclimate proxies demands a cautious approach. Apparent "signals" need to be tested statistically against a null hypothesis that they have arisen randomly - and this null hypothesis must be appropriately chosen, based on the nature of the time-series. Furthermore, filtering or smoothing a time-series in order to make the signals clearer may produce artefacts; for example, crude filters such as weighted moving averages can induce periodic signals in a time-series consisting entirely of noise. Simple spectral analysis is adequate for strongly-periodic signals such as Milankovitch cyclicity, but is little use for the weaker and more variable cyclicity that characterises Holocene climate; techniques such as filtered spectral analysis and

evolutionary time-series analysis are useful in identifying such weak and/or changing periodic signals in the data.

The methods of time-series analysis used are summarised in chapter 4. In addition, appendix A contains a detailed discussion of time-series analysis and its applications to palaeoclimate data, especially data derived from image analysis of varved sediments, and justifies in depth the choice of methods described in chapter 4.

1.9 Aims of the thesis

1.9.1 Image analysis as part of multi-proxy palaeoclimate research

As discussed in section 1.5, varves can contain many different palaeoclimate proxies. Counting and measuring of varves, and of the colour and thickness of their component sublayers, and possibly linkage of these to climatic influences, is best carried out in the context of a multi-proxy investigation. This will allow the image-derived data to be compared with independent data such as pollen, microfossil, and isotope records, which may also preserve climatic signals.

So the general aim of the thesis was to develop techniques for measuring image-derived data from laminated sediment cores, and to integrate these data into broader palaeoclimatic research on the same sediment cores. On the basis that image analysis would be entirely non-invasive and would not affect the sediment in any way, the UCL Palaeoclimate Research Group aimed to produce a low-cost research program. Unfortunately, the unwillingness of UCL to contribute towards coring and core storage costs greatly restricted the range and quality of available core material, and tended to isolate the image analysis research from the programs of collaborative research that it sought to join.

Nonetheless, access to two sets of varved sediment cores was obtained, both fulfilling the initial criteria of suitability for image analysis: having relatively long sequences of relatively thin Holocene varves. The coring locations were Drammensfjord, Norway, and Lake St Moritz, Switzerland. Reviews of these two basins form chapters 2 and 3 respectively. The next two sections briefly summarise the aims of the research on these specific sediment cores.

1.9.2 Aims of the Drammensfjord research

The Drammensfjord varve record had not been previously studied. In addition, of the small amount of research that had been done on Drammensfjord, most had been written in Norwegian. Therefore, the first aim of the Drammensfjord research was to produce a full literature review, drawing on translated research papers. The second was to photograph and digitise the varved cores, to build a chronology, to develop and test image analysis techniques for measuring the varves, to investigate the varve mechanism, and to investigate the possible presence of climatic signals in the image-analysis-derived data.

1.9.3 Aims of the Lake St Moritz research

In contrast to Drammensfjord, a body of palaeolimnological research on Lake St Moritz had already been published, so a brief literature review was all that was required. The varved core to be analysed had already been the subject of published research, and had a newly-measured set of uncalibrated radiocarbon dates, a lithological description, and a range of compositional data. Here, the aim was to investigate what image analysis could specifically add to this body of information, by developing a high-resolution chronology based on varves and calibrated radiocarbon dates, measuring varve thicknesses, and comparing sediment colour data with previously-published compositional data, to see if the crude palaeoclimatic record already inferred from the core could be improved.

1.9.4 Summary of aims and thesis structure

The application of image analysis to varved sediment is not new, but nor is it an established technique whose methodology can be taken for granted. Thus the overall aim of the thesis was not so much the generation of new palaeoclimate proxy data, but in demonstrating how image analysis could be used to obtain meaningful proxy data, and how the problems associated with using unfamiliar and complex techniques (namely, image analysis and the time-series analysis that it entrains) could be minimised or avoided.

Chapter 1 has introduced the research subject and its context. Chapters 2 and 3 are literature reviews of the two basins involved: Drammensfjord, Norway, and Lake St Moritz, Switzerland. Chapter 4 describes the research methods. Chapter 5 presents the most important results. Chapter 6 describes the interpretation of the results. Chapter 7 describes the conclusions and suggestions for further research. Appendix A is a detailed review of time-series analysis which can be read in conjunction with chapter 4. Appendix B contains supplementary results on paper and on CD-ROM.

Chapter 1 References

[1] Davis, M., 2001, Early signs of a thaw in Bush's attitude to global warming, News Article, Nature, 410:133.

[2] Kennedy, D., 2001, An unfortunate U-turn on carbon, Editorial, Science, 291:2,515.

[3] Singer, S. F., inter alios, 2001, Global warming: an insignificant trend?, and other replies to [2], Letters, Science, 292:1,063-1,066.

[4] Bradley, R. S., 2001, Many citations support global warming trend: reply to [3], Letter, Science, 292:2,011.

[5] Hansen, J., Ruedy, R., Sato, M., and Lo, K., 2002, Global warming continues, Letter, Science, 295:275.

[6] Houghton, J. T., Ding, Y., Griggs, D. J., Noguer, M., van der Linden, P. J., and Xiaosu, D., (Eds.), 2001, Climate Change 2001: The Scientific Basis, Contribution of Working Group I to the Third Assessment Report of the Intergovernmental Panel on Climate Change (IPCC), Cambridge University Press, 944 pp.

[7] Jones, P. D., New, M., Parker, D. E., Martin, S., and Rigor, I. G., 1999, Surface air temperature and its changes over the past 150 years, Reviews of Geophysics, 37:173-199.

[8] Hays, J. D., Imbrie, J., and Shackleton, N. J., 1976, Variations in the Earth's orbit: pacemaker of the ice ages, Science, 194:1,121-1,132.

[9] Imbrie, J., and Imbrie, K. P., 1979, Ice Ages: Solving the Mystery, Harvard University Press, 224 pp.

[10] Stuiver, M., Grootes, P. M., and Braziunas, T. F., 1995, The GISP2 delta O-18 climate record of the past 16,500 years and the role of the sun, ocean, and volcanoes, Quaternary Research, 44:341-354.

[11] Jansen, E., Fronval, T., Rack, F., and Channell, J. E. T., 2000, Pliocene-Pleistocene ice rafting history and cyclicity in the Nordic Seas during the last 3.5 Myr, Paleoceanography, 15:709-721.

[12] Dansgaard, W., Johnsen, S. J., Clausen, H. B., Dahljensen, D., Gundestrup, N. S., Hammer, C. U., Hvidberg, C. S., Steffensen, J. P., Sveinbjornsdottir, A. E., Jouzel, J., and Bond, G., 1993, Evidence for general instability of past climate from a 250-kyr ice-core record, Nature, 364:218-220.

[13] Bond, G., Broecker, W., Johnsen, S., McManus, J., Labeyrie, L., Jouzel, J., and Bonani, G., 1993, Correlations between climate records from North Atlantic sediments and Greenland ice, Nature, 365:143-147.

[14] Heinrich, H., 1988, Origin and consequences of cyclic ice rafting in the northeast Atlantic Ocean during the past 130,000 years, Quaternary Research, 29:142-152.

[15] Bianchi, G. G., and McCave, I. N., 1999, Holocene periodicity in North Atlantic climate and deep ocean flow south of Iceland, Nature, 397:515-517.

[16] Chapman, M. R., and Shackleton, N. J., 2000, Evidence of 550-year and 1,000-year cyclicities in North Atlantic circulation patterns during the Holocene, The Holocene, 10:287-291.

[17] Bond, G., Showers, W., Cheseby, M., Lotti, R., Almasi, P., deMenocal, P., Priore, P., Cullen, H., Hajdas, I., and Bonani, G., 1997, A pervasive millennial-scale cycle in North Atlantic Holocene and glacial climates, Science, 278:1,257-1,266.

[18] Bond, G., Kromer, B., Beer, J., Muscheler, R., Evans, M. N., Showers, W., Hoffman, S., Lotti-Bond, R., Hajdas, I., and Bonani, G., 2001, Persistent solar influence on North Atlantic climate during the Holocene, Science, 294:2,130-2,136.

[19] McDermott, F., Mattey, D. P., and Hawkesworth, C., Centennial-scale Holocene climate variability revealed by a high resolution speleothem delta O-18 record from SW Ireland, Science, 294:1,328-1,331.

[20] Hoyt, D. V., and Schatten, K. H., 1997, The Role of the Sun in Climate Change, Oxford University Press, 288 pp.

[21] Friis-Christensen, E., and Lassen, K., 1991, Length of the solar cycle: an indicator of solar activity closely associated with climate, Science, 254:698-700.

[22] Mahlman, J. D., 2001, Global warming: misuse of data and ignorance of science: a review of the "Global Warming" chapter of Bjorn Lomborg's "The Skeptical Environmentalist", Union of Concerned Scientists, 8 pp.

[23] Thejll, P., and Lassen, K., 2000, Solar forcing of the Northern hemisphere land air

temperature: new data, Journal of Atmospheric and Solar-Terrestrial Physics, 62:1,207-1,213.

[24] Sigvaldason, G., Annerts, K., and Nilsson, M., 1992, Effect of glacier loading/deloading on volcanism: postglacial volcanic production rate of the Dyngjufjöll area, central Iceland, Bulletin Volcanologique, 54:385-392.

[25] Briffa, K. R., Jones, P. D., Schweingruber, F. H., and Osborn, T. J., 1998, Influence of volcanic eruptions on Northern Hemisphere summer temperature over the past 600 years, Nature, 393:450-455.

[26] Rampino, M. R., and Self, S., 1993, Climate-volcanism feedback and the Toba eruption of ~74,000 years ago, Quaternary Research, 40:269-280.

[27] Philander, S. G., 1990, El Niño, La Niña, and the Southern Oscillation, International Geophysics Series, v. 46, Academic Press, 293 pp.

[28] Paegle, J. N., and Mo, K. C., 2002, Linkages between summer rainfall variability over South America and sea surface temperature anomalies, Journal of Climate, 15:1,389-1,407.

[29] Diaz, H. F., Hoerling, M. P., and Eischeid, J. K., 2001, ENSO variability, teleconnections and climate change, International Journal of Climatology, 21:1,845-1,862.

[30] Siegert, F., Ruecker, G., Hinrichs, A., and Hoffmann, A. A., 2001, Increased damage from fires in logged forests during droughts caused by El Niño, Nature, 414:437-440.

[31] Kumar, K. K., Rajagopalan, B., and Cane, M. A., 1999, On the weakening relationship between the Indian monsoon and ENSO, Science, 284:2,156-2,159.

[32] Visbeck, M. H., Hurrell, J. W., Polvani, L., and Cullen, H. M., 2001, The North Atlantic Oscillation: past, present, and future, Proceedings of the National Academy of Sciences of the USA, 98:12,876-12,877.

[33] Groetzner, A., Latif, M., and Barnett, T. P., 1998, A decadal climate cycle in the North Atlantic Ocean as simulated by the ECHO coupled GCM, Journal of Climate, 11:831-847.

[34] Dickson, R. R., Meincke, J., Malmberg, S.-A., and Lee, A. J., 1988, The "Great Salinity Anomaly" in the northern North Atlantic 1968-82, Progress in Oceanography, 20:103-151.

[35] Cook, E. R., D'Arrigo, R. D., and Briffa, K. R., 1998, A reconstruction of the North Atlantic Oscillation using tree-ring chronologies from North America and Europe, The Holocene, 8:9-17.

[36] Wallace, J. M., 2000, North Atlantic oscillation/annular mode: Two paradigms - one phenomenon, Quarterly Journal of the Royal Meteorological Society, 126:791-805.

[37] Barnston, A. G., and Livezey, R. E., 1987, Classification, seasonality, and persistence of low-frequency atmospheric circulation patterns, Monthly Weather Review, 115:1,083-1,126.

[38] Wang, B., and Ding, Y., 1991, An overview of the Madden-Julian Oscillation and its relation to monsoon and mid-latitude circulation, Advances in Atmospheric Science, 9:93-111.

[39] Tsonis, A. A., and Elsner, J. B., 1989, Chaos, strange attractors, and weather, Bulletin of the American Meteorological Society, 70:14-23.

[40] Hansen, J., Sato, M., Ruedy, R., Lacis, A., Asamoah, K., Beckford, K., Borenstein, S., Brown, E., Cairns, B., Carlson, B., Curran, B., deCastro, S., Druyan, L., Etwarrow, P., Ferede, T., Fox, M., Gaffen, D., Glascoe, J., Gordon, H., Hollandsworth, S., Jiang, X., Johnson, C., Lawrence, N., Lean, J., Lerner, J., Lo, K., Logan, J., Luckett, A., McCormick, M. P., McPeters, R., Miller, R., Minnis, P., Ramberran, I., Russell, G., Russell, P., Stone, P., Tegen, I., Thomas, S., Thomason, L., Thompson, A., Wilder, J., Willson, R., and Zawodny, J., 1997, Forcings and chaos in interannual to decadal climate change, Journal of Geophysical Research - Atmospheres, 102:25,679-25,270.

[41] Briffa, K. R., Jones, P. D., Schweingruber, F. H., and Osborn, T. J., 1998, Influence of volcanic eruptions on Northern Hemisphere summer temperature over the past 600 years, Nature, 393:450-455.

[42] Kirov, B., and Georgieva, K., 2002, Long-term variations and interrelations of ENSO, NAO and solar activity, Physics and Chemistry of the Earth, 27:441-448.

[43] Goudie, A., 2000, The Human Impact on the Natural Environment, Fifth Edition, MIT Press, 527 pp.

[44] Vitousek, P. M., Mooney, H. A., Lubchenco, J., and Melillo, J. M., 1997,

Human domination of Earth's ecosystems, Science, 277:494-499.

[45] Rojstaczer, S., Sterling, S. M., and Moore, N. J., 2001, Human appropriation of photosynthesis products, Science, 294:2,549-2,552.

[46] Leggett, J., 2000, The Carbon War: Global Warming and the End of the Oil Era, Penguin Books, 342 pp.

[47] Herzog, H., 2001, What future for carbon capture and sequestration?, Environmental Science and Technology, 35:148-153.

[48] Timmermann, A., Oberhuber, J. M., Bacher, A., Esch, M., Latif, M., and Roeckner, E., 1999, Increased El Niño frequency in a climate model forced by future greenhouse warming, Nature, 398:694-696.

[49] Bigg, G. R., 1997, The Oceans and Climate, Cambridge University Press, 256 pp.

[50] Linacre, E., 1992, Climate Data and Resources: a Reference and Guide, Routledge, 366 pp.

[51] Bates, J. J., 1994, A decade of multispectral sea surface temperature observations from space, Advances in Space Research, 14:5-14.

[52] Lamb, H. H., 1995, Climate, History, and the Modern World, Second Edition, Routledge, 433 pp.

[53] Karl, T. R., Derr, V. E., Easterling, D. R., Folland, C. K., Hofmann, D. J., Levitus, S., Nicholls, N., Parker, D. E., and Withee, G. W., 1995, Critical issues for long-term climate monitoring, Climatic Change, 31:185-221.

[54] Folland, C. K., and Parker, D. E., 1995, Correction of instrumental biases in historical sea surface temperature data, Quarterly Journal of the Royal Meteorological Society, 121:319-367.

[55] Chandler, T. J., 1965, The Climate of London, Hutchinson, 292 pp.

[56] Chatfield, C., 1996, The Analysis of Time-series: An Introduction, Fifth Edition, Chapman and Hall / CRC, 283 pp.

[57] Wunsch, C., 1999, The interpretation of short climate records, with comments on the North Atlantic and Southern Oscillations, Bulletin of the American Meteorological Society, 80:257-270.

[58] Garcia, A., and Mouradian, Z., 1998, The Gleissberg cycle of minima, Solar Physics, 180:495-498.

[59] Hughes, M. K., and Graumlich, L. J., 1996, Multi-millennial dendroclimatic studies from the western United States, In: Climatic Variations and Forcing Mechanisms of the Last 2,000 years, NATO ASI Series, 141:109-124.

[60] Wefer, G., Berger, W. H., Bijma, J., and Fischer, G., 1999, Clues to ocean history - a brief overview of proxies, In: Fischer, G., and Wefer, G., (Eds.), Use of Proxies in Paleoceanography: Examples from the South Atlantic, Springer Verlag, p. 1-68.

[61] Lowe, J. J., and Walker, M. J. C., 1997, Reconstructing Quaternary Environments, Second Edition, Longman, 446 pp.

[62] Imbrie, J., and Imbrie, K. P., 1979, Ice Ages: Solving the Mystery, Harvard University Press, 224 pp.

[63] Hays, J. D., Imbrie, J., and Shackleton, N. J., 1976, Variations in the Earth's orbit: pacemaker of the ice ages, Science, 194:1,121-1,132.

[64] Bowman, S., 1990, Radiocarbon Dating, Interpreting the Past, Number 1, University of California Press, 64 pp.

[65] Pilcher, J., 1991, Radiocarbon dating for the Quaternary scientist, In:, Lowe, J. J., (Ed.), Radiocarbon Dating: Recent Applications and Future Potential, Quaternary Proceedings v. 1, Quaternary Research Association, p. 27-34.

[66] Eckstein, D., Ogden, J. C., Jacoby, G. C., and Ash, J., 1981, Age and growth rate determination in tropical trees: the application of dendrochronological methods, Bulletin No. 94, School of Forestry and Environmental Studies, Yale University.

[67] Glock, W. S., 1937, Principles and Methods of Tree-ring Analysis, Carnegie Institution of Washington, Publication No. 486, 100 pp.

[68] Baillie, M. G. L., 1995, A Slice through Time: Dendrochronology and Precision Dating, Routledge, 176 pp.

[69] Alley, R. B., and Bentley, C. R., 1988, Ice-core analysis on the Siple Coast of West Antarctica, Annals of Glaciology, 11:1-7.

[70] Thomson, L. G., Mosley-Thompson, E., Bolzan, J. F., and Koci, B. R., 1985, A

1,500-year record of tropical precipitation recorded in ice cores from the Quelccaya Icecap, Peru, Science, 229:971-973.

[71] Meese, D. A., Gow, A. J., Alley, R. B., Zielinski, G. A., Grootes, P. M., Ram, K., Taylor, K. C., Mayewski, P. A. and Bolzan, J. F., 1997, The Greenland Ice Sheet Project 2 depth-age scale: methods and results, Journal of Geophysical Research, 102:26,411–26,423.

[72] Weidman, C. R., Jones, G. A., and Lohmann, K. C., 1994, The long-lived mollusc Arctica islandica - a new paleoceanographic tool for the reconstruction of bottom temperatures for the continental shelves of the northern North Atlantic Ocean, Journal of Geophysical Research: Oceans, 99:18,305-18,314.

[73] Jones, D. S., and Quitmyer, I. R., 1996, Marking time with bivalve shells: oxygen isotopes and season of annual increment formation, Palaios, 11:340-346.

[74] Dunbar, R. B., Wellington, G. M., Colgan, M. W., and Glynn, P. W., 1994, Eastern Pacific sea surface temperature since 1600 AD - the delta O-18 record of climate variability in Galapagos corals, Paleoceanography, 9:291-315.

[75] Barnes, D. J., and Lough, J. M., 1996, Coral skeletons: storage and recovery of environmental information, Global Change Biology, 2:569-582.

[76] Baker, A., Smart, P. L., Edwards, R. L., and Richards, A., 1993, Annual growth banding in a cave stalagmite, Nature, 364:518-520.

[77] De Geer, G., 1912, Geochronology of the last 12,000 years, Proceedings of the 11th International Geological Congress, Stockholm, 1910, 1:241-253.

[78] De Geer, G., 1940, Geochronologia Suecica Principles, Svenska Vetenskapsakademiens Handlingar, 3:18(6), 367 pp. and atlas.

[79] Boygle, J., 1993, The Swedish varve chronology - a review, Progress in Physical Geography, 17:1-19.

[80] Andrén, T., Björck, J., and Johnsen, S., 1999, Correlation of Swedish glacial varves with the Greenland (GRIP) oxygen isotope record, Journal of Quaternary Science, 14:361-371.

[81] Wohlfarth, B., Holmquist, B., Cato, I., and Linderson, H., 1998, The climatic significance of clastic varves in the Ångermanälven Estuary, northern Sweden, AD 1860 to 1950, The Holocene, 8:521-534.

[82] Barrell, J., 1917, Rhythms and the measurements of geologic time, GSA Bulletin, 28:745-904.

[83] Wright, H. E. Jr., Cushing, E. J., and Livingstone, D. A., 1965, Coring devices for lake sediments, in: Kummel, B., and Raup, D., (Eds.), Handbook of paleontological techniques, W. H. Freeman and Co., p. 494-520.

[84] Mackereth, F. J. H., 1948, A portable core sampler for lake deposits, Limnology and Oceanography, 3:181-191.

[85] Livingstone, D. A., 1955, A lightweight piston sampler for lake deposits, Ecology, 36:137-139.

[86] Calvert, S. E., 1966, Origin of diatom-rich, varved sediments from the Gulf of California, Journal of Geology, 74:546-565.

[87] Gross, M. G., Gugluer, S. M., Creager, J. S., and Dawson, W. A., 1963, Varved marine sediments in a stagnant marine basin, Science, 141:918-919.

[88] Libby, W. F., 1946, Atmospheric Helium three and radiocarbon from cosmic radiation, Physical Review, 69:671-672.

[89] De Vries, H., 1958, Variation in concentration of radiocarbon with time and location on earth, Koningklijke Nederlandse Akademie van Wetenschappen Proceedings, B61:94-102.

[90] Reading, H. G., (Ed.), 1996, Sedimentary Environments: Processes, Facies, and Stratigraphy, Blackwell Science, 744 pp.

[91] Shanmugam, G., 2000, 50 years of the turbidite paradigm (1950s-1990s): deep water processes and facies models - a critical perspective, Marine and Petroleum Geology, 17:285-342.

[92] Fischer, A. G., and Roberts, L. T., 1991, Cyclicity in the Green River Formation (Lacustrine - Eocene) of Wyoming, Journal of Sedimentary Petrology, 61:1,146-1,154.

[93] Garner, P., 1997, Green River blues: evidence against one of the most common "proofs" of an old Earth, Creation Magazine, 19:18-19.

[94] Williams, G. E., 1988, Cyclicity in the Late Precambrian Elatina Formation, South Australia: solar or tidal signature?, Climatic Change, 13:117-128.

[95] Anderson, R. Y., 1996, Seasonal sedimentation: a framework for reconstructing climatic and environmental change, in: Kemp, A. E. S., (Ed.), 1996, Palaeoclimatology and Palaeoceanography from Laminated Sediments, Geological Society Special Publication No. 116, p. 1-15.

[96] O'Sullivan, P. E., 1983, Annually-laminated lake sediments and the study of Quaternary environmental changes - a review, Quaternary Science Reviews, 1:245-313.

[97] Anderson, R. Y., 1986, The varve microcosm: propagator of cyclic bedding, Paleoceanography, 1:373-382.

[98] Thunell, R., Pride, C., Tappa, E., and Mullerkarger, F., 1993, Varve formation in the Gulf of California - insights from time-series sediment trap sampling and remote sensing, Quaternary Science Reviews, 12:451-464.

[99] Grimm, K. A., Lange, C. B., and Gill, A. S., 1996, Biological forcing of sedimentary laminae: evidence from ODP site 893, Santa Barbara Basin, California, Journal of Sedimentary Research, 66:613-624.

[100] Prof. I. N. McCave, personal communication, December 1997.

[101] Von Rad, U., Schaaf, M., Michels, K. H., Schulz, H., Berger, W. H., and Sirocko, F., 1999, A 5,000-year record of climate change in varved sediments from the Oxygen Minimum Zone off Pakistan, northeastern Arabian Sea, Quaternary Research, 51:39-53.

[102] De Diego, T., and Douglas, R. G., 1999, Oxygen-related sediment microfabrics in modern "black shales", Gulf of California, Mexico, Journal of Foraminiferal Research, 29:453-464.

[103] McIlroy, D., and Logan, G. A., 1999, The impact of bioturbation on infaunal ecology and evolution during the Proterozoic-Cambrian transition, Palaios, 14:58-72.

[104] Kemp, A. E. S., and Baldauf, J. G., 1993, Vast Neogene laminated diatom mat deposits from the eastern equatorial Pacific Ocean, Nature, 362:141-144.

[105] Mackereth, F. J. H., 1966, Some chemical observations on post-glacial lake sediments, Philosophical Transactions of the Royal Society, B250:165-213.

[106] Lamoureux, S. F., 1999, Spatial and interannual variations in sedimentation recorded in nonglacial varved sediments from the Canadian High Arctic, Journal of Paleolimnology, 21:73-84.

[107] Petterson, G., 1996, Varved sediments in Sweden: a brief review, in: Kemp, A. E. S., (Ed.), 1996, Palaeoclimatology and Palaeoceanography from Laminated Sediments, Geological Society Special Publication No. 116, p. 73-77.

[108] Ojala, A., 2001, Varved lake sediments in southern and central Finland: long varve chronologies as a basis for Holocene palaeoenvironmental reconstructions, PhD Thesis, Geological Survey of Finland, 41 pp.

[109] Züllig, H., 1989, Role of carotenoids in lake sediments for reconstructing trophic history during the late Quaternary, Journal of Paleolimnology, 2:23-40.

[110] Van Kolfshoten, T., and Gibbard, P. L., 2000, The Eemian - local sequences, global perspectives: introduction, Netherlands Journal of Geosciences, 79:129-133, and references therein.

[111] Kitagawa, H., and van der Plicht, J., 1998, A 40,000-year varve chronology from Lake Suigetsu, Japan: extension of the C-14 calibration curve, Radiocarbon, 40:505-515.

[112] Schimmelmann, A., and Lange, C. B., 1996, Tales of 1,001 varves: a review of Santa Barbara Basin sediment studies, in: Kemp, A. E. S., (Ed.), 1996, Palaeoclimatology and Palaeoceanography from Laminated Sediments, Geological Society Special Publication No. 116, p. 121-141.

[113] Kirby, M. E., Mullins, H. T., Patterson, W. P., and Burnett, A. W., 2001, Lacustrine isotopic evidence for multidecadal natural climate variability related to the circumpolar vortex over the northeast United States during the past millennnium, Geology, 29:807-810.

[114] Teranes, J. L., and McKenzie, J. A., 2001, Lacustrine oxygen isotope record of 20th-century cliamte change in central Europe: evaluation of climatic controls on oxygen isotopes in precipitation, Journal of Paleolimnology, 26:131-146.

[115] Pitkänen, A., and Grönlund, E., 2001, A 600 year fire history record of a varved lake sediment (Lake Ristijärvi, North Karelia, East Finland), Annales Botanici Fennici, 38:63-73.

[116] Snowball, I., Zillén, L., and Gaillard, M.-J., 2002, Rapid early-Holocene environmental changes in northern Sweden based on studies of two varved lake-sediment sequences, The Holocene, 12:7-16.

[117] Tinner, W., and Lotter, A. F., 2001, Central European vegetation response to abrupt climate change at 8.2ka, Geology, 29:551-554.

[118] Zhao, M., Eglinton, G., Read, G., and Schimmelmann, A., 2000, An alkenone (UK-37) quasi-annual sea surface temperature record (A.D. 1440 to 1940) using varved sediments from the Santa Barbara Basin, Organic Geochemistry, 31:903-917.

[119] Brännvall, M.-L., Bindler, R., Emteryd, O., and Renberg, I., 2001, Four thousand years of atmospheric lead pollution in northern Europe: a summary from Swedish lake sediments, Journal of Paleolimnology, 25:421-435.

[120] Blais-Stevens, A., and Clague, J. J., 2001, Paleoseismic signature in late Holocene sediment cores from Saanich Inlet, British Columbia, Marine Geology, 175:131-148.

[121] Hausmann, S., Lotter, A. F., van Leeuwen, J. F. N., Ohlendorf, C., Lemcke, G., Grönlund, E., and Sturm, M., 2002, Interactions of climate and land use documented in the varved sediments of Seebergsee in the Swiss Alps, The Holocene, 12:279-289.

[122] Anderson, R. Y., 1982, A long geoclimatic record from the Permian, Journal of Geophysical Research: Oceans and Atmospheres, 87:7,285-7,294.

[123] Wohlfarth, B., and Possnert, G., 2000, AMS 14-C measurements from the Swedish varved clays, Radiocarbon, 42:323-333.

[124] Hughen, K. A., Overpeck, J. T., and Anderson, R. F., 2000, Recent warming in a 500-year palaeotemperature record from varved sediments, Upper Soper Lake, Baffin Island, Canada, The Holocene, 10:9-19.

[125] Moore, J. J., Hughen, K. A., Miller, G. A., and Overpeck, J. T., 2001, Little Ice Age recorded in summer temperature reconstruction from varved sediments of Donard Lake, Baffin Island, Canada, Journal of Paleolimnoology, 25:503-517.

[126] Bull, D., Kemp, A. E. S., and Weedon, G. P., 2000, A 160 k.y.-old record of El Niño Southern Oscillation in marine production and coastal runoff from Santa Barbara Basin, California, USA, Geology, 28:1,007-1,010.

[127] Dean, J. M., Kemp, A. E. S., and Pearce, R. B., 2001, Palaeoflux records from electron microscope studies of Holocene laminated sediments, Saanich Inlet, British Columbia, Marine Geology, 174:139-158.

[128] Nederbragt, A. J., and Thurow, J. W., 2001, A 6,000 yr varve record of Holocene climate in Saanich Inlet, British Columbia, from digital sediment colour analysis of ODP Leg 169S cores, Marine Geology, 174:95-110.

[129] Lotter, A. F., and Birks, H. J. B., 1997, The separation of the influence of nutrients and climate on the varve time-series of Baldeggersee, Switzerland, Aquatic Sciences, 59:362-375.

[130] Ohlendorf, C., Niessen, F., and Weissert, H., 1997. Glacial varve thickness and 127 years of instrumental climate data: a comparison, Climatic Change, 36:391-411.

[131] Brauer, A., Endres, C., and Negendank, J. F. W., 1999, Lateglacial calendar year chronology based on annually laminated sediments from Lake Meerfelder Maar, Germany, Quaternary International, 61:17-25.

[132] Godsey, H. S., Moore, T. C., Rea, D. K., and Shane, L. C. K., 1999, Post-Younger Dryas seasonality in the North American midcontinent region as recorded in Lake Huron varved sediments, Canadian Journal of Earth Sciences, 36:533-547.

[133] Livingstone, D. M., and Hajdas, I., 2001, Climatically relevant periodicities in the thicknesses of biogenic carbonate varves in Soppensee, Switzerland (9740-6870 calendar yr BP), Journal of Paleolimnology, 25:17-24.

[134] Vos, H., Sanchez, A., Zolitschka, B., Brauer, A., and Negendank, J. F. W., 1997, Solar activity variations recorded in varved sediments from the crater lake of Holzmaar - a maar lake in the Westeifel Volcanic Field, Germany, Surveys in Geophysics, 18:163-182.

[135] Scargle, J. D., 2000, Publication bias: the "file drawer" problem in scientific inference, Journal of Scientific Exploration, 14:91-106.

[136] Young, R., Walanus, A., and Goslar, T., 2000, Autocorrelation analysis in search of short-term patterns in varve data from sediments of Lake Gosciaz, Poland, Boreas, 29:251-260.

[137] Wohlfarth, B., Björck, S., Cato, I., and Possnert, G., 1997, A new middle Holocene varve diagram from the River Ångermanälven, northern Sweden: indications for a possible error in the Holocene varve chronology, Boreas, 26:347-353.

[138] De Geer, G., 1927, Late Glacial clay varves in Argentina, measured by Dr. Carl Caldenius, dated and connected with the Solar Curve through the Swedish Timescale, Geografiska Annaler, 1927, Parts 1-2, p. 1-8.

[139] Antevs, E., 1929, Conditions of varve correlations (abstract only), GSA Bulletin, 40:126.

[140] Sauramo, M., 1923, Studies on the Quaternary varve sediments in southern Finland, Bulletin de la Commission Géologique de Finlande, v. 60, 164 pp.

[141] Zeuner, F. E., 1952, Dating the Past, Third Edition, Methuen and Co., 494 pp.

[142] Potter, P. E., Maynard, J. B., and Pryor, W. A., 1980, Sedimentology of Shale, Springer Verlag, 314 pp.

[143] Ojala, A., 2001, Varved lake sediments in southern and central Finland: long varve chronologies as a basis for Holocene palaeoenvironmental reconstructions, PhD Thesis Synopsis, Geological Survey of Finland, 41 pp.

[144] Renberg, I., 1981, Improved methods for sampling, photographing and varve-counting of varved lake sediments, Boreas, 10:255-258.

[145] Russ, J. C., 1999, The Image Processing Handbook, Third Edition, CRC Press, 771 pp.

[146] Varem-Sanders, T. M. L., and Campbell, I. D., 1996, Dendroscan: tree-ring width and density measurement system, Canadian Forest Service, Special Report 10, 131 pp.

[147] Cooper, M. C., 1997, The use of digital image analysis in the study of laminated sediments, Journal of Paleolimnology, 19:33-40.

[148] Saarinen, T., and Petterson, G., 2001, Image analysis techniques, In: Last, W. M., and Smol, J. P., (Eds.), Tracking Environmental Change Using Lake Sediments, Vol. 2, Physical and Geochemical Methods, Ch. 3, p. 23-39.

[149] Zolitschka, B., 1996, Image analysis and microscopic investigation of annually laminated lake sediments from Fayetteville Green Lake (NY, USA), Lake C2 (NWT, Canada), and Holzmaar (Germany): a comparison, in: Kemp, A. E. S., (Ed.), 1996, Palaeoclimatology and Palaeoceanography from Laminated Sediments, Geological Society Special Publication No. 116, p. 49-55.

[150] Schaaf, M., and Thurow, J., 1994, A fast and easy method to derive highest-resolution time-series datasets from drillcores and rock samples, Sedimentary Geology, 94:1-10.

Chapter 2: Drammensfjord, Norway

2.1 Introduction

A detailed review of the Drammensfjord basin system and its components is a necessary precursor to any research on palaeoclimate records that might be obtained from it. In addition, such a review is valuable in its own right, for two reasons. Firstly, because Drammensfjord is little-known. Previously-published research is sparse, hard to find, and mostly in Norwegian; information is drawn here from newly-translated papers. Secondly, varved sediment from fjords has not been the subject of as much research as more typical biogenic lake varves, or clastic glacial varves, perhaps because fjords are not as widely distributed as lakes, and in many cases are deeper and more difficult to core.

The fjord environment is complex: fjords are influenced by glacial, fluvial, climatic, geographic, and geotechnical controls [1]. There is no obvious point to begin a comprehensive description of Drammensfjord, so the different aspects of the fjord which are described next are best considered in parallel. A general literature review (in sections 2.2 to 2.13) is followed by an introduction to the specific Drammensfjord research program involving image analysis of varved sediment (in section 2.14).

2.2 The Oslo Rift and its silled fjords

Drammensfjord and the surrounding Oslo region are located at the apex of the Inner Skagerrak, which cuts northward into the Scandinavian landmass. The structure of the apex is a graben: a fault-bounded sunken block. The area is referred to as the Oslo Rift [2-5].

The surrounding rocks are Precambrian basement, and to the north, rocks of the Caledonian Nappe. The Oslo Rift itself has a varied geology, with Lower Palaeozoic sediments, Carboniferous sediments, and a variety of Permo-Carboniferous igneous rocks. The area includes the type locality for larvikite [6], which can be found as distinctive blue glacial erratics on the Yorkshire Coast.

The Oslo graben continues offshore into the Skagerrak graben, forming a rift oriented approximately N-S, of c. 400km in length; seismic profiles show that the region's crust has been thinned [7]. Rifting began in the Late Carboniferous [8], coeval with the volcanism, and continued until the earliest Triassic. The detailed tectonics of the area are poorly understood because uplift has eroded much of the sediment cover. Rifting is no longer occurring - it is a failed rift - but occasional seismic activity still occurs on its faults. One of the largest earthquakes in Scandinavia in the last 500 years, of magnitude c. 6, occurred in the Oslofjord area in 1904 [9].

The present morphology of the Drammensfjord region has been influenced as much by glacial activity as by its underlying tectonic structure. Drammensfjord was most probably initiated by a river following a fault, but the proto-river-valley was excavated to its present shape by ice [1].

Following the Last Glacial, numerous ice-gouged valleys in the region's basement rocks flooded to become fjords. Several silled fjords occur along the coast of the Oslo Rift, such as Drammensfjord and Inner Oslofjord, which are adjacent, Frierfjord to the west, and Iddefjord to the east [10]. Cores from many silled fjords could potentially contain varves [11], though investigations are currently at an early stage.

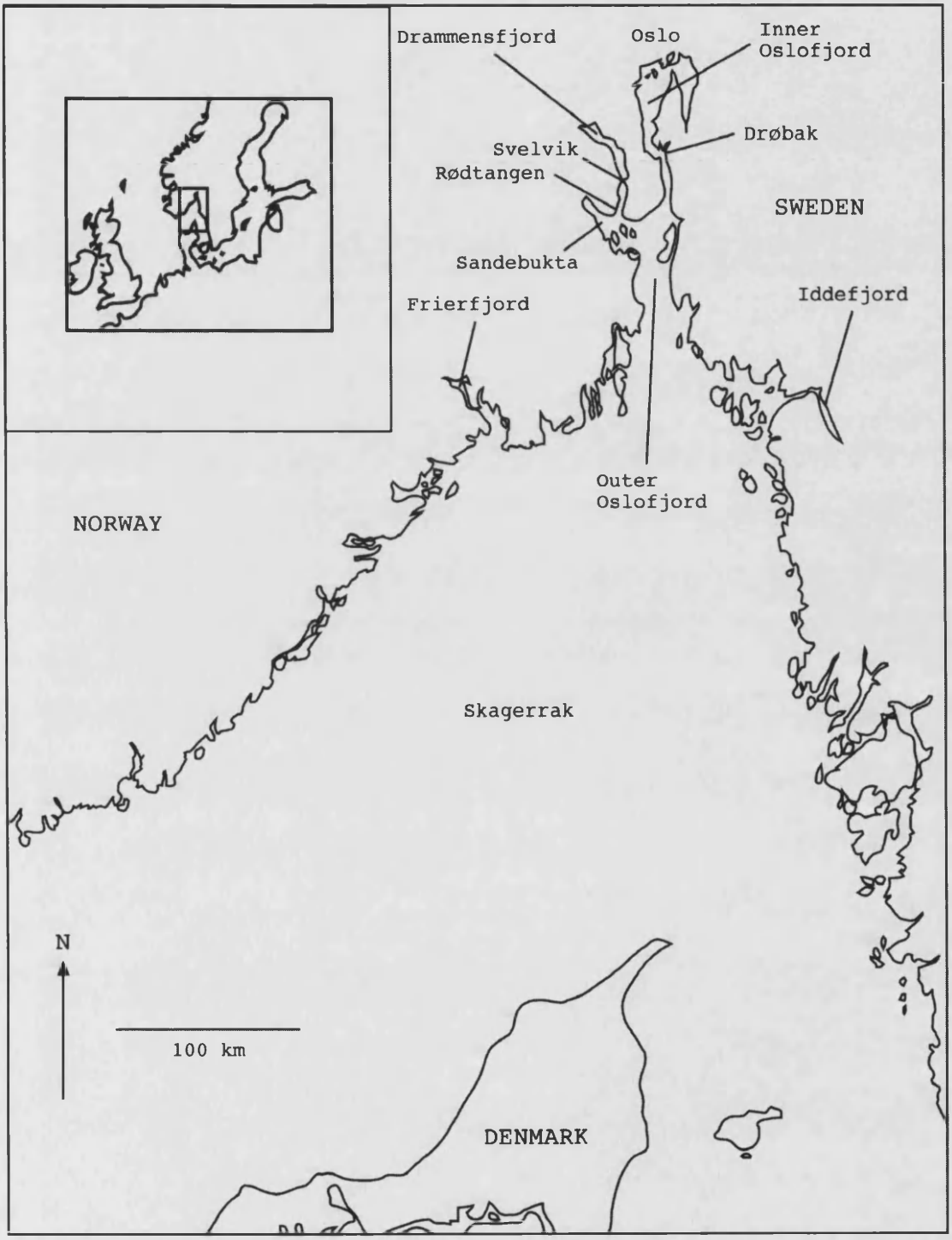

Figure 2.1: Map of the Drammensfjord region showing nearby silled fjords and the location of the region on the Scandinavian landmass. Modified from Pederstad *et al.* [10].

A precise nomenclature is useful in distinguishing between the different depositional basins along this coastline. "Outer Oslofjord" includes numerous smaller fjords and inlets and extends south over more than 100km, merging at its southern margin into the Skagerrak [10]. It is not open ocean; it is estuarine in character, owing to the large freshwater influx from the River Glomma and the Kattegat. Its bathymetry is complex, reaching depths of c. 200m, and it includes an archipelago of many small islands. Numerous sidearms project from Outer Oslofjord; most of these, such as Sandebukta [12], are not silled. The two silled sidearms are "Inner Oslofjord" and Drammensfjord.

The depocentre of Drammensfjord is located at 59°37'99"N, 10°25'39"E, c. 50km southwest of the city of Oslo. The fjord itself trends approximately northwest-southeast and is c. 30km long, extending from Drammen in the north to Rødtangen in the south. It is divided by a shallow sill, at Svelvik, north of which is found "Inner Drammensfjord", and south of which "Outer Drammensfjord". Based on the shape of the coastline, then, Inner and Outer Drammensfjord form a single unit, but because of the location of the sill, Outer Drammensfjord is hydrographically continuous with the larger Outer Oslofjord [13]; it is less than 35m deep and contains no other sills [14]. The reasons for the sill being so important are explained later. For convenience, "Drammensfjord" will only be used to refer to Inner Drammensfjord, i.e. the part of the fjord behind the sill. This is most clearly understood by reference to figure 2.1.

Note that Drammensfjord has also been referred to as "Dramsfjord" [e.g. 15], and that before 1900, Oslofjord was named "Christianiafjord" [e.g. 16], then "Kristianiafjord" until 1925. The Inner Oslofjord has two arms, named Bunnefjord and Vestfjord.

What is the nature of the sills that separate Drammensfjord and Inner Oslofjord from Outer Oslofjord? The Inner Oslofjord sill at Drøbak and the Drammensfjord sill at Svelvik are both formed by the same terminal moraine. This is the Ski moraine, whose eroded remnants can be traced laterally across the surrounding land area for c. 60km. It consists of boulder clay and glacial outwash sediments with ice-compressional structures, and is one of a set of parallel moraine ridges formed by minor ice readvances during the last deglaciation [17]. The Ski moraine represents an ice readvance at c. 10,000 to 10,200 ^{14}C years BP, at the end of the Younger Dryas Stadial; the initial, major Younger Dryas ice readvance produced the Ra moraine, which is found to the south of the Ski moraine [18].

The sill at Svelvik strongly influences the depositional regime in Drammensfjord. This regime, therefore, has only arisen since the start of the Holocene, when the sill was formed.

2.3 The Drammensfjord basin [13]

Drammensfjord is a typical silled fjord or "poll", 20km long, 1.6 to 3km wide (average width 2.3km), and roughly rectangular in shape. Its area is c. 45.1km^2 and its volume c. 3.33bn m^3 [19]. Water depth slowly increases southwards, reaching a maximum of 124m just inside the sill at Svelvik. Average water depth is 74m. It has a typical fjord bathymetry, reflecting its glacial origin: steep sides and a smooth bottom. This is

clear in side-scan sonar images obtained by NIOZ during the *Pelagia* cruise, which is described in section 2.14 [20].

Effectively, the River Drammen is the sole source of freshwater to the fjord. Of a measured mean freshwater input of 290m^3/s over the interval 1982 to 1984, 97% was from the River Drammen, 2% from the River Lier, and the remainder from many smaller rivers [14].

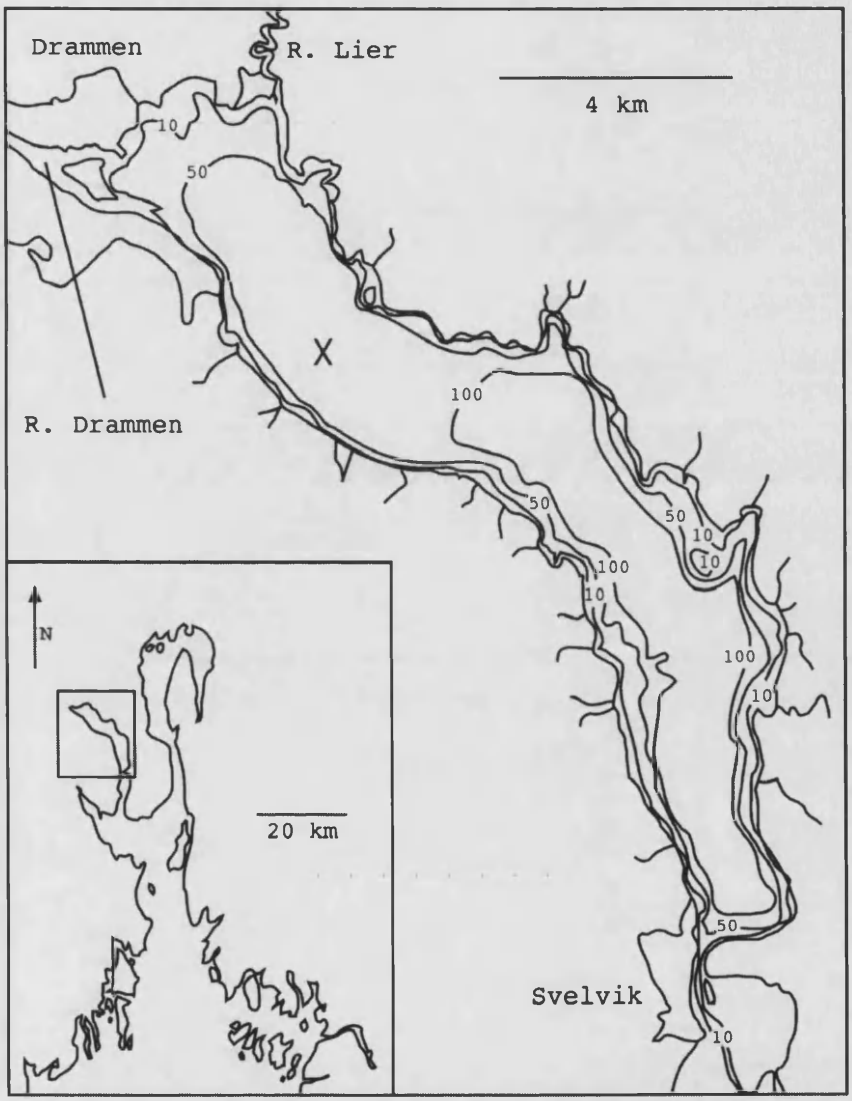

Figure 2.2: Map of Drammensfjord basin showing bathymetry: contours at 10m, 50m, and 100m depths. Redrawn from Alve [13]. The cross marks the location of a sampling site (see figure 2.4).

Most fjords (c. 70%) have a direct glacial input at the fjord head [1]. This is not the case for Drammensfjord. Some mountainous parts of its catchment area do contain glaciers, and it drains a number of freshwater lakes of glacial origin (e.g. Lake Tyrifjord), but it has had no direct glacial input since the early Holocene. Recent sediments from Drammensfjord therefore lack characteristic glacial components such as dropstones, ice-rafted debris (IRD), and glacial "rock flour". Fjords with a direct glacial input can contain laminated sediments [e.g. 21], but they are not comparable to those found in Drammensfjord.

Drammensfjord is underlain by Holocene and Lateglacial clays [22], above a granite basement. No studies have been made into the nature of the pre-Holocene sediments under Drammensfjord; however, they are presumably very similar to those under Inner Oslofjord. Between c. 13,000 and 10,000 ^{14}C years BP, whilst the Oslofjord area was depressed below sea-level, vast amounts of postglacial marine clay were deposited adjacent to the ice margin [23]. During the deglaciation of Scandinavia, shortly after the start of the Holocene, when relative isostatic rise and sea-level regression were fastest, extensive submarine deposits of this clay were exposed to wave erosion, and rivers rapidly eroded down through these to a new base level [24]. Thus, most of the 30-100m thick sediment drape revealed by seismic surveys of Outer Oslofjord is either primary or reworked postglacial marine clay. This has now been subaerially exposed across a wide coastal belt by isostatic uplift. Within the Inner Oslofjord, Holocene deposits form only a thin veneer above this clay, c. 5 to 15m thick [10].

The region has undergone significant uplift since the last deglaciation as a result of isostatic rebound; the oldest known early Holocene shoreline is 220m above present sea-level [16]. Uplift continues today at a rate of c. 3mm per year [22]. Uplift and sedimentary deposition at the northern end of Drammensfjord have contributed to the formation of Holmen Island, a mouth bar on the delta of the River Drammen, which is now part of the modern port; the area upon which the modern city is built only emerged from the fjord c. 1,000 years ago [22].

Over the region as a whole, large amounts of Lateglacial sediment are now above sea-level and are being eroded down into by rivers. This is an important source of sediment for Drammensfjord. Most importantly of all, the Drammensfjord sill is getting gradually shallower, because of the uplift, and the sill depth strongly affects the hydrography of the fjord. This is described in the next section.

2.4 Drammensfjord hydrography

The hydrography of Drammensfjord has been studied by Hjort and Gran [16], Braarud and Ruud [25], Beyer [26], Richards and Benson [15], Dahl [27], Schaanning [19], and in most detail, Magnusson and Næs [14].

The sill at Svelvik is currently 10m deep. Water circulation in Drammensfjord is characteristic of a small silled fjord: there is a fresh-to-brackish surface layer, typically extending down to the same depth as the sill, overlying a body of deep water which has a salinity slightly less than ordinary seawater. The two are separated by a strong pycnocline, and the density difference between them inhibits mixing of deep and surface water. In Drammensfjord a small amount of mixing does occur, near the river mouth and in the area just inside the sill, producing a thin transitional layer, 20-30m thick [28].

The existence of a low-salinity surface layer is favoured by several criteria [29] which are met by Drammensfjord: high freshwater input to the fjord, short fjord length, narrow fjord exit, and very weak tidal mixing via internal waves. Internal waves, driven by streaming tidewater, cannot currently flow across the sill; it would have to be c. 12-15m deep to allow this [14]. Thus, a slight deepening of the sill

would cause much more vertical mixing in Drammensfjord, with consequent aeration of the deep water [14]. The shallowness of the sill is the most important factor in maintaining the stratified hydrography of Drammensfjord [14].

However, Drammensfjord shows a pronounced annual cycle in its hydrography. The freshwater surface layer is thickest following the spring flood, when it can reach 25m thick [1]. Surface water flows out of the fjord, driven by the "head" created by the spring flood, and the surface layer thins. The monsoonal wind field of Drammensfjord, alternating onshore and offshore during the year, also contributes to the removal of surface water. Strong northerly winds in winter facilitate the loss of the surface layer, and water that is more saline appears at the fjord surface later in the year. The surface may then be covered with a thin layer of ice over winter and early spring. When the ice melts, saline water is again exposed at the surface, until the spring flood re-occurs, replenishing the freshwater surface layer. So, the freshwater surface layer may only be present during six months of the year: surface water is continually flowing out of Drammensfjord, though at a changing rate over the year. The flushing time of the surface layer varies from 6 to 18 days [30].

Wind stress does not simply drive water out of Drammensfjord. Surface water currents instigate frictionally driven countercurrents operating just below the surface. Drammensfjord has a three-layer circulation in June and a five-layer circulation in December [1] owing to the stronger winds in winter. Wind-driven mixing can be intense, but only affects the top 20m or so of the fjord [29], so it does not cause significant mixing of surface and deep water.

The basin's positive water balance requires a continual outflow of surface water, in order to stabilise its water volume. This outflow entrains salt from the saline water beneath as it flows out of the fjord. Salt conservation therefore requires inflow of saline water into the fjord at depth. Water and salt content in the fjord are kept balanced by these "renewal events" [29]. Constant entrainment of salt by outflowing surface water makes the deep water slightly hyposaline: deep water in Drammensfjord has a salinity of 30-31.5‰ [31]. Seawater from outside is therefore able to flow into the fjord because it is slightly denser than the fjord's deep water.

However, renewals are restricted in scope and irregular. Deep water outside Drammensfjord may also become hyposaline, since the Outer Oslofjord and Skagerrak are themselves effectively part of a large estuary [32]. This inhibits renewals. Also, a thick freshwater surface layer in Drammensfjord inhibits renewals, preventing deep saline water being able to get over the sill. Wind stress also affects renewals, although there is no obvious relation between the wind stress field and renewal events because of countercurrents being set up at depth, as mentioned above [33]. During renewal events, a plume of saline water moves over the sill and sinks until it reaches water of an equal density to itself. The fjord then gets renewed from this depth upwards. Of course, if the renewal event is restricted in duration, then the deep water in the fjord will not be completely renewed either [33].

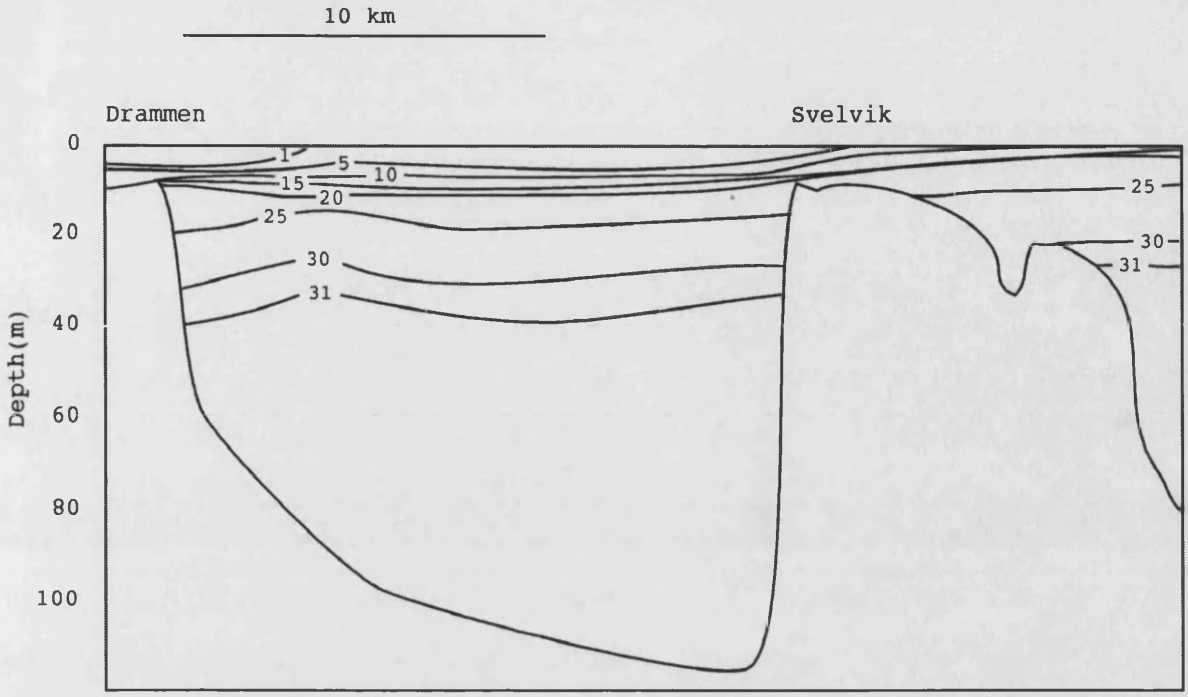

Figure 2.3: Cross-section of Drammensfjord in summer 1982 showing salinity variations in parts per thousand. Redrawn from Magnusson and Næs [14].

Renewal events in Drammensfjord currently occur every 3-5 years [13], during November to May, when the thermocline is weak and saline water upwells outside the fjord. They show up in salinity records of deep water as sudden increases. They can also be recorded by measuring the height of the water surface: inflowing deep water "pushes up" the surface level of the fjord, allowing the volume of inflowing water to be calculated [33].

Partial and irregular renewals, combined with the oxygen-depleting effects of organic matter sinking into Drammensfjord, cause near-permanent anoxia in the deep water, and resultant production of hydrogen sulphide. The "anoxic zone" varies in depth and lateral extent, both seasonally and over longer time periods (e.g. between renewal events). In 1987-88, anoxia occurred below 35m in the northern part of Drammensfjord, and below 60m in the southern part [31]. Some "interfingering" of oxygenated and anoxic water masses is known to occur [15].

As already mentioned, water flowing out of Drammensfjord discharges not into the open ocean but into the Skagerrak, part of the Baltic "giant estuary". This, too, has a brackish surface layer with a strong pycnocline: the surface layer is part of the Norwegian Coastal Current, which flows west around the tip of Norway then north up the Norwegian coast. It contributes to the cooling and dilution of the warm, saline surface water of the North Atlantic Conveyor, affecting its density, and thereby its propensity to sink and form North Atlantic Deep Water. The North Atlantic Conveyor, in turn, affects the precipitation over Drammensfjord's catchment, which affects the output of freshwater from Drammensfjord into the Skagerrak, which feeds back into the North Atlantic Conveyor. In this sense, Drammensfjord is a tiny part of the system of ocean-atmosphere feedbacks which influence climate in the North Atlantic region.

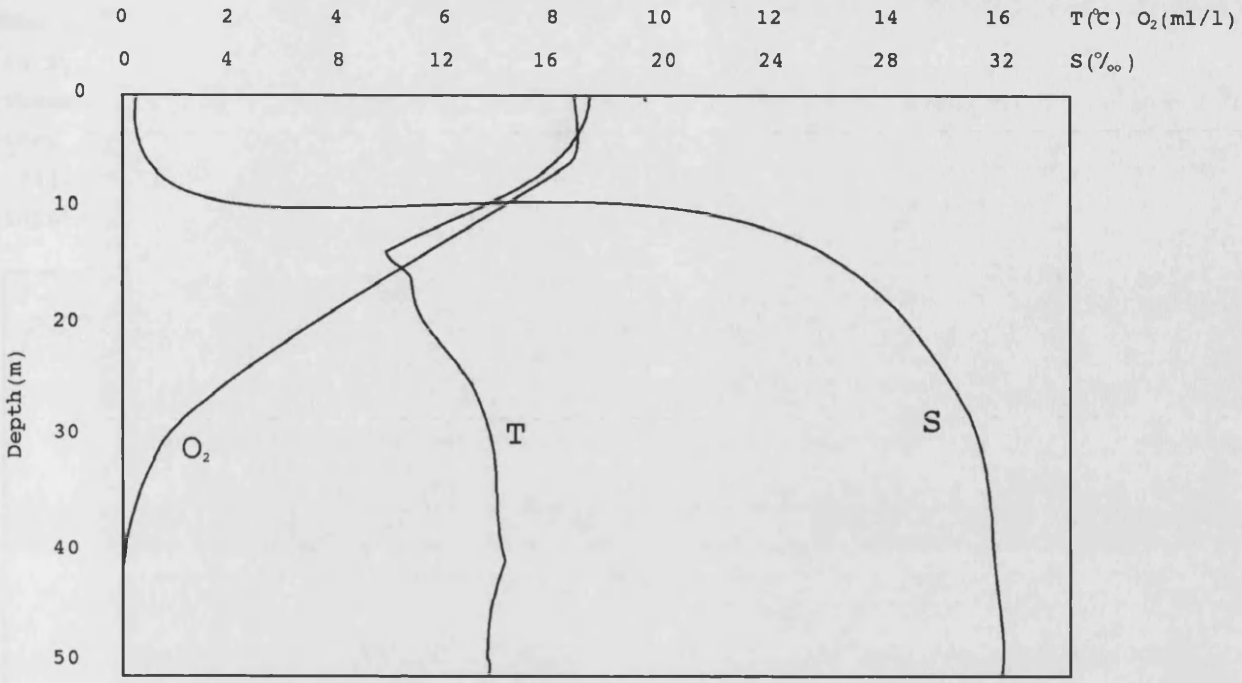

Figure 2.4: Changes in temperature, salinity and oxygen availability with depth in Drammensfjord in summer 1982. The measurement site is indicated by the cross in figure 2.2. Redrawn from Magnusson and Næs [14].

2.5 The Drammensfjord catchment

The thickness of the surface freshwater layer, and therefore the likelihood of a renewal event, is just one aspect of Drammensfjord that changes with the annual climate cycle. The following sections consider the nature of the annual cycle in southern Scandinavia, and its effects on Drammensfjord's catchment area and on the fjord itself. First, the catchment area of the River Drammen is described.

The River Drammen drains the third largest catchment area in Norway, after the Glomma and the Pasvikelv: 17,096km^2 [34]. Mean specific runoff is 608mm/year. The mean discharge of the River Drammen is 330m^3/s; the maximum recorded discharge is c. 2,100m^3/s [34]. The Drammen catchment is mostly hilly terrain; the bedrock is predominantly impermeable Archaean gneiss and Permian granite. The area was scoured by ice during the last glacial, and the soil cover is thin [35]. Following deglaciation, sea-level rise happened faster than isostatic rebound, such that most of the Drammen catchment was under the sea, becoming covered with a layer of marine clay. Marine regression has occurred gradually over the Holocene, as sea-level has stabilised and isostatic rebound has continued [36].

The Drammen catchment spans the boundary between two natural vegetation zones, with deciduous forest to the south, and mixed deciduous-coniferous forest to the north. Even in recent times, much of the area close to Drammen and Oslo has remained forested, with cleared "islands" in the forest for agriculture and other purposes [37]. Further to the north, mountainous areas of the catchment are covered by boreal forest; the highest parts are covered by alpine-type vegetation [36].

The drainage pattern is dendritic, and includes many large lakes, the largest of which is Tyrifjord, a "fjord-lake" which is glacial in origin, like Drammensfjord itself. These fjord-lakes have been isolated from the sea by post-glacial isostatic uplift, so they are generally close to the coast, i.e. well downstream in the catchment area [34]. The catchment reaches up into the mountains of western Norway, and includes input from mountain glaciers.

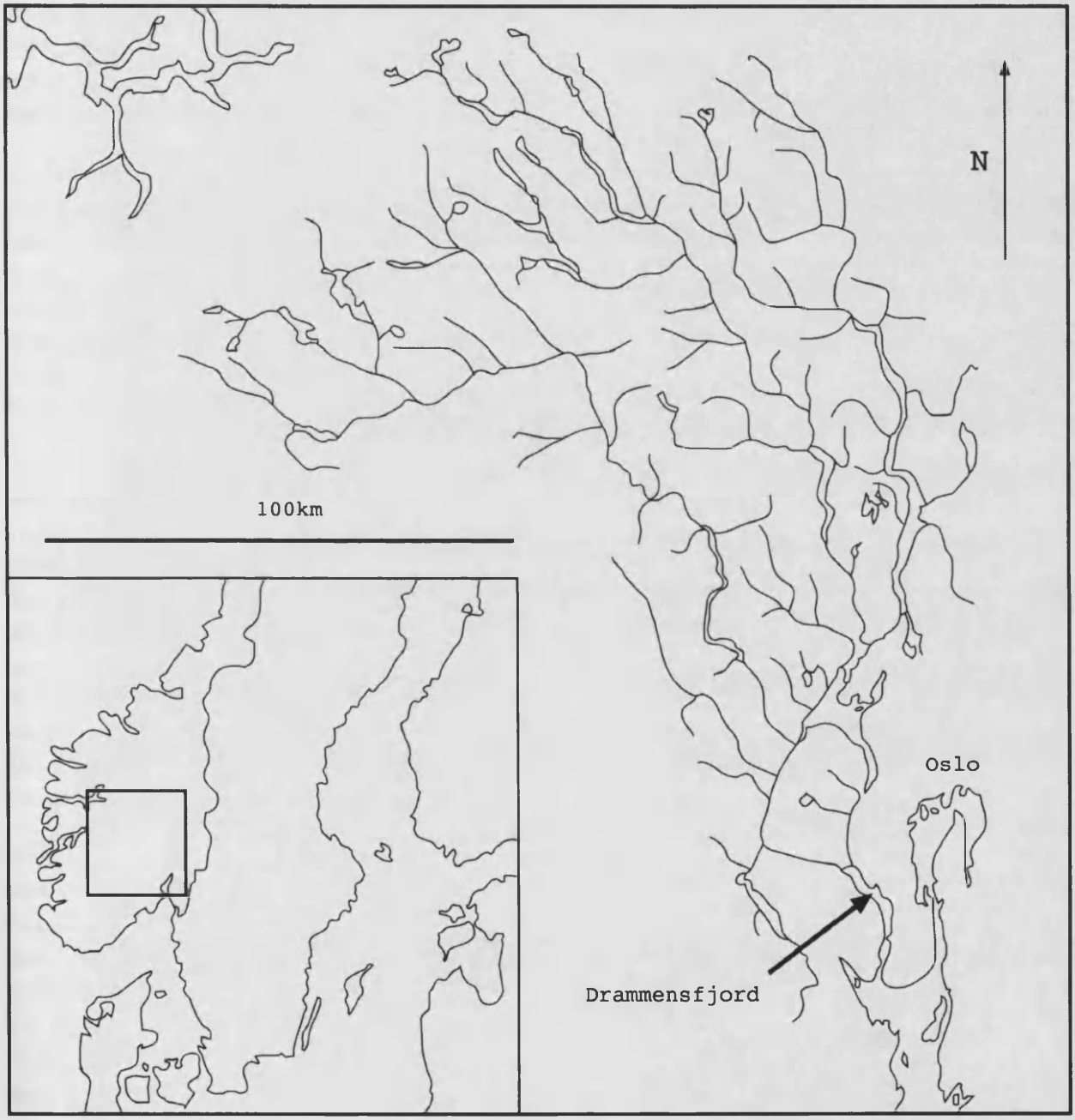

Figure 2.5: Drammensfjord catchment area showing lakes and drainage pattern. Redrawn from Braarud *et al.* [30].

2.6 Seasonal temperature change in the Drammensfjord catchment

This very large catchment undergoes substantial change with the seasonal cycle. Contrasts between winter and summer insolation become greater nearer the poles, such that in Scandinavia, there is a pronounced seasonal cycle in solar energy input. The northernmost part of Norway experiences c. 50 days of continual darkness in winter, and a comparable period of "midnight sun" in summer. The contrasts are not so extreme in Drammen, at c. 60°N, but there remains a pronounced seasonal cycle, in terms of both day length and insolation during daylight hours. "Spring" and "autumn" conditions are fleeting: the seasons essentially alternate between winter and summer conditions, separated by short transitions [36].

On latitudinal grounds, Scandinavia would be expected to be a very cold landmass, with its climate dominated by polar air masses, like the northernmost parts of North America [37]. As with all areas of the globe at latitudes greater than c. 50°, it has a negative energy balance [38]: incoming solar energy per unit area is less than energy lost from the Earth's surface. This deficit is compensated for by poleward atmospheric and oceanic heat transport from lower latitudes, where the energy balance is positive. John [36] gives three reasons why the climate of Scandinavia is very much less severe than expected.

First, the North Atlantic Conveyor (NAC) brings warm water northward from the tropics, and this warm current (the "Gulf Stream") warms the air above it. This warm, moist air rises, producing low pressure systems which move westward over Scandinavia. Condensation of the moist air releases latent heat, warming the air further. Second, the presence of the North Atlantic Ocean itself, even without the Gulf Stream, results in a significant warming effect [39] simply because evaporation leads to the latent warming effect of precipitation as described above: westerly winds blowing across the North Atlantic Ocean warm Scandinavia, via precipitation which releases this latent heat, and via direct transfer of "sensible heat". Third, the mixed distribution of land and sea allows these maritime aspects of the climate to penetrate across much of Scandinavia.

Southern Scandinavia, including Drammen, has a transitional climate, affected both by maritime air masses to the west, and continental air masses to the east [38]. Maritime influence tends to reduce seasonal temperature fluctuations, owing to the high specific heat capacity of the oceans; continental influence works the opposite way, giving stronger seasonal contrasts, i.e. warmer, drier summers and colder winters [37]. There is a 20-25°C difference between the coldest and warmest months in Drammen; by comparison, the maritime climate of Reykjavik has a difference of less than half as much [38].

2.7 Seasonal precipitation change in the Drammensfjord catchment

Seasonal changes in precipitation are more complex than those in temperature. Average precipitation in the Oslo area is 800-900mm [40], and precipitation occurs year-round, without a pronounced seasonal maximum [37]. The prevailing westerly winds mean that the west coast of Norway receives more precipitation than the interior. On the west

coast, most of the rain falls during winter because of stronger cyclonic activity: more depressions move in over the coast, releasing more precipitation [38].

In addition, there is a near-continuous orographic barrier, 1,200-2,470m high, running north-south over most of the length of Norway, close to the west coast. This mountainous area receives most of the precipitation, since it forces warm, moist air masses upwards, promoting condensation of the water vapour [35]. Behind this barrier there are areas of "rain shadow" which receive the least precipitation in Norway. Smaller-scale orographic influence occurs across Scandinavia: local variations in precipitation are large across the whole landmass, owing to its variable topography [38].

Drammen itself is just far north enough to be behind this orographic barrier. In consequence, it has an inland precipitation regime, with maximum rainfall in late summer and early autumn: July and August are the wettest months [34]. A slow, stable inflow of air is exposed to convective heating, which is most effective during the warmer parts of the year, when the air is more humid and convective heating is more intense. So, for Drammen, convective precipitation dominates during the summer [35].

Drammen also receives much cyclonic precipitation, however, especially in late winter. Then, the polar front moves southward, allowing cyclones to come in from the south and southwest, bringing rain to Denmark and, augmented by orographic uplift, southern Norway: the latter falls mostly as snow. It is these systems which bring in acid rain from the industrial areas of Britain and Germany [35]. Early spring is the time of least precipitation in Drammen [34].

Southern Norway generally has snow cover from November until April [38]. In addition, the Gulf of Bothnia and the northern Baltic Sea freeze every year. Oslofjord and Drammensfjord only freeze during very cold winters [37].

So, there is no distinct "wet season" in the Drammen catchment. Seasonal changes in sedimentation result from the *temperature* contrast between the seasons: most of the precipitation that falls on Drammen is rain, but a significant amount also falls between November and April, and this is stored in the Drammen catchment as snow. This difference in behaviour (snow being largely stored, rain being largely discharged) is of great importance in understanding the Drammensfjord sediment record.

2.8 Seasonal changes in river discharge in the Drammensfjord catchment

It is assumed that the amount of snow that falls is largely determined by the same controls as rainfall: the passage of cyclones over the area during the winter. These are driven by westerly winds from the North Atlantic, so presumably more intense westerly winds would bring in more snow. However, the warmth of the North Atlantic, even in winter, tends to inhibit snowfall from westerly systems: the snow often melts before it reaches the ground [41]. The role of other air masses in winter also needs to be recognised, e.g. colder continental air masses from the south and east. But snowfall is only one part of snow hydrology. The other crucial part is snowmelt. This

is an important process to understand (e.g. to predict floods) and has been closely studied, yet the controls on snowmelt are complex and poorly understood.

Maintenance of snow on the ground requires both air temperature and ground surface temperature to be below 0°C; the most important meteorological variable controlling snowmelt is air temperature [41]. Some models show both reduced snow amount and shorter snow cover duration in a warmer setting, even with increased precipitation [e.g. 42]. However, if a model is to be constructed, including other variables gives a much better fit to known behaviour. In addition, the melting snow surface can affect the air temperature itself, complicating the picture. The system controlling runoff from a snowpack is "enormously complex" [41], especially where the catchment is forested, and except for very small catchments, even the best models are still too inaccurate to be of much use. It is simplest to assume that snowmelt in the Drammen catchment is near-instantaneous and complete, occurring during the rapid switch from winter to summer conditions, usually in May.

High in the Drammensfjord catchment, glaciers are maintained by the low temperatures at altitude and fed by orographic precipitation. These presumably influence the runoff regime of the catchment; this would occur even if only a small area of glaciers were involved [35]. Typical glacial runoff regimes have a prolonged summer peak, between May and August [35]. Glacial runoff is controlled by temperature, since it is due to ablation of the glacier. Precipitation trends only affect glacial runoff over the long term (decades or more) as they affect how the glacier waxes and wanes: the year-to-year signal is temperature-controlled.

Next, consider runoff and river discharge patterns in the Drammen catchment. Note that strictly speaking, "catchment" and "watershed" refer to surface runoff only; "drainage basin" includes both surface runoff and groundwater input [43]. But for the Drammen region, groundwater input is minimal, so the terms are roughly equivalent. The Drammen catchment has a low groundwater potential, because of its thin soil cover and impermeable crystalline bedrock. Following rainfall and snowmelt, most of the water runs straight into the river: there is a high runoff coefficient [35]. The Drammen basin could therefore be described as "flashy": heavy rainfall is quickly translated into swollen rivers.

On a larger scale, however, the size of the Drammen basin means that runoff mechanisms are not important in controlling river discharge into the fjord; this is because the time that water spends within the river channels is so much greater than the time it spends reaching the channels in the first place [44]. The Drammen basin is "network-dominated". Thus runoff can be considered as an instantaneous process. Nonetheless, modelling the precipitation-discharge relationship in the basin is still difficult. There is not a straightforward correspondence between the rainfall input and the river discharge (i.e. between hyetograph and hydrograph), because of both the overwhelming influence of snowmelt, and various damping effects on rainfall variations.

It should also be borne in mind that groundwater does play a significant role in maintaining the flow of the River Drammen through the winter, when precipitation falls as snow; at this time, the river is fed only by groundwater draining into it.

Groundwater supplies charged up by large storm events can be gradually discharged over long time periods: months, or even years.

A simplified model of seasonal discharge for the River Drammen consists of a sharp peak starting in May/June, when spring melting occurs, relatively high flow through the summer, then a fall to a minimum in winter when precipitation is stored as snow, and the river is fed only from groundwater. The maximum river discharge coincides with the early summer rainfall minimum around Drammen itself.

However, real river discharge patterns are more complicated. Some Scandinavian rivers have two, or even three, discharge maxima. The first is due to snowmelt in lowland, forested regions; the second, and third, are due to melting of snow in higher, mountainous regions, which occurs later, in late spring and early summer, because of the colder temperatures at altitude. Local terminology names these the "home flood" and the "mountain flood" [38]. Together, these can merge into an extended flood period, lasting up to 2 or 3 months [34]; glacial ablation also starts later than lowland snowmelt, continues throughout the summer, and may contribute to the prolonged flood period.

Another cause of secondary discharge maxima is heavy rainfall in summer and autumn; this occurs owing to convective precipitation. However, in major rivers like the Drammen, summer rainstorms only produce minor fluctuations in discharge because of the limited extent of convective precipitation: rain only falls over a small area of the catchment at any one time [35]. Only in small river basins does this have a significant effect.

The drainage pattern of the Drammen basin is significant in controlling how its discharge varies. The dendritic drainage favours higher and sharper spring and summer flood peaks, because it allows separate flood flows to coalesce. A more elongate drainage pattern would allow "evacuation" of downstream flood events before arrival of others from upstream [41].

Lakes within a river's drainage basin serve to regulate its flow, reducing or removing entirely the effect of seasonal rainfall variations. Some rivers in Scandinavia have a smoothed discharge pattern because of such lakes; their role as a storage element for water is made even more significant by the lack of groundwater capacity in most areas. Several vast lakes exist in southern Scandinavia, and these reduce the annual variation in discharge of the rivers they feed to near zero [38]. However, although the River Drammen drains many lakes (e.g. Lake Tyrifjord), these are not large enough to dampen the seasonal variations. The Drammen basin is "large" in the sense that it filters out high-frequency variation in rainfall, via channel storage and its lakes, but it still shows a pronounced seasonal variation due to snowmelt. A discharge station at Drammen is maintained by the Norwegian Meteorological Institute (DMNI). Discharge records are available for a number of years, and they show the expected pattern of a pronounced peak in spring, falling to a lower level in summer and autumn and then to a very low level in winter. They are considered in more detail in section 2.12, since mankind has had a major influence in recent times on the seasonal discharge cycle of the River Drammen.

2.9 Seasonal sediment transport in the Drammensfjord catchment

This seasonal peak in river discharge during the spring results in a strong seasonal cycle in sediment transport and deposition. The River Drammen deposits much of its sedimentary load immediately upon entering Drammensfjord, building up a delta at the river mouth. Cores from the deeper, anoxic part of Drammensfjord contain only fine-grained suspended sediment, which is carried much further out into the fjord. Thus, only mud-grade sediment (mixed clay and silt, with particle diameters < 0.062mm) is significant for the deep Drammensfjord cores: its sources, transport, and deposition. This is fine enough to be kept suspended in the water column by turbulence. Coarser bed load, and dissolved sediment load, can be ignored.

Suspended sediment comes from several sources [44]: surface erosion supplies sediment to the river channel; this is supplemented by channel erosion, bank collapse, and so on, occurring within the channel itself. Together these processes produce "wash load", which is continuously suspended, and "suspended bed load", which is kept suspended via interaction with the stream bed. Such erosion of cohesive sediment is not related to particle grain size but involves attractive forces between the particles themselves, and is thus very complex to model [44]. For simplicity, it is perhaps best considered as occurring proportionally to runoff.

Indeed, it is unlikely in a basin the size of the River Drammen's that there will be any clear relationship between upstream erosion and sediment output at the fjord head [44]. This is because as drainage area increases, so do the opportunities for sediment storage: the further downstream, the lower the concentration of suspended sediment owing to deposition along the way. Of course, this sediment is also frequently remobilised. So the sediment input to the fjord is only a good proxy for river discharge; its relationship with upstream runoff and erosion is more complex.

The grain size of the suspended bed load also depends on river discharge: a river in full flood may be able to carry coarse silt and fine sand in suspension because of the high turbulence of its flow, whereas during periods of low flow this material would be transported as bed load. However, any sediment coarser than mud-grade is unlikely to reach the deep fjord, except via the separate mechanism of mass movements.

Runoff and river discharge control the amount of suspended sediment carried by the river, and obviously these two processes are closely linked. Thus, the amount of sediment entering the deep fjord, and possibly its grain size, should vary annually, with peaks reflecting the seasonal changes in river discharge. The relation between the two may not be exact, but sediment concentrations will be maximised during brief, high-discharge periods [45]. Globally, this behaviour is characteristic of suspended sediment: it is the dominant form of river sediment transport, but it is more erratic than the dissolved load and is mostly associated with high-magnitude discharges [44]. In detail, suspended bed load is proportional to river discharge, whereas wash load has a more complex set of controls [1].

The highest concentration of suspended sediment occurs during the spring flood; this may be increased beyond the amount expected by discharge changes alone, because of the

"bed clearing" that occurs after a prolonged period of low discharge [46]. High-discharge events of similar magnitude later in the year may not bring as much suspended sediment into the fjord. The relationship between discharge and sediment supply may be more complex than a power function [47]: there may be thresholds above which the function changes, for example.

Directly-measured experimental data concerning sediment accumulation in Drammensfjord are scarce. The Norwegian Institute for Water Research (NIVA) installed sediment traps in Drammensfjord in 1982-83 [14]. As expected, clastic sediment is mainly supplied to the fjord by the spring flood. The relationship between discharge and sediment supply is exemplified by the difference between 1982, where the very small spring flood supplied 5 g/m^2 per day of sediment to the trap nearest Drammen, and 1983, where a much larger spring flood supplied c. 90-100 g/m^2 per day of sediment to the same trap [14]. The relationship between river discharge and particulate sediment input to the fjord has been further confirmed by sediment trap investigations in 1991 and 1995 by Magnusson [48].

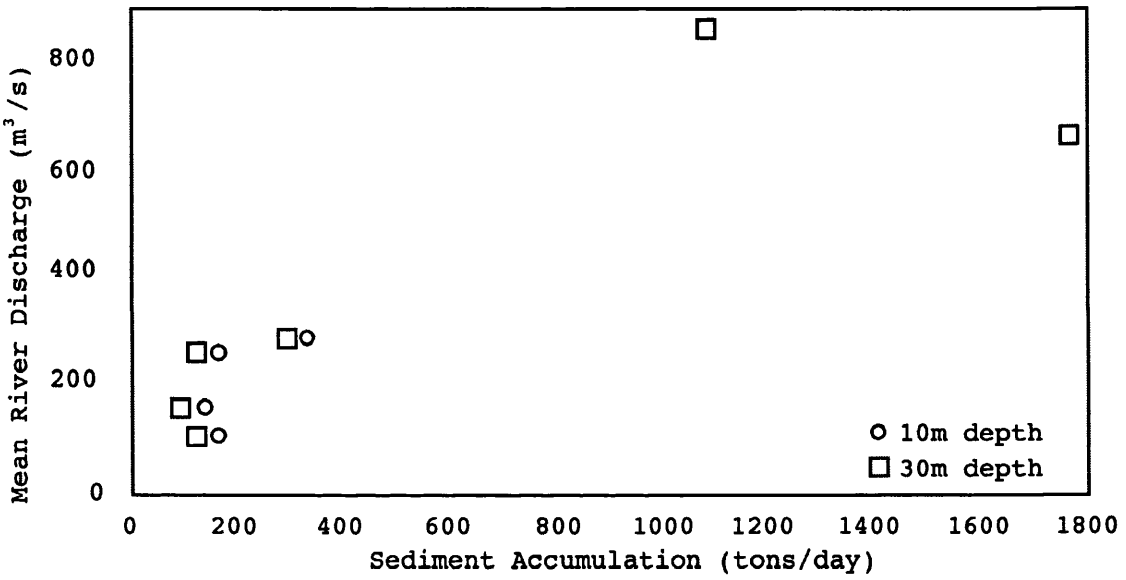

Figure 2.6: Relationship between river discharge and sediment accumulation in Drammensfjord, as estimated from sediment trap studies. Redrawn from Magnusson and Næs [14].

At low river discharges, the traps show that sediment accumulation is dominated by autochthonous sediment: mainly phytoplankton [14]. This is discussed in more detail in the next section. In essence, Drammensfjord acts as a natural, large-scale sediment trap: very little sediment is transported over the sill into the outer fjord. The seasonal pulse of terrigenous sediment brought by the River Drammen in flood settles within the fjord as a distinct "spring layer" each year, forming one component of each varve.

2.10 Seasonal changes in the Drammensfjord biota

Drammensfjord is generally an inhospitable environment. The major seasonal changes in fjord conditions that have been described tend to restrict the flora and fauna to

fast-flourishing opportunist species, which bloom when conditions are right, then rapidly die off. A detailed picture of the seasonal plankton cycle in Drammensfjord is given by Braarud *et al.* [30]. However, this study was made during 1951, at a time when the fjord was much more polluted than it is today, and than it has been during most of the Holocene. More recent work by NIVA [14,48-50] gives additional insight into the seasonal cycle of productivity in Drammensfjord.

Primary productivity in Drammensfjord is constrained by the limited availability of light, and changing water temperature and salinity during the seasonal cycle. Between late November and early March, the surface water of Drammensfjord is at around 0°C [14], and as for the Inner Oslofjord [51], at least part of the fjord freezes each winter. In exceptional years (c. 10-25% of the time [52]) the fjord surface freezes entirely. This reduces sediment flux to the deep fjord by 90-95% [1], by inhibiting wind and wave action, and reducing the shallow water resuspension of sediment. In contrast, the deep water in the fjord remains at c. 7°C all year round [14], although low oxygen availability greatly restricts the deep water biota. The deep fjord biota is discussed in section 2.12, since anthropogenic anoxia has affected it so strongly.

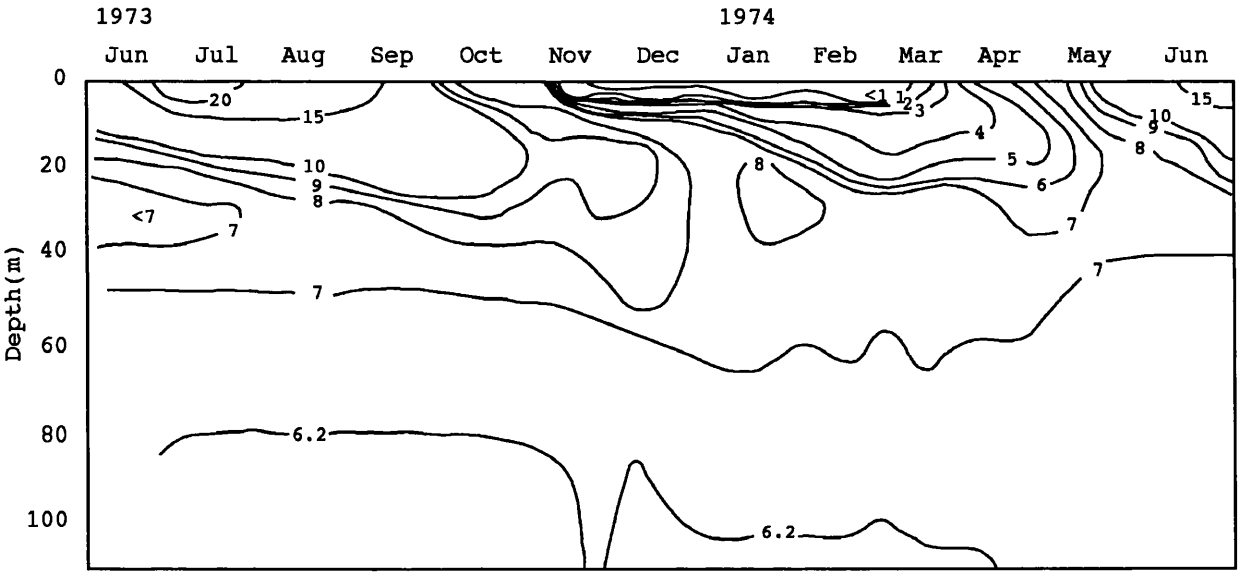

Figure 2.7: Seasonal variations in temperature (indicated in °C) with water depth in Drammensfjord in 1973-1974. The measurement site was just inside the sill, at the deepest point of the fjord. Redrawn from Magnusson and Næs [14].

So, the first opportunity for primary productivity to start up is in March or April, when the winter ends, the ice melts, and the days become longer, increasing the availability of light for photosynthesis. The spring flood brings a layer of freshwater to the fjord which is relatively rich in nutrients, although its high sediment load makes it very turbid. This restricts the depth to which sunlight can penetrate; Braarud *et al.* [30] found that the depth at which light availability was 0.01% of its surface value was only 6.5-7m in April. More recently, Alve [13] found photosynthesis restricted to the upper 4-5m of the fjord; Magnusson [48] established that the lack of visibility is caused by terrigenous sediment: suspended clay particles and organic matter (e.g. humus).

Outward flow of the freshwater surface layer also tends to reduce the possibility of extensive phytoplankton blooms: the flushing time of the surface layer is only 6 to 18 days [30]. Nonetheless, during the interval of approximately May to November, conditions are suitable for freshwater phytoplankton blooms in Drammensfjord, mainly of diatoms, initiated by organisms carried into the fjord by the River Drammen [30]. Maxima tend to occur in late summer and early autumn, as with many lakes in eastern Norway [30].

After the ice melts, but before the freshwater surface layer becomes established, there is a brief "window" in March and April when there is saline water at the surface of the fjord. Similarly, as winter approaches, the river discharge declines, the surface freshwater is carried out of the fjord entirely, and there is another saline "window" in October to November. During these two intervals, there are occasional blooms of marine phytoplankton, typically diatoms, dinoflagellates, and silicoflagellates, though they are limited by the low light availability at these times of year [30]. The 1951 study of Braarud *et al.* [30] found "no definite indications of any considerable growth" in marine diatom populations during these intervals, but in 1951 they were hindered by pollution increasing the fjord turbidity - though eutrophication of the fjord may have compensated for this.

So, the annual cycle in Drammensfjord productivity consists of an unproductive winter, two brief intervals either side of winter where marine phytoplankton have a chance to bloom, and a long summer during which freshwater phytoplankton can bloom. The depth of the freshwater "lid" is sufficient to prevent any photosynthesis in the saline water beneath it during the summer [30]. So in effect, there are three separate environments: the anoxic deep water, the oxygenated saline surface layer, and the seasonal freshwater "lid". The alternation in surface conditions means that marine and freshwater diatom populations in Drammensfjord have to be restocked every year: marine diatoms from the outer fjord, beyond the sill, and freshwater diatoms from the river input [30].

Overall fjord productivity is low: Braarud *et al.* [30] describe Drammensfjord as a "desert" compared to Inner Oslofjord and the outer fjord: "The inner Drammensfjord basin is doubtless the least productive area of the Norwegian coastal region which has been investigated so far".

No figures are available for total production, and its distribution amongst different plankton types, in Drammensfjord. For purposes of comparison, daily primary production in neighbouring Inner Oslofjord is 1-7gCm^{-2} in summer and 0.011-0.024gCm^{-2} in winter [53]. Ultraplankton (<5μm diameter) blooms, including bacteria and cyanobacteria, account for 70-90% of the primary production in Inner Oslofjord [54]. Nanoplankton blooms, such as of the coccolithophorid *Emiliania huxleyi*, occur in some Scandinavian fjords, e.g. Samnangerfjord, western Norway [55], but are not known to occur in Drammensfjord.

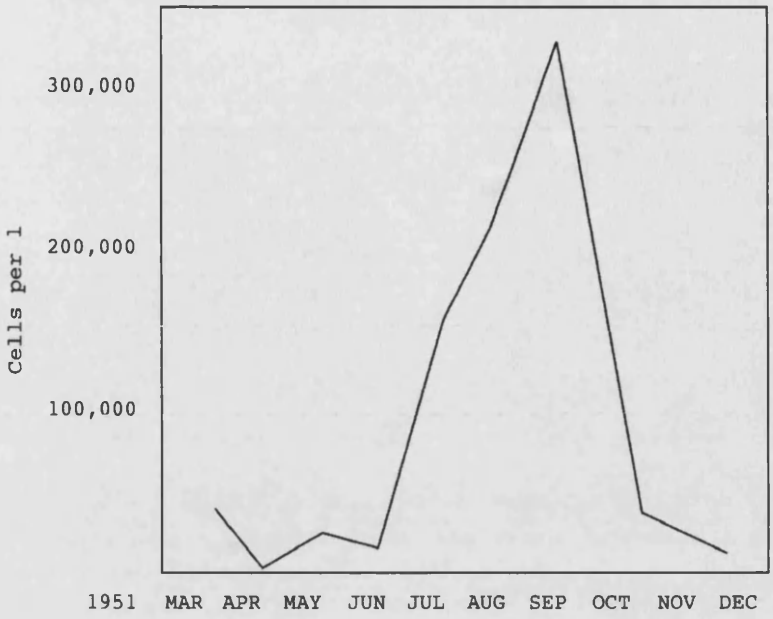

Figure 2.8: The annual cycle in freshwater phytoplankton abundance in Drammensfjord as measured in 1951, with a peak during August and September. The measurements are monthly, so the peak does not reflect one individual phytoplankton bloom (which would be expected to show exponential growth). Redrawn from Braarud *et al.* [30].

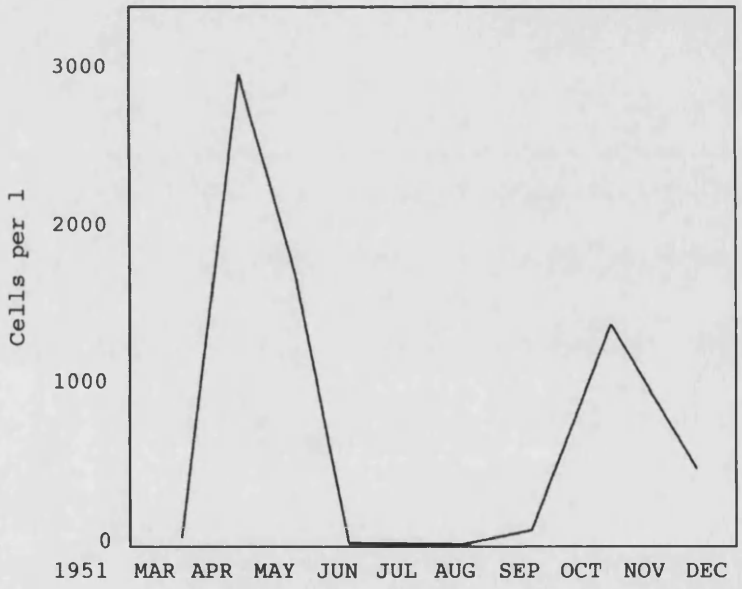

Figure 2.9: The annual cycle in marine dinoflagellate abundance in Drammensfjord in 1951, showing peaks in April and November. Redrawn from Braarud *et al.* [30].

The limits on production in Drammensfjord probably change seasonally, as they do in Inner Oslofjord. Any brief period of increased river discharge into Inner Oslofjord can induce a phytoplankton bloom; such floodwater is usually very turbid, making the rate of photosynthesis light-limited, and favouring species that can cope with low light levels [56]. The major annual bloom in spring in Inner Oslofjord is limited by the availability of nitrogen and phosphorus [57]; subsequent summer blooms are restricted by the amount of nutrients left over from the spring bloom, such that their sizes are inversely related [58]. Detailed sampling of Drammensfjord during plankton

blooms is required to establish whether these limitations on production apply to both fjords.

Plankton blooms in Drammensfjord result in a rain of planktonic material to the fjord bottom. But they are not the only biological contributor to the fjord sediment. It is also necessary to consider the Drammen catchment, and the sediment input from the soil and vegetation that are found there. These have been continuously present since the early Holocene, albeit in varying states depending on, for example, the stage of postglacial ecological progression, and the impact of mankind (see section 2.12). What contribution does this terrestrial biota (which is mostly coniferous forest, at present) make to sediment accumulation in Drammensfjord?

First, it is useful to establish the total organic carbon (TOC) content of the sediments. Surface sediments below 10m water depth in Drammensfjord have TOC contents of c. 2-3%, and up to 4-5% in deeper water [13]. Deeper-water sediment naturally contains more organic carbon for two reasons: coarser sediment in shallow water allows greater interstitial circulation of water, supplying more oxygen to break down organic carbon, and the deeper water is a lower energy environment, allowing fine-grained organic matter to settle out.

However, these surface sediment values are elevated by recent anthropogenic pollution; below 20cm depth in the sediment, TOC content falls to c. 1% [28], which is also a representative figure for the NIOZ Drammensfjord cores [59]. Overall, TOC content in Drammensfjord is higher than in the outer fjord (Sandebukta, for example, has TOC contents of c. 0.8-2.2% [12]), and is comparable to the Inner Oslofjord (which has a surface sediment TOC content of c. 3% [60,61]).

What are the main sources of this organic matter in the fjord sediment? Autochthonous sediment, that produced within the fjord, includes phytoplankton such as diatoms and dinoflagellates, zooplankton that feed on the phytoplankton, plus bacteria and amorphous organic matter. But there is also a substantial contribution from allochthonous organic matter, including windblown pollen grains, dissolved organic compounds from the soil, and vascular plant material: from microscopic fibres up to leaves and tree branches.

The relative contributions of different sources can be assessed using carbon:nitrogen (C:N) ratios. Marine plankton has a C:N ratio of c. 6.6. Marine humics (decay-resistant, refractory compounds from marine plankton) have C:N ratios of c. 12-14. Terrestrial humics have C:N ratios of c. 48, and vascular plant material has C:N ratios of c. 100 [62]. Sediment trap investigations could potentially reveal seasonal changes in C:N ratios [1], but overall values are all that are available.

Drammensfjord sediment has a C:N ratio of c. 20 in the northern part of the fjord, c. 17 in the central part, and c. 15 in the southern part [13]. This shows that the sediment closer to the mouth of the River Drammen receives a greater contribution of allochthonous organic matter. Overall, the C:N ratios are relatively high, indicating low productivity and a substantial contribution from terrestrial organic matter. This is borne out by the appearance and composition of organic matter extracted from the

NIOZ Drammensfjord cores [63]. In contrast, sediments of the Inner Oslofjord have C:N ratios of c. 6.6 [64], indicating that virtually all their organic matter is produced within the water column.

So, the various seasonal phytoplankton blooms that occur during the year in Drammensfjord are complemented by terrigenous organic matter carried in by the River Drammen. It is likely that the latter reaches a maximum with the spring flood, at least in the form of particulate organic carbon (POC). It may be that for dissolved organic carbon (DOC), maximal terrigenous input occurs during the winter, when low temperatures inhibit its decomposition [65]. In any case, variations in organic carbon supply to the fjord are not directly reflected in variations in supply to the sediment, because of the behaviour of organic matter in the water column.

POC, defined as particles larger than 1μm in diameter (and therefore too large to be kept suspended indefinitely by Brownian motion), is colonised by bacteria as it sinks. Only the larger particles (e.g. faecal pellets) sink fast enough to reach the sediment without significant bacterial degradation [66]. Some develop into mucoid filaments or "streamers", which join up at depth to form interconnected webs [1]. Agglomerations of "marine snow" are very common in fjords owing to the lack of turbulence in the water column [1].

Bacterial degradation converts POC to dissolved organic carbon (DOC): indeed, the preservation of any organic matter in the sediments implies partial or interrupted bacterial degradation [67]. However, DOC can also be converted to POC: the process is reversible. For example, during estuarine mixing, seawater can cause humic substances to flocculate [68]. In addition, some bacteria secrete "slime" which traps other organic molecules, converting DOC to POC [69]. In the open ocean, the visual appearance of most organic particles suggests that they are not recognisable parts of any particular organism but have been formed within the water column by these various processes [69]. It is easy to see how repeated conversion between DOC (which does not settle out) and POC (which does) could significantly delay deposition of waterborne organic matter, smoothing out variations in input to the water column.

In the deep, quiet parts of Drammensfjord, then, there is a continuous "background" deposition of fine-grained clastic sediment, sinking plankton, and organic matter: in appearance, an unconsolidated black sludge. It is this which forms the remainder of the annual cycle of deposition in Drammensfjord, in addition to the clastic pulse from the spring flood.

2.11 Episodic sedimentation events in Drammensfjord

Sediment in Drammensfjord tends to get finer-grained as water depth increases [13], since coarse sediment is not transported so far into the fjord, leaving fine sediment to settle out in the low-energy environment of the deep water. At water depths of less than 10m, the sand content of the surface sediment can exceed 50% [13]; below this, mud-grade sediments dominate, and in the deepest parts of the fjord, continuous sediment accumulation is entirely mud-grade.

However, as well as the "rain" of fine-grained clastic and biogenic sediment which changes with the seasons, there are also episodic sedimentation events, some of which bring coarser sediment into the deep fjord. The term "episodic" is used in this context to denote random events that do not follow a predictable rhythm, in contrast to "periodic" events. In the terminology of time-series analysis, "periodic" events follow a predictable cycle, like the swinging of a pendulum. In Drammensfjord, then, there are periodic changes in sedimentation through the seasonal cycle, but there are also episodic sedimentation events superimposed on this cycle.

So, where does the coarser sediment in the deep fjord originate? Some of this sandy sediment comes from erosion of the moraine sill at Svelvik [13], but the main source is another terminal moraine deposit that is being eroded by the River Drammen, upstream from Drammensfjord, erosion of which began c. 3,000 years ago [22]. The main sand input to the fjord is, therefore, the mouth of the River Drammen. Sand is deposited at the river mouth, where there is a prograding delta front, and by smaller rivers in other shallow areas of the fjord.

Furthermore, like most fjords, Drammensfjord has very steep sides, and sediment deposited on them is liable to become unstable, initiating mass movement down the slope onto the flat fjord bottom. Indeed, such mass movement is a characteristic feature of fjord sedimentation [1]. This results in episodic deposition of "event beds" in the deep fjord. Another source of event beds is the river itself, which under certain conditions can form dense, sediment-rich plumes that can reach the deep fjord. These two categories of event beds are considered separately.

2.11.1 Event beds originating within Drammensfjord

Unconsolidated sediment originally deposited in shallow water can be re-sedimented into deep water by various types of flow under gravity [70]. Plastic flows retain some mechanical strength and will, therefore, "freeze" at some point, preserving some of the original sediment structure; fluidal flows, in contrast, have no strength and retain no structure. In both cases, flow is initiated in fjord settings because of a high rate of sediment accumulation on a high-angle slope, possibly aided by the generation of methane gas during low-temperature diagenesis of organic matter [1].

Whole blocks of sediment can move as slumps and slides. More significant for the transfer of coarse sediment to the deep fjord are non-cohesive debris flows [70], which result from grain avalanching when deposition causes the angle of rest to be exceeded. These remain mobile owing to intergranular collisions. Dilution of slumps and debris flows can produce turbidity currents, which remain mobile via autosuspension and which can flow downslope over long distances [70].

The event beds that result from these flows depend not only on the flow mechanism but also on the sediment source and the distance travelled. In fjords such as Drammensfjord, sand-grade debris flows produce massive sandstones sometimes termed "homogenites" [70]. Classical turbidites should produce a sequence of bedforms corresponding to a decelerating flow regime [70], but distal turbidites in the deep fjord are likely to be restricted to thin, normally-graded sand beds.

Bute Inlet, a fjord in British Columbia, is a useful comparator because its episodic sedimentation events have been closely studied [71]. Slumped blocks can be identified using sidescan sonar; such slumps can evolve downslope into debris flows and turbidity currents. These produce well-sorted, medium-to-fine grained sand beds with sharp tops and bases. Some have faint laminations. Thick event beds (50-200cm) result from transitional flows; thinner ones (10-30cm) from true turbidites; all are likely to be triggered by slope failures within the fjord, rather than by river-borne plumes (see below). Such a detailed picture was obtained by using underwater sensors to track sediment flows: this would be necessary to get a comparable picture for Drammensfjord.

2.11.2 Event beds originating outside Drammensfjord

There are also events that originate outside Drammensfjord that can transport large amounts of sediment to the deep fjord. These require an exceptionally high sediment load in the river input. Understanding how these conditions arise requires some discussion of the geotechnical aspects of the Drammen catchment.

Large areas of the Drammen catchment are covered by sensitive clay or "quickclay", so named for its geotechnical properties [23]. It was rapidly deposited adjacent to the ice margin towards the end of the Last Glacial, and consists mostly of rock flour produced by glacial grinding and outwash. It is a distinctive type of sediment found only in Scandinavia, Canada, New Zealand, and Greenland [23]. Not all of the clay has the same properties, but two aspects of its behaviour are significant: so much so that the Norwegian Geotechnical Institute was set up in Oslo in 1953 to do research on quickclay [e.g. 72]. The first aspect is the tendency of quickclay to cause serious ground distortion, owing to shrinkage as its moisture content is reduced [23]; for example, the Old Town Hall in Drammen has sunk 90cm in the last 100 years, causing severe damage [22]. The second aspect, which is relevant to the Drammensfjord sediment record, is the high frequency of landslips in quickclay.

Landslips are common in quickclay because it is structurally weak. Because it was deposited in a marine environment, its pore water was originally saline. A combination of downward percolation of groundwater and upward artesian pressure gradients reduces the electrolytic concentration of the pore water, causing a reduction in the clay's shear strength over time [23]. After an initial landslip, quickclay forms a viscous slurry and flows rapidly downhill. Landslips develop retrogressively, slice by slice, and can occur on very gentle slopes and cover large areas [23]. Perhaps the best known example, because it was fortuitously filmed, is the landslip at Rissa, Norway, in 1978: the largest landslip in Norway in the last 100 years. This was initiated artificially, by an ill-advised small excavation. Published research on landslips in the Drammen catchment is scarce, but a large quickclay landslip is known to have occurred at Ullensaker, c. 40km northeast of Oslo, in 1953 [73].

Landslips can be initiated by riverbank erosion, or simply by rainfall loading a quickclay slope. Small events occur yearly [23], mostly in the spring, when river erosion and pore water pressure are at their highest. Major events are rarer; multiple landslips can be triggered by storms, floods, and earthquakes, all of which affect the Drammen catchment. A useful analogue is Saguenay Fjord, Canada, which suffered major

events in AD 1663 after an earthquake [74], in 1971 after a month of heavy rain [75], and in 1996 after a 36-hour storm [76]. These events caused direct mobilisation of large amounts of sediment. In addition, some landslips caused damming of rivers, leading to the build-up of a "head" followed by damburst and release of an exceptionally-swollen sediment-laden flow.

It is this mobilisation of large amounts of sediment that causes sediment-laden plumes in the form of "hyperpycnal flows" [77] to enter the fjord. These are the other source of the event beds discussed earlier in the section.

Hyperpycnal flows occur when river water is significantly more dense than the basin into which it flows [70]. In the case of Drammensfjord and other stratified fjords, the river becomes more dense than the salt water of the fjord when it is carrying a large load of suspended sediment. The suspended sediment increases the density of the inflowing freshwater plume such that it is denser than the saltwater - it is "negatively buoyant" - so that the plume flows along the basin floor. As with slumps and debris flows, hyperpycnal flows can ignite turbidity currents [77]. This is another way, then, for sediment to be transported from the river mouth into the deep fjord.

The sedimentary impact of hyperpycnal flows can be enormous. For example, around the Saguenay Fjord basin in AD 1663, a violent earthquake caused widespread landslips, mobilising c. 210 $\times$ 10^6 m^3 of sediment [74]. The earthquake immediately resulted in debris flows and turbidity currents within the fjord. In addition, landslips dammed the River Saguenay, causing a build-up of freshwater and a very large spring flood in the next year. This initiated a prolonged hyperpycnal flow, fed by erosion of the landslipped sediment, which lasted approximately one month according to eyewitness accounts [74]. Its density maintained by super-elevated sediment concentrations, this flow eroded parts of the basin floor, and resulted in deposition of a turbidite which is 10m thick in places. Similar trains of events occurred after the 1971 and 1996 landslips and flooding.

Deposits from hyperpycnal flows share some features with those from mass movement events within the fjord: sharp tops and bases, and sometimes normal grading. They can be identified [78] based on their sedimentary composition: since they consist mostly of quickclay, they have much lower organic carbon contents than the background sediment, and may contain reworked Lateglacial foraminifera. Incidentally, hyperpycnal flows also bring oxygenated water into the deep fjord; the AD 1663 event caused complete renewal of the deep water in Saguenay Fjord [77].

How often do hyperpycnal flows occur in Drammensfjord? Such flows will only occur regularly in situations where the density contrast between river water and basin water is large, such as when cold, sediment-laden water flows into a warm lake, as occurs in tropical settings [70]. In the case of fjords, there is little temperature difference between river water and basin water, so a very high concentration of suspended sediment is needed, especially considering that the fresh river water needs to become denser than the saline deep fjord water. For this reason, hyperpycnal flows are more

common in fjords with direct glacial input, since these produce higher sediment concentrations in inflowing rivers [79].

Fjords without a direct glacial input, such as Drammensfjord, ordinarily experience deposition of coarse sediment at the river mouth and only gradual diffusion of finer sediment into the deep fjord. Landslipping on the scale of the AD 1663 Saguenay Fjord event, however, is not necessary to produce a hyperpycnal flow. Mulder *et al.* [77] suggest a minimum frequency of once per hundred years for generation of hyperpycnal flows by rivers entering the sea, and there is no reason why this estimate cannot also be applied to Drammensfjord.

In summary, "natural" sedimentation in the deep parts of Drammensfjord includes both a continuous, seasonally-changing rain of fine-grained sediment, and a variety of rapidly-deposited event beds including slumps, debris flows and turbidites that originate within the fjord, and hyperpycnal flows and turbidites that originate from the river mouth. Triggers for these event beds include storms, flooding, earthquakes, and landslips.

2.12 Anthropogenic influences on Drammensfjord

2.12.1 Human settlement around Drammensfjord

Ships have sailed around Drammensfjord for at least 1,000 years. The Vikings used Drammensfjord as a harbour: it is mentioned in the Sagas of Snorre (c. AD 1070) as "Drofn", meaning "grey river water", the original name for Drammen harbour [80]. The neighbouring settlement of Oslo was founded in AD 1024.

The port of Drammen was established in the 14th century. Timber was floated down the River Drammen to be loaded onto ships. By the mid 18th century, the river was affected by sawdust and woodchips from many sawmills [28]. The timber industry continued to grow until the end of the 18th century when paper and pulp mills were first constructed. The combined pollution from these soon threatened the local fishing industry [28]. Meanwhile, settlement around Drammensfjord continued, often originating along rivers which were used to generate power. Svelvik, at the fjord entrance, became a significant centre for timber export and shipbuilding after it was used as the winter port for Drammen during the worst of the Little Ice Age, when Drammensfjord froze too often for shipping to be feasible.

The River Drammen was until recently "an open sewer" [80]. It flows through some of the most densely populated areas of Norway [28], and it carried to Drammensfjord large amounts of industrial and agricultural pollution, as well as sewage from the many settlements in the area. The river is now clean, but much of the pollution that it supplied to Drammensfjord is still in the fjord. Unlike a port on the open coast, a port on a silled fjord faces the issue of pollution becoming trapped within the fjord. Remediation of fjord pollution, which can become concentrated in small fjord basins, is an important issue [1], and the Drammensfjord sediments are expected to record a significant human influence.

2.12.2 Regulation of river discharge into Drammensfjord

Winter storage of snow in the Drammen catchment produces a strong seasonal cycle in river discharge. Mankind has regulated this cycle, producing a more predictable level of discharge, which is more useful for power generation, and which reduces the need for flood defences. The overall mean annual discharge of the River Drammen is unchanged at c. 330m^3/s, but it varies less over the year, with the spring flood reduced, and a higher discharge during the winter. The time of minimum discharge has shifted from its natural position in winter to being in late summer [14].

Regulation has also increased the residence time of the freshwater surface layer in Drammensfjord, which alongside an increase in nutrient availability due to sewage pollution, served to increase the production of freshwater phytoplankton between 1961 and 1980 [14].

River flow regulation began in c. 1900 [81]. Further regulations were applied in the 1920s, and again in the 1950s and 1960s [14]. Unfortunately, there are no records of river discharge from the time before flow regulations: the earliest published discharge data begin in 1921. A summary of the discharge data, as published by NIVA [14], shows a distinct peak beginning in April and May across all the summarised intervals.

Interval	Year Mean	Jan	Feb	Mar	Apr	May	Jun	Jul	Aug	Sep	Oct	Nov	Dec
1921-50	314	66	50	58	240	842	721	463	375	357	290	184	113
1951-60	296	159	160	156	193	558	525	410	387	325	271	229	171
1961-70	305	189	191	196	239	563	492	269	304	338	374	306	197
1971-80	257	203	214	221	248	505	429	246	212	173	221	210	195
1982	257	232	232	244	304	502	352	190	91	121	300	271	238
1983	326	245	253	240	267	1011	554	215	182	240	248	236	219
1984	294	219	223	209	236	506	418	169	248	179	453	389	292

Figure 2.10: Table showing River Drammen monthly average discharge records, measured in m^3/s, for 1921-50, 1951-60, 1961-70, 1971-80, and 1982, 1983, and 1984. Data from [14].

More recently, the discharge data resolution has improved from monthly totals to mean discharges recorded over 24-hour intervals, allowing river flow variation to be studied in more detail. Such data are available for three years: 1982, 1991, and 1995. Comparing these three records illustrates the modern year-to-year variation in river discharge. 1995 was an exceptional year because of the very large spring flood across southern Norway [48]. 1991 was also an exceptional year, because of its near-absence of a spring flood peak [48]. 1982 is generally representative of typical conditions. However, under natural, pre-regulated conditions, it is likely that most years would more closely resemble 1995, and that the seasonal cycle in sedimentation would be correspondingly more pronounced [81].

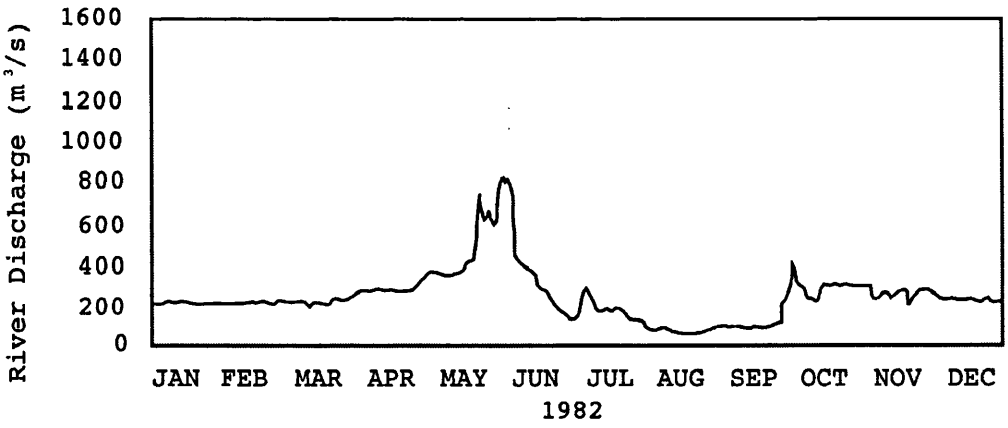

Figure 2.11: 24-hr mean discharge record for the River Drammen, 1982, showing a low, single peak in June. Redrawn from Magnusson [48].

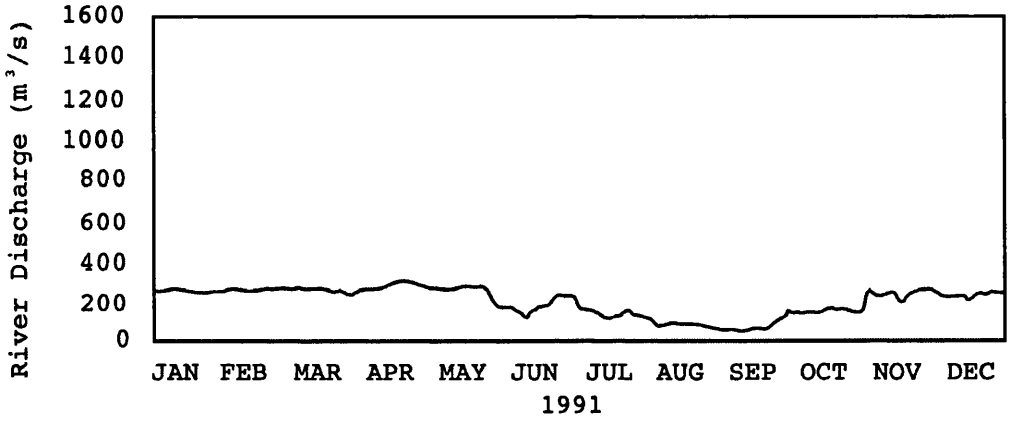

Figure 2.12: 24-hr mean discharge record for the River Drammen, 1991, showing no seasonal peak at all. Redrawn from Magnusson [48].

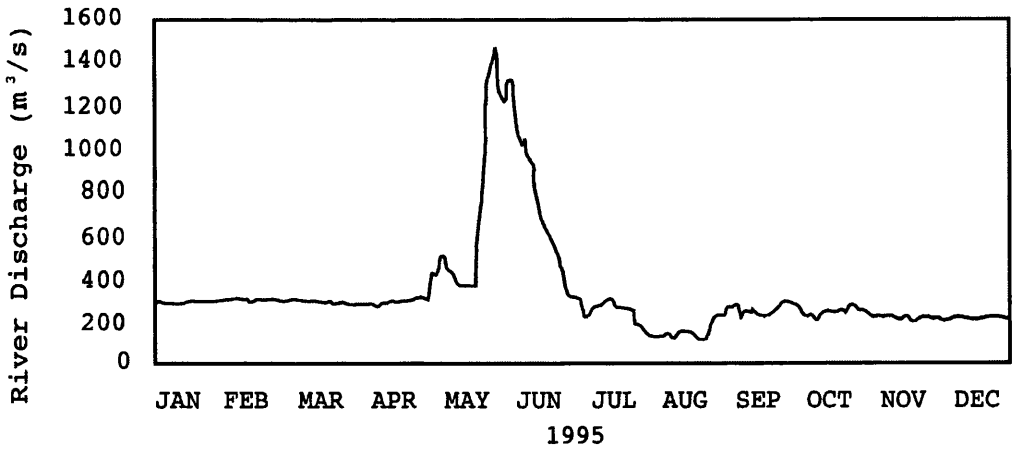

Figure 2.13: 24-hr mean discharge record for the River Drammen, 1995, showing very large single peak in June. Redrawn from Magnusson [48].

2.12.3 Sill excavation and natural stagnation of Drammensfjord

All ships entering Drammensfjord must pass through the narrow channel at Svelvik. The sill has been progressively excavated over the last hundred years to allow bigger ships to enter; the channel now allows ships up to the same size limit as the Panama Canal. In detail, the sill was c. 6m below sea-level in 1900 [16]; in 1933 it was excavated to 8m depth [82]; and in 1951 to 10m depth [26], at which it has remained [28]. This deepening has made renewal events in Drammensfjord more likely to occur. However, as discussed in section 2.4, the hydrography of Drammensfjord is such that a slight further excavation of the sill, to 12-15m depth, would be required to effect a major increase in oxygen availability in the deep fjord [14]. Excavation of the sill during the last century has not affected oxygen availability greatly.

The depth of the Svelvik sill has also been affected by isostatic rebound, which is occurring at c. 3mm per year [22]. In effect, the sill is slowly closing off the fjord: without excavation, Drammensfjord is destined to become fully isolated from the sea. The deep fjord water in Drammensfjord is stagnant, containing free hydrogen sulphide: this apparent "pollution" is a natural phenomenon. Fortunately, the surface layer in Drammensfjord is thick enough to prevent wind from skimming it off and exposing the deep water, which could result in "malodorous conditions for the population nearby", as occurs in Nævestadfjord [30].

Early in the Holocene, then, the Drammensfjord sill was much deeper below sea-level, at as much as 40m depth. Renewals would have been unimpeded, and the deep fjord fully oxygenated. The gradual onset of anoxia in the deep fjord is recorded in the Drammensfjord sediments. Using foraminiferal assemblages, Alve [28] suggests a date of c. AD 900 for the onset of periodic oxygen depletion and c. AD 1375 for the development of total anoxia in the deep fjord; from visual inspection of fjord sediments, Strøm [82] similarly suggested a date of c. AD 1300 for a sudden reduction in deep water renewals.

However, over the last c. 300 years, the most important influence on anoxia in Drammensfjord has been anthropogenic carbon loading, whose negative effects on oxygen availability far outweigh the positive effects of sill excavation [28]. This is described in the next section.

2.12.4 Carbon loading and anoxia in the deep fjord

Decomposition of organic carbon compounds in the deep fjord uses up free oxygen. This process is mainly carried out by bacteria in the "microbial loop", which has been studied in detail in the Inner Oslofjord [83]. Once all the available oxygen has been used, organic carbon is preserved in the sediment. However, this is a simplified description of a controversial subject. Anoxia is not the only factor influencing organic carbon preservation in sediments [e.g. 84,85]. Conventionally, decomposition of organic carbon under anoxic conditions is thought to be slow [66], partly because in order to produce anoxia, the labile compounds have already been preferentially decomposed, leaving refractory compounds behind. But this has also been disputed [86]. Nonetheless, it is clear that carbon loading of Drammensfjord has promoted anoxia in

the deep water. A typical depth for the modern redox cline (the boundary between oxidising and reducing conditions) is c. 40m, though this varies across the fjord and with time [14].

What is the nature of the organic carbon load? In addition to the natural input of carbon from plankton, soil, and vegetation, there are woodchips and sawdust from the timber industry, and cellulose fibres from pulp and paper mills, totalling c. 38,000 tons in 1970 [87]. Population growth has also increased the sewage input to Drammensfjord, to c. 14 - 17,000 tons per year over 1982-83 [14]. Productivity in Drammensfjord has remained low; unlike the Inner Oslofjord, it has not experienced significant eutrophication [58], so there has been little additional carbon load as a result of anthropogenic fertilisation of the fjord. Nonetheless, the natural tendency of Drammensfjord to become anoxic, as a result of its shallow sill, has been made permanent and more extensive by direct anthropogenic carbon loading.

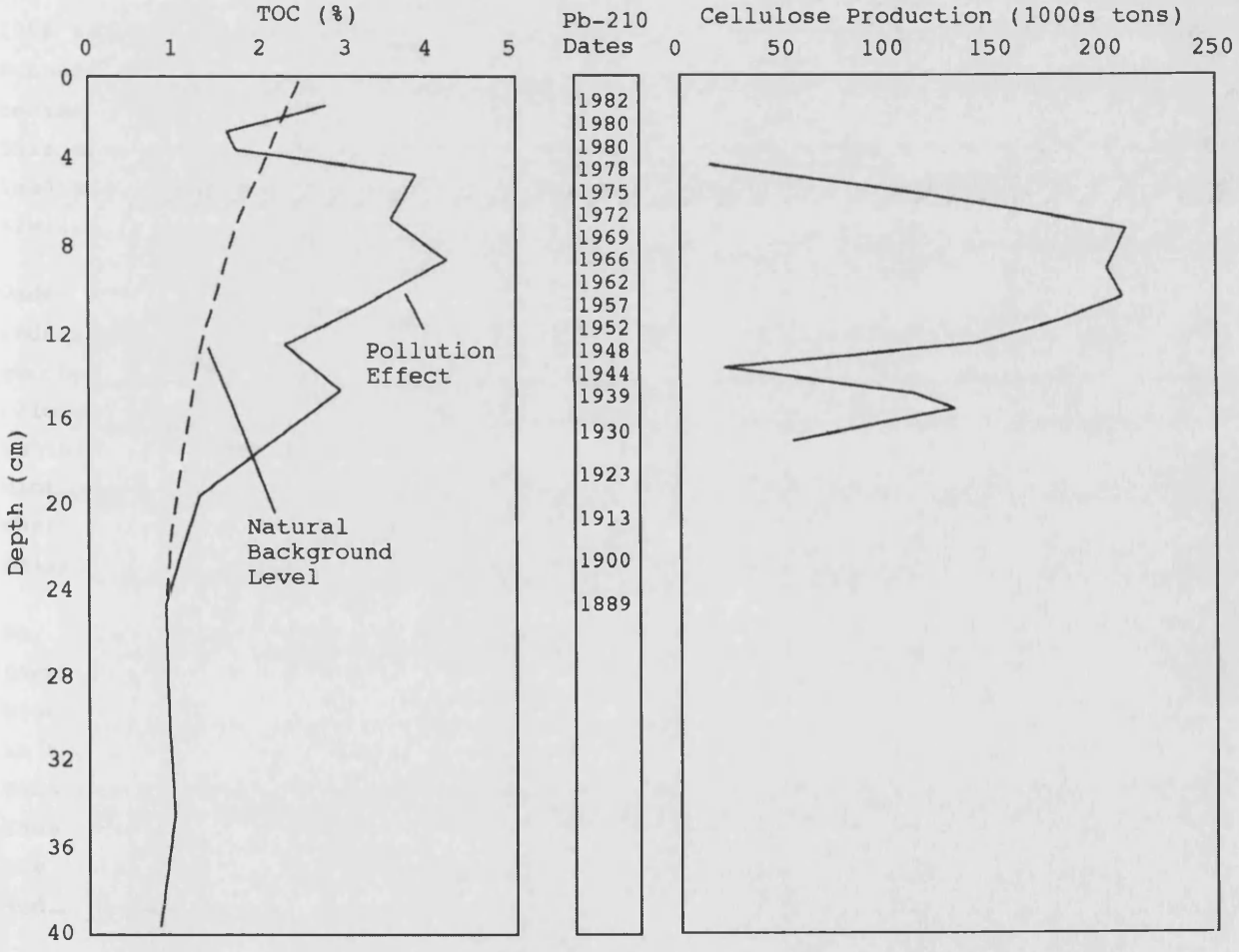

Figure 2.14: Sedimentary evidence for wood-product pollution history in Drammensfjord, redrawn from [49]. The natural background level indicated is not explained in [49]; a decrease in TOC with depth is expected due to decomposition of labile organic compounds within the sediment, and most probably, the only purpose of this curve is to clarify that the pollution effect should not be considered to be the deviation from a vertical line.

Research by NIVA has shown that the history of carbon loading in Drammensfjord can be reconstructed using the organic carbon content of sediment cores [49]. The observed decline in organic carbon content with depth in the sediment is partly due to natural decomposition, but the uppermost sediment is especially rich in refractory organic compounds which represent pollution from the wood products industry. Furthermore, sediment records from the last century can be closely correlated with records of cellulose production around Drammensfjord: a fall during World War 2, then a rise to a peak in the early 1970s, then a rapid decline around 1980 [49].

What are the effects of carbon loading? Dissolved oxygen is absent from the deep fjord except during occasional renewal events. These are not annual; they only occur every 3-5 years, during winter [14]. For example, renewal events occurred in 1983-84, and 1987-88 [13]; in both cases, renewal was only partial and anoxia was quickly re-established. Drammensfjord is more vulnerable to carbon-loading-induced anoxia than the Inner Oslofjord because of its lack of mixing and shallower sill [14]. Between 1956 and 1963, oxygen conditions in Drammensfjord were similar to those in the Bunnefjord arm of the Inner Oslofjord [14], but between 1963 and 1975, Drammensfjord became near-permanently anoxic whereas Bunnefjord remained only intermittently so. This difference arose owing to the vulnerability of Drammensfjord to high carbon loading; in a sense, the deeper sill of Bunnefjord allowed it to "cope" with a similarly high carbon load without developing anoxia [14].

Under anoxic conditions in the deep fjord, organic carbon is decomposed by sulphate-reducing bacteria, producing free hydrogen sulphide in the water [49]. The geochemistry of anoxic fjord water is of some interest [e.g. 88,89] though it is not relevant here. The anoxia is significant because it inhibits the establishment of benthic macrofauna: animals that burrow and feed at the sediment-water interface, bioturbating the sediment. In the Vestfjord arm of the Inner Oslofjord, for example, where the redox cline is below the sediment-water interface [62], a "carpet" of polychaete worms covers the sediment surface, burrowing to c. 5cm depth [61].

So, although Inner Oslofjord does have a seasonal cycle in sediment input, no varves form because of this bioturbation of the sediment. Alve [28] did find evidence of bioturbation in the shallower parts of Drammensfjord, where oxygen is available, but in the deep fjord the fauna is restricted to a few anoxia-tolerant species such as the foraminifer *Stainforthia fusiformis* [28] which do not cause significant bioturbation. Thus, both near-permanent anoxia, and the seasonal cycle in sedimentary deposition, are necessary for the formation and preservation of varves in the Drammensfjord sediment.

Beginning in c. 1980, measures have been taken to clean up Drammensfjord and to return it to its natural state. The timber and pulp industries have greatly declined, and sewage treatment has been initiated; both of these developments have reduced the carbon load on the fjord. Unlike most industrialised fjords, Drammensfjord has never been severely polluted by metals [28], but it is still contaminated by organic pollutants such as PCBs and DDT, which are concentrated in some kinds of fish [48]. Harmful bacteria from sewage also persist, making the northern half of the fjord

unsuitable for open-air bathing [48]. Most persistent of all the effects is the anoxia in the deep fjord. Despite the reduction of carbon loading to a level close to the assumed "background" level [49], anoxia in the deep fjord is unchanged and is likely to remain so for a long time. This is partly because there is a lot of carbon still present in the deep fjord, and its decay is very slow [14]; furthermore, river flow regulation has reduced the frequency of renewals by prolonging the existence of a freshwater surface layer through the winter; finally, the River Drammen is still eroding down into wood-fibre-rich sediment deposited over the last few centuries [14]. For now, deep fjord anoxia remains near-permanently established.

2.12.5 Anthropogenic influence on Drammensfjord in context

- Anoxia originally developed in Drammensfjord without any assistance from mankind. However, a continual increase in carbon loading over the last c. 300 years has resulted in near-permanent anoxia in the deep fjord and consequent inhibition of bioturbation.

- The composition of the sediment has also been changed by mankind: recent sediments contain more fibrous organic carbon from the timber products industry, and possibly more phytoplanktonic sediment because of a minor increase in nutrient availability [14]. Recent sediment accumulation rates are also higher.

- The annual cycle in sedimentation has been altered, with seasonal variations smoothed out, resulting in a year-round input of organic-rich sediment, e.g. from sewage discharge and agricultural erosion, and a reduction in event sedimentation from floods, landslides, and so on.

So, modern sediment accumulation patterns (e.g. as derived from sediment trap investigations) are not entirely representative of Drammensfjord in its natural state. It is important to consider the extent to which recent sedimentation in Drammensfjord, especially from the last century, is a suitable "uniformitarian" analogue for past Holocene sedimentation.

2.13 Why Drammensfjord is significant

Drammensfjord is significant because it is a silled anoxic fjord with a pronounced annual cycle in sedimentation. This situation arises because of a combination of climatic and geographic factors, notably its shallow sill, large catchment area, and seasonal changes in climate and hydrography. This combination of factors has produced a potential record of past climate change in the Drammensfjord varves.

The disadvantage of Drammensfjord as a site for palaeoclimatic research is the lack of previous research, except for the work of Alve on anoxia and foraminifers [13,28,31,90]; hence, the attempt at a comprehensive review in this chapter. The Drammensfjord varves have not been previously studied.

2.14 The NIOZ Drammensfjord project

The Drammensfjord research originated in a project organised by the Department of Marine Biogeochemistry at NIOZ (the Royal Netherlands Institute for Sea Research). This project investigated the fate of natural organic compounds, tracing their origins and the diagenetic pathways they follow as they move amongst marine organisms, the sea itself, and marine sediments. The project ran from 1998 to 2002 and was led by Jaap Sinninghe Damste [e.g. 91]. As part of the project, a cruise was made to recover sediment from Drammensfjord, Norway. Research Vessel *Pelagia*, owned by NIOZ, was used. Cruise number 64PE147 departed from Texel, Netherlands, on 25 October 1999, returning on 5 November with core material from Drammensfjord.

The aim of the Drammensfjord coring was to recover varved fjord sediments, so that organic material in the sediment could be precisely dated using varve counting. These dates could then be compared with dates obtained by a new technique, of extracting specific phytoplankton biomarkers from the sediment, and performing radiocarbon dating on them. This technique was developed at NIOZ by Rienk Smittenberg, who supervised the coring and storage of the Drammensfjord material; it has also been applied to varved cores from Saanich Inlet, Canada [92]. In addition, Matthias Paetzel, at HSF University College, Sogndal, Norway, obtained funding between 1999 and 2001 to study Holocene sediments in Drammensfjord. His research is based on anthropogenic pollution of anoxic fjord environments [e.g. 93,94]. None of his research on Drammensfjord has yet been published, though similar collaborative research with NIOZ on Kyllarenfjord, Norway, has been published [95,96].

The UCL Palaeoclimate Research Group were granted access to the Drammensfjord cores for the purpose of "varve counting" without having to contribute to the costs of the project, on the basis that any work done would be entirely "remote" and would not disturb the sediment cores in any way. The aims of the UCL research were subsequently expanded to include: producing a detailed literature review; an interpretation of the varve mechanism using smear slides and backscatter electron imagery (BSEI); and varve counting, thickness measurement, and sediment colour measurement, using traditional techniques and digital image analysis. The Drammensfjord cores remain in storage at the Department of Marine Biogeochemistry, Royal Netherlands Institute for Sea Research (NIOZ), P.O. Box 59, 1790 AB, Den Burg, The Netherlands.

Chapter 2 References

[1] Syvitski, J. P. M., Burrell, D. C., and Skei, J. M., 1987, Fjords: Processes and Products, Springer, 379 pp.

[2] Dons, J. A., and Larsen, B. T., (Eds.), 1978, The Oslo Paleorift: a review and guide to excursions, Norges Geologiske Undersøkelse, Special Edition, v. 337.

[3] Neumann, E.-R., Olsen, K. H., Baldridge, W. S., and Sundvoll, B., 1992, The Oslo Rift: a review, Tectonophysics, 208:1-18.

[4] Neumann, E.-R., 1994, The Oslo Rift: P-T relations and lithospheric structure, Tectonophysics, 240:159-172.

[5] Sundvoll, B., and Larsen, B. T., 1995, Architecture and early evolution of the Oslo Rift, Tectonophysics, 240:173-189.

[6] Petersen, J. S., 1978, Structure of the larvikite-lardalite complex, Oslo region, Norway, Geologische Rundschau, 67:330-342.

[7] Kinck, J. J., Husebye, E. S., and Larsson, F. R., 1993, The Moho depth distribution in Fennoscandia and the regional tectonic evolution from Archaean to Permian times, Precambrian Research, 64:23-51.

[8] Torsvik, T. H., Eide, E. A., Meert, J. G., Smethurst, M. A. and Walderhaug, H. J., 1998, The Oslo Rift: new palaeomagnetic and 40-Ar/39-Ar age constraints, Geophysical Journal International 135:1,045-1,059.

[9] Husebye, E. S., Bungum, H., Fyen, J., and Gjøystdal, H., 1978, Earthquake activity in Fennoscandia between 1497 and 1975 and intraplate tectonics, Norsk Geologisk Tidsskrift, 58:51-68.

[10] Pederstad, K., Roaldset, E., and Ronningsland, T. M., 1993, Sedimentation and environmental conditions in the Inner Skagerrak - Outer Oslofjord, Marine Geology, 111:245-268.

[11] Petterson, G., 1996, Varved sediments in Sweden: a brief review, in: Kemp, A. E. S., (Ed.), 1996, Palaeoclimatology and Palaeoceanography from Laminated Sediments, Geological Society Special Publication No. 116, p. 73-77.

[12] Alve, E., and Nagy, J., 1986, Estuarine foraminiferal distribution in Sandebukta, a branch of the Oslofjord, Journal of Foraminiferal Research, 16:261-284.

[13] Alve, E., 1990, Variations in estuarine foraminiferal biofacies with diminishing oxygen conditions in Drammensfjord, S. E. Norway, in: Hemleben, C., Kaminski, M. A., and Kuhnt, W., (Eds.), Paleoecology, Biostratigraphy, Paleoceanography and Taxonomy of Agglutinated Foraminifera, NATO ASI Series C (Mathematical and Physical Sciences) v. 327, p. 661-694.

[14] Magnusson, J., and Næs, K., 1986, Basis undersøkelser i Drammensfjorden 1982-84: Delrapport 6: Hydrografi, vannkvalitet og vannutskiftning, NIVA-rapport, Overvåkningsrapport 243/86, 77 pp.

[15] Richards, F. A., and Benson, B. B., 1961, Nitrogen/argon and nitrogen isotope ratios in two anaerobic environments, the Cariaco Trench in the Caribbean Sea and Dramsfjord, Norway, Deep-Sea Research, 7:254-264.

[16] Hjort, J., and Gran, H. H., 1900, Hydrographic-biological investigations of the Skagerrak and the Christianiafjord, Rep. Norwegian Fishery Mar. Invest., 1:1-40.

[17] Holtedahl, H., 1989, Submarine end moraines and associated deposits off the south coast of Norway, Marine Geology, 88:23-48.

[18] Sørenson, R., 1979, Late Weichselian deglaciation in the Oslofjord area, south Norway, Boreas, 8:241-246.

[19] Schaanning, M., 1983, Chemical investigations in the inner Dramsfjord, an anoxic basin, with particular reference to various redox and solubility equilibria, Cand. Real. Thesis, Unpublished, University of Oslo, 155 pp.

[20] Rienk Smittenberg, personal communication, January 2000.

[21] Cowan, E. A., Seramur, K. C., Cai, J., and Powell, R. D., 1999, Cyclic sedimentation produced by fluctuations in meltwater discharge, tides and marine productivity in an Alaskan fjord, Sedimentology, 46:1109-1126.

[22] Bjerrum, L., 1967, Engineering geology of Norwegian normally-consolidated marine clays as related to settlements of buildings, Geotechnique, 17:83-117.

[23] Bentley, S. P., and Smalley, I. J., 1984, Landslips in sensitive clays, Chapter 11, In: Brunsden, D., and Prior, D. B.,

(Eds.), Slope Instability, John Wiley and Sons, p. 457-490.
[24] Solheim, A., and Gronlie, G., 1983, Quaternary sediments and bedrock geology in the Outer Oslofjord and northernmost Skagerrak, Norsk Geologisk Tidsskrift, 63:55-72.

[25] Braarud, T., and Ruud, J. T., 1937, The hydrographic conditions and aeration of the Oslofjord 1933-1934, Hvalrådets Skrifter, v. 15, 56 pp.

[26] Beyer, F., 1954, Studies of a threshold fjord - Drammensfjord - in Southern Norway. I. Hydrography, and II. Zoology, Unpublished Masters Thesis, University of Oslo.

[27] Dahl, F.-E., 1970, Utskiftning og sirkulasjon i Drammensfjorden, Hovedfagsoppgave i geofysikk, University of Oslo, 77 pp.

[28] Alve, E., 1991, Foraminifera, climatic change, and pollution: a study of late Holocene sediments in Drammensfjord, southeast Norway, Holocene, 1:243-261.

[29] Pedersen, F. B., 1977, A brief review of present theories of fjord dynamics, in: Nihoul, J. C. J., (Ed.), 1978, Hydrodynamics of Estuaries and Fjords, Proceedings of the 9th International Colloquium on Ocean Hydrodynamics, Elsevier Oceanography Series, 23:407-422.

[30] Braarud, T., Foyn, B., and Hasle, G. R., 1958, The marine and freshwater phytoplankton of the Dramsfjord and the adjacent part of the Oslofjord March - December 1951, Hvalrådets Skrifter, v. 43, 102 pp.

[31] Alve, E., 1995, Benthic foraminiferal distribution and recolonisation of formerly anoxic environments in Drammensfjord, Southern Norway, Marine Micropaleontology, 25:169-186.

[32] Gustafsson, B., 1997, Dynamics of the seas and straits between the Baltic and North Seas - a process-oriented oceanographic study, PhD thesis, Department of Oceanography, University of Gothenburg, 148 pp.

[33] Gade, H. G., and Edwards, A., 1979, Deep water renewal in fjords, in: Freeland, H. J., Farmer, D. M., and Levings, C. D., (Eds.), 1980, Fjord Oceanography, NATO Conference Series IV: Marine Sciences, 715 pp, p. 453-489.

[34] Nordseth, K., 1987, Climate, hydrology, and biogeography of Norway, In: Varjo, U, and Tietze, W, (Eds.), 1987, Norden: Man and Environment, Gebrüder Borntrager, p. 159-168.
[35] Nordseth, K., 1987, Climate and hydrology of Norden, In: Varjo, U, and Tietze, W, (Eds.), 1987, Norden: Man and Environment, Gebrüder Borntrager, p. 120-128.

[36] John, B., 1984, Scandinavia: A New Geography, Longman, 365 pp.

[37] Fullerton, B., and Williams, A. F., 1972, Scandinavia, Chatto and Windus, 374 pp.

[38] Wallén, C. C., 1968, Chapter 4: Climate, In: Sømme, A., 1968, A Geography of Norden, Heinemann, 399 pp.

[39] Bryant, E., 1997, Climate Process and Change, Cambridge University Press, 209 pp.

[40] Gade, H. G., 1963, Some hydrographic observations of the Inner Oslofjord during 1959, Hvalrådets Skrifter, v. 46, 62 pp.

[41] Ward, R. C., and Robinson, M., 1989, Principles of Hydrology, Third Edition, McGrawHill, 365 pp.

[42] Xu, C. Y., and Halldin, S., 1997, The effect of climate change on river flow and snow cover in the NOPEX area simulated by a simple water balance model, Nordic Hydrology, 28:273-282.

[43] Viessman, W., and Lewis, G. L., 1996, Introduction to Hydrology, Fourth Edition, HarperCollins, 624 pp.

[44] Knighton, D., 1998, Fluvial Forms and Processes: A New Perspective, Arnold, 383 pp.

[45] Richards, K., 1982, Rivers: Form and Process in Alluvial Channels, Methuen and Co., 361 pp.

[46] Rodda, J. C., Downing, R. A., and Law, F. M., 1976, Systematic Hydrology, Newnes-Butterworths, 399 pp.

[47] Nash, D. B., 1994, Effective sediment-transporting discharge from magnitude-frequency analysis, Journal of Geology, 102:79-95.

[48] Magnusson, J., 1996, Overvåkning av Drammensfjorden 1995. Vannkvaliteten i overflatelaget, NIVA-Rapport OR-3515, 35 pp.

[49] Næs, K., 1984, Basis undersøkelser i Drammensfjorden 1982-83, Delrapport: Sedimenter, NIVA-rapport, Overvåkningsrapport 158/84, 28 pp.

[50] Hvoslef, S., Kirkerud, L., Knutzen, J., Kvalvågnæs, K., Magnusson, J., Mjelde, M., Næs, K., Pedersen, A., Rygg, B., and Wiik, Ö, 1987, Basis undersøkelser i Drammensfjorden 1982-84, Konklusjonsrapport, NIVA-rapport, Overvåkningsrapport 266/86, 38 pp.

[51] Qvale, G., Markussen, B., and Thiede, J., 1984, Benthic foraminifers in fjords: response to water masses, Norsk Geologisk Tidsskrift, 64:235-249.

[52] Grasshoff, K., 1975, The hydrochemistry of landlocked basins and fjords, In: Riley, J. P., and Skirrow, G., (Eds.), 1975, Chemical Oceanography, Second Edition, v. 2, p. 455-597.

[53] Haugen, J. E., and Lichtentaler, R., 1991, Amino acid diagenesis, organic carbon and nitrogen mineralisation in surface sediments from the Inner Oslofjord, Norway, Geochimica et Cosmochimica Acta, 55:1,649-1,661.

[54] Ypma, J. E., and Throndsen, J., 1996, Seasonal dynamics of bacteria, autotrophic picoplankton and small nanoplankton in the Inner Oslofjord and the Skagerrak in 1993, Sarsia, 81:57-66.

[55] Kristiansen, S., Thingstad, T. F., Vanderwal, P., Farbrot, T., and Skjoldal, E. F., 1994, An *Emiliania-huxleyi* dominated subsurface bloom in Samnangerfjorden, western Norway - importance of hydrography and nutrients, Sarsia, 79:357-368.

[56] Kristiansen, S., 1998, Impact of increased river discharge on the phytoplankton community in the Outer Oslofjord, Norway, Hydrobiologia, 363:169-177.

[57] Andersen, T., Schartau, A. K. L., and Paasche, E., 1991, Quantifying external and internal nitrogen and phosphorus pools, as well as nitrogen and phosphorus supplied through remineralisation, in coastal marine plankton by means of a dilution technique, Marine Ecology - Progress Series, 69:67-80.

[58] Dale, B., Thorsen, T. A., and Fjellsa, A., 1999, Dinoflagellate cysts as indicators of cultural eutrophication in the Oslofjord, Norway, Estuarine, Coastal, and Shelf Science, 48:371-382.

[59] Rienk Smittenberg, personal communication, January 2002.

[60] Alve, E., and Olsgard, F., 1999, Benthic foraminiferal colonisation in experiments with copper-contaminated sediments, Journal of Foraminiferal Research, 29:186-195.

[61] Alve, E., and Bernhard, J. M., 1995, Vertical migratory response of benthic foraminifera to controlled oxygen conditions in an experimental mesocosm, Marine Ecology - Progress Series, 116:137-151.

[62] Abdullah, M. I., and Danielsen, M., 1992, Chemical criteria for marine eutrophication with special reference to the Oslofjord, Norway, Hydrobiologia, 235:711-722.

[63] Rienk Smittenberg, personal communication, January 2000.

[64] Næs, K., Bakke, T., and Konieczny, R., 1995, Mobilisation of PAH from polluted seabed and uptake in the blue mussel (*Mytilus edulis L*), Marine and Freshwater Research, 46:275-285.

[65] Artemyev, V. E., 1996, Geochemistry of organic matter in river-sea systems, Kluwer Academic Publishers, 190 pp.

[66] Killops, S. D., and Killops, V. J., 1993, An Introduction to Organic Geochemistry, Longman, 265 pp.

[67] McLane, M., 1995, Sedimentology, Oxford University Press, 423 pp.

[68] Aston, S. R., 1978, Estuarine chemistry, In: Riley, J. P., and Chester, R., (Eds.), Chemical Oceanography, Second Edition, v. 7, p. 361-440.

[69] Parsons, T. R., 1975, Particulate organic carbon in the sea, In: Riley, J. P., and Skirrow, G., (Eds.), 1975, Chemical Oceanography, Second Edition, v. 2, p. 365-383.

[70] Reading, H. G., (Ed.), 1996, Sedimentary Environments: Processes, Facies, and Stratigraphy, Blackwell Science, 744 pp.

[71] Zeng, J., Lowe, D. R., Prior, D. B., Wiseman Jr, W. J., and Bornhold, B. D., 1991, Flow properties of turbidity currents in Bute Inlet, British Columbia, Sedimentology, 38:975-996.

[72] Moum, J., Loeken, T., and Torrance, J. K., 1971, A geochemical investigation of the sensitivity of a normally-consolidated clay from Drammen, Norway, Geotechnique, 21:329-340.

[73] Kenney, T. C., and Drury, P., 1973, Case record of the slope failure that initiated the retrogressive quickclay

landslide at Ullensaker, Norway, Geotechnique, 23:33-47.

[74] Syvitski, J. P. M., and Schafer, C. T., 1996, Evidence for an earthquake-triggered basin collapse in Saguenay Fjord, Canada, Sedimentary Geology, 104:127-153.

[75] Schafer, C. T., Smith, J. N., and Seibert, G., 1983, Significance of natural and anthropogenic sediment inputs to the Saguenay Fjord, Quebec, Sedimentary Geology, 36:177-194.

[76] Locat, J., Gagnon, C., and Pelletier, É., (Eds.), 1998, Synopsis of the symposium on the Saguenay flood, Part of the Québec 1998 Carrefour des Sciences de la Terre, Emergency Preparedness Canada, Scientific/Technical Reports, 26 pp.

[77] Mulder, T., Syvitski, J. P. M., and Skene, K. I., 1998, Modeling of erosion and deposition by turbidity currents generated by river mouths, Journal of Sedimentary Research, 68:124-137.

[78] Smith, J. N., and Schafer, C. T., 1987, A 20th-Century record of climatologically modulated sediment accumulation rates in a Canadian fjord, Quaternary Research, 27:232-247.

[79] Gilbert, R., 1983, Sedimentary processes of Canadian arctic fjords, In: Syvitski, J. P. M., and Skei, J. M., (Eds.), Sedimentology of Fjords, Sedimentary Geology, 36:147-175.

[80] Carlsson, Y., 2001, Somewhere between Venice and "Harry-town": Drammen - identity, image, and attributes, Norwegian Institute for Urban and Regional Research, January 2001, Noord XXI Report No. 18, 20 pp.

[81] Elisabeth Alve, personal communication, September 2002.

[82] Strøm, K. M., 1936, Land-locked waters, Skrifter utgitt av det Norske Vitenskaps-akademi i Oslo, 1, Matematisk-naturvidenskapelige klasse 1, no. 7, p. 1-85.

[83] Tobiesen, A., 1991, The succession of microheterotrophs and phytoplankton within the microbial loop in Oslofjord, May-October 1984, Journal of Plankton Research, 13:197-216.

[84] Pedersen, T. F., and Calvert, S. E., 1990, Anoxia vs productivity: what controls the formation of organic-carbon-rich sediments and sedimentary rocks?, AAPG Bulletin, 74:454-466. See also Discussion, AAPG Bulletin, 75:499, and Reply, AAPG Bulletin, 75:500-501.

[85] Canfield, D. E., 1994, Factors influencing organic carbon preservation in marine sediments, Chemical Geology, 114:315-329.

[86] Bastviken, D., Ejlertsson, J., and Tranvik, L., 2001, Similar bacterial growth on dissolved organic matter in anoxic and oxic lake water, Aquatic Mircobial Ecology, 24:41-49.

[87] Alsaker-Nøstedahl, H., 1988, Tiltaksplan mot forurensning i Drammenselva og Drammensfjorden, Fylkesmannen i Buskerud, Miljøvernavdelingen, Rapport nr. 19, 42 pp.

[88] Schaanning, M., Næs, K., Egeberg, P. K., and Bome, F., 1988, Cycling of manganese in the permanently anoxic Drammensfjord, Marine Chemistry, 23:365-382.

[89] Ozturk, M., 1995, Trends of trace-metal (Mn, Fe, Co, Ni, Zn, Cd and Pb) distributions at the oxic-anoxic interface and in sulphidic water of the Drammensfjord, Marine Chemistry, 48:329-342.

[90] Bernhard, J. M., and Alve, E., 1996, Survival, ATP pool, and ultrastructural characterisation of benthic foraminifera from Drammensfjord (Norway): Response to anoxia, Marine Micropaleontology, 28:5-17.

[91] Van Dongen, B. E., Rijpstra, W. I. C., Philippart, C. J. M., de Leeuw, J. W., and Sinninghe Damste, J. S., 2000, Biomarkers in upper Holocene eastern North Sea and Wadden Sea sediments, Organic Geochemistry, 31:1,533-1,543.

[92] Smittenberg, R. H., Hopmans, E. C., Eglinton, T. I., Hayes, J. M., Whiticar, M. J., Schouten, S., and Sinninghe Damste, J. S., 2001, Validation of compound-specific 14-C dating using the varved sedimentary record of Saanich Inlet, Canada, Talk given at 20th International Meeting on Organic Geochemistry, 13 September 2001, Nancy, France.

[93] Paetzel, M., and Schrader, H., 1992, Recent environmental changes recorded in anoxic Barnesfjord sediments - western Norway, Marine Geology, 105:23-36.

[94] Paetzel, M., and Schrader, H., 1995, Sewage history in the anoxic sediments of the fjord Nordåsvannet, western Norway: 2. The origin of the sedimented organic matter fraction, Norsk Geologisk Tidsskrift, 75:146-155.

[95] Smittenberg, R. H., Pancost, R. D., Paetzel, M., and Sinninghe Damste, J. S., 1999, Biomarkers in varved, late Holocene fjord sediments: a study of the anoxic Kyllarenfjord, Norway, Abstract Only, in Special Abstract Volume, 19th International Meeting on Organic Geochemistry, Istanbul, 6-10 September 1999.

[96] Smittenberg, R. H., Pancost, R. D., Paetzel, M., and Sinninghe Damste, J. S., 2000, Late Holocene environmental changes in the euxinic Kyllarenfjord as revealed by its sedimentary biomarker record, Abstract Only, in Abstract Volume, 5th Dutch Earth Science Conference (NAC 5), Amsterdam, 20-21 April 2000.

Chapter 3: Lake St Moritz

3.1 Introduction

Anoxic fjords are not the only places where varved sediment is formed. The necessary requirements of a seasonal cycle in sediment input, together with inhibition of bioturbation (e.g. by anoxia), are met by numerous other depositional environments, including oceanic basins and shelves [e.g. 1 and 2], small temperate lakes such as the Norfolk Meres [3], and Alpine lakes such as Lake St Moritz.

The European Alps, and other alpine regions, are especially sensitive to global environmental change. For example, recent climatic warming in the Alps has been much greater than the global average: a warming of c. 1°C between 1895 and 1985, then a further c. 1°C between 1985 and the present day [4]. Climatic warming also has more severe consequences in alpine environments, because average temperatures are close to 0°C, such that warming causes permafrost melting, glacial recession, and resultant hydrological changes such as reduction in lake stratification, alongside changes in the altitude of the tree line, the snow line, and various vertically distributed biomes [4]. Climatic change in alpine regions is, therefore, a matter of pressing concern.

Records of past climate change in the Alps are available from various sources. Instrumental coverage is good, and there are some long historical records, e.g. Basel and Geneva both have homogeneous temperature records going back to c. AD 1750 [5]. However, trees in the Alps have an average age of only c. 100 years, and the longest dendrochronological record, from Lauenen in western Switzerland, only covers the last 1,000 years [5]. So, sedimentary records preserved in Alpine lakes are important as recorders of the effects of pre-instrumental climatic change in the Alps.

Small lakes such as Lake St Moritz, which contain Holocene sediment records, are common in the European Alps; they formed after the last deglaciation in glacial overdeepenings or moraine-dammed basins. Some smaller lakes have been completely filled by sediment. Research on Holocene climate records has been published on numerous Alpine lakes, from small ponds [6] to large "pre-alpine" lakes such as Lake Zürich [7], Lake Constance [8], Lake Neuchâtel [9], and Lake Lugano [10]. All of these papers address the contentious question of millennial climate change during the Holocene (see section 1.2.1) using lake sediment records. The Holocene sediment record from Lake St Moritz has the potential to add to this debate, with its varves both recording long-term climate change, as they themselves change in nature, and acting as a high-resolution chronometer.

There are some similarities between Drammensfjord and Lake St Moritz: both contain varves with biogenic and clastic components, and the climate of the Swiss Alps is warmed by the same Gulf Stream and westerly weather systems as that of southern Norway, and is similarly transitional in nature, experiencing both maritime and continental influences. However, the Alps lie in a quite different climatic zone to Scandinavia: at a major boundary, where the climate changes abruptly from Mediterranean to Northern European [11]. Furthermore, Alpine climate is locally

dominated by the effects of mountain topography, such that there is little reason to expect any similarity between palaeoclimate records from Drammensfjord and Lake St Moritz except on a very broad scale. The value of the comparison is methodological rather than climatological: it enables the robustness of the digital image analysis techniques developed to be assessed, by applying them to records from different settings.

3.2 The geographical setting of Lake St Moritz

The geographical setting of Lake St Moritz, and its sedimentary inputs and depositional processes, are described in detail in [12], [13] and [14]. There is no need for an extended review here. Thus, this chapter is much shorter than chapter 2.

Lake St Moritz [12] is located at 46°30'N and 9°51'E in the Upper Engadine area of the Canton of Graubünden, southeast Switzerland. It is at an altitude of 1,768m and has an area of 0.78km^2, with a maximum length of 1,600m and width of 600m. It is roughly rectangular in shape. Its maximum depth is 44m, its average depth 25m, and its volume 20 × 10^6 m^3.

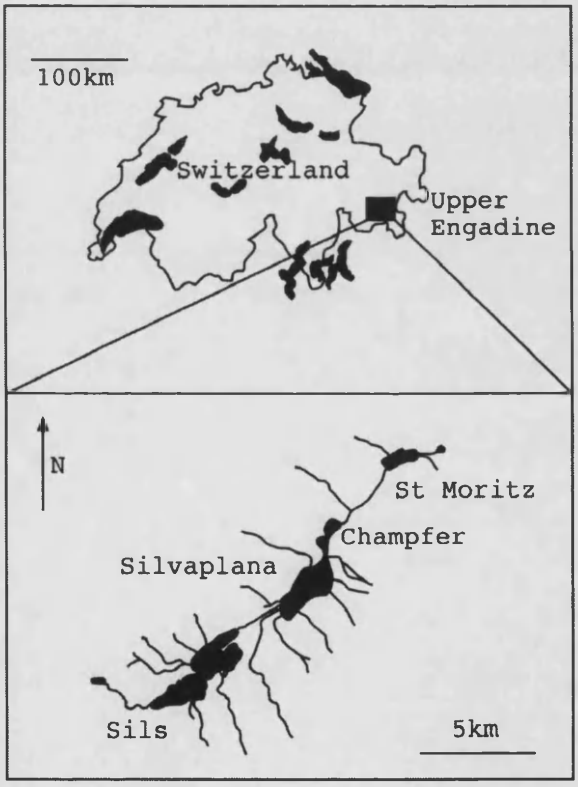

Figure 3.1: Location of Lake St Moritz and the other three lakes in the chain linked by the River Inn. Redrawn from Ariztegui and Dobson [12].

The main river input to Lake St Moritz is the River Inn, which enters at the southeast corner. This river links a chain of four alpine lakes: Lake Sils, Lake Silvaplana, Lake Champfer, and finally Lake St Moritz. Outflow from Lake St Moritz continues into the River Inn, which flows away northeastwards. The average residence time of water in the lake is 0.1 years. The position of Lake St Moritz as the last member of a chain of lakes linked by the same river tends to dampen variations in river flow, such as the

diurnal cycle seen during summer in glacial streams. What remains is a seasonal discharge cycle, with a rapid increase following the spring melt, rising to a peak during maximal glacial melting in June, July, and August, then falling to a low level during the winter.

The climate of St Moritz is famously characterised by warm summers, cold winters, low humidity and many hours of sunshine. Lake St Moritz and the other lakes in the chain remain frozen during every winter. This situation produces a dimictic water column - one that mixes completely twice a year. The resulting seasonal changes in the water column contribute towards producing varves in the sediment record: this seasonal cycle of deposition is described in more detail in section 3.5. Since Lake St Moritz assumed its present form during the last deglaciation, it should contain a complete, varved Holocene sediment record, overlying glacial sediments. For most of the Holocene, this will reflect natural environmental fluctuations. More recently, of course, the lake has been greatly influenced by mankind.

A small settlement by Lake St Moritz had existed for hundreds of years before the first Alpine tourism in the late 19th century led to the development of the modern town of St Moritz. In 1850 the resident population was only c. 500, but by 1910, when the first hotel was built, it had increased to c. 2,500. By 1970 the resident population had stabilised at 5,000, but the additional tourist population fluctuated between a low of 120,000 during World War 2 to a high of 1,100,000 in recent years [15]. Measures to reduce pollution of Lake St Moritz began in the 1960s, but its effects persist. Eutrophication of the lake began in the 1900s [15], resulting from pollution (e.g. by sewage) increasing the nutrient concentration of the water. Other effects of mankind include changes in sediment input due to deforestation, and dredging and dumping of sediment [15].

3.3 The ETH-Zürich cores from Lake St Moritz

Prior to the extraction of the ETH-Zürich cores, research on Lake St Moritz was confined to the surface sediments and the recent history of the lake [13,15-18]. In 1990, coring to recover the entire Holocene sequence for the first time was done by the Swiss Federal Institute of Technology (ETH-Zürich). Four long piston cores were taken from the deepest part of the lake. The third of these, varved core PSM90.3, was chosen for the application of digital image analysis. It was c. 11m long in total, split into sections of c. 1m length.

Since 1990, these cores have been the subject of a range of research projects, led by Daniel Ariztegui, including studies of organic matter content (TOC) and hydrogen index (HI) [14], $\delta^{13}C$ [19], concentrations of fatty acids and other biomarkers [20], magnetic minerals such as greigite [12], and most recently, pollen profiles [21]. So, Lake St Moritz already has a crude multi-proxy record of palaeoenvironmental change, though the varves themselves have not been investigated in detail, and image analysis has not been applied to the cores.

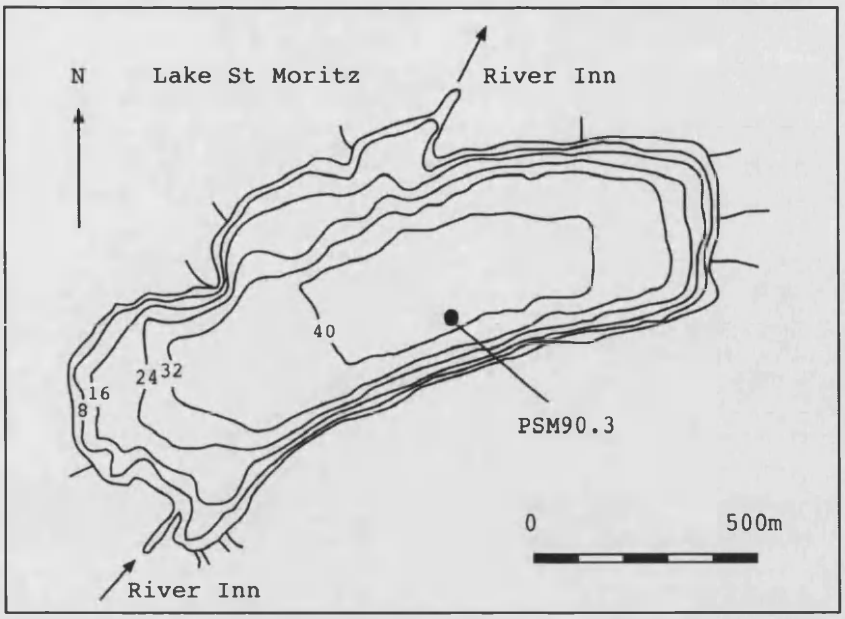

Figure 3.2: Bathymetry of Lake St Moritz showing PSM90.3 core location. Depth contours are in metres. Redrawn from Ariztegui and Dobson [12].

The situation of the Lake St Moritz research is, therefore, different from that of the Drammensfjord research: not only have some data from the Lake St Moritz cores already been obtained, but interpretations of these data have also already been published. The remainder of chapter 3 describes the nature of this existing Lake St Moritz record, and its palaeoclimatic interpretation as offered in already-published literature; it also considers the role that image analysis of the varved core can potentially play in refining this record and its interpretation.

All original data derived from the image analysis research are presented in summary form in chapter 5, and in full in appendix B. Similarly, all original interpretations of the Lake St Moritz data are in chapter 6. Sections 3.4 to 3.6 summarise a body of already-published data and interpretation, which the intention is to improve upon by using results derived from image analysis.

3.4 Lake St Moritz core PSM90.3 lithological description and chronology

Ariztegui *et al.* [14] divide the Lake St Moritz core PSM90.3 into four lithostratigraphic units, which are apparent simply by looking at downcore sediment colour changes (and which also show up in compositional data). Described from bottom to top, these are: very pale pre-Holocene glacial clay, a dark early-to-mid Holocene interval, a paler late Holocene interval, and a very dark recent interval. The latter three Holocene intervals are denoted Unit III, Unit II, and Unit I respectively [14]. The base of the Holocene - the base of Unit III - is especially clear in the core as a sharp transition from pale to dark sediment.

The Holocene sediment is fine-grained throughout, and is a mixture of biogenic and clastic components. The core contains an apparently-continuous sequence of laminations throughout the Lateglacial and Holocene, which are assumed to be varves: the varve mechanism of Lake St Moritz is reviewed separately in section 3.5. In addition, there

are occasional thin turbidites. The four larger-scale stratigraphic units described above, and the climatic changes they represent (as interpreted by Ariztegui *et al.* [14]) are reviewed in section 3.6. First, it is necessary to consider the core chronology used by Ariztegui *et al.* [14].

This was based on a small number of radiocarbon dates [22], some of which were problematic as they were derived from bulk sediment and were, therefore, vulnerable to contamination by old carbon. Furthermore, these dates were uncalibrated, and irregularities in the chosen radiocarbon calibration curve could potentially alter the age-depth curve for the core. Calibration of these dates is an essential precursor to a comparison with varve-derived data (since each varve should correspond to one seasonal cycle, equivalent to one calendar year). These problems are discussed in more detail in chapter 5. Evidently, the simple Holocene chronology of Ariztegui *et al.* [14] could potentially be much improved by calibrating the dates and incorporating the varve sequence.

Two additional sources of chronological information were available. Recent work on the pollen profile of core PSM90.3 [23] included the production of twenty AMS radiocarbon dates taken from terrigeneous plant material, which (after calibration) should be much more representative of the age of their surrounding sediment. These data are given in the table below.

Laboratory No.	Depth (cm)	Age (Uncal. BP)	$\delta^{13}C$ (‰)	Material dated
UtC-9871	142-144	1120±30	-29.3	Needles
UtC-9870	226-228	1870±40	-27.5	Needles
UtC-9869	330-332	3140±40	-29.1	Needles
UtC-9868	382-384	3920±60	-28.7	Needles
UtC-9867	400-402	3950±40	-28.3	Needles
UtC-9865	436-438	4750±50	-29.4	Needles
UtC-9519	454-456	5300±50	-28.0	Needles
UtC-9864	462-464	5280±50	-28.8	Needles
UtC-9863	476-478	5880±50	-28.5	Needles
UtC-9862	500-502	6400±50	-28.1	Needles, *Betula* fruit
UtC-9861	522-524	6670±50	-29.1	Needles
UtC-9860	536-538	7700±70	-29.7	Needles
UtC-9859	548-550	8110±60	-30.0	Needles
UtC-9526	578-580	9070±70	-28.3	Needles
UtC-9525	584-586	9340±60	-28.6	Fruits, needles, bark
UtC-9524	596-598	9260±130	-28.0	Anthers, needles
UtC-9857	760-765	10200±70	-28.6	Wood, leaves
UtC-9522	795-800	9660±120	-29.6	Leaves, wood, bark
UtC-9521	895-900	10100±100	-28.0	Wood
UtC-9520	925-930	10050±90	-24.1	Charcoal, leaves

Figure 3.3: Lake St Moritz core PSM90.3 AMS radiocarbon dates from terrigenous plant material, from Gobet *et al.* [23].

Further independent chronological data were available for the most recent c. 100 years of sediment, namely ^{137}Cs data (taken from [22]) and two historically-dated event beds

(taken from [15]). ^{137}Cs data were measured from the top 20cm of a short core taken adjacently to core PSM90.3. Fallout peaks occur at 1cm, 15cm, and 19cm depth, which can be correlated with the Chernobyl event in 1986, and nuclear testing events in 1963 and 1954, respectively [22]. Dredging operations during the summers of 1911 to 1914 on the northwestern shore of Lake St Moritz led to the dredged material being dumped into the deepest part of the lake, where it forms a distinctive pale grey, massive, clay-rich interval at 58cm depth [15]. A second event bed, again distinctively thick and pale grey in colour, occurs at 11cm depth, and was produced in 1969 by deforestation work (and consequent increased runoff) prior to a ski event in 1974.

These high-resolution chronological data are useful in confirming that the laminations are annual (i.e. varves), as noted by Ariztegui and Dobson [12]; the development of a newly-extended high-resolution chronology for core PSM90.3, incorporating these data and varve counting, is discussed in chapter 5. Further evidence for the annual nature of the laminations comes from the seasonal affinities of their components, which are described in the next section.

3.5 Review of the Lake St Moritz varves and varve mechanism

The seasonal cycle affects Lake St Moritz as follows. Warming of the upper part of Lake St Moritz during the summer causes the lake to become stratified. The upper warm layer, the epilimnion, is less dense than the lower cold layer, the hypolimnion, and this density difference inhibits mixing between the two. The availability of light and warmth in the epilimnion allows photosynthetic plankton to grow, releasing oxygen into the water. In the dark, cold hypolimnion, in contrast, below the thermocline, the presence of decomposing organic matter promotes seasonal anoxia. Nutrients are transported from the epilimnion to the hypolimnion via sinking biogenic material.

This stratification only persists as long as the epilimnion is warmed through the spring and summer. In the autumn, the surface water cools, and the density stratification is lost, causing overturn: the lake water becomes homogenised. Nutrients are brought back up to the surface. During the winter, ice forms on the lake surface, typically up to 50cm thick [22]. This cuts off wind-driven circulation in the lake and produces a winter stratification. Here, water just below the ice is colder than the water further beneath it, but it is less dense (since water has a maximum density at 4°C): the winter stratification is inverse. This breaks down in spring, when the ice melts, producing cold, dense meltwater at the lake surface. A second overturn occurs, before the summer warming and resultant stratification begins anew. Thus, Lake St Moritz overturns twice each year: it is dimictic.

This seasonal cycle can be linked to changes in sedimentation [12]. Increased runoff associated with the spring melt produces sediment-rich plumes that flow into the lake, depositing a dark, silty spring layer. It is not clear whether the turbidites mentioned earlier grade laterally into these silty layers, as is the case in other lakes such as Brienzersee [24], indicating that both are deposited from hyperpycnal flows, or whether the thinner silty varve layers are deposited separately. The spring silty layer is followed by a pale biogenic layer formed by sinking plankton and amorphous organic matter during the spring, summer, and autumn. Occasionally a third,

clayey layer is deposited during the late autumn and winter, low in organic carbon and representing fine-grained sediment settling beneath the ice. Seasonal development of anoxia, observed at the present day by Züllig [15], inhibits bioturbation of the sediment during the summer and autumn, enabling the varve fabric to be preserved.

Water Depth (m)	Temp (°C)	Oxygen availability (mg/l)	pH	NH_4 availability (mg/l)	NO_3 availability (mg/l)	Phosphate availability (mg/l)
0.0	0.4	10.2	7.6	0.019	0.62	0.171
1.0	2.5	10.0	7.7	0.012	1.01	0.198
2.5	2.3	8.4	7.6	0.012	0.96	0.195
5.0	3.3	7.7	7.4	0.012	0.57	0.131
7.5	3.2	7.4	7.4	0.007	0.37	0.120
10.0	3.2	7.4	7.4	0.053	1.10	0.103
12.5	3.1	7.4	7.4			
15.0	3.1	7.4	7.4	0.028	0.14	0.102
20.0	3.1	7.3	7.4	0.010	0.29	0.129
30.0	3.1	7.2	7.4	0.012	0.02	0.113
35.0	3.1	7.1	7.4			
40.0	3.2	4.1	7.2	1.260	1.48	0.169
40.5	3.4	1.3	7.1			
43.0	3.8	0.0	6.9			

Figure 3.4: Züllig [15] studied the Lake St Moritz water column over the deepest part of the lake on 25th March 1981, under a 50cm thick cover of ice. Whilst they are limited to one point in time, and are likely to be distorted by anthropogenic eutrophication, these data do at least illustrate the contrast between surface and deep water in Lake St Moritz.

The nature of the varves changes over the Holocene at core locality PSM90.3 [13]. Firstly, the relative contributions of clastic and biogenic components change. For example, in Unit I, biogenic components are most abundant, whereas in Unit II, clastic components are most abundant. Secondly, the clastic and biogenic layers themselves vary in composition. The clastic layers consist of different proportions of mica flakes, clay, and amorphous organic matter, for example; the biogenic layers consist of different proportions of diatoms, chrysophyte cysts, and cladoceran remains. Changes in the nature of the organisms contributing to the organic matter in the sediment can also be traced using biomarkers [14].

The Lake St Moritz varves, then, are mixed in nature, containing both biogenic and detrital components. This situation arises from the position of Lake St Moritz: it receives sediment from a glacier-fed river, but only after this river has flowed through three previous lakes. The three lakes upstream from Lake St Moritz are dominated by detrital sediment: Lake Silvaplana, for example, contains glacial varves defined by changes in grain size. Annual records of sediment grain size and varve thickness in Lake Silvaplana can be correlated with mean summer temperature (in the short term) and precipitation-linked glacier size changes (over the Holocene) [25,26]. The mixed varves in Lake St Moritz are more complex, and no such direct correlations have been obtained so far, though some much lower-resolution climatic signals have

been inferred from the Lake St Moritz sediment record. These are described in the next section.

3.6 Palaeoclimatic interpretation of core PSM90.3 by Ariztegui *et al.* [14]

The palaeoclimatic reconstruction of Ariztegui *et al.* [14] is based on a chain of reasoning that links climate change, lake productivity, and sedimentation of organic matter. Measurements of Total Organic Carbon (TOC) were made from core PSM90.3 at 2cm intervals (in the top 80cm of the core) and at c. 10cm intervals (for the remainder of the core), enabling the following record to be produced.

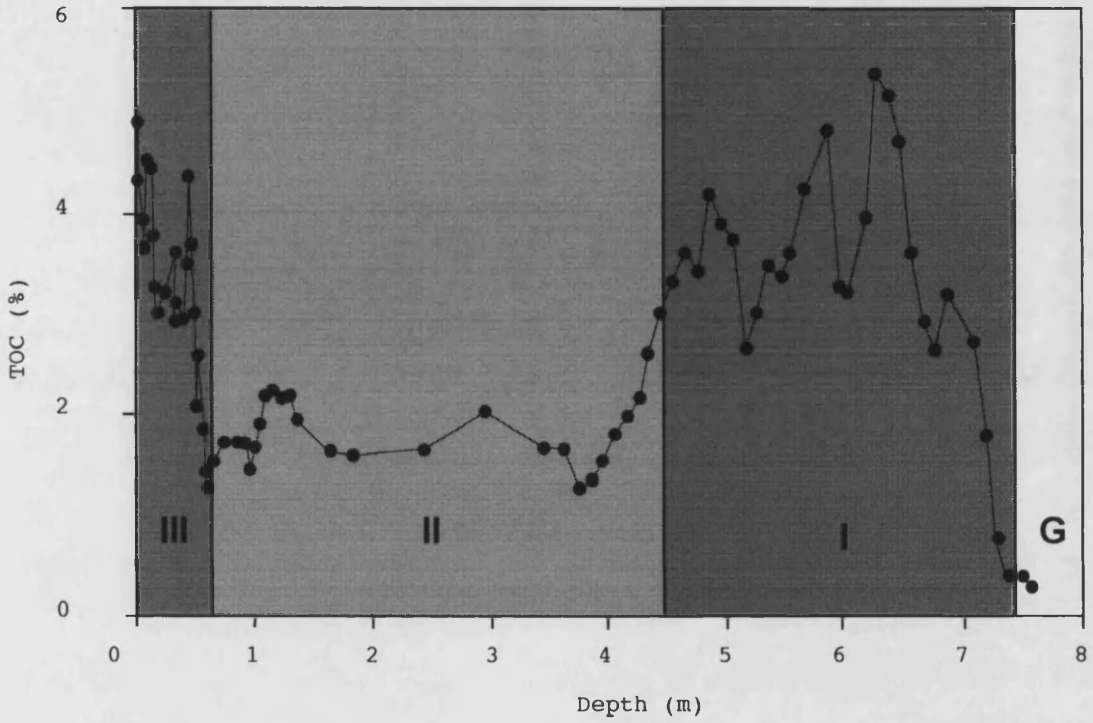

Figure 3.5: Sediment TOC versus depth for Lake St Moritz core PSM90.3, modified from Ariztegui *et al.* [14]. The approximate boundaries of the three-way Holocene division are marked; G indicates glacial sediment, and the darker intervals of increased TOC at the top and base of the sequence correspond to Units I and III respectively.

There is a clear link between the stratigraphic units described in section 3.4, and the organic carbon content of the sediment: evidently, the higher the TOC, the darker the sediment. It is known that Unit I, the very dark sediment from the last c. 100 years, represents an interval of anthropogenic eutrophication: this can be inferred from the recent chronological data from the uppermost part of the sediment sequence (described in section 3.4), combined with contemporary accounts of the onset of eutrophication [16,17] and evidence from carotenoid biomarkers and cladoceran remains in the sediment [15]. The high TOC content of Unit I is the result of an interval of high lake productivity.

By the same reasoning, Ariztegui *et al.* [14] suggest that the earlier Unit III, which has a similarly high TOC content and similar biomarker signature, also reflects an increased supply of organic carbon to the sediment as a result of high productivity. The sequence therefore represents, crudely, a change from eutrophic conditions in the

early to mid Holocene, to oligotrophic conditions in the late Holocene (Unit II, with a lower TOC), ended by anthropogenic eutrophication beginning c. 100 years ago. Superimposed on these changes are numerous other "wiggles" in the TOC record. Lake productivity, in turn, is taken to be influenced by climate, predominantly temperature - at least, in the interval prior to mankind having a significant impact - such that a crude Holocene temperature curve can be inferred [14].

Additional support for this interpretation is derived from measurements of the Hydrogen Index (HI) and $\delta^{13}C$ of the organic matter in the core. HI correlates with TOC, suggesting that intervals of high TOC reflect greater anoxia, i.e. an absolutely larger supply of organic carbon to the sediment. $\delta^{13}C$ anticorrelates with TOC, suggesting that intervals of high TOC are linked to low availability of CO_2 for photosynthesis in the surface waters of the lake, i.e. high productivity.

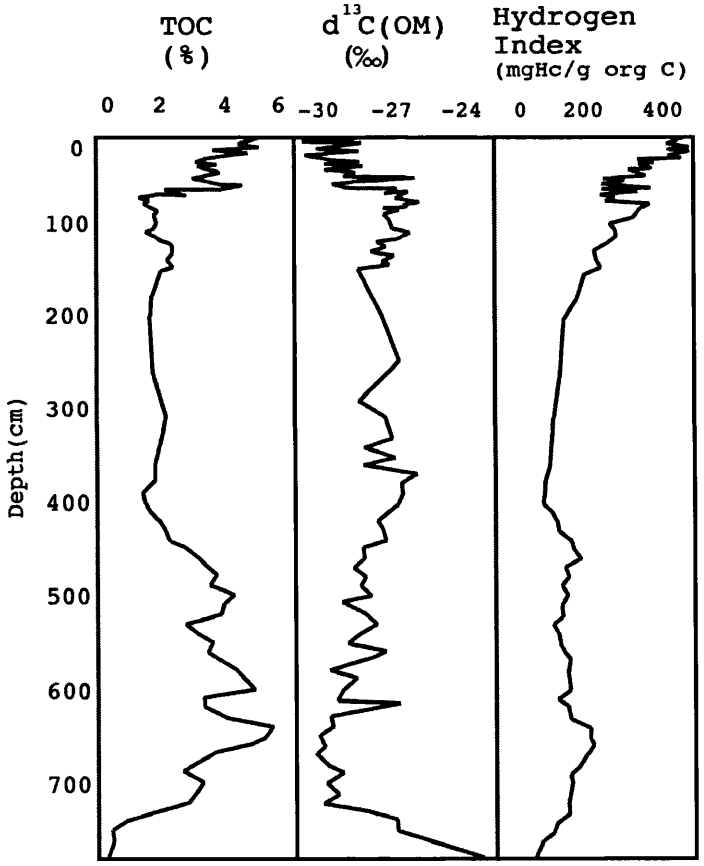

Figure 3.6: TOC, HI, and $\delta^{13}C$ curves from Lake St Moritz core PSM90.3, showing an anticorrelation between TOC and $\delta^{13}C$, and a correlation between TOC and HI. Redrawn from Ariztegui *et al.* [14].

This interpretation of the Lake St Moritz record, and its possible weaknesses, are scrutinised in chapter 6; in particular, the links between climate change, lake productivity and sediment TOC content. There is clear potential for digital image analysis of the sediment core to add to this work. The relationship between sediment colour, sediment composition and environmental change can be explored in more depth. There is obvious colour banding in the cores on scales of a few cm to c. 1m, and the varves have not yet been investigated in detail.

3.7 Integration of image analysis into the Lake St Moritz research

As described in section 1.9.3, the aim of the Lake St Moritz research in this thesis is to integrate image analysis of the varved sediment core into the existing research. There are two strands to the new research, as follows.

First, can the varves and the new radiocarbon dates be integrated into a high-resolution, calendar year chronology for core PSM90.3, and can varve thickness then be linked to sedimentary input to the lake and thereby to climatic signals?

Second, can the correlation between sediment colour and sediment composition which is noted by Ariztegui *et al.* [14] be improved using digital image analysis, and what bearing does this have on the suggested links between sediment composition and climate change?

Essentially, both of these involve an advance from describing the record in terms of a succession of zones (a dark unit followed by a light unit, for example), to describing it in terms of numerical time-series. This requires an increased degree of rigour in order to maintain the quality of the data and of any causal interpretations.

Chapter 3 References

[1] Schaaf, M., and Thurow, J., 1997, Tracing short cycles in long records: the study of inter-annual to inter-centennial climate change from long sediment records: examples from the Santa Barbara Basin, Journal of the Geological Society, London, 154:613-622.

[2] Von Rad, U., Schaaf, M., Michels, K. H., Schulz, H., Berger, W. H., and Sirocko, F., 1999, A 5000-yr record of climate change in varved sediments from the oxygen minimum zone off Pakistan, northeastern Arabian Sea, Quaternary Research, 51:39-53.

[3] Peglar, S., 1993, The mid-Holocene *Ulmus* decline at Diss Mere, Norfolk: a year by year pollen stratigraphy from annual laminations, The Holocene, 3:1-13.

[4] Psenner, R., 2002, Alpine waters in the interplay of global change: complex links - simple effects?, In: Steininger, K. W., and Weck-Hannemann, H., (Eds.), Global Environmental Change in Alpine Regions, Edward Elgar, Chapter 2, p. 15-40.

[5] Lister, G. S., Livingstone, D. M., Ammann, B., Ariztegui, D., Haeberli, W., Lotter, A. F., Ohlendorf, C., Pfister, C., Schwander, J., Schweingruber, F., Stauffer, B., and Sturm, M., 1998, Alpine paleoclimatology, Chapter 3, In: Cebon, P., Dahinden, U., Davies, H. C., Imboden, D. M., and Jaeger, C. C., (Eds.), Views from the Alps: Regional Perspectives on Climate Change, MIT Press, p. 73-169.

[6] Haas, J. N., Richoz, I., Tinner, W., and Wick, L., 1998, Synchronous Holocene climatic oscillations recorded on the Swiss Plateau and at timberline in the Alps, The Holocene, 8:301-309.

[7] Lister, G. S., 1988, A 15,000-year isotopic record from Lake Zurich of deglaciation and climatic change in Switzerland, Quaternary Research, 29:129-141.

[8] Wessels, M., 1996, Natural environmental changes indicated by Late Glacial and Holocene sediments from Lake Constance, Germany, Palaeogeography, Palaeoclimatology, Palaeoecology, 140:421-432.

[9] Schwalb, A., Hadorn, P., Thew, N., and Straub, F., 1998, Evidence for Late Glacial and Holocene environmental changes from subfossil assemblages in sediments of Lake Neuchâtel, Switzerland, Palaeogeography, Palaeoclimatology, Palaeoecology, 140:307-323.

[10] Niessen, F., Wick, L., Bonani, G., Chondrogianni, C., and Siegenthaler, C., 1992, Aquatic system response to climatic and human changes: productivity, bottom water oxygen status, and sapropel formation in Lake Lugano over the last 10,000 years, Aquatic Sciences, 54:257-276.

[11] Egli, E., 1978, Switzerland: A Survey of its Land and People, Paul Haupt Berne Publishers, 229 pp.

[12] Ariztegui, D., and Dobson, J., 1996, Magnetic investigations of framboidal greigite formation: a record of anthropogenic environmental changes in eutrophic Lake St Moritz, Switzerland, The Holocene, 6:235-241.

[13] Schelske, C. L., Züllig, H., and Boucherle, M. M., 1987, Limnological investigation of biogenic silica sedimentation and silica biogeochemistry in Lake St Moritz and Lake Zurich, Swiss Journal of Hydrology, 49:42-50.

[14] Ariztegui, D., Farrimond, P., and McKenzie, J. A., 1996, Compositional variations in sedimentary lacustrine organic matter and their implications for high Alpine Holocene environmental changes: Lake St Moritz, Switzerland, Organic Geochemistry, 24:453-461.

[15] Züllig, H., 1982, Die Entwicklung von St Moritz zum Kurort in Spiegel der Sedimente des St Moritzersees, Wasser, Energie, Luft, 74:177-83.

[16] Bonner, R. A., 1922, Die Bodenfauna des St Mortizer Sees, Archives Hydrobiologie, 13:1-99.

[17] Schmassman, W., and Schmassman, H. J., 1948, Chemische Untersuchungen im St Moritzersee, Swiss Journal of Hydrology, 10:21-35.

[18] Boucherle, M. M., and Züllig, H., 1983, Cladoceran remains as evidence of change of trophic state in three Swiss lakes, Hydrobiologia, 103:141-146.

[19] Ariztegui, D., and McKenzie, J. A., 1995, Temperature-dependent carbon isotope fractionation of organic matter: a potential paleoclimate indicator in Holocene lacustrine sequences, In: Frenzel, B., Stauffer, B., and Weiss, M. M., (Eds.), Problems of stable isotopes in tree-rings, lake sediments and peat bogs as climatic evidence for the Holocene, Paleoclimate Research, 15:17-28.

[20] Ariztegui, D., McKenzie, J. A., and Farrimond, P., 1993, Fatty acid distributions in Holocene sediments from Lake St Moritz, Switzerland: A record of fluctuating trophic conditions, Advances in Organic Geochemistry, 10:470-472.

[21] Gobet, E., Hochuli, P. A., and Ariztegui, D., 2001, Human impact on the vegetation of the Upper Engadine (Central Swiss Alps), Presented at EUG 11, Strasbourg, France, April 2001.

[22] Ariztegui, D. R., 1993, Palaeoenvironmental and palaeoclimatic implications of sedimented organic matter variations in lacustrine systems: Lake St Moritz, a case study, PhD Thesis (unpublished), ETH-Zürich, Switzerland, Nr. 10225, 188 pp.

[23] Gobet, E., Tinner, W., Hochuli, P. A., Van Leeuwen, J. F. N., and Ammann, B., 2003, Middle to Late Holocene vegetation history of the Upper Engadine (Swiss Alps): the role of man and fire, Vegetation History and Archaeobotany, 12:143-163.

[24] Sturm, M., and Matter, A., 1978, Turbidites and varves in Lake Brienz (Switzerland): deposition of clastic detritus by density currents, In: Matter, A., and Tucker, M., (Eds.), Modern and Ancient Lake Sediments, IASP Special Publication, No. 2, p. 145-166.

[25] Leemann, A., and Niessen, F., 1994, Varve formation and the climatic record in an Alpine proglacial lake, The Holocene, 4:1-8.

[26] Leemann, A., and Niessen, F., 1994, Holocene glacial activity and climatic variations in the Swiss Alps: reconstructing a continuous record from proglacial lake sediments, The Holocene, 4:259-268.

Chapter 4: Methods

4.1 Preliminary work on the Drammensfjord cores

4.1.1 Sediment coring and core preparation

The RV *Pelagia* cruise in 1999 cored at three sites within Drammensfjord, denoted D1, D2, and D3 in figure 4.1 below. Site D1 was just inside the sill at Svelvik, in the deepest part of the fjord (water depth c. 124m), site D2 was in the central part of the fjord (water depth c. 100m), and site D3 was further towards the northwest end of the fjord (water depth c. 75m). Multiple cores were taken from each site; all the cores from a given site were taken within 10m of each other [1].

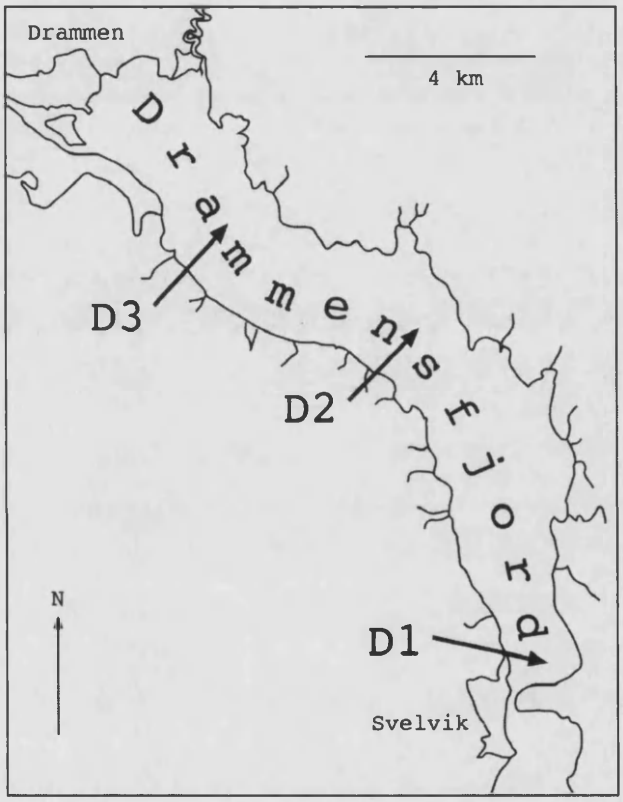

Figure 4.1: Map of Drammensfjord showing approximate positions of the three coring sites D1, D2, and D3.

Various coring devices were used: boxcorers to recover the uppermost sediment and sediment-water interface, and piston and gravity corers to recover deeper sediment. Letters were used to identify the various cores as follows:

Site D1

Core D1G: 110mm piston core	Total length 10.00m
Core D1H: 90mm piston core	Total length 13.99m
Core D1L: 110mm gravity core	Total length 8.15m
Core D1M: 110mm gravity core	Total length 8.48m

Site D2

Core D2G: 90mm piston core	Total length 8.89m
Core D2H: 110mm piston core	Total length 10.47m
Core D2L: 110mm gravity core	Total length 3.56m

Site D3

Core D3G: 90m piston core	Total length 9.17m
Core D3H: 110mm piston core	Total length 10.28m
Core D3L: 110mm gravity core	Total length 1.83m

Only the long piston and gravity cores above were suitable for image analysis of the laminations. The boxcores were unsuitable, because they were too short and did not recover properly-laminated sediment. The lengths given above include core sections that were obviously corrupted, or where no proper sediment was recovered: these include the deepest parts of cores D1H and D2H. The sediment extruded from the piston and gravity cores was sliced into core sections, each c. 1m long, and transported to NIOZ. The core sections were then split, numbered (D1G1, D1G2, etc.), marked with a way-up, wrapped in foil, then sealed in plastic wrapping along with a dampened sponge to stop them drying out. They were packed into cold storage at c. 4°C, although owing to temperature fluctuations, unfortunately some small intervals of the sediment subsequently froze, greatly disrupting the sedimentary fabric. This did not affect the best-quality core, D1G.

Prior to the cores being placed in storage, rapid preliminary logging was carried out in order to identify laminated intervals. A brief description was made of each metre-long section. The cores were initially disappointing, in that of nearly 60m of recovered sediment, less than 10% was properly laminated, the remainder being homogeneous or containing faint and/or disrupted laminations. However, some intervals, especially at the top of core D1G, showed very well-preserved laminations, and these intervals were prioritised for subsequent high-resolution imaging. Even so, in retrospect, perhaps too much time was expended in imaging homogeneous sediment, and too little time in detailed imaging of the well-preserved laminations. The imaging process itself is described in detail in section 4.4.

Substantial preparation was required prior to imaging of the cores. Each core section was split into an archive half and a sampling half; the archive halves were used for imaging. The act of splitting tended to smear the surface of the sediment, obscuring any laminations present. An undisturbed surface was obtained by scraping away the smeared surface layer, using a metal scraper c. 10cm wide. The sediment was scraped in a direction parallel to the laminations, using a smooth and rapid action: slow scraping tended to leave ridges on the sediment surface, parallel to the core. The scraper was wiped clean after each pass over the core surface, to avoid contamination of adjacent intervals. The aim was to get as flat a surface as possible, since sloping surfaces are very difficult to correct geometrically after image capture; they are unevenly illuminated and may be partly out of focus. The scraper was applied in overlapping sections, in order to avoid producing small ridges in the sediment every 10cm.

Many intervals of the Drammensfjord cores were obscured by mobilised sand that had flowed around the inside surface of the plastic core liner. In some cases, several centimetres of sandy sediment had to be scraped off before an undisturbed sediment fabric was visible across the full core width. Standing water on the core surface, seeping out of sandy intervals, also tended to obscure the true sediment fabric. This

was removed as far as possible by soaking it up with paper towels. The core scraping process turned up numerous fragments of wood, and one small bivalve shell, all of which were extracted, bottled, and labelled, and their locations noted. Where this left voids in the sediment, expanded polystyrene blocks were cut to shape and used to fill the voids, to stop the core collapsing into them. Immediately after the core scraping, each section was logged in detail. This is described in the next section.

4.1.2 Sediment core logging

The entire set of nine piston and gravity cores were logged using a vertical resolution of 3cm: any beds thinner than 3cm were ignored. Four different lithologies were identified: solid black mud, laminated mud with alternating black and grey sublayers, homogeneous grey mud, and sand. The laminations were also assessed as flat or distorted, and as continuous or discontinuous. This simple key was adequate for almost all of the sediment; there was relatively little lithological disparity. In particular, this 3cm-resolution log was designed to highlight the locations of well-laminated intervals where varve measurements could potentially be made. It can be found in the results (figure 5.2 in chapter 5).

The above log proved inadequate as a means of correlating the cores, except within the top few metres. An attempt was made to improve this by repeating the logging with a 1cm vertical resolution, noting all lithological variations as well as the presence of voids, wood fragments, shells, etc. This produced a very detailed description of the cores which can be found on CD-ROM in appendix B. Further attempts were made to correlate the cores using these more detailed descriptions.

4.1.3 Preliminary varve counting and investigation of the varve mechanism

Varved sediments are widespread, but it is important to confirm the assumption that any given laminations are indeed annual before embarking on further research (see section 1.4.2). Evidence from the literature review (chapter 2) suggests that the Drammensfjord laminations are indeed varves: the fjord is anoxic, there is a seasonal sedimentation cycle, and previous estimates of sediment accumulation rates are concordant (from first impressions) with the thicknesses of the laminations. However, as noted by Anderson [2], suspected varves should pass the following two tests: they should broadly agree with an independent chronology, and it should be possible to link their component sublayers to known seasonal changes in sedimentation. Both of these tests were carried out on the Drammensfjord laminations in order to confirm that the laminations were indeed annual, and to investigate the *varve mechanism*: the seasonal changes in sedimentation that lead to varves being deposited.

Radiocarbon dating was performed on two wood fragments from Drammensfjord core D1G, located approximately at either end of a long sequence of laminations. The remaining cores from site D1 lacked wood fragments at suitable depths for comparative dating with the varves, and unfortunately the laminations in the cores from sites D2 and D3 were poorly-preserved, such that most of the varve research was necessarily restricted to core D1G. In addition, Rienk Smittenberg, at NIOZ, supplied four AMS radiocarbon dates on biomarkers extracted from core D1G, and ^{210}Pb and ^{137}Cs data from a boxcore

from site D1 [3], and these data have also been used in confirming that the laminations are annual and in constructing an overall core chronology. Calibration of the radiocarbon dates, and the details of the integrated core chronology, can be found in the results (chapter 5).

Varve counting was performed on core D1G "by eye", counting the numbers of varves visible between distinct marker beds (defined at frequent intervals, to reduce counting errors) in order to produce a total. Each varve was defined as a couplet: a black sublayer and a pale grey sublayer. This was slow and laborious, but was an essential precursor to the automated image-analysis-based techniques developed later on (see section 4.4). The resulting count could also be immediately compared with the independent radiometric dates described above to confirm that the laminations were annual.

The second test described above, of linking component sublayers to known seasonal changes in sedimentation, could not be done simply by logging the cores. Except for the coarser sand grains, the components of the Drammensfjord sediment were too fine to be seen with the naked eye. Smear slides [4,5] were used to give an idea of the detailed composition of the sediment. A tiny amount of sediment was extracted from the core on the point of a toothpick, and transferred to a microscope slide; a drop of distilled water was then added and the sediment was smeared such that the components were distributed across the slide. It was then dried on a hot-plate, and a cover-slip was mounted. The sediment components could then be examined under a petrological microscope. In total, 22 smear slides were made, sampling most of the different sediment intervals from core D1G that were identified during the sedimentary logging.

In addition, a further trip to NIOZ was made to recover sediment slabs for backscatter electron imaging (BSEI). BSEI [6] is valuable for fine-grained laminated sediment because unlike smear slides it preserves the fabric of the sediment intact whilst allowing high-magnification study. BSEI works by firing a beam of electrons at a slab of sediment; some of these collide with atoms in the sediment and are backscattered. The image is constructed by detecting the paths of backscattered electrons. Strictly speaking, the proportion of electrons backscattered depends on the "backscatter coefficient" (η) of the sample material; this is basically controlled by its atomic number, such that larger, heavier atoms backscatter more electrons and therefore appear brighter. So, BSEI produces a high-resolution greyscale image, showing both the structure and the composition of the sediment.

The slab to be imaged must be stable under high vacuum and under heating by the electron beam, and must be polished perfectly flat to avoid topographical effects. For these reasons, the slab must be totally dehydrated, and impregnated with epoxy resin. The epoxy resin appears black in the backscatter images, making BSEI an easy way to estimate the porosity of the sediment. A more detailed use of BSEI of sediment slabs is for studying the fabric of fine-grained sediment: the morphology and composition of individual grains, and overall changes in the composition of the sediment.

For example, quartz, feldspar, and carbonate grains appear bright white, whereas clay is darker. In laminated sediment, terrigenous layers generally appear lighter than

diatomaceous layers: the opposite of their appearance under plane-polarised light, where the diatomaceous layers normally appear lighter [7]. This is because of the high porosity of diatom-rich sediment. It is important to note that the greyvalue of BSEI images is controlled by atomic number and not by the "photographic" greyvalue of the components in question. The application of BSEI to sediment slabs was pioneered at Southampton University by Alan Kemp and co-workers [8]. Low-resolution mosaics are first prepared, covering the whole slab, then areas of interest can be imaged at higher magnification. The maximum resolution is c. 1μm.

Sediment-slab BSEI is a relatively recent development, so it has only been used in a few studies. Published research includes BSEI on laminated sediment slabs from five locations: the Japan Sea [9], the Peruvian Shelf [10], the Mediterranean [11,12], Antarctica [13], and Scandinavian lakes [14]. This technique has not previously been used on laminated fjord sediments, so a number of backscatter images are presented in the results (chapter 5). BSEI is likely to become a standard technique in the future for studying unconsolidated laminated sediments of every kind, because it allows description of the fine-scale structural fabric of the sediment.

Of five slabs extracted from the Drammensfjord cores, two were selected for BSEI, which was performed at Southampton Oceanography Centre. This low rate of success was partly due to the difficulty of wielding a "cookie-cutter" - a slab-extracting device - in such soft sediment. Some slabs were only partly extracted, or became distorted during handling. None were taken from core D1G, in order to avoid disturbing the best-quality varves. Of the two chosen slabs, one (from core D1M) was structurally the most sound, since it was from deep down in the cores, where the sediment was more competent; the other (from core D1L) contained the best-preserved laminations, though it was slightly distorted. The two slabs were denoted D1M-CC3 and D1L-CC5, where "CC" is for "cookie-cutter". As extracted from the cores, the slabs were c. 12-14cm long, 2-5cm wide, and 1cm thick. They were transported between panes of glass, to keep them undistorted as much as possible. The BSEI results, and the insights they give into the Drammensfjord varve mechanism, are discussed in chapter 5.

4.2 Preliminary work on the Lake St Moritz core

The Lake St Moritz coring was done in July 1990 by ETH-Zürich, prior to UCL joining the Lake St Moritz research program. The location of core PSM90.3, at the deepest part of the lake (according to a seismic survey [15]), is given in section 3.3. It was obtained using a modified Kullenberg piston-corer. The sampling halves of the Lake St Moritz cores were subsequently destroyed by geochemical and micropalaeontological sampling; the archive halves of the cores were stored and subsequently used for the imaging.

Preparation of core PSM90.3 was identical to that for the Drammensfjord cores: the oxidised surface sediment was removed and the core was then scraped smooth. Since the entire core was only c. 11m long, there was no need for a preliminary survey to identify laminated intervals - and indeed, at first glance the entire core appeared to be laminated, including the lower glacial interval.

A short description was made of core PSM90.3, with reference to the framework given in Ariztegui *et al.* [16], dividing the Holocene into three stratigraphic units and describing changes in sediment colour and texture, and in the nature of the laminations (their thickness, lateral continuity, and colour contrast). As regards confirmation of the annual nature of the laminations via independent dating techniques, seasonal linkage of the varve components, and other aspects of the sediment core as a palaeoenvironmental record, attention is drawn to the large amounts of both data and interpretation already available [e.g. 16-18]; these are summarised and fully referenced in chapter 3.

4.3 Development of image analysis methods

4.3.1 Introduction

The image analysis methods used in this thesis were developed for application to *any* digital images of varved sediment cores, not just the two specific cores used. Development of these methods began before the Drammensfjord and Lake St Moritz cores had been obtained. This development initially used "idealised" digital images of varves, before progressing to selected high-quality images of real varves, then finally being adapted for use with the chosen Holocene varved sediment core images. Two reviews of the application of image analysis to laminated sediments have been previously published, by Cooper [19], and Saarinen and Petterson [20], but neither of these were detailed enough to be of use in developing the specific image analysis methods described in this chapter.

At an early stage, the decision was made to restrict the research to greyscale images: to study changes in the luminosity component of the sediment colour but not the colour itself. Lighting that maintains a constant "colour" (that is, temperature) over time is extremely expensive [21]; furthermore, changes in the *brightness* of illumination with time also cause colour shifts in the resulting images. "Most materials have a spectral response that is a function of total brightness, so that color shifts may occur ... These make attempts to perform colorimetry extremely difficult to standardise or keep in calibration" [22]. Without great expense, it is difficult to obtain a sufficiently stable illumination source and sensor for controlled colour imaging of varved sediment. The use of greyscale images enabled both of these problems to be avoided.

4.3.2 Digital image analysis software and programming

Greyscale digital images consist of a two-dimensional array of pixels, each with an assigned greyvalue, which can be manipulated using image analysis software. For 8-bit images, as used here, greyvalue takes integer values between 0 and 255; 0 is pure white and 255 is pure black. All images were stored as Tagged Image File Format (TIFF) files, which can be read by both Macs and PCs. This is also a "lossless" file format, which is essential for scientific image analysis: even when compressed, it allows reconstruction of all the original pixel values, unlike lossy formats such as JPEG files.

The software package NIH Image [23] was used for virtually all of the image analysis done in this thesis. Image analysis for presentational purposes (such as removing "red-eye") is commonly done using software such as Adobe Photoshop, but there are major advantages to using NIH Image for numerical image analysis. NIH Image, which runs on Macintosh computers, and Scion Image, its PC equivalent, can be downloaded for free from the internet [23]. Furthermore, it is "open source" and so can easily be modified using macros. Open source programs [24] do not encrypt their source code; this results in programs whose operations are transparent - it is easy to find out exactly what NIH Image is doing to the images it is modifying. NIH Image in particular is very versatile because its macros are written in Pascal, such that simple procedural programming can be used to locate or adjust individual array values, or to apply procedures to the entire pixel array [25].

4.3.3 Idealised digital varve images and thresholding

The simplest varves are repeating couplets of lighter and darker sublayers: on an idealised digital image, these can be represented as alternating black and white layers. A linescan perpendicular to these varves shows a "binary" alternation between two values: a right-angled waveform. The varve image only has two different greyvalues: one for pixels in the black layers, and one for pixels in the white layers (see figure 4.2).

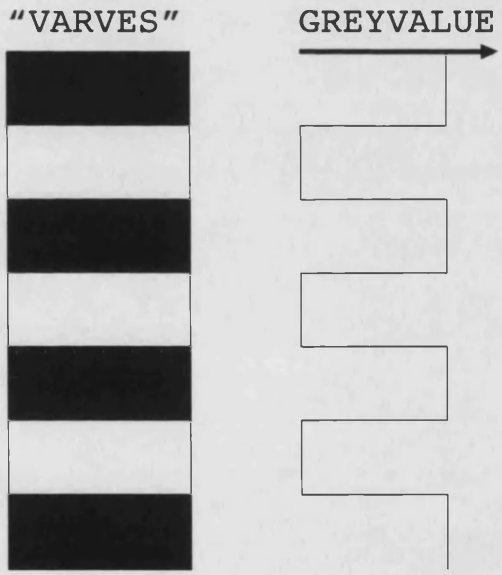

Figure 4.2: Idealised alternating black and white varve sublayers.

Introducing noise into this image results in pixels with a variety of different greyvalues. If the greyvalue frequency histogram is considered, the introduction of noise will cause the two sharp spikes representing the layers to spread out into two broader distributions, most likely normal distributions, since the most common type of noise in images is Gaussian [26]. The technique of *thresholding* can then be used to separate the different layers.

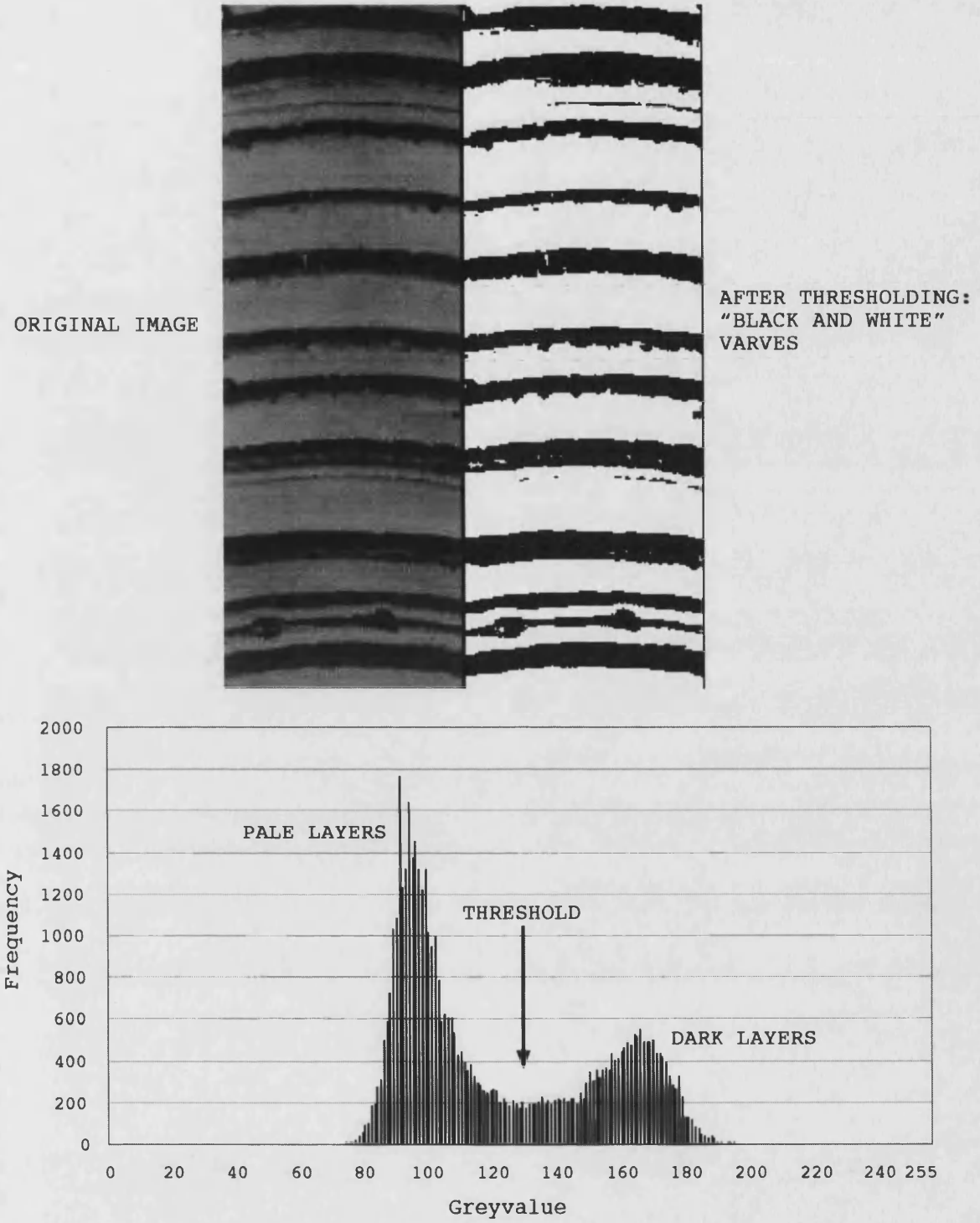

Figure 4.3: Thresholding to produce a "binary" black and white image, using varves from Keeseville, New York State, USA. The bimodal greyvalue frequency distribution is shown. For original image source, see [27].

Given two distinct distributions (or image "phases"), a greyvalue can be chosen from anywhere in the region between them to act as a threshold. This allows the two types of layers in the image to be separated. This threshold value is unlikely to be equal to the mean. For example, if the lighter layers are thicker than the darker layers, the mean pixel greyvalue will be biased towards lighter values, such that a thresholding operation using it will underestimate the thickness of the lighter

layers. The result of thresholding is to assign each pixel to either above or below the threshold, which can be represented by black and white pixels: essentially, it converts noisy images of dark and light layers back to the black and white idealised varves described above.

The thresholding technique was tested in NIH Image using an image showing thick, regular glacial varves (see figure 4.3). A slider control allows rapid preliminary inspection of how a thresholded image will look, and whether a simple thresholding operation alone will result in clear, alternating black and white layers, or whether additional image processing is required. If the greyvalue frequency histogram is sufficiently bimodal, then thresholding will be successful, and it is a simple matter to write an NIH macro (a user-written Pascal program [25]) to locate varve sublayer boundaries, count the varves, measure the thicknesses of their sublayers, and store the relevant array addresses such that sediment greyvalue can be measured from the original image (which is unchanged in size by the thresholding process).

However, this approach was rarely found to be successful in practice, unless the varves were exceptionally clear and uniform (as is the case for the image in figure 4.3). Testing the method on a range of digital images of varves identified two distinct problems that reduced the efficacy of simple thresholding.

The first problem was that the image may not have a bimodal greyvalue frequency distribution because of other phases in the image in addition to the varve couplets. Varves may form triplets [28], for example, or more commonly, there are additional image components such as turbidites or other event beds, or cracks and voids in the sediment core [29]. Each of these components will add one or more further distributed variables to the greyvalue frequency distribution. The solution to this is to select a linescan path down the image which avoids, where possible, features other than the varve sequence; for poor-quality varved cores this has to be done manually.

The second problem is the effect of noise on the greyvalue frequency distribution. Too much noise will blur separate normal distributions together, preventing thresholding from producing coherent sublayers. This problem was found in almost every varve image investigated. The varves are clear to the naked eye, but the sediment greyvalue is so variable that a thresholded image contains no distinct varve boundaries. This noise comes from several sources. All digital cameras and scanners produce some randomly-distributed internal noise; lighting irregularities and detached sediment particles can obscure the camera's "view" of the sediment; the surface of the sediment core itself may not have been scraped perfectly smooth; and the sediment fabric is not always well-preserved. However, the signal-to-noise ratio of an image of varved sediment can be greatly improved using appropriate image filters.

These problems can be demonstrated using a sample of digital images of varved sediment. These are shown, unmodified, with their greyvalue frequency distributions (all plotted at the same scale) in figure 4.4.

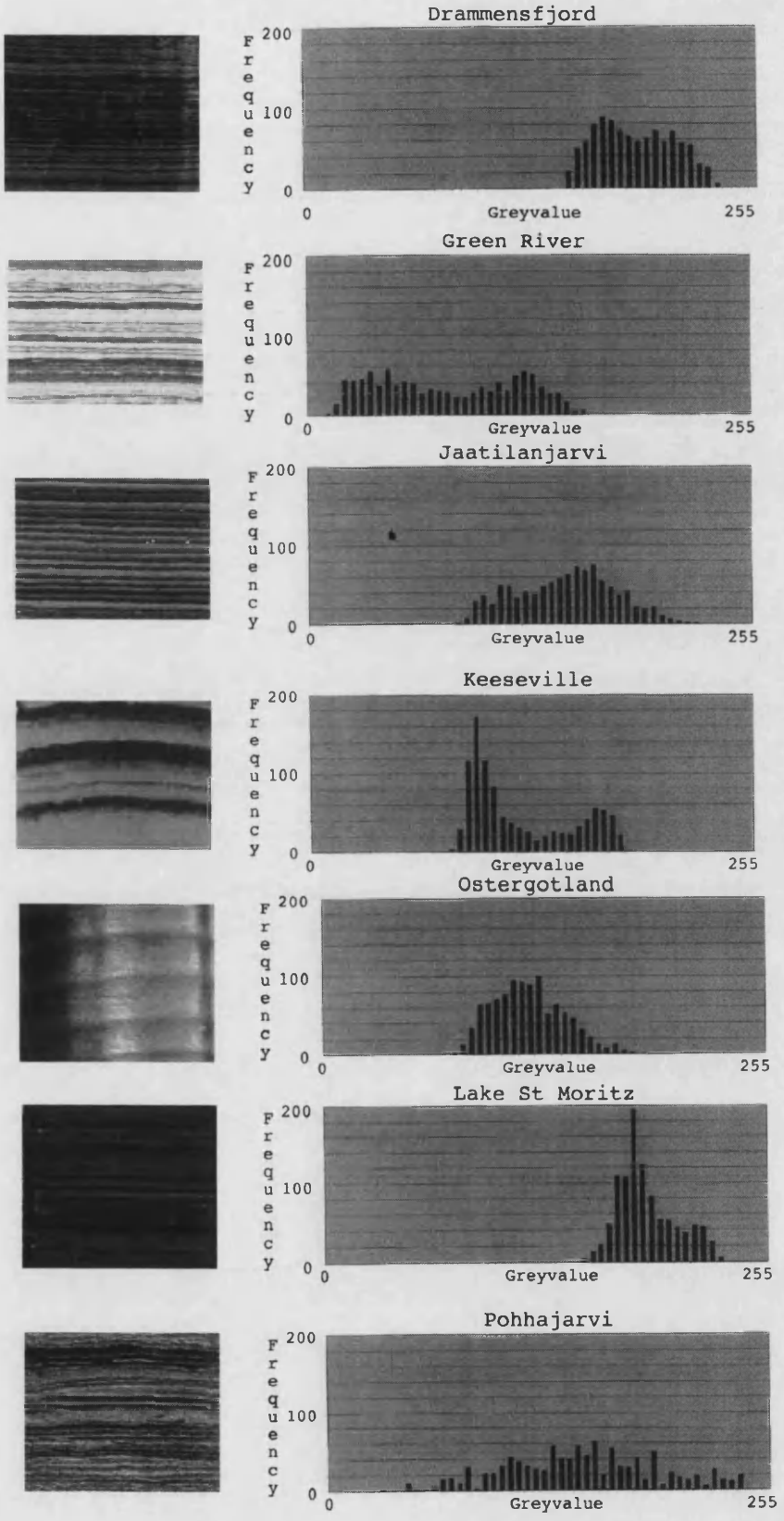

Figure 4.4: Greyscale images and greyvalue frequency histograms (with outliers removed) for varved cores from Drammensfjord, the Eocene Green River Formation, USA, Lake Jaatilanjärvi, Finland, Keeseville, USA, Östergötland, Sweden, Lake St Moritz, and Lake Pohhajärvi, Finland. The distributions are all plotted at the same scale. For original image sources, see [30].

Evidently, it is unusual for unprocessed varve images to have strongly bimodal greyvalue frequency distributions. This is primarily because of image noise, and a method is required that can reduce the noise levels of real varve images sufficiently so that thresholding can be used. Filtering methods that can achieve this are described in the next section.

4.3.4 Filtering to remove noise from actual varve images

Post-thresholding noise removal was investigated using so-called morphological processing [31], which repeatedly erodes and dilates regions (of black or white) in the thresholded image, filling in gaps and removing extraneous single pixels. This produces distinct, morphologically coherent black and white structures. However, as with various other methods of image processing such as texture-based thresholding [22], morphological processing requires each region to have a relatively large number of pixels across each dimension, such that it only worked with very high resolution images. Varve images where the thinnest varve sublayers may be only three or four pixels thick were unsuitable for this type of processing.

Filtering the images *before* thresholding was more successful. A number of small, high-quality digital varve images from Finnish lakes [30] were used to investigate various filtering methods.

All of these methods are underpinned by two assumptions: "that the pixels in the image are much smaller than any of the important details, and that for most of the pixels present, most of their neighbours represent the same structure" [22].

Images of varves, especially very thin biogenic varves, are a special case, in that perpendicular to the varves, a rapid alternation in image phases is expected - a single varve sublayer may only be a few pixels thick - but parallel to the varves, there is a strong prior expectation that the image phases will show no change, and this allows lateral averaging to be used to improve confidence in the resulting filtered linescan record. This averaging, in turn, depends on the quality of the sediment cores, and is vulnerable to disruption where the core surface is distorted, or contains voids, mobilised sand, and so on.

The first filtering method that was investigated was *neighbourhood averaging*. This works by replacing the greyvalue of a given pixel with the mean greyvalue of all the pixels within a predefined "kernel" centred on it. It is based on the assumption given above, that most of the surrounding pixels which form the kernel represent the same structure as the central pixel. Neighbourhood averaging does increase the signal-to-noise ratio of the image; however, it is an unsuitable method for varve measurement since it blurs edges, displaces boundaries, reduces contrast, and can introduce "pseudo-resolution artefacts" [22].

Median filtering was found to be a more useful process. Again, this is a kernel operation: all the pixels in the kernel are ranked in order of greyvalue, then the median value in the list is assigned to the central pixel. This technique is an excellent way of removing "shot noise": isolated extreme values which may result from

reflections, sand grains, foraminifers, and so on. This is because it replaces "extreme" greyvalues with "reasonable" ones. Importantly, this technique does not reduce the greyvalue contrast across steps in the image, such as varve boundaries. No new intermediate greyvalues are introduced, unlike with neighbourhood averaging, because only the original greyvalues are available for selection. Furthermore, it does not shift boundaries, making it suitable for varve measurement.

Because it does not affect the position of edges in the image, median filtering can be repeatedly applied to the same image. This has the effect of smoothing out the fine detail, leaving broader areas with the same greyvalue: an effect called *posterisation*. This can produce a sharp, uniform image of alternating varve sublayers, given sufficient resolution in the original image.

The effects of neighbourhood averaging and median filtering can be compared using figures 4.5 and 4.6, which show the effects of these filters on the same image. Note the difference in the resulting greyvalue frequency distributions.

Other filters also exist which can improve the signal-to-noise ratio of varve images, such as greyscale erosion and dilation, and variable thresholding methods such as using "top hat" and "rolling ball" filters [22]. For high-quality images, these can work better than the simple median filter, but they are also more prone to amplifying irregularities in the image. For example, if the varves in an image are all of very similar thicknesses, then a rolling ball filter at an appropriate scale will successfully amplify the varves and ignore the noise. But if there is significant variation in varve thickness, or varve colour contrast, then this filter will not be as effective as a simple median filter.

Repeated investigations suggested two general results. First, that there is no optimum way of filtering varved images; what works well for one core may not be suitable for another. Second, that the scale over which a filter is applied is just as important as its type: the area of the kernel for a median filter, for example, or the width of a rolling ball filter applied to a linescan. The median filter was chosen as a suitably simple and effective filter to apply to the Drammensfjord and Lake St Moritz images in the first instance.

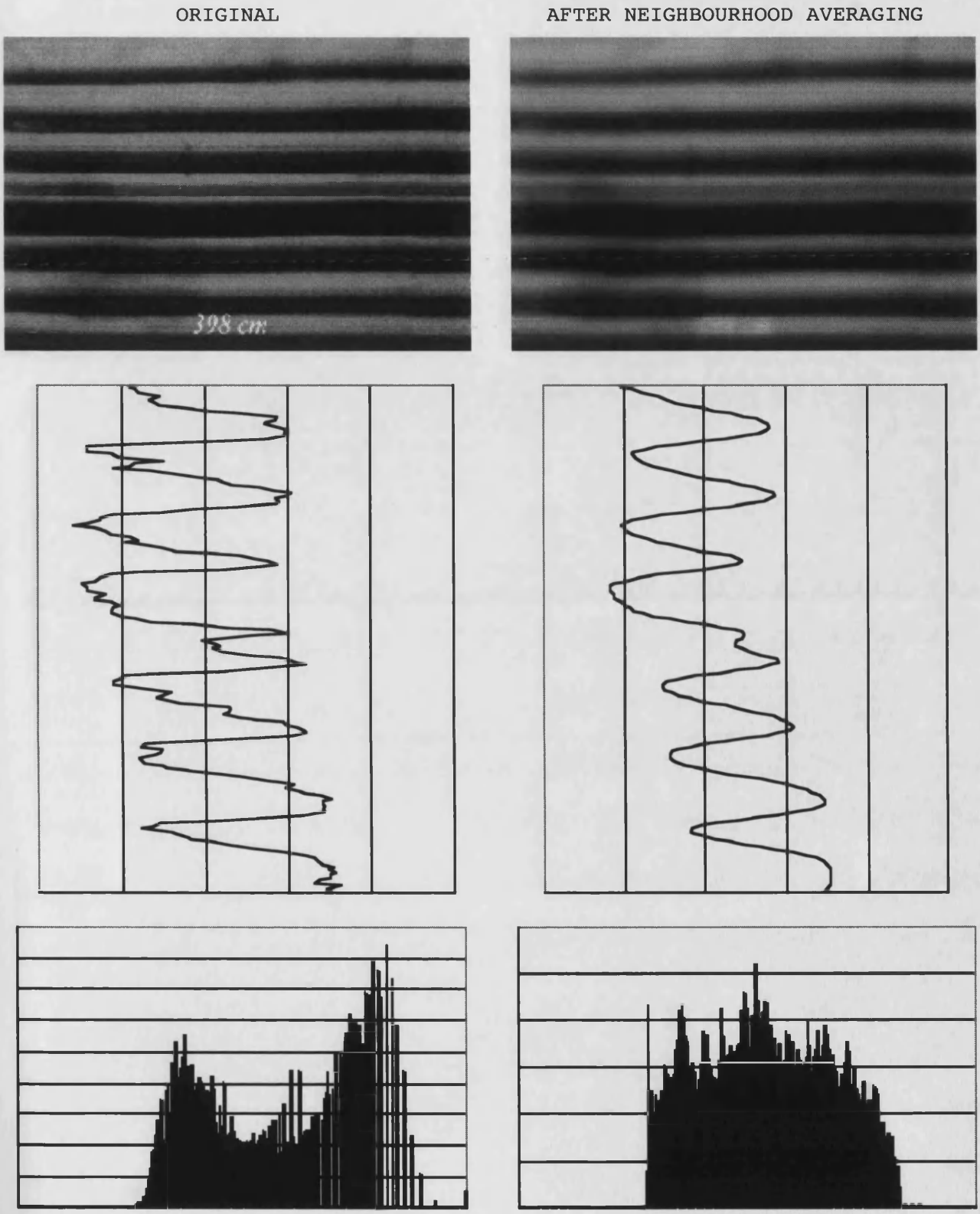

Figure 4.5: Effects of neighbourhood averaging. The original image of varves from Lake Korttajärvi [30] is on the left, and the averaged image on the right. Linescans and greyvalue frequency distributions are below.

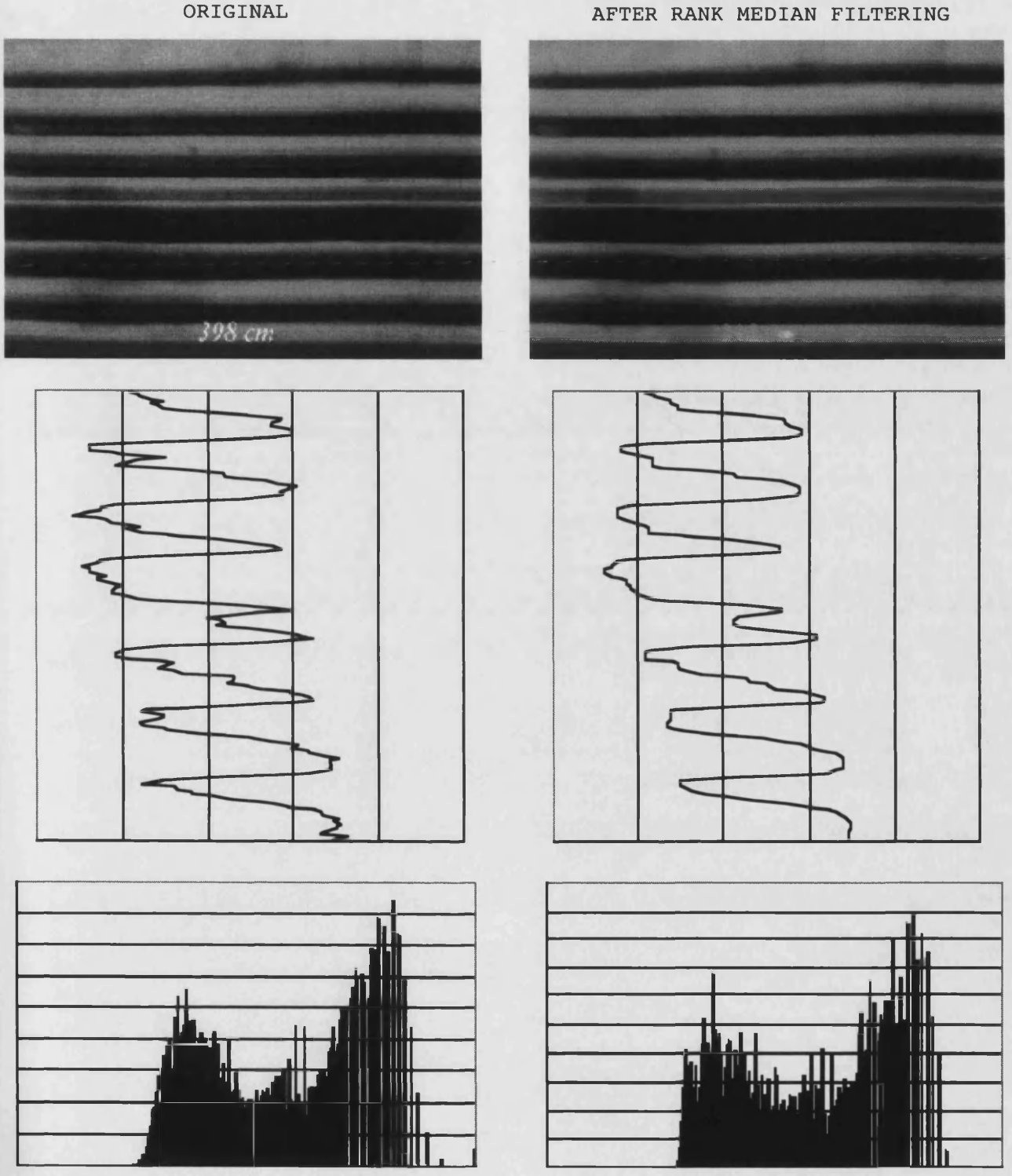

Figure 4.6: Effects of median filtering. The original image is as figure 4.5, but here the processed version remains sharp, and the frequency distribution remains bimodal, allowing thresholding.

4.3.5 Methodological conclusions from the preliminary image analysis

Before the specific methods applied to the Drammensfjord and Lake St Moritz cores are described, it is useful to draw some methodological conclusions from the preliminary image analysis investigations, since this is a relatively new and little-used technique.

- As discussed in section 1.7.2, the aim of image analysis is to enable objective and consistent criteria to be used in varve measurement, especially in low-quality varve sequences. Image analysis in this sense is not limited to methods such as inverting the greyvalue look-up table, using false colour, and stretching the greyvalue histogram, all of which can be done in order to make the varves clearer to the human eye, but none of which affect the information content of the image. It is concerned with the more complex aim of enabling the computer itself to identify varve boundaries and derive varve-based data, using the filtering and thresholding techniques above to reduce image noise levels to a point at which this is possible.

- Image resolution is of critical importance. Images should be captured at the maximum, rather than the minimum, possible resolution, since the resulting redundancy in the images will make image processing more effective: a high-resolution image can be processed in such a way as to compensate for irregular and poorly-preserved varves. This may mean initially dealing with very large file sizes. Image resolution can always be reduced later to save time and reduce memory usage, but it cannot be increased!

- The second critically important factor is consistency in imaging conditions. The preliminary image analysis concentrated on individual images from different varved cores, so the importance of this factor was not fully realised until the work on the Drammensfjord and Lake St Moritz cores began. Images captured under differing conditions will not be comparable until those differences have been corrected for, which may well take much longer than arranging to have consistent imaging conditions in the first place. Once again, the aim should be to approach as close as possible to an ideal situation before the images are digitised: this will result in the strongest possible signal in the data, and will minimise the necessary image processing that needs to be carried out afterwards.

4.4 Application of image analysis to the Drammensfjord cores

4.4.1 The Drammensfjord imaging process

The Drammensfjord core imaging took place in January 2000 at NIOZ. The original intention was to use a high-resolution OptoTech digital camera to capture digital images of the cores directly, but this proved to be too unreliable and lacked technical support. Instead, photographs were taken using an ordinary camera, and later converted to digital images. No darkroom was available at NIOZ, so a long, L-shaped laboratory with a window only at one end was used, such that one arm of the "L" received no direct lighting from outside, in order to reduce lighting fluctuations.

The camera stand was erected on a table, with the camera bolted to a sliding unit on a vertical column mounted on the stand. This column was calibrated in centimetres, allowing the height of the camera lens to be recorded. The camera was positioned c. 20cm above the sediment, then adjusted such that the depth of focus was sufficient to include both the ordinary core surface height, and those parts of the cores that had been lowered by extra scraping in order to expose the undisturbed sediment fabric. The focus of the camera was periodically checked throughout the photography. A polarising filter was used to reduce reflections in the images. The sediment surface was illuminated by two fluorescent strip lights, mounted on the camera stand such that their positions were constant, and angled at 45° to the sediment surface (see figure 4.7). The lamps were at c. 5,400K, that is, "daylight" lamps. This set-up is similar to that described by Schaaf and Thurow [29].

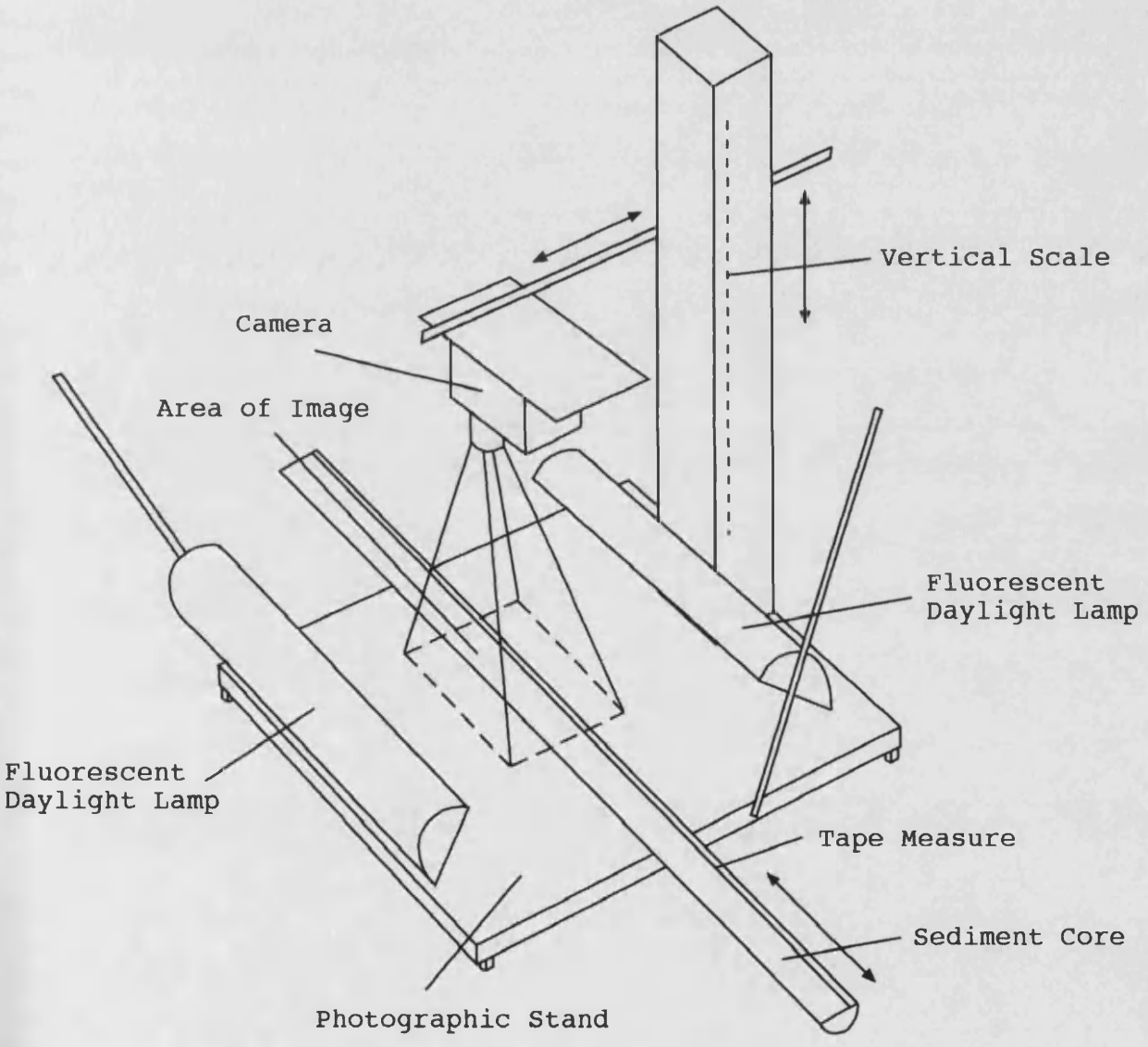

Figure 4.7: The Drammensfjord core imaging apparatus. Guide tape on the photographic stand was used to keep the core correctly aligned under the camera.

Each core section was photographed in turn, after placing a flat tape measure on the freshly-scraped sediment surface to act as a core depth scale in the images. The relevant core depths were recorded as each image was taken, along with the film and

image number. Between each 1m core section, a Kodak photographic colour card was photographed in exactly the same position each time. After conversion of the images to greyscale, this would provide a range of greyvalues which could be used to correct for variation in imaging conditions (since the "real" greyvalues of the colour card were unchanging). The photography was done at two settings, high magnification and low magnification, corresponding to 10cm depth of core in one image (plus c. 1cm of overlap on each side), and to 20cm depth of core in one image (plus c. 2cm of overlap on each side) respectively. For most of the cores, laminated intervals were photographed at high magnification, and homogeneous intervals at low magnification; in addition, a few core sections were photographed under both settings, to enable detection of any systematic bias that the change in settings might have introduced.

Since the initial thesis plan involved working with colour images, 35mm colour slide film was used. However, the resulting images were not colour-stable, as could have been foreseen given the unpredictable changes in illumination that occurred because of the lack of a suitable darkroom. Furthermore, attempts to remedy a colour bias in the camera set-up (saturation of the blue channel, resulting in an inability to capture variation in the blue component of the sediment colour) by adjusting the camera aperture, only served to reduce the quality of the later core images, especially the images from core D3, making varve measurement very difficult even after the conversion to greyscale.

The core sections were photographed in order of priority, with the laminated sections being done first. 35 films were used in total, producing c. 550 images. These films were developed cheaply at "Hema", rather than at a dedicated photographic developer, which resulted in further problems with image consistency. Pale bands appeared across some of the developed images, presumably artefacts from the developing process; in addition, some of the images were darkened at the margins or even truncated. 37 images were taken on each 36-image film, and this may have contributed to the latter problem. Fortunately, these problems did not affect the crucial images of the well-preserved varves from core D1G. Overall, however, comparing the developed photographs to the original cores, there was a significant loss of information during the Drammensfjord imaging, which could have been reduced if the imaging process had been better designed.

The slide films were framed as 36mm x 24mm slides, and numbered 01-01 to 01-37, 02-02 to 02-37, and so on for each film. These slides were then scanned, using a Nikon LS-1000 35mm slide scanner, into Adobe Photoshop where they were saved as TIFF files, each being 7.2MB in size. The claimed resolution of the scanner, of 1,350 dots per inch - which refers to the slide dimensions, of course, not to the imaged area - translated into a real resolution of c. 10 pixels per mm for the "high resolution" images and c. 16 pixels per mm for the "low resolution" images. The only deliberate modification made to the images during the scanning process was to increase the brightness. Within Photoshop, the images were then converted to greyscale, discarding the colour values and keeping only the luminosity for each pixel, then saved onto CD-ROM.

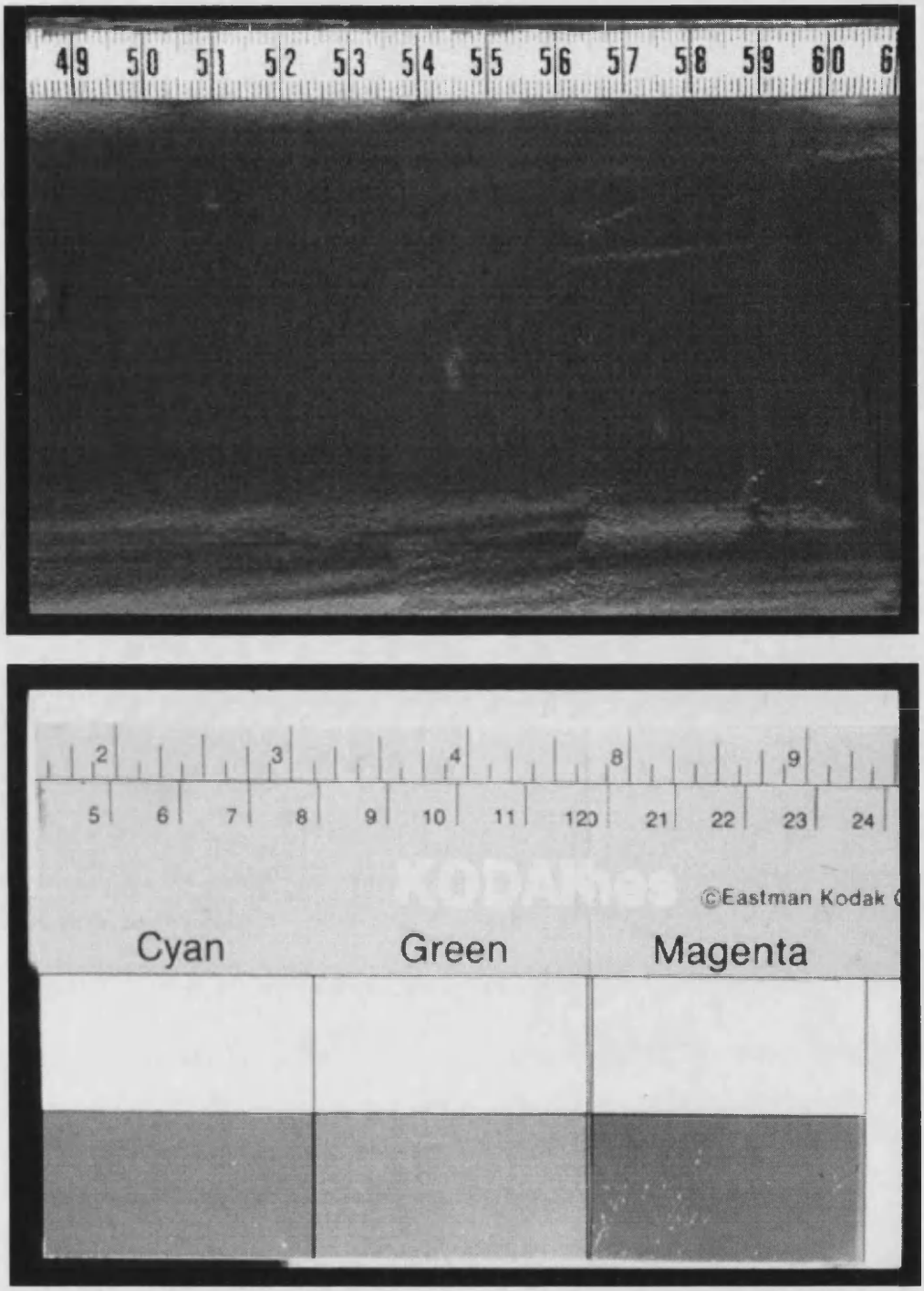

Figure 4.8: Drammensfjord greyscale example image (top), in this case showing homogeneous sediment at the "high magnification" setting, and Kodak colour card (bottom) used to correct for changing imaging conditions. The reflections at the bottom edge of the sediment reveal where the soft surface has not been scraped perfectly flat.

Prior to the greyscale conversion, a brief investigation of downcore changes in colour (measured on the RGB system) suggested that in fact, there was little extra information preserved in sediment colour: R, G, and B values were closely correlated, suggesting that the sediment components were basically varying in shades of grey anyway, although this cannot be confirmed without a properly-controlled colorimetric investigation.

4.4.2 Correction for changes in imaging conditions

Under brightly-lit conditions, a given sediment surface will appear lighter than under dimly-lit conditions. Thus, it is important to keep the degree of illumination uniform across the sediment surface. Unfortunately, even elaborate arrangements of lights can only approximate uniform illumination [22]. After image capture, then, each image needed to be corrected for uneven illumination.

Lateral variation in illumination was found to be minimal, at least within the smoothed area of the sediment surface from within which the linescans were extracted. Downcore variation, in contrast, was significant. This was quantified by averaging all the downcore linescans extracted from the images, based on the reasoning that averaging would cause genuine "sedimentary" variations in greyvalue to cancel out. This would leave a curve which represented the consistent "background" illumination, assuming that the lighting configuration was identical for each image. Images at different magnifications were treated separately, of course. The resulting curve for the high-magnification images is shown in figure 4.9.

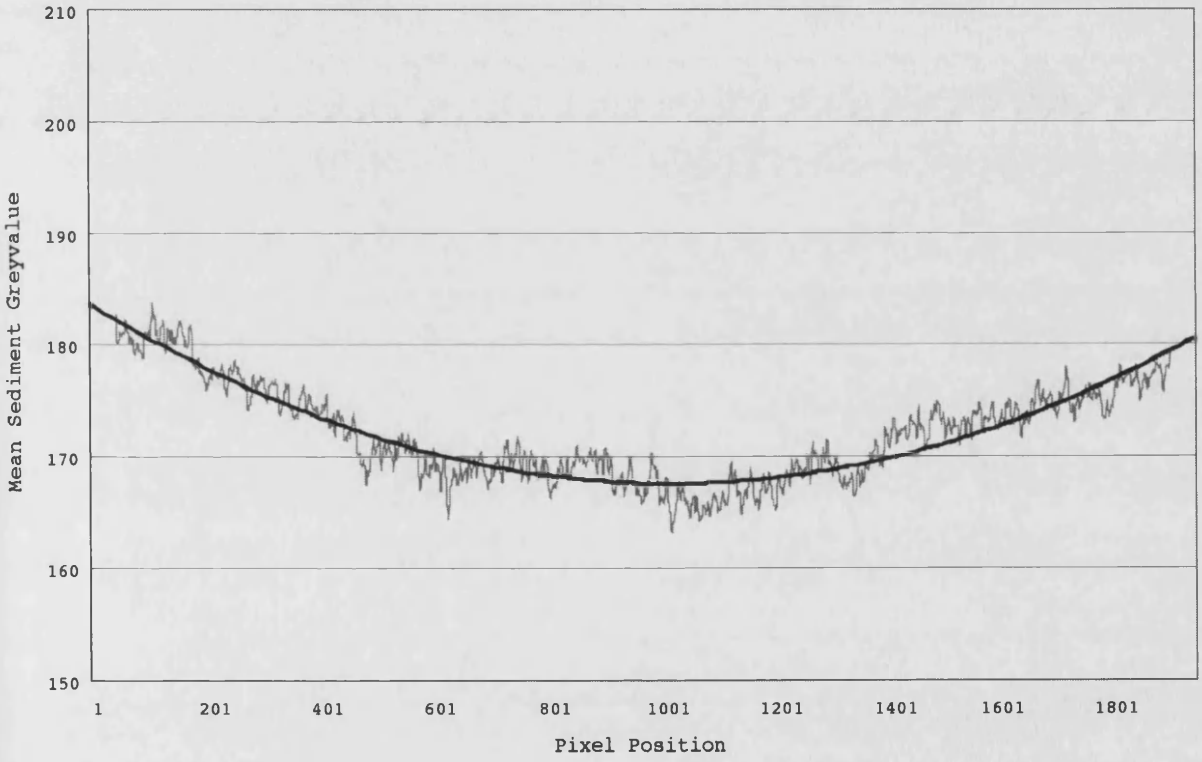

Figure 4.9: Averaged greyvalue (light grey) and quadratic approximation curve (black) showing uneven illumination of Drammensfjord high-magnification images, obtained by averaging vertical linescans. The quadratic curve may be thought of as the apparent greyvalue of a uniformly grey sheet of paper under the Drammensfjord imaging set-up.

Conventionally, such curves are approximated by simple polynomials [22] and the Drammensfjord vertical background variation can be closely approximated by a quadratic curve. This curve shows that the unmodified images are slightly brighter in the middle than at the top and bottom; the correction was done by flattening each linescan by the amount necessary to flatten this averaged curve.

In addition, changes in illumination *between one image and the next* needed to be corrected for. The fluorescent lights were fixed in the same position throughout, but there were changes both intentional (such as raising the camera to switch to low-resolution imaging, which reduced the effective image illumination) and unintentional (such as changes in the amount of sunlight entering the laboratory) which were apparent when the control images of Kodak colour cards were studied.

Gradual drift in illumination conditions, as was originally expected, would have been simple to correct, but the chaotic changes shown in figure 4.10 reduced the degree of confidence in the correction process. For example, if the illumination was much greater just before a 1m core section was imaged than just after, did the illumination evenly decline over that core section, or was there a sudden change at one point? Further information can be gleaned by looking at the individual images, though this risks problems with circular reasoning, since without external controls there is no way to distinguish gradual changes in real sediment greyvalue from gradual changes in background illumination. This could have been resolved by incorporating a full greyscale control card into every image, as was later done for the Lake St Moritz images. For the Drammensfjord images, linear interpolation was used to match each sediment core image with an estimated degree of illumination; this was the most parsimonious method of correcting the images, and did not introduce any discontinuities into the greyscale linescans.

Figure 4.10: Changes in background illumination during the Drammensfjord photography, as measured from the Kodak colour cards. Intentional changes (e.g. because of camera aperture adjustment) are marked with arrows.

Even after these corrections, there remained a small number of evident irregularities within the images, such as in image 09-37, which was significantly darker than all the other images, despite no recorded changes in imaging conditions. These were assumed to result from irregularities in the developing process, and they demonstrate how much

more useful direct image capture by a digital camera can be, in allowing *in situ* assessment of image quality and image recapture if necessary. However, the fact that most of the well-preserved varves in the Drammensfjord cores were contained in a relatively small interval (<10% of the total core length that was photographed) meant that the above problems with consistency of imaging conditions were not as damaging as they might otherwise have been. For metre-scale variation in sediment greyvalue, for example, it would be impossible to resolve fully the effects of changing imaging conditions and changing sediment composition.

Even with perfectly-uniform illumination and developing methods, there were other sources of "noise" within the Drammensfjord cores that prevented the digital images being truly representative of the Drammensfjord sediment record. The sediment surface was not always scraped perfectly smooth, and the resulting ridges in the sediment surface caused reflections in the images which the polariser reduced, but could not eliminate. Mobilised sand and accidentally-frozen intervals also obscured the original fabric of the sediment in places.

The pixel-by-pixel greyvalue record was also disrupted by original sedimentary components such as wood fragments, voids, and reflecting facets of sand grains. Indeed, changes in sediment reflectivity resulted in *the sediment itself* contributing to uneven illumination, such that no generalised method of correction was possible. For example, sand intervals in the clay-rich Drammensfjord cores tended to seep standing water, producing reflective "highlights" on the sediment surface which changed position as the viewing angle changed. This problem occurs in other imaging situations, such as photographing leaves [32], where the reflectivity of the leaf surface causes an apparent variation in leaf colour. For measurement of its shape, a leaf can be illuminated from behind, producing a silhouette - but a similar solution is impossible for varved sediment cores. This is a fundamental imperfection in the imaging technique [33].

4.4.3 Method of varve measurement using digital image analysis

The Drammensfjord varves were typically c. 1mm thick, and consisted of a grey sublayer and a black sublayer, producing a couplet. They were clearer in some intervals than in others: there was significant downcore variation in sublayer contrast, thickness, and sharpness/blurriness. Manual counts were made of the varves in the digital images from core D1G, using "Object Image" [34], a modified version of NIH Image which allows image measurement to be done using a transparent overlay that can be edited without affecting the original image. This enabled a computerised version of the traditional method of varve measurement (using pins placed in the sediment at varve boundaries); markers were manually fixed on the overlay above the digital image, then their pixel array locations were exported to Excel. This process is shown in figure 4.11.

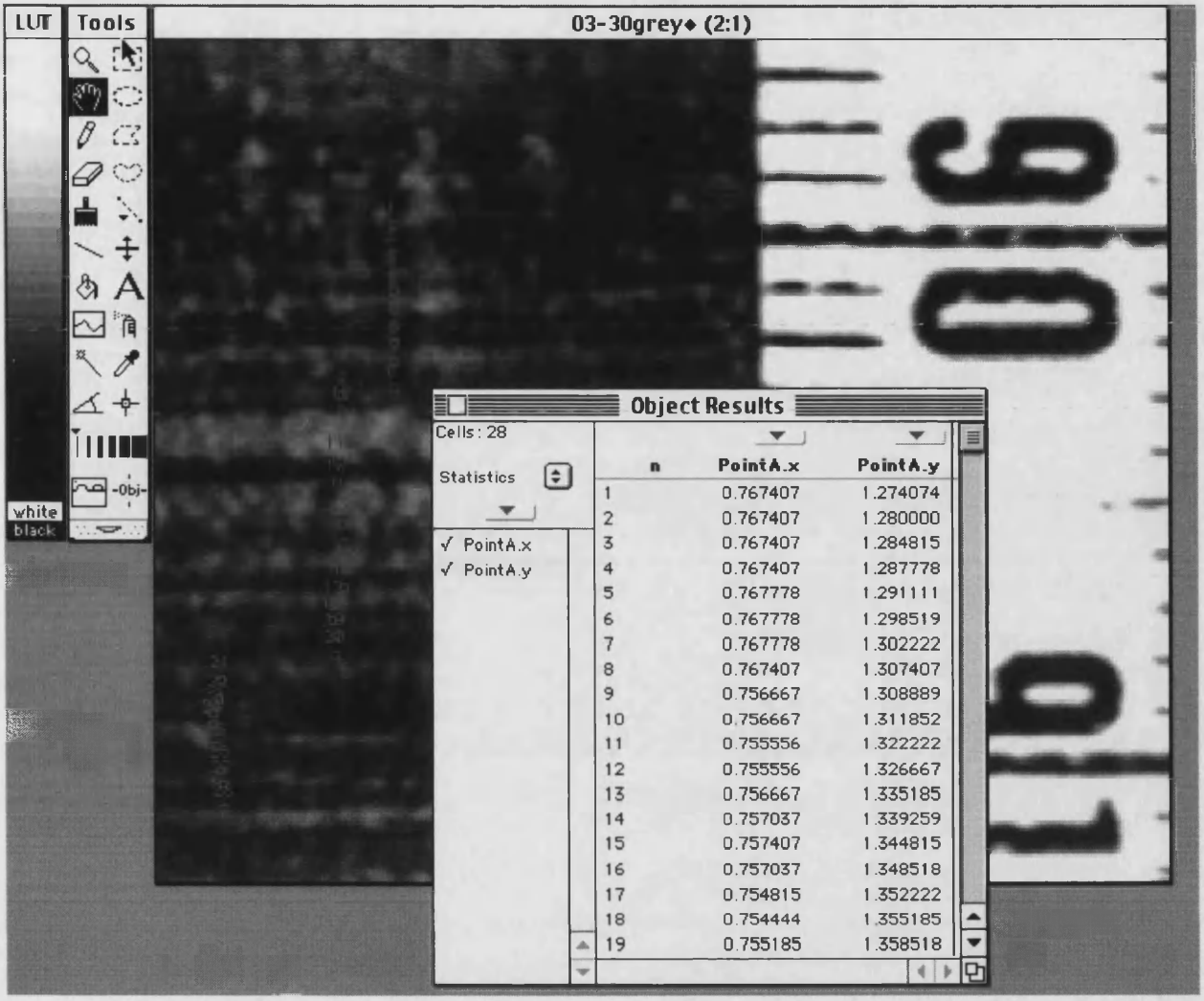

Figure 4.11: Manual measurement of varve thicknesses from a digital image using the Object Image package. The enlarged tape measure on the right is in centimetres, i.e. 90-91cm depth in core D1G. The varves are much clearer on the computer screen than on the printer because of the limited dynamic range of the latter.

These positions were then converted to millimetric depth measurements using the tape measure present in each image. This was a simple linear conversion, since repeated investigations proved that the area represented by each pixel was constant except at the extreme margins of the images, where no measurements were required because of the overlap between images. The varves were clear enough to allow consistent manual counting; the resolution was just high enough to capture the thinnest sublayers, though not as high as it ideally should have been to allow large-scale image processing. But this manual counting was not the main aim of the research (see section 1.7.2). The next step was to develop a method for computer-based automatic varve measurement.

This required that greyvalue linescans be obtained from selected columnar parts of the images, to avoid blurred intervals, voids, reflections, and so on. Only rarely were the images of sufficient quality that the entire width of the core image displayed undisturbed varves. A linescan thickness of a single pixel was used for varve measurement, since in most parts of the core, the varves were not perfectly horizontal

(perhaps as a result of the core not penetrating exactly vertically into the sediment, or of post-coring deformation of the sediment, e.g. during extrusion); averaging multiple pixels would therefore have caused undesirable smoothing of the data. Furthermore, varying the width of the linescan was not feasible, since this would have acted as a frequency filter on the greyvalue depth-series, making it non-stationary. An optimal linescan path was manually constructed down each core section, using multiple overlapping linescans on each image.

To produce a master linescan record, these overlapping linescans needed to be joined. This was done using cross-correlation via an Excel macro named "LinescanJoiner", written in Visual Basic for Applications (VBA). For two overlapping linescans, correlation coefficients were measured for each possible overlap, and the highest one taken as the correct position (as long as the overlap was greater than 200 pixels, to avoid anomalies with very small counting statistics). The VBA code for LinescanJoiner can be found on CD-ROM in appendix B. The resulting master linescans for each core were resampled at a lower resolution (to make them easier to process) and then plotted side-by-side to provide an alternative to the original lithological log (see section 4.1.2). These master linescans should theoretically have allowed the varves to be measured, via thresholding. However, the noise levels of the original images were frequently too high for this to be possible; the greyvalue frequency distribution was often non-bimodal.

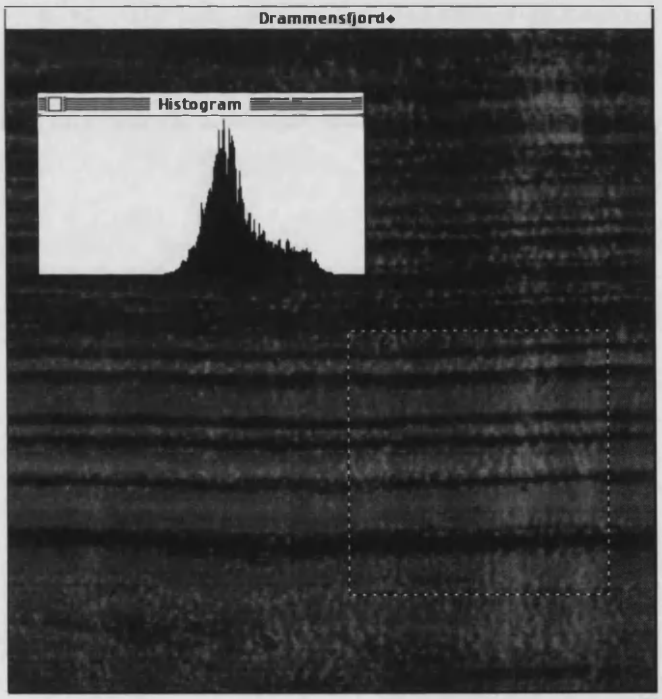

Figure 4.12: Unmodified Drammensfjord varve image and inset greyvalue frequency distribution, showing that thresholding is not possible because noise pixels have made the distribution non-bimodal. The noise arises in part from the obvious reflections on the right of the image.

The signal-to-noise ratio of the images needed to be increased before the varves could unambiguously be detected in the numerical data. A rank median filter was applied to the images (see section 4.3.4) to remove "unlikely" pixel values (based on their

frequency of adjacent occurrence) and to produce a more uniform series of horizontal bands of different greyvalues. These processed images could then be successfully thresholded, and using macros within NIH Image [25] the positions of the varve boundaries could then be extracted, allowing sublayer thicknesses to be calculated; the mean greyvalues of the component sublayers could be found by reference to the original images.

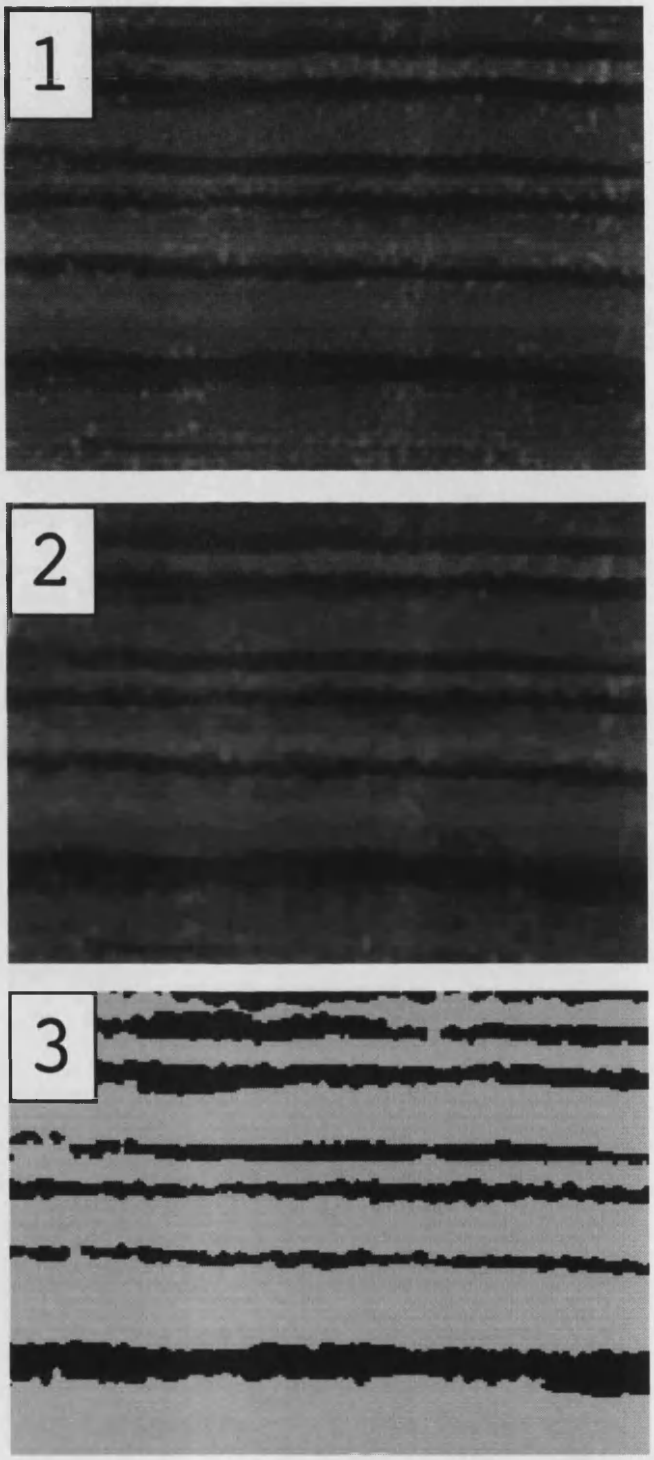

Figure 4.13: Two-stage thresholding of the Drammensfjord varves. 1 = Original unmodified image. 2 = Image 1 after application of rank median filter. 3 = Image 2 after thresholding.

The size of the interval over which a single threshold could be successfully applied was generally small - no more than a few hundred varves, or several tens of centimetres - as a result of gradual overall shifts in greyvalue. The filtered images retained a bimodal greyvalue distribution, but these gradual shifts caused the frequency distribution peaks to blur together if a linescan was used that was too long. Despite the attempts to correct for changing image illumination (see section 4.4.2), the most likely explanation for this is that these shifts result from changing imaging conditions, although they could also arise from gradual changes in sediment composition.

Locally-tailored thresholds were used wherever necessary to avoid any ambiguity about the locations of varve boundaries: a process that was slow and painstaking, though still objectively designed to separate the two phases of the varve images. This contrasted with the "fast and easy" approach to sediment colour measurement of Schaaf and Thurow [29] who were able to assume that in their case these measures were unnecessary (justifiably, since they were using images with a much higher signal-to-noise ratio).

It was originally hoped that this extent of image processing would suffice for all of the images. However, in order to obtain a continuous varve record, some intervals needed additional processing. For "noisy" regions of the images that also contained many thin varves, it was necessary *in extremis* to compare a set of one-pixel-wide linescans covering the same interval, in order to identify laterally continuous peaks and troughs in image greyvalue. The pixels of *maximum greyvalue gradient* were then located and assumed to represent the contacts between varve sublayers. The need for this additional processing could have been obviated by a higher initial image resolution.

The varve results (see chapter 5) were taken from core D1G. This site was jointly identified by UCL and NIOZ as containing the best-quality sediment record, and was chosen for radiocarbon dating, ^{210}Pb and ^{137}Cs dating, biomarker investigation, and detailed varve measurement. Repeated image measurements from core D1G using slightly different criteria (such as laterally-shifted linescans or different threshold values) showed that for the most part, the data were robust, unlike the data from the other cores, where the varves were mostly discontinuous, wavy, and possibly bioturbated. Furthermore, although there were probable varves in the cores from sites D2 and D3, they were much fainter in the images, which was partly, though not wholly, a result of a change in the imaging conditions (see section 4.4.1); even seen with the naked eye, the varves in these cores were much fainter. It seemed probable that attempts to measure varves from these cores would simply result in measuring high-frequency noise, as described by Zolitschka [35] when measuring comparably indistinct varves.

So, a suite of NIH Image macro programs [25] were used to generate a sequentially-numbered list of varves from core D1G, each with the thicknesses (in pixels) of the black and grey sublayers (defining one varve as black on top of grey), and the mean greyvalues of these sublayers: that is, four data points per varve. The programs treated the entire image sequence as a set of varves, such that homogeneous grey

intervals, even those which were tens of cm thick, were identified only as grey varve sublayers; these were manually identified within the results afterwards.

4.5 Application of image analysis to the Lake St Moritz core

4.5.1 Digitisation of the Lake St Moritz core

The photographing of the Lake St Moritz core used a similar set-up to that of the Drammensfjord core (see section 4.4.1), except that a darkroom was available, which resulted in less variability in the imaging conditions. The shorter length of core also helped here, as this resulted in a shorter duration for the photography rather than it having to be done over several days as was the case for Drammensfjord. The settings of the camera and illumination were kept constant during the photography. Images were captured on colour slide film as before. Each image covered c. 20cm of core, with overlaps of up to 6cm at each end. As before, each image contained a tape measure placed alongside the core. In addition, a Kodak greyscale calibration card with twenty different greyvalues was captured in each image, always in the same location in the image. 55 colour slides were taken in total.

The colour slides of Lake St Moritz core PSM90.3 were digitised using the same process as for the Drammensfjord images: they were scanned using a Nikon LS-1000 35mm slide scanner, then converted to greyscale TIFF files using Adobe Photoshop. Prior to the conversion to greyscale, a preliminary investigation into changes in colour components suggested that unlike the Drammensfjord sediment, there was significant information preserved in the changing sediment colour; the central part (sections 4-6) of the core, in particular, showed some variation in colour between grey, dark brown, and olive sediment. Colorimetric research, which has been applied to laminated sediments [e.g. 36,37], could therefore perhaps be worthwhile on the Lake St Moritz sediment record, although it is beyond the scope of this thesis.

The resulting image resolution was c. 11 pixels per millimetre. This is a lower real resolution than the high-resolution Drammensfjord images, but the greater thickness of the Lake St Moritz varves actually meant that more information was captured in the Lake St Moritz images in terms of data points per varve.

The large size of the Lake St Moritz image files (28.8 MB each) made working with them slow and unwieldy. To assist with the image processing, a set of reduced-resolution images were prepared, then conjoined into a mosaic covering the entire core PSM90.3 that was small enough to be displayed on two pages of A4. This mosaic can be found in the results, and was convenient for studying downcore changes in the nature and quality of the varves using NIH Image.

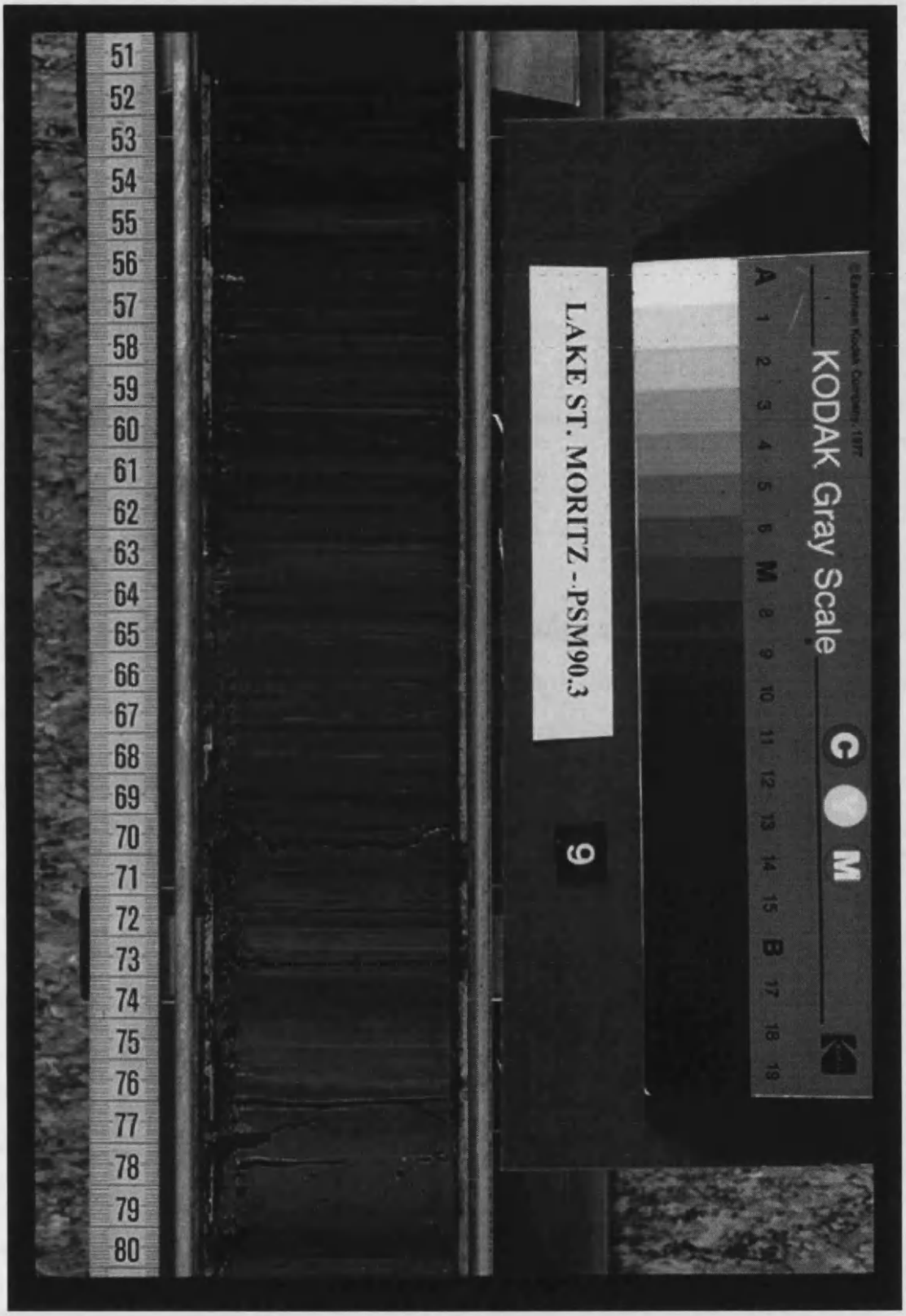

Figure 4.14: Unmodified digital image of laminated sediment from Lake St Moritz core PSM90.3 showing alternating couplets of dark silty and pale biogenic layers.

4.5.2 Correction for changes in imaging conditions

The Kodak greyscale calibration card imaged alongside the sediment cores was used to correct for changes in illumination during image capture. The card had 20 boxes, each with a different greyscale value. Each box should have had *the same greyvalue in each image*, although, as figure 4.15 shows, illumination was not constant during image capture.

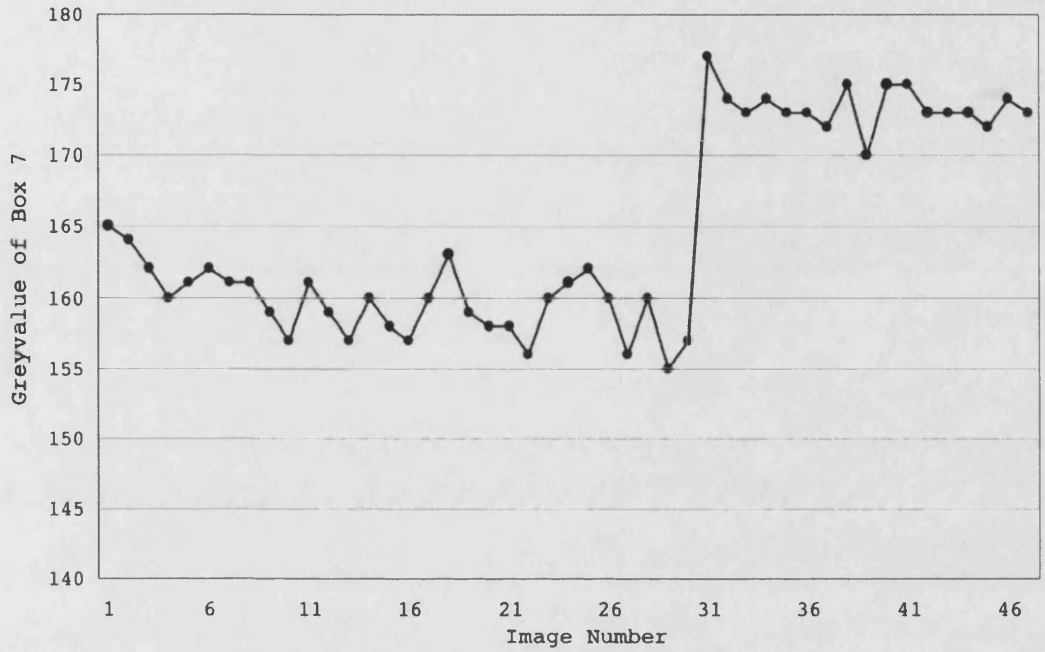

Figure 4.15: Greyvalue of box 7 on the Kodak calibration card for each image from Lake St Moritz, showing one major change in illumination conditions, plus minor background noise.

Consider the darkening in illumination between image 30 and image 31. The change in the greyvalue of box 7 on the calibration card is +20, since box 7 has a greyvalue of 157 in image 30, and 177 in image 31. However, in order to lighten image 31 so that it has an equivalent illumination to image 30, it is not correct just to subtract 20 from the greyvalue of every pixel. Different greyvalues (as found on the Kodak calibration card) respond differently to changes in illumination. Qualitatively speaking, lighter pixels change more than darker ones: the camera response is non-linear.

Using the 20 boxes on the calibration card, it was possible to obtain 20 data points which showed how the change in illumination between image 30 and image 31 affected certain values in the greyvalue scale of 0 to 255. This curve was then approximated by a fourth-order polynomial. It is shown in figure 4.16.

Using this curve, it is possible to correct image 31 so that it appears to be illuminated to the same degree as image 30. Taking image 30 as a "target image", is it possible to correct all the other images so that they, too, have this same degree of illumination? The curve in figure 4.16 only applies to the difference between image 30 and image 31, but fortunately, smaller changes in illumination resulted in greyvalue differences that were linearly-scaled versions of this curve. For example, the

increase in box 7 greyvalue between image 1 and image 38 was +10, i.e. half as big as the increase between image 30 and image 31, and the rest of the points on the curve were also half as big as their equivalents in figure 4.16 when measured on the two images' calibration cards. Using an NIH Image macro, written in Pascal, each image was processed so that it appeared to have the same illumination as image 30, using a linear scaling factor on the polynomial curve shown below.

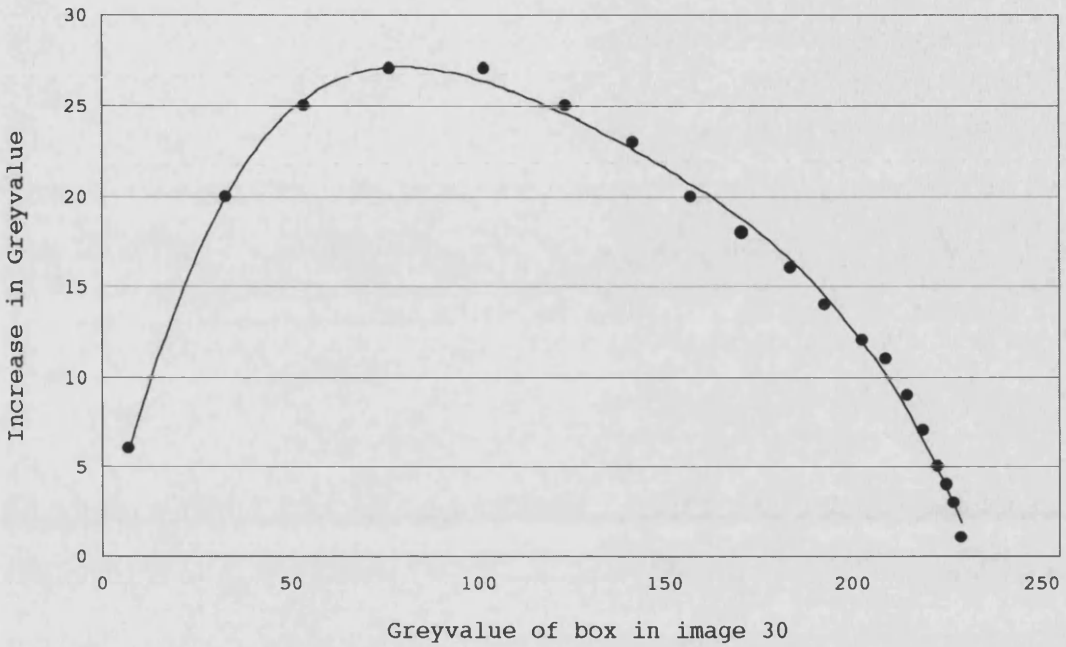

Figure 4.16: Effect of the change in illumination between images 30 and 31 across the greyvalue scale: the increase is non-uniform, but can be approximated with a polynomial.

A further correction was necessary because each image was itself not uniformly illuminated: as noted earlier, uniform illumination of a single photograph is very difficult to achieve. In the Lake St Moritz images, the upper half of each was darker than the lower half, because of the lighting arrangement.

A quantitative estimate of how illumination varies over each image was obtained by averaging all the images. This smoothed out any variations resulting from differences in the sediment, leaving only changes in "background" greyvalue, equivalent to the image that would have resulted if a uniformly grey sheet of paper had been photographed. The average image was obtained using another NIH Image macro.

Downcore variation in illumination was modelled by fitting a quadratic curve to the vertical greyvalue profile of the average image, as shown in figure 4.18. Using this profile, each image was processed so that the minimum value was left unchanged and the other values were reduced appropriately, so that the resulting profile was flat, as it would have been with uniform illumination. This correction was done using a third NIH Image macro. The outcome of this processing was to approach more closely the "true", uniformly-illuminated greyvalue of the Lake St Moritz sediment.

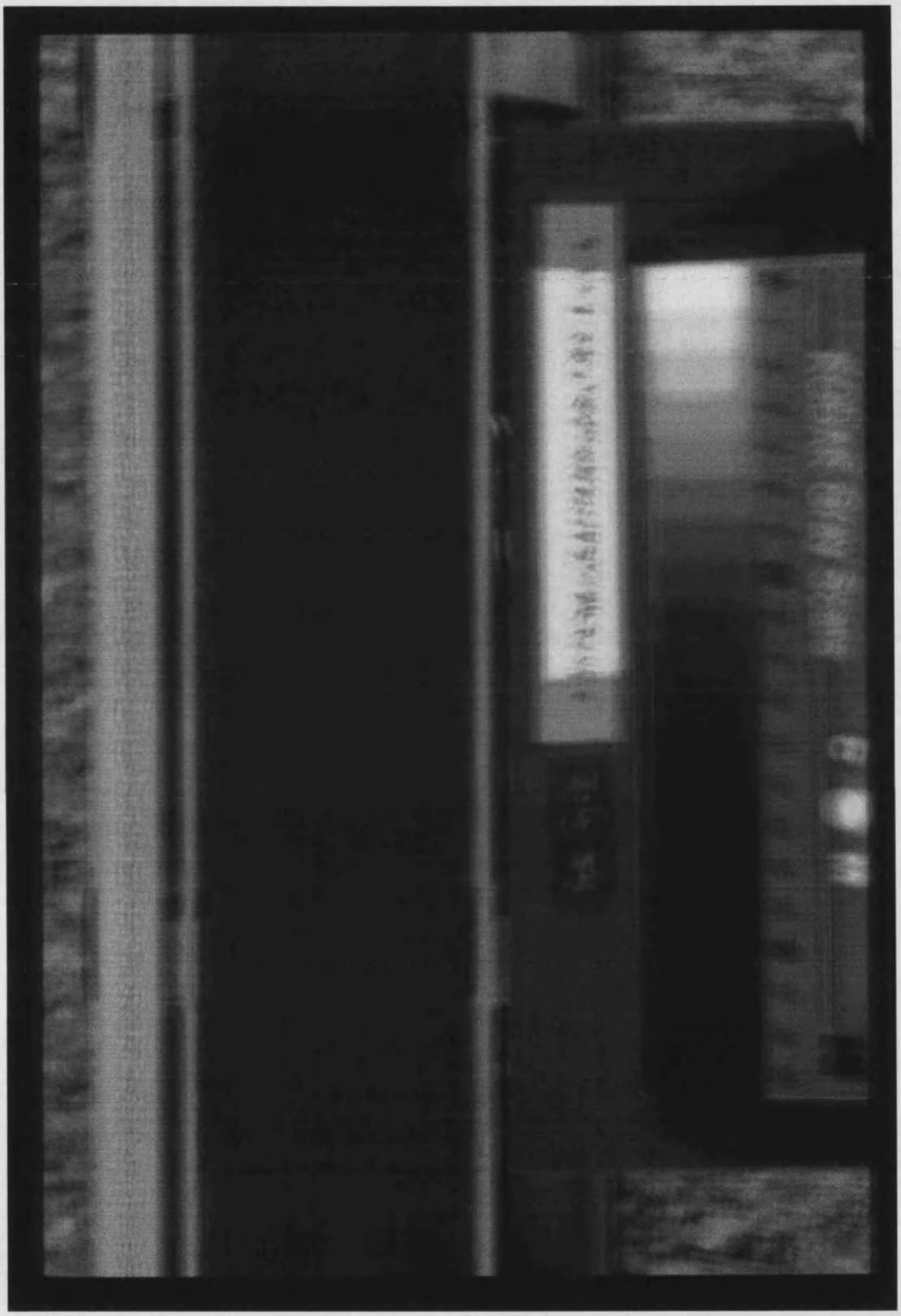

Figure 4.17: Averaged Lake St Moritz image, obtained by superimposing all the images and averaging the pixel values at each location. Most sedimentary greyvalue variation has been averaged out, leaving changes caused by uneven illumination. (These are too subtle to be visible in the printed image; it is actually darker at the top than at the bottom.)

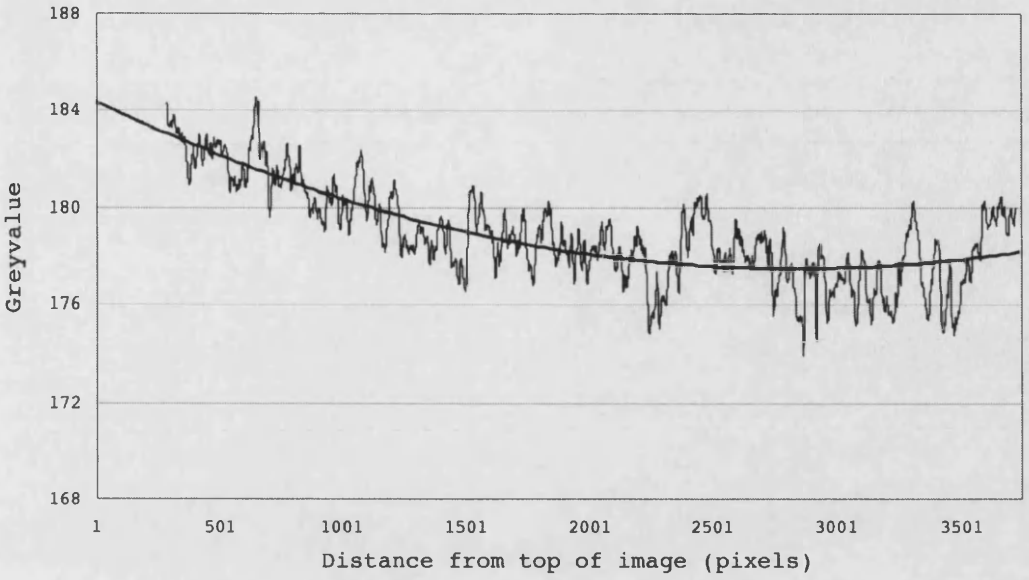

Figure 4.18: Vertical greyvalue profile of the average Lake St Moritz image (as shown in figure 4.17), showing brighter illumination in the lower half of each image. The profile is approximated using a quadratic line of best fit.

4.5.3 Method of varve measurement using digital image analysis

Image enhancement techniques were used, as for the Drammensfjord images, in order to show up the Lake St Moritz varves more clearly. The greater "pixel thickness" of the varves allowed more effective filtering; a multiple-pass rank median filter was used to remove noise, then attempts were made to threshold intervals of varves in order to allow automated varve measurement. In places, this was successful, as shown in figure 4.19, allowing the thicknesses of the dark and pale varve sublayers to be measured. However, two problems were encountered.

The first was that, as for Drammensfjord, despite the corrections for changing imaging conditions, individual thresholds were only applicable to relatively short intervals of sediment owing to changing sediment greyvalue. This made the varve measurement time-consuming, as many separate greyvalue frequency histograms had to be calculated in order to apply an appropriate threshold to each interval. Another way of expressing this problem is that the darkest of the light sublayers were not significantly different from the lightest of the dark sublayers.

This is related to the second problem, which is that not all the varves showed a typical couplet structure of a light and dark sublayer. Multiple sublayers were common, such as the triplet structure of an additional medium-grey clayey winter sublayer. Sublayers frequently graded into each other, producing boundaries which could not be located by thresholding anyway. For the topmost section of the core, where a sequence of 239 varves was measured, efforts were made to separate out dark and pale sublayers, but for subsequent measuring operations, it was decided to measure only the thickness of the entire varve, using the most distinct point in the whole depositional cycle as a boundary, this being the top of the darkest sublayer, which indicates the start of silt deposition after the spring flood.

Ambiguity was further avoided by concentrating further work on a specific interval of older varves where the sediment greyvalue changes that defined the varves appeared to be reasonably consistent, in addition to the varves being distinct and undisturbed. Nonetheless, numerous intervals in the record required measurement "by eye", using Object Image, in order to generate a continuous series of results. These results were: a set of varve counts (for comparison with the other chronological data) and a set of varve thickness measurements (for investigation as a possible climatic proxy).

4.5.4 Measurement of sediment greyvalue

Measurement of sediment greyvalue was also difficult because of the above problems concerning the ambiguity of the varve sublayers. The most important consideration in generating these data was to avoid inhomogeneity resulting from measuring non-comparable sediment intervals, rather than to maximise the resolution of the data. Therefore, sediment greyvalue was measured by dividing the whole of core PSM90.3 into depth intervals that were large enough to average each measurement over even the thickest varves. Two sets of measurements were made, using intervals of 5cm and 3cm, via an NIH Image macro. These intervals spanned the entire core width; cracks, voids, and other irregularities in the sediment which could have given misleading greyvalues did not influence the results significantly, since the areas of sediment affected were small. The results are statistically robust, since each measurement is the mean of at least 100,000 pixels.

These linescans showing downcore changes in sediment greyvalue could then be compared with compositional data in order to judge the value of sediment greyvalue as a compositional proxy. The presence of varves, resulting from a lack of bioturbation of the sediment, should also result in a link between the relative contributions of different sediment components (i.e. sediment composition) and the relative thicknesses of different varve sublayers. This can be understood by reference to the "varve microcosm" [38]; averaging sediment greyvalue over 3cm and 5cm intervals in the core removes the partitioning effects of the varve mechanism, in order to reveal longer-than-annual changes in sediment composition. In its undisturbed state, these changes should be manifest in modulations of varve sublayer thicknesses, but as discussed above, these were not straightforward to measure.

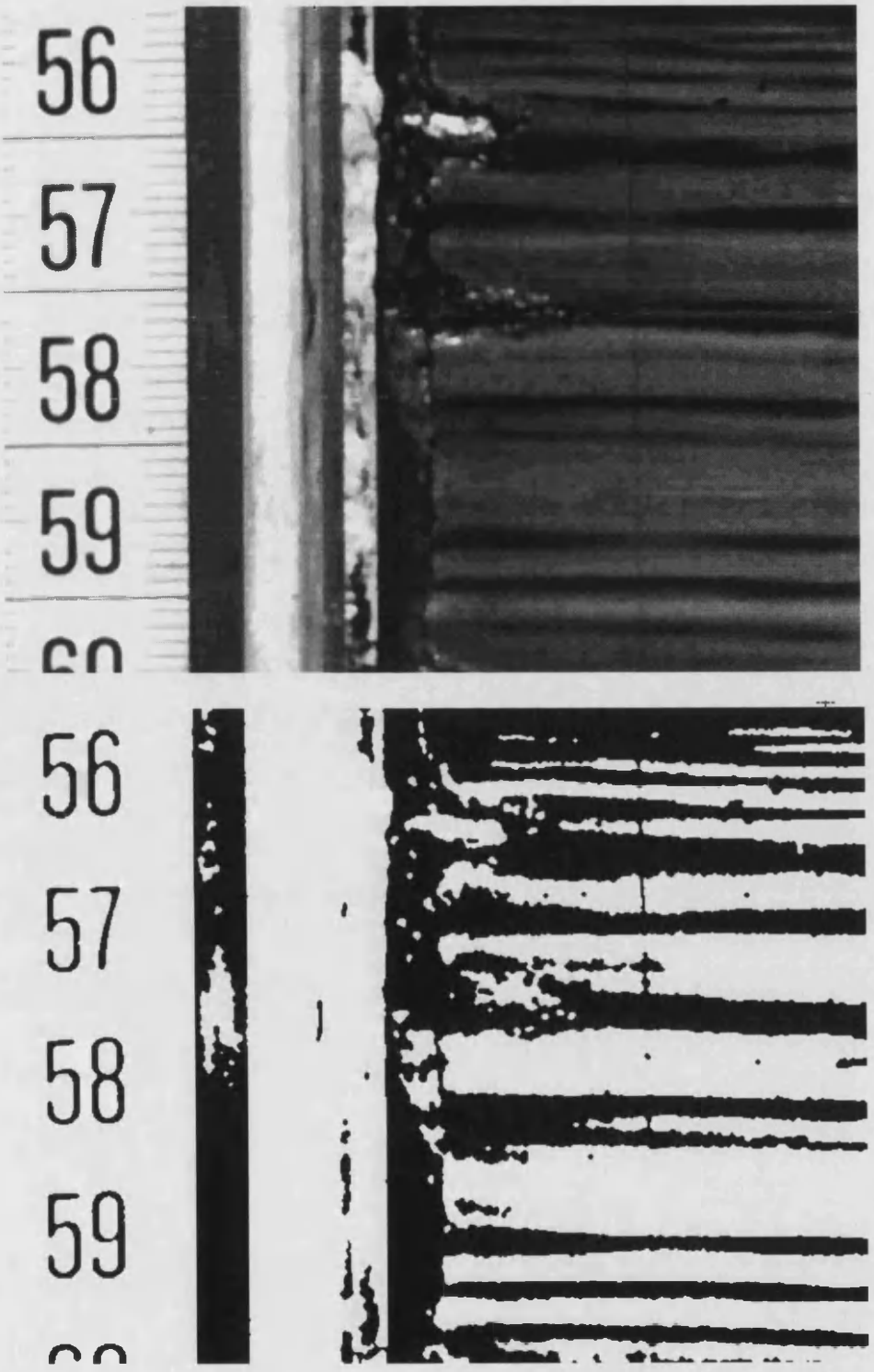

Figure 4.19: Demonstration images showing a 4cm interval of Lake St Moritz core PSM90.3, after application of 10-pass rank median filter (top) and subsequent binary thresholding (bottom) revealing alternating, laterally continuous varve sublayers. These couplets are unusually distinct for core PSM90.3; most of the varves in this core are not as clear as in this image.

4.6 Time-series analysis methods

Time-series analysis methods are complex and frequently misapplied. Additional explanation of the methods that were used is given in appendix A.

The results of the image analysis research were either time-series (sequences of data points in time order, such as one data point per varve, equivalent to one data point per seasonal cycle) or "depth-series" (sequences of data points in depth order, such as downcore measurements of sediment greyvalue). These results were initially generated as Excel spreadsheets, from which they were transferred to the time-series program AnalySeries [39], and to custom-written programs in Matlab, to enable frequency-domain spectral analysis to be performed. Chronological data were used to construct integrated core chronologies in order to allow the conversion of depth-series to time-series; details are given in chapter 5.

Spectral analysis was performed on the resulting time-series, followed by "window-closing" using a variety of spectral filters. Spectral peaks were tested for significance by choosing an appropriate null hypothesis, performing a variety of significance tests, and considering whether the overall outcome suggested a convincingly significant result, rather than relying on a single technique. Maximum Entropy Spectral Analysis (MESA) and evolutionary spectral analysis were also performed in order to study the frequency characteristics of the data in more detail, bearing in mind that sharp, isolated spectral peaks are rare in Holocene proxy palaeoclimate data, and that overinterpretation of spectral peaks is common, especially with "desirable" frequencies such as the 11-year Schwabe sunspot cycle [40]. Statistical guidance was taken from Von Storch and Zwiers [41], Janacek [42], and Priestley [43].

Chapter 4 References

[1] Rienk Smittenberg, personal communication, January 2000.

[2] Anderson, R. Y., 1996, Seasonal sedimentation: a framework for reconstructing climatic and environmental change, in: Kemp, A. E. S., (Ed.), 1996, Palaeoclimatology and Palaeoceanography from Laminated Sediments, Geological Society Special Publication No. 116, p. 1-15.

[3] The data are taken from: Smittenberg, R. H., 2003, Holocene environmental changes disclosed from anoxic fjord sediments by biomarkers and their radiocarbon content, PhD thesis, Geologica Ultraiectina, v. 227, 143 pp.

[4] Kelts, K., 1998, Components in lake sediments: smear slide identifications, Limnological Research Centre Core Facility, University of Minnesota, January 1998, 8 pp.

[5] Schrader, H., 2000, The secret of smear slides in marine sedimentology - there is none!, Department of Geology, University of Bergen, November 2000, 5 pp.

[6] Goldstein, J. I., Newbury, D. E., Echlin, P., Joy, D. C., Fiori, C., and Lifshin, E., 1981, Scanning electron microscopy and X-ray microanalysis, Plenum Press, 673 pp.

[7] Pike, J., 2000, Data report: Backscattered electron imagery analysis of Early Pliocene laminated *Ethmodiscus* ooze, site 1010, Proceedings of the Ocean Drilling Program, Scientific Results, 167:207-212.

[8] Pike, J., and Kemp, A. E. S., 1996, Preparation and analysis techniques for studies of laminated sediments, in: Kemp, A. E. S., (Ed.), 1996, Palaeoclimatology and Palaeoceanography from Laminated Sediments, Geological Society Special Publication No. 116, p. 37-48.

[9] Grimm, K. A., 1992, High-resolution imaging of laminated biosiliceous sediments and the oceanographic significance (Quaternary, Site 798, Oki Ridge, Japan Sea), Proceedings of the Ocean Drilling Program, Scientific Results, 127/128:547-557.

[10] Brodie, I., and Kemp, A., 1994, Variation in biogenic and detrital fluxes and formation of laminae in late Quaternary sediments from the Peruvian coastal upwelling zone, Marine Geology, 116:385-398.

[11] Pearce, R. B., Kemp, A. E. S., Koizumi, I., Pike, J., Cramp, A., and Rowland, S. J., 1998, A lamina-scale SEM-based study of a late Quaternary diatom-ooze sapropel from the Mediterranean Ridge, Site 971, Proceedings of the Ocean Drilling Program, Scientific Results, 160:349-363.

[12] Kemp, A. E. S., Pearce, R. B., Pike, J., and Marshall, J. E. A., 1998, Microfabric and microcompositional studies of Pliocene and Quaternary sapropels from the Eastern Mediterranean, Proceedings of the Ocean Drilling Program, Scientific Results, 160:333-348.

[13] Pike, J., Moreton, S. G., and Allen, C. S., 2001, Data report: microfabric analysis of postglacial sediments from Palmer Deep, Western Antarctic Peninsula, Proceedings of the Ocean Drilling Program, Scientific Results, v. 178, 17 pp., available online at http://www-odp.tamu.edu/publications/178 SR/chap 18/c18 .htm.

[14] Ojala, A. E. K., and Francus, P., 2002, Comparing X-ray densitometry and BSE-image analysis of thin sections in varved sediments, Boreas, 31:57-64.

[15] Ariztegui, D. R., 1993, Palaeoenvironmental and palaeoclimatic implications of sedimented organic matter variations in lacustrine systems: Lake St Moritz, a case study, PhD Thesis (unpublished), ETH-Zürich, Switzerland, Nr. 10225, 188 pp.

[16] Ariztegui, D., Farrimond, P., and McKenzie, J. A., 1996, Compositional variations in sedimentary lacustrine organic matter and their implications for high Alpine Holocene environmental changes: Lake St Moritz, Switzerland, Organic Geochemistry, 24:453-461.

[17] Ariztegui, D., and Dobson, J., 1996, Magnetic investigations of framboidal greigite formation: a record of anthropogenic environmental changes in eutrophic Lake St Moritz, Switzerland, The Holocene, 6:235-241.

[18] Gobet, E., Tinner, W., Hochuli, P., van Leeuwen, J. F. N., and Ammann, B., 2003, Middle to Late Holocene vegetation history of the Upper Engadine (Swiss

Alps): the role of man and fire, Vegetation History and Archaeobotany, 12:143-163.

[19] Cooper, M. C., 1997, The use of digital image analysis in the study of laminated sediments, Journal of Paleolimnology, 19:33-40.

[20] Saarinen, T., and Petterson, G., 2001, Image analysis techniques, in: Last, W. M., and Smol, J. P., (Eds.), Tracking Environmental Change Using Lake Sediments, Vol. 2, Physical and Geochemical Methods, Ch. 3, p. 23-39.

[21] Merrill, R. B., and Beck, J. W., 1995, The ODP color digital imaging system: color logs of Quaternary sediments from the Santa Barbara Basin, Site 893, Proceedings of the ODP, Scientific Results, 146:45-59.

[22] Russ, J. C., 1999, The Image Processing Handbook, Third Edition, CRC Press, 771 pp.

[23] NIH, 2002, The public domain NIH Image program was developed at the U.S. National Institutes of Health and is available on the Internet at http://rsb.info.nih.gov/nih-image/. Note that recently NIH Image has been replaced by ImageJ, an improved version written in Java.

[24] Raymond, E. S., 2001, The Cathedral and the Bazaar, O'Reilly Press, 255 pp.

[25] A manual for writing macros for NIH Image by the author of this thesis is available online at http://rsb.info.nih.gov/nih-image/more-docs/macros-into.html. This describes in detail how the varve-measuring macros operate.

[26] Petrou, M., and Bosdogianni, P., 1999, Image Processing: The Fundamentals, John Wiley and Sons, 333 pp.

[27] Original image supplied by D. A. Franzi, Center for Earth and Environmental Science, Plattsburgh State University, USA.

[28] Bull, D., and Kemp, A. E. S., 1995, Composition and origins of laminae in late Quaternary and Holocene sediments from the Santa Barbara Basin, Proceedings of the ODP, Scientific Results, 146:77-87.

[29] Schaaf, M., and Thurow, J., 1994, A fast and easy method to derive highest-resolution time-series datasets from drillcores and rock samples, Sedimentary Geology, 94:1-10.

[30] Keeseville image: see [27]. Green River Formation image: H. P. Eugster. Lake Jaatilanjärvi, Lake Pohhajärvi, and Lake Korttajärvi images: Geological Survey of Finland.

[31] Jähne, B., 1997, Digital Image Processing - Concepts, Algorithms, and Scientific Applications, Fourth Edition, Springer, 555 pp.

[32] Jähne, B., 1997, Practical Handbook on Image Processing for Scientific Applications, CRC Press, 589 pp.

[33] Nederbragt, A. J., Thurow, J. W., and Merrill, R. B., 2000, Data report: Color records from the California margin: proxy indicators for sediment composition and climatic change, Proceedings of the ODP, Scientific Results, 167:319-329.

[34] Vischer, N. O. E., Huls, P. G., and Woldringh, C. L., 1994, Object-Image: an interactive image analysis program using structured point collection, BioLine Binary, 6.

[35] Zolitschka, B., 1996, Image analysis and microscopic investigation of annually laminated lake sediments from Fayetteville Green Lake (NY, USA), Lake C2 (NWT, Canada), and Holzmaar (Germany): a comparison, in: Kemp, A. E. S., (Ed.), 1996, Palaeoclimatology and Palaeoceanography from Laminated Sediments, Geological Society Special Publication No. 116, p. 49-55.

[36] Merrill, R. B., and Beck, J. W., 1995, The ODP color digital imaging system: color logs of Quaternary sediments from the Santa Barbara Basin, Site 893, Proceedings of the ODP, Scientific Results, 146:45-59.

[37] Cramer, B. S., 2001, Latest Paleocene-earliest Eocene cyclostratigraphy: using core photographs for reconnaissance geophysical logging, Earth and Planetary Science Letters, 186:231-244.

[38] Anderson, R. Y., 1986, The varve microcosm: propagator of cyclic bedding, Paleoceanography, 1:373-382.

[39] Paillard, D., Labeyrie, L., and Yiou, P., 1996, Macintosh program performs time-series analysis, Eos, Transactions of the American Geophysical Union, 77:379, and available online at http://www.agu.org/eos_elec/96097e.html.

[40] Burroughs, W. J., 1992, Weather Cycles: Real or Imaginary?, Cambridge University Press, 201 pp.

[41] Von Storch, H., and Zwiers, F. W., 2002, Statistical Analysis in Climate Research, Cambridge University Press, 528 pp.

[42] Janacek, G., 2001, Practical Time-series, Arnold Texts in Statistics, 156 pp.

[43] Priestley, M. B., 1997, Chapter 5: Detection of periodicities, In: Subba Rao, T., Priestley, M. B., and Lessi, O., (Eds.), Applications of Time-series Analysis in Astronomy and Meteorology, Chapman and Hall, p. 65-88.

Chapter 5: Results

5.1 Introduction

As a technique for generating geological time-series, digital image analysis is unusual because it can produce very large numbers of data points [1]; $>10^5$ data points for the Drammensfjord cores alone. For convenience, all of the data in this chapter can be found on CD-ROM in appendix B, as Excel files.

The primary results for this research are downcore sediment greyvalue and varve thickness data. This chapter presents these results and describes their conversion from sediment-core-based measurements into evenly-sampled time-series data, by using independent chronological data to construct age-depth models for the cores. It also describes the sedimentary sequences imaged from the cores, the varve mechanisms that were investigated, and the various components that make up the varved sediment. Following this, chapter 6 interprets the chronologically-calibrated image data in terms of possible signals of environmental change, and discusses what these reveal about Holocene climate change in the regions of Drammensfjord and Lake St Moritz respectively.

5.2 Drammensfjord results

5.2.1 Drammensfjord core image mosaics

After conversion to greyscale, the original Drammensfjord images were reduced in resolution and then combined to produce core-section image mosaics, all at the same scale (14.5cm : 1m of core). These illustrate the lithological changes seen in the cores, although this variation is partly obscured by the poorer quality of the images of the cores from sites D2 and D3, a result of changes in imaging conditions (see section 4.4.1). The uneven illumination from top to bottom of each image is also apparent in the mosaics, though this was simple to correct for (see section 4.4.2).

The core section numbering system, originally applied by NIOZ, is the reverse of conventional numbering, as the deepest (i.e. oldest) section of each core is numbered 1, and the numbers increase towards the top of the core. Thus, the top section of D1G is D1G7, but for D1M, because it has 8 sections, the top section is D1M8, even though this contains the same sequence as D1G7. The following list details the core sections that were photographed.

D1G: only top 2 sections photographed (D1G7 and D1G6)
D1L: all 7 sections photographed (D1L7 to D1L1)
D1M: all 8 sections photographed (D1M8 to D1M1)

D2G: all 7 sections photographed (D2G7 to D2G1)
D2H: top 2 sections not recovered; remaining 5 sections photographed (D2H5 to D2H1); D2H4 in two parts (D2H4II the top part and D2H4I the bottom part)
D2L: all 4 sections photographed (D2L4 to D2L1)

D3G: all 7 sections photographed (D3G7 to D3G1)
D3H: top 7 of 9 sections photographed (D3H9 to D3H3)
D3L: both sections photographed (D3L2 and D3L1)

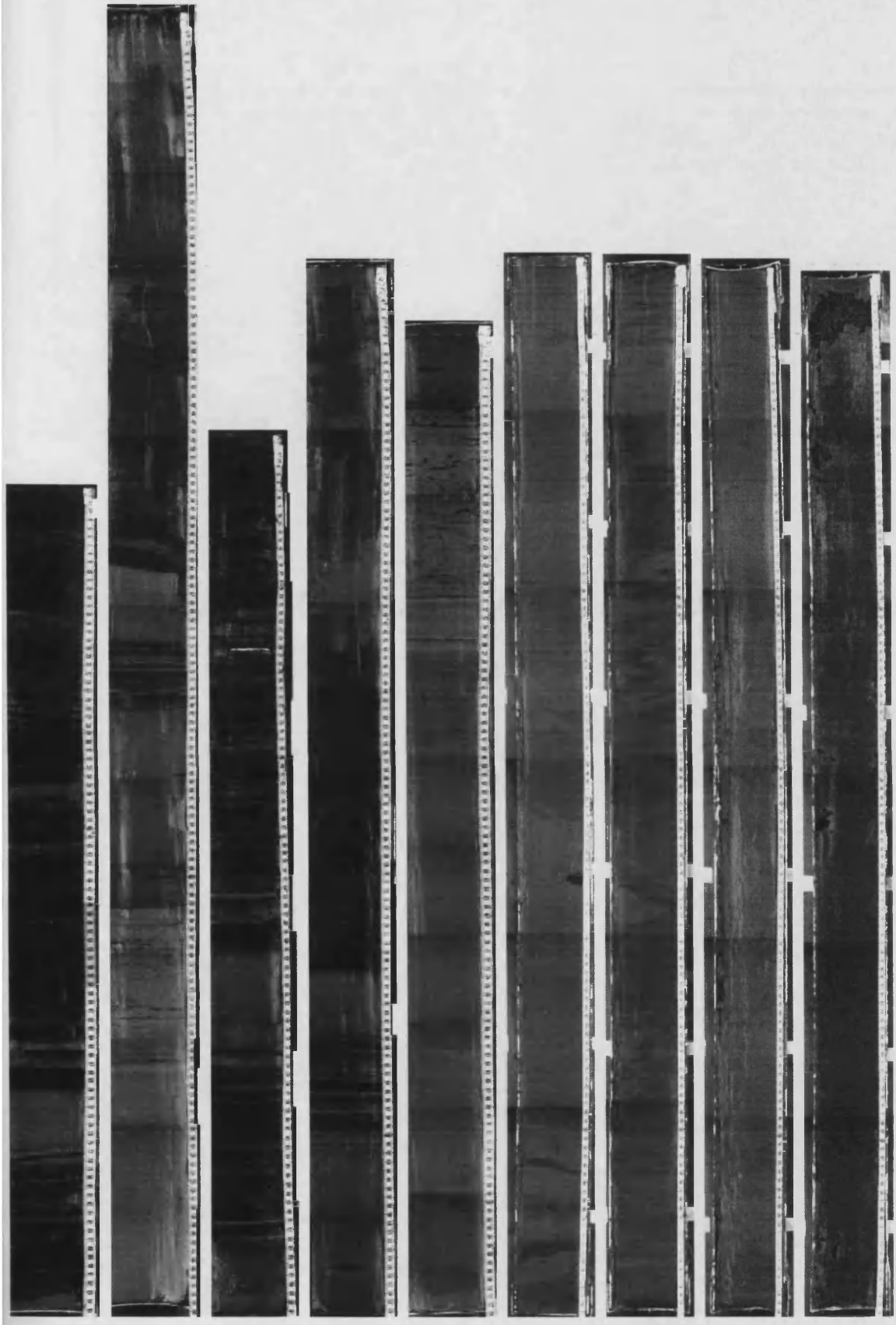

Figure 5.1.1: Left to right, Drammensfjord core sections D1G7, D1G6, D1L7, D1L6, D1L5, D1L4, D1L3, D1L2, and D1L1.

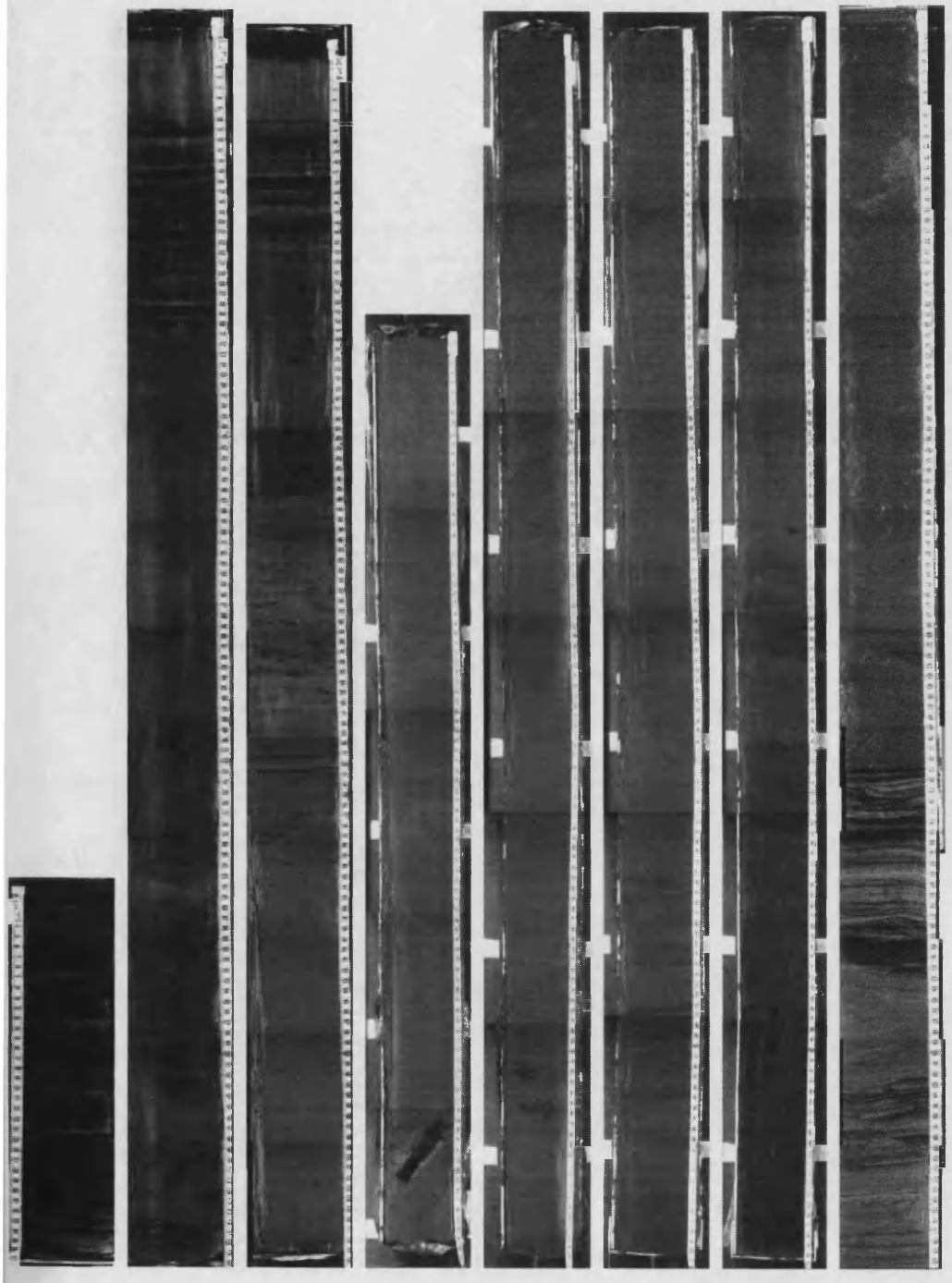

Figure 5.1.2: Left to right, Drammensfjord core sections D1M8, D1M7, D1M6, D1M5, D1M4, D1M3, D1M2, and D1M1.

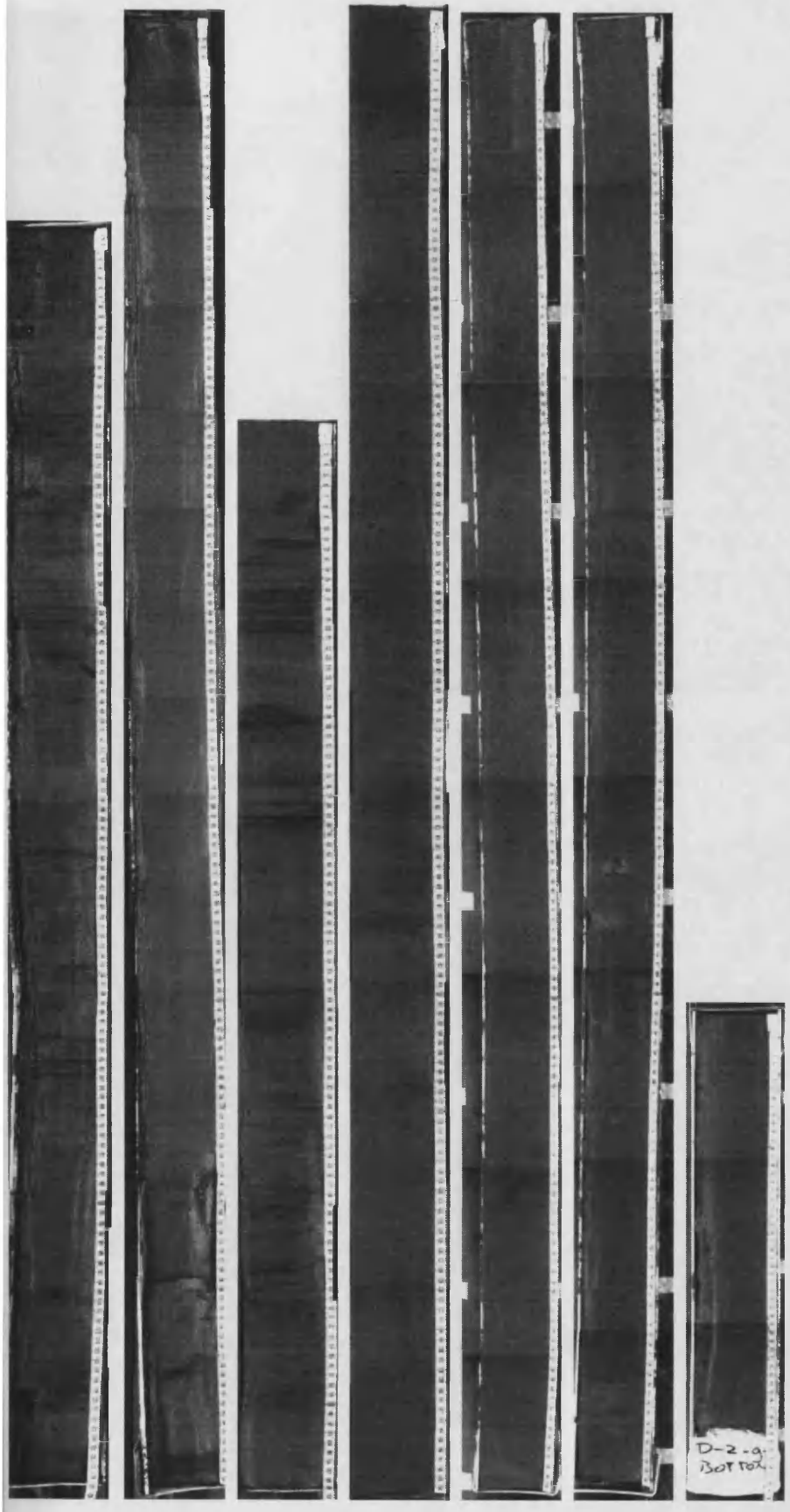

Figure 5.1.3: Left to right, Drammensfjord core sections D2G7, D2G6, D2G5, D2G4, D2G3, D2G2, and D2G1.

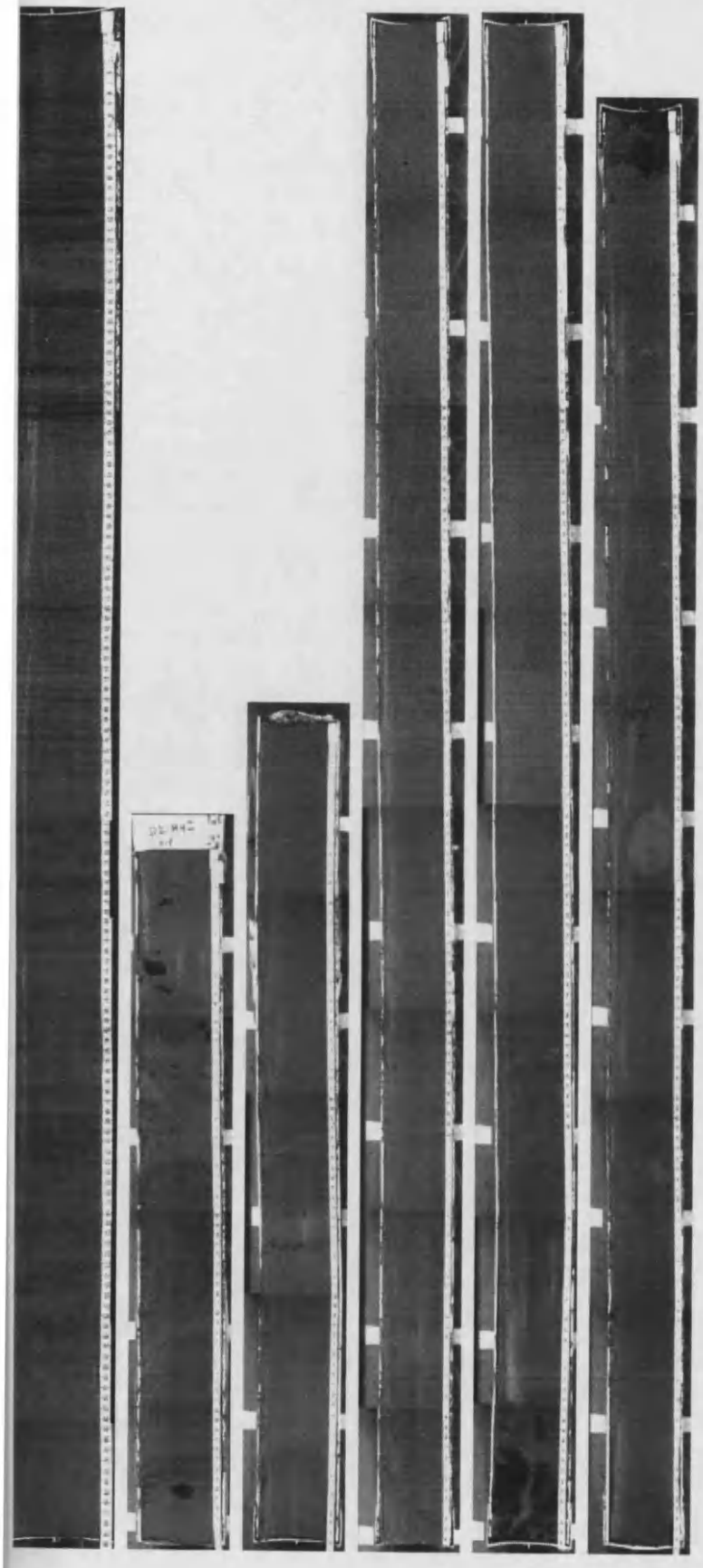

Figure 5.1.4: Left to right, Drammensfjord core sections D2H5, D2H4II, D2H4I, D2H3, D2H2, and D2H1.

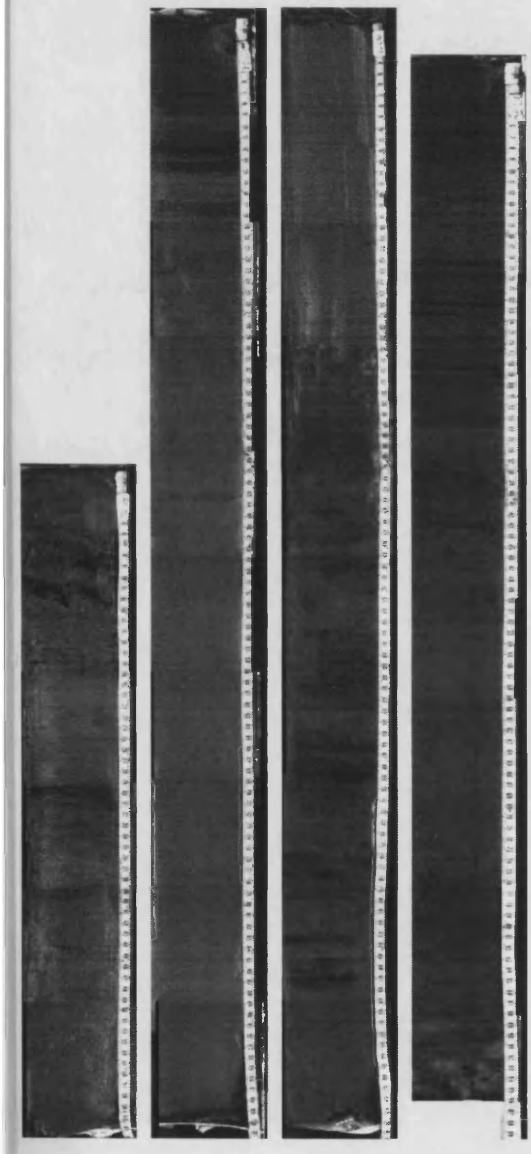

Figure 5.1.5: Left to right, Drammensfjord core sections D2L4, D2L3, D2L2, and D2L1.

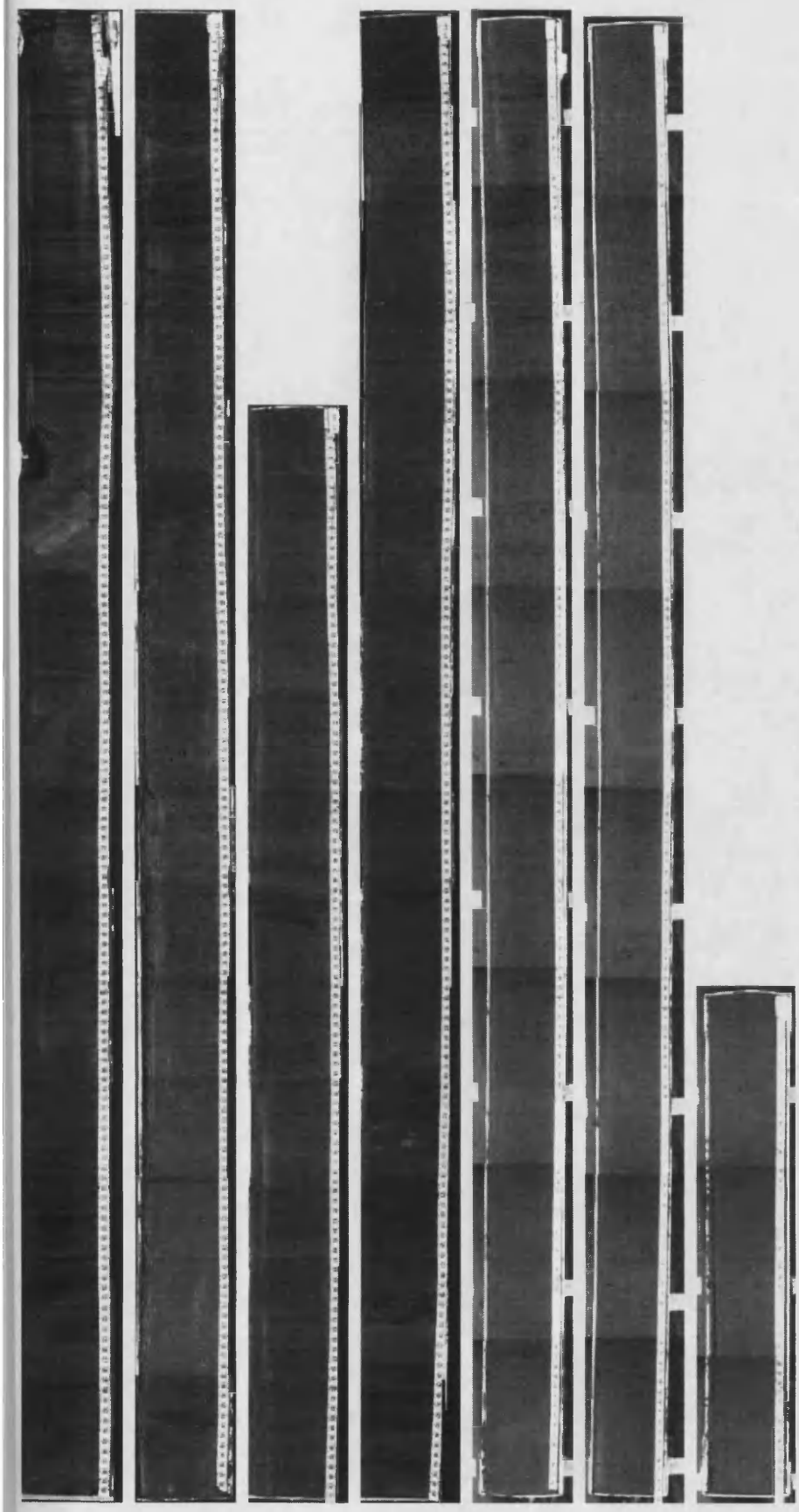

Figure 5.1.6: Left to right, Drammensfjord core sections D3G7, D3G6, D3G5, D3G4, D3G2, and D3G1.

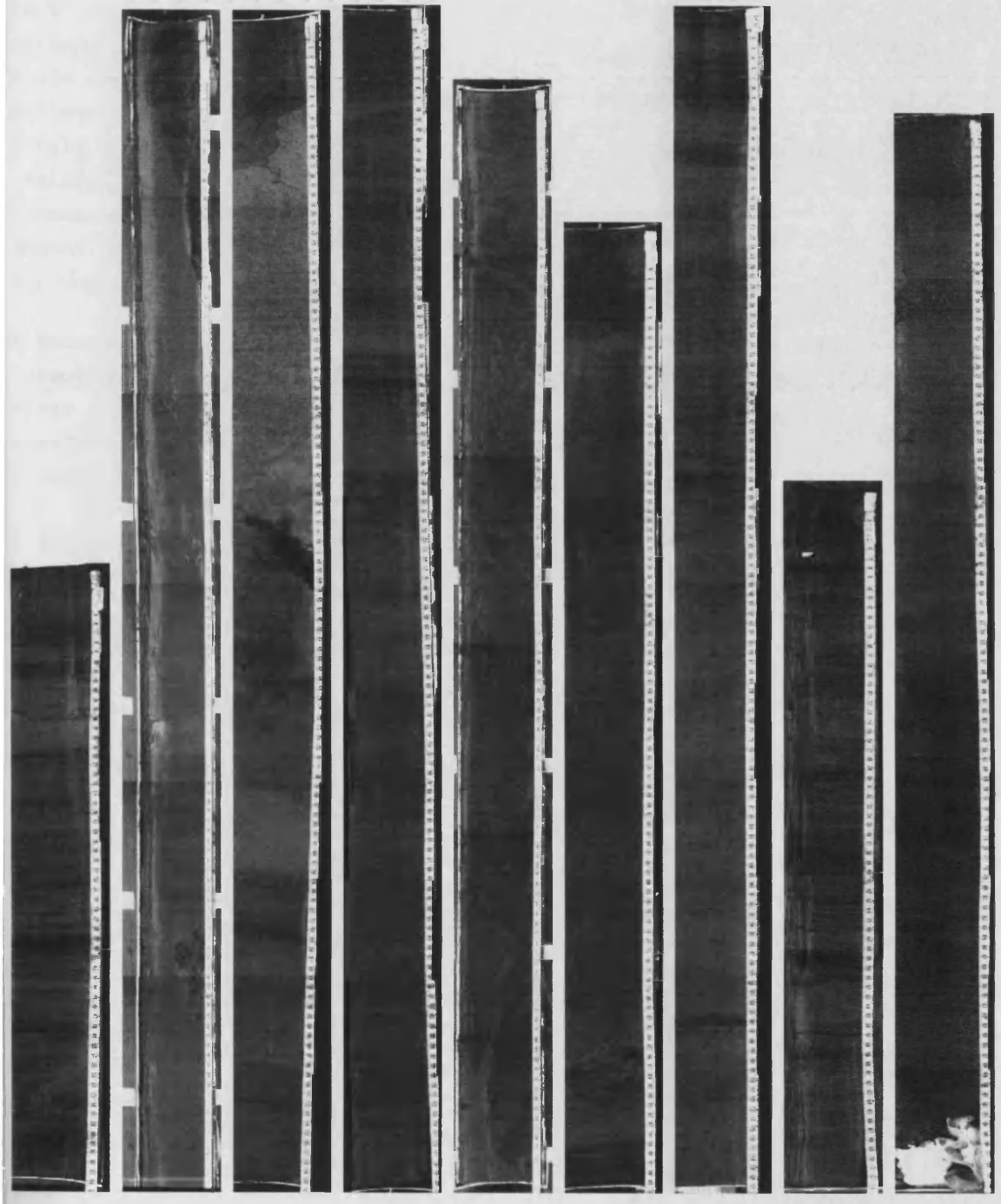

Figure 5.1.7: Left to right, Drammensfjord core sections D3H9, D3H8, D3H7, D3H6, D3H5, D3H4, D3H3, D3L2, and D3L1.

5.2.2 Drammensfjord sedimentary logs and lithological correlation

The simple sedimentary log of the Drammensfjord cores described in section 4.1.2, prepared at 3cm resolution and designed to highlight laminated intervals of sediment, is shown in figure 5.2. The correlations indicated are tentative and are based only on visible changes in sediment lithology.

A comparison between the cores from sites D1, D2, and D3 shows a number of interesting features. First, the solid black sediment at the top of the cores from site D1. The lack of visible laminations in this sediment is likely to be a result of recent anthropogenic influences on sedimentation in Drammensfjord: smoothing of the annual cycle via flood control, and a near-continuous input of black, organic-carbon-rich sediment. Why is this black sediment only found in the cores from site D1? It is likely that it is missing from the other cores because the corers disturbed the sediment surface as they penetrated it. The surface sediment in the deep parts of Drammensfjord is a semi-consolidated "soup" [2], and it is likely that a substantial amount of sediment is missing from the tops of all the cores (see section 5.2.7). Only accidentally did some of this sediment survive at the tops of cores D1G and D1L.

A second feature of interest is the sand content of the cores, which follows the expected pattern of being highest in the D3 cores - those closest to the mouth of the River Drammen - lower in the D2 cores, and almost absent in the D1 cores. The sand is mostly concentrated in distinct beds, presumably deposited by debris flows and turbidity currents; the remainder of the sediment is almost entirely mud-grade.

A final feature of interest is the alternation between laminated and homogeneous intervals, and for the D2 cores, the near-absence of laminations. There are two possible explanations for this. The first is that the homogeneous mud intervals are event beds. This would explain why, in some cases at least, they can be correlated amongst cores from the same site but not amongst different coring sites: for example, the 7cm thick homogeneous interval seen in the top 1m of all three D1 cores. Presumably, as with most event beds in Saguenay Fjord [3], mass movement deposits in Drammensfjord have a limited lateral extent: only rarely will an event bed be large enough to cover the whole fjord bottom.

Alternatively, the homogeneous mud could originally have been identical to the laminated mud, but the laminations have since been lost. This could occur via rapid decomposition of the organic carbon in the black layers, owing to microbial activity, and/or via mechanical mixing of the sediment layers during bioturbation. Both require oxygenation of the deep fjord water. There is little evidence of burrows and other large ichnofabrics in the Drammensfjord cores, but this does not mean the sediments have not been disturbed. Close study of the cores reveals a continuum from flat, continuous laminations to wavy, discontinuous laminations, passing into completely homogeneous sediment.

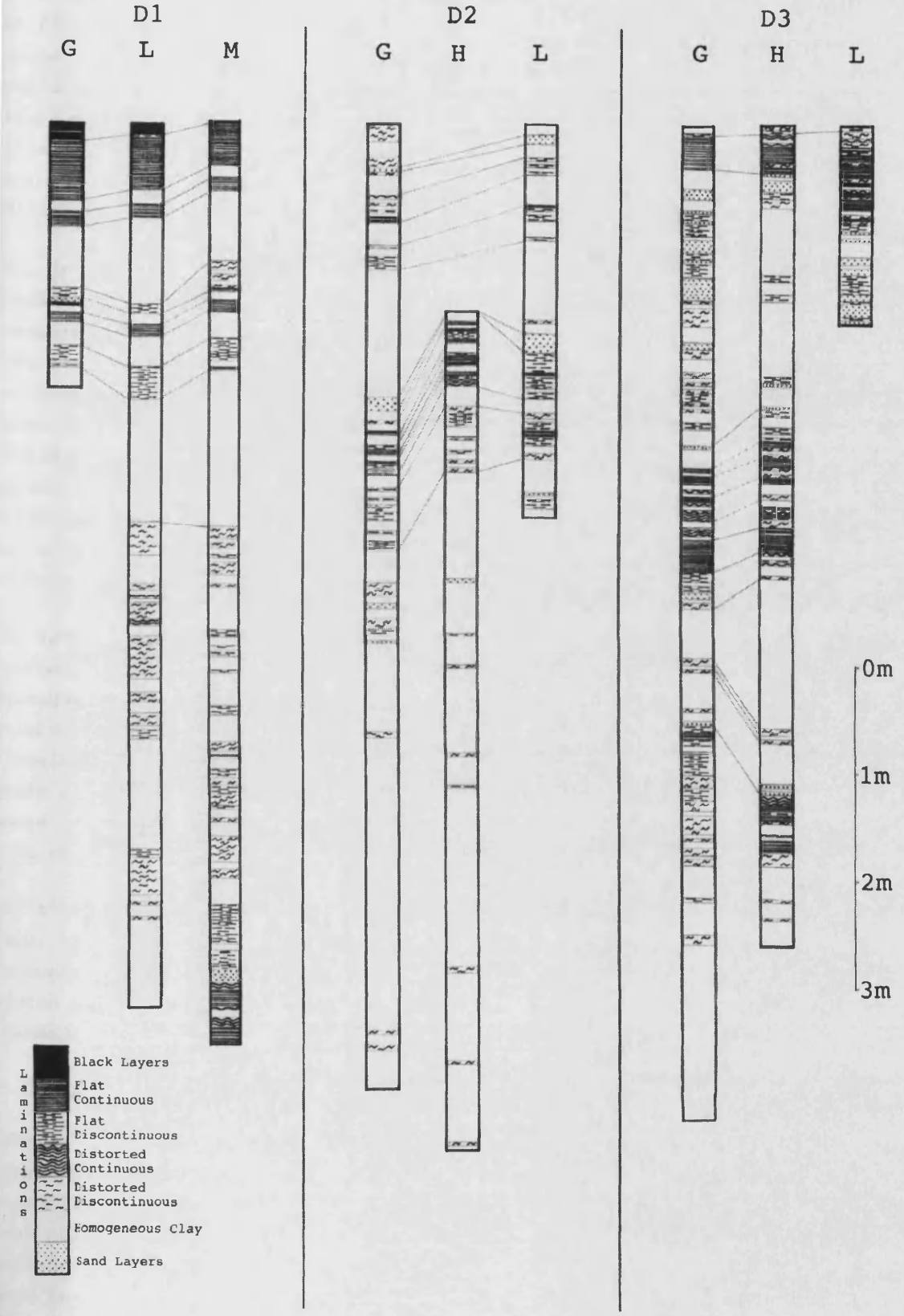

Figure 5.2: Simplified sedimentary log of the nine Drammensfjord cores, at 3cm resolution, showing location of laminated, homogenous, and sandy intervals.

This can be explained by "microbioturbation", perhaps by benthic foraminifers that are tolerant of low-oxygen conditions. Comparable microbioturbated structures have been found in laminated sediments from the Peruvian Shelf [4] and the Arabian Sea [5]. This explanation also fits with the limited lateral extent of the homogeneous intervals, since different parts of Drammensfjord are oxygenated at different times: the coring sites are at different depths, and in any case the redox cline is not a flat surface across the whole fjord. Thus, laminated intervals will have been preserved at different times in different locations.

So, do the homogeneous intervals represent event beds or homogenised background sedimentation? By way of comparison, 50% of the sediment column in Hardangerfjord is composed of slumps and turbidites [6], though this is much deeper than Drammensfjord. The sand layers in Drammensfjord are definitely event beds; on the other hand, the thickest homogeneous mud intervals, such as the 3m thick interval at the base of core D2G, are very unlikely to be event beds. So, there is evidence for both types of deposition. The answer lies somewhere between the extremes of all the homogeneous sediment being event beds and all being homogenised background sediment. Detailed examination of foraminifers from the homogeneous intervals may enable identification of event beds containing reworked Lateglacial clay, as in comparable fjords [7], though this is beyond the scope of this thesis.

In fact, with the exception of intervals containing well-preserved laminations, correlation even amongst cores from a single site is difficult. This is not so much because the cores are different, as because intervals with faint, wavy, or discontinuous laminations are so difficult to distinguish. The method of lithological logging chosen is of limited use; this was confirmed by attempting to correlate the more detailed 1cm-resolution log, which produced sedimentary sequences that were even more dissimilar rather than increasing the level of correlatable detail. This detailed log of the cores can be found on CD-ROM in Appendix B.

To a first approximation, then, the Drammensfjord cores are entirely made up of grey mud, with not really enough lithological variation to allow correlation via conventional logging. Indeed, this is one reason why digital image analysis of the cores can be useful. The next section describes attempts to correlate the cores using records of sediment greyvalue derived from the digital images.

5.2.3 Drammensfjord core linescans and greyvalue correlation

The following records of sediment greyvalue were derived from downcore linescans measured from the Drammensfjord images following correction for changing imaging conditions, but no other image processing. The resolution of these overall linescans was reduced to 0.05mm (that is, 20 data points per cm) in order to keep the data manageable and to allow comparable data to be extracted from both the high-resolution and the low-resolution images. The numerical data are given on CD-ROM in appendix B. Note that these are not the data from which varve measurements were made; this required processed versions of the original, highest-resolution data (see section 4.4.3).

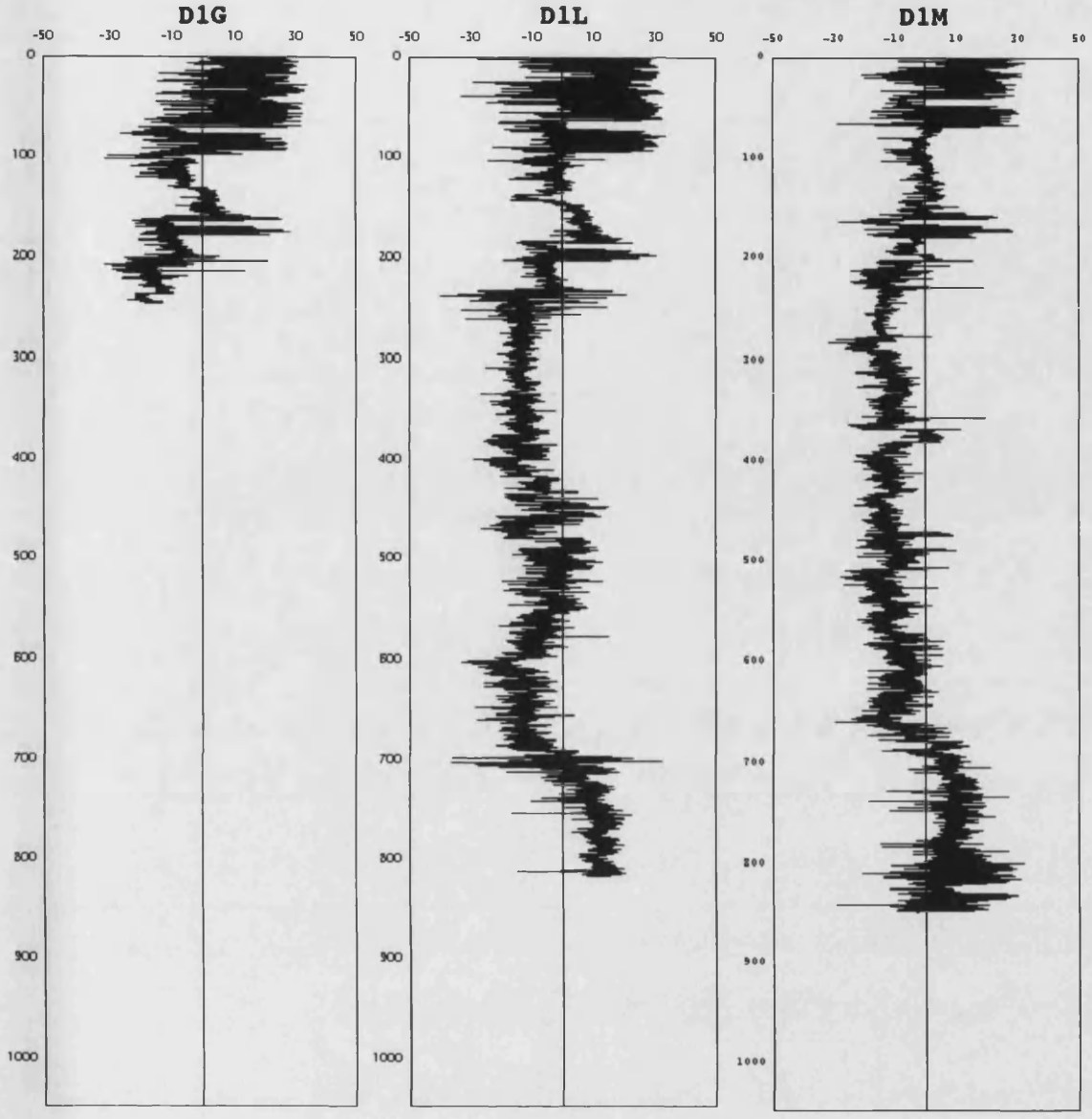

Figure 5.3.1: Composite linescans showing sediment greyvalue from core site D1. Left to right, cores D1G, D1H, and D1M. The depth scale is in centimetres; sediment greyvalue has been normalised to a mean of zero. Negative greyvalues are paler; positive greyvalues darker.

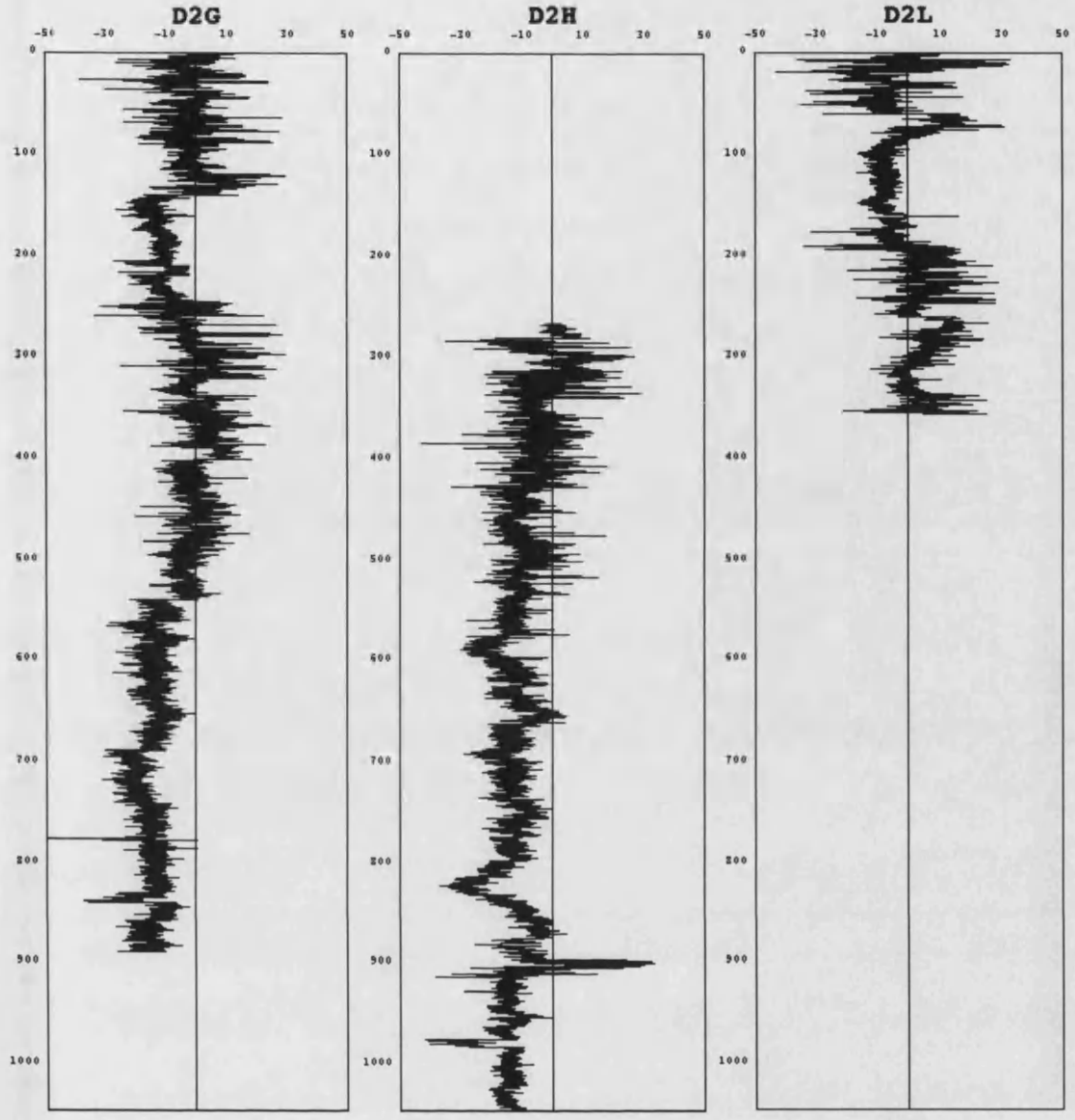

Figure 5.3.2: Composite linescans showing sediment greyvalue from core site D2. Left to right, cores D2G, D2H, and D2L. The depth scale is in centimetres; sediment greyvalue has been normalised to a mean of zero. As noted earlier, the top two sections of core D2H were not recovered.

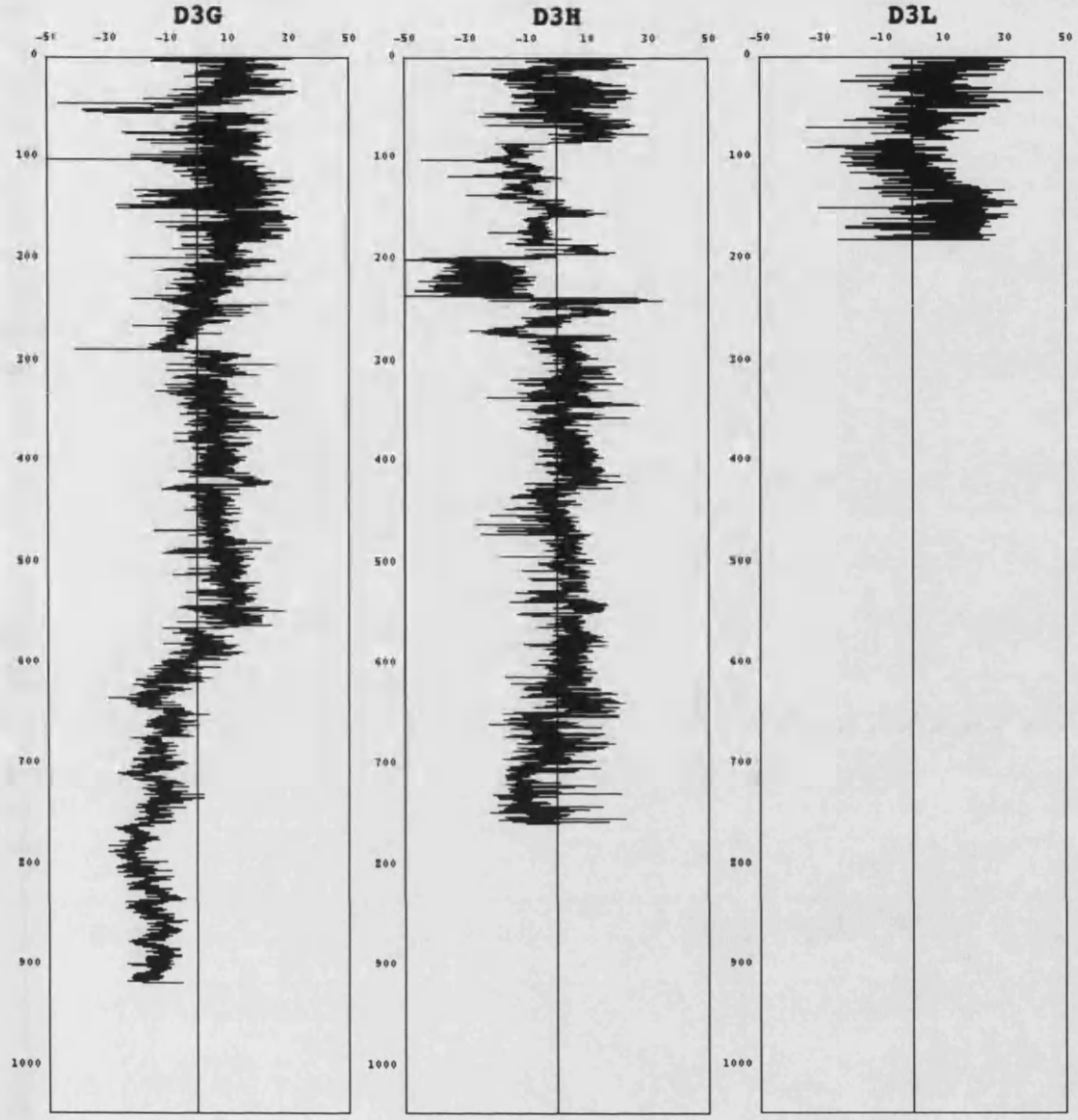

Figure 5.3.3: Composite linescans showing sediment greyvalue from core site D3. Left to right, cores D3G, D3H, and D3L. The depth scale is in centimetres; sediment greyvalue has been normalised to a mean of zero.

These linescans allow an alternative technique for correlating the Drammensfjord cores, using sediment greyvalue rather than lithological description (as used in figure 5.2). Statistical analysis using the Pearson correlation coefficient shows that intra-site correlation is good within the top 2-3m of the cores, but poor below this, and (as is evident by inspection of the above data) inter-site correlation is always poor. Two sets of correlation coefficients illustrate this.

First, the three cores from site D1 were compared with each other. Only the top 2.44m of data could be used, since this was the depth of the shortest imaged core sequence, that from core D1G. Sediment greyvalue was measured at intervals of 0.05cm, such that there were 4,881 data points in each record.

Core Comparison	Correlation Coefficient r
D1G vs D1L	0.454
D1L vs D1M	0.370
D1G vs D1M	0.531

These correlations are excellent, as could be anticipated just by comparing the three records by eye. Lateral alignment of the cores to compensate for missing material at the core tops makes the correlations even better.

This is not the case for the second comparison, across the three different coring sites in the fjord. Comparing D1G, D2G and D3G, again using the top 2.44m of each core at the same interval, gives the following results.

Core Comparison	Correlation Coefficient r
D1G vs D2G	0.189
D1G vs D3G	0.085
D2G vs D3G	-0.034

It is clear that on a large scale, the three sites have different sediment greyvalue sequences. Explaining these differences requires an understanding of the link between sediment lithology and greyvalue. Each lithology shows a characteristic pattern of greyvalue variability: laminated intervals oscillate between fairly constant dark and light greyvalues, sand intervals flicker chaotically between a range of greyvalues, and homogeneous intervals show little variation. Homogeneous grey event beds in core D1G can be detected in the sediment greyvalue record because they are noticeably paler than the surrounding sediment, perhaps because of the lower organic carbon content of the reworked glacial clay that they contain. This is illustrated in figure 5.4.

The differences in core greyvalue records arise because of differences in the distribution of lithological units within the fjord sediment system; they do not necessarily invalidate the continuity of individual laminations. For example, event beds such as those in figure 5.4 are not laterally continuous along the whole fjord, so cannot be correlated amongst the three sites. Similarly, the depth of the redox cline has not always been constant across the fjord, producing coeval laminated sediment in some locations and homogeneous sediment in others. These factors combine

to produce the best-quality record at site D1, in the deepest part of the fjord, where event beds are rarest and thinnest, and where anoxia has been most consistent; here, the varve record is the both the best-preserved by anoxia and the least-interrupted by event beds.

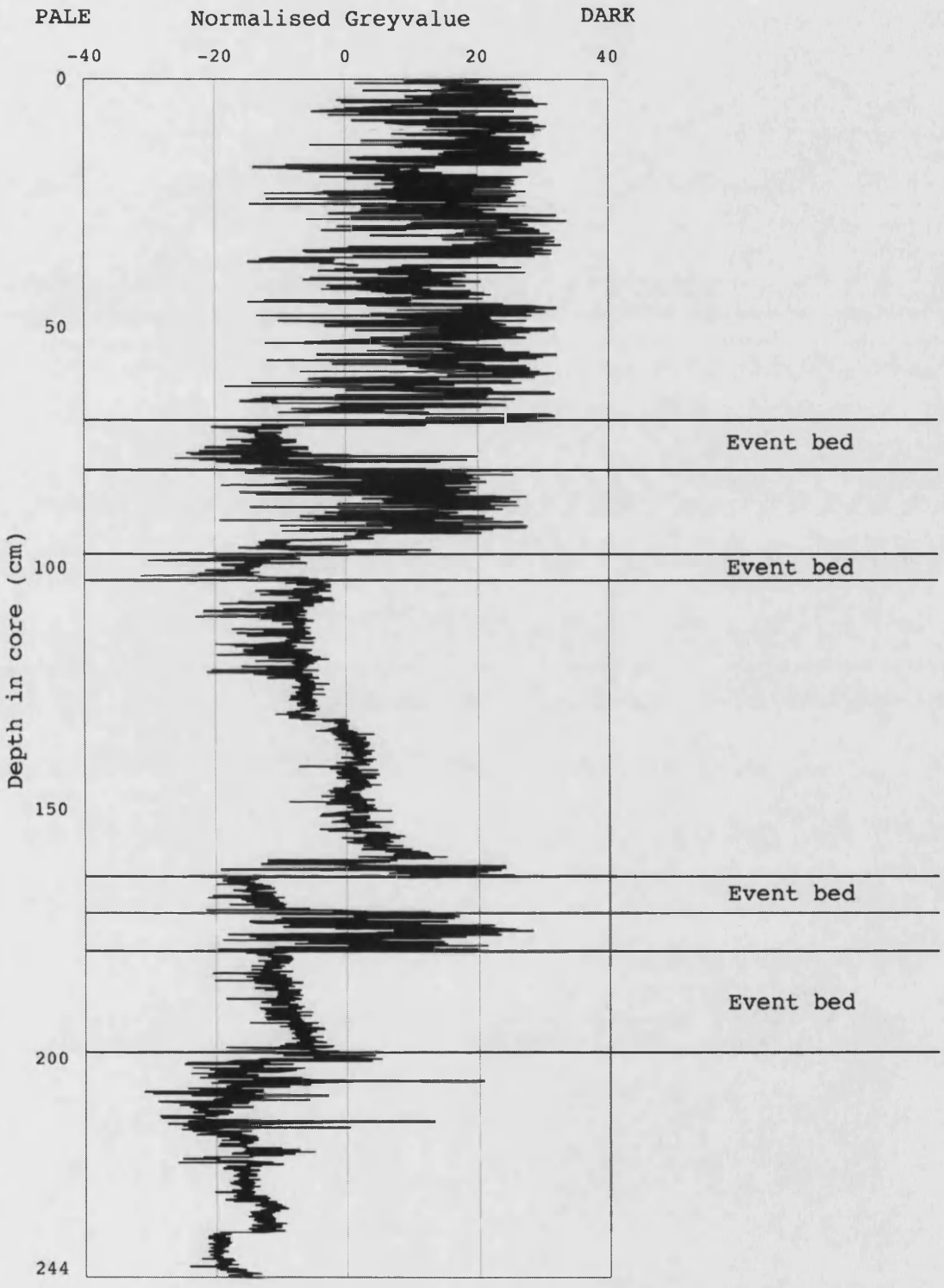

Figure 5.4: Greyvalue linescan from Drammensfjord core D1G, showing event beds identified using sediment greyvalue: they are noticeably paler and more homogeneous than the rest of the sediment. At the base of this record, there is a change to a paler background sediment which (according to the neighbouring core D1L) continues for several metres without interruption.

5.2.4 Drammensfjord varve mechanism investigation results

5.2.4.1 Smear slide results

The different components of the Drammensfjord sediment observed in the smear slides could be classified as clastic or biogenic.

- Clastic components included sand- and silt-size fragments of quartz, feldspar, pyroxene, and various other minerals, of which quartz was by far the most common: c. 90% of all clastic grains.

- Biogenic components included filamentous and amorphous organic matter, plant material (such as fibrous fragments and pollen grains), silicoflagellates [8], and diatoms, which were the commonest biogenic component. Calcite grains were also present: these were blocky and crystalline, rather than being fine micrite, so they were probably biogenic rather than inorganic. The amorphous organic matter was often aggregated with small clastic grains.

Since diatoms are so common in the Drammensfjord sediment, it is worth considering them in more detail. Approximately 40 different genera were noted. Diatom frustules in the sediment were often well-preserved, indicating that the diatoms were not predated upon, and suggesting (in accordance with [9]) that peaks of primary producers and consumers in Drammensfjord do not always coincide. The diversity of ecological niches occupied by diatoms [10] may explain their abundance in the Drammensfjord sediment.

Diatoms in the Drammensfjord sediment include the well-known and abundant coastal marine genera *Chaetoceros* and *Skeletonema*. The remainder can be divided into centric, planktonic genera (e.g. *Cyclotella*, *Porosira*, and *Coscinodiscus*) or pennate, benthic genera (e.g. *Fragilaria*, *Navicula*, *Nitzschia*, *Thalassionema*, and *Tabellaria*). The latter group could not feasibly live in the deep fjord, because there is no light available there, so they are presumably reworked from shallower water. Rarer genera seen in some slides include the distinctive *Oxyneis* and *Odontella*. Braarud *et al.* [11] studied only marine planktonic diatoms, but the smear slide diatom data agree with the assemblage described therein. Further work on the diatom assemblages in the Drammensfjord cores would undoubtedly be worthwhile, though it is beyond the scope of this thesis.

Could the different sediment components be quantified, as well as described? This was difficult with the smear slides, since different amounts of sediment were used for each slide. An apparent high concentration of diatoms on one slide may have been a result of more densely packed sediment. Without using a calibration method, such as adding a known quantity of microspheres [12], only a very approximate idea could be gained of the concentrations of sediment components. Furthermore, the process of smearing tended to sort the sediment components, so that (for example) diatoms tended to clump together in certain areas of the slide; this made sediment composition very difficult to quantify. Slides from the uppermost sediment contained noticeably more organic matter than the others, and the sand interval at 156-157cm depth in core D1G had a clear predominance of sand grains. But aside from these two examples, all the

other smear slides were similar, each containing all the sediment components described - clay, silt, diatoms, and so on - in roughly similar proportions.

So, the smear slides cannot definitely answer the question concerning the nature of the homogeneous mud intervals discussed in section 5.2.2. The similarity of the smear slides taken from laminated and homogeneous intervals might be taken to suggest that the homogeneous intervals were just homogenised laminated intervals. However, it is not clear that the expected difference in composition, if the homogeneous intervals were event beds - fewer diatoms, and more and coarser clastic grains - would be detectable using smear slides.

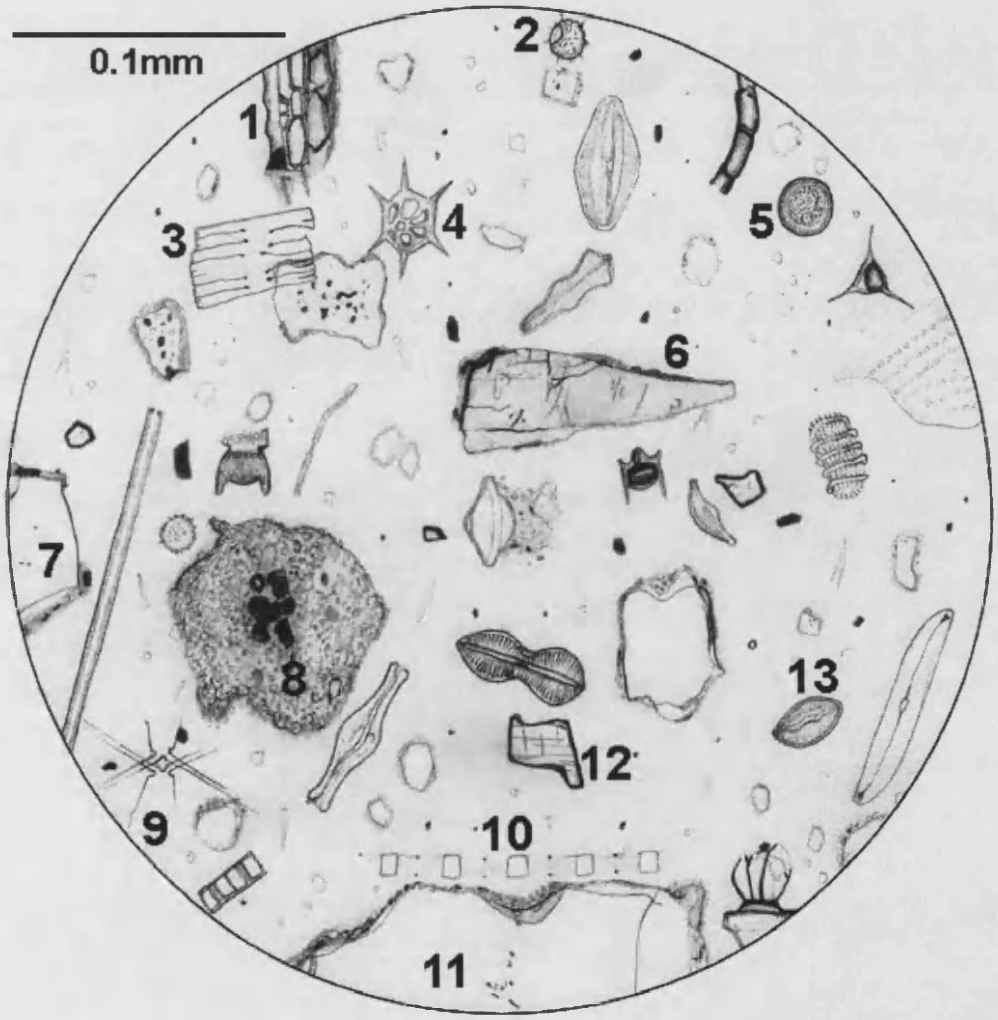

Figure 5.5: Drawing of an "idealised" smear slide at high power showing the range of components in the Drammensfjord sediment. 1 = wood fragment; 2 = dinoflagellate?; 3 = diatom; 4 = silicoflagellate; 5 = *Cyclotella* (diatom); 6 = pyroxene grain; 7 = quartz grain; 8 = amorphous organic matter; 9 = *Chaetoceros* (diatom); 10 = *Skeletonema* (diatom); 11 = large quartz grain; 12 = calcite grain; 13 = diatom.

As for the laminations themselves, attempts to sample black and grey sublayers separately were unsuccessful. Even the point of a toothpick could not separate two distinct lithologies without such heavy cross-contamination as to make them virtually indistinguishable. Once again, all the slides basically contained a similarly-proportioned mixture of the same components. It is important here to note the importance of "reinforcement syndrome" [cf.13]. Because a suggested lamination mechanism was already in mind, based on the depositional system described in chapter 2, then there was a risk that the eye would "see" evidence to support this in the smear slides, for example by selective counting of different components. It was thought best to leave the smear slide results ambiguous rather than risk endorsing a potentially biased set of descriptions.

So, the results from the smear slide investigations are limited to a typical composition of Drammensfjord sediment, with "typical" in this instance meaning all sediment except sand layers and the most recent organic-rich sediment. This is shown in figure 5.5. Better results concerning the nature of the laminated sediment and the homogeneous intervals were obtained using BSEI, which enabled the fabric of the sediment to be kept intact whilst allowing high-magnification study.

5.2.4.2 Backscatter electron imaging (BSEI) results

BSEI images were captured at three magnifications, denoted here as low, medium, and high magnification, as follows:

Low magnification:	1cm on image = c. 780μm	(approximately × 12)
Medium magnification:	1cm on image = c. 350μm	(approximately × 30)
High magnification:	1cm on image = c. 130μm	(approximately × 75)

- The D1M-CC3 slab

Slab D1M-CC3 originally covered c. 75cm to 90cm depth in core section D1M1, which was itself located c. 10m below the sediment-water interface. D1M was the only core that contained well-preserved laminations at this depth. Figure 5.6 shows a digital image of this region of the sediment core.

Three images were taken of slab D1M-CC3, from an area of undisturbed laminations at c. 82cm depth in core section D1M1. The laminations in this area are thinner than most of the others in the cores: only c. 0.6 to 0.9mm thick. Images 000 and 002 are both at medium magnification. Image 000 (figure 5.7.1) shows five or six complete varve couplets; image 002 (figure 5.7.2) shows 7 or 8 slightly thinner varve couplets. Image 005 (figure 5.7.3) is an area of image 000 expanded to high magnification. From bottom to top, it shows the top half of a dark layer, a complete pale layer, a complete dark layer, and another complete pale layer: almost two complete varves.

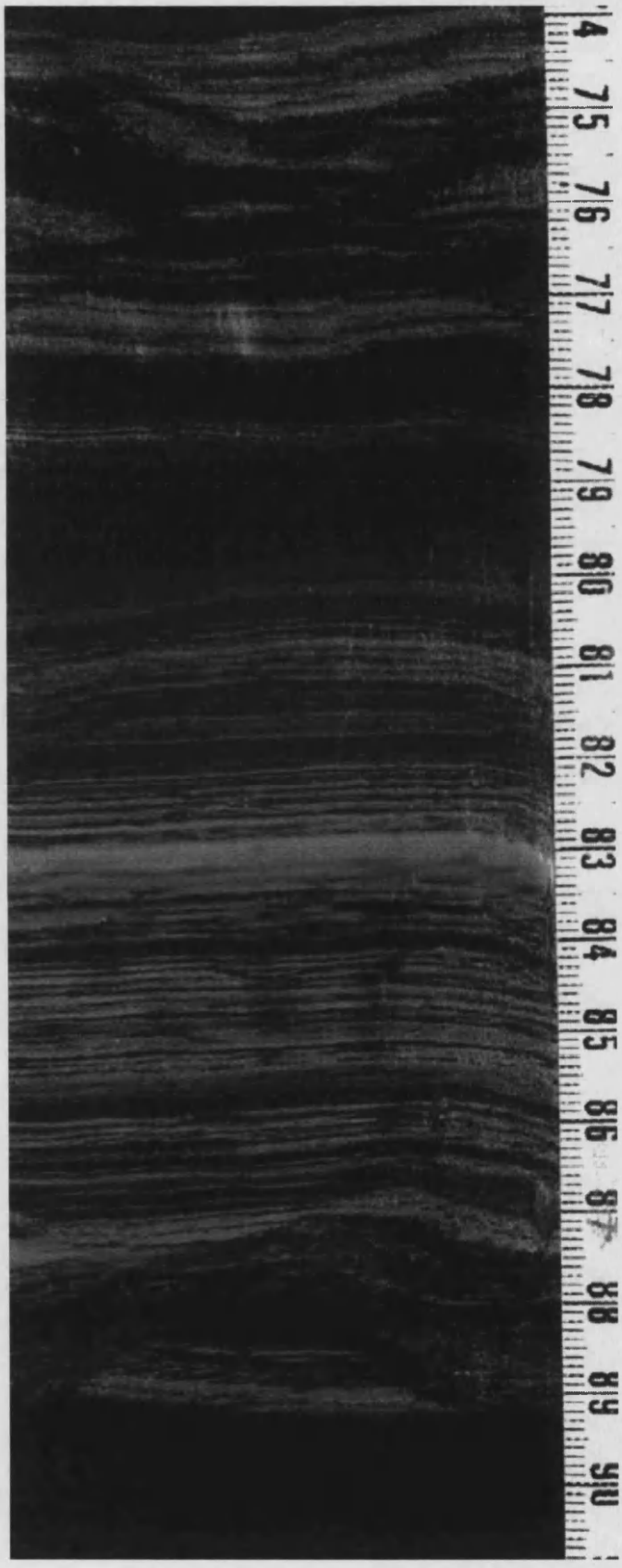

Figure 5.6: Digital image of the sediment core interval from which slab D1M-CC3 was obtained. Note the synsedimentary faulting which has presumably been caused by the sand-rich event bed deposited just above this interval. The varved interval selected for BSEI was unaffected by this faulting.

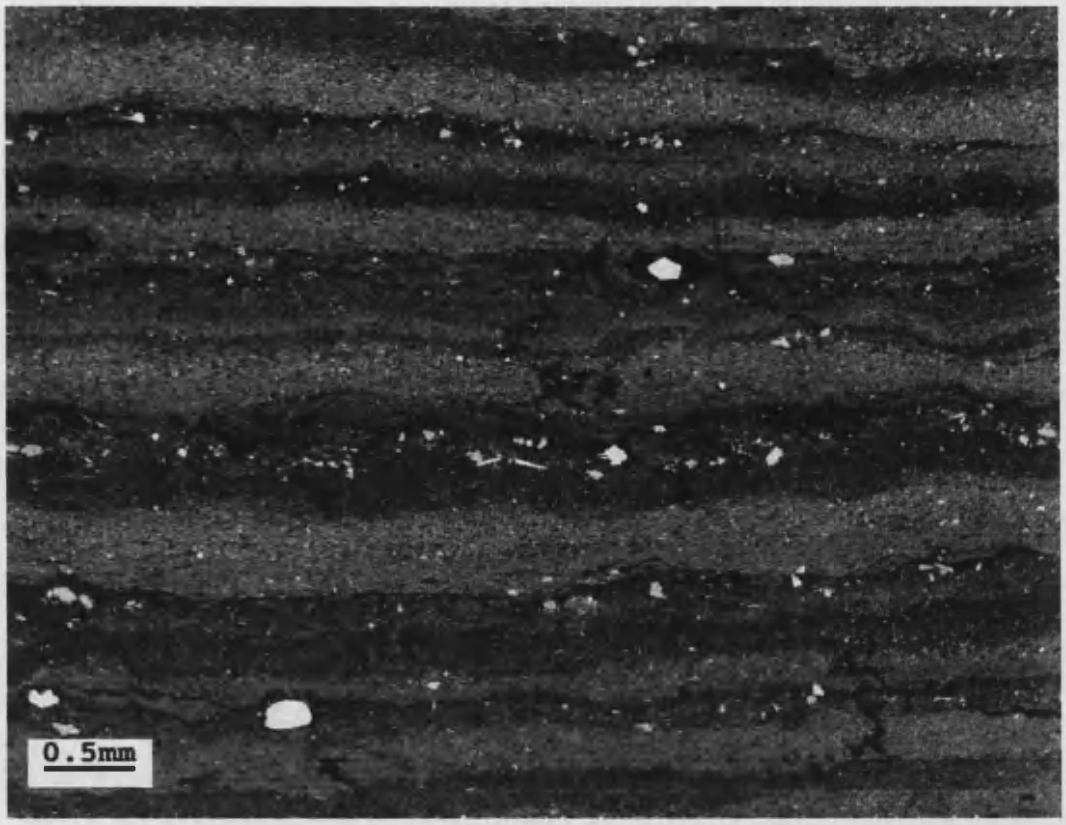

Figure 5.7.1: Image 000 from slab D1M-CC3, showing a laminated region at medium magnification.

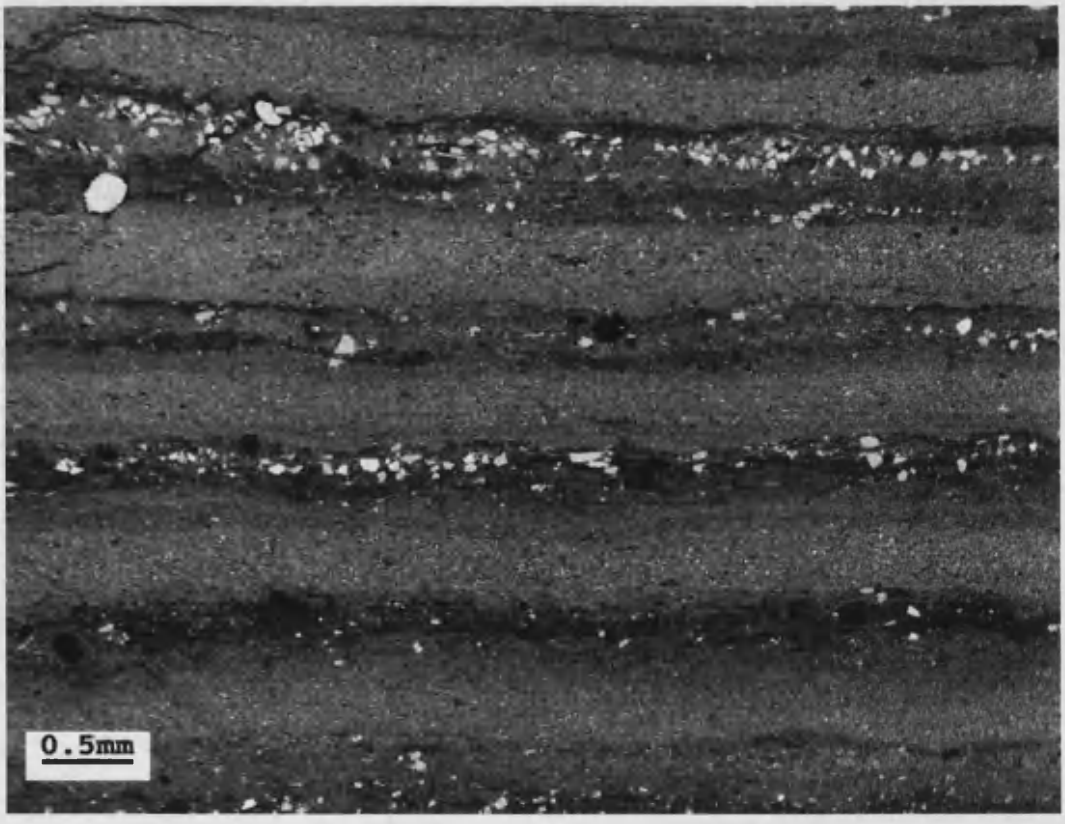

Figure 5.7.2: Image 002 from slab D1M-CC3, showing a region of slightly thicker varves.

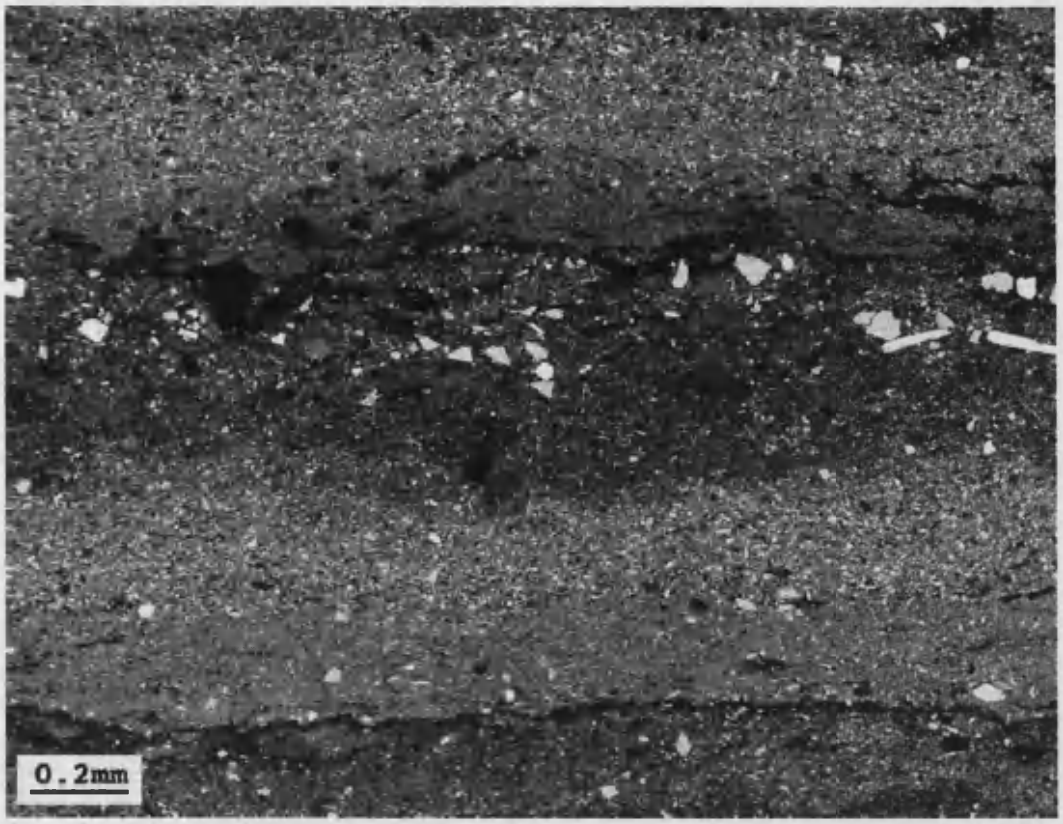

Figure 5.7.3 : Image 005 from slab D1M-CC3, part of image 000 expanded to high magnification.

- The D1L-CC5 slab

Slab D1L-CC5 was originally located at c. 75cm to 90cm depth in core section D1L6, corresponding to c. 180cm below the top of the core. This section of this particular core contained perhaps the best-preserved laminations of all the Drammensfjord cores.

Slab D1L-CC5 was imaged in its entirety at low magnification, producing a mosaic of five images (021 to 025) which is displayed in three parts, in vertical sequence, in figures 5.9.2 to 5.9.4. In addition, image 000 is an area of image 024 expanded to medium magnification and is shown in figure 5.9.1. The low-magnification mosaic as a whole shows a slab c. 8.3mm wide, 38mm long on its left edge, and 36mm long on its right edge: it is a trapezoid shape. The top part of the slab has become separated from the lower part during the impregnation process. This trimmed section of slab D1L-CC5 forming the mosaic is from c. 89 to 92.5cm depth in core section D1L6.

The top part of the D1L-CC5 mosaic is relatively coarse siliciclastic sediment, with a sharp, possibly erosive lower contact with fine-grained, well-laminated sediment. This coarse unit is not homogeneous: the upper part of it is noticeably coarser than the lower, with a sharp rather than graded change in grain size. Comparison with the digital image of the same area (see figure 5.8.1) shows that this sandy sediment is at the base of a 7cm-thick homogeneous interval within the laminated sequence, which fines upwards into clay-grade sediment at the top. The presence of coarser sediment at the base, and the abrupt contact with well-laminated sediment, strongly suggests that this is an event bed. This bed can be seen in all the cores from site D1. Within the

silt and sand fraction, most of the grains are quartz and feldspar, though there are also heavy minerals: zircons, apatite, Fe and Fe-Ti oxides, and pyroxenes [14].

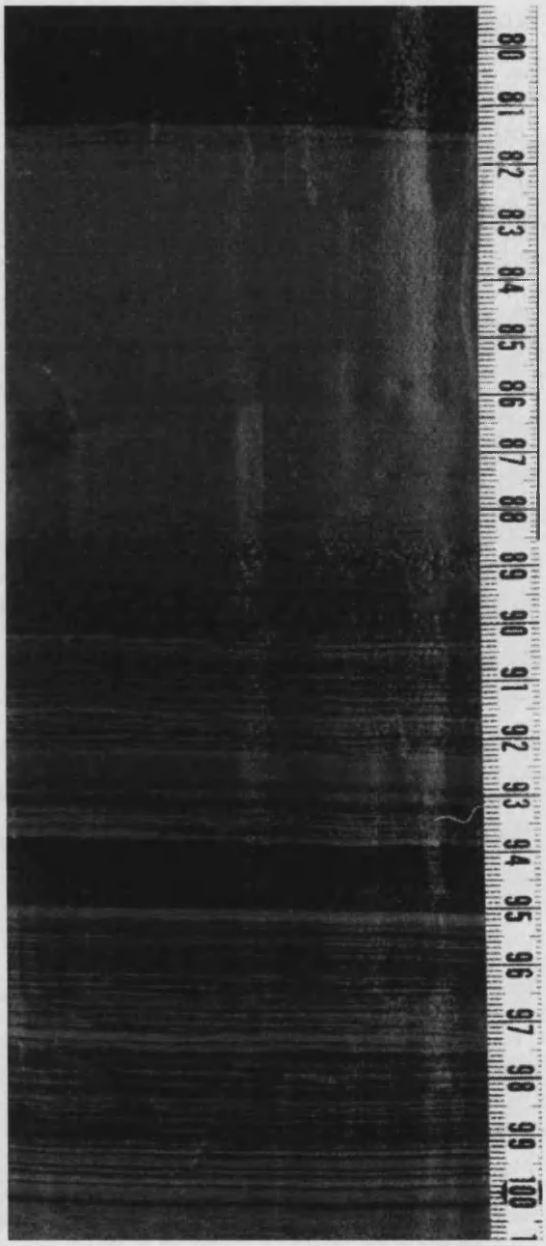

Figure 5.8.1: Digital image of the sediment core interval from which slab D1L-CC5 was taken. Note the thick homogeneous bed (c. 81.5 to 89cm depth) between two varved intervals.

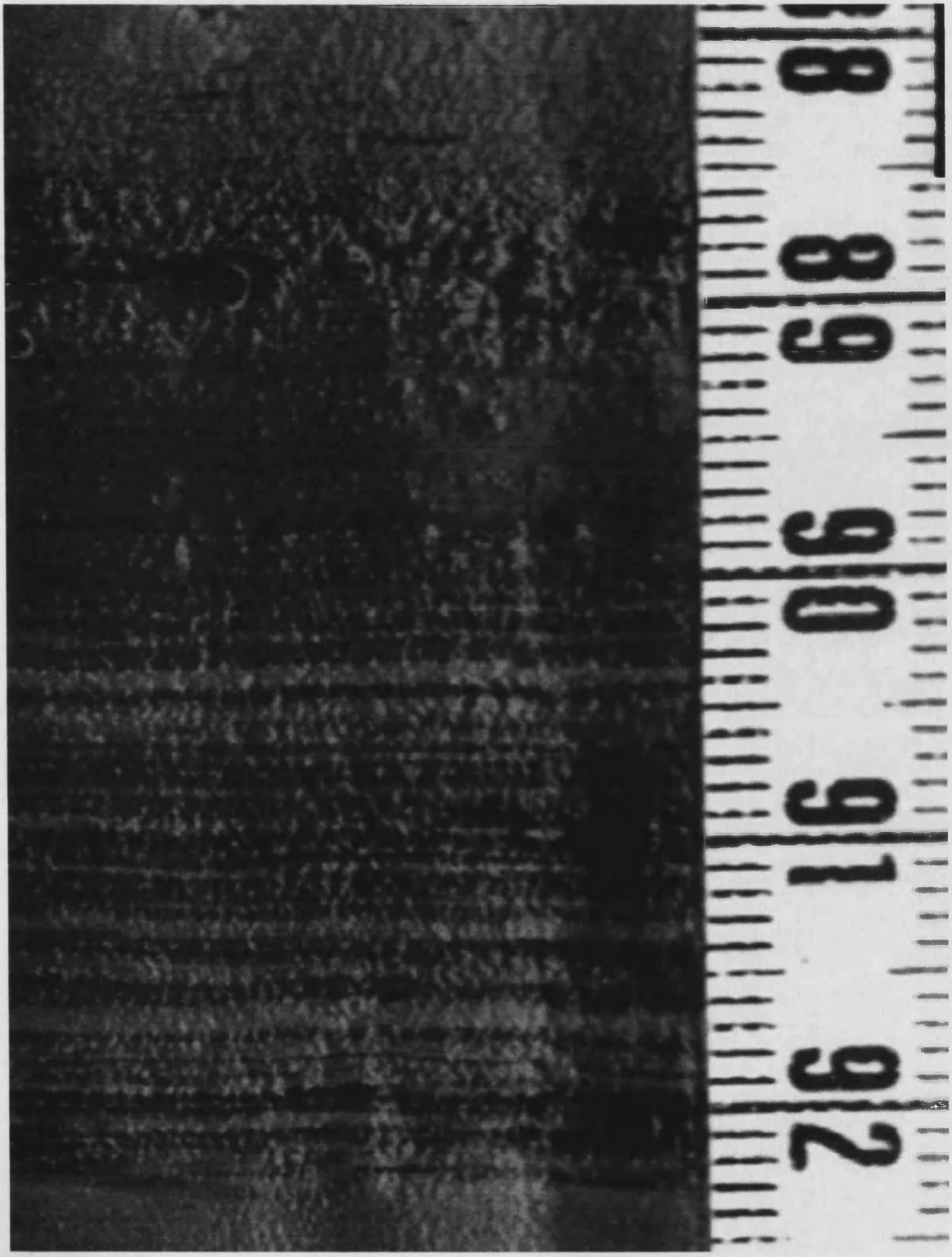

Figure 5.8.2: Close-up of the previous image showing the region used for the backscatter mosaic images that follow. Note the abrupt change from well-preserved varves at the bottom to the sandy base of the homogeneous interval at the top.

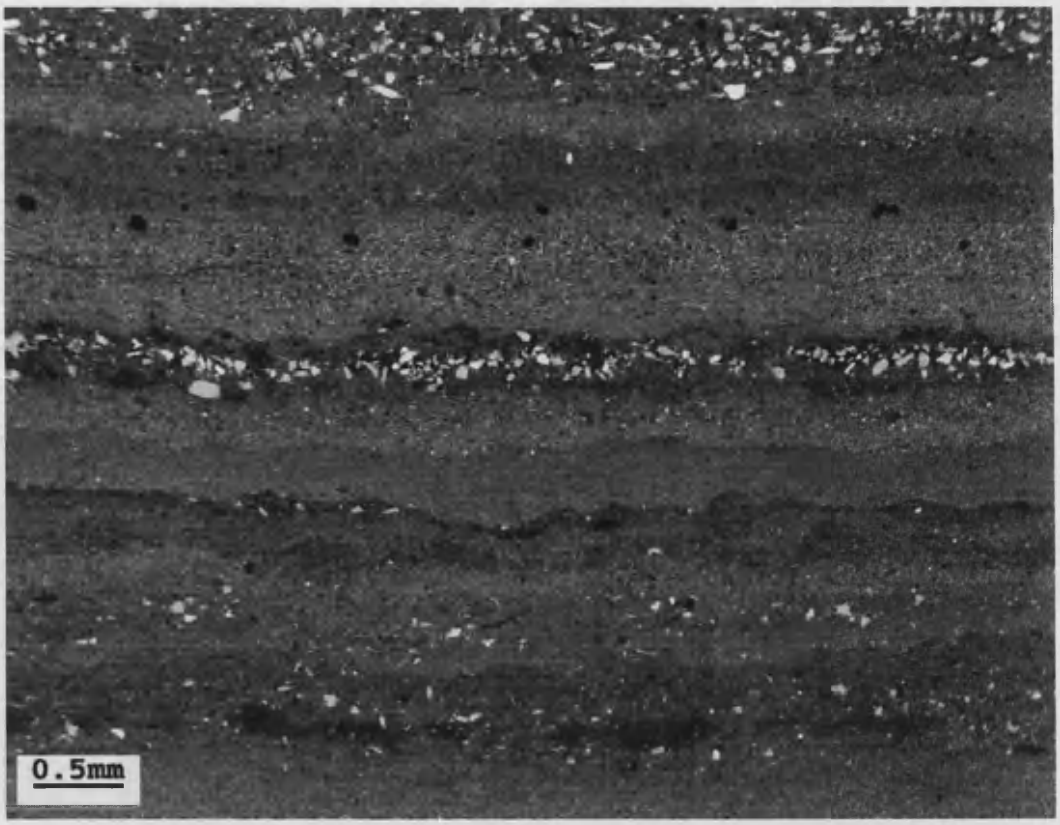

Figure 5.9.1: Image 000 from slab D1L-CC5, showing the laminated fabric at increased (medium) magnification.

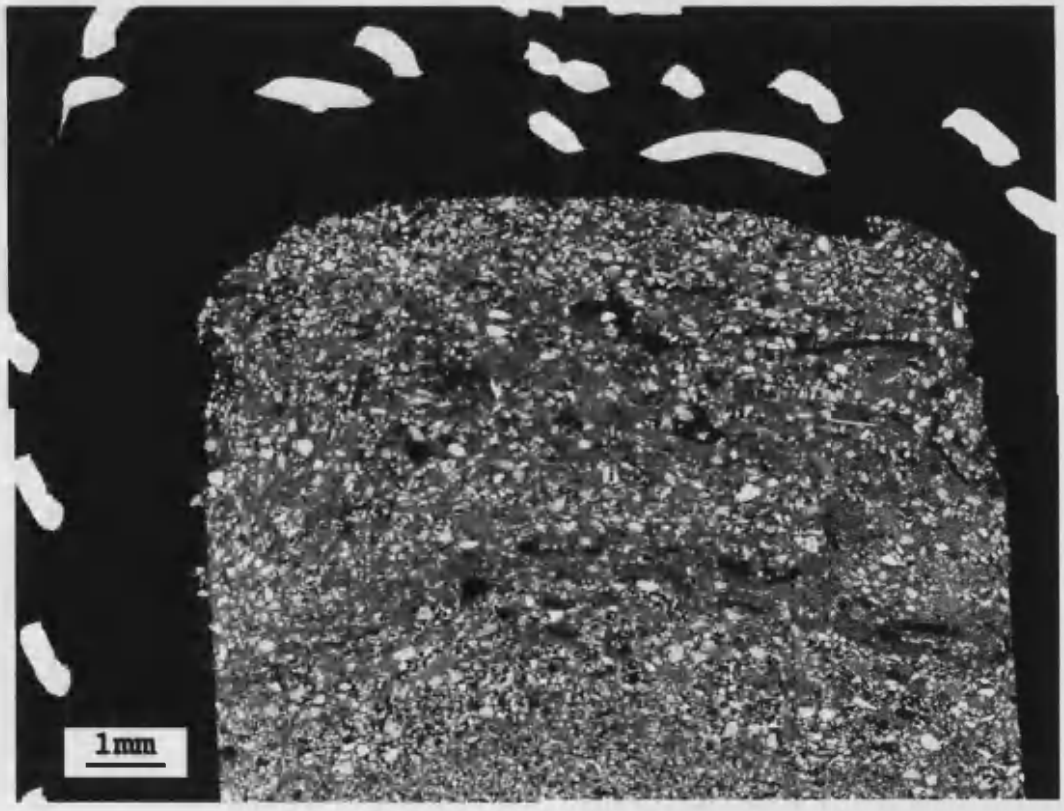

Figure 5.9.2: Uppermost part of the BSEI mosaic covering slab D1L-CC5, showing the coarse upper interval. The width of the slab is approximately 8.3mm.

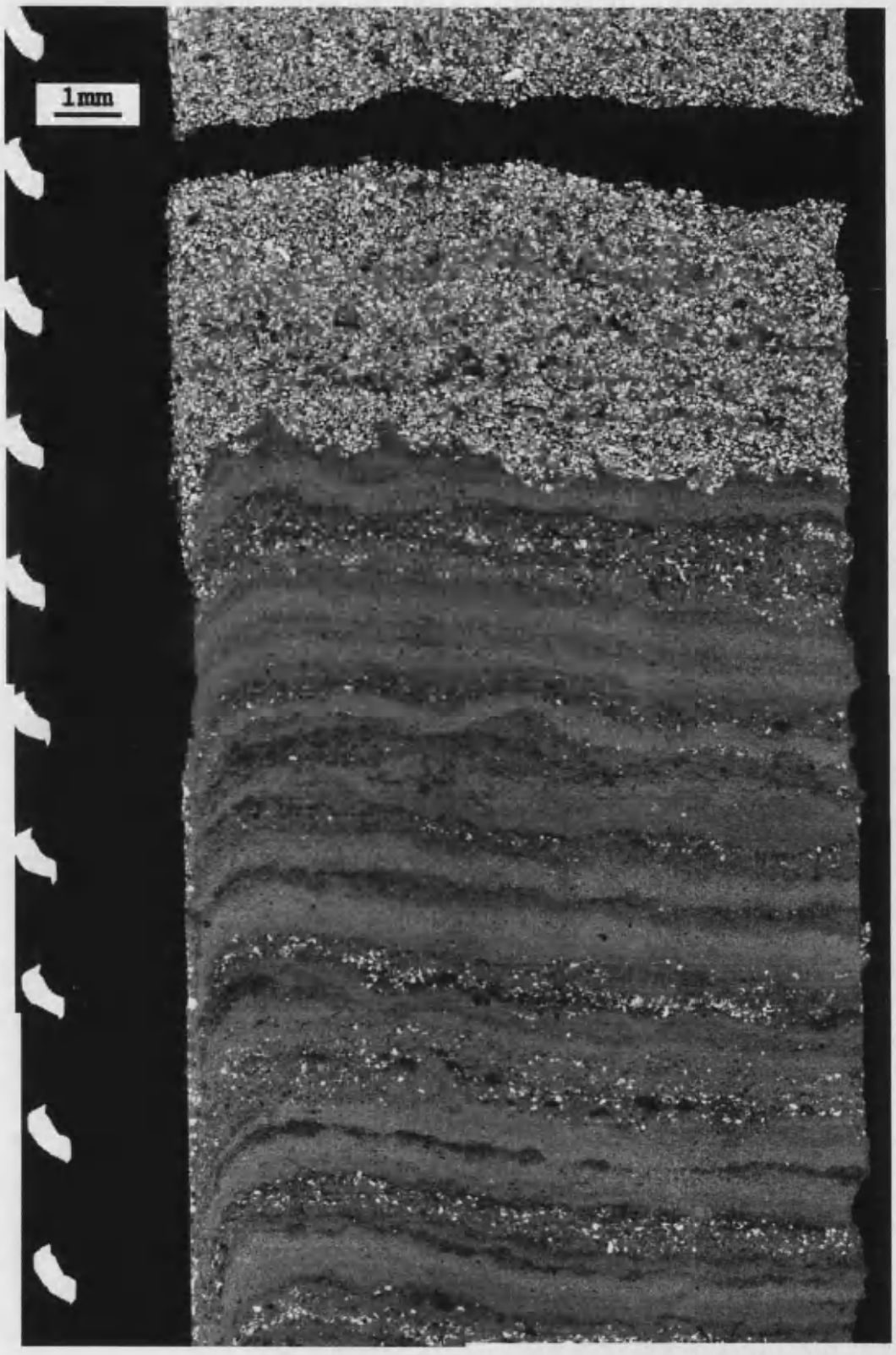

Figure 5.9.3: Central region of the D1L-CC5 mosaic, showing the abrupt change from well-preserved varves to coarse, homogeneous sediment. The width of the slab is approximately 8.3mm. Image 000 (figure 5.9.1) is taken from this section of the slab.

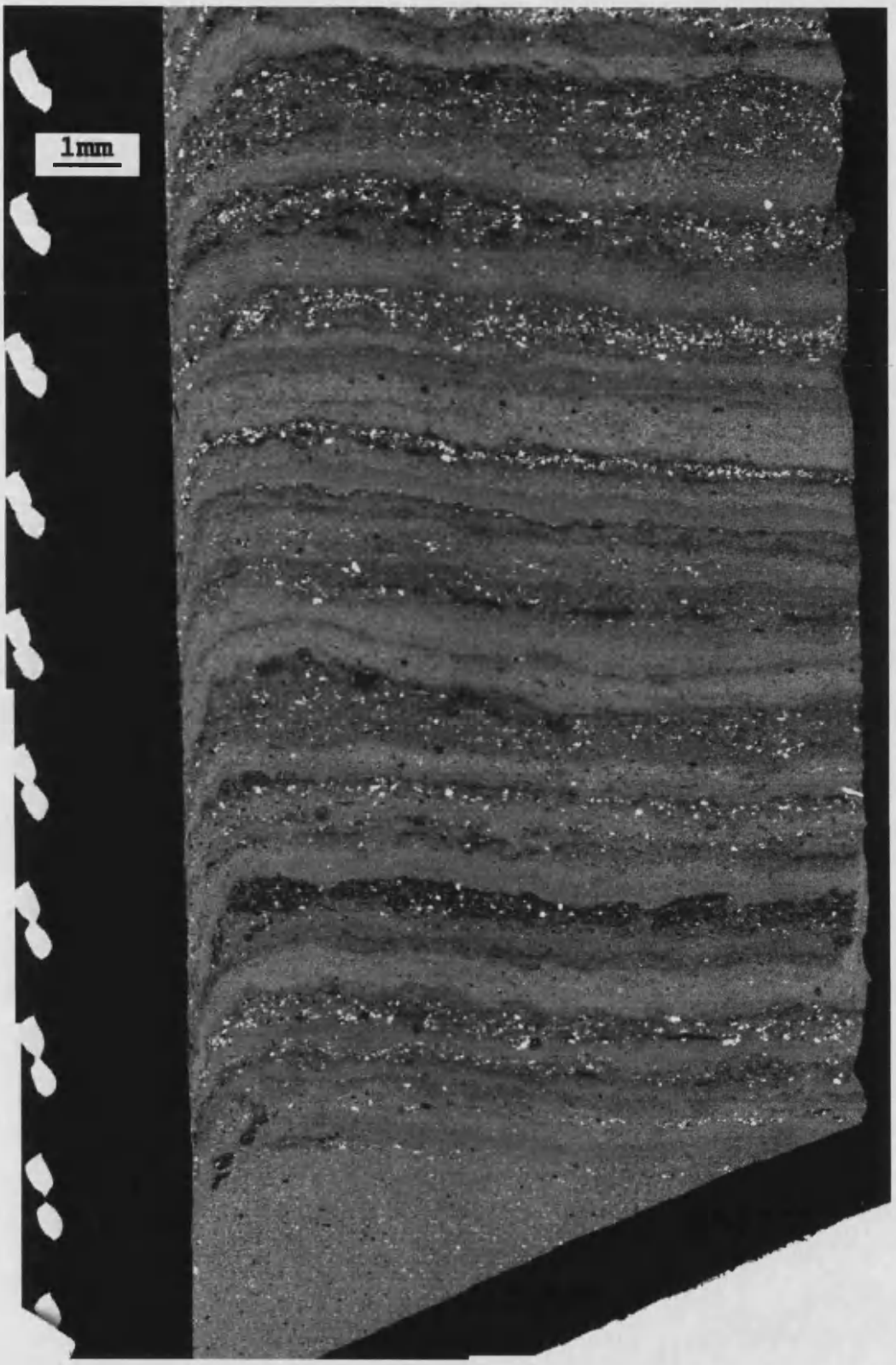

Figure 5.9.4: Lower region of the D1L-CC5 mosaic, showing a fine-grained homogeneous interval visible at the very base, above which are well-preserved varves. The width of the slab is approximately 8.3mm.

The images from slab D1M-CC3 show the lamination fabric in detail. Angular clastic grains show up as bright white. They are mostly confined to darker layers in the sediment, which are separated by paler, fine-grained layers. Dark, fibrous organic matter is apparent throughout the sediment. The lamination cycle is an alternation in grain size, between relatively coarse clastic sediment and finer sediment. However, this is not the only cycle: indeed, in some cycles the coarse sediment is barely present, yet the cycle is still clear.

This is because there is a "background" cycle in BSEI brightness. After each relatively bright clastic-rich layer, there is a darkening into a layer containing more diatoms, without much change in grain size. This darker fine-grained layer is covered by or interspersed with a much coarser clastic layer, but this can be very thin. Then there is a return to clastic-rich fine-grained sediment. The lamination cycle in the backscatter images can be summed up as white-coarse-grained, then pale-fine-grained, then dark-fine-grained, then white-coarse-grained again, and so on.

Here it should be noted that there is no straightforward correspondence between the alternation of black and pale grey layers in the digital images and the layers in the backscatter images. Similar components result in similar changes in greyvalue in both cases, but for totally different reasons. In the digital images, the clastic-rich layers are pale grey, and the fine-grained layers are black. The concentration of diatoms in the latter is insufficient to produce pale "diatomite"-type sediment; it remains black because of the presence of organic matter, and possibly also iron sulphides produced in the anoxic bottom water.

The lamination cycle can be interpreted in the light of the BSEI results and the nature of the annual cycle in the Drammensfjord basin, as follows. The grain size cycle - deposition of the relatively coarse, clastic-rich layer - results from the spring flood, which occurs once a year in March and April. This layer may be very thin if the flood is small. In between spring floods, there is a constant rain of fine-grained sediment to the deep fjord. The composition of this rain changes throughout the year: diatoms and other plankton bloom in spring and summer, then die off as temperature and light are reduced in autumn and winter. The sediment rain becomes richer in clay and organic matter. At the end of the winter, when the snow melts, a new clastic layer is formed and the cycle begins anew.

In the digital images of the Drammensfjord cores, the varves appear as simple couplets: alternating pale grey and black layers. The BSEI results show that the sediment components cycle in a more complex way than is revealed by sediment greyvalue. There is potential for more insight to be gained into deposition in Drammensfjord via close examination of changes in varve type (cf. [4], figure 9). Image 000 is interesting in this respect. Unlike the D1M-CC3 images, the varve cycle does not always appear to follow the same pattern. The sediment is still clearly laminated, but there is not a simple progression of the layers described above, and it is not immediately clear how many varves there are in this backscatter image. Such sub-varve complexity did not present any hindrance to the varve analysis based on digital images, but its presence means that there is yet more information that can

potentially be extracted from the Drammensfjord varves, beyond the scope of this thesis.

The style of lamination seen in Drammensfjord, which could be described as a "clastic-organic" varve fabric, is found in numerous other silled fjords, such as Nordåsvannet [15] and Framvaren [16] in Norway, and Saguenay Fjord, Canada [17]. The existence of these varves in Drammensfjord has been known about since the 1930s [18], though only recently has their potential value as a record of palaeoclimatic information been appreciated.

5.2.5 Drammensfjord varve measurement results

The Drammensfjord varve data were extracted from a composite linescan from core D1G, which was located to cover the best-preserved varves, and subsequently enhanced using the image processing and thresholding techniques discussed in section 4.4.3. Varve thickness was measured, for convenience, in pixels. To confirm the linear relationship between "pixel depth" and depth in millimetres, 54 tie-points were located (using the tape measure present in every image) to construct the following calibration curve.

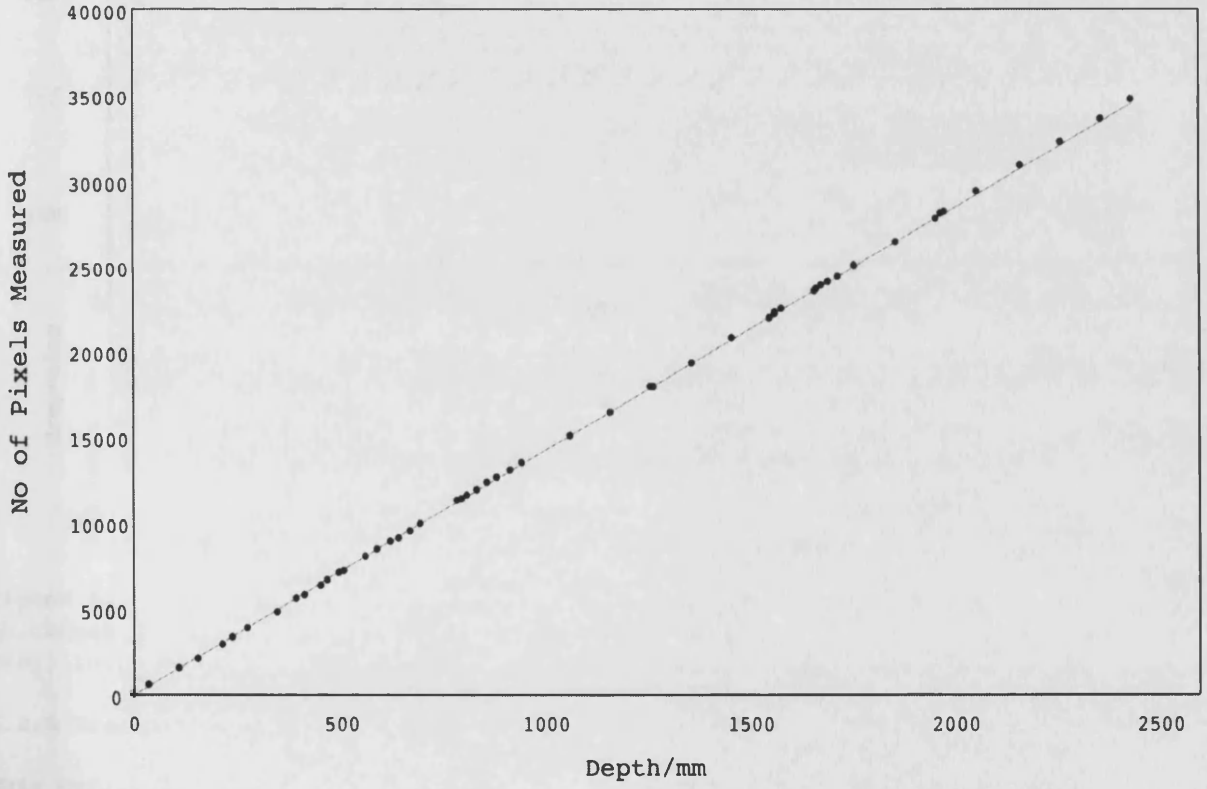

Figure 5.10: Calibration curve showing actual depth in core D1G (measured from the tape measure in the images) against the number of pixels in the composite linescan up to that depth.

The linear relationship between pixel depth and millimetre depth is near-exact, with 14.14 pixels per millimetre in the final linescan. Even though hundreds of overlapping linescans were used to construct this, it is noteworthy that the total length of the final D1G curve is 34,739 pixels, almost identical to the figure of 34,735 pixels obtained using just one linescan per image to produce the preliminary greyvalue logs

presented in section 5.2.3. This corresponds to 2,439mm of sediment: the top c. 2.5m of core D1G. Despite the presence of some poor-quality varves, in the topmost part of the core, for example, the varve counts are similarly replicable: there are 896 varves in the final data, as compared with an earlier, less detailed count which gave a total of 906 varves, and several counts "by eye" which gave totals within 900 ± 10. The varve results themselves are in section B.1 in appendix B. A summary graph of the data is below.

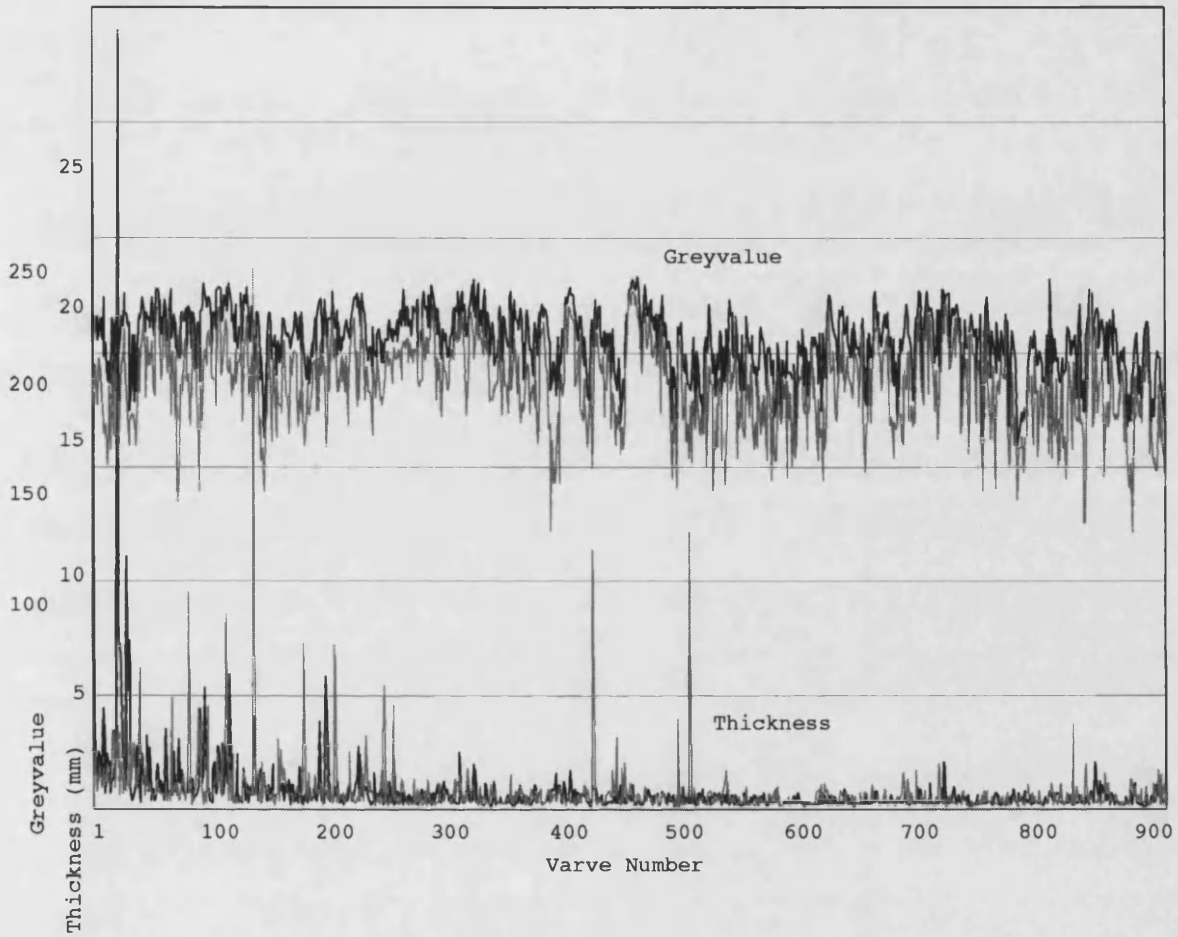

Figure 5.11: Graph showing all four variables obtained from the Drammensfjord varves: thickness and mean greyvalue of both black and grey sublayers (plotted in black and grey, respectively).

5.2.6 Drammensfjord integrated core chronology

This section describes the use of independent chronological data to calibrate the varve data described in section 5.2.5 so that it can be treated as a time-series.

Radiocarbon dates were obtained from two wood fragments in core section D1G7, at 11-12cm depth (a wood chip, possibly from a sawmill) and 94cm depth (a twig). Neither showed any signs of erosion, though this by no means proved that they were the same age as the surrounding sediment: for woody plant fragments, transport into sedimentary basins may take hundreds of years or more [e.g. 19]. Radiocarbon dating measures the relative concentration of ^{14}C in the sample, which is then converted into an uncalibrated age by assuming a constant past supply of ^{14}C and a standardised half-

life of 5,568 ± 30 years [20]. Uncalibrated ages are expressed in ^{14}C years. The two D1G7 ages are as follows, quoted with a 2σ error:

Depth below top of core D1G	Uncalibrated age
11-12cm	240 ± 45 ^{14}C yrs BP
94cm	1,030 ± 35 ^{14}C yrs BP

Because atmospheric production of ^{14}C varies with changing solar activity and other factors, the ages above need to be calibrated using a calibration curve; in this case, INTCAL98 [21] was used. Wiggles in this curve distort the originally symmetrical errors of the uncalibrated ages, and for some uncalibrated ages, also result in multiple possible calibrated ages. The calibration process for the D1G ages is illustrated in figure 5.12.

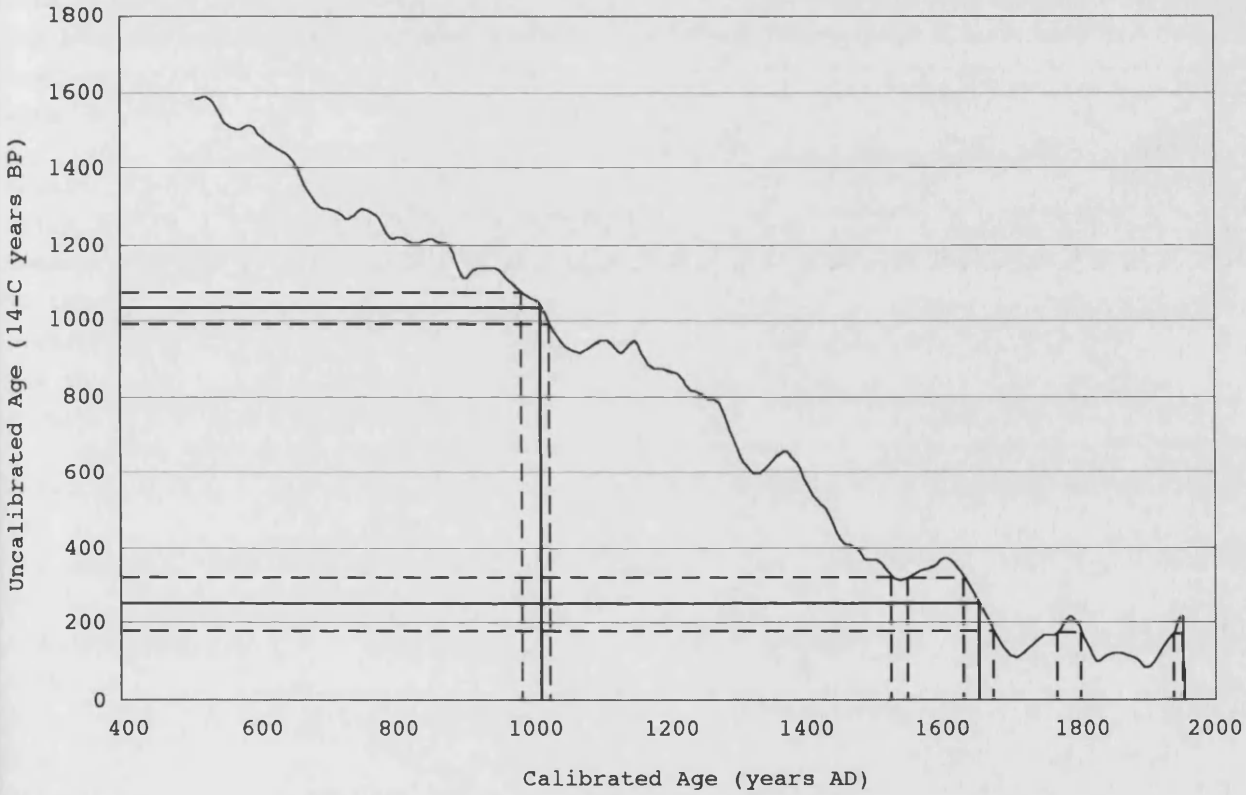

Figure 5.12: INTCAL98 radiocarbon calibration curve [21], plus uncalibrated dates and calibration lines, indicating an unambiguous calibrated age for the older wood fragment, but multiple possible calibrated ages for the more recent fragment.

The INTCAL98 calibration curve results in an unambiguous calibrated age of 942 calendar years BP for the older wood fragment (with a 2σ error of 927-965 years), but the younger wood fragment has an ambiguous calibrated age because of wiggles in the curve. It could lie in any one of a number of different intervals. The most likely three intervals are as follows, with the probabilities based on a 2σ error once more:

Calibrated age interval	Probability
265 to 322 ^{14}C yrs BP	34.3%
141 to 220 ^{14}C yrs BP	31.4%
0 to 24 ^{14}C yrs BP	11.7%

The remainder of the 100% consists of other, smaller intervals which are much less likely (c. 1-2% probability). This ambiguity in calibration arises because the calibration curve levels off after c. AD 1700, as a result of the release of large amounts of "fossil" carbon dioxide from the burning of fossil fuels during the industrial revolution. This carbon contains almost no ^{14}C [22]. More recently, atomic testing has generated (relatively) large amounts of atmospheric ^{14}C, distorting the ^{14}C content of extant living tissue to such a degree that AD 1950 is used as the "present" for radiocarbon purposes [22]. "24 BP" refers, then, to AD 1926, and so on.

The radiocarbon dating results can now be compared with the varve counts. Based on the final varve measurements, given in appendix B, a depth of 11.1cm in core D1G corresponds to varve number 21, and the lowest varve in D1G, at 92.2cm depth, is varve number 733. This means that there are 712 varves between the two dated wood fragments, with a probable counting error of c. 1% based on repeated counts. This is caused by the blurred, smeared appearance of some of the thinnest varves; the precision of the computer-assisted counting is nonetheless much greater than could have been achieved with the naked eye.

Within the interval between 11cm and 94cm, there are also event beds (such as the 7cm-thick bed seen in the BSEI mosaic of slab D1L-CC5, in figure 5.9.3); 4cm of poorly-laminated sludge at the top of the interval (11-15cm); and 2cm of homogeneous grey mud at the bottom, below the final counted varve (92-94cm). Together these represent perhaps several tens of years of deposition. This means that the total time between the two wood fragments - assuming they are the same age as the surrounding sediment - should be c. 750 calendar years, if the varve sequence is truly annual and continuous.

Using 942 calendar years BP as the age of the older wood fragment, this predicts an age of c. 192 calendar years BP for the younger wood fragment, which fits well with the middle interval of 141-220 calendar years BP obtained from the calibration curve in the table above. Thus, the radiocarbon and varve data fit together well, defining a sequence of 712 varves that cover the interval from c. 192 to 942 calendar years BP, with an error on both these dates of c. 50 years; that is, the interval c. AD 1000 to AD 1750. This is only a fragment of the entire Holocene, but it is a time of significant climate change, manifest in many historical accounts as well as in other natural climate proxies. The palaeoclimatic value of the varve record is discussed in chapter 6.

Four additional radiocarbon dates were supplied by Rienk Smittenberg at NIOZ, obtained from biomarkers sampled from bulk sediment in core D1G.

Depth below top of core D1G	Biomarker	Uncalibrated age
0-7.5cm	Crenarchaeol	860±120 ^{14}C yrs BP
0-7.5cm	GDGT-0	520±75 ^{14}C yrs BP
85-92cm	Crenarchaeol	1,020±240 ^{14}C yrs BP
85-92cm	GDGT-0	1,050±80 ^{14}C yrs BP

Crenarchaeol and GDGT-0 (Glycerol Dialkyl Glycerol Tetraether) are derived from marine methanogenic archaebacteria [23]: unlike the wood fragments, these are autochthonous,

and their radiocarbon ages reflect the radiocarbon age of the fjord water. This explains why these dates appear to be too old, especially the two dates from the 0-7.5cm interval. The ^{14}C content of Drammensfjord water is evidently not in equilibrium with the atmosphere; Lowe and Walker [22] note that Norwegian fjord water can have an apparent age of 450±40 years, and this is not incompatible with the ages given above for the 0-7.5cm depth interval. When compared with the varve-and-wood chronology, the older pair of dates suggest a much lower reservoir age, of 100 years or less, and this may be related to changes in circulation in the fjord, though in any case these biomarker dates add nothing to the integrated core chronology and are not considered further.

Using the combined varve-and-wood chronology for core D1G, it is possible to estimate the amount of sediment missing from the top of the core. It would not be surprising to have a significant amount missing [24], owing to the soft, soupy nature of the surface sediment in Drammensfjord, and the high-energy impact of the sinking core barrel. Using the two radiocarbon ages, two age-depth curves can be drawn, showing the maximum and minimum amounts of missing sediment (based on the 2σ errors, and assuming a constant rate of sediment accumulation).

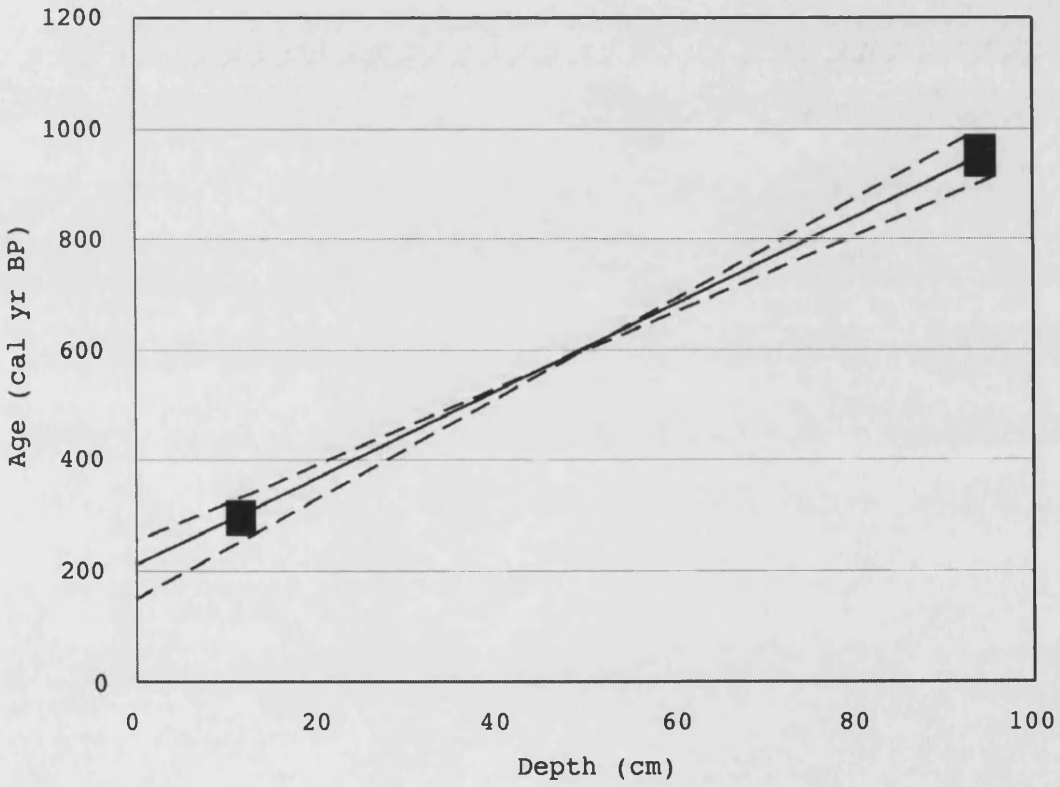

Figure 5.13: Age-depth curves for core D1G, showing the range of possible radiocarbon ages (indicated by black blocks) and consequent range of age-depth curves (all assuming a constant rate of sediment accumulation - see later).

These results suggest that between 3cm and 14cm of sediment are missing from the top of core D1G. However, recent sediment accumulation rates in Drammensfjord are likely to have been much increased by anthropogenic activity. This is supported by additional chronological data derived from the surface sediments at Drammensfjord site D1, which

were sampled by a 35cm-long boxcore that captured the sediment-water interface intact. ^{137}Cs and ^{210}Pb measurements were obtained from this boxcore, producing the curves below.

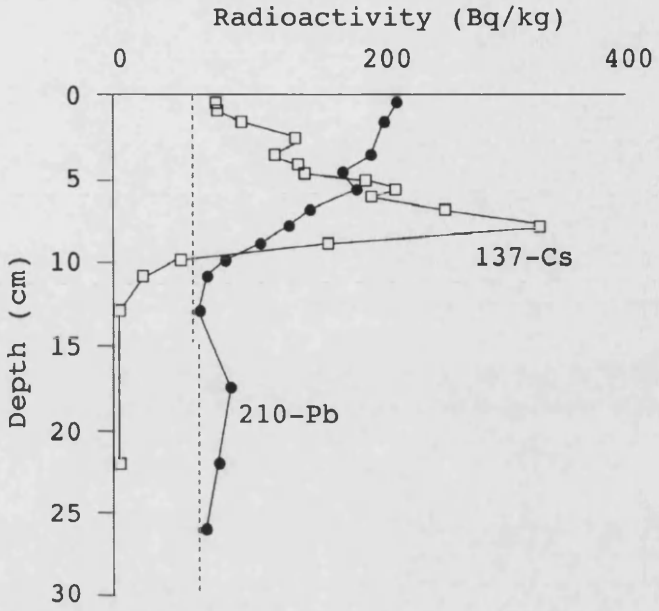

Figure 5.14: ^{137}Cs (squares) and ^{210}Pb (circles) curves from the Drammensfjord site D1 boxcore. The vertical dotted line is the background ^{210}Pb activity.

The maximum ^{137}Cs activity, at 8cm depth in the boxcore, corresponds to the 1986 Chernobyl nuclear event. ^{137}Cs activity drops to zero at 12cm depth, which corresponds to the early 1950s, when nuclear testing was initiated. These dates indicate a much faster recent rate of sediment accumulation in Drammensfjord, though the thickness of sediment involved appears to be much greater mostly because of its high water content; there is a substantial reduction in sediment bulk density down the boxcore, unlike the piston core section D1G7, which shows no significant change in bulk density from top to bottom [24].

Similarly, ^{210}Pb activity falls to the background level at c. 25cm depth in the boxcore, indicating an age of c. AD 1850 for this depth [25]. The general pattern is of exponential decay, as would be expected in a core which has not been bioturbated (as indicated lower in the sediment column by the undisturbed varves). However, there is some additional variability in the ^{210}Pb activity, such as the slight increase seen between 15cm and 20cm depth. It is unclear whether this is a result of distortion of the boxcore sediment during coring, or whether it is a true sedimentary signal.

Direct linkage of these chronological data from the boxcore to the varve-and-wood chronology derived earlier from the piston core D1G is not possible, because the oldest boxcore date (from the ^{210}Pb, of c. AD 1850 at c. 25cm depth) is younger than the youngest varve-and-wood date (of c. AD 1750 for the uppermost varves, at c. 15cm below the top of the piston core). However, bulk ^{210}Pb activity measured from the interval 0-7cm depth in piston core D1G is slightly above the background level [24], indicating that this upper part of the piston core is slightly younger than AD 1850. This suggests that a depth of c. 25cm in the boxcore corresponds to a depth in the

region of c. 7cm in the piston core, meaning that c. 15-20cm are missing from the top of piston core D1G.

A coherent overall chronology can, therefore, be constructed for Drammensfjord site D1 by combining the boxcore ^{137}Cs and ^{210}Pb dates with the piston core varve-and-wood chronology, although attempts to expand this into the deeper parts of the piston core material would be difficult, even with additional radiocarbon dates, because of the lack of varves.

5.3 Lake St Moritz results

5.3.1 Lake St Moritz core image mosaics

Image mosaics were prepared for Lake St Moritz core PSM90.3 in the same way as for the Drammensfjord cores. These are shown in figures 5.15.1 and 5.15.2. As before, depth increases from left to right. The printed image mosaics have a limited greyvalue range because of the half-toning effect of the printer, whereby each greyvalue is constructed from black dots, but there are two visible transitions worthy of note (further details are given in section 5.3.2). The first is in the very first core section at c. 60cm depth, where the sediment changes from pale to dark; this marks the abrupt onset of anthropogenic eutrophication in c. AD 1900. The second is the base of the Holocene, which is visible in core section 9 (second from the left in figure 5.15.2) at c. 60cm depth, where again there is an obvious change from pale to dark sediment over an interval of c. 15cm.

5.3.2 Lake St Moritz sedimentary log

The Lake St Moritz sedimentary log shown in figure 5.16 uses the stratigraphic framework devised by Ariztegui *et al.* [26], and describes and briefly interprets the lithology of each unit.

The Holocene sediment is laminated throughout; its colour varies from a pale grey-brown to black. In comparison with the Drammensfjord sediment, there are no distinct homogeneous intervals, although there are event beds, which are mostly little thicker than the laminations. These beds, which are turbidites, show up as very pale layers, paler than any components of the laminations. Upon close inspection, the laminations are not as clear as those in Drammensfjord: rather than a simple alternation of dark and pale layers, there is a more complex sequence of layers with different greyvalues. "Triplet" varves are frequent, with spring clastic sublayers, summer biogenic sublayers, and winter clayey sublayers; additional sublayers within this scheme may represent separate diatom blooms.

There is also an obvious large-scale greyvalue banding, on a scale of 10cm to several metres, part of which is the threefold division of the Holocene sequence described in [26]. Leaving the varves aside, there is clear large-scale variability, of alternating intervals of hundreds to thousands of years when predominantly dark, or predominantly light, sediment is being deposited, with this variability continuing through the Holocene. This is also apparent in the Lake St Moritz sediment greyvalue results, which are in the next section.

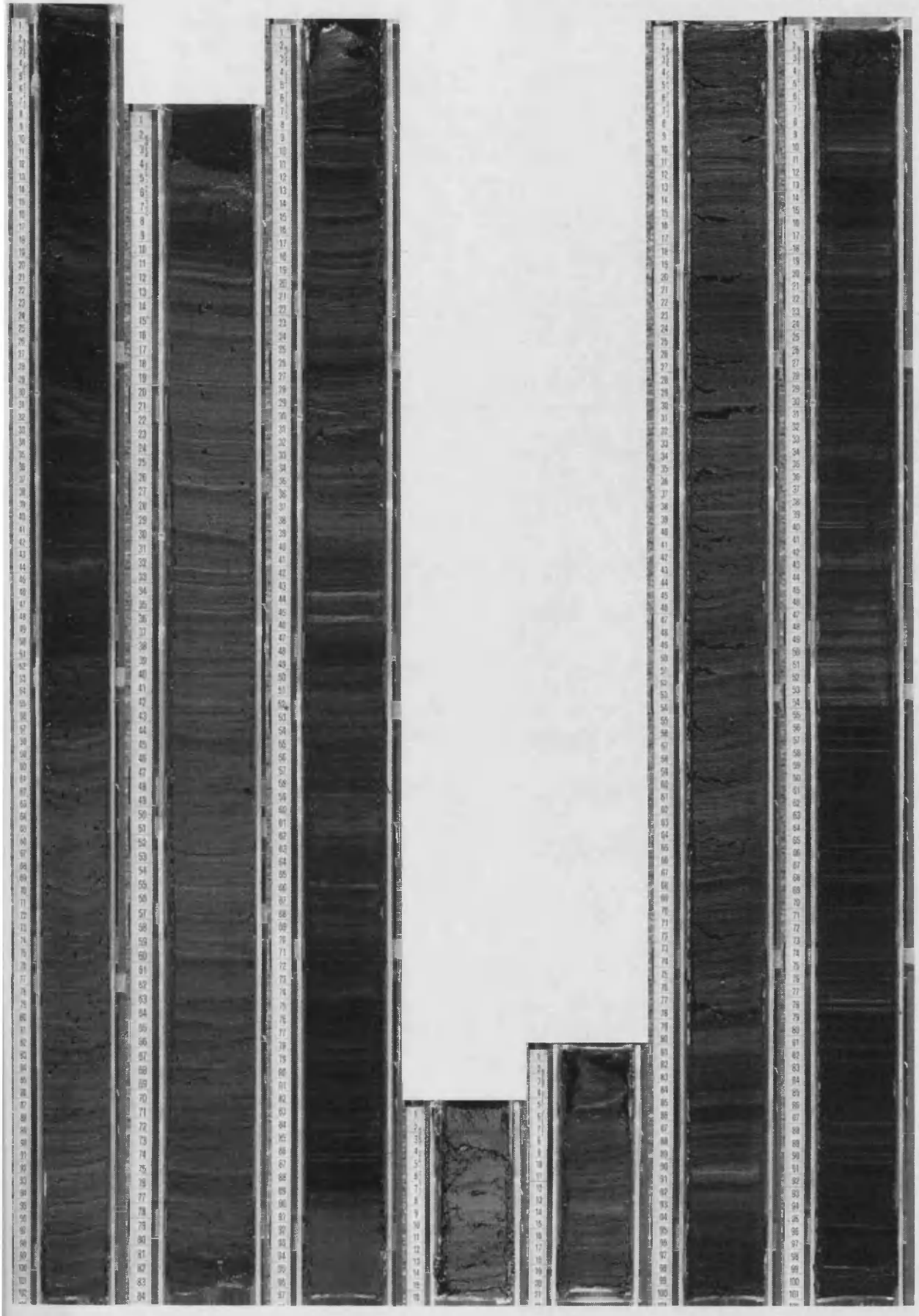

Figure 5.15.1: Core image mosaic of Lake St Moritz Core PSM90.3: L-R sections 1-7.

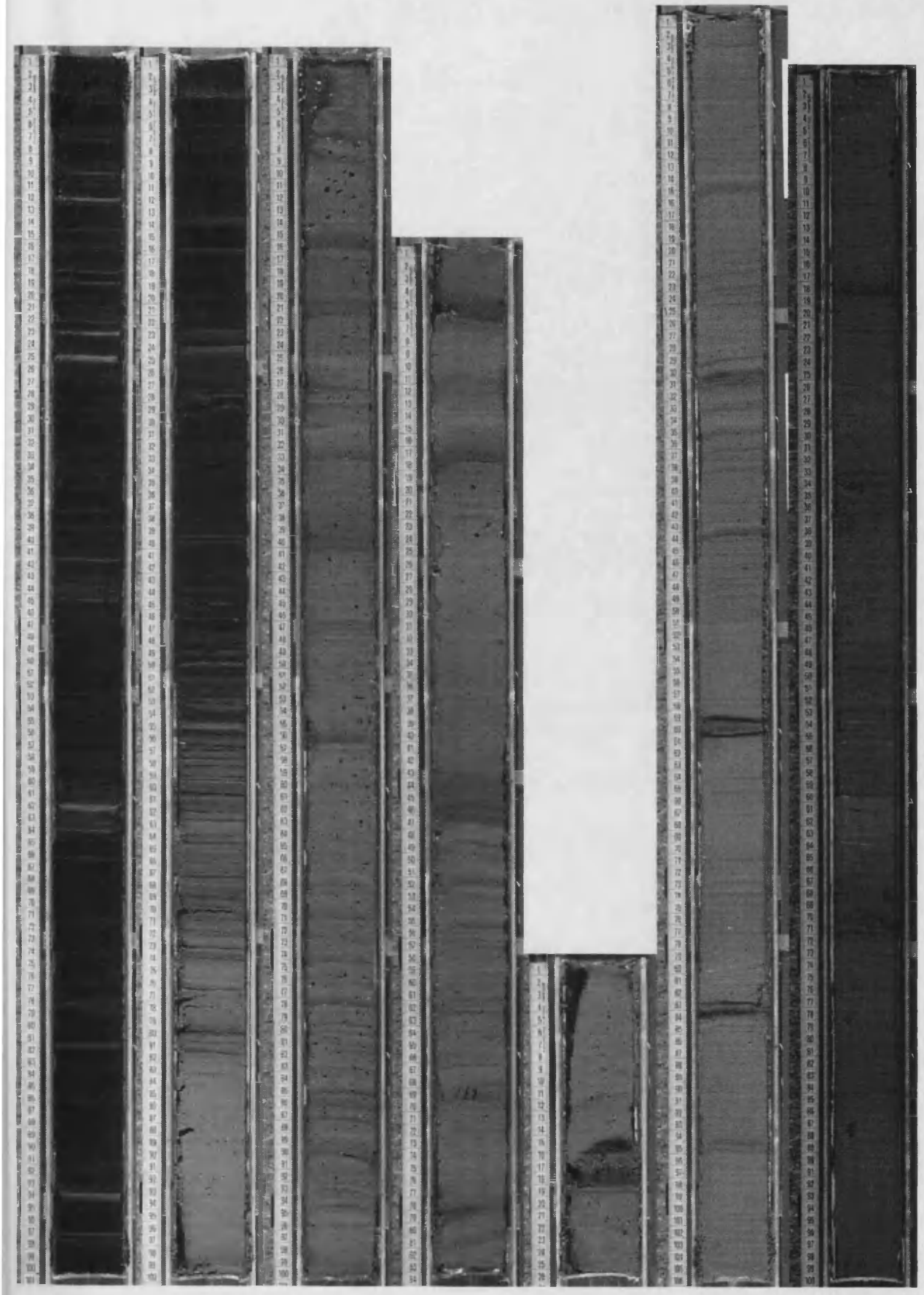

Figure 5.15.2: Core image mosaic of Lake St Moritz Core PSM90.3: L-R sections 8-14.

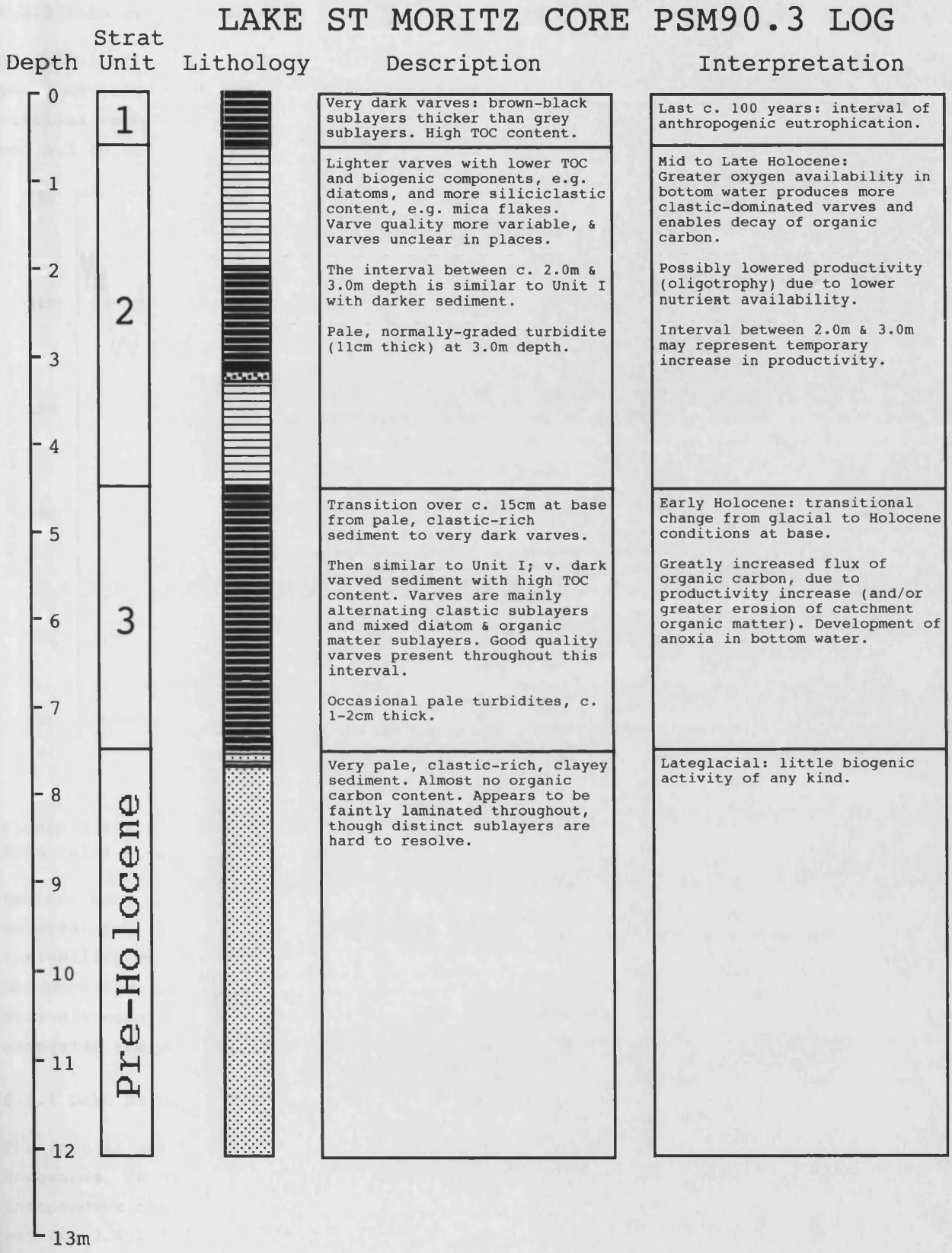

Figure 5.16: Simplified log of Lake St Moritz core PSM90.3, summarising the changes in sediment type. The interpretation section and its chronological assignations are discussed in much more detail in section 5.5 and in chapter 6, and are given for summary purposes only.

5.3.3 Lake St Moritz sediment greyvalue results

As described in section 4.5.4, whole-core-width records of sediment greyvalue were measured (after correction for uneven illumination) from the Lake St Moritz core using vertical resolutions of 3cm and 5cm. The numerical data can be found in sections B.2 and B.3 in appendix B. A summary plot of the 5cm-resolution greyvalue data is below.

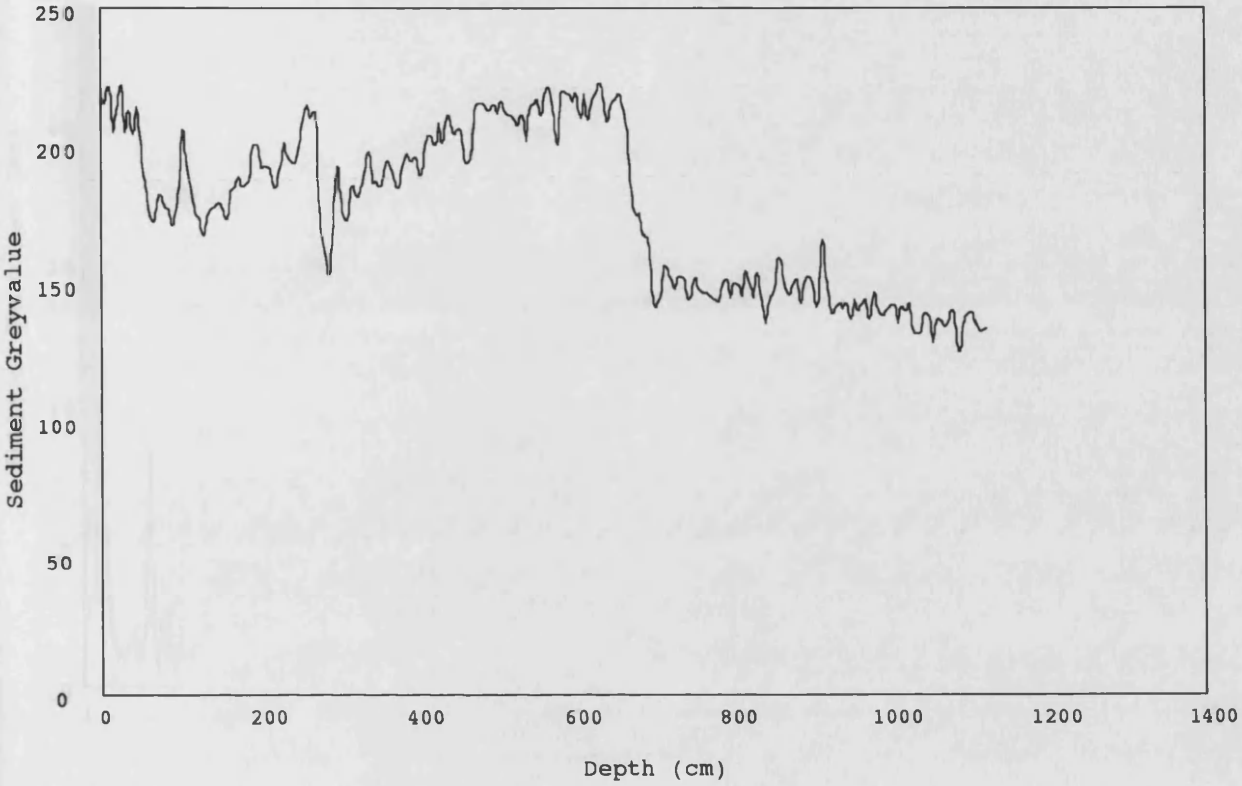

Figure 5.17: Plot showing variation of sediment greyvalue (averaged over 5cm vertical intervals) against depth for Lake St Moritz core PSM90.3.

Records were also kept of the standard deviation of sediment greyvalue in each interval for the 3cm-resolution record, in order to investigate whether greyvalue variability within each interval could be related to lithological changes. This was not possible, and the standard deviation data appeared simply to fluctuate randomly around a mean of c. 10 greyvalue units. These data are included in appendix B alongside the mean greyvalue data, for completeness.

5.3.4 Lake St Moritz varve measurement results

The initial set of varve measurements were made from the top of core PSM90.3 downwards, in order to enable a comparison between these most recent varves and the independent chronological data obtained from event beds and ^{137}Cs (as described in section 3.4). The observed anthropogenic eutrophication, and consequent anoxia of the bottom water, were also expected to have preserved good quality varves in the uppermost part of the core, and this was mostly the case. The top c. 60cm of the core contained c. 90 varves. Below this, however, varve quality decreased: the colour contrast of the varve sublayers was reduced, and the varves showed signs of disturbance, probably as a result of bioturbation. Early studies on Lake St Moritz

surface sediments note the presence of the oligochaete *Tubifex tubifex*, for example, at the start of the 20th century [27,28]. Nonetheless, varve measurement was continued down to a depth of c. 1m, producing a record of c. 239 varves in total, although the continuity of the latter part of the sequence is in doubt. The numerical data can be found in appendix B; they are summarised in the figure below.

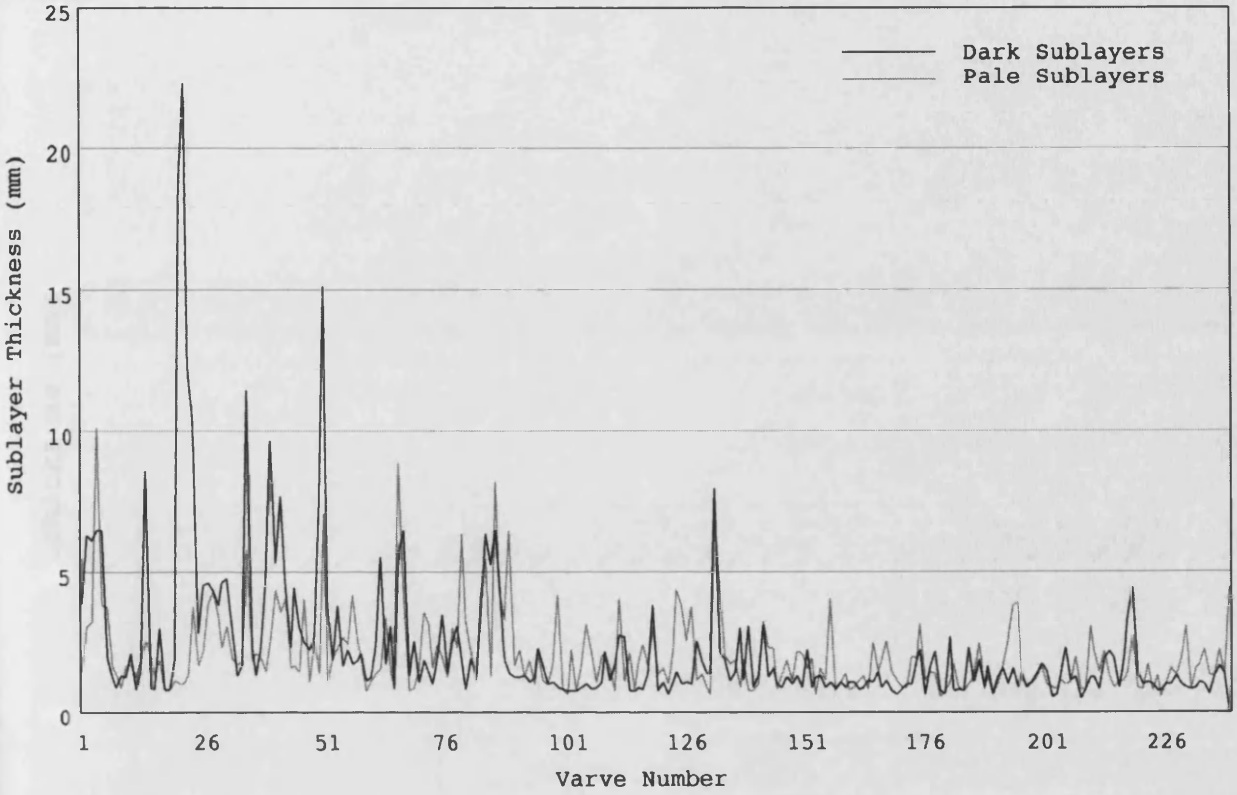

Figure 5.18: Upper sequence of Lake St Moritz varve thickness data; varve number 1 is at the top of core PSM90.3 and varve number increases with depth. The sequence is only believed to be reliable for the first c. 90 varves; the greater thicknesses of the dark sublayers in this topmost part reflects the overall dark colour of the sediment.

A further interval of varves was measured, in order to allow an older comparison with the new radiocarbon chronology (which was to be constructed from the terrestrial macrofossil dates given in section 3.4). The most recent of these dates was at 142-144cm depth in the core, so an interval was sought which was below this depth, and which contained better-quality varves than those immediately below the base of Unit I (i.e. those with varve numbers > c.90 in figure 5.18).

The interval selected was c. 200-275cm depth in Unit II, which was visually similar to Unit I, in that the sediment was noticeably dark and the varves apparently well-preserved. The measurement was done before the new chronology was constructed, in order to avoid introducing any biases. Overall varve thickness was the only variable measured, from top-of-black-sublayer to top-of-black-sublayer, to reduce inhonogeneities arising from the presence of multiple sublayers (see section 4.5.3) and in the knowledge that a continuous record of sediment greyvalue already existed (see section 5.3.3). The data are summarised in figure 5.19. Three turbidites, identifiable by their anomalous thicknesses (22mm, 4mm, and 6mm) and by their

distinctive pale grey colour, have been deleted from this sequence in order to improve its stationarity. They are identified as such within the original numerical data, which can be found in appendix B. The varves within this core interval are noticeably thinner than those in the topmost part of the core, presumably as a result of compaction. Comparative images showing the differing varved fabrics within the measured intervals are shown in figure 5.20.

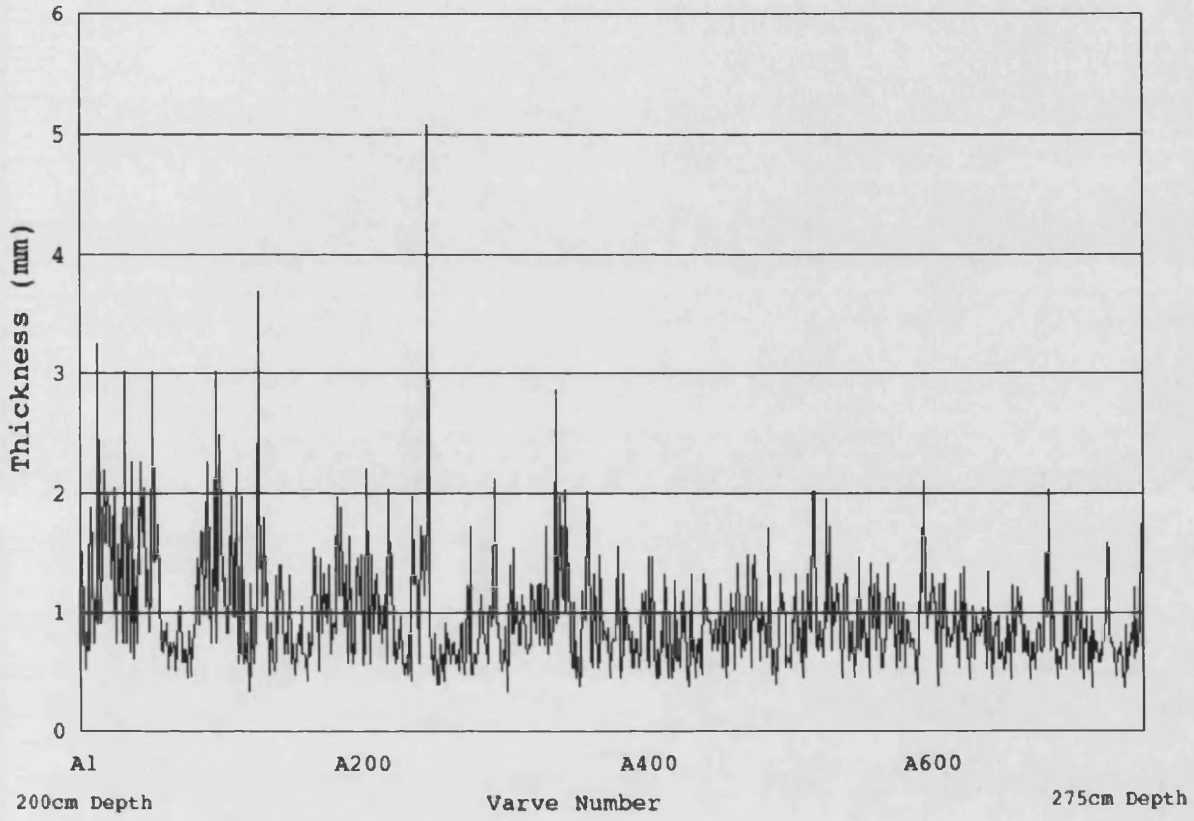

Figure 5.19: Overall varve thickness for the 745 varves measured within the interval c. 200-275cm depth in Lake St Moritz core PSM90.3. This interval begins just above an 11cm-thick turbidite (below which it seems reasonable to expect possible erosion of varves) and ends just below a noticeable deterioration in the quality of the varves. Varves are numbered from the top downwards, thus: A1, A2, etc, in order to avoid any confusion with the more recent varve sequence described earlier. As before, these are just identifiers, and are not intended to represent any chronological information.

5.3.5 Lake St Moritz integrated core chronology

As described in section 3.4, chronological data for the uppermost part of the Lake St Moritz sediment sequence are available from ^{137}Cs activity [29] and from two event beds [30] measured in a parallel short core. ^{137}Cs activity peaks at 1cm, 15cm, and 19cm depth, corresponding to 1986, 1963, and 1954, respectively. The two event beds described by Züllig [30] occur at depths of 11cm and 58cm, corresponding to 1969 and 1911-14 respectively. From inspection, these beds are believed to be located in core PSM90.3 at respective depths of 12.3cm (varve number 21) and 56.5cm (varve number 87), as indicated in section B.3.1 in appendix B. The uppermost varves, ^{137}Cs data and event beds can then be integrated as shown in figure 5.21.

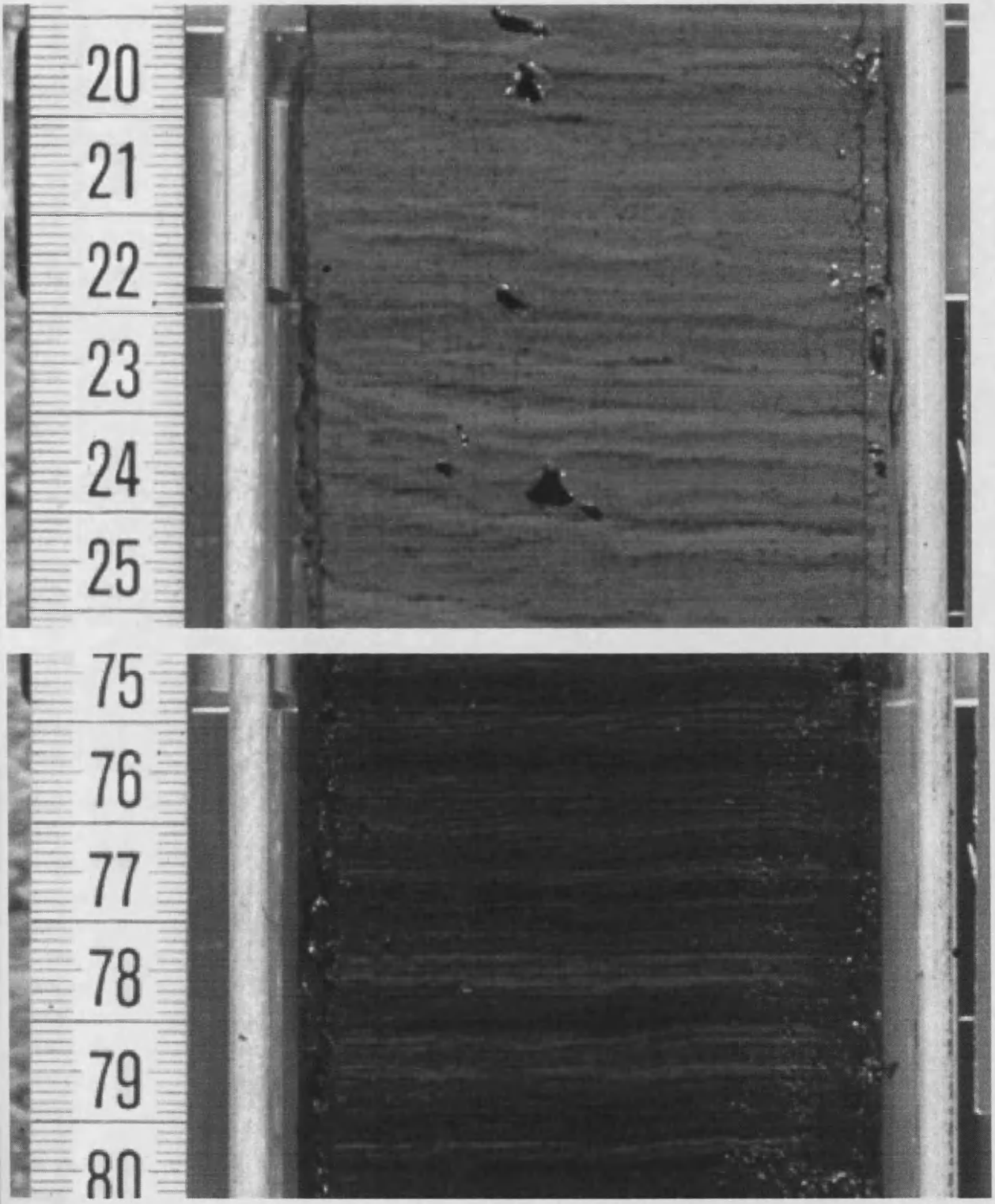

Figure 5.20: Images illustrating the variation in the Lake St Moritz varves. At the top are varves from the pale upper part of Unit II (c. 122-127cm depth) which are difficult to trace laterally. At the bottom, shown at the same scale, are varves from the darker interval of Unit II (c. 261-266cm depth) which form part of the second, deeper sequence of varves measured above. These are darker, thinner, and laterally flat and continuous. This image contains c. 55 varves, corresponding to c. A584-A639 in figure 5.19. The printed output is of a much lower quality than the original high-resolution digital images.

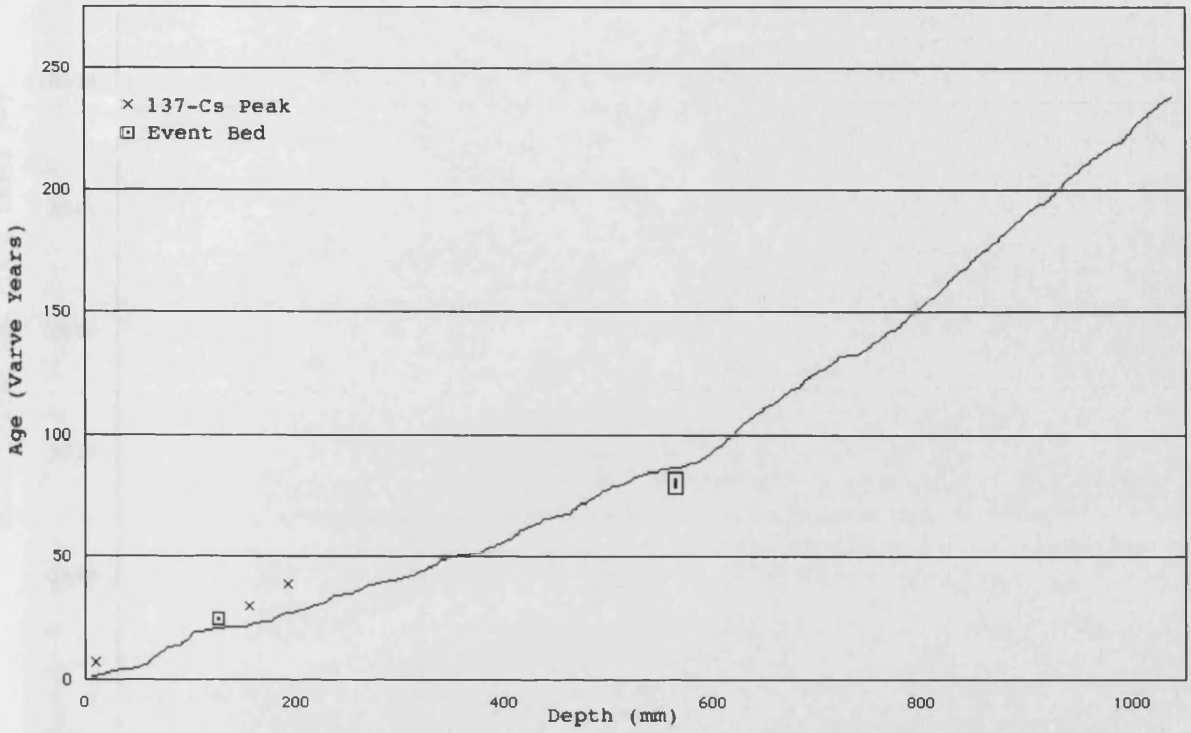

Figure 5.21: Combined age-depth data for the uppermost part of core PSM90.3. The solid line is the age-depth curve derived from the varve thickness data, on the assumption that the varve sequence is continuous from AD 1993 backwards, and that each varve represents one year. The crosses and boxes represent ^{137}Cs dates and event bed dates respectively, plotted on the assumption that varve years are equal to calendar years.

There is a good agreement amongst the three sources of chronological data in figure 5.21, notwithstanding minor disagreement at the very top of the core which may have arisen because the varves in this topmost section are not very clear. This suggests that the assumptions made are valid, and that the varve sequence is continuous, at least within the top 60cm. Below this, as noted earlier, varve quality decreases, but in the absence of any other chronological information these earlier varves are also assumed to form a continuous, annual sequence. The uncalibrated radiocarbon dates given in [29] and derived from bulk sediment from this core have not been included in this comparison; they suggest ages that are significantly older than the above curve, most probably as a result of contamination with older carbon from reworked soils and sediments [31].

The radiocarbon dates taken from terrigenous plant macrofossils in core PSM90.3 by Gobet *et al.* [32] should not suffer from this contamination since the ^{14}C content of living plant tissue is in equilibrium with the atmosphere at the time of growth. However, these dates require calibration, via tree-rings, in order to produce a calendar-year chronology for the core. This chronology will then suggest an absolute age for the deeper varve sequence measured from the core (described in section 5.3.4), and will enable conversion of the sediment greyvalue data described in section 5.3.3 from a depth-series into an evenly-sampled time-series. The uncalibrated dates are plotted in figure 5.22.

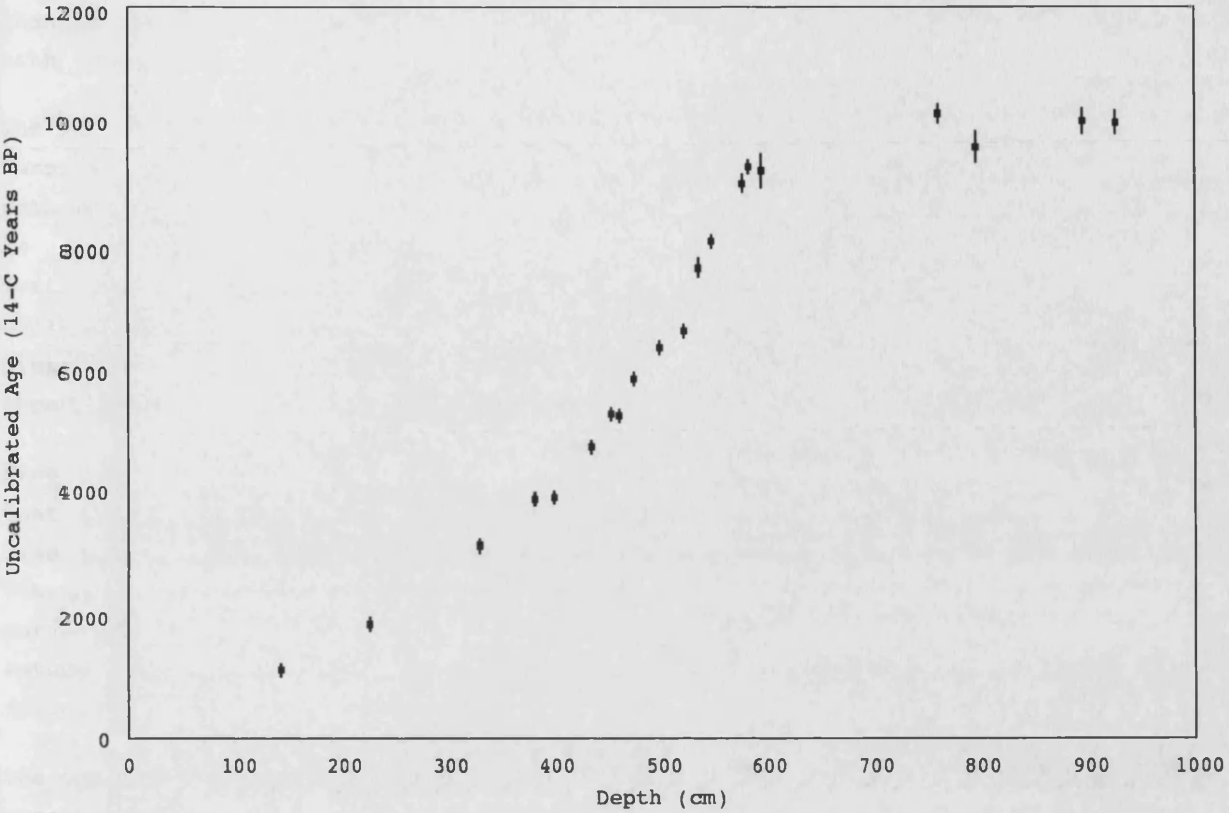

Figure 5.22: Uncalibrated age-depth plot for Lake St Moritz core PSM90.3, based on 20 dates from terrigenous plant macrofossils obtained by Gobet *et al.* [32]. Errors are plotted as vertical bars. Code numbers, numerical data, and source materials are given in section 3.4.

There is a clear "plateau" in the uncalibrated dates beyond c. 600cm depth. Considering both figure 5.22 and the core lithology (see figure 5.16), the base of the Holocene in this core occurs at c. 750cm depth, such that the oldest four dates in the figure above are from glacial sediment. For the Holocene dates alone, however, the orderly increase in ^{14}C-year age with depth indicates that the uncalibrated dates are sound, and that calibration of these dates is worthwhile.

The calibration process is more complex than that for the Drammensfjord material, since here the aim is to produce an entire *core chronology* rather than just to date isolated *events*. The complexity arises because of the multiple variables involved. Even for a single radiocarbon date, multiple possible calibrated ages can arise from the combination of the known error in the radiocarbon count and wiggles in the calibration curve, as found for the younger Drammensfjord radiocarbon date, for example. Many possible age-depth curves therefore exist for any set of calibrated radiocarbon ages.

In the context of a core chronology, it is reasonable that the other ages will affect what is considered to be the most probable calendar age for an "ambiguous" result [33] - in other words, there is a prior expectation (at least with material such as the well-preserved pine needles that form the basis of the Lake St Moritz chronology) that the "true" calendar chronology is at least in stratigraphic order, and notwithstanding

changes in sediment accumulation rate, that it should show a smooth increase of age with depth.

The 20 radiocarbon ages plotted in figure 5.22 were calibrated using the program CALIB version 4.4 [34] together with the calibration curve INTCAL98 [21]. The intercept method was not used, since although it is simple, the resulting single point estimate is not stable with respect to small changes in the counting statistics [35]; furthermore, it may unintentionally underplay the possible variability of the calibrated age. Instead, as for the Drammensfjord results, full probability distributions were calculated for each date; these data can be found in section B.4 in appendix B.

Even then, because these are 2σ distributions (that is, c. 95% probability), and given that there are 20 dates, it would not be unexpected for an accurate age-depth curve to miss one of the intervals entirely, or even more than one of them. As above, the "most likely" statistical values should be traded off against the most likely age-depth curve on geological criteria, such as smooth changes in sediment accumulation rate rather than straightforward linear interpolation. There is no agreed standard definition of the most parsimonious age-depth model [35,36].

The chosen age-depth model, shown in figure 5.23, was derived from range mid-point weighted averages of the 2σ probability distributions, producing more stable central-point estimates, as suggested by Telford *et al.* [35]. These were calculated to the nearest 10 years, as recommended by [34], bearing in mind the errors of ≥ 50 years on the original uncalibrated dates. These data are also given in section B.4 in appendix B. They were then approximated by a sixth-order polynomial curve over the interval 100cm to 750cm depth, augmented by the varve data in the interval 0-100cm. It is helpful that for this core, at least, the relatively smooth increase of the Holocene part of the age-depth data means that the final age-depth curve is not particularly sensitive to the precise model chosen.

The deeper varve data measured from core PSM90.3, those plotted in figure 5.19, were *not* used in construction of the age-depth model, in order to allow independent comparison of the implied ages of the interval c. 200-275cm depth. 745 varves were measured from this interval; according to the smoothed radiocarbon-derived curve (given with the sediment greyvalue data in appendix B), this interval represents c. 1,571-2,398 BP, that is, c. 827 calendar years. This agreement is close enough to justify using the varves as an annual-resolution time-series, and they are analysed as such in chapter 6.

The pre-Holocene dates are more problematic, especially the anomalously young date of c. 10,937 cal BP at c. 797 cm depth. Extension of the age-depth curve beyond the base of the Holocene has not been attempted; there is good reason to expect major changes in sediment accumulation rate to have occurred during the last glacial-to-interglacial transition [37], and in any case, this time interval is beyond the scope of this thesis.

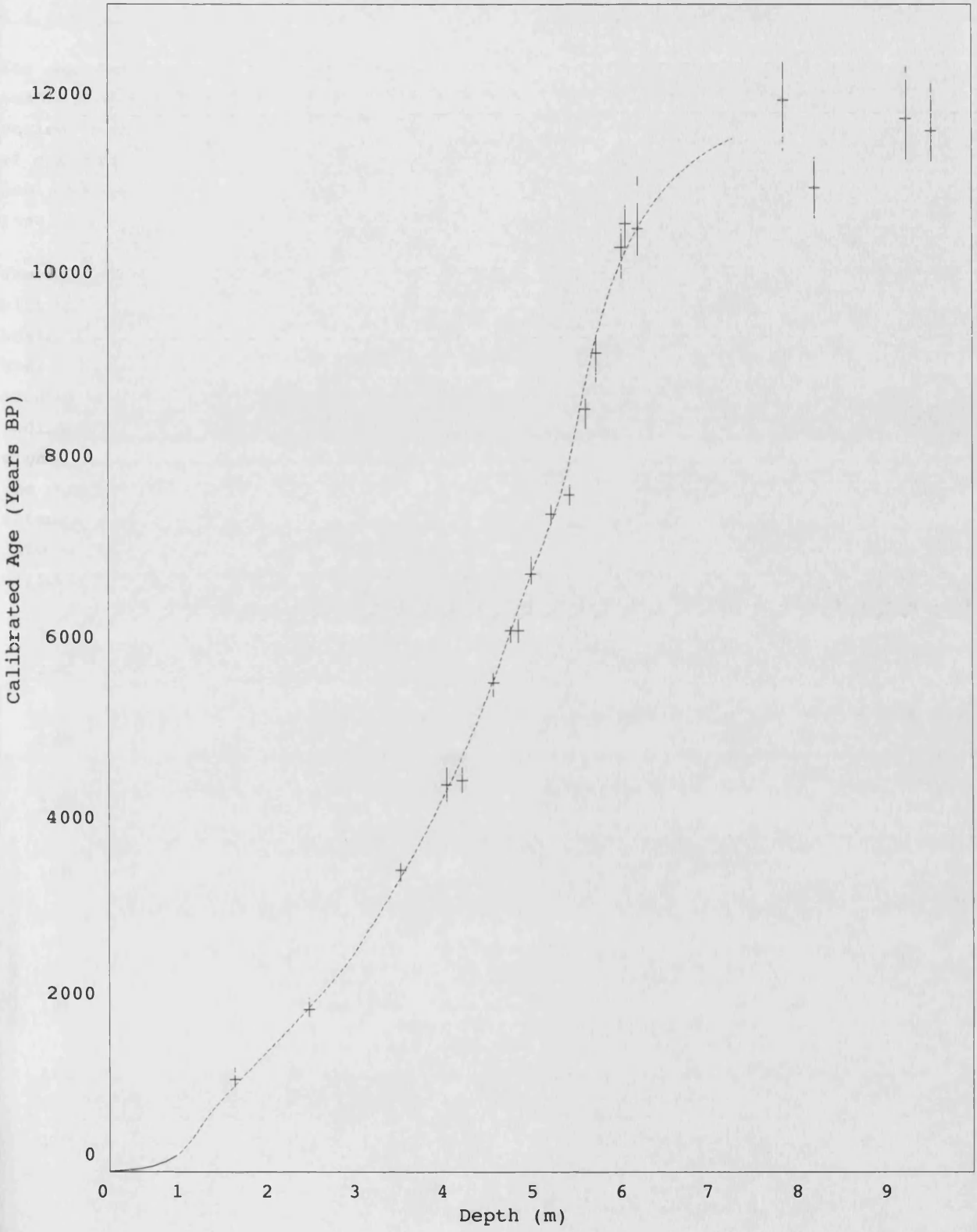

Figure 5.23: Smoothed age-depth curve, based on calibrated radiocarbon dates and varve data, for Lake St Moritz core PSM90.3. The vertical lines indicate the 2σ range for each calibrated date; the horizontal line in each case is the weighted average. The solid line close to the origin is the age-depth curve derived from the varve counts (see figure 5.21).

5.3.6 Conversion of sediment greyvalue data from depth-series to time-series

The age-depth model constructed in the previous section was used to convert the 3cm-resolution sediment greyvalue depth-series described in section 5.3.3 into a time-series with a constant sampling interval of c. 30 years, suitable for the application of spectral analysis. This was done by resampling the data, using the program AnalySeries [38]. The numerical data and the ages used are given in appendix B; the resulting time-series is plotted below.

The difference between figures 5.17 and 5.24 is noteworthy; the same information is plotted in each case, but significant modifications are necessary to the horizontal scale in order to represent the data as a time-series rather than as a depth-series. These arise from changes in sediment accumulation rate. The most significant of these occurs at c. 200-300 cal yr BP, and is presumably anthropogenic, caused by increased sediment discharge resulting from forest clearance and other land-use changes. Further significant changes probably occurred during the end of the last glacial [37], though the difficulty in extending the age-depth model to cover this interval meant that no attempt could be made to convert the very pale, glacial sediment "tail" of figure 5.17 into a time-series. Figure 5.24 extends back to the start of the Holocene, at c. 11,500 cal yr BP.

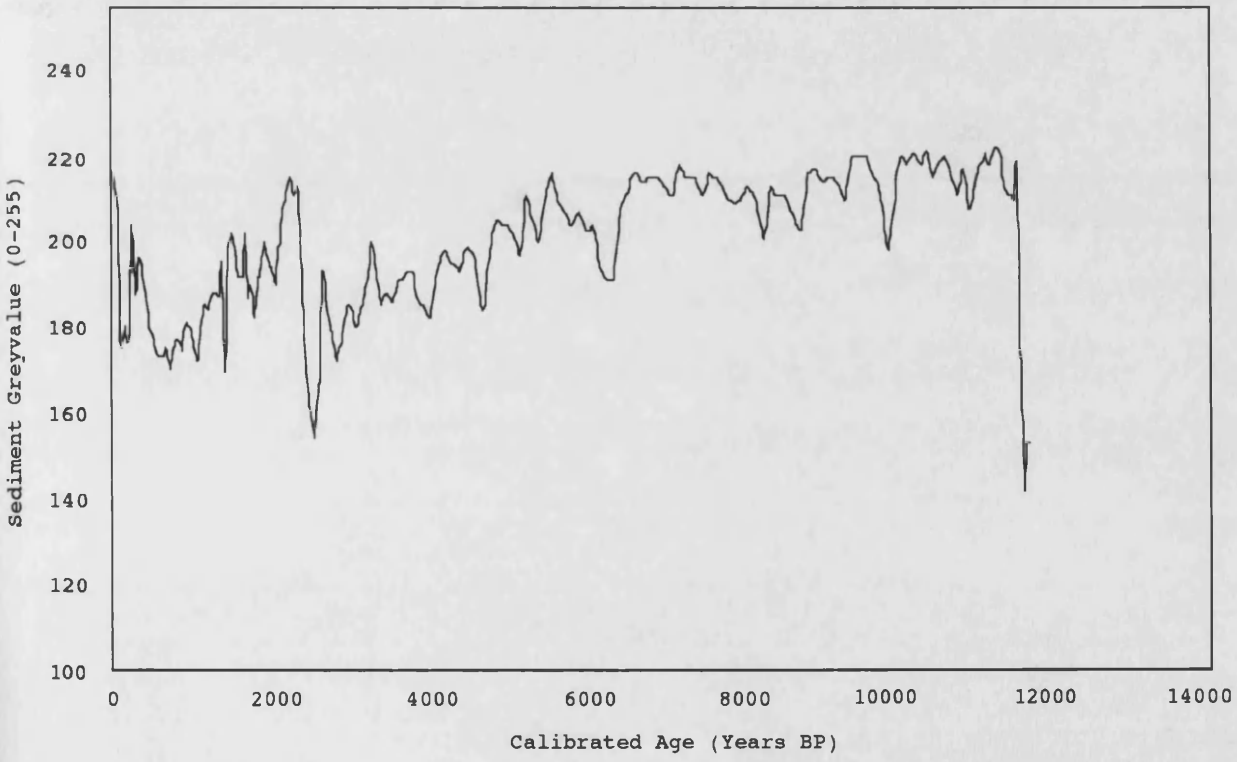

Figure 5.24: Sediment greyvalue data from Lake St Moritz core PSM90.3 plotted as an time-series with a sampling interval of c. 30 years.

Resampling can introduce serious bias into time-series data, and to avoid this, spectral analysis of unevenly-sampled data can be carried out without modification, using the Lomb-Scargle periodogram [39,40] or another suitable technique [e.g. 41]. However, a judgment needs to be made as to whether the additional complexity of these

methods (such as the loss of the connection between spectrum and autocorrelation function) is justified by the degree of clustering in the time-series. For most deep-sea sediment records, for example, the relationship between depth and time is almost uniform, such that the bias introduced by resampling is small [42]. This argument also applies to the Lake St Moritz record, since prior to c. 2,000 cal yr BP the age-depth curve is almost linear (see figure 5.23). So, most of the data were left unchanged, and those that were changed are mostly in the interval where the record is vulnerable to anthropogenic interference anyway, and so may need to be modified if climatic signals are to be sought. Nonetheless, it is important to consider the potential biases introduced by resampling [43].

Resampling creates new data points by interpolating between existing ones. So, it makes the spectrum ordinates no longer independent, i.e. it increases the bandwidth of the spectrum. It also smoothes the original data, being equivalent to a low-pass filter, and thereby serves to "redden" the spectrum. The degree to which this reddening occurs depends both on the degree of irregularity in the time-sampling, and the method of interpolation used. For example, using cubic splines results in less bias than using linear interpolation [42]. The latter was used for the Lake St Moritz data, for simplicity, since the increase in bias was slight. The important point is that the spectrum is *a priori* suspected to be slightly redder than its true shape: the shape that would have been produced by even time-sampling to start with.

Chapter 5 References

[1] Schaaf, M., and Thurow, J., 1994, A fast and easy method to derive highest-resolution time-series datasets from drillcores and rock samples, Sedimentary Geology, 94:1-10.

[2] Alve, E., 1991, Foraminifera, climatic change, and pollution: a study of late Holocene sediments in Drammensfjord, southeast Norway, Holocene, 1:243-261.

[3] Smith, J. N., and Walton, A., 1980, Sediment accumulation rates and geochronologies measured in the Saguenay Fjord using the Pb-210 dating method, Geochimica et Cosmochimica Acta, 44:225-240.

[4] Brodie, I., and Kemp, A., 1994, Variation in biogenic and detrital fluxes and formation of laminae in late Quaternary sediments from the Peruvian coastal upwelling zone, Marine Geology, 116:385-398.

[5] Von Rad, U., Schulz, H., Riech, V., den Dulk, M., Berner, U., and Sirocko, F., 1999, Multiple monsoon-controlled breakdown of oxygen-minimum conditions during the past 30,000 years documented in laminated sediments off Pakistan, Palaeogeography Palaeoclimatology Palaeoecology, 152:129-161.

[6] Holtedahl, H., 1965, Recent turbidites in the Hardangerfjord, Norway, Colston Research Society Proceedings, University of Bristol, 17:107-141.

[7] Smith, J. N., Schafer, C. T., and Loring, D. H., 1979, Depositional processes in an anoxic, high sedimentation regime, in the Saguenay Fjord, in: Freeland, H. J., Farmer, D. M., and Levings, C. D., (Eds.), Fjord Oceanography, NATO Conference Series IV: Marine Sciences, p. 625-631.

[8] McCartney, K., 1995, Silicoflagellates, In: Blome, C. D., Whalen, P. M., and Reed, K. M., (Eds.), Siliceous Microfossils, Short Courses in Paleontology, No. 8, p. 159-176.

[9] Wassmann, P., 1983, Sedimentation of organic and inorganic particulate material in Lindåspollene, a stratified, land-locked fjord in western Norway, Marine Ecology Progress Series, 13:237-248.

[10] Tomas, C. R., (Ed.), 1996, Identifying Marine Diatoms and Dinoflagellates, Academic Press, 598 pp.

[11] Braarud, T., Foyn, B., and Hasle, G. R., 1958, The marine and freshwater phytoplankton of the Dramsfjord and the adjacent part of the Oslofjord March - December 1951, Hvalrådets Skrifter, v. 43, 102 pp.

[12] Battarbee, R. W., and Kneen, M. J., 1982, The use of electronically counted microspheres in absolute diatom analysis, Limnology and Oceanography, 27:184-188.

[13] Watkins, N. D., 1971, The reinforcement syndrome, Comments on Earth Sciences - Geophysics, 2:36-43.

[14] R. B. Pearce, personal communication, May 2002.

[15] Paetzel, M., Schrader, H., and Croudace, I., 1994, Sewage history in the anoxic sediments of the fjord Nordåsvannet, western Norway: (1) Dating and trace-metal accumulation, The Holocene, 4:290-298.

[16] Skei, J., 1983, Geochemical and sedimentological considerations of a permanently anoxic fjord: Framvaren, South Norway, Sedimentary Geology, 36:131-145.

[17] Smith, J. N., and Schafer, C. T., 1987, A 20th-Century record of climatologically modulated sediment accumulation rates in a Canadian fjord, Quaternary Research, 27:232-247.

[18] Strøm, K. M., 1936, Land-locked waters, Skrifter utgitt av det Norske Vitenskaps-akademi i Oslo, 1, Matematisk-naturvidenskapelige klasse 1, no. 7, p. 1-85.

[19] Turney, C. S. M., Coope, G. R., Harkness, D. D., Lowe, J. J., and Walker, M. J. C., 2000, Implications for the dating of Wisconsinan (Weichselian) Lateglacial events of systematic radiocarbon age differences between terrestrial plant macrofossils from a site in SW Ireland, Quaternary Research, 53:114-121.

[20] Mook, W. G., 1986, Recommendations / resolutions adopted by the Twelfth International Radiocarbon Conference, Radiocarbon, 28:799.

[21] Stuiver, M., Reimer, P. J., Bard, E., Beck, J. W., Burr, G. S., Hughen, K. A., Kromer, B., McCormac, G., van der Plicht, J., and Spurk, M., 1998, INTCAL98 radiocarbon age calibration, 24,000 - 0 cal BP, Radiocarbon, 40:1,041-1,083.

[22] Lowe, J. J., and Walker, M. J. C., 1997, Reconstructing Quaternary Environments, Second Edition, Longman, 446 pp.

[23] Schouten, S., Hopmans, E. C., Pancost, R. D., and Sinninghe Damste, J. S., 2000, Widespread occurrence of structurally diverse tetraether membrane lipids: evidence for the ubiquitous presence of low-temperature relatives of hyperthermophiles, Proceedings of the National Academy of Sciences of the USA, 97:14,421-14,426.

[24] Rienk Smittenberg, personal communication, April 2002.

[25] Appleby, P. G., Oldfield, F., Thompson, R., Huttunen, P., and Tolonen, K., 1979, ^{210}Pb dating of annually laminated lake sediments from Finland, Nature, 280:53-55.

[26] Ariztegui, D., Farrimond, P., and McKenzie, J. A., 1996, Compositional variations in sedimentary lacustrine organic matter and their implications for high Alpine Holocene environmental changes: Lake St Moritz, Switzerland, Organic Geochemistry, 24:453-461.

[27] Bonner, R. A., 1922, Die Bodenfauna des St Mortizer Sees, Archives Hydrobiologie, 13:1-99.

[28] Schmassman, W., and Schmassman, H. J., 1948, Chemische Untersuchungen im St Moritzersee, Swiss Journal of Hydrology, 10:21-35.

[29] Ariztegui, D. R., 1993, Palaeoenvironmental and palaeoclimatic implications of sedimented organic matter variations in lacustrine systems: Lake St Moritz, a case study, PhD Thesis (unpublished), ETH-Zürich, Switzerland, Nr. 10225, 188 pp.

[30] Züllig, H., 1982, Die Entwicklung von St Moritz zum Kurort in Spiegel der Sedimente des St Moritzersees, Wasser, Energie, Luft, 74:177-83.

[31] Oldfield, F., Crooks, P., Harkness, D., and Petterson, G., 1997, AMS radiocarbon dating of organic fractions from varved lake sediments: an empirical test of reliability, Journal of Paleolimnology, 18:87-91.

[32] Gobet, E., Tinner, W., Hochuli, P. A., Van Leeuwen, J. F. N., and Ammann, B., 2003, Middle to Late Holocene vegetation history of the Upper Engadine (Swiss Alps): the role of man and fire, Vegetation History and Archaeobotany, 12:143-163.

[33] Biasi, G. P., and Weldon, R., 1993, Quantitative refinement of calibrated ^{14}C distributions, Quaternary Research, 41:1-18.

[34] Stuiver, M., and Reimer, P. J., 1993, Extended 14C database and revised CALIB radiocarbon calibration program, Radiocarbon, 35:215-230. CALIB v. 4.4 is available at http://radiocarbon.pa.qub.ac.uk/calib/.

[35] Telford, R. J., Heegaard, E., and Birks, H. J. B., 2004, The intercept is a poor estimate of a calibrated radiocarbon age, The Holocene, 14:296-298.

[36] Bennett, K. D., 1994, Confidence intervals for age estimates and deposition times in late-Quaternary sediment sequences, The Holocene, 4:337-348.

[37] Ariztegui, D., personal communication, May 2002.

[38] Paillard, D., Labeyrie, L., and Yiou, P., 1996, Macintosh program performs time-series analysis, Eos, Transactions of the American Geophysical Union, 77:379, and available online at http://www.agu.org/eos_elec/96097e.html.

[39] Scargle, J. D., 1982, Studies in astronomical time-series: II. Statistical aspects of spectral analysis of unevenly-sampled data, Astrophysical Journal, 263:835-853.

[40] Lomb, N. R., 1976, Least-squares frequency analysis of unequally-spaced data, Astrophysics and Space Science, 39:447-462.

[41] Wilcox, J. Z., and Wilcox, T. J., 1995, Algorithm for extraction of periodic signals from sparse, irregularly-sampled data, Astronomy and Astrophysics Supplement, 112:395.

[42] Schulz, M., and Stattegger, K., 1997, SPECTRUM: Spectral analysis of unevenly-spaced paleoclimatic time-series, Computers and Geosciences, 23:929-945.

[43] Horne, J. H., and Baliunas, S. L., 1986, A prescription for period analysis of unevenly-sampled time-series, Astrophysical Journal, 302:757-763.

Chapter 6: Interpretation

6.1 Interpretation of the Drammensfjord results

6.1.1 Varve preservation and the onset of anoxia

Below c. 92cm depth in Drammensfjord core D1G, there are no well-preserved varves. There are, however, intervals containing faint and/or disturbed laminations, in addition to the homogeneous grey mud (see figure 5.2 for a lithological log of core D1G). Presumably the gradual depletion of oxygen in Drammensfjord, owing to the shallowing sill restricting circulation (see section 2.12.3), has caused this change in lithology from homogeneous mud deep in the core, to "semi-laminated" mud at c. 220cm depth, then to well-preserved laminations at 92cm depth. Similar progressions occur in other silled fjords at various times during the Holocene: anoxia in Sulafjord, western Norway, began in c. 2,700 BP [1], for example, whereas in Havstens Fjord and Koljö Fjord, in Sweden, it only began within the last two centuries [2].

If the first appearance of well-preserved laminations coincides with the onset of total anoxia, then this occurred at c. AD 1000 in the deepest part of Drammensfjord. Alve [3] gives a date of c. AD 1375 for the onset of anoxia in Drammensfjord at depths shallower than 70m, which concurs with the D1G estimate, since anoxia would have initially developed in the deepest part of the fjord and then spread to shallower depths. However, there is also an interval of well-preserved varves, c. 30cm thick in total, at the very bottom (8m depth) of core D1M. This is not found in the other two cores from site D1, but this may be because they were just not long enough to reach it. This is interesting because it suggests that anoxia may have temporarily been established in Drammensfjord much earlier than AD 1000.

No precise age can be given for these varves, because of the lack of radiocarbon dates; nor can they be counted and measured properly, because they are distorted by synsedimentary faulting; immediately above them is a thick sandy event bed whose rapid deposition presumably caused the faulting (see figure 6.1). Nonetheless, they suggest that there are additional varves present deeper in the Drammensfjord sediment record, which could be recovered by deeper coring. Undisturbed intervals of these very early varves could provide a valuable counterpoint to the more recent varves to which this section of the thesis is restricted.

The remainder of the interpretation concentrates on the varve record obtained from core D1G, especially the 712-varve sequence between the two radiocarbon dates and the information it contains as an evenly-sampled time-series.

6.1.2 The varve thickness and sediment greyvalue time-series

From the c. 900 varves in core D1G, four time-series were obtained: of thickness for both grey and black sublayers, and of mean greyvalue for both grey and black sublayers. These are plotted in chapter 5, in figure 5.11. As expected, there is no correlation between the thicknesses of adjacent grey sublayers and black sublayers, since the controlling factors on their thicknesses are unrelated.

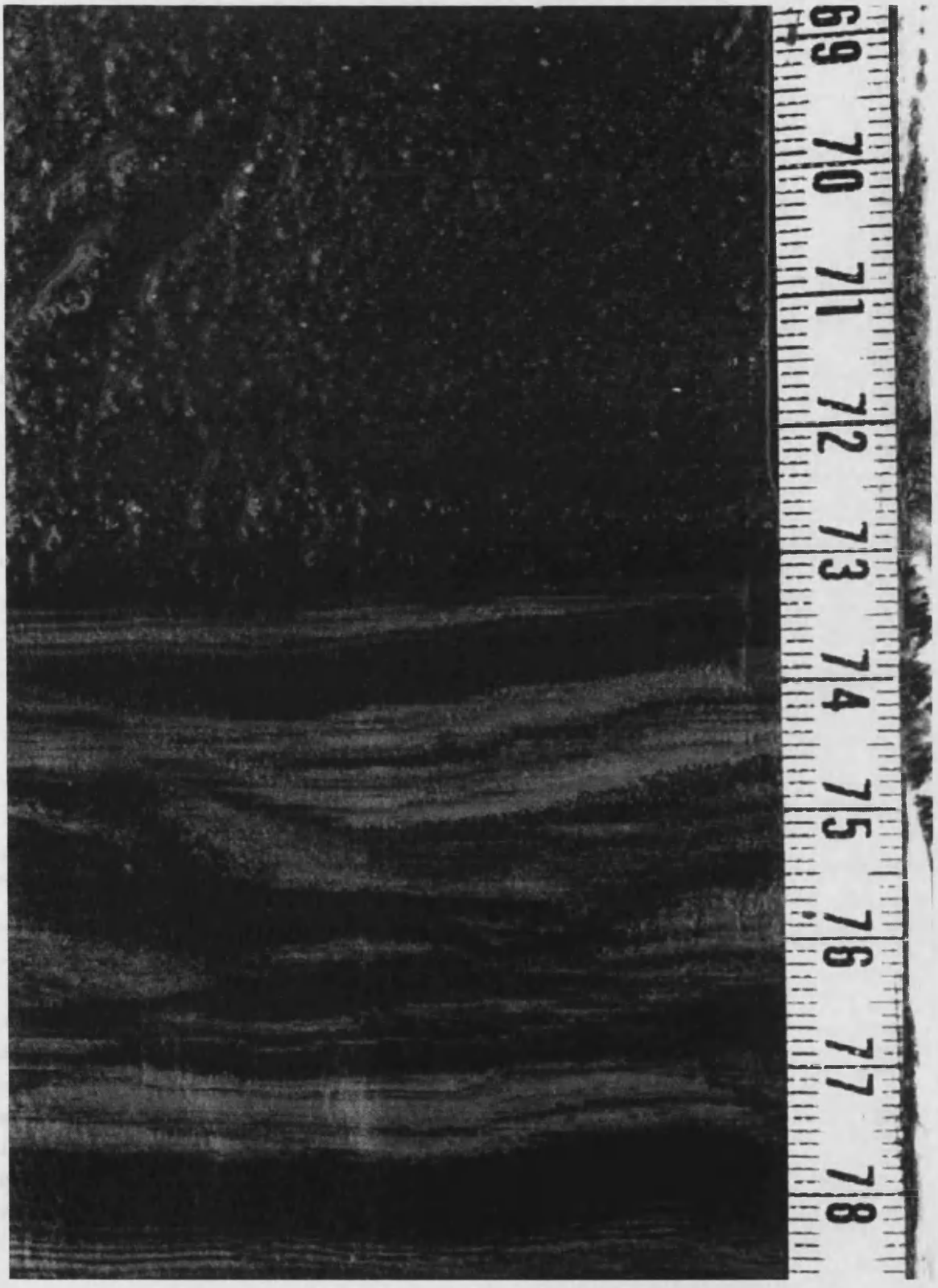

Figure 6.1: Synsedimentary faulting in varves at c. 8m depth in core D1M; above the varves is a thick sand bed.

A scatter plot of these two variables was distorted by the presence of a few very thick sublayers; to generate the plot that follows in figure 6.2, all sublayers thicker than 100 pixels (c. 6mm) were removed. The resulting plot, which is still statistically representative of the varve population, shows no correlation: the line-of-best-fit has an r^2 value of only 0.06.

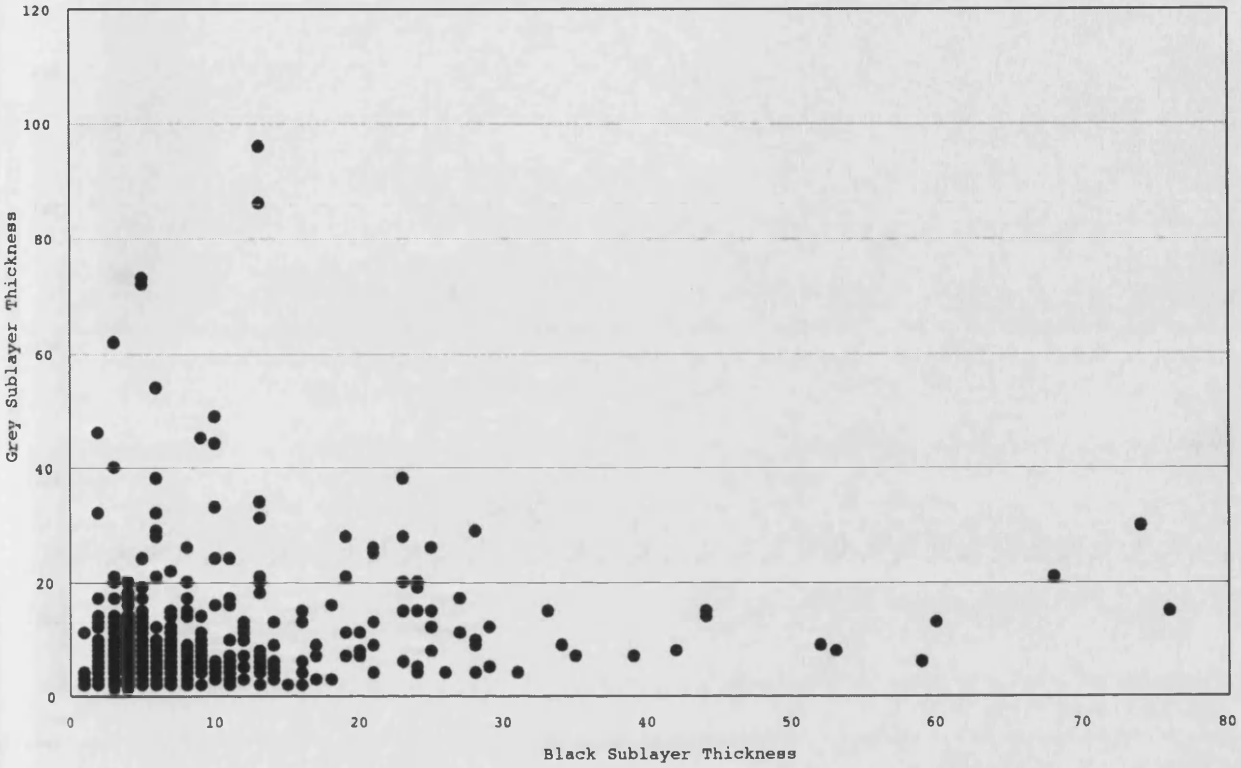

Figure 6.2: Scatter plot showing no correlation between black sublayer and grey sublayer thicknesses. Sublayer thickness is plotted in pixels; 14.1 pixels = 1mm.

Similarly, there is no correlation between the thickness of a given sublayer and its mean greyvalue, either for black or grey sublayers. Scatter plots for both are shown in figure 6.3; r^2 values are 0.03 and 0.004 respectively. This non-correlation can be explained by plotting the greyvalue of a black sublayer against the greyvalue of its accompanying grey sublayer: here, there is a significant correlation, with $r^2 = 0.5076$ (see figure 6.4). This suggests that the dominant control on sediment greyvalue in the Drammensfjord images, at greater length-scales than the varves themselves, is the *illumination of the sediment surface*, not the sediment composition. This is to be expected, since (in comparison with the Lake St Moritz images) the Drammensfjord photography was carried out under fluctuating lighting conditions, which were difficult to correct for (see figure 4.10).

The scatter plot in figure 6.4 is bounded at the top by the line y = x, i.e. the situation where the greyvalue of a black sublayer is equal to the greyvalue of the adjacent grey sublayer. Clearly this situation, or the situation where grey sublayer greyvalue exceeds black sublayer greyvalue, is impossible; the uppermost points on the scatter plot are those where the contrast between black and grey sublayers is very small but still measurable. The degree of scatter on this plot indicates that the two

sublayers have strongly overlapping greyvalue frequency distributions; again, this is most likely to be a result of changing illumination of the sediment images, and it explains why thresholding of the unmodified Drammensfjord images was impossible.

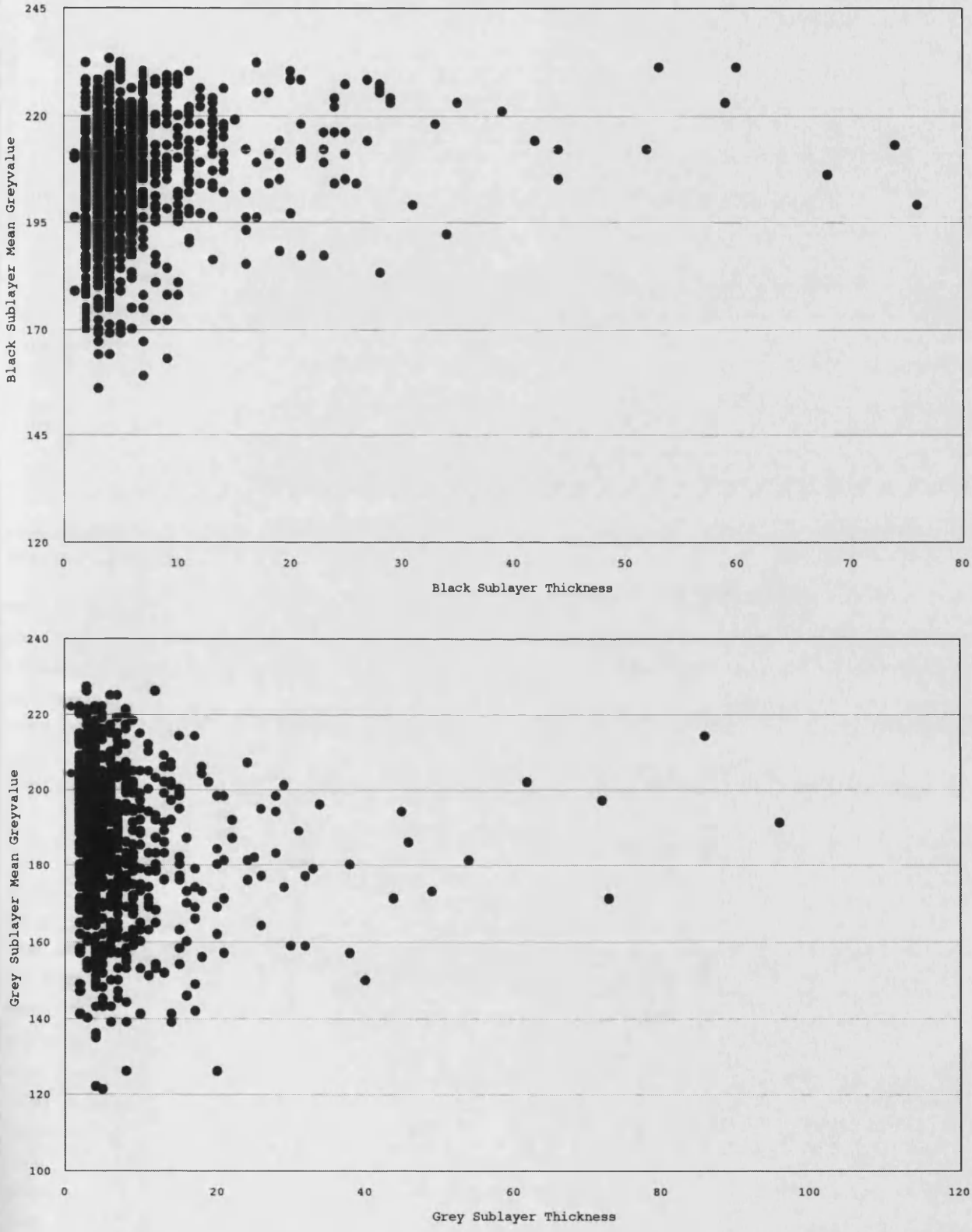

Figure 6.3: Scatter plots of thickness against greyvalue for both black (top) and grey (bottom) sublayers, showing no correlation for both.

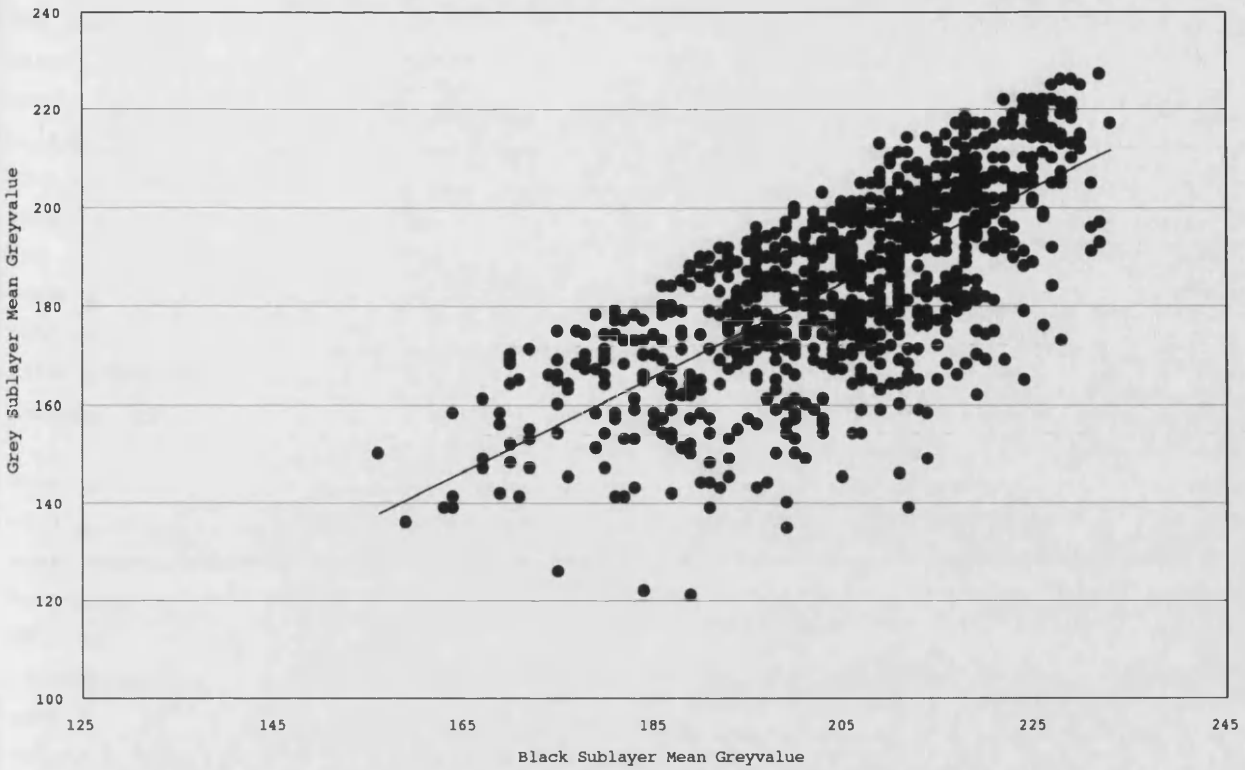

Figure 6.4: Scatter plot of black sublayer greyvalue against adjacent grey sublayer greyvalue, showing an obvious correlation. The line-of-best-fit is also shown.

Re-photographing of the Drammensfjord cores under carefully controlled lighting conditions could potentially separate these two distributions, allowing simple thresholding and perhaps greyvalue-based quantification of sediment components on a varve-to-varve scale, as achieved by Petterson *et al.* [4] using sediments from Lake Kassjön, Sweden. For now, the "illumination effects" on the greyvalue time-series prohibit further worthwhile research. The remaining sections concentrate on the varve sublayer thickness time-series.

6.1.3 Attempts at calibration with other palaeoclimate records

Given the varve mechanism discussed in section 5.2.4.2, grey sublayer thickness (which is proportional to the amount of sediment deposited in the fjord) can be related to the river discharge into the fjord, as indicated by sediment trap studies carried out by NIVA [5]. The size of the spring flood, in turn, is controlled primarily by the amount of winter precipitation over the Drammen catchment. However, there are no direct records of flooding, river discharge, or sediment input into Drammensfjord for the period c. AD 1000 to 1750. Instead, it is possible to assume *a priori* that the grey sublayer thickness time-series is an imperfect climatic time-series - the approach used by Anderson and Koopmans [6] - then to compare other palaeoclimate records from the Drammen area with this time-series, looking for common features, while bearing in mind the imperfections of the varve series as a climate record (which are discussed later). Convincing similarities between records may then allow some form of calibration of the varve thickness time-series.

The most useful type of records for calibration are instrumental meteorological data. Detailed records of multiple meteorological elements are available for the Drammen area, but only for the last 100 years or so. For example, the North Atlantic Climatological Dataset NACD-1 [7] contains monthly climate records for the weather station at Oslo-Blindern, only a few kilometres from Drammen, but only for the interval AD 1896 - 1990. Other instrumental records are available from earlier years, but none go back as far as AD 1750, and these records suffer from problems that data sets such as NACD-1 were designed to address, such as non-stationarity because of changing recording instruments and techniques. Calibration of the Drammensfjord varves with instrumental data is not feasible unless more recent varves can be recovered, perhaps by X-ray studies of freeze-cored sediment.

Even in the absence of suitable instrumental climate data, the varve time-series can still be compared with proxy-based climate data. Here, numerous records are available that overlap with the AD 1000 - 1750 time interval, such as the Central England Temperature record (since AD 1659) [8], the record of the date of ice break-up on Lake Mälaren, Sweden (since AD 1720) [9], and several records from Scandinavian tree rings (since c. AD 1100) [e.g. 10,11]. Which proxy records should be compared? It may seem best to use geographical proximity as a measure of relevance, but the nature of the palaeoclimate proxy records involved also needs to be considered.

First, different types of palaeoclimate proxies respond to different climate elements. Tree ring data, for example, may contain signals from temperature or precipitation depending on the nature of the tree and the location concerned [12]; in Scandinavia, where water stress is infrequent, tree ring width depends mostly on the length of the growing season. Similarly, ice break-up dates indicate the length and severity of winter conditions, which are not necessarily related to winter precipitation and the size of the spring flood. Furthermore, because of the large size of the Drammen catchment, the Drammensfjord record of river discharge is an integrated record of hydrological change over a large area, unlike records such as tree rings which can be affected by events peculiar to the individual site concerned. Differences in climatic meaning, in areal extent, and in timescale dependence, make it impossible to tell whether similarities between such palaeoclimate time-series are meaningful, or whether they are statistical coincidences. Proper integration of multiple proxy records [e.g. 13] is beyond the scope of this thesis.

What is needed is not a comparison between a few isolated, noisy, and possibly unrelated time-series, but a regionally-representative integrated climate record, for whose influence the Drammensfjord record can be scrutinised. Despite the complexity of the global climate, there is a significant statistical pattern that influences the climate of the North Atlantic sector, including the succession of weather systems that cross the Drammen catchment: a coherent spatial pressure variation called the North Atlantic Oscillation (NAO). Multiple-source proxy reconstructions of the NAO can be calibrated against instrumental data, giving them a known climatic meaning, and they are regionally representative. As such, they are suitable comparators for the Drammensfjord data.

The North Atlantic Oscillation [14] is a teleconnection in atmospheric pressure between northern and southern regions of the North Atlantic, conventionally defined using pressure measurements from Stykkisholmur, Iceland, and Ponta Delgada in the Azores. The NAO is numerically expressed as the North Atlantic Oscillation Index (NAOI): this is positive when pressure is relatively low in Iceland and high in the Azores, and negative when pressure is relatively high in Iceland and low in the Azores. Atmospheric pressure in Iceland only becomes absolutely greater than atmospheric pressure in the Azores during extreme negative events. A positive NAOI favours strong westerlies across the North Atlantic, bringing a maritime climate to northwest Europe: typically more rain, and warmer temperatures. A negative NAOI directs this storm track further south, producing a more continental climate in northwest Europe: typically colder and drier. The NAO signal is strongest in winter, when atmospheric circulation has a greater spatial coherence: c. 30% of the variance in mean winter extratropical temperature variation in the Northern Hemisphere can be explained by the NAO [14].

The influence of the North Atlantic Oscillation extends across Iberia, southern Europe, northern Africa, and the Middle East [15,16]. As for the Drammen catchment, winter precipitation in Norway is strongly linked to the NAO [17], as are many other features of Scandinavian climate including air temperatures [18], Baltic ice cover [19], and glacial mass balance [20]. The strongly positive state of the NAO over the last two decades has resulted in Norwegian glaciers advancing (because of increased precipitation), in contrast to the dramatic retreat of glaciers seen in almost every other part of the world in response to recent warming [21].

So, it is reasonable to expect that the Drammensfjord grey sublayer thickness time-series should record the influence of the NAO on precipitation and subsequent flooding in the Drammen catchment. Comparable sediment cores from the adjacent Inner Oslofjord contain a detectable NAO signal in both the record of dinoflagellates [22] and of lipid biomarkers [23]. To compare the varve thickness time-series with the NAO, it is necessary to find an NAO record which overlaps with the varved time interval (c. AD 1000 - 1750). Instrumental data from this period are scarce [e.g. 24], but several multiple-source proxy reconstructions are available [25-27]. The record used here was obtained by Luterbacher *et al.* [28] using various proxy records including tree-rings and ice cores. It covers the interval AD 1500 - 1658, with one NAOI data point per season, i.e. four data points per year. The expectation is that grey sublayer thickness will correlate with the winter NAOI, since a positive NAOI should result in more winter precipitation and a consequently larger spring flood.

The Luterbacher *et al.* NAO reconstruction [28] covers 159 years, so the correlation coefficient between this and the same number of varve sublayer thicknesses has 159 - 2 = 157 degrees of freedom. This gives significant correlation coefficients of 0.155 at the 95% level and 0.204 at the 99% level. As discussed in section 5.2.6, the 712 varves in the Drammensfjord record lie somewhere in the chronological interval AD 1000 - 1750. Because the absolute dates of the varve series are inexact, the 159 years of winter NAO data need to be tested against different possible alignments. It is simple enough to measure the correlation coefficient of every possible alignment of the NAO

data which has a complete overlap with the varve data. (Partial overlaps introduce problems with non-comparable correlation coefficients.)

As a starting point, the uppermost varve was taken to represent AD 1720. Aligning the NAO data thus, the correlation coefficient was 0.1280 which is not significant. With this alignment, the NAO index for winter AD 1658 - the final value - aligned with the winter sublayer of the varve representing AD 1658. But this varve is not necessarily from exactly AD 1658. Correlation coefficients were measured for all possible complete alignments, with the AD 1658 NAO value aligned with each varve back to AD 1167; earlier dates than this did not allow complete overlaps. The expectation is that if there is an NAO signal in the varve record, then the maximum correlation coefficient will correspond to an alignment of the records which is close to the originally-chosen alignment.

In fact, the alignment with the highest correlation coefficient (of 0.2163) aligns the final AD 1658 NAO value with the varve at AD 1656: only two years less than the originally-chosen alignment. Superficially, this suggests that the Drammensfjord record does contain an NAO signal: of all possible alignments, the one with the highest correlation coefficient is almost exactly where it was expected to be, and is significant at the 99% level.

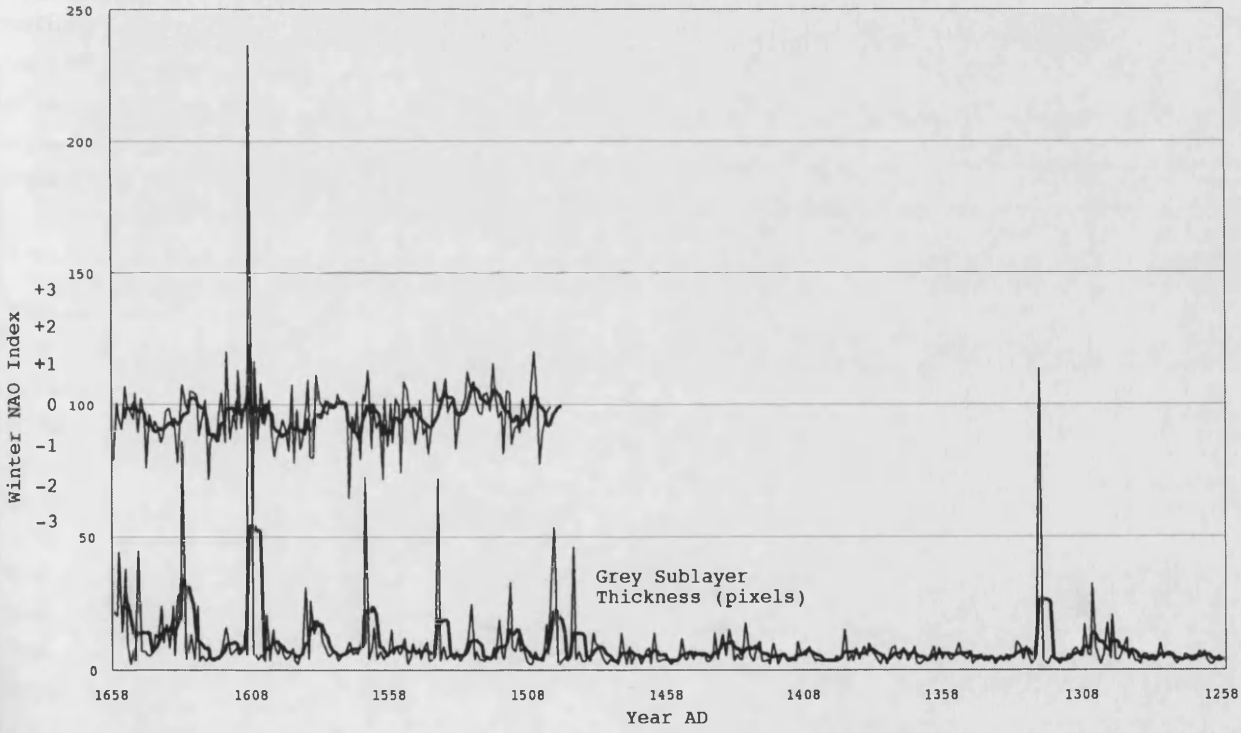

Figure 6.5: Optimal alignment of North Atlantic Oscillation Index and grey sublayer thickness time-series, plotted as raw data (thin lines) and as 5-year moving averages (thick lines).

However, closer analysis suggests that this is a statistical fluke. The correlation coefficient of 0.2163 is "significant" at the 99% level, but this is undermined by the large number of alignments tested. The result is more likely to be a type I error, since it is not much higher than other "significant" values obtained from deliberately

misaligned comparisons ($0.17 < r < 0.22$) of both grey and black sublayer thicknesses with NAOI values from all four seasons. For example, comparing the thicknesses of the *black* varve sublayers with the winter NAOI at different alignments gave a maximum correlation coefficient of 0.2161, but this required the NAOI value from AD 1658 to be aligned with the varve from AD 1474: an unacceptably large difference, and a definite type I error.

The position of optimal alignment is influenced by outliers in the varve thickness data: a small number of very thick layers that disrupt the correlation coefficients. In statistical terms, the data are heteroscedastic; this also means that they are non-stationary, which causes problems for spectral analysis (see section 6.1.5). Plotting varve thickness against NAO index shows that alignment of outliers in both data sets controls the position of optimal alignment, rather than alignment of more general features.

It is notable that published examples of significant NAO signals in palaeoclimate proxy records exhibit much higher correlation coefficients than statistical convention demands. The proxy NAO record described by Appenzeller *et al.* [29] from Greenland ice cores, for example, has correlation coefficients of c. 0.4 to 0.6 when aligned with instrumental NAO data. A conservative interpretation of the Drammensfjord data requires a similarly-good agreement - good enough to allow visual "wiggle-matching" - before rejecting the null hypothesis that a signal from the North Atlantic Oscillation is not preserved in the Drammensfjord varves, perhaps because it is masked by local climate variability and general background noise. The next two sections consider the signals that *are* preserved in the Drammensfjord varves, in the absence of any numerical calibration.

6.1.4 Drammensfjord flood records and the Little Ice Age

Visual analysis of plotted data is the starting point of all time-series analysis [30]. Plotting the Drammensfjord grey sublayer thickness time-series immediately reveals that thick layers are concentrated in the most recent half of the data; the time-series can be divided into two halves, before and after c. AD 1470, with the former almost entirely lacking in thick layers and the latter having many. How can this be explained?

The pattern is not simply that the grey sublayers, on average, get thicker towards the top of the sediment core. If this were the case, it could be ascribed to compaction of the deeper layers and would be unremarkable. Differential compaction is a concern in very long varved sediment cores, such as those from the Santa Barbara Basin [31], and in unconsolidated recent sediment with a very high water content, such as the topmost seven varves (corresponding to AD 1986-1992) from Baldeggersee, Switzerland [32]. But its effect is not significant in Drammensfjord, since the topmost sediment does not contain measurable varves anyway, yet the interval of varved sediment is short. If grey sublayers thicker than 1.5mm are ignored, then there is no significant change in the sublayer thickness distribution with depth, whereas if compaction had occurred, then the thinner sublayers should also become compacted, not just the thicker ones. Compaction is only likely to be significant in the Drammensfjord cores if the much

deeper varves (as found in core D1M: see section 6.1.1) are to be investigated. Here, at c. 8m depth below the sediment-water interface, the sediment is much stiffer and more compacted, as demonstrated by the ease with which slabs could be extracted for BSEI using a "cookie-cutter". For the more recent 712-varve sequence, as with many other short varve records, the influence of differential compaction on the thickness record is not significant.

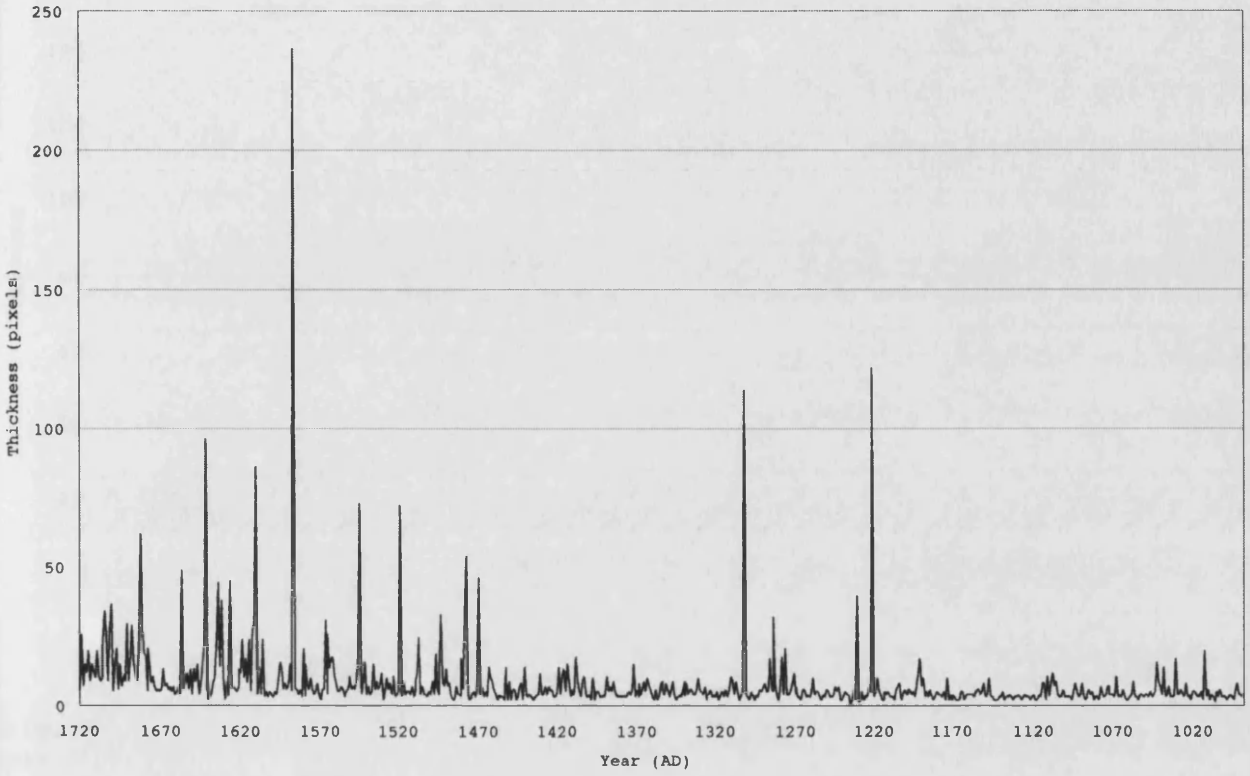

Figure 6.6: Plot of the grey sublayer thickness time-series from Drammensfjord core D1G. Thickness is in pixels, as before: 14.1 pixels = 1 mm.

So, it is the frequency of thick sublayers that increases in the second half of the time-series. How can a "thick" sublayer be defined? The thickness frequency histogram of the grey sublayers (figure 6.7) shows a smooth decline from 0.3mm (the mode) to c. 1.8mm, then above this there is a long "tail" to the distribution, up to c. 5.5mm, before the frequency falls to zero. The fact that the distribution is smooth and unimodal means that the positioning of a threshold to separate "thick" sublayers from "ordinary" ones is necessarily arbitrary. Yet the resultant division of the time-series is statistically robust: because of the long tail in the frequency distribution, it makes little difference where the threshold is drawn. However a "thick" sublayer is defined, within the range c. 1.8-5.5mm thick, the time-series is divided at c. AD 1470.

The frequency distribution shows that the thick layers are not actually "outliers" as suggested in section 6.1.3, but part of a continuous, very extended distribution. They are not anomalies that need to be removed from the record, but indicators of a change in the nature of the varve-thickness time-series. This change is best defined as an increase in the variance of the time-series rather than an increase in its mean. Changes in variance such as this, and concomitant changes in the frequencies of

extreme events, significantly influence the impacts of climate change [33]. Abrupt changes in variance are common in climatic time-series [34], owing to the highly non-linear "almost intransitive" [35] nature of the climate system. Statistical methods to detect change points in climatic time-series are reviewed by Tsay [36]; they are not necessary here because the change point is obvious.

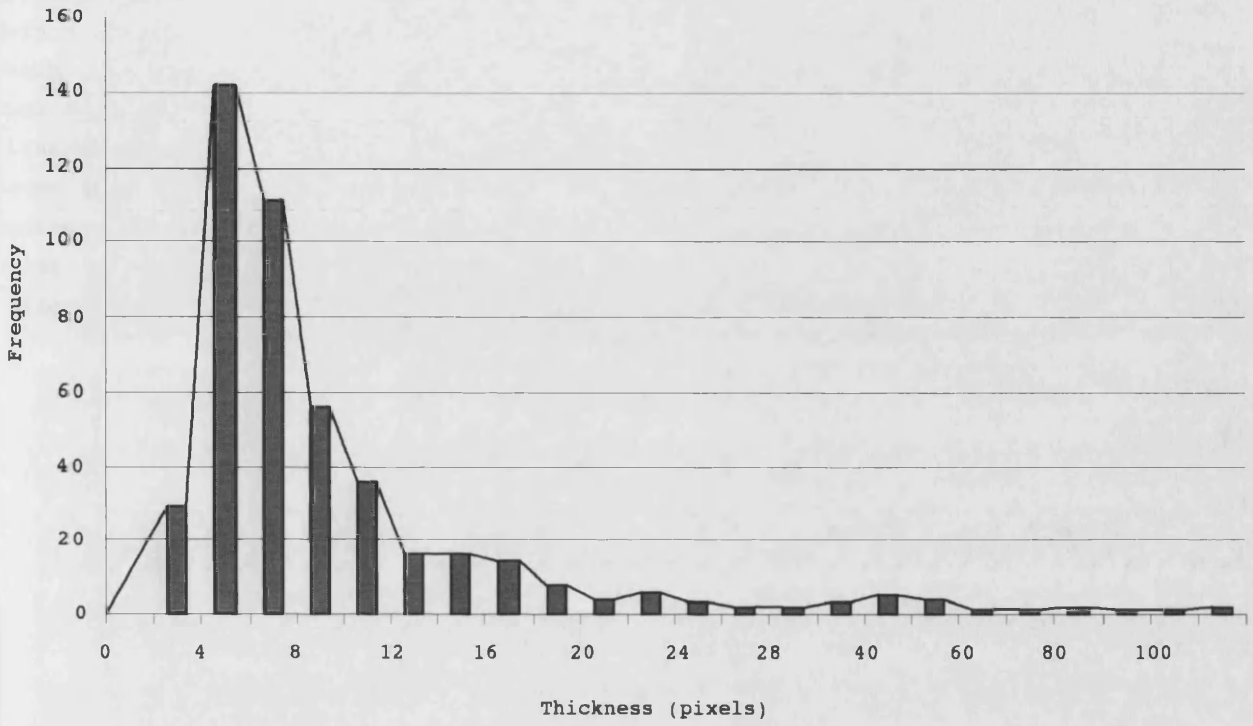

Figure 6.7: Grey sublayer thickness histogram: a strongly skewed unimodal distribution. Note that the bin widths are not constant, in order to show all the data on a single plot.

What controls sediment sublayer thickness? It is proportional to sediment input to Drammensfjord, which is controlled by the discharge of the River Drammen [5]. However, this relationship is poorly known because of the small number of sediment-trap results. A fuller picture can be gained by comparison with other sediment-trap studies. The classic Scandinavian example of this is the estuary of the River Ångermanälven, in northern Sweden, where varve formation can be observed at the present day [37]. The link between river discharge and varve thickness was established 50 years ago [38] and has been repeatedly confirmed [37,39]. For the River Ångermanälven, maximum river discharge and varve thickness follow a non-linear relationship: a slight increase in discharge leads to a much thicker varve (see figure 6.8).

The detailed controls on the Ångermanälven varves are different to those for Drammensfjord: the former are typically several centimetres thick, are much coarser than the Drammensfjord varves, and are mostly deposited over just a few days during the height of the spring flood. This means that varve thickness is most closely related to the maximum *daily* discharge, rather than the integrated size of the spring flood [37], and that monthly and seasonal relationships between discharge and varve thickness are non-stationary: liable to be altered by a discharge "spike" in one

particular month or another, for example [37]. The Drammensfjord varves, in contrast, settle out more slowly into much deeper water, so a clearer relationship between integrated discharge and sedimentation is expected. It is likely, however, that Drammensfjord has a similar non-linear relationship between river discharge and clastic sublayer thickness, as is also seen in various other Alpine and North American basins [40]. This explains the extremely-skewed grey sublayer thickness distribution, since river discharge events in themselves typically also have a skewed distribution: each discharge event has a probabilistically-constant recurrence interval, such that log discharge against log frequency plots as a straight line [41], so given the non-linear relationship in figure 6.8, the grey sublayer thickness distribution should be even more skewed. And importantly, it means that the thick layers do not necessarily correspond to major floods, along the lines of the "palaeoflood" layers identified in some varved records [e.g. 42]; thick layers just mean higher-than-normal river discharge.

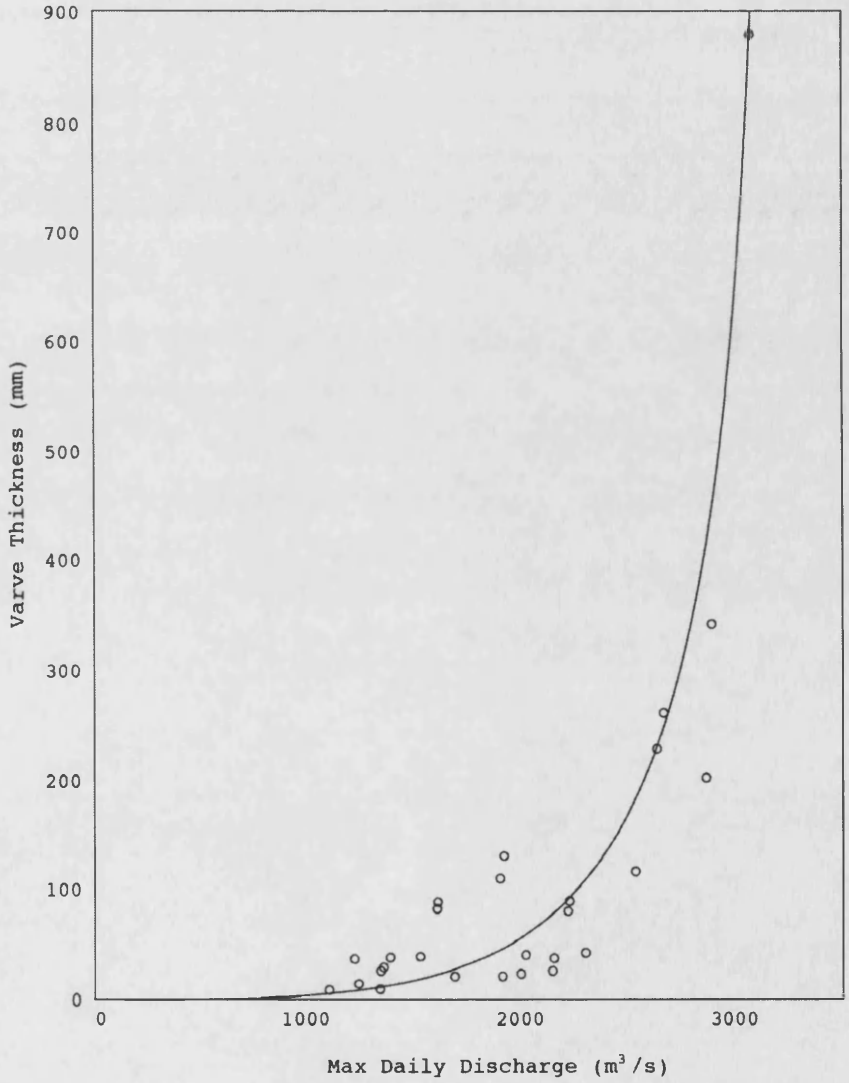

Figure 6.8: Relationship between varve thickness and river discharge for the Ångermanälven estuary, Sweden, as determined from sediment-trap data. Redrawn from Cato [39].

So, what are the controls on river discharge? These vary from basin to basin. For basins fed directly by glacial meltwater, the main influence is summer temperature, because this controls ice melting. There is usually little biogenic input into such lakes and fjords, so "whole varve thickness" correlates well with mean summer temperature [e.g. 43,44], although summer rainfall may also be important for extreme sedimentation events [e.g. 43]. For Drammensfjord, in contrast, the clastic element of sedimentation first needs to be isolated, by measuring only the grey sublayers. The most likely correlates for this variable are winter and spring *precipitation*, since river discharge into Drammensfjord is dominated by the spring flood [5], and this is precipitation-controlled. This is because virtually all the snow in the Drammen catchment melts in the spring; spring flood size depends not on the amount of melting but on the total precipitation supply, as is also the case for the River Ångermanälven [45].

However, the climate-sedimentation relationship is inevitably more complex than this. The presence of glaciers high in the Drammen catchment, together with the influence of temperature on the rate of spring snowmelt and hence the maximum flood discharge, plus co-deposition of clastic and biogenic sediment, all introduce additional variability into the record. Varves from most basins lacking direct glacial input have multiple climatic controls on varve thickness, including both temperature and precipitation [e.g. 32,46,47]. The expectation for Drammensfjord is only that grey sublayer thickness is *predominantly* controlled by winter and spring precipitation. Given this, can the change in the variability of the thickness time-series at c. AD 1470 be explained by reference to a known climate change?

Around this time, a major climate change did occur: the transition from the Mediaeval Warm Period (MWP) to the Little Ice Age (LIA). This is part of a generalised centennial-scale alternation of climate between cold and warm intervals over the last c. 2,000 years, defined by Lamb [48] using historical accounts and climate proxy data. These used to be regarded as global phenomena, but are now known to be restricted mainly to the North Atlantic region [21]: only c. 10% of the global surface [49]. In contrast, the current warming identified by the IPCC is truly global in scale [21]. Even in those regions where the LIA did occur as a definite cooling, there is uncertainty over its timing, and hence over the nature of any common forcing factors involved [50].

Nonetheless, the significance of the Little Ice Age in Scandinavia is undisputed: it is recorded in colder temperatures, glacial advances, and a range of resultant impacts [48,51] including collapses of the fishing industry and crop harvests, famine, depopulation, and the movement of the Norwegian court from Trondheim south to Oslo, and later to Copenhagen, as from AD 1536 to 1815 Norway ceased to exist as a separate country. The LIA was not only a climatic cooling; climate variability also increased during this time, producing frequent biennial alternations of cold and warm years, and some very hot summers amidst cold winters. For example, Baltic sea-ice reached a maximum during the winter of AD 1658-1659 at the nadir of the Little Ice Age, but its recorded *minimum* extent occurred only shortly before, during AD 1651-1653 [48]. This variability brought more heavy rain and floods: the LIA is the most recent of several

phases of high flood frequency across Europe [52], which resulted in more landslides [53], the combination of all these impacts causing great hardship for human populations [48,51,54].

The Little Ice Age ended between AD 1850 and 1900, and was followed by abrupt warming at the start of the 20th century [21]. Its cause is still disputed: it falls within the little-understood centennial-to-millennial variability introduced in chapter 1, and may be linked to the 1,500-year Holocene climate cyclicity mentioned therein. Global forcing factors such as sunspot minima and volcanic dust veils fail to explain the regional distribution of climatic change; internal changes in ocean circulation in the North Atlantic, perhaps linked to decadal and centennial-scale variability in the NAO, may be more likely [21]. In any case, the Little Ice Age in Scandinavia was a real event, and began at approximately the same time as the change in the varve sublayer thickness time-series. So do the thicker varve sublayers record the effect of the LIA on Drammensfjord?

Lower temperatures during the LIA resulted in longer, more severe winters, allowing more snow to accumulate, producing bigger spring floods. However, the climatic changes involved are more complex than this. The LIA was not just an interval of lower temperatures [55]; there were also hydrological changes which can only be understood in terms of changes in atmospheric circulation. Such understanding is difficult because of the need to integrate changes over centuries, how these are expressed as modulations of the seasonal cycle, and how these, in turn, are produced by synoptic-scale weather systems that cross Scandinavia over days or weeks. Climate variability on different timescales needs to be considered in order to understand the mechanisms involved.

Simplistically, recent atmospheric circulation over Scandinavia [17] has been strongly zonal: westerlies and southwesterlies bring storms and moisture from over the North Atlantic. Condensation of this moisture to form precipitation releases heat, such that strong westerlies correlate with Scandinavia being relatively warm; on the other hand, the effect of the increased precipitation on glaciers outweighs that of the increased warmth, such that glaciers have advanced over the last two decades [21]. The opposite situation is that of "blocking", where a high pressure system - an anticyclone - lies over Scandinavia, bringing very cold, dry air across from the continent to the south and east. "Blocking" conditions are the most likely explanation for the very worst winters of the LIA, such as those during the 1690s [21]. However, for much of the LIA, conditions were not extremely cold and dry. The initial phase of the LIA (c. AD 1500-1750) in southern Scandinavia was marked by *increased* precipitation, noted historically as more frequent floods and snow avalanches [55,56], and clearly recorded in the Drammensfjord varves. Significant glacial advances also occurred in northern and western Norway, which by comparison with recent conditions suggests more winter storms and stronger westerlies, not "blocking" conditions.

Furthermore, there is little to be gained from referring to the North Atlantic Oscillation as an explanatory factor. The previous section (6.1.3) showed that there is no record of the NAO index preserved in varve thicknesses; it is also not accurate

to argue that the LIA resulted from a prolonged negative state of the NAO, not just because predominant "blocking"-type circulation is insufficient to explain the LIA, as noted above, but also because synoptic-scale circulation over Scandinavia is not necessarily linked to the NAO, anyway. There *is* evidence for a strongly negative NAO index during parts of the LIA, notably from storms and floods across southern Europe at this time [57-59] which suggest that North Atlantic storm tracks were terminating much further south; however, there is no essential link between "blocking" in Scandinavia and a negative NAO index. As is shown by comparing the NAO index with records of storminess in northern Europe over the last century [60], a negative NAO index does not preclude winter storms and precipitation occurring over Scandinavia. The NAO is just a statistical correlation, not a mechanistic explanatory measure. For the maritime regions of southern Scandinavia, weaker zonal (westerly) circulation may bring colder winters but also *more* precipitation, resulting from persistent anticyclones increasing southerly, moist airflow across the Norwegian Sea [61]; a combination of local and regional circulation changes may be required to account for the combination of colder temperatures, increased climate variability, glacial advances and more frequent heavy spring floods. In summary, then, both the underlying causes and the atmospheric changes involved in the LIA are ambiguous and poorly-understood.

The impact of the LIA on Drammensfjord has already been noted by Alve [3], who described an abrupt change in foraminiferal assemblages indicating reduced salinity and lower temperatures. However, the dating of this change was very crude, being dependent on pollen stratigraphy and extrapolated sediment accumulation rates: it could only be placed sometime after c. AD 1375. The increase in thick flood layers seen in the NIOZ Drammensfjord cores is more useful because the abrupt onset of heavier flooding can be dated very accurately. This is of interest because the date of onset of the LIA at many locations over Scandinavia is presently unsure, and records such as the one from Drammensfjord may help to constrain the changes in atmospheric circulation that brought it about [e.g. 61]. The varve sublayer thickness record can also be compared with year-by-year historical flood records from the Drammen region, should any exist [62], bearing in mind the biases of many such historical records, and the possibility that, as mentioned earlier, the increase in the size of the spring flood necessary to produce a noticeably thicker grey sublayer in Drammensfjord may not be very large.

In the absence of historical confirmation, it is apposite to note other possible explanations for the abrupt change in the thickness time-series. The date is probably too early for human interference in the catchment (such as deforestation) to have affected flood frequency, but is it possible that it could be a natural, localised effect? The size of the Drammen catchment means that a natural change in flow regime, brought about by capture of a new tributary, for example, is very unlikely. An enhanced seasonal signal could also result from glacial advance during the LIA - bigger glaciers releasing more meltwater - but modelling suggests that glaciers east of the Scandinavian watershed changed little in size, even at the height of the LIA [63]; an increase in winter precipitation and consequent flood magnitude is more likely. To confirm the interpretation given above, it would be useful to have other

climate proxy data from the Drammensfjord cores: temperature-sensitive isotopes and micropalaeontological proxies, for example. At present, it is better to conclude only that there is a *probable* signal of the Little Ice Age recorded with high temporal resolution in the Drammensfjord varve thicknesses.

6.1.5 Spectral analysis of variability on interannual to decadal scales

6.1.5.1 Solar influence on climate and the 11-year sunspot cycle

The annual resolution of the Drammensfjord varve time-series means that it can potentially record cyclicity up to a frequency of one cycle per two years (the Nyquist frequency). So, in addition to the centennial-scale change in flood magnitude discussed in the previous section, it is also possible to study changes on interannual to decadal timescales. Many previous studies of varves in various settings have looked for similar variability using spectral analysis of varve thickness.

For example, Vos *et al.* [64] found periodicities of 11, 88, and 208 years in varves from Holzmaar, Germany; Renberg *et al.* [65] found a periodicity of 30-40 years in varves from Judesjön, northern Sweden; Mingram [66] found a periodicity of 5.5 years in varves from Eckfeld, Germany; and Sonett and Williams [67] and Svenonius and Olausson [68] both found periodicities of 11 and 22 years in glacial varves, from Skilak Lake, Alaska, and Scandinavia, respectively. Many such studies claim that "solar periodicities" recorded in the varve thicknesses indicate the influence of the Sun on the Earth's climate. Before testing whether the Drammensfjord record contains any evidence of solar influence on climate, it is necessary to consider the relationship between solar variability and climate records in more detail.

Such a relationship has long been sought, and the search has intensified recently because the identification of solar-influenced variability is a crucial step in resolving the natural and anthropogenic components of current climate change. The observational record of changing solar output, which extends back to c. AD 1700, is based on sunspots [69]. These are dark regions on the Sun's surface which are cooler than their surroundings; they coexist with brighter regions called faculae, such that total solar irradiance increases when sunspots are numerous. Sunspot abundance follows an 11-year cycle; consecutive 11-year cycles have alternating magnetic polarities, and slightly changing amplitudes, producing in addition a 22-year cycle. Longer cycles in sunspot numbers occur with periods of c. 55, 80-90 and 150-220 years. The latter is manifest as prolonged periods of sunspot minima, the one recent period being the "Maunder Minimum", c. AD 1645-1715, which may be linked to the Little Ice Age [70]. The Drammensfjord varve record is too short to allow a proper study of this cycle. Traditionally, the detection of cyclicity in palaeoclimate records at solar frequencies like those mentioned above was used to infer the influence of the Sun on the Earth's climate. Classic studies include those of Bradley [71] on Eocene varves, and of Douglass [72] on tree rings in Arizona. However, this simple method needs to be updated, to take into account recent research on the links between solar output and climate.

Total Solar Irradiance (TSI) varies by only 0.08% over the 11-year sunspot cycle [21]. So, an amplification mechanism is required if the influence of this 11-year cycle on the Earth's climate is to be believed. Several have been suggested, such as changes in atmospheric ozone concentration linked to ultraviolet solar radiation [73], and changes in cloudiness linked to cosmic rays which are influenced by solar activity [74], but the level of scientific understanding in this area remains very low [21]. In the absence of a definite mechanism, solar influence on climate can only be established by searching for characteristic solar patterns: by a statistical comparison of time-series. This is analogous to the detection of Milankovitch frequencies in longer-timescale palaeoclimate data, where again there is no definite mechanism. The Milankovitch "signature" is unambiguous: coupled cycles of eccentricity, obliquity and precession, with regular, predictable frequencies and amplitudes. For solar variability on interannual to decadal scales, the situation is not as simple.

Firstly, not all changes in TSI are linked to changes in sunspots. Sunspot numbers essentially return to zero at each solar minimum, but this cycle is superimposed on longer-term variability in solar output, including changes in regions of the Sun where sunspots are absent [21]. Direct measurement of TSI using satellites only began in 1979, such that this time-series is too short to characterise longer-term variation in TSI; reconstruction of TSI is therefore dependent on combinations of the sunspot record and other proxy evidence such as cosmogenic isotopes in tree rings and ice cores. Current reconstructions of TSI over the last few centuries are very uncertain [21].

Secondly, even if attention is focused solely on the 11-year sunspot cycle, in order to detect at least one component of past variation in TSI, the spectral identification of this cycle is difficult. The sunspot cycle has a mean period of 11.1 years, but it is quasi-periodic, varying in length from c. 8 to 14 years, and its amplitude varies by a factor of 3 [75,76]. This results in the unmodified spectrum of the Wolfer sunspot data having two peaks at c. 10 and 11 years, plus minor peaks at 12.1 and 8.5 years [76], rather than a single distinct peak. Shorter sections of the Wolfer data produce different spectra, indicating that the 11-year cycle is non-stationary. Moreover, the variation in length of the sunspot cycle may have a stronger climatic influence than the cycle itself [77].

Thirdly, spectral identification of the 11-year cycle in real climatic data is made more difficult by the presence of many other kinds of climate variability at similar frequencies. For example, the Quasi-Biennial Oscillation (QBO) is a change in the direction of winds in the tropical stratosphere that takes place every c. 26-28 months, and which influences the distribution of weather systems in the troposphere both within and without the tropics [78]. The beat between this cycle and the 2-year harmonic of the annual cycle can alone produce a 12 to 14-year cycle which may be spectrally indistinguishable from the 11-year sunspot cycle [79]. It has also been suggested that the influence of the 11-year solar cycle is partitioned into the opposite phases of the QBO [80] which would make it impossible to extract a signal of the 11-year cycle from unpartitioned climate data; since records of the QBO only

extend back to 1952, this would preclude any attempts at long-term study of the influence of the 11-year cycle. The statistical support for this claim has been questioned [81], but interactions of solar-driven variability with other modes of climate variability are to be expected. In fact, cyclicity of all kinds at similar frequencies to sunspot cycles is so common, that the Wolfer numbers are commonly used as a pedagogical example of how easy it is to find nonsense correlations with climate data [82].

Climate change on interannual to decadal timescales is noisy and complex; early research concentrated on solar-influenced variability because this was thought to consist of clear-cut cycles which could be distinguished from the background noise. The above discussion has shown that this is not the case, and that any apparent cyclicity in the data must not be too hastily ascribed to solar influence or any other forcing factors. In the light of this, the Drammensfjord data can now be analysed.

Both the correlogram and the unmodified power spectrum of the raw data suggest that the series is no different to white noise. The correlogram falls rapidly to zero, then oscillates close to zero in a random fashion. The power spectrum contains four "significant" ordinates at the 95% level according to Schuster's test, which is one less than the number of type I errors expected. None of the peaks are significant according to Fisher's test: the largest ordinate occurs at a frequency of 0.04301075, which corresponds to a period of 23.25 years; Fisher's g statistic, the ratio of this largest ordinate to the mean of all the ordinates with two degrees of freedom, is 4.4004, for n = 231; using the table of values in Fuller [83], this is nowhere near significance at the 95% level.

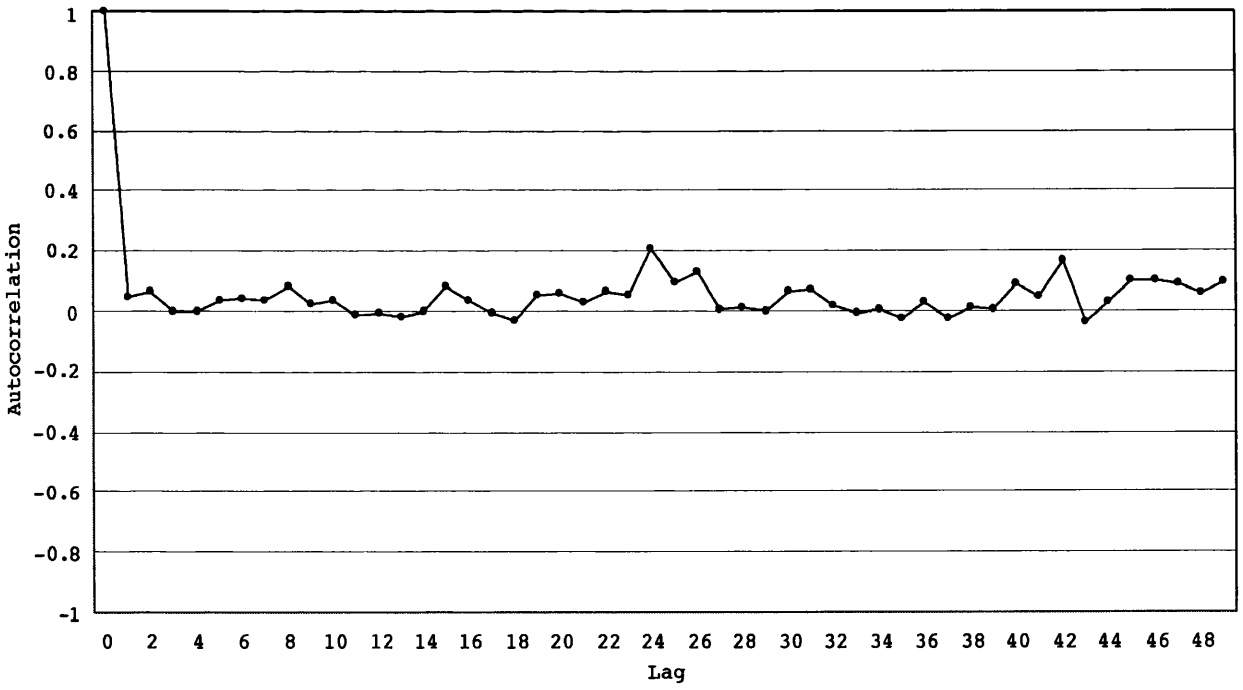

Figure 6.9: Correlogram for the Drammensfjord grey sublayer thickness time-series.

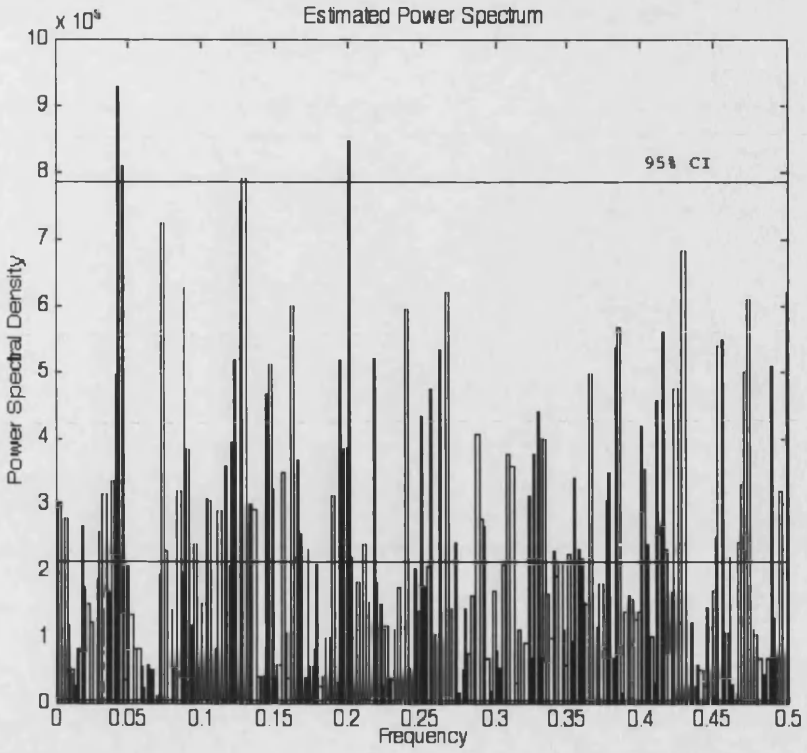

Figure 6.10: Power spectrum for the unmodified Drammensfjord grey sublayer thickness time-series, which is not significantly different from that of white noise.

However, there is an obvious problem with the time-series plotted in figure 6.6: it is strongly non-stationary. The variance of the time-series is not independent of time, perhaps, as noted above, a consequence of the onset of the Little Ice Age. This non-stationarity makes time-series analysis of the data difficult. The unmodified spectrum above is based on converting the data into sinusoids, but these are poor approximators of the large, isolated spikes ("singularities") and transient cycles in the real data. The result of this is that spectral power is redistributed over the spectrum, creating spurious peaks and concealing real ones [84]. The proliferation of power across the whole spectrum, right down to the Nyquist frequency, as seen in figure 6.10, is typical of a time-series with many singularities and transient cycles. If there are any signals in the data, the distorting effects of non-stationarity are causing them to be overlooked.

One answer to this could be to process the time-series to make it more stationary. For example, by multiyear averaging, or applying a moving average, the spikes can be smoothed out. However, the former can produce very misleading results [85], and the latter, whilst less distorting, acts as a low-pass frequency filter, removing interannual variability from the data which could contain climatic signals. It is better in this situation to apply only those filters whose effects in both the time and frequency domains have been considered (see section A.6.3 in appendix A); modifying the time-series data without such consideration is likely to undermine the statistical validity of the results [86]. A better solution is to analyse stationary parts of the unmodified time-series.

The most suitable interval to use from the grey sublayer thickness time-series is between the large peak at c. AD 1321 and the onset of more frequent peaks at c. AD 1488: a stationary interval of 167 years which lacks any sublayers thicker than c. 2mm, and therefore contains no distorting singularities.

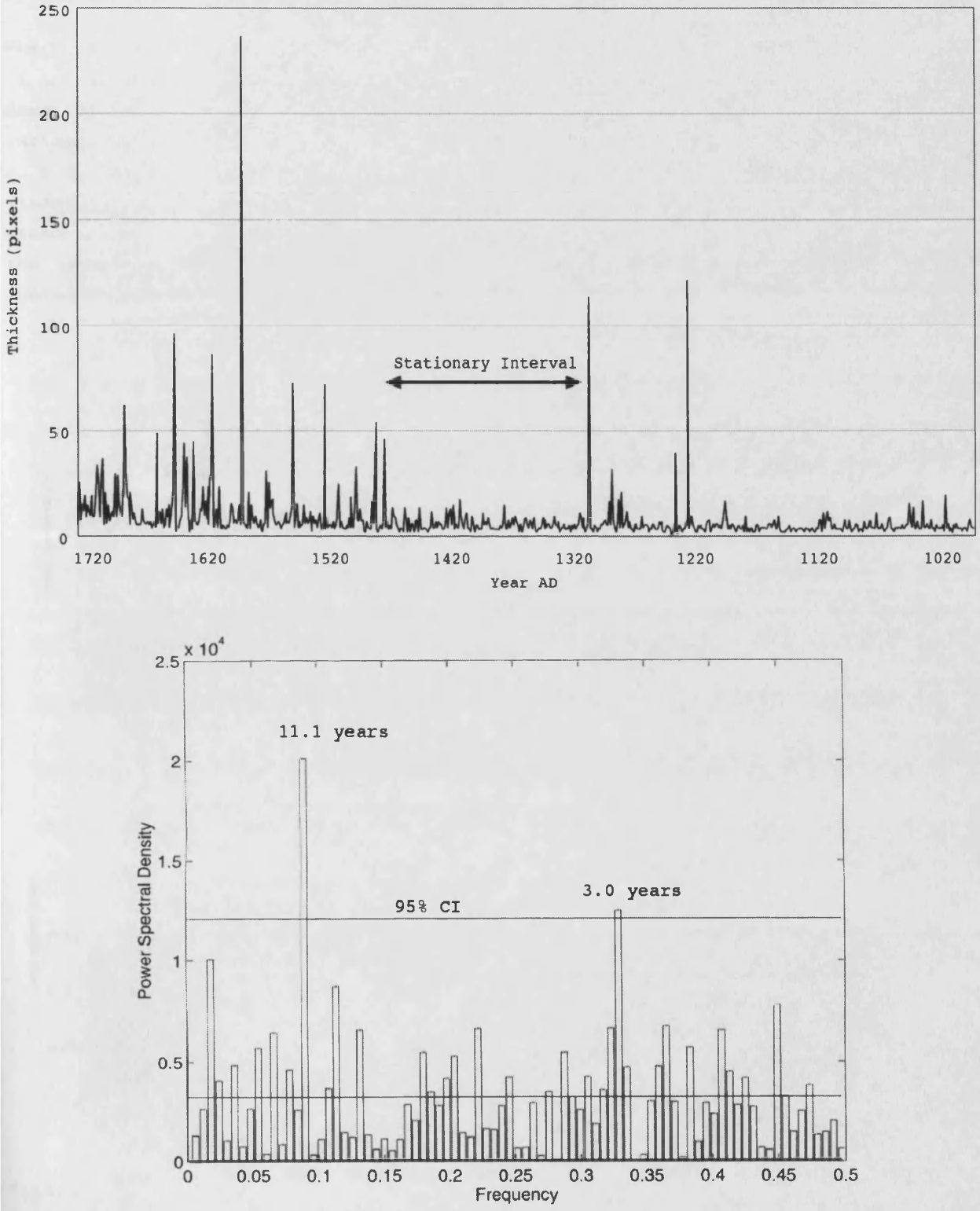

Figure 6.11: The Drammensfjord time-series with the stationary interval indicated by the arrow (top) and the unmodified spectrum of this interval (bottom) showing a prominent peak at a period of 11.1 years.

The unmodified spectrum of this interval is instructive because it has two peaks: a barely significant one at 3.0 years and a highly significant one at 11.1 years - the latter matching exactly with the mean length of the sunspot cycle discussed earlier. Is there, then, an underlying 11-year solar signal in the varve data which is obscured by the non-stationarity, or is this peak a statistical accident?

There is always a possibility that this is a type I error, but the *a priori* prediction of an 11.1-year cycle seems to make a case for it being a genuine signal. However, does the detailed structure of the spectrum match the structure of the solar variability described earlier? The unmodified periodogram has no subsidiary peaks at c. 8.5, 10, 12, and 22 years as occur in the Wolfer data spectrum. Furthermore, window-closing of the spectrum, to reduce the variance of the ordinates, reveals three broad concentrations of spectral power, at c. 2-3 years, 5 years, and 8-12 years, but the latter is no longer statistically significant. So it seems that the lone 11-year spectral peak is a statistical accident.

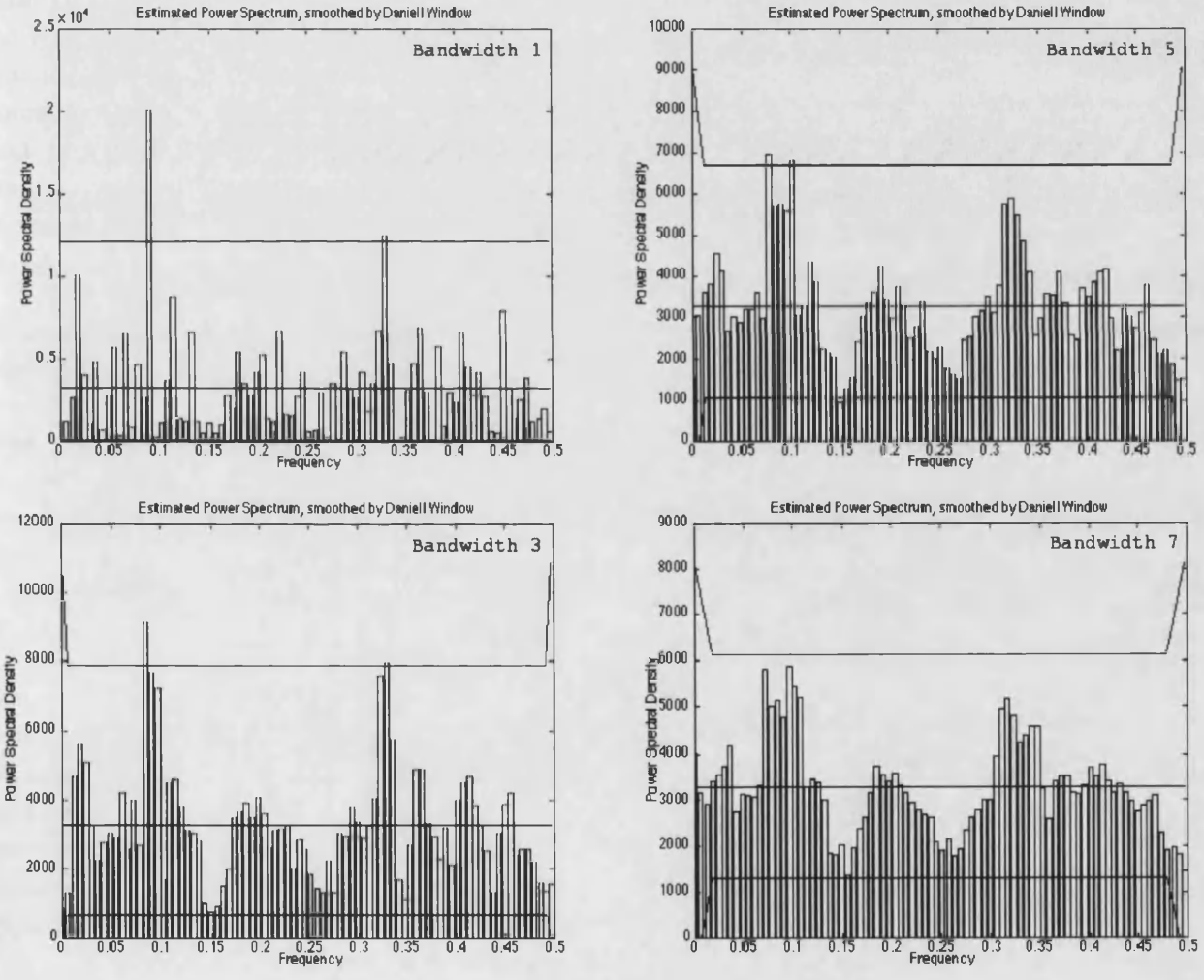

Figure 6.12: "Window-closing" of the 167-year stationary interval labelled in figure 6.11, using a Daniell window and a progressively increasing bandwidth. The three horizontal lines show the expected value for white noise, and the 95% confidence interval for this null hypothesis.

If there was any overlap with observational sunspot data, this could be confirmed by checking the *phase* of the 11-year peak with the phase of the sunspot cycle: a very powerful test which unfortunately cannot be done because observational sunspot data only extend back to c. AD 1700. This limitation affects many annual-resolution palaeoclimate records, and has some complex statistical consequences. It makes it harder to produce a convincing solar explanation, but it also makes it harder to *reject* such an explanation: perhaps one reason why suggestions of solar cycles are so commonly found in pre-AD-1700 annual palaeoclimate records [e.g. 64,66,68,71]. Without further confirmation, a solar explanation for the 11-year peak in the spectrum in figure 6.13 is unconvincing.

6.1.5.2 Evolutionary time-series analysis and the need for other records

The approach used in the previous section to cope with non-stationarity can be broadened to include the whole of the time-series by juxtaposing the spectra of many short intervals, which tend to be more stationary than the entire parent time-series. This is evolutionary spectral analysis, as described in section A.7.3 in appendix A, and has been used for various climatic time-series including data from varves [87] and hydrological data [88]. There will still be spectral distortion because of singularities and changes in variance, but this will not be constant with time: it will be different for each short interval. Evolutionary spectral analysis thus allows the *persistence* of cyclicity at different frequencies to be assessed, providing a form of statistical verification which is not available for the spectrum of the whole time-series.

To generate the evolutionary spectrum in figure 6.13, the grey sublayer thickness time-series was divided into 20 non-overlapping subseries of equal length (37 data points), then a spectrum was generated for each subseries. These were then arranged in time order, creating a three-dimensional surface which is shown in figure 6.13 as a shaded contour plot. Evolutionary plots such as this are frequently constructed using overlapping subseries, which gives a smoothly-changing distribution of spectral power with time. The advantage of using non-overlapping subseries is that the expectation is a random pattern: any persistence in spectral power from one subseries to the next is of interest, because there is no *a priori* reason to expect it.

The distribution of spectral power with time is, indeed, random for periods of c. 7 years or less: only in the leftmost third of the plot is there any suggestion of persistent cyclicity. For the first half of the time-series as a whole, there is a persistent concentration of spectral power in the range c. 9 - 12.5 years; in the second half of the time-series this moves to the range c. 20 - 30 years. Cyclicity at longer timescales than this cannot be studied without a longer overall time-series; it is not possible to generate sufficient non-overlapping subseries that are long enough.

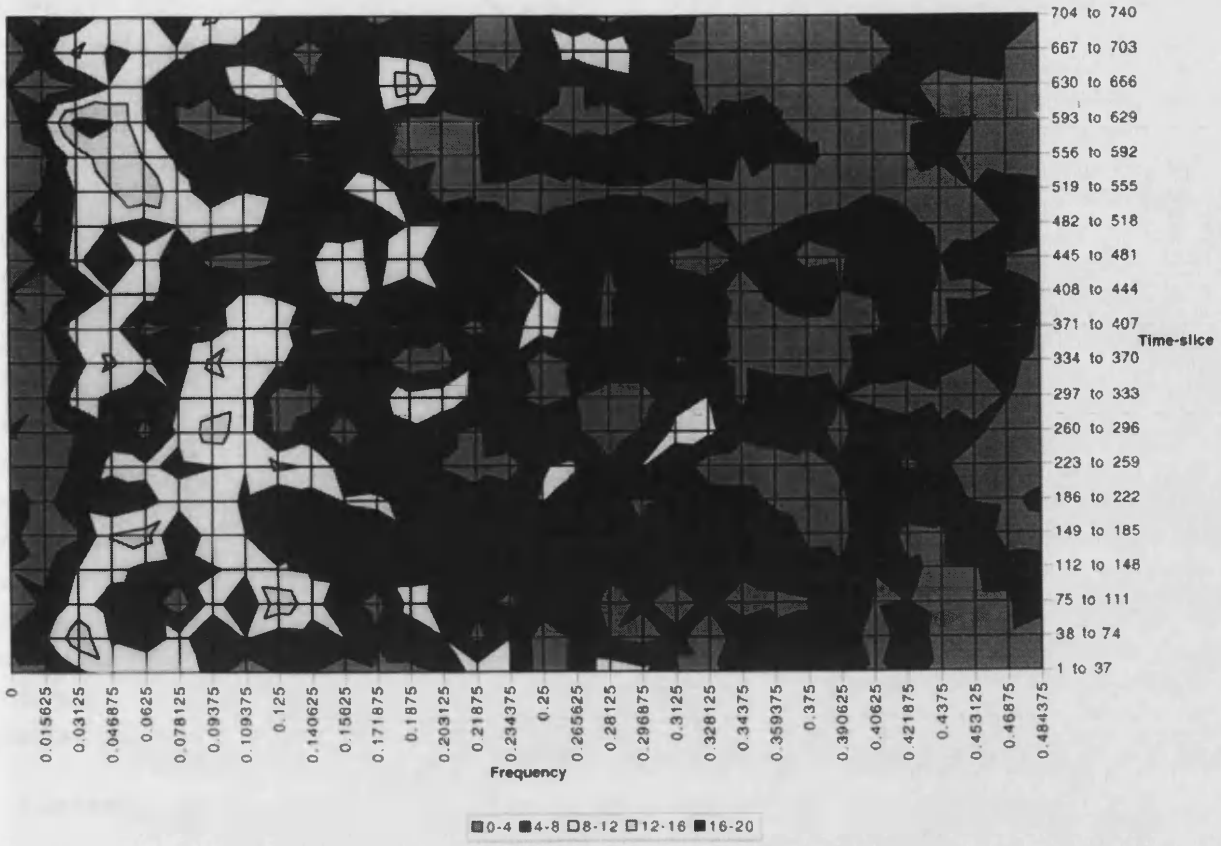

Figure 6.13: Evolutionary power spectrum of the Drammensfjord grey sublayer time-series, divided into 20 non-overlapping time-slices of equal length.

What do these patterns mean? At periods of less than c. 7 years, random behaviour is unsurprising, given the lack of known periodic climatic influences on Scandinavia: the North Atlantic Oscillation, for example, has a near-white-noise spectrum over this frequency range [89]. Broad concentrations of power within bands which include the 11-year period, for the first half of the data, and the 22-year period, for the second half, allow a claim to be made for a solar influence on the data, but care is necessary with such reasoning. For example, consider the hypothesis (derived from figure 6.13) that "the data record a solar influence from c. AD 1000 to 1400 as an 11-year cycle, which then breaks down until c. AD 1500, when it returns, now locked to a 22-yr cycle, until c. AD 1750". This is difficult to test statistically, because these *ad hoc* complications add degrees of freedom [90], even though this sort of transient locking of different cycles is exactly what is seen in some instrumental climate data [91]. The difficulty is precisely that the null hypothesis is difficult to reject, because it is so similar to the expected results.

More complex techniques of time-series analysis may provide more powerful statistical tests: wavelet analysis [84,92], for example, can mimic non-sinusoidal cycles in the data more successfully than ordinary harmonic analysis, though it requires a relatively long time-series. This may become in future a standard technique in palaeoclimatology for spectral analysis, especially in detecting solar cyclicity [93]. But a simpler and better next step is to seek *independent confirmation from elsewhere*. As discussed in appendix A, statistical processing can help to reveal patterns in the

data, but can also create supposedly significant results where there are none, by the process of trying different techniques until one is found that delivers a "significant" result. If the relationship between the proposed source mechanism and the time-series that is supposedly a realisation of it becomes too distant - after filtering, partitioning, and other *a posteriori* modifications - then the results are unlikely to be convincing. Successful palaeoclimate reconstruction relies on coherent patterns in both space and time, and therefore on comparisons amongst sites rather than endless reanalysis of single time-series in isolation.

Several other palaeoclimate records are in the process of being obtained from localities near Drammensfjord. Lake sediment from Torsby, in southern Sweden, c. 120km east of Drammensfjord, contains c. 9,000 varves which are being studied at Lund University [94], and there are many other Scandinavian lakes which contain unstudied varves [95]. Anoxic fjords similar to Drammensfjord occur along the southern coast of Scandinavia (see figure 2.1) and there is much future potential for regional palaeoclimate reconstruction using varved fjord sediments, which are only just beginning to be cored and studied [e.g. 1,2]. The value of the Drammensfjord record is not so much as a stand-alone climatic history, as an indicator of the potential availability of a robust regional palaeoclimate reconstruction derived from many similar sources.

6.2 Interpretation of the Lake St Moritz results

6.2.1 Comparison of the Lake St Moritz varve data with meteorological data

Approximate agreement amongst independent chronological data from varve counting, historically-dated event beds, and ^{210}Pb activity, suggests that the topmost c. 239 varves measured from core PSM90.3 form a continuous, annual-resolution sequence (see section 5.3.5) representing the interval c. AD 1750 to 1990. The measured varve thickness data can be compared with two series of climatological observations from the St Moritz area: a homogeneous April temperature record (AD 1872 onwards) from the meteorological station at Sils Maria, 8km southwest of St Moritz along the same valley [96], and a long series (AD 1832 onwards) of historically-observed ice break-up dates from Lake St Moritz itself [97]. These data are compared in figure 6.14.

Not surprisingly, there is an excellent correlation between the April temperature data and the ice break-up date ($r = 0.787$). But there is only a weak correlation between the temperature and the average varve thickness data ($r = 0.259$, for $n = 93$). This is a better correlation than would be expected for two random time-series, but not usefully so.

Using the separate sublayer thicknesses fails to produce improved correlations, though these data are in any case less reliable because the separate sublayers are difficult to identify. There is an apparent correlation between adjacent dark and pale sublayer thicknesses ($r = 0.368$, for $n = 239$) but its significance is unclear because of the distorting effects of outliers: the sublayer thicknesses are not normally-distributed, as the Pearson coefficient strictly requires, but heavily-skewed.

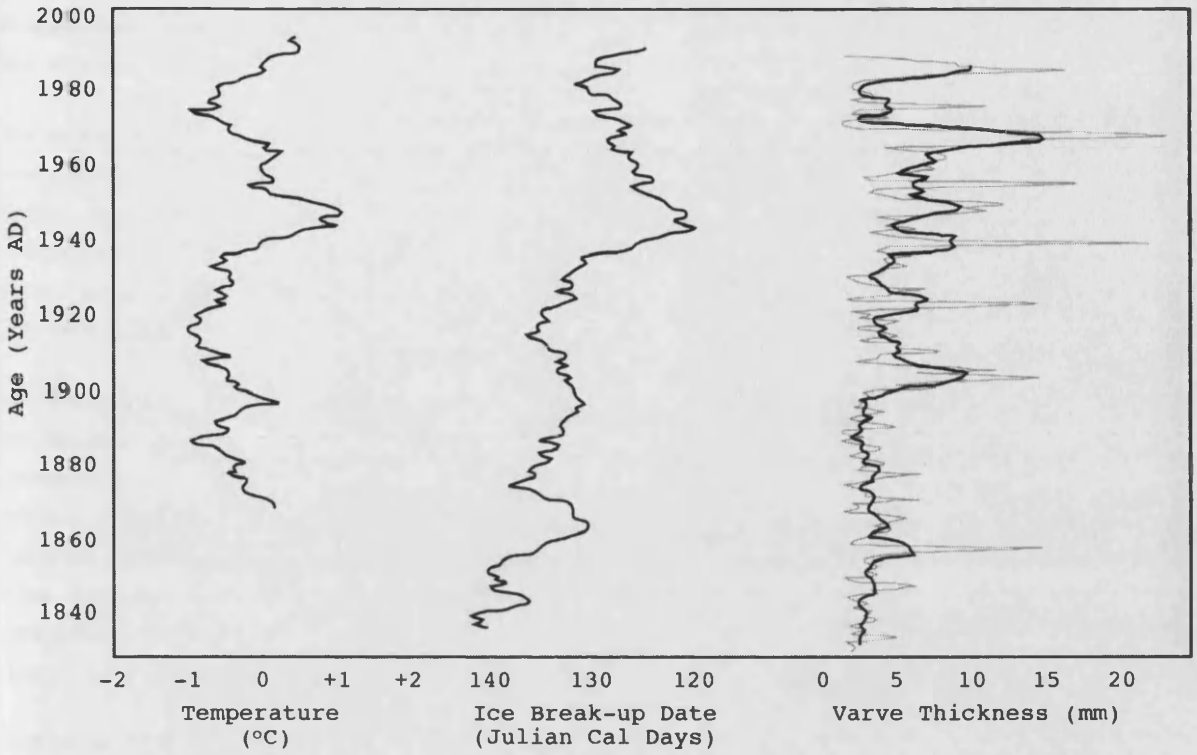

Figure 6.14: Five-year moving averages of April temperature data from the Sils Maria station (left), ice break-up date from Lake St Moritz (centre), and varve thickness from Lake St Moritz (right).

The absence of a straightforward relationship between climatic variables (such as air temperature and ice melt) and sediment accumulation (represented by varve thickness) is not unexpected. In the Alpine environment, processes such as runoff, erosion, and sediment transport are influenced by a range of interdependent climate elements including air temperature, precipitation, and snow cover duration [98]. So, for Alpine lakes such as Lake St Moritz, it is expected that individual climate elements will only explain small amounts of the observed variability in varve thickness; this is especially likely in recent times when there has also been significant anthropogenic disruption to the natural processes of lake sediment supply.

For example, as observed in Lake Silvaplana, part of the same chain of lakes as Lake St Moritz, low-frequency (decadal to centennial) variability in varve thickness is controlled by glacial extent [99], but higher-frequency variability reflects the combined influences of temperature, precipitation, and snow cover duration, and these multiple influences cannot easily be separated [96]. Similarly, changes in temperature and precipitation only explain one-third of the variability observed in recent varve thickness changes in Baldeggersee, Switzerland [100].

The presence of multiple, unresolvable influences has meant that attempts to develop climatic transfer functions using sediment accumulation proxies such as varve thickness in Alpine lakes have not yet been successful. Better results have been obtained from remote lakes where there has been little anthropogenic disturbance, and where strong climatic thresholds exist. For example, proglacial lakes where there is a long frozen interval each year and little biogenic activity, such that sediment

accumulation, almost entirely of clastic sediment, is influenced at high frequencies by summer temperature, and at low frequencies by glacial extent [e.g. 101].

In some lakes, varve thickness may be primarily controlled by different climatic variables in different time intervals [96]. For example, varve thickness in Mirror Lake, Northwest Territories, Canada, has been primarily controlled by summer temperature during some decadal-scale intervals in the past, and by winter precipitation during others [102], though statistical confirmation of such intervals is not simple.

A detailed study of separate varve components could potentially enable better links to be made between climate variability and sediment accumulation in Lake St Moritz; for example, the separation of autochthonous and allochthonous sediment accumulation, which image analysis alone cannot achieve. However, for the varve measurements given above, from c. AD 1750 to 1990, there remains the problem of anthropogenic effects on the sediment record. The record can be edited to remove distinct, historically-documented anthropogenic event beds, but undocumented disturbances such as changes in land use [e.g. 103] are likely to be just as important.

Anthropogenic disturbances may be less of a problem for the deeper varves from core PSM90.3, although these of course cannot be calibrated against instrumental data. The next section uses spectral analysis to search for signals within both sets of varve thickness data in the frequency domain.

6.2.2 Spectral analysis of the Lake St Moritz varve data

Spectral analysis was used to test the varve measurements for the presence of signals in the frequency domain. The same method was used for both intervals of varves: the upper one, representing c. AD 1750 to 1990, and the lower one, representing c. 2,400 ± 100 to 1,600 ± 100 BP (see section 5.3.5).

A linear detrend was performed, to improve the stationarity of the data. The unmodified spectrum was then calculated. Finally, the technique of "window-closing" was used with a Blackman-Tukey filter until comparable filtered spectra had also been obtained for each interval.

These filtered spectra are shown in figure 6.15. The upper varve spectrum was smoothed using a Blackman-Tukey parameter of 0.33; the lower varve spectrum with a parameter of 0.15. These values produced spectra of comparable "peakiness": the greater length of the lower varve sequence (745 data points, compared with 239 for the upper sequence) resulted in more spectral information and hence required a greater degree of smoothing to attain the same bandwidth. In both cases, white noise was clearly an unsuitable null hypothesis, and a greatly-smoothed version of the actual spectrum was used instead. The 95% confidence level was estimated from this and is indicated by the upper grey line.

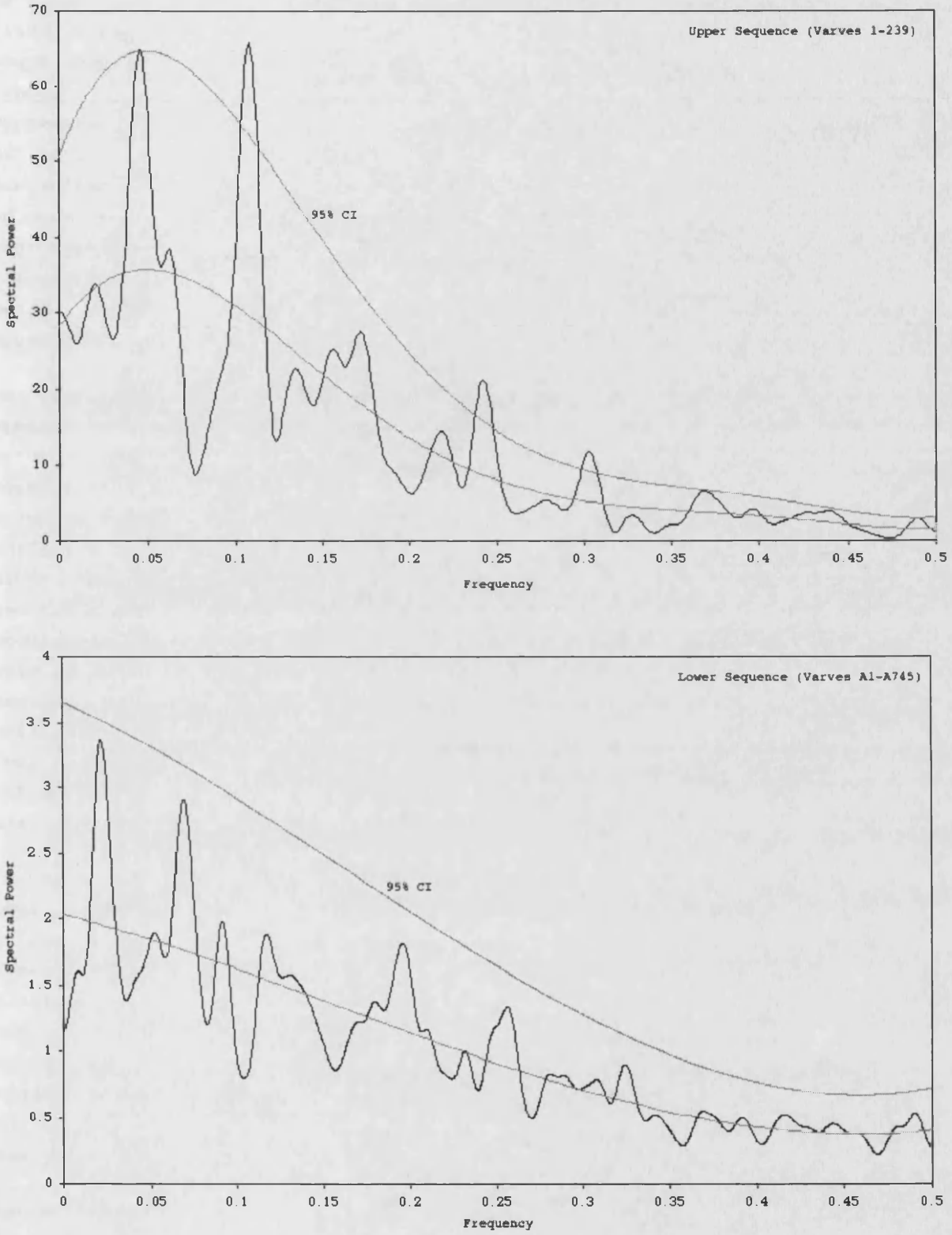

Figure 6.15: Spectra for the upper (top) and lower (bottom) varve sequences, smoothed using Blackman-Tukey filters of parameters 0.33 and 0.15 respectively. The lower grey line is the expected spectrum for the null hypothesis; the upper grey line, the 95% confidence level.

The upper varve sequence contains three significant spectral peaks, at frequencies of 0.1084, 0.2421, and 0.3031, corresponding to cycle periods of 9.2, 4.1, and 3.3 years, though only the first of these is noticeably large, such that all three may arise from harmonics of a single c. 8-10-year cycle. The lower varve spectrum resembles the null hypothesis more closely: it contains no significant peaks, and also no spectral peaks that match those in the upper varve spectrum. This lower spectrum is also possibly more reliable, since it is constructed from a varve time-series which is both longer and more stationary. The upper varve spectrum is likely to have been distorted by large changes in the thicknesses of recent varves, such as have resulted from differential compaction in the topmost varves, and anthropogenic eutrophication, sewage output, land-use and drainage changes, and so on, which make it virtually impossible to ascribe any meaning to the observed cyclic variability.

The "reddened" (low-frequency-dominated) shape of the upper varve spectrum, then, is expected because of this non-stationarity in sediment deposition during the last century: this is clear in the plot of the time-series data (see figure 5.18). The presence of a similar domination of low frequencies in the lower varve spectrum, though to a lesser degree, is more interesting because it suggests that there may be a consistent underlying reddened spectral power distribution for the Lake St Moritz varves. This raises the possibility of analysing the data in terms of a continuous spectral signal, the inverse of the "cycles plus noise" approach: of assuming that the smoothed curves in figure 6.15 represent the signal and disregarding any spectral peaks as noise. It may be more parsimonious, especially in the case of the lower varve spectrum, to model these time-series not as the sum of a number of independent oscillating elements but as the outcome of a single process, producing a self-affine power distribution across the entire spectrum (or, since this is varve-derived data, with a lower bound to the self-affinity at an annual resolution). Further detail of this approach is given in appendix A, section A.6.1.

A continuous spectrum of this type can be modelled using a power law, where spectral power at frequency f (S(f)) is equal to $k * f^{-\beta}$. The parameter β describes the degree of "reddening" of the spectrum, and can be simply calculated as the gradient of the line-of-best-fit through a plot of the unmodified periodogram on log-log axes. This is illustrated in figure 6.16. Note that the apparent poor fit of the left-hand "tail" of both spectra can be ignored: it is a consequence of the logarithmic x-scale, which shifts almost all of the information in the spectrum to the right-hand side. Using a single line-of-best-fit is preferable to constructing *ad hoc* multi-part models of the log-log spectrum [e.g. 104,105] which may fit the spectral data better, but which have less explanatory power.

Figure 6.16 produces values for β of 0.498 for the upper varve spectrum and 0.209 for the lower varve spectrum, on a scale where white noise has $\beta = 0$, "1/f noise" has $\beta = 1$, and red noise has $\beta = 2$. Repeated modelling using randomised time-series suggests that genuine white noise time-series of the same length and variance have $\beta = 0 \pm 0.1$, such that both varve sequences are significantly different from white noise. A brief comparison was made with the frequency scaling characteristics of several other annual-resolution palaeoclimate records, as follows.

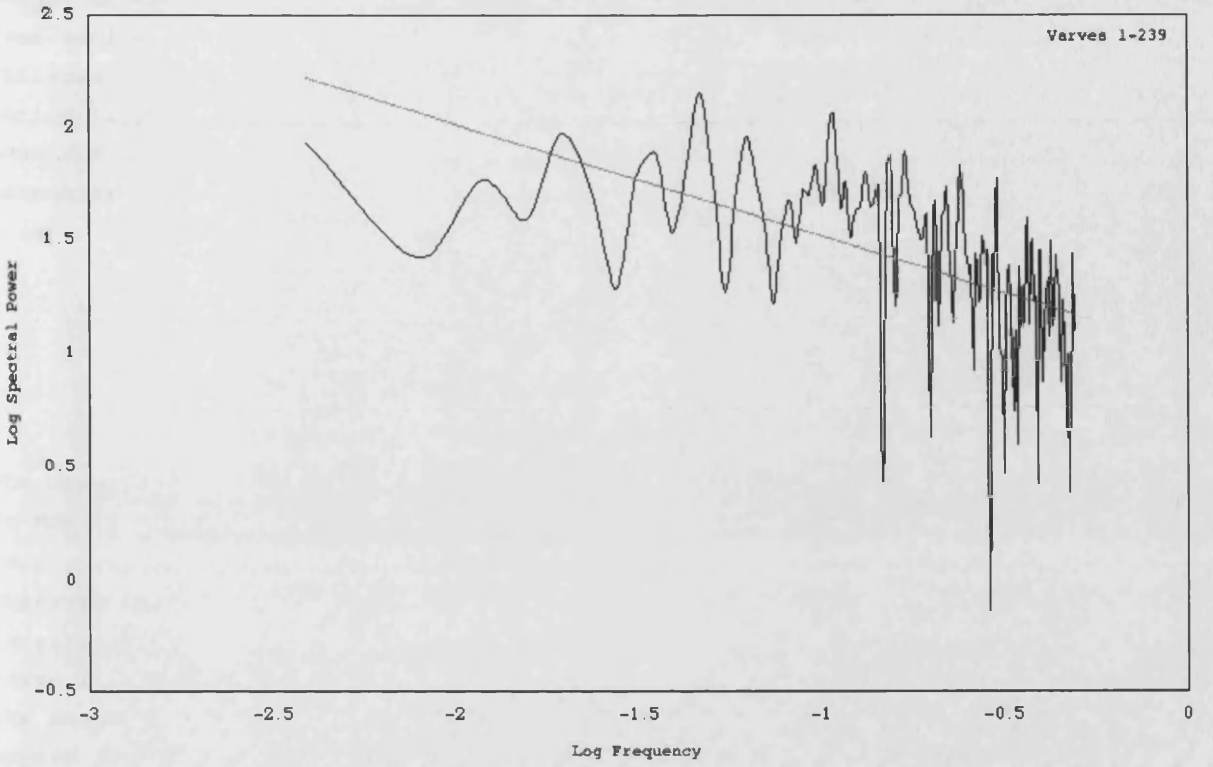

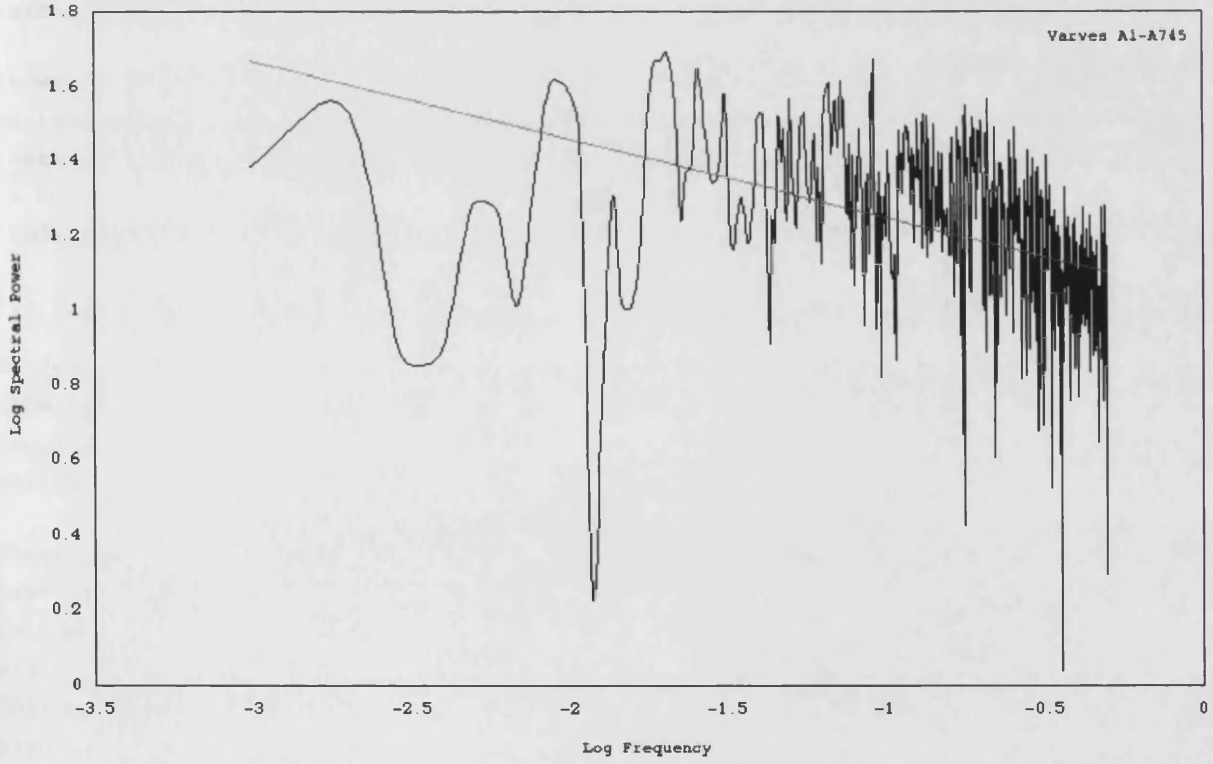

Fig 6.16: Unmodified periodograms for the upper (top) and lower (bottom) varve data, plotted on log-log axes. The grey line in each case is the regression line-of-best-fit.

Annual-resolution data from four other sources were used: the total varve thickness time-series from Drammensfjord (given in section B.1); a series of Pleistocene varve thicknesses from Glacial Lake Hitchcock, New England [106]; another varve thickness series from Elk Lake, Minnesota [107]; and a series of annual-resolution bands measured from a speleothem in Assynt, northwest Scotland [108]. The values of the parameter β were as follows:

Record Location	β value
Drammensfjord, Norway	0.2029
Glacial Lake Hitchcock, New England	0.3528
Elk Lake, Minnesota	0.9981
Assynt speleothem, Scotland	1.1195

The Drammensfjord and Glacial Lake Hitchcock records are scaled similarly to the Lake St Moritz record, in contrast to the Elk Lake and speleothem records which are have β very close to 1, that is, "1/f noise": a form a frequency scaling that has been observed in a range of environmental systems (see section A.6.1). This brief pilot investigation cannot assist with interpreting any physical mechanisms to explain why varve thickness should vary in the way that it does, except to emphasise that even in the absence of any significant cyclicity, the varve time-series investigated do not appear to be simply progressions of random numbers. There is structure in the series, in the form of frequency scaling, which is perhaps a response to mechanisms such as self-organised criticality which may pervade global climate variability [109].

It would be interesting to investigate other varve thickness data from the Lake St Moritz cores, though the variable quality of varve preservation will significantly restrict its availability. This would enable the consistency of the frequency scaling to be assessed and may provide stronger evidence that this approach is superior to the traditional one of modelling "cycles plus noise".

6.2.3 Sediment greyvalue and its links to sediment composition

As described in section 4.5.4, a continuous record of sediment greyvalue was obtained from Lake St Moritz core PSM90.3 using the digital images. Figure 6.17 shows the 5-cm resolution "depth-series" of 224 sediment greyvalue measurements, compared with the series of total organic carbon (TOC) measurements given in Ariztegui *et al.* [110].

There is an obvious strong correlation between sediment greyvalue and TOC content. The same features can be seen in the greyvalue record as in the TOC record: low greyvalues in the lowest part of the core - pale glacial sediment - then a sudden increase at the start of the Holocene, followed by a decline in the mid Holocene and a recent increase following anthropogenic eutrophication. Several smaller peaks in the two records can also be correlated; for example, two occur just below the sudden increase at c. 60cm depth in both curves.

The relationship between sediment greyvalue and TOC content can be clarified by plotting these variables against each other (figure 6.18). At TOC contents above c. 4%, the greyvalue curve levels off, most likely because of the limited dynamic range of the digital imaging system used; nonetheless, the sensitivity of the greyvalue

curve is sufficient to reflect all the major features of the TOC curve. The plot shows what may be an unexpected degree of scatter when the obvious correlation in figure 6.17 is considered; close inspection suggests that the correlation could be improved by minor realignments of the data, perhaps a result of core shrinkage in the time interval between the imaging and the TOC sampling.

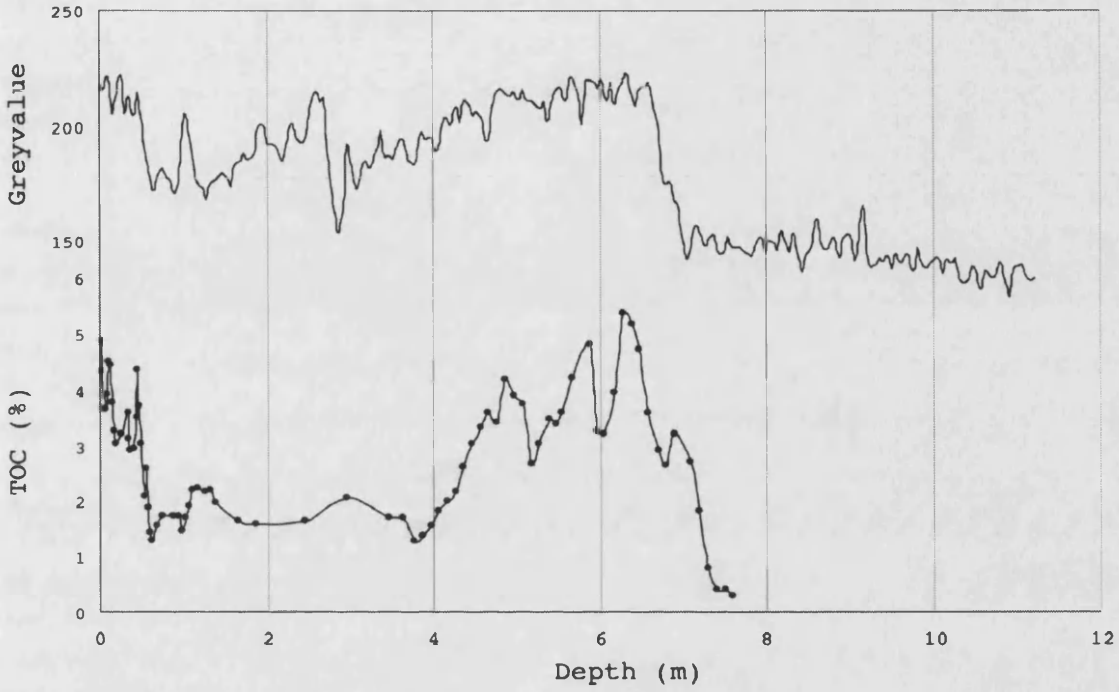

Figure 6.17: Sediment greyvalue (top) and TOC content (bottom) for Lake St Moritz core PSM90.3.

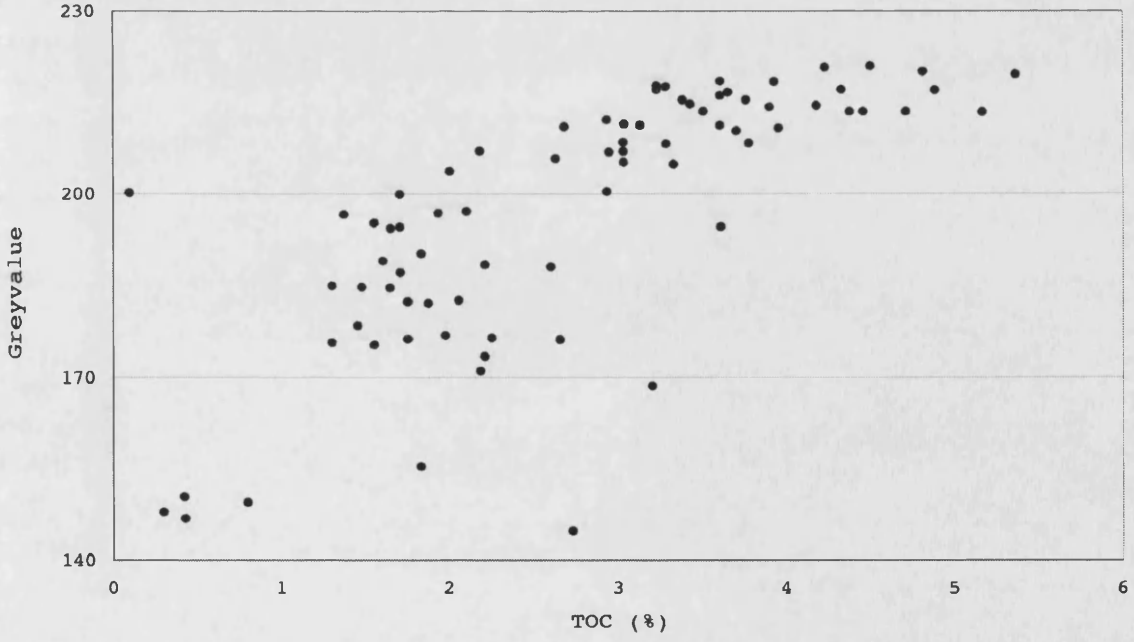

Figure 6.18: Sediment greyvalue plotted against TOC content for Lake St Moritz core PSM90.3.

In addition, there is a further source of scatter in figure 6.18 that limits the usefulness of sediment greyvalue as a proxy for TOC content, namely, the multiple components in the Lake St Moritz sediment. The correlation would be much better if the sediment were to be homogeneous grey clay, with a varying concentration of finely-disseminated organic carbon (which is black in colour), as observed in "black shales" and other carbon-rich sedimentary rocks [111]. In Lake St Moritz, in contrast, greyvalue is influenced by both relatively dark components (e.g. algal organic matter, humics) and relatively light components (e.g. clay, diatoms) whose individual contributions to TOC content are not comparably proportional to their greyvalues. Sediment greyvalue, then, is a proxy for TOC content, though the correlation between the two is inexact.

So, what is the value of having this proxy? Compare the two curves in figure 6.17. There is more detail visible in the greyvalue curve, including a major increase between 2.5m and 3m depth, whereas the TOC curve remains fairly flat in this interval. Conversely, there are also major "troughs" in the TOC curve, for example, at c. 6m depth, which are not present in the greyvalue curve. How can these discrepancies be explained? Firstly, sampling for TOC content is not continuous: there are gaps between the data points, especially in Unit II where the measurements are widely spaced. This is because such destructive sediment sampling is concentrated in intervals where the most interesting features are believed to lie: in the case of Ariztegui *et al.* [110], in the most recent sediment and in the early Holocene. Thus, Unit II is only sparsely sampled, which explains why the peak in the TOC curve is much less noticeable than the peak in the greyvalue curve. (Furthermore, Ariztegui *et al.* [110] note an interval between 2.5m and 3.5m depth of similar dark appearance to the modern eutrophicated interval; presumably this corresponds to the peak seen in the greyvalue record.)

Selective sampling also explains the dip in the TOC curve at c. 6m depth which is not seen in the greyvalue curve. This represents a turbidite, which consists of terrigenous sediment with a very low TOC content [110]. This interval does have a very low greyvalue - it is whitish in colour - but it does not show up on the greyvalue curve because it is too thin (c. 1cm): the 5cm-scale averaging removes it. The 3cm-resolution greyvalue record showed minor features like this turbidite more clearly; however, this curve also had a lower signal-to-noise ratio in terms of representing the continuous background sedimentation of the lake system, which is the focus of the research.

So, the value of sediment greyvalue as a TOC proxy is that it is *continuous* and *high-resolution*. There are many more data points on the greyvalue curve, so it is better supported than the TOC curve - allowing a higher level of confidence that the features seen are "real" - and contains no gaps. It was also relatively easy to obtain, once the TOC data were available. This should enable the investigation of Holocene environmental change at a much higher temporal resolution than that used by Ariztegui *et al.* [110]. However, complications arise because of the proxy nature of the image-derived TOC record, and because of the multiple influences on sediment TOC content over the Holocene. These are discussed in the next section.

6.2.4 Palaeoclimatic inferences from the sediment greyvalue data

6.2.4.1 Environmental influences on organic carbon in lake sediments

The total organic carbon (TOC) content preserved in lake sediments is influenced by multiple environmental factors. For example, organic carbon supply to the lake bottom is linked to productivity in the lake, which is influenced by climate change. This is the chain of reasoning used by Ariztegui *et al.* [110] to link the Lake St Moritz TOC record to Holocene temperature fluctuations, with dark and light intervals within the sediment core arising thereby from a larger or smaller supply of phytoplankton sinking from the surface waters. Sedimentary organic carbon content has also been used as a crude measure of lake productivity variation during the Holocene for Sägistalsee, Switzerland [112], and Lake Kässjön, Sweden [113], among others.

Corroborating evidence for Holocene productivity changes in Lake St Moritz comes from measurements of the hydrogen index (HI) and $\delta^{13}C$ of organic matter from core PSM90.3 (see figure 3.6). The HI correlates with the TOC content [110], indicating that higher TOC reflects increasing preservation of the labile components within the sinking organic matter, owing to a higher degree of productivity-induced anoxia. The $\delta^{13}C$ curve from core PSM90.3 can also be explained by changing productivity over the Holocene: $\delta^{13}C$ anticorrelates with TOC, suggesting that intervals of high TOC are accompanied by increased productivity lowering the availability of CO_2 in the surface waters [110].

However, climate-driven changes in lake productivity are not the only possible causes of changes in sediment TOC content [114]. Changing patterns of organic carbon transport, deposition, and preservation may affect sediment TOC over the Holocene [115], and even if a constant level of diagenetic loss of organic carbon is assumed, there are further complications in the nature of organic carbon supply to the sediments.

- Firstly, not all changes in lake productivity are climate-driven. The most significant of these non-climatic changes is the recent anthropogenic eutrophication seen in many Alpine lakes as a result of fertiliser and sewage discharge [114]; however, anthropogenic effects on lake productivity are not limited to the last century or so, and have affected some lakes over thousands of years. These effects are discussed in more detail with regard to Lake St Moritz in section 6.2.4.2.

- Secondly, not all organic matter within lake sediment comes from biological productivity within the lake; it can also come from vegetation or soils in the catchment area, for example. Autochthonous and allochthonous organic matter can in some cases be distinguished by studying their compositions [116]. For example, Cranwell [117] used the chain length of *n*-alkanes to distinguish between allochthonous sources (e.g. deciduous trees, peat) and autochthonous sources (e.g. algae) of organic matter. In some oligotrophic upland lakes, such as those studied by Mackereth [118] and Cranwell [117], most of the organic matter in the sediment

is allochthonous, and the Holocene sediment TOC record essentially represents a series of soils eroded from the catchment [118].

- Thirdly, sediment TOC content is a percentage measure, and as such is influenced by factors other than the supply of organic matter, especially by the supply of clastic material to the lake. Differential dilution of organic matter arising from a changing rate of clastic sediment accumulation will result in fluctuations in the TOC record that are independent of changes in productivity [119].

These multiple influences on sediment composition are certain to have influenced the Lake St Moritz record, and must be acknowledged before any interpretation of this record can be attempted. Consider first the expected evolution of sedimentary organic carbon content over the Holocene, as originally explained by Mackereth (1966) working in the English Lake District [118]. During intervals when vegetation cover is lacking, such as at the start of the Holocene, rapid erosion occurs, bringing relatively unweathered material into the lake, and producing sediment with a high clastic content and a low organic carbon content. During intervals when vegetation cover is well-developed, in contrast, the bedrock is weathered more deeply *in situ*, leaching out ions which promote lake productivity and reducing the input of clastic material to the lake, resulting in a relatively higher organic carbon content.

As a result of this differential leaching, the concentration of cations such as Na^+ and K^+ is a proxy for relative soil erosion intensity in the catchment [120]. Mackereth combined this proxy with several observed TOC records, in order to explain changes in organic matter accumulation over the Holocene with reference to changes in erosion intensity [118]. The concentration of these cations was linearly proportional to the percentage of clastic material in the lake sediment, indicating that "the variation in gross composition of the lake sediments with time must then be related primarily to variation in time of the intensity of erosion in the drainage system rather than to variation in the rate of production and deposition of organic matter" [118].

As noted above, weathering in the catchment can itself influence lake productivity, such that the overall record of sediment TOC should preserve both the direct effect of clastic dilution of organic matter and the indirect effect of increased productivity stimulated by leached nutrients during intervals of slower erosion. The direct effect of climate change on productivity itself, e.g. via changing water temperature, is likely to be overshadowed by these effects of changing catchment erosion. However, two factors combine to make the Lake St Moritz record a more sensitive proxy for lake productivity than those lakes studied by Mackereth [118]: firstly, the latter were oxygenated, with the redox cline at the sediment surface, such that only refractive organic matter was preserved, weakening the productivity signal in the sediment record, unlike in Lake St Moritz, whose varved fabric indicates at least seasonal anoxia throughout the Holocene; secondly, Lake St Moritz is at the end of a chain of four Alpine lakes, which reduces the clastic input it receives from the River Inn, again serving to increase the productivity signal by decreasing the effect of clastic dilution of organic matter.

The direct effect of changing temperature on the balance between eutrophy and oligotrophy in alpine lakes occurs via the following two pathways described by Psenner [121]: warming increases lake productivity, leading to eutrophication, and cooling decreases lake productivity, leading to oligotrophication. Psenner notes that these pathways are gross simplifications of complex natural systems [121]. There is evidence, however, for links between palaeotemperature and palaeoproductivity records from alpine lakes, at least for centennial-to-millennial-scale variability.

- For example, from Lake Zürich, a large pre-Alpine lake: a productivity record derived from the same proxies as that of Lake St Moritz: sediment TOC content and $\partial^{13}C$ [122]. Inferred productivity shows a considerable increase at the start of the Holocene, reaches a maximum at c. 3,850 BP, then declines. Furthermore, a temperature proxy record from $\partial^{18}O$ is also available. The $\partial^{13}C$ curve is a mirror image of the $\partial^{18}O$ curve, suggesting that warmer and cooler periods correspond to periods of enhanced and reduced productivity, even for minor climate changes [122].

- Similarly, from Lake Candia, northern Italy, a productivity record based on algal pigments is available [123]. This only goes back to c. 2,000 BP, but it shows how the productivity of the lake is affected by centennial-to-millennial climate change: at 2,000 BP, productivity is low; it then rises during the "Mediaeval Warm Period" (c. 900-700 BP), then falls again during the "Little Ice Age" (c. 450-300 BP).

Nonetheless, sediment TOC content in Lake St Moritz is heavily influenced by the degree of clastic dilution, as explained above, in addition to lake productivity. The HI and $\delta^{13}C$ evidence described by Ariztegui *et al.* [110] is inconclusive in its support for the productivity-based explanation of TOC variations: HI varies with the source organism of the organic matter as well as its degree of anoxia-induced preservation, and a reduction in $\delta^{13}C$ is only a distinctive signature for intra-water-column algal blooms as long as variation in other factors such as temperature, pH, nutrient availability, and growth rates, is minimal [116]. As observed at the present day, in Lake St Moritz [124] and in other Alpine lakes such as Greifensee [125], TOC, HI, $\delta^{13}C$, and lake productivity are linked, but the current interval of significant anthropogenic eutrophication may not be representative of the remainder of the Holocene. The analogy drawn between this recent eutrophicated interval and the early Holocene rise in sediment TOC in Lake St Moritz by Ariztegui *et al.* [110] may, therefore, be flawed.

Some changes in lake productivity over the Holocene fit a common pattern. For example, a significant spike in productivity is expected during the earliest Holocene [114] as a result of high availability of nutrients from adjacent deglaciated terrestrial areas. A prolonged increase in early Holocene productivity may be caused by the establishment of anoxia arising from increased organic matter supply, as noted by Livingstone in his study of Linsley Pond [126], resulting in *more intense recycling* of nutrients. Further Holocene productivity changes vary depending on the ontogeny of the particular lake in question.

For example, as the lake fills with sediment and becomes shallower, productivity will tend to increase, causing a progression from oligotrophy to eutrophy over the Holocene; in contrast, some lakes undergo the reverse process, so-called meiotrophication, as a result of progressive leaching of the catchment leaving behind nutrient-poor acid soils which can no longer support high lake productivity. Deevey [127] notes that lakes will simply become "as eutrophic as the geological conditions allow"; the levels of nutrient loading and internal nutrient recycling, and hence the pseudo-equilibrium productivity level, will vary from lake to lake [114]. Even if the TOC record were unaffected by clastic dilution, subtracting these ontogenetic processes from a record of lake productivity in order to isolate wiggles driven directly by climate change would not be simple.

6.2.4.2 Anthropogenic effects on lake productivity and sediment accumulation

As noted earlier, further complications in interpreting Holocene records of lake sediment composition arise from anthropogenic effects on lakes and their surroundings. For example, detailed work on Frains Lake, Michigan [128], showed that following forest clearance in AD 1830, sediment yields rose seventy-fold as a result of ploughing and construction, later stabilising (c. AD 1900) at a level ten times greater than the Holocene "background". As well as this increase in sediment accumulation, the increased erosion drove an increase in lake productivity after AD 1830, resulting in a 13% increase in the organic matter content of the lake sediment [128]. Comparable effects have been found for much earlier anthropogenic activity recorded in other lakes: in Linsley Pond, New England, for example, an increased silt yield, mobilised by prehistoric agriculture, is apparent in the sediment record after c. 5,000 BP [126].

As far as the Lake St Moritz area is concerned, archaeological finds are rare in the Upper Engadine valley. Isolated Neolithic artefacts are known from c. 5,500 BP onwards, and it is known that Neolithic man could travel over high alpine passes (e.g. "Iceman Ötzi", found at Hauslabjoch, in the Austrian Alps, at 3,200m altitude, and dated to c. 5,300 - 5,050 BP [129]). However, the earliest evidence of continuous settlement in the Lake St Moritz area is in the Bronze Age, after c. 3,950 BP [130].

A massive wooden water trough, used to collect water from the St Moritz spring, has been dated to 3,416 BP [131], and a knife blade is known from c. 3,550 BP [110]. Better evidence of continuous disturbance comes from pollen records from Lake St Moritz [132], which show the rise of *Alnus viridis* (alder) and *Larix decidua* (larch) after c. 3,900 BP, a pattern which occurs widely across the western Alps [133] and which is thought to have been induced by anthropogenic deforestation. Evidence from charcoal analysis and fern spores suggests that controlled burning was used to produce "larch meadows", used for grazing [132]; in addition to the production of farmland, trees were felled to fuel copper smelting [134].

So, there have been substantial pre-industrial anthropogenic effects on the catchment of Lake St Moritz, in addition to the more recent changes in sediment accumulation and lake productivity resulting from the development of tourism detailed in section 3.2. Indeed, the combination of a gradual ecological progression over the early Holocene,

with the Bronze Age and later effects of mankind, mean that there is only a relatively short interval in the mid-Holocene where sedimentation in Lake St Moritz is expected to be influenced directly by climate change. The next section considers the implications of this for the application of time-series analysis to the Lake St Moritz sediment greyvalue record.

6.2.4.3 Spectral analysis of the Lake St Moritz sediment greyvalue record

Spectral analysis treats the Lake St Moritz record as a realisation of a single, stationary climate process, so the data need to be edited accordingly. Obviously, the data from the last century need to be removed, since the cultural eutrophication that they reflect is unconnected to climate change. The dramatic rise in productivity at the start of the Holocene also needs to be removed, since although this does represent a response to natural climate change, it is part of a low-frequency cycle which cannot be adequately studied given the timespan of the data. If it were not removed, it would dominate the spectrum and obscure the minor, within-Holocene variability which is of interest. The Lake St Moritz record thus needs to be truncated at each end. A linear detrend is also necessary to improve the stationarity of the time-series.

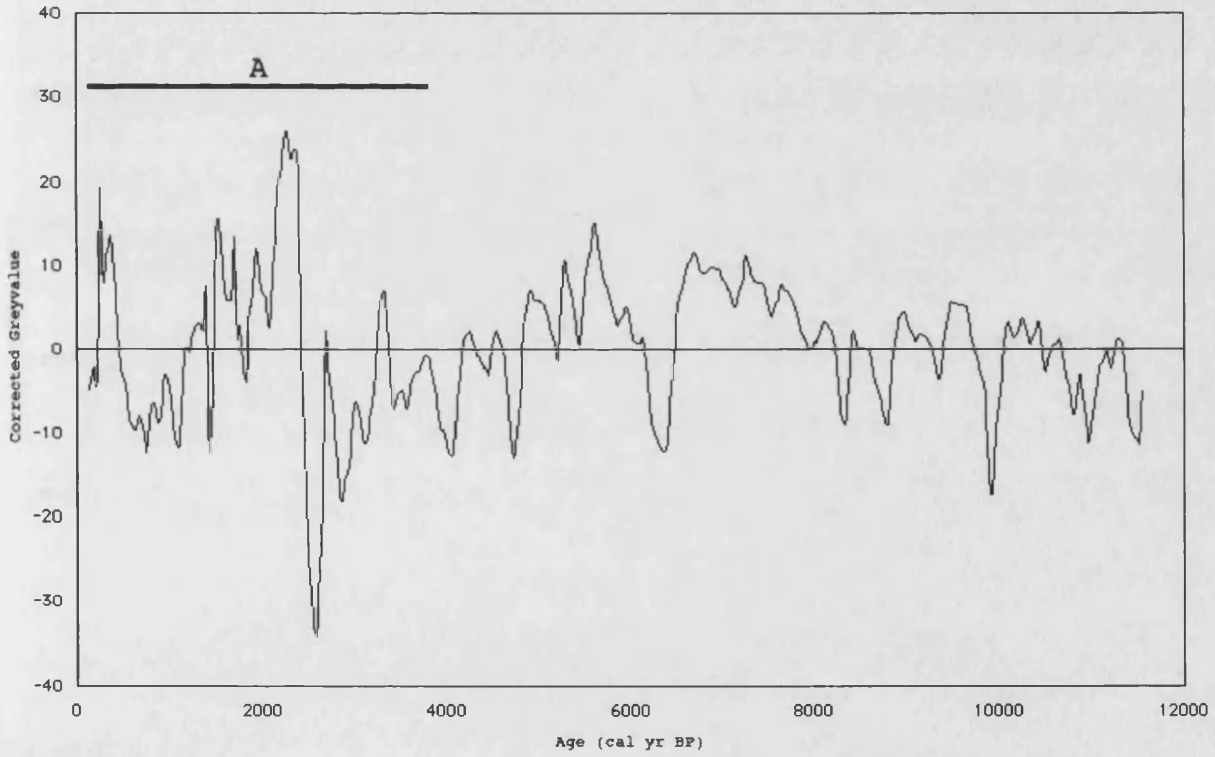

Figure 6.19: Sediment greyvalue time-series from Lake St Moritz core PSM90.3, as shown in Figure 5.24, following truncation at both ends and linear detrend. The horizontal bar marked 'A', beginning at c. 3,900 BP, denotes the interval during which significant anthropogenic disturbance is suspected (see section 6.2.4.2).

The removal of pre-AD-1900 anthropogenic disturbances from the sediment greyvalue record is more difficult; all variability within the zone marked 'A' in figure 6.19 must be suspect in this respect. Land-use changes may have caused greater clastic dilution of the organic matter in the lake sediment, and possibly also increased lake

productivity and hence organic matter flux to the sediment; the age model (shown in figure 5.23) shows no major changes in sediment accumulation rate since c. 3,900 BP, but this part of the radiocarbon chronology is poorly constrained, meaning that centennial-scale variability in sediment accumulation could have been overlooked. One possibility is to perform spectral analysis with and without this zone of anthropogenic disturbance in order to reveal its effect on the stability of the results, bearing in mind that filtered spectra should be relatively insensitive to the addition of low levels of noise, providing that any underlying signals are consistent (which may not, of course, be the case for Holocene climate variability).

The highest frequency that can be detected in the data is 0.5 (the Nyquist frequency; see section A.4.3.2) which is equivalent to 0.5 cycles in 30 years, or a period of 60 years. The lowest frequency that can adequately be detected depends on the technique used; for the filtered periodogram, Chatfield [30] suggests a limit of N/4, which is approximately 2,850 years for the Lake St Moritz record. The spectrum of the full Lake St Moritz sediment greyvalue record is shown in figure 6.20.

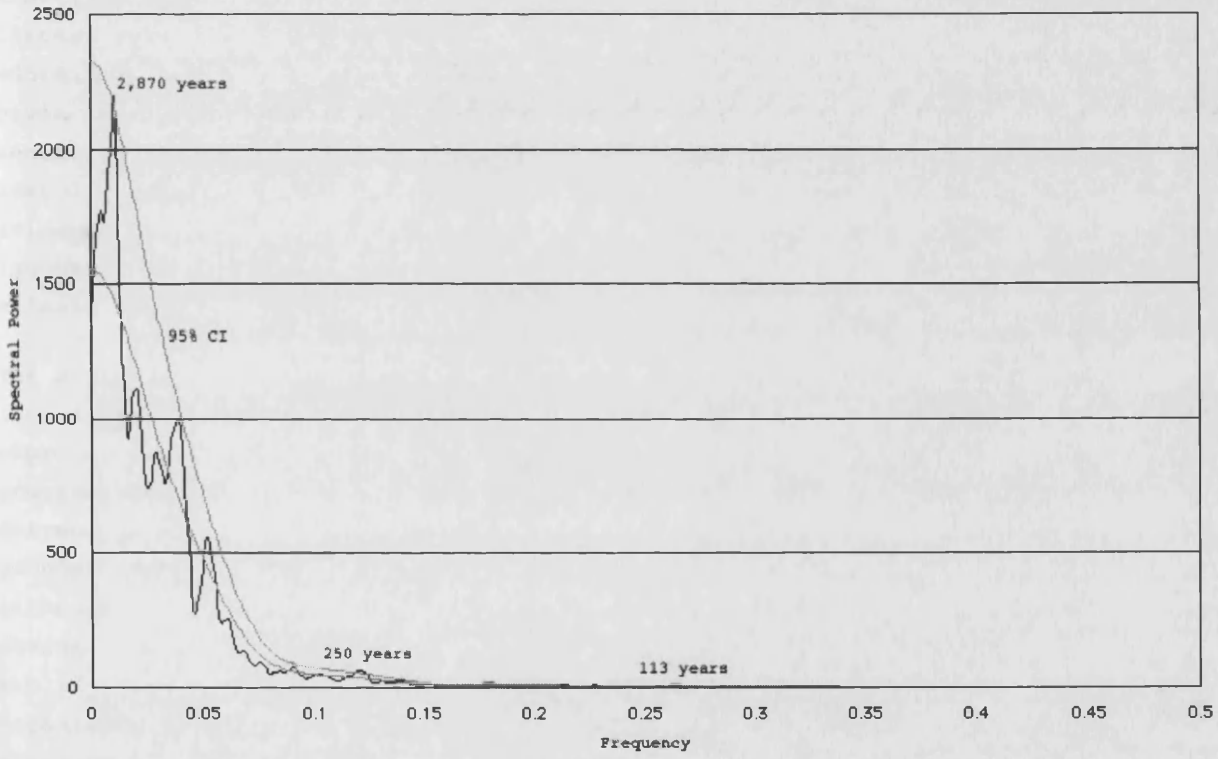

Figure 6.20: Spectrum of the Lake St Moritz sediment greyvalue record, filtered using a Blackman-Tukey parameter of 0.333. The lower grey line is the null hypothesis: the same spectrum with a Blackman-Tukey parameter of 0.05. The upper grey line is the 95% significance level estimated from this. The periods of significant stable peaks are labelled.

Almost all of the spectral power in figure 6.20 is at frequencies less than 0.1; that is, at periods greater than 300 years. The sediment greyvalue spectrum is, therefore, very much redder than the varve thickness spectra in figure 6.15; this is partly a result of the presence of non-stationary features in the time-series, even following the processing described earlier: for example, the linear interpolation described in

section 5.3.6 will have reddened the spectrum. One consequence of this is that when plotted on a linear scale as in figure 6.20, spectral power at frequencies greater than 0.1 appears to be close to zero, although there can still be significant spectral peaks at these frequencies: selecting an appropriate null hypothesis is important. The reddened shape of the spectrum also holds for the greyvalue time-series that omits the anthropogenic zone indicated in figure 6.19. In this spectrum, the two peaks in figure 6.20 at periods of c. 600 and 800 years become stronger, but these are of less interest than spectral peaks that are statistically significant in both spectra, i.e. which appear to be persistent over the Holocene. There are three of these, at periods of c. 2,870, 250, and 113 years, as labelled in figure 6.20.

The peak at c. 2,870 years is poorly-constrained because of the length of the time-series, as noted earlier: suspected cycles of this length require time-series longer than the Holocene in order to characterise them adequately. Furthermore, the peak at 250 years is close to the expected frequency of *one cycle per digital image* and is thus suspect. This leaves the third peak at 113 years; rejecting this as a type I error, a conservative approach could interpret the whole Lake St Moritz sediment greyvalue record as reddish noise. Pre-whitening of the spectrum, combined with a flatter null hypothesis curve, could potentially result in as many as twelve additional "significant" spectral peaks at frequencies greater than 0.1; however, given the complexity of the influences on sediment greyvalue discussed earlier in section 6.2.4, it is doubtful as to whether such additional spectral detail could be usefully interpreted. It is worth noting, finally, that there is definitely no evidence for a c. 1,500-year cycle in this time-series: a cycle which has long been suggested to have occurred over the Holocene [135] and which has been found in various climate proxy records [136-139].

The major difficulty in interpretation of the sediment greyvalue data, as noted above, lies in separating the different factors influencing sediment composition. The expected early Holocene decrease in clastic dilution of organic matter, arising from progressive development of catchment vegetation, may have been largely removed by the detrend of the time-series, but the remaining variability is impossible to partition amongst direct climatic effects, catchment erosion effects, and anthropogenic effects, although the latter two categories are expected to be strongly influenced by climate change. Prehistoric anthropogenic variability, especially, has been observed to amplify natural climate variability, e.g. where areas of Alpine pasture have been repeatedly abandoned during cold intervals and re-cultivated during warm intervals, as observed in sediment records from other Swiss lakes such as Sägistalsee [112] and Seebergsee [140]. But there are also technological and political influences on human history, which have no climatic affinity.

High-resolution records of sediment greyvalue from digital images can evidently refine the quality of compositional data from laminated lake sediments, revealing a history of centennial-scale variability, but similar refinements in data interpretation are difficult without additional historical and proxy data. Some suggestions are made in the conclusions about possibilities for further progress.

Chapter 6 References

[1] Mikalsen, G., Sejrup, H. P., and Aarseth, I., 2001, Late-Holocene changes in ocean circulation and climate: foraminiferal and isotopic evidence from Sulafjord, western Norway, The Holocene, 11:437-446.

[2] Gustafsson, M., and Nordberg, K., 2002, The impact of climate and shore-level displacement on the late-Holocene environmental development of Havstens Fjord and Koljö Fjord, Swedish west coast, The Holocene, 12:325-338.

[3] Alve, E., 1991, Foraminifera, climatic change, and pollution: a study of late Holocene sediments in Drammensfjord, southeast Norway, The Holocene, 1:243-261.

[4] Petterson, G., Odgaard, B. V., and Renberg, I., 1999, Image analysis as a method to quantify sediment components, Journal of Paleolimnology, 22:443-455.

[5] Magnusson, J., and Næs, K., 1986, Basis undersøkelser i Drammensfjorden 1982-84: Delrapport 6: Hydrografi, vannkvalitet og vannutskiftning, NIVA-rapport, Overvåkningsrapport 243/86, 77 pp.

[6] Anderson, R. Y., and Koopmans, L. H., 1963, Harmonic analysis of varve time-series, Journal of Geophysical Research, 68:877-893.

[7] Frich, P., Alexandersson, H., Ashcroft, J., Dahlström, B., Demarée, G. R., Drebs, A., van Engelen, A. F. V., Førland, E. J., Hanssen-Bauer, I., Heino, R., Jónsson, T., Jonasson, K., Keegan, L., Nordli, P. Ø., Schmith, T., Steffensen, P., Tuomenvirta, H., and Tveito, O. E., 1996, North Atlantic Climatological Database (NACD Version 1) - Final Report, Danish Meteorological Institute Scientific Report 96-1, 71 pp.

[8] Manley, G., 1974, Central England Temperatures, monthly means from 1659 to 1973, Quarterly Journal of the Royal Meteorological Society, 79:242-261. See also Parker, D. E., Legg, T. P., and Folland, C. K., 1992, A new daily Central England Temperature series, 1772-1991, International Journal of Climatology, 12:317-342.

[9] Eklund, A., 1999, Long observation series of ice freeze and break-up data in Swedish lakes, In: Proceedings from the Northern Research Basins 12th International Symposium and Workshop, Reykjavik, Iceland, 23-27th August 1999.

[10] Schweingruber, F. H., 1978, Scots Pine Tree ring data set, Gotland, Sweden, IGBP PAGES/World Data Center for Paleoclimatology Data Contribution Series 5630-1500, NOAA/NGDC Paleoclimatology Program, Boulder, Colorado, USA.

[11] Schweingruber, F. H., 1978, Scots Pine Tree ring data set, Jamtland, Sweden, IGBP PAGES/World Data Center for Paleoclimatology Data Contribution Series 5330-1530, NOAA/NGDC Paleoclimatology Program, Boulder, Colorado, USA.

[12] Lowe, J. J., and Walker, M. J. C., 1997, Reconstructing Quaternary Environments, Second Edition, Longman, 446 pp.

[13] Jones, P. D., Briffa, K. R., Barnett, T. P., and Tett, S. F. B., 1998, High-resolution palaeoclimatic records for the last millennium: interpretation, integration and comparison with General Circulation Model control-run temperatures, The Holocene, 8:455-471.

[14] Perry, A., 2000, The North Atlantic Oscillation: an enigmatic see-saw, Progress in Physical Geography, 24:289-294.

[15] Rodo, X., Baert, E., and Comin, F., 1997, Variations in seasonal rainfall in southern Europe during the present century: relationships with the NAO and the El Niño-Southern Oscillation, Climate Dynamics, 13:275-284.

[16] Cullen, H. M., Kaplan, A., Arkin, P. A., and deMenocal, P. B., 2002, Impact of the North Atlantic Oscillation on Middle Eastern climate and streamflow, Climatic Change, 55:315-338.

[17] Hanssen-Bauer, I., and Førland, E., 2000, Temperature and precipitation variations in Norway 1900-1994 and their links to atmospheric circulation, International Journal of Climatology, 20:1,693-1,708.

[18] Chen, D., and Hellström, C. H., 1999, The influence of the North Atlantic Oscillation on the regional temperature variability in Sweden: spatial and temporal variations, Tellus, 51A:505-516.

[19] Koslowski, G., and Loewe, P., 1994, The western Baltic ice season in terms of mass-related severity index: 1879-1992. Part I: temporal variability and association with the North Atlantic Oscillation, Tellus, 46A:66-74.

[20] Pohjola, V. A., and Rogers, J. C., 1997, Atmospheric circulation and variations in Scandinavian glacier mass balance, Quaternary Research, 47:29-36.

[21] Houghton, J. T., Ding, Y., Griggs, D. J., Noguer, M., van der Linden, P. J., and Xiaosu, D., (Eds.), 2001, Climate Change 2001: The Scientific Basis, Contribution of Working Group I to the Third Assessment Report of the Intergovernmental Panel on Climate Change (IPCC), Cambridge University Press, 944 pp.

[22] Dale, B., Thorsen, T. A., and Fjellså, A., 1999, Dinoflagellate cysts as indicators of cultural eutrophication in the Oslofjord, Norway, Estuarine and Coastal Shelf Science, 48:371-382.

[23] Pinturier-Geiss, L., Méjanelle, L., Dale, B., and Karlsen, D. A., 2002, Lipids as indicators of eutrophication in marine coastal sediments, Journal of Microbiological Methods, 48:239-257.

[24] Jones, P. D., Jónsson, T., and Wheeler, D., 1997, Extension to the North Atlantic Oscillation using early instrumental pressure observations from Gibraltar and south-west Iceland, International Journal of Climatology, 17:1,433-1,450.

[25] Cook, E. R., D'Arrigo, R. D., and Briffa, K. R., 1998, The North Atlantic Oscillation and its expression in circum-Atlantic tree-ring chronologies from North America and Europe, The Holocene, 8:9-17.

[26] Luterbacher, J.,Schmutz, C., Gyalistras, D., Xoplaki, E., and Wanner, H., 1999, Reconstruction of monthly NAO and EU indices back to AD 1675, Geophysical Research Letters, 26:2,745-2,748.

[27] Glueck, M. F., and Stockton, C. W., 2001, Reconstruction of the North Atlantic Oscillation, 1429-1983, International Journal of Climatology, 21:1,453-1,465.

[28] Luterbacher, J., Xoplaki, E., Dietrich, D., Jones, P.D., Davies, T.D., Portis, D., Gonzalez-Rouco, J.F., von Storch, H., Gyalistras, D., Casty, C., and Wanner, H., 2002. Extending North Atlantic Oscillation reconstructions back to 1500, Atmospheric Science Letters, 2:114-124. The NAO data are freely available from the UEA website at http://www.cru.uea.ac.uk/cru/data/naojurg.htm.

[29] Appenzeller, C., Stocker, T. F., and Anklin, M., 1998, North Atlantic Oscillation dynamics recorded in Greenland ice cores, Science, 282:446-449.

[30] Chatfield, C., 1996, The Analysis of Time-series: An Introduction, Fifth Edition, Chapman and Hall / CRC, 283 pp.

[31] Baumgartner, T. R., Michaelsen, J., Thompson, L. G., Shen, G., Soutar, A., and Casey, R., 1989, The recording of interannual climatic change by high-resolution natural systems: tree-rings, coral bands, glacial ice layers, and marine varves, Geophysical Monograph, 55:1-14.

[32] Lotter, A. F., and Birks, H. J. B., 1997, The separation of the influence of nutrients and climate on the varve time-series of Baldeggersee, Switzerland, Aquatic Sciences, 59:362-375.

[33] Katz, R. W., and Brown, B. G., 1992, Extreme events in a changing climate: variability is more important than averages, Climatic Change, 21:289-302.

[34] Lockwood, J. G., 2001, Abrupt and sudden climatic transitions and fluctuations: a review, International Journal of Climatology, 21:1,153-1,179.

[35] Lorenz, E. N., 1976, Nondeterministic theories of climate change, Quaternary Research, 6:495-506.

[36] Tsay, R. S., 1988, Outliers, level shifts, and variance changes in time series, Journal of Forecasting, 7:1-20.

[37] Wohlfarth, B., Holmquist, B., Cato, I., and Linderson, H., 1998, The climatic significance of clastic varves in the Ångermanälven Estuary, northern Sweden, AD 1860 to 1950, The Holocene, 8:521-534.

[38] Granar, L., 1956, Dating of recent fluvial sediments from the estuary of the Ångermanälven river, Geologiska Föreningens i Stockholm Förhandlingar, 78:654-658.

[39] Cato., I., 1985, The definitive connection of the Swedish geochronological time scale with the present, and the new date of the zero year in Döviken, northern Sweden, Boreas, 14:117-122.

[40] Zolitschka, B., 1996, High resolution lacustrine sediments and their potential for palaeoclimatic reconstruction, In: Jones, P. D., Bradley, R. S., and Jouzel, J., (Eds.), Climatic Variations and Forcing Mechanisms of the Last 2,000 years, NATO ASI Series, Vol. 141, p. 453-478, and references therein.

[41] Viessman, W., and Lewis, G. L., 1996, Introduction to Hydrology, Fourth Edition, HarperCollins, 759 pp.

[42] Brown, S. L., Bierman, P. R., Lini, A., and Southon, J., 2000, 10,000 year record of extreme hydrologic events, Geology, 28:335-338.

[43] Lamoureux, S., 2000, Five centuries of interannual sediment yield and rainfall-induced erosion in the Canadian High Arctic recorded in lacustrine varves, Water Resources Research, 36:309-318.

[44] Hardy, D. R., Bradley, R. S., and Zolitschka, B., 1996, The climatic signal in varved sediments from Lake C2, northern Ellesmere Island, Canada, Journal of Paleolimnology, 16:227-238.

[45] Sonett, C. P., Williams, C. R., and Mörner, N.-A., 1992, The Fourier spectrum of Swedish riverine varves: evidence of sub-arctic quasi-biennial (QBO) oscillations, Palaeogeography, Palaeoclimatology, Palaeoecology, 98:57-65.

[46] Ohlendorf, C., Niessen, F., and Weissert, H., 1997, Glacial varve thickness and 127 years of intrumental climate data: a comparison, Climatic Change, 36:391-411.

[47] Leemann, A., and Niessen, F., 1994, Varve formation and the climatic record in an Alpine proglacial lake: calibrating annually-laminated sediments against hydrological and meteorological data, The Holocene, 4:1-8.

[48] Lamb, H. H., 1995, Climate, History, and the Modern World, Second Edition, Routledge, 433 pp.

[49] Flohn, H., 1993, Climatic evolution during the last millennium: what can we learn from it?, In: Eddy, J. A., and Oeschger, H., (Eds.), Global Changes in the Perspective of the Past, John Wiley and Sons, p. 295-316.

[50] Grove, J. M., 2001, The initiation of the "Little Ice Age" in regions round the North Atlantic, Climatic Change, 48:53-82.

[51] Grove, J. M., 1988, The Little Ice Age, Routledge, 500 pp.

[52] Starkel, L., 2002, Change in the frequency of extreme events as the indicator of climatic change in the Holocene (in fluvial systems), Quaternary International, 91:25-32.

[53] Starkel, L., 1985, The reflection of the Holocene climatic variations in the slope and fluvial deposits and forms in the European mountains, Ecologia Mediterranea, 11:91-97.

[54] Fagan, B., 2002, The Little Ice Age: How Climate Made History 1300-1850, Basic Books, 272 pp.

[55] Nesje, A., and Dahl, S. O., 2002, The "Little Ice Age" - only temperature?, The Holocene, 13:139-145.

[56] Grove, J. M., and Battagel, A., 1983, Tax records from western Norway, as an index of Little Ice Age environmental and economic deterioration, Climatic Change, 5:265-282.

[57] Straffin, E. C., and Blum, M. D., 2002, Holocene fluvial response to climate change and human activities: Burgundy, France, Netherlands Journal of Geosciences, 81:417-430.

[58] Mazzarella, A., and Diodato, N., 2002, The alluvial events in the last two centuries at Sarno, southern Italy: their classification and power-law time occurrence, Theoretical and Applied Climatology, 72:75-84.

[59] Maas, G. S., and Macklin, M. G., 2002, The impact of recent climate change on flooding and sediment supply within a Mediterranean mountain catchment, southwestern Crete, Greece, Earth Surface Processes and Landforms, 27:1,087-1,105.

[60] Dawson, A. G., Hickey, K., Holt, T., Elliott, L., Dawson, S., Foster, I. D. L., Wadhams, P., Jonsdottir, I., Wilkinson, J., McKenna, J., Davis, N. R., and Smith, D. E., 2001, Complex North Atlantic Oscillation (NAO) Index signal of historic North Atlantic storm-track changes, The Holocene, 12:363-369.

[61] Winkler, S., 2003, A new interpretation of the date of the "Little Ice Age" glacier maximum at Svartisen and Okstindan, northern Norway, The Holocene, 13:83-95.

[62] It is likely that historical flood records for the Drammen catchment are somewhere in existence - there has been a concentration of important industry in the region for centuries - though if so, they are inaccessible from the UK. The ongoing rediscovery of historical records is covered in PAGES News, v. 10(3), December 2002, and includes an exactly comparable pattern of increased river floods during the LIA for the River Pegnitz, Nuremburg, Germany, derived from historical records. See Brázdil, R., Glaser, R., Pfister, C., and Stangl, H., 2002, Floods in Europe - a look into the past, PAGES News, 10:23-25.

[63] Lie, Ø., Dahl, S. O., and Nesje, A., 2003, Theoretical equilibrium-line altitudes and glacier build-up sensitivity in southern

Norway based on meteorological data in a geographical information system, The Holocene, 13:373-380.

[64] Vos, H., Sanchez, A., Zolitschka, B., Brauer, A., and Negendank, J. F. W., 1997, Solar activity variations recorded in varved sediments from the crater lake of Holzmaar - a maar lake in the Westeifel volcanic field, Germany, Surveys in Geophysics, 18:163-182.

[65] Renberg, I., Segerström, U., and Wallin, J.-E., 1984, Climatic reflection in varved lake sediments, in: Mörner, N.-A., and Karlén, W., (Eds.), Climatic Changes on a Yearly to Millennial Basis, D. Reidel Publishing Company, p. 249-256.

[66] Mingram, J., 1998, Laminated Eocene maar-lake sediments from Eckfeld (Eifel region, Germany) and their short-term periodicities, Palaeogeography, Palaeoclimatology, Palaeoecology, 140:289-305.

[67] Sonett, C. P., and Williams, G. E., 1985, Solar periodicities expressed in varves from glacial Skilak Lake, southern Alaska, Journal of Geophysical Research, 90:12,019-12,026.

[68] Svenonius, B., and Olaussen, E., 1979, Cycles in solar activity, especially of long periods, and certain terrestrial relationships, Palaeogeography, Palaeoclimatology, Palaeoecology, 26:89-97.

[69] Bryant, E., 1997, Climate Process and Change, Cambridge University Press, 209 pp.

[70] Wigley, T. M. L., and Kelly, P. M., 1990, Holocene climatic change, ^{14}C wiggles and variations in solar irradiance, Philosophical Transactions of the Royal Society of London, A, 330:547-560.

[71] Bradley, W. H., 1929, The varves and climate of the Green River Epoch, U.S. Geological Survey Professional Papers, 158:87-110.

[72] Douglass, A. E., 1919, A study of the annual rings of trees in relation to climate and solar activity, Carnegie Institution of Washington, 127 pp.

[73] Haigh, J. D., 1994, The role of stratospheric ozone in modulating the solar radiative forcing of climate, Nature, 370:544-546.

[74] Svensmark, H., and Friis-Christensen, E., 1997, Variation of cosmic ray flux and global cloud coverage - a missing link in solar-climate relationships, Journal of Atmospheric and Solar-Terrestrial Physics, 59:1,225-1,232.

[75] Weiss, N. O., 1990, Periodicity and aperiodicity in solar magnetic activity, Philosophical Transactions of the Royal Society of London, A, 330:617-625.

[76] Berger, A., Mélice, J. L., Van Der Mersch, I., 1990, Evolutive spectral analysis of sunspot data over the past 300 years, Philosophical Transactions of the Royal Society of London, A, 330:529-541.

[77] Friis-Christensen, E., and Lassen, K., 1991, Length of the solar cycle: an indicator of solar activity closely associated with climate, Science, 254:698-700.

[78] Baldwin, M. P., Gray, L. J., Dunkerton, T. J., Hamilton, K., Haynes, P. H., Randel, W. J., Holton, J. R., Alexander, M. J., Hirota, I., Horinouchi, T., Jones, D. B. A., Kinnersley, J. S., Marquardt, C., Sato, K., and Takahashi, 2001, The quasi-biennial oscillation, Reviews of Geophysics, 39:179-229.

[79] Teitelbaum, H., and Bauer, P., 1990, Stratospheric temperature eleven-year variations: solar cycle influence or stroboscopic effect?, Annales Geophysicae, 8:239-242.

[80] Labitzke, K., and van Loon, H., 1990, Associations between the 11-year solar cycle, the quasi-biennial oscillation and the atmosphere: a summary of recent work, Philosophical Transactions of the Royal Society of London, A, 330:577-589.

[81] Dewan, E. M., and Shapiro, R., 1991, Are sunspot-weather correlations real?, A discussion of [147], Journal of Atmospheric and Terrestrial Physics, 53:171-174.

[82] Trefil, J., 1987, Meditations at Sunset, Chapter 3, MacMillan, 208 pp.

[83] Fuller, W. A., 1976, Introduction to Statistical Time-series, John Wiley and Sons, 470 pp.

[84] Yiou, P., Baert, B., and Loutre, M. F., 1996, Spectral analysis of climate data, Surveys in Geophysics, 17:619-663.

[85] Parkinson, C. L., 1989, Dangers of multiyear averaging in analyses of long-term climate trends, Climate Dynamics, 4:39-44.

[86] Hernandez, G., 1999, Time series, periodograms, and significance, Journal of Geophysical Research, 140:10,355-10,368.

[87] Schaaf, M., and Thurow, J., 1997, Tracing short cycles in long records: the study of inter-annual to inter-centennial climate change from long sediment records, examples from the Santa Barbara Basin, Journal of the Geological Society, London, 154:613-622.

[88] Kottegoda, N. T., 1985, Assessment of non-stationarity in annual series through evolutionary spectra, Journal of Hydrology, 76:381-402.

[89] Stephenson, D. B., Pavan, V., and Bojariu, R., 2000, Is the North Atlantic Oscillation a random walk?, International Journal of Climatology, 20:1-18.

[90] Pittock, A. B., 1983, Solar variability, weather and climate: an update, Quarterly Journal of the Royal Meteorological Society, 109:23-55.

[91] Currie, R. G., 1995, Luni-solar and solar cycle signals in Lake Saki varves and further experiments, International Journal of Climatology, 15:893-917, and references therein.

[92] Bultheel, A., 1995, Learning to swim in a sea of wavelets, Bulletin of the Belgian Mathematical Society, 2:1-46.

[93] Lawrence, J. K., and Ruzmaikin, A. A., 1998, Transient solar influence on terrestrial temperature, Geophysical Research Letters, 25:159-162.

[94] Ian Snowball, personal communication, June 2001.

[95] Petterson, G., 1996, Varved sediments in Sweden: a brief review, in: Kemp, A. E. S., (Ed.), 1996, Palaeoclimatology and Palaeoceanography from Laminated Sediments, Geological Society Special Publication No. 116, p. 73-77.

[96] Ohlendorf, C., Niessen, F., and Weissert, H., 1997. Glacial varve thickness and 127 years of instrumental climate data: a comparison, Climatic Change, 36:391-411. The relationship between temperature and ice break-up was noted by Bigler, C., Ammann, B., and Sturm, M., 2003, Diatoms as environmental indicators in the Alps - a high-resolution reconstruction of the past century using sediments of Lake St Moritz, Switzerland, Poster Presentation, 2nd International NCCR Climate Summer School, Grindelwald, Switzerland, 30 August - 6 September 2003.

[97] Ohlendorf, C., 1998, High Alpine lake sediments as chronicles for regional glacial and climate history in the Upper Engadine, southeastern Switzerland, PhD Thesis (Unpublished), ETH-Zürich, Switzerland, Nr. 12705, 203 pp.

[98] Rebetez, M., 1996, Seasonal relationship between temperature, precipitation and snow cover in a mountainous region, Theoretical and Applied Climatology, 54:99-106.

[99] Leemann, A., and Niessen, F., 1994, Holocene glacial activity and climatic variations in the Swiss Alps: reconstructing a continuous record from proglacial lake sediments, The Holocene, 4:259-268.

[100] Lotter, A. F., and Birks, H. J. B., 1997, The separation of the influence of nutrients and climate on the varve time-series of Baldeggersee, Switzerland, Aquatic Sciences, 59:362-375.

[101] Desloges, J. R., 1994, Varve deposition and the sediment yield record at three small lakes of the southern Canadian Cordillera, Arctic and Alpine Research, 26:130-140.

[102] Tomkins, J. D., and Lamoureux, S. F., 2004, Decadal hydroclimatic variability as evidenced by the sedimentary record of Mirror Lake, Northwest Territories, Canada, Presentation, 34th Annual International Arctic Workshop, Institute of Arctic and Alpine Research, Boulder, Colorado, 11-13 March 2004.

[103] Hausmann, S., Lotter, A. F., Van Leeuwen, J. F. N., Ohlendorf, C., and Sturm, M., 2001, The influence of land-use and climate change on Alpine lakes: a high-resolution study focusing on the past 1000 years, Terra Nostra, 3:96-99.

[104] Pelletier, J. D., 1997, Analysis and modeling of the natural variability of climate, Journal of Climate, 10:1,331-1,342.

[105] Pelletier, J. D., and Turcotte, D. L., 1997, Long-range persistence in climatological and hydrological time-series: analysis, modeling, and application to drought hazard assessment, Journal of Hydrology, 203:198-208.

[106] Rittenour, T. M., Brigham-Grette, J., and Mann, M. E., 2000, El Niño-like climate teleconnections in New England during the Late Pleistocene, Science, 288:1,039-1,042.

[107] Bradbury, J. P., and Dean, W. E., (Eds.), 1993, Elk Lake, Minnesota: Evidence for Rapid Climate Change in the North Central United States, Geological Society of America Special Paper, v. 276, 336 pp.

[108] Proctor, C. J., Baker, A., Barnes, W. L., and Gilmour, M. A., 2000, A thousand-year speleothem proxy record of North Atlantic climate from Scotland, Climate Dynamics, 16:815-820.

[109] Selvam, A. M., and Fadnavis, S., 1998, Signatures of a universal spectrum for atmospheric interannual variability in some disparate climatic regimes, Meteorology and Atmospheric Physics, 66:87-112.

[110] Ariztegui, D., Farrimond, P., and McKenzie, J. A., 1996, Compositional variations in sedimentary lacustrine organic matter and their implications for high Alpine Holocene environmental changes: Lake St Moritz, Switzerland, Organic Geochemistry, 24:453-461.

[111] Potter, P. E., Maynard, J. B., and Pryor, W. A., 1980, Sedimentology of Shale, Springer Verlag, 314 pp.

[112] Ohlendorf, C., Sturm, M., and Hausmann, S., 2003, Natural environmental changes and human impact reflected in sediments of a high alpine lake in Switzerland, Journal of Paleolimnology, 30:297-306.

[113] Renberg, I., and Segerström, U., 1981, Application of varved lake sediments in palaeoenvironmental studies, Wahlenbergia, 7:125-133.

[114] Wetzel, R. G., 2001, Limnology: River and Lake Ecosystems, Third Edition, Academic Press, 1,006 pp.

[115] Tyson, R. V., 1995, Sedimentary Organic Matter: Organic Facies and Palynofacies, Chapman and Hall, 615 pp.

[116] Meyers, P. A., and Ishiwatari, R., 1995, Organic matter accumulation records in lake sediments, in: Lerman, A., Imboden, D., and Gat, J., (Eds.), Physics and Chemistry of Lakes, Second Edition, Springer Verlag, p. 279-328.

[117] Cranwell, P. A., 1973, Chain-length distribution of n-alkanes from lake sediments in relation to post-glacial environmental change, Freshwater Biology, 3:259-265.

[118] Mackereth, F. J. H., 1966, Some chemical observations on post-glacial lake sediments, Philosophical Transactions of the Royal Society, B250:165-213.

[119] Rowan, D. J., Kalff, J., and Rasmussen, J. B., 1992, Profundal sediment organic content and physical character do not reflect lake trophic status, but rather reflect inorganic sedimentation and exposure, Canadian Journal of Fisheries and Aquatic Sciences, 49:1,431-1,438. See also: Dean, W. E., 1999, The carbon cycle and biogeochemical dynamics in lake sediments, Journal of Paleolimnology, 21:375-393.

[120] Engstrom, D. R., and Wright, H. E., 1984, Chemical stratigraphy of lake sediments as a record of environmental change, in: Haworth, E. Y., and Lund, J. W. G., (Eds.), Lake Sediments and Environmental History, Leicester University Press, p. 11-67.

[121] Psenner, R., 2002, Alpine waters in the interplay of global change: complex links - simple effects?, In: Steininger, K. W., and Weck-Hannemann, H., (Eds.), Global Environmental Change in Alpine Regions, Edward Elgar, Chapter 2, p. 15-40.

[122] Lister, G. S., 1988, A 15,000-year isotopic record from Lake Zurich of deglaciation and climatic change in Switzerland, Quaternary Research, 29:129-141.

[123] Lami, A., Marchetto, A., Lo Bianco, R., Appleby, P. G., and Guilizzoni, P., 2000, The last *ca* 2000 years palaeolimnology of Lake Candia (N. Italy): inorganic geochemistry, fossil pigments, and temperature time-series analyses, Journal of Limnology, 59:31-46.

[124] Züllig, H., 1982, Die Entwicklung von St Moritz zum Kurort in Spiegel der Sedimente des St Moritzersees, Wasser, Energie, Luft, 74:177-83.

[125] Hollander, D. J., McKenzie, J. A., and Lo ten Haven, H., 1992, A 200-year sedimentary record of progressive eutrophication in Lake Greifen (Switzerland): implications for the origin of organic-carbon-rich sediments, Geology, 20:825-828.

[126] Livingstone, D. A., 1957, On the sigmoid growth phase in the history of Linsley Pond, American Journal of Science, 255:364-373.

[127] Deevey, E. S. Jr., 1984, Stress, strain, and stability of lacustrine ecosystems, in: Haworth, E. Y., and Lund, J. W. G., (Eds.), Lake Sediments and Environmental History, Leicester University Press, p. 203-229.

[128] Davis, M. B., 1976, Erosion rates and land-use history in southern Michigan, Environmental Conservation, 3:139-148.

[129] Baroni, C., and Orombelli, G., 1996, The Alpine "Iceman" and Holocene climatic change, Quaternary Research, 46:78-83.

[130] Rageth, J., 2000, Kleine Urgeschichte Graubündens, Archäologie der Schweiz, 23:32-46.

[131] Seifert, M., 2000, Vor 3,466 Jahren erbaut! Die Quellfassung von St Moritz, Archäologie der Schweiz, 23:63-75.

[132] Gobet, E., Tinner, W., Hochuli, P. A., Van Leeuwen, J. F. N., and Ammann, B., 2003, Middle to Late Holocene vegetation history of the Upper Engadine (Swiss Alps): the role of man and fire, Vegetation History and Archaeobotany, 12:143-163.

[133] Markgraf, V., 1970, Palaeohistory of the spruce in Switzerland, Nature, 228:249-251.

[134] Schaer, A., 2003, Untersuchungen zum prähistorischen Bergbau im Oberhalbstein (Kanton Graubünden), Jährbuch der Schweizerischen Gesellschaft für Ur- und Frühgeschichte, 86:7-54.

[135] Denton, G. H., and Karlen, W., 1973, Holocene climatic variations - their pattern and possible cause, Quaternary Research, 3:155-205.

[136] Campbell, I. D., Campbell, C., Apps, M. J., Rutter, N. W., and Bush, A. B. G., 1998, Late Holocene ~1,500 yr climatic periodicities and their implications, Geology, 26:471-473.

[137] Grootes, P. M., and Stuiver, M., 1997, Oxygen 18/16 variability in Greenland snow and ice with 10^3- to 10^5-year time resolution, Journal of Geophysical Research, 102:26,455-26,470.

[138] Bianchi, G. G., and McCave, I. N., 1999, Holocene periodicity in North Atlantic climate and deep-ocean flow south of Iceland, Nature, 397:515-517.

[139] Bond, G., Showers, W., Cheseby, M., Lotti, R., Almasi, P., deMenocal, P., Priore, P., Cullen, H., Hajdas, I., and Bonani, G., 1997, A pervasive millennial-scale cycle in North Atlantic Holocene and glacial climates, Science, 278:1,257-1,266.

[140] Hausmann, S., Lotter, A. F., Van Leeuwen, J. F. N., Ohlendorf, C., Lemcke, G., Grönlund, E., and Sturm, M., 2002, Interactions of climate and land use documented in the varved sediments of Seebergsee in the Swiss Alps, The Holocene, 12:279-289.

Chapter 7: Conclusions

7.1 Methodological conclusions

- An extensive literature review suggests that work on the application of digital image analysis to sediment cores needs to be better coordinated, in order to avoid the duplication of research effort. Both theoretical developments in image processing [e.g. 1-3] and the development of practical imaging apparatus [e.g. 4-6] have previously tended to be published as secondary parts of papers that are primarily concerned with specific sediment records. Standardisation of image analysis techniques, driven by techniques-based review papers [e.g. 7], will assist this coordination process. The use of open source software, such as NIH Image [8] and its successor ImageJ [9], which can be freely obtained from the internet, is recommended. The increasing ease of storage of large data files should also allow high-resolution digital images of sediment cores to be made available on the internet in future, together with descriptions of imaging techniques and conditions, allowing image measurements to be corroborated and new software to be tested by other researchers.

- Experience gained during this research indicates that digital image analysis needs to be integrated fully with other research techniques in order to realise its full value. Indeed, within a multi-proxy sediment core study, it may be best to perform image analysis of sediment cores *before* any major destructive sampling is done: image analysis may offer guidance as to the most valuable or interesting core intervals to sample, for example. The proxy nature of image-derived data also means that all additional data should be immediately taken into consideration as the research progresses, allowing the image-derived proxies to be calibrated and if necessary refined.

- There is a need to emphasise what digital image analysis applied to sediment cores can, and cannot, achieve. Digital image analysis can produce very-high-resolution records of sediment colour or greyvalue, and these can be calibrated in terms of changes in sediment composition (as found, for example, with the Lake St Moritz core). It can also characterise sedimentary structures, such as varves, at high resolution and in a consistent, objective way (as was done for the Drammensfjord varves). However, the success of image analysis is crucially dependent on two factors.

  Firstly, the imaging conditions need to be suitable: especially the consistency of illumination and the real resolution of the resulting images. The limiting factor on the Drammensfjord results, for example, was the quality of the images; this could have been improved by investing more time in planning and calibrating the imaging set-up.

  Secondly, the sediment core material needs to be suitable, ideally exhibiting well-understood variation in a small number of sediment components and not *vice versa*. There is a danger of over-interpretation, given a sediment core record with multiple influences, both climatic and non-climatic, such as the Lake St Moritz

TOC record; in cases such as this, it may be preferable to concentrate on publishing standardised, high-quality data (as is frequently the case for tree-ring records [e.g. 10]) rather than to search for new and important climatic results with each new record.

- Finally, it is worth a reminder that remote-sensing techniques that can be applied to sediment cores, such as digital image analysis and X-ray fluorescence [11], augment, but do not supersede, the direct physical study of sediment core components. Despite the passage of 60 years, the approach taken by Deevey in the 1940s [12] in sediment core analysis, of combining physical and chemical analysis with an exhaustive study of all preserved biological remains, is still worthwhile: the primary source of information in sediment core research remains the sediment itself.

7.2 Palaeoenvironmental and palaeoclimatic conclusions

- The laminations in the Drammensfjord cores reflect the seasonal cycle: they are varves. This has been deduced from independent evidence from sediment traps, radiocarbon dating of wood fragments, semi-automated varve counting from digital images, and investigation of the lamination fabric using backscatter electron imagery (BSEI), which has not previously been applied to laminated fjord sediments.

- The first appearance of varves in the deepest part of Drammensfjord at c. AD 1000 suggests that the onset of anoxia occurred at this time, as a result of the shallowing of the fjord sill, driven by isostatic rebound, though this anoxia was subsequently greatly strengthened by anthropogenic carbon loading of the fjord. Deeper varves found in core D1M hint at a much earlier, possibly early-to-mid-Holocene, interval of anoxia, though this cannot be accurately dated.

- The thicknesses of the grey varve sublayers in Drammensfjord are a proxy for the magnitude of the annual spring flood, which is expected to be linked to the amount of winter precipitation. An interval of more frequent large spring floods, beginning in c. AD 1470, may be linked to the onset of the Little Ice Age in southern Scandinavia. Regional historical observations would be useful in validating this interpretation. Spectral analysis of the Drammensfjord varves reveals cyclicity at "solar" frequencies, but a solar explanation is unconvincing. There is no signal of the North Atlantic Oscillation in the Drammensfjord record.

- The laminations in Lake St Moritz core PSM90.3 are also annual: image-derived varve counts fit well, although not perfectly, with independent chronological data from ^{137}Cs-activity peaks and historically-recorded event beds. However, the variable quality of the varves, especially below a depth of c. 60cm, corresponding to dates before c. AD 1900, makes measurement of a continuous Holocene varve record difficult even though the laminated fabric is evident throughout the Holocene. Deeper in the core, an independent calibrated radiocarbon chronology derived from terrestrial plant macrofossils enables estimation of the true calendar-year duration (c. 827 years) of an interval containing c. 745 measurable

varves: again, a fit that is not perfect but that is sufficient to support the annual-lamination hypothesis.

- Total varve thickness in Lake St Moritz has only a very weakly significant correlation with available local meteorological data, as expected from previously-published research on comparable Alpine lakes: the thickness record is likely to be influenced by multiple, unresolvable environmental factors. Measurement of the accumulation of separate sediment components, as was achieved for the Drammensfjord record, may reveal stronger climatic links, but this was hindered by frequent minor bioturbation of the varves, and their variable structure: both the number of varve sublayers within one seasonal cycle, and their sedimentary composition, varies over the Holocene.

- Sediment greyvalue in Lake St Moritz core PSM90.3 is closely linked to sediment TOC content, enabling the production of a high-resolution record over the entire Holocene. The early Holocene rise in TOC is probably not comparable to the recent interval of anthropogenic eutrophication and is more likely to have been driven by reduced clastic sediment supply as soil and vegetation became established. Increased variability in the record after c. 3,900 BP is probably a result of anthropogenic disturbances in the lake catchment, some of which may represent amplified natural climate changes. Spectral analysis of the sediment greyvalue record reveals stable significant cyclicity at periods of c. 2,870, 250, and 113 years; a conservative interpretation might describe the spectrum as reddish noise, although this is likely to have arisen from the juxtaposition of erosion-driven and anthropogenic signals with direct climate-driven signals rather than truly stochastic behaviour internal to the lake system.

- Additional data from other components and/or properties of the sediment cores in question would greatly strengthen the climatic inferences for both of the above locations. In both cases, the laminations have been demonstrated to be varves, allowing a high-resolution chronology to be constructed; future research could profitably concentrate on extracting proxies from individual varves or blocks of consecutive varves and linking these to the image-derived data. For example, work is underway on the construction of a diatom record [13] and a pollen record [14] from Lake St Moritz; research on Holocene laminated sediments from Norwegian fjords is at an early stage [e.g. 15,16] but there is future potential for the combination of additional sediment core data with the results of the image analysis, in order to produce more detailed reconstructions of Holocene climate change.

Chapter 7 References

[1] Francus P. and Karabanov E., 2000, A computer-assisted thin-section study of Lake Baikal sediments: a tool for understanding sedimentary processes and deciphering their climatic signal, International Journal of Earth Sciences, 89:260-267.

[2] Nederbragt, A. J., Thurow, J. W., and Merrill, R. B., 2000, Data report: Color records from the California margin: proxy indicators for sediment composition and climatic change, Proceedings of the ODP, Scientific Results, 167:319-329.

[3] D'Argenio, B., Fischer, A. G., Richter, G. M., Longo, G., Pelosi, N., Molisso, F., and Duarte Morais, M. L., 1998, Orbital cyclicity in the Eocene of Angola: visual and image-time-series analysis compared, Earth and Planetary Science Letters, 160:147-161.

[4] Dartnell, P., and Gardner, J. V., 1993, Digital imaging of sediment cores for archives and research, Journal of Sedimentary Petrology, 63:750-752.

[5] Schaaf, M., and Thurow, J., 1994, A fast and easy method to derive highest-resolution time-series datasets from drillcores and rock samples, Sedimentary Geology, 94:1-10.

[6] Christensen, J. Q., and Björck, S., 2001, Digital sediment colour analyses, DSCA, of lake sediments - pitfalls and potentials, Journal of Paleolimnology, 25:531-538.

[7] Saarinen, T., and Petterson, G., 2001, Image analysis techniques, In: Last, W. M., and Smol, J. P., (Eds.), Tracking Environmental Change Using Lake Sediments, Vol. 2, Physical and Geochemical Methods, Ch. 3, p. 23-39.

[8] NIH, 2002, The public domain NIH Image program was developed at the U.S. National Institutes of Health and is available at http://rsb.info.nih.gov/nih-image/.

[9] NIH, 2003, The public domain ImageJ program was developed at the U.S. National Institutes of Health and is available at http://rsb.info.nih.gov/ij/.

[10] The International Tree-Ring Data Bank is based at the WDC-A in Boulder, Colorado, USA; it is available at http://www.ngdc.noaa.gov/paleo/treering.html.

[11] Gunn, D. E., and Best, A. I., 1998, A new automated nondestructive system for high resolution multi-sensor core logging of open sediment cores, Geo-Marine Letters, 18:70-77.

[12] Deevey, E. S. Jr., 1942, Studies on Connecticut lake sediments III: The biostratonomy of Linsley Pond, parts I and II, American Journal of Science, 240:233-264 and 313-338.

[13] Bigler, C., Ammann, B., and Sturm, M., 2003, Diatoms as environmental indicators in the Alps - a high-resolution reconstruction of the past century using sediments of Lake St Moritz, Switzerland, Poster Presentation, 2nd International NCCR Climate Summer School, Grindelwald, Switzerland, 30 August - 6 September 2003.

[14] Gobet, E., Tinner, W., Hochuli, P. A., Van Leeuwen, J. F. N., and Ammann, B., 2003, Middle to Late Holocene vegetation history of the Upper Engadine (Swiss Alps): the role of man and fire, Vegetation History and Archaeobotany, 12:143-163.

[15] For example, the SPINOF programme (Sedimentary Processes and Palaeoenvironment in Northern Fjords). Details are available at http://www.ibg.uit.no/geologi/spinof.

[16] Smittenberg, R. H., 2003, Holocene environmental changes disclosed from anoxic fjord sediments by biomarkers and their radiocarbon content, Geologica Ultraiectina, 227, 143 pp.

Appendix A: Time-series Analysis

A.1 Rationale for this appendix

Time-series analysis, as discussed in section 1.8, is a valuable technique for interpreting palaeoclimate data such as those derived from image analysis of laminated sediments, yet it is a complex subject which requires experience to interpret correctly. There is a large variety of possible techniques that can be used, and there occur frequent misinterpretations and incomparabilities of results in the literature. The aim of this appendix is to clarify the method and purpose of basic time-series analysis. Using this is preferable to producing impressive but meaningless results by using some complex and unsuitable technique. Examples from palaeoclimate-related literature are given where possible.

A.2 Introduction to time-series and correlation

Consider a set of palaeoclimate data arranged in time order: a time-series. It may be possible to define "zones" within this time-series without using any statistical methods, just from inspection with the naked eye. Two examples are the Blytt-Sernander climatic division of the Holocene into Pre-Boreal, Boreal, Atlantic, Sub-Boreal, and Sub-Atlantic periods [1] which, post-1930, was based primarily on pollen evidence from northwestern Europe, and the division of the Late Holocene into climatic phases such as the Little Ice Age and the Mediaeval Warm Period by Lamb [2], based primarily on historical evidence of climate change from northern Europe.

These divisions are convenient, but are vulnerable to self-reinforcement via circular reasoning. The Blytt-Sernander scheme, for example, has been only rarely used since the development of radiocarbon dating, which showed that pollen zone boundaries were often diachronous [3]. Lamb's scheme, also, has suffered problems with palaeoclimate data being forcibly fitted to the same succession of warm and cold intervals, with the result that the dates of the supposed "Little Ice Age" are very uncertain, if indeed it should be regarded as a distinct historical event at all [4].

There is a need to analyse palaeoclimatic time-series using objective methods, both to detect patterns within the data and to correlate one palaeoclimate record with another in a systematic way. A distinction can be drawn between an evenly-sampled time-series x_1, x_2, x_3, and so on, where Δt (the time interval between measurements) is constant, and an unevenly-sampled time-series, where Δt is not constant. For the varve-derived data, time-series such as varve thickness, where there is one data point per varve, are evenly sampled, with Δt equal to one year. For sediment greyvalue, on the other hand, Δt is not constant because age does not increase exactly linearly with depth. In this sense, a greyscale record is a "depth-series" rather than a "time-series". This makes its statistical analysis more complicated (see later), although it is easier to obtain than varve thickness or other evenly-sampled series. As such it is ideal for core correlation. The mathematics of time-series correlation underpin the more complex methods of time-series analysis described later in the appendix, so they are described in detail here.

Correlation is based on pairs of data points. The degree to which the pairs tend to vary together can be calculated by multiplying them, then adding together all the products. This sum will be at its largest when the data pair in such a way that the largest numbers multiply together and the smallest numbers multiply together: when there is a high correlation. This can be taken a stage further by subtracting the appropriate mean from each data point before multiplication; this gives the Corrected Sum of Products, or CSP, which is defined as

$$CSP_{x,y}=\Sigma((x-\mu_x)\times(y-\mu_y))$$

where x and y represent the paired data points, and μ_x and μ_y the means of x and y respectively. The CSP is useful because the sign of each term to be added is controlled by the degree of correlation of the data pair. So, if x and y are both greater than, or both less than, their means, the sign of the CSP term will be positive; if one data point is less than its mean, and one greater, the sign of the CSP term will be negative. From this, it follows that data pairs which tend to correlate will produce a large positive CSP, data pairs which tend to anticorrelate will produce a large negative CSP, and data pairs which are, on average, uncorrelated, will produce a mixture of negative and positive terms which should cancel when added, giving a CSP near zero.

Clearly, the magnitude of the CSP will depend on sample size. To correct for this, it is necessary to divide by the number of data pairs. This gives the covariance of the data, which is defined as

$$Cov_{x,y}=(\Sigma((x-\mu_x)\times(y-\mu_y)))/n$$

where n is the number of data points. Strictly speaking, the division should be by (n-1) but n is usually large enough to ignore this. The covariance depends on the units of measurement. To allow different types of series to be compared, it is necessary to convert the covariance to a form which has no units, i.e. a dimensionless number. This is the Pearson product-moment correlation coefficient, or "correlation coefficient" for short. It is denoted by ρ (for a population) or r (for a sample) and is defined as

$$r=Cov_{x,y}/(\sigma_x\times\sigma_y)$$

where σ_x and σ_y are the standard deviations of x and y respectively. In essence, the measured covariance is divided by the maximum possible covariance for the data sets given. Thus, r has a maximum value of +1, which indicates perfect correlation, and a minimum value of -1, which indicates perfect anticorrelation. r=0 indicates that there is no correlation between the data sets. Squaring r produces a value between 0 and 1: the coefficient of determination. This value r^2 indicates what proportion of the variance of x can be explained by y, or vice versa.

Understanding the properties of r is important. First, it is non-linear: an r of 0.8 indicates a correlation much more than twice as good as an r of 0.4. Second, its significance depends upon the number of data points. Significance tables can be consulted which give critical values of r. An r-value of 0.4, given 10 pairs of data points, indicates that there is no significant correlation. In contrast, an r-value of

0.4, given 100 data points, indicates a highly significant correlation. As the number of data points rises, the r-value necessary for a significant result falls counterintuitively low: given 120 pairs of data, to get a significant result at the 1% level r only needs to be 0.2343 or greater. However, the values level off as n increases, such that even with a very large data set, r must still be greater than 0.1 if any significant correlation is to be claimed.

The correlation coefficient is bidirectional, unlike the regression of one variable on another; the latter is not appropriate here, since there is not an independent and a dependent variable, and the nature of the correlation trend is not required, just how good it is. The correlation coefficient also assumes that the relationship between the variables is linear, and that both variables are normally distributed. Strictly speaking, the correlation coefficient also assumes that the data are homoscedastic; that is, the variation in the correlation between x and y is independent of x.

A.3 Autocovariance, autocorrelation, and the correlogram

Instead of correlating pairs of time-series, consider the alternative use of time-series analysis mentioned earlier: looking for patterns within a single time-series. The obvious feature to search for is cyclicity: some form of repeated pattern within the data which suggests a simple, predictable underlying mechanism rather than just randomness which cannot be analysed further. The remainder of appendix A concerns the search for cyclic patterns in varve-based time-series, using statistical means rather than naked-eye inspection.

The *correlogram* applies the method of correlation described in section A.2 to develop a simple technique for detecting cyclicity and trends in time-series. It has long been surpassed by more sophisticated methods, but is included here for two reasons: first, those later methods build on the mathematics of the correlogram, and second, it is still a useful first step in analysing any time-series [5].

Two terms need to be defined. The *autocovariance* of a time-series is the covariance of the original time-series with the same time-series shifted by a specified "lag". Similarly, the *autocorrelation* is the correlation of a time-series with itself, again with a certain specified lag. Lag is usually denoted by k, and each of these two quantities can be calculated for k=1, 2, 3, etc. So, with reference to the derivation of the basic equations in section A.2, the autocovariance can be defined as

$$(\sum(x_t-\mu)(x_{t+k}-\mu))/n$$

where x_t is a term in the time-series, k is the lag, μ is the mean, and n the number of data points. This expression is similar to that for ordinary correlation - the corrected sum of products, corrected again for sample size - except that different members of the *same* time-series are being compared. Note that strictly there are only n-k corresponding pairs of data to compare, so that the division should be by n-k, instead of n. However, if k is small relative to n, then this is not important. Similarly, two different means should strictly be used, since the two time-series are slightly different - each includes some data that the other does not - but the

difference between their means is likely to be insignificant, such that μ can be used in both terms. This also makes the equation simpler.

As with the covariance, the autocovariance varies with the units of measurement. To convert it to a dimensionless number, the division by n is removed, then it is divided by the square of the standard deviation of the original time-series. This is the autocorrelation:

$$\sum(x_t-\mu)(x_{t+k}-\mu)/(\sum(x_t-\mu))^2$$

which varies between -1 (perfect anti-autocorrelation) and +1 (perfect autocorrelation). Zero indicates no autocorrelation. Consider the situation where there is no lag: k=0. Clearly, this produces the same expression for the numerator and denominator, so that the autocorrelation is 1. Notice that the division by n has been removed from the above equation: it could be added to numerator and denominator if required. This would convert both into "autocovariance" equations, leading to the following result:

autocorrelation (lag k) = autocovariance (lag k) / autocovariance (lag 0)

where the autocovariance of a lag of zero is simply the variance of the original time-series. This, in fact, is the easiest way to calculate the autocorrelation for a time-series for lags from zero upwards: find the appropriate autocovariances, then divide by the variance: autocorrelation (lag k) = autocovariance (lag k) / variance.

A plot of autocorrelation as a function of lag is the *correlogram*. The vertical axis, r_k, runs from -1 to +1; the horizontal axis, k, is discrete: 0, 1, 2, 3, etc. For how far should r_k be calculated? This is a matter of personal preference, though Chatfield [5] suggests that there is "often little point" in calculating r_k for $k > n/4$. Correlogram interpretation demands experience. The time-series data must also be appropriate. For example, outliers must be removed, otherwise they will tend to reduce the autocorrelation to zero at all lags, except when there are two outliers exactly one lag apart, in which case a very large, spurious autocorrelation will be introduced. Correlograms from four types of time-series are shown in figure A.1 overleaf.

Random time-series (1) should show r_k close to zero for all non-zero values of k. In fact, for a truly random time-series, r_k is distributed as N(0, 1/N); that is, a normal distribution with mean zero and variance 1/N. The standard deviation of this distribution is $1/\sqrt{N}$, so that at the level of 95% significance (which is c. ±2 standard deviations) is $\pm 2/\sqrt{N}$. Any autocorrelation coefficient outside these limits is, therefore, significant. However, "falsely significant" autocorrelation coefficients at low lag values are not unusual, such that it is best if it is specified that coefficients should be either (a) well outside the significance limits, or (b) have an "interpretable" lag time (e.g. an annual cycle) before their significance is seriously considered [5].

Short-term correlation (2) gives a different kind of correlogram. Here, r_k also falls to zero, but not immediately: instead, it declines over several lag terms. This common

behaviour indicates that there is some "short-term memory" in the time-series: each data point is influenced by the several terms preceding it, rather than a rapid flickering between random values.

Linear trends (3) in time-series result in r_k values that never decrease to zero: the trend results in a long run of data points that are the same side of the mean, such that the correlation between them stays high. In fact, the presence of a linear trend tends to obscure any interesting features in the time-series, and it is usual to carry out a linear detrend before plotting the correlogram. This problem is only part of a large and complex issue in time-series analysis: that of *stationarity*. Stationarity, crudely, refers to whether a time-series behaves in a consistent way or not. Linear trends must be removed in order to get stationary time-series, which can then be analysed further.

Cyclicity (4) in a time-series translates into cyclicity in the correlogram. A sinusoidal time-series, for example, will produce a sinusoidal correlogram. The addition of noise will make the correlation between cycles less good over time, such that the cyclicity in the correlogram dies away as k increases. However, the correlogram can be used to look for cyclic correlations in the time-series over a range of suspected cycle lengths: a high value of r_k at a certain value k indicates the presence of cyclicity with period k in the data.

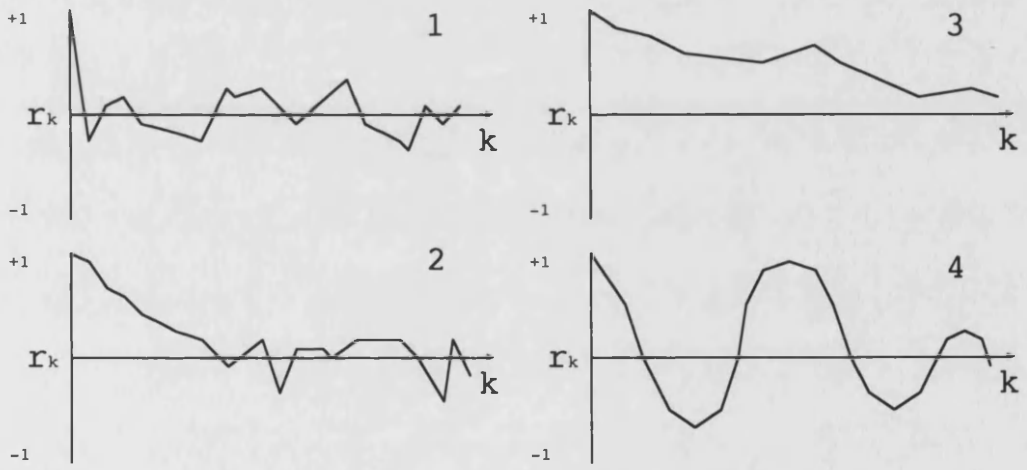

Figure A.1: Correlograms of four different kinds of time-series.

The correlogram is the basis of time-series analysis in the time domain. However, it has been superseded where cyclicity analysis is concerned, by tools based in the frequency domain. The time domain refers simply to a succession of values in time order; the frequency domain, instead, treats the data as a group of periodic functions. The data are unchanged: they are just expressed in a different form.

A.4 The frequency domain and the spectrum

A.4.1 Introduction to the frequency domain

A time-series is considered in the frequency domain as a set of periodic functions. For a periodic function f(t):

$$f(t) = f(t + T)$$

for all t, where t is a time counter and T is the period of the function. Such a function will also have periods of 2T, 3T, 4T, and so on. Most frequency-domain analysis uses sinusoid functions, for simplicity, since they are easy to manipulate: for example, the sum of two sinusoids with a common frequency is another sinusoid with the same frequency; and if the time origin or timescale of a sinusoid is altered, then the amplitude is unchanged and the frequency and phase change in easily-predictable ways. Nonetheless, working in the frequency domain is not as intuitive as in the time domain. So why do it? A simple justification is to consider the example of noise added to a single sine wave (see figure A.2).

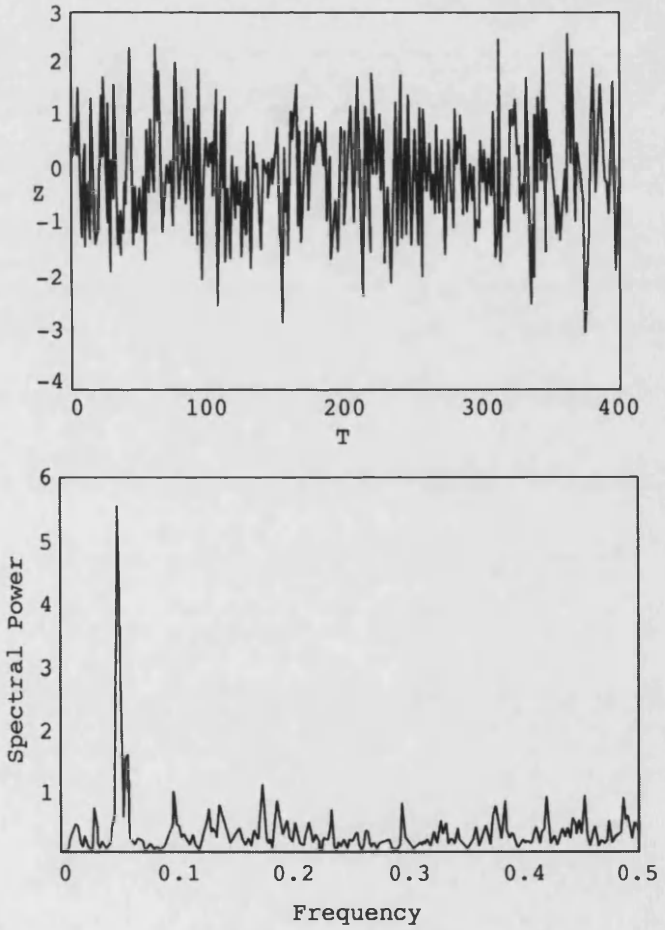

Figure A.2: The time-series data (at top) appear random but actually consist of a single sine wave with random noise added. The sine wave cannot be detected. It is clear, however, in the frequency spectrum plotted below, as a large spike at the correct frequency.

To the human eye, this just looks like noise: the sine wave is lost. But frequency analysis shows that a strong signal is still present. We cannot "see" in the frequency domain, so we must rely on the tools of frequency analysis to reveal any cyclicity that may be present.

A.4.2 Fitting sinusoid functions to the data

Consider a simple model of a time-series as the sum of a sinusoid and an error term. This model will have the equation

$$x_t = u + R \cos 2\pi (ft + \phi) + e_t$$

where x_t is the term in the time-series: the whole series can be denoted x_0, x_1, x_2, ... up to x_{t-1}, such that there are T terms in total. Since all sinusoid functions oscillate about zero, u, an added constant, needs to be included; in the models used later, u will be the mean of the time-series. (Alternatively, the mean can be subtracted from the data before modelling is attempted, such that the time-series itself oscillates about zero in the same manner as a sinusoid.)

The term R cos 2π (ft + ϕ) corresponds to the sinusoid function. R is the amplitude; unmodified sinusoids oscillate only between +1 and -1. The frequency is given by f. Frequency is equal to the proportion of one cycle represented by a single data point. So, given twenty data points and four identical cycles, then each point represents one-fifth of a cycle, such that the frequency is 0.2. Another way of calculating it is to consider the period, which is the reciprocal of the frequency: 1/f. If each cycle is ten data points long, then the period is 10, so the frequency is 1/10 = 0.1.

Time is represented by t: in this case, and in all others in this section, it is assumed that the time-series is evenly sampled, i.e. at time points t_0, t_1, t_2, ... t_{n-1}, where Δt is a constant, and it is assumed for simplicity that the frequency is expressed in terms of Δt units. The timespan of the time-series is therefore $\Delta t \times T$. ϕ (phi) is the phase: a term that shifts the maxima and minima of the sinusoid forward or backward such that they can match the peaks and troughs in the time-series. The only difference between sine and cosine curves is in their phases. e_t is the error term or "residual", at time t: that part of the time-series which is not explained by the sinusoid model. If the model is successfully fitted to the data, then e_0, e_1, e_2 ... etc., should be small.

Finally, the 2π term is required because angles here are expressed in radians, i.e. the angle subtended by an arc whose length is equal to the radius. There are 2π radians in 360°. The period of an unmodified cosine (or sine) function is 2π, so that the frequency is not 1 but $1/2\pi$. However, it is much simpler to work with a sinusoid of frequency 1, which can then just be multiplied by f to get the desired frequency. The frequency of cos(t) is $1/2\pi$, so the frequency of cos(2πt) is 1, so the frequency of cos(2πft) is f, as required.

Alternatively, the function can be defined as R cos (ωt + ϕ) where ω is the "angular frequency": the number of cycles in 2π units of time, rather than in one unit of time.

In this case, $f=\omega/2\pi$, so the period=$2\pi/\omega$. However, this complicates matters, so is not used here.

This equation allows a single sinusoid function to be manipulated, using frequency, amplitude, and phase. How can these parameters be adjusted to get the best possible fit to the time-series data? The aim is to minimise e_t, the error term. Assume that the frequency, f, is pre-specified: the reasons for this will become clear later. For now, the aim is to choose values of u, R, and ϕ, such that e_t is minimised. From the equation of the model:

$$x_t = u + R \cos 2\pi (ft + \phi) + e_t$$

$$\text{so } e_t = x_t - (u + R \cos 2\pi (ft + \phi))$$

$$\text{so } e_t = x_t - u - R \cos 2\pi (ft + \phi)$$

This latter expression is the quantity to be minimised. The least-squares criterion is used to achieve this: the error terms are squared (to avoid negative values cancelling out positive ones) then added together to give an idea of the overall goodness of fit of the model. So the expression to be minimised is:

$$\Sigma (x_t - u - R \cos 2\pi (ft + \phi))^2$$

by fixing f, then choosing appropriate values of u, R, and ϕ.

Here, a problem arises: the expression $\cos 2\pi (ft + \phi)$ is non-linear in the phase parameter ϕ. Further progress cannot be made without converting this expression to a linear equivalent. This is done by using the trigonometric identity:

$$\sin (a + b) = \cos a \sin b + \sin a \cos b$$

such that $R \cos 2\pi (ft + \phi)$ can be converted to:

$$R (\cos 2\pi ft \sin \phi + \sin 2\pi ft \cos \phi)$$

which equals:

$$A \cos 2\pi ft + B \sin 2\pi ft$$

$$\text{where } A = R \sin \phi \text{ and } B = R \cos \phi.$$

This is a more complicated way of expressing the sinusoid function, which is now linear in its phase parameters. Two important points need to be stressed about this "two-layer" expression. First, the original parameters R and ϕ are not lost. They can be simply recovered from A and B:

$$R = \sqrt{(A^2 + B^2)}$$

$$\phi = \tan^{-1} (A / B)$$

Second, although it may seem obvious, it should be stressed that the new, linear form of the sinusoid expression only defines a single sinusoid curve, even though it now

contains multiple sine and cosine terms. When plotted, it still only results in a single wave with a single frequency.

It is now possible to calculate the best-fit values of A and B, from which R and ϕ can be derived if necessary. First, the fixed frequency must be chosen. For example, given monthly data, in order to model an annual cycle, a frequency of 1/12 would be used. Then, the best-fit annual cycle could be subtracted from the data, leaving a minimised residual which could be investigated for other patterns.

The best-fit values of A and B are found by taking a partial derivative, setting it equal to zero and then solving. To go straight to the solutions - the values of A and B that, given a pre-specified frequency, produce the sinusoid which fits the data with the smallest residual:

$$A = (2/T) \sum (x_t \cos 2\pi ft) \quad \text{for } t = 0, 1, 2, \ldots t-1$$
$$B = (2/T) \sum (x_t \sin 2\pi ft) \quad \text{for } t = 0, 1, 2, \ldots t-1$$

Note that these equations look very similar to the initial expressions. This is because sinusoid functions differentiate to give other sinusoid functions, and it is potentially confusing. The best-fit estimators for A and B, above, are not sinusoid functions that fit the data. They are purely for number-crunching, in order to obtain coefficients which can then be fed into the previous expression (A cos $2\pi ft$ + B sin $2\pi ft$) which will then produce a sinusoid that matches the data. It is important to keep these different levels of operation separate, as far as possible.

To summarise so far: best-fit estimates of A and B can be obtained from the data, which can then be substituted into the equation

$$x_t = A \cos 2\pi ft + B \sin 2\pi ft$$

to produce a best-fit sinusoid of a pre-specified frequency. The residuals can then be examined. Since the frequency must be specified beforehand, this is not a very useful technique: it "was used in the last century to search for hidden periodicities, but has now gone out of fashion" [5]. A method is needed that can look at different frequencies within a time-series, and ultimately, work without any pre-specified frequencies at all. However, this single-frequency method is a useful step towards achieving these goals.

A.4.3 Fourier analysis

A.4.3.1 Introduction

Consider again what happens when the best-fit sinusoid defined above is subtracted from the original time-series. What remains is a residual time-series, which will hopefully have a smaller variance than the original (if the frequency of the subtracted sinusoid has been chosen appropriately). Then, another sinusoid can be fitted to the residual time-series, subtracted, and this method repeated, until the residual gets very small. If the time-series is dominated by several different frequencies, plus a small amount of noise, then it should be possible to express it,

in essence, as a sum of several sinusoids. But the question remains: how to choose which frequencies to fit?

One obvious, though labour-intensive, way is to take the original time-series and try fitting different frequencies to it, keeping track of the size of the residual each time. A plot can then be drawn, showing size of residual against subtracted frequency. The best frequency to fit, then, is the one which results in the smallest residual: that is, the one that has the largest correlation with the time-series. This process can then be repeated with the residual time-series, again choosing the frequency with the best fit, constructing term-by-term an acceptable model for the data constructed only of sinusoids. Once the residual becomes insignificant, it can be ignored.

This "poor man's spectral analysis" is intuitively easy to understand. However, it results in a major, and intractable, problem. The first sinusoid to be added works fine. But consider the second. It is being modelled so that it fits the residual time-series, but actually it should fit the first sinusoid plus the residual time-series (i.e. the original data). Consider subtracting the second sinusoid from the original data: will the resulting residual still have a best-fit sinusoid equal to the first sinusoid? The answer is no. The upshot of this is that each time another sinusoid is added to the model, the coefficients of all the preceding sinusoids need to be modified in order to accommodate the new one. The sinusoids all "interfere" with one another. This is a difficult and inefficient way to model the data.

Is there a better way? Experience of using the method above shows that the necessary alteration in the preceding sinusoid term's coefficients is related to the ratio of the frequencies used. Thus, by trial and error, or (more elegantly) by mathematical reasoning, frequencies can be found that require no alteration of the preceding ones: frequencies that are "independent" of each other. These frequencies form the basis of Fourier analysis.

A.4.3.2 Fourier frequencies

So, successive subtraction of different frequencies can be used to build up a model of the data, but with the problem that the fit of one frequency is biased by the presence of the others, meaning that the sinusoid parameters have to keep being changed. The way to avoid this problem is to use Fourier frequencies. These are "orthogonal": they do not interfere with each other. They are also evenly-spaced across the data, so if the method were just to fit a "grid" of frequencies to the data, these are probably the ones that would be used anyway.

Given T data points in a time-series, then the Fourier frequencies are integer multiples of 1/T (2/T, 3/T, 4/T, etc). In other words, they have periods which occur a whole number of times in the data: they are "harmonic" with regard to the timespan of the data. The first Fourier frequency is 1/T, corresponding to one cycle occurring over the whole of the data: it makes little sense to try to model cycles occurring over longer periods than this. The last (highest) Fourier frequency is defined differently depending on whether T is even or odd. If T is even, then it has a frequency of (T/2)/T, which is equal to 0.5. This makes intuitive sense, since the

fastest cyclicity in the data that can be detected has one cycle every two data points, i.e. a period of 2. This "highest-possible frequency" is called the Nyquist frequency. If T is odd, then the definition is slightly different: not T/2 but the last integer before T/2. The highest frequency is therefore ((T/2)-1/2)/T.

Note that the periods of Fourier frequencies are not usually integers: it is the periods themselves which occur an integer number of times over the span of the data. For example, given 10 data points, the periods of the Fourier frequencies are 10/1, 10/2, 10/3, 10/4, and 10/5, that is 10, 5, 3.333, 2.5, and 2, and the frequencies themselves are 1/10, 2/10, 3/10, 4/10, and 5/10.

Now the data can be modelled once more, without having to go back and adjust parameters that have already been defined. There has been a change in approach. Before, the hunt was for frequencies that were thought to be appropriate for the data. Now, because they must be orthogonal, the frequencies are totally fixed in advance. Only the number of data points, T, needs to be known in order to know exactly which frequencies will be used. This applies regardless of the actual data themselves.

This leads to an elegant property of Fourier analysis: any time-series, regardless of its data values, can be fully approximated (i.e. with zero residual) by the best fit of its Fourier frequencies. This is not proved here, but from this point on, there will be no more error terms. The data are no longer being approximated: they are being converted into the frequency domain. The sinusoid-based construction is not a model: it is the same data, looked at from a different perspective. This conversion of a time-series into the frequency domain was originally developed by Jean Baptiste Fourier [6].

A.4.3.3 The integral Fourier transform

The equation for the integral Fourier transform is long, but simple. The expressions that make up the transform are of similar form to the least-squares estimators for a single sinusoid function given earlier. The integral Fourier transform, for any T numbers x_0, x_1, x_2, ..., x_{T-1}, is:

$$x_t = 1/T(\sum x_t) + 2(\sum(A(f_j) \cos 2\pi f_j t + B(f_j) \sin 2\pi f_j t)) \; [\; + A(f_{T/2}) \cos 2\pi f_{T/2} t \;]$$

$$\text{where } A(f) = 2/T \sum(x_t \cos 2\pi f_j t)$$

$$\text{and } B(f) = 2/T \sum(x_t \sin 2\pi f_j t)$$

$$\text{and } f_j = j/T$$

where T is the total number of data points in the time-series, f_j is the Fourier frequency (these are dealt with in order, thus, f_1, f_2, f_3, ... for j=1, 2, 3, 4, ... up to the last integer before T/2), and t is a counter (run through completely for each term) which runs t=0, 1, 2, 3, ... T-1. The part in square brackets [+ $A(f_{T/2})$ cos $2\pi f_{T/2} t$] is added only if T is even, such that the "sum of" operation in the middle term applies only for $0<j<T/2$. The first expression ($1/T(\sum x_t)$) is just the arithmetic mean of the data. The remainder of the expressions are sinusoids which are added to this to produce the oscillations of the data. As before, the calculation is

in two stages: first, number-crunching to produce the sinusoid coefficients, then evaluation of successive best-fit sinusoid curves from these.

Overall, T sinusoid expressions are obtained when a time-series consisting of T data points is transformed. The first expression can be thought of as a sinusoid with frequency zero; two sinusoids are also produced for each Fourier frequency (one using $A(f_j)$ and one using $B(f_j)$) and if T is even, a single extra sinusoid is added using $A(f_{T/2})$. Since t is just a counter, and T is known beforehand, and the frequencies can be calculated straight from it, the important parts of the transform are the values of A(f) and B(f) - the Fourier coefficients. It is these that need to be recorded, in order to express the time-series as a mathematical function in the frequency domain. Again, there are T such coefficients, with the first one being trivial and the rest derived using A(f) and B(f).

Because of the repeating nature of sinusoids, if a value for t outside the range 0, 1, 2, ... T-1, is substituted, the same pattern is obtained: the Fourier transform defines a periodic time-series of period T, consisting of the values x_0, x_1, x_2, ..., x_{T-1}, repeated cyclically.

A.4.3.4 The discrete Fourier transform (DFT) and fast Fourier transform (FFT)

The reason behind transforming the data into the frequency domain is to study cyclicity at different frequencies. Recall that the output of the integral Fourier transform is a set of coefficients $A(f_j)$ and $B(f_j)$, from which it is possible to reconstruct the amplitudes and phases of a set of sinusoids, of known frequencies, which constitute the data transformed into the frequency domain. It is the amplitudes of these sinusoids which are relevant, because they indicate the strength of the cyclicity at each frequency within the time-series. The phases of the different sinusoids are not relevant, except as a means of recovering the exact time-series values.

The next step, then, is to plot some measure of amplitude against frequency for the component sinusoids that have been defined. Before doing this, an automated method of computing the Fourier transform is needed, since the pen-and-paper method of the integral Fourier transform described in section A.4.3.3 is far too slow.

The integral Fourier transform above can be expressed in different ways. It is simpler when written in complex form, as the discrete Fourier transform (DFT), which is derived from the integral Fourier transform using DeMoivre's equality:

$$e^{ix} = \cos x + i \sin x \text{ (where } i = \sqrt{-1})$$

The original, real-valued, time-series is regarded as complex, with each value having a zero imaginary part. The DFT itself is expressed as follows:

$$d(f_j) = 1/T \sum(x_t\, e^{-2\pi i f_j t}) \text{ for } t = 0 \text{ to } T-1$$

where the frequency f_j is j/T for j = 0, 1, 2, ... T-1, and T is the number of data points. Note that this is different from the integral Fourier transform: here, in

addition to the Fourier frequencies, there are also frequencies greater than 0.5. These bring no new information to the data (provided that the original time-series consists only of real numbers). They are completely determined by the frequencies between 0 and 0.5. The DFT is only significant here because the output of the standard method for rapidly computing Fourier transforms is in "DFT format". This method is the fast Fourier transform (FFT). It is *not* another form of the Fourier transform; it is just a *method* for calculating it, developed in 1965 [7].

The FFT can also rapidly retrieve the original time-series values from the FFT output, using the *inverse* FFT. Its workings are not of interest here, except that it is faster than the original DFT calculation because it has complexity of order T × log T instead of T^2. For long time-series (T>1,000), the FFT is the only feasible method of Fourier transformation, and it is used by all serious time-series analysis programs, so it is important to have a good understanding of the FFT output.

A time-series consisting of T values produces an FFT that also consists of T values. Each of these is a complex number, of the form a + bi. These correspond to frequencies ranging from 0 to (T-1)/T, in steps of 1/T, as for the traditional DFT described above. All frequencies greater than 0.5 are determined by their counterparts in the frequency range 0 to 0.5: in fact, they are complex conjugates. The second half of the FFT output is a "mirror image" of the first: the real parts are the same, although in reversed order, and the complex parts have changed sign.

$A(f_j)$ and $B(f_j)$, as used in the integral Fourier transform, can be obtained from the real and imaginary parts of the DFT output. The equations are:

$$A(f_j) = 2 \times \text{Re (DFT)} \text{ and } B(f_j) = -2 \times \text{Im (DFT)}$$

but care is needed when working with the FFT. It is only an efficient computer algorithm to calculate the DFT, but over time, certain shortcuts have developed within it, such that the FFT output is commonly *not* the same as the output of the traditional DFT.

The first number in the FFT output is the sum of the data (not the mean, as with the integral Fourier transform), i.e. a real number, and represents a "frequency" of zero. If the time-series has been detrended beforehand, then its first FFT term should be zero (or perhaps a very small real number, owing to rounding errors). After this, there are complex numbers corresponding to frequencies 1/T, 2/T, 3/T, etc., until a frequency of (T/2)/T (=0.5) is reached, the Nyquist frequency. Here, again, the FFT term will always be real: because it is in the middle of the data, it must be its own complex conjugate, i.e. a real number. As before, it may have a tiny complex part owing to rounding errors, but this can be ignored. So, there are only T/2 + 1 values of the FFT output that are of interest.

Two tables can be drawn up to compare the output of the integral Fourier transform and the FFT, which will hopefully make the latter more comprehensible.

Integral Fourier Transform

Component	Frequency	A(f)	B(f)	$R(f)=\sqrt{(A^2+B^2)}$
Mean	(0/T)	...	0	...
Fundamental	1/T	...	...	...
2nd Harmonic	2/T	...	...	...
3rd Harmonic	3/T	...	...	...
...	...	...	...	...
...	...	...	...	...
T/2th Harmonic	(T/2)/T (if even)	...	0	...

Fast Fourier Transform

Component	Frequency	Form	A(f)	B(f)	$R(f)=\sqrt{(A^2+B^2)}$
Sum	(0/T)	a+0i	2a	0	...
Fundamental	1/T	a+bi	2a	-2b	...
2nd Harmonic	2/T	a+bi	2a	-2b	...
3rd Harmonic	3/T	a+bi	2a	-2b	...
...	...	...	...	...	...
...	...	...	...	...	...
T/2th Harmonic	(T/2)/T (if T even)	a+0i	2a	0	...
Further Harmonics	>Nyquist ((T/2)/T)	(a-bi)	(n/a)	(n/a)	(not required)

Setting aside differences in the method (and speed) of calculation, the desired outcome in either case is equivalent: a set of Fourier frequencies and their associated amplitudes (R values). Now it is possible to return to plotting amplitude against frequency, as mentioned earlier. This is done using the periodogram.

A.4.4 The periodogram

For each Fourier frequency, some measure of the strength of oscillation at that frequency can be obtained by looking at the amplitude, R, of the appropriate sinusoid. This measure can be expressed in several different ways, but all are designed in order to enable the plotting of frequency f against some function of R(f). Because Fourier frequencies are orthogonal, the strength of oscillation of each is independent of the others, which is crucial if the plot is to be meaningful.

Such a plot is called a periodogram. The name is unfortunate, since it makes more sense for a plot of *period* against strength of oscillation to be called a periodogram! A better name for the frequency-based plot might be a "spectrogram", and this term is occasionally used. However, the terminology is unlikely to change, for historical reasons.

Since there are several different ways of expressing "strength of oscillation" at a given frequency, there are several different types of periodogram. All have the same basic shape - such that a time-series with one dominant frequency will always produce

a peak in the same place - but the numerical value assigned to this peak will differ. None of the expressions are objectively better or worse than the others. The simplest version, used here, plots *average power* against frequency.

Given that the average power of a sinusoid of amplitude R is $R^2 / 2$, which need not be derived, this can be used as a measure of "strength of oscillation", since each of the Fourier frequencies has a corresponding sinusoid. Denoting average power at frequency f as I(f), this gives:

$$I(f) = R_f^2 / 2$$

$$\text{given } R_f = \sqrt{(A^2 + B^2)}$$

$$R_f^2 = (A^2 + B^2)$$

$$=(2a)^2 + (-2b)^2$$

$$=4a^2 + 4b^2$$

$$=4(a^2 + b^2)$$

$$\text{then } I(f) =4(a^2 + b^2) / 2$$

$$I(f) = 2(a^2 + b^2) = 2 \left|a + bi\right|^2$$

This applies to all values of f between (but not including) zero and 0.5. These two "end frequencies" have $I(f) = (a^2 + b^2)$: only half as big. These two frequencies are not "doubled" like all the others, such that they do not have complex conjugates somewhere else in the FFT output. So, an average power for each of the Fourier frequencies can now be obtained.

One additional point needs to be made. According to Parseval's Theorem, the sum of squares of a time-series is equal to the total average power, i.e. the sum of all the values of I(f) which have just been defined, for frequencies between zero and 0.5. However, many FFT algorithms are coded so that this is not the case! The code will always contain a summation of the frequency terms. Strictly, this should have $1/\sqrt{T}$ in front of it, and if it does, then the values of I(f) defined above will fit with Parseval's Theorem. But very often, the forward FFT summation term has no multiplier in front of it, and the inverse term has 1/T in front of it. This still allows the data to be transformed into the frequency domain, then back into the time domain, without alteration, and it makes the forward FFT algorithm simpler, but the results no longer fit Parseval's Theorem. To get the correct values for the average power, it is necessary to divide each term by T [8]. This correction applies to the FFT routines in both Excel and Matlab. So the power equation is now:

$$I(f) = (2 / T) \times \left|a + bi\right|^2$$

This defines a periodogram with a discrete set of lines: one is plotted at each Fourier frequency. The sum of these ordinates is the total average power of the time-series.

A.4.5 The power spectrum

This "line periodogram" is not a very useful representation, because it suggests that the total average power of the time-series is contained only within the Fourier frequencies. For most real time-series, including all those related to varves and palaeoclimate, the total average power is distributed continuously over the range of frequencies. The "true" periodogram should not consist of isolated lines - it should be a continuous curve. The area under this curve should be the total average power of the time-series.

This curve can be approximated by plotting a histogram: instead of a line, each frequency is plotted as a column. The width of each column is equal to the interval between Fourier frequencies, i.e. 1/T (with the exception of the column representing the Nyquist frequency 0.5, which is half the width of all the others, so its height is only $T \times R_f^2$. However, the amplitude at the Nyquist frequency is rarely of interest, anyway, so this difference can be ignored if desired). The area of the column should equal the average power I(f). So:

$$\text{area} = \text{width} \times \text{height}$$

$$I(f) = 1/T \times \text{height}$$

$$\text{height} = I(f) \; / \; (1/T)$$

$$\text{height} = T \times I(f)$$

This is a new kind of periodogram, where the height of each column measures not power, but power per frequency interval: a quantity known as power spectral density (PSD). This is denoted

$$P_{xx} = T \times I(f)$$

where P_{xx} represents the power spectral density of time-series x. A plot of power spectral density against frequency gives a form of the periodogram known as the "power spectrum", the "variance spectrum", or just the spectrum. It has the property that the area under the curve is equal to the total average power (i.e. the sum of squares) of the time-series. It is not a smooth curve: it is still a discrete data set. However, it is an approximation - an estimator - of the true, continuous power spectral density function.

Examples of both types of periodogram are shown in figure A.3, which uses greyvalue data from Drammensfjord core D1G. Note that the shapes and frequencies are identical: the only difference is in the scales of the ordinates. The strongest cyclicity occurs at a frequency of 0.0703125, which corresponds to a period of 14.2 pixels (this is a "depth-series", rather than a "time-series"). This fits well with the observation that the 256 data points span 17 varves (core D1G varves number 176-192, inclusive), so that the mean varve thickness is 15.1 pixels. The highest peak on the periodogram, therefore, corresponds to the annual cycle, recorded in the sediment as varves. In this simple example, the periodogram reveals the cyclicity in the data.

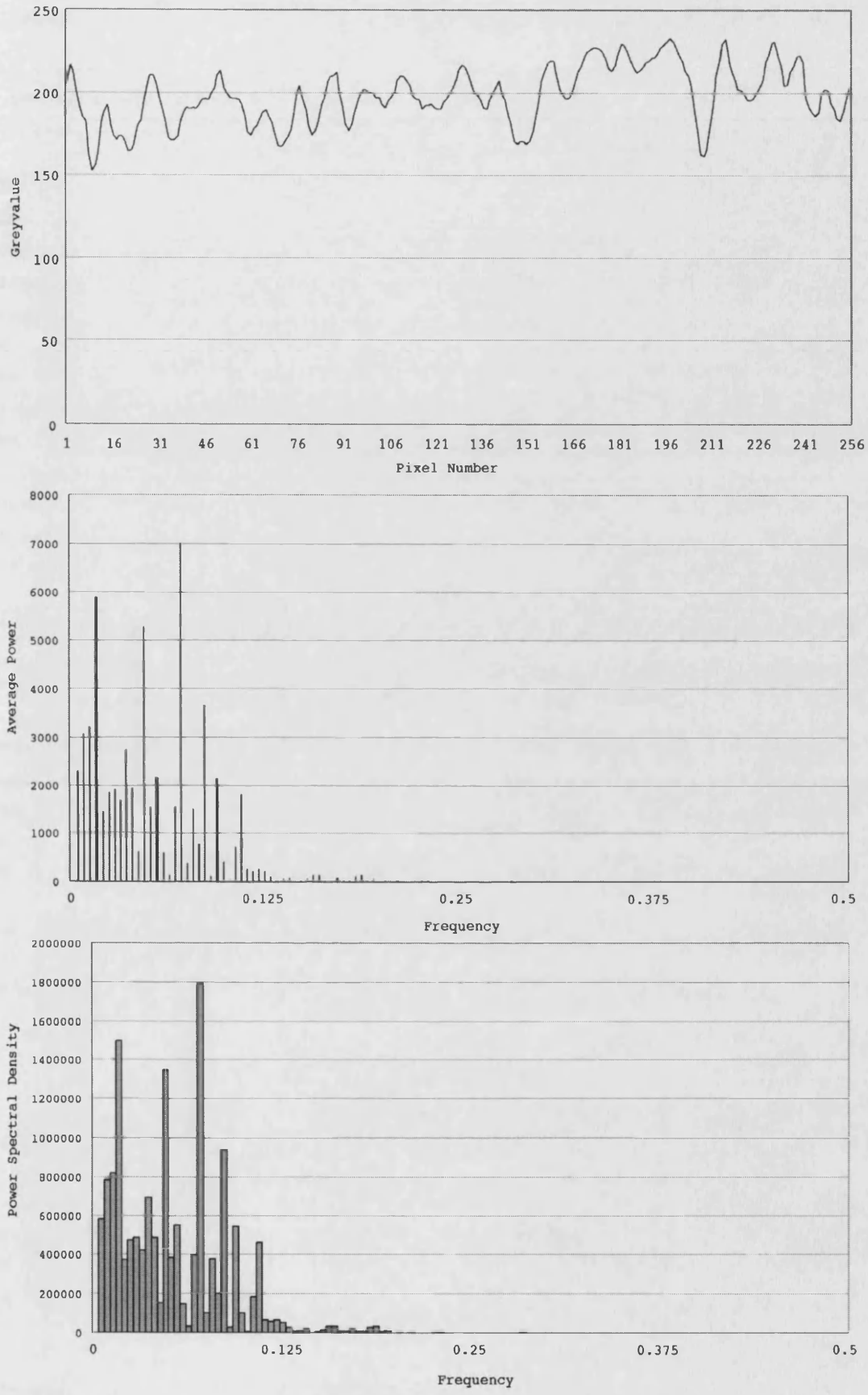

Figure A.3: Greyvalue linescan data from Drammensfjord core D1G, showing 17 varves (at top). Below this are the "line periodogram" of the data (middle) and the power spectrum (bottom).

A.4.6 Interpreting the spectrum

As with the correlogram, interpretation of the spectrum requires some experience in order to know which features may be important and which may just result from random noise. This section discusses in turn aliasing, non-stationarity, and harmonics.

Recall that the grid of frequencies is determined only by the number of data points in the time-series. To study cyclicity at longer frequencies, data must be collected over *a longer period of time*. The highest measurable frequency - the Nyquist frequency - is equivalent to one whole cycle per two data points. So, to increase this frequency, it is necessary to *collect more data points per unit time*. These two improvements are not "symmetrical": the highest measurable frequency depends only on the time interval between data points, and is independent of the total length of the time-series. The improvement that does occur if the time-series is lengthened is that there are more Fourier frequencies, within the same limits, such that the grid of frequencies becomes finer. Thus, the frequency resolution of the spectrum can be increased by collecting more data: peaks in the spectrum can be located more precisely. Varve-based time-series data, where Δt is one year, allow a finer frequency grid to be used than for most other palaeoclimate proxy data.

Aliasing occurs when cyclicity in the data occurs at frequencies higher than the Nyquist frequency. This cyclicity is not lost, since the Fourier transform is a complete representation of the data. Instead, it is "folded back" into frequencies below the Nyquist frequency: the Nyquist frequency is also called the "folding frequency". So, if there are higher-than-Nyquist frequencies present in the data, the spectrum will be distorted by them. Frequencies that are indistinguishable from one another given a certain sampling frequency are called "aliases"; they arise from the interplay of a real frequency and a sampling frequency, as occurs when stagecoach wheels in old westerns sometimes appear to spin backwards.

How can aliasing be detected? There are two ways. First, the sampling frequency should be chosen such that the Nyquist frequency is definitely higher than the highest suspected frequency of cyclicity in the time-series in question. For example, if the highest-frequency cycle in a greyvalue depth-series represents varves in the sediment, then to avoid aliasing, there need to be at least two pixels per varve, and preferably more.

The second way to test for aliasing is to consider the shape of the spectrum. Average power should approach zero well before the Nyquist frequency is reached, showing that the Nyquist frequency is comfortably higher than the fastest cyclicity in the data. A spectrum with this shape indicates that the sampling was well-designed, such that the higher frequencies are there just to provide "headroom", making sure that all the frequencies in the data are captured properly and that there is no aliasing. The spectra in figure A.3 exhibit this shape.

Non-stationarity of the time-series can also affect the spectrum. A peak at zero frequency indicates a linear trend in the data which should have been removed. In general, a concentration of power at very low frequencies suggests that the time-

series is non-stationary. In this situation, strong cyclicity at higher frequencies can go unnoticed because of low-frequency irregularities in the data. Successful spectral analysis requires that every effort be made to make the time-series stationary beforehand.

Harmonics in the spectrum are the final point of interest. Ordinarily, peaks in the spectrum indicate cyclicity in the data. However, strong cyclicity, such as the annual cycle in varve-derived greyvalue data, can produce harmonics: "false" peaks at integer multiples of the basic frequency. These result from cyclic components in the time-series which are *non-sinusoidal*, such as "sawtooth"-type waves. These require more than one sinusoid to approximate, so they introduce power into the spectrum at the wrong frequencies. There are complex forms of frequency analysis which use non-sinusoidal periodic functions, and these can be tailored to avoid the problems of harmonics; however, they are difficult and rarely used. It is usually sufficient just to be aware of the existence of harmonics, and not to be misled into thinking that they indicate many different cycles within the data. A classic example of this mistake is the twenty or so "cycles" found by Beveridge in historical wheat prices [9].

A.4.7 A note on the difference between time and depth

It has already been emphasised that a "depth-series" is not the same as a "time-series" unless age is directly proportional to depth, i.e. the sediment accumulation rate is constant. This is clearly not the case in a varved core where the varves show variation in thickness, nor is it likely to be the case in most sediment cores. Sampling from each varve produces a proper time-series, but sampling sediment greyvalue (or colour) continuously down the core produces a depth-series from which cyclicity should strictly be expressed as cycles on a length scale, not a time scale.

What would happen if a greyvalue depth-series across, say, 500 varves of varying thickness, were to be analysed as if it were a time-series, i.e. as if age were exactly proportional to depth? The resulting spectrum would not be nonsense, it would just be a distorted version of the true spectrum. The nature of the distortion depends on both the magnitude of variation in varve thickness, and its frequency relative to the frequency changes in sediment greyvalue. Rapid changes in thickness introduce "chatter" into the spectrum, moving spectral power from "real" peaks to higher frequencies, where false peaks may develop. Slow changes in varve thickness introduce "drift" into the spectrum, again moving spectral power, but this time not far from the "real" peaks, serving only to broaden them. The effects of chatter and drift are to weaken the true signal in the spectrum [10].

So, a depth-series analysed as if it were a time-series can give a rough idea of where cyclicity may be in the data, but the peaks in the spectrum cannot safely be statistically tested, because they are lower than they should be. Perhaps more importantly, there are also likely to be false peaks at high frequencies as a result of chatter. Care should be taken not to over-interpret such spectra [e.g. 11,12]. Dealing with changing sediment accumulation rates is a complex problem, and a large literature has developed around the problem, centred on the technique of "tuning" accumulation rates to match the Milankovitch hypothesis [10]. There is no need to go

into details here, except to say that it is one of the major advantages of varved sediment cores that they have a built-in annual-resolution chronology, allowing this complication to be avoided.

A.5 Significance testing of the unmodified spectrum

Peaks in the spectrum correspond to strong frequencies that are present in the data. Interpretations for these can be offered in terms of climatic cycles such as the 11-year Schwabe sunspot cycle, and the 2.2-year Quasi-Biennial Oscillation (QBO), which are known to produce peaks in spectral analysis of instrumental climate data. However, spectral analysis of random time-series data can also produce "peaks" which have no mechanistic interpretation. So how can a genuine climatic signal be distinguished in proxy time-series data?

One method is to consider the expected climatic influences on the palaeoclimate record in question: a proxy record from the west coast of South America, for example, should show a strong ENSO signal, and a lake-sediment-based record from Laguna Pallcacocha, Ecuador [13] does indeed show the influence of ENSO in a frequency band with periods from 2.5 to 7.5 years. However, this method is vulnerable to circular reasoning, especially with supposedly global climate influences such as solar cycles. Regardless of mechanism of formation, it seems that an explanation can be contrived to explain the influence of solar activity on almost any palaeoclimate record. A more convincing method in this case is to consider the statistical significance of the peaks in the spectrum which supposedly match solar (or other) frequencies, in order to demonstrate that they are unlikely to have arisen by chance.

It is an axiom of statistics that the significance of a hypothesis cannot be tested in isolation, only in relation to an alternative "null hypothesis". Here, a series of random numbers - "white noise" - is used, for simplicity.

Given a time-series which is totally random, each Fourier coefficient will be normally distributed. Because the Fourier frequencies are orthogonal, the coefficients are independent, so each can be separately tested for significance. Amplitude, on the spectrum, is obtained by squaring the Fourier coefficients, so the amplitudes are distributed as the square of a normal distribution: a chi-squared distribution, with two degrees of freedom [14]. This is denoted $\chi^2_{(2)}$ and is equivalent to a negative exponential distribution. Using white noise as a null hypothesis, peaks on the spectrum can be tested against this distribution to see whether they qualify as significant.

The probability of a given ordinate arising by chance can be obtained by referring to the area under the $\chi^2_{(2)}$ curve, using a statistical table. This determines whether or not each ordinate is "significant", based on whether it exceeds a previously-defined deviation from the expected value. What is this expected value? For a null hypothesis of white noise, which contains no periodic components, the expectation is the same average power at each frequency, i.e. a flat line with no peaks.

Since there are T/2 Fourier frequencies (ignoring zero, which never has any power, even in white noise), which must have equal ordinates and add up to give the sum of squares, the expected value E(I(f)) for each frequency is:

$$E(I(f)) = \text{Sum of Squares} / (T/2)$$

$$\text{Sum of Squares} = \sigma^2 \times T$$

$$\text{So } E(I(f)) = \sigma^2 \times T / (T/2)$$

$$E(I(f)) = (\sigma^2 \times T) \times (2/T)$$

$$E(I(f)) = \sigma^2 \times 2$$

where σ^2 is the variance. The expected spectrum for white noise, therefore, is a horizontal line at the level of $2\sigma^2$ average power. Significance testing considers deviation of the values from this level.

Conventionally, significance is defined at the 95% level, i.e. lying outside that part of the x-axis which underlies 95% of the area under the distribution curve. Since the deviations are being measured from a positive expected value, the test should strictly be two-sided: the 95% confidence interval is bounded by a 2.5% area at the far left of the $\chi^2_{(2)}$ curve, and another 2.5% area at the far right. The table of $\chi^2_{(2)}$ values gives 0.051 and 7.38 as the relevant threshold values. These apply to a standardised data set, with a variance equal to one. For real data, the distribution is simply $\sigma^2 \times \chi^2_{(2)}$ such that the threshold values can just be multiplied up appropriately; alternatively, the time-series can be standardised beforehand so that it has a variance of one.

This two-sided test is testing for deviation from white noise, where a deficiency of power at a given frequency is just as significant as an excess. For palaeoclimate research, however, models are rarely encountered which use the absence of certain frequencies from a broad spectrum; only the peaks, and not the troughs, are of interest, in which case it is better to use a one-sided test, with a threshold value of 5.99. Every spectral ordinate is tested against this except the first and last, f = 0 and f = 0.5, since these two have only one degree of freedom, not two [15]. There is no point doing significance testing on these "end ordinates", anyway, since significant power at either frequency would only indicate a problem with the time-series: for f = 0, this would indicate an underlying trend which should have been removed, and for f = 0.5, a peak would strongly suggest that the series had been undersampled, and that frequencies above the Nyquist had been aliased into a misleading spectrum.

This simple test for significant peaks in the spectrum was first described by Schuster [16]. It has an obvious weakness in that it is not stringent enough: the choice of a 95% confidence level entails that one in twenty spectral ordinates should be "significant" just owing to chance. How can the genuinely significant peaks be identified, without making the test so stringent that it does not detect any significant peaks at all?

Schuster's test was improved upon by Fisher [17]. Fisher's test locates the largest spectral ordinate, than asks if it is reasonable that this could be the largest ordinate in a random sample from a $\chi^2_{(2)}$ distribution. The largest ordinate is divided by the mean of all the ordinates (except those at f = 0 and f = 0.5) to produce Fisher's g statistic. This can then be compared with values from a statistical table for different values of n and different confidence levels. The longer the time-series, the more likely it is that a large spectral peak will crop up randomly, so the higher the significance threshold. This may seem counterintuitive with a time-series of random numbers, but becomes clearer if the independent spectral ordinates are considered. A longer time-series simply gives more chance for a large spectral ordinate to appear at random, since it generates more spectral ordinates.

Fisher's test is an improvement on Schuster's test, because it uses an unbiased estimate of the true variance of the time-series [18]. It is also more stringent than the Schuster test [19]. However, as described above it can only be applied to the largest spectral ordinate. Palaeoclimate data characteristically contain multiple frequencies, some of which may be significant despite their lesser amplitude. So, there is a need to extend Fisher's test to the rest of the ordinates. As Priestley [18] writes: "This seemingly simple problem has proved to involve both mathematical complexity and intractability, and among the array of techniques which now exist there is none which can be guaranteed to deal successfully with all its variants". For example, the height of a peak is only a good representation of amplitude if the frequency present in the data coincides exactly with a Fourier frequency; if not, then there is "leakage" of the spectral power onto adjacent ordinates, reducing the apparent significance of the peak.

Whittle [20,21] extended Fisher's test by applying it sequentially until all the significant peaks on the spectrum had been identified. There are two problems with this approach: first, the number of peaks to be tested needs to be known beforehand, and second, the sequential nature of the testing means that the level of "significance" keeps changing depending on the nature of the peaks already measured. The meaning of this "conditional significance" is not clear [22].

A whole menagerie of other tests exists in the literature, described by Hartley [23], Grenander and Rosenblatt [24], Shimshoni [25], Siegel [26], Bolviken [27], Quinn [28], and Chiu [22], among others. The situation is further complicated if the null hypothesis is not white noise, but some other form of "background variability", since this affects the significance of any peaks. All of these different tests have advantages and disadvantages; none is preferable to the others in all situations. Ultimately, the approach of significance-testing of peaks in the unmodified spectrum is not suitable for most palaeoclimate data. It is not a dead end, since it can still give some information about the nature of a time-series, but it cannot cope with the complex nature of climate cyclicity. Further understanding of this requires a brief discussion of the history of spectral analysis.

Before the development of relativity and quantum mechanics, classical physics viewed the universe as a "clockwork", predictable entity running according to Newton's laws,

where experiments in spectral analysis could be designed so as to minimise noise and generate strong spectral peaks [29]. The aim of spectral analysis was to construct a model for the data which consisted of a trend, if required, plus a number (K) of independent oscillations, plus a white noise residual. These K frequencies could be identified on the spectrum, and could have their phases and amplitudes derived; they could then be linked to physical phenomena, thus "explaining" the time-series in its entirety.

This "cycles plus noise" approach to time-series analysis was dominant until the 1920s [29]. It works for astronomical cycles, such as Milankovitch cycles, because of the relative absence of friction in celestial mechanics [10]; it is also successful in distinguishing the annual cycle in instrumental temperature records because this cycle is so much stronger than temperature changes from year to year, for example. It is less successful in revealing the cyclic structure of sunspot numbers, producing only low, broad peaks at 11, 22, and 90-year periods, because of the influence of noise on the data. The correlogram of the Wolfer sunspot data shows how the autocorrelation of the time-series dies away to insignificant levels because of the incorporation of noise into the cycles - in effect, noise and cycles become mixed.

This is not the same situation as with noisy time-series which lack *any kind of* cyclicity. Here, spectral analysis will always produce "false" peaks: consider the many attempts to find cycles in stock market prices, for example, which have been unsuccessful because this time-series seems to follow a random walk [30]. The "cycles plus noise" approach, as described above, is also not suitable for studying time-series containing "impure" cyclicity: cyclicity that is itself influenced by noise. Most climatic and meteorological time-series are pseudoperiodic in this way. As Burroughs [31] writes: "The history of meteorology is littered with the whitened bones of claims to have demonstrated the existence of reliable cycles in the weather". Simple models such as that of Lorenz [32], based on non-linear differential equations, suggest that although the weather system continually follows similar patterns, it never returns to exactly the same state, and thus does not contain "pure" sinusoidal cyclicity.

Returning to the Wolfer sunspot data, to give another example, comparable behaviour occurs. Yule used these data in the 1920s to develop more sophisticated models for pseudoperiodic time-series [33]. He reasoned that the effect of noise on a cyclic time-series should be analogous to the effect of slightly disturbing the swings of a pendulum: the noise becomes incorporated into the swings of the pendulum, i.e. into the cyclicity itself. He attempted to model this effect using the Wolfer sunspot data, which behave similarly to the hypothetical pendulum: the 11-year cycle is clear, but some cycles are asymmetrical, for example, and the frequency is not exactly constant (see figure A.4).

Yule developed autoregressive (AR) models, in the time domain, which explain the Wolfer sunspot data more parsimoniously - using fewer explanatory variables - than the old "cycles plus noise" approach, which coped badly with the changing frequencies and waveforms. Time-domain models such as this are beyond the scope of this thesis. The

alternative approach, used here, is to stay in the frequency domain and to consider the whole spectrum as the output of a pseudoperiodic mechanism, rather than looking for isolated perfect sinusoids. This approach is considered in the next section.

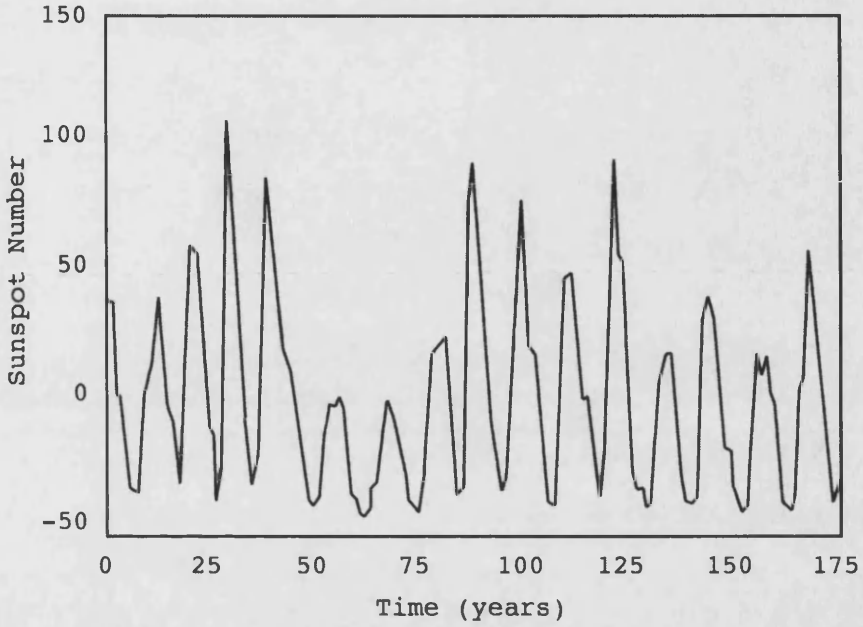

Figure A.4: The Wolfer sunspot data, covering 175 years of observations. The 11-year Schwabe cycle is clear, though it is not by any means a perfect sinusoid.

A.6 Modifying the spectrum

A.6.1 Continuous spectra and spectral instability

The unmodified spectrum is designed for use with the "cycles plus noise" model described above. The value of the unmodified spectrum method depends on the nature of the time-series involved: as with all methods of time-series analysis, no absolute judgement can be made as to whether a given method is good or bad, only as to its degree of suitability for the particular circumstances concerned. The unmodified spectrum is especially suitable for time-series that produce prominent spectral peaks, such as those containing Milankovitch cycles [10]. It is less suitable for pseudoperiodic time-series, which tend to produce more continuous spectra with broad areas of increased spectral power indicating periodicity in the data. In this case, instead of looking for isolated peaks, it is better to consider the shape of the entire spectrum, as a function of frequency: the spectral density function. This section first discusses the nature of simple continuous spectra, then describes how the original periodogram can be modified to better approximate a continuous spectrum.

Continuous spectra are difficult to understand intuitively, since they consist of many superimposed frequencies. A time-series consisting of random numbers, as already mentioned, is called "white noise" because in the frequency domain it consists of a mixture of all frequencies, analogous to white light which is a mixture of all colours. So, it has an expected spectrum that is a flat line: the same average power at each frequency. However, this is not the only form of "random" (*sensu lato*) time-series. Consider a time-series where the next data point is generated by adding a

random number to the previous data point: equivalent to a "random walk". This time-series will not "flicker" so rapidly as white noise, since the value of each data point is influenced by the value of the previous one: the time-series is autocorrelated, and is generated by what is described as an AR(1) process. The lower-frequency flickerings result in a spectrum dominated by low frequencies, which by analogy with visible light once more is referred to as "red noise". For ideal red noise, the spectral density function is proportional to $1/f^2$, so power gets much larger at low frequencies.

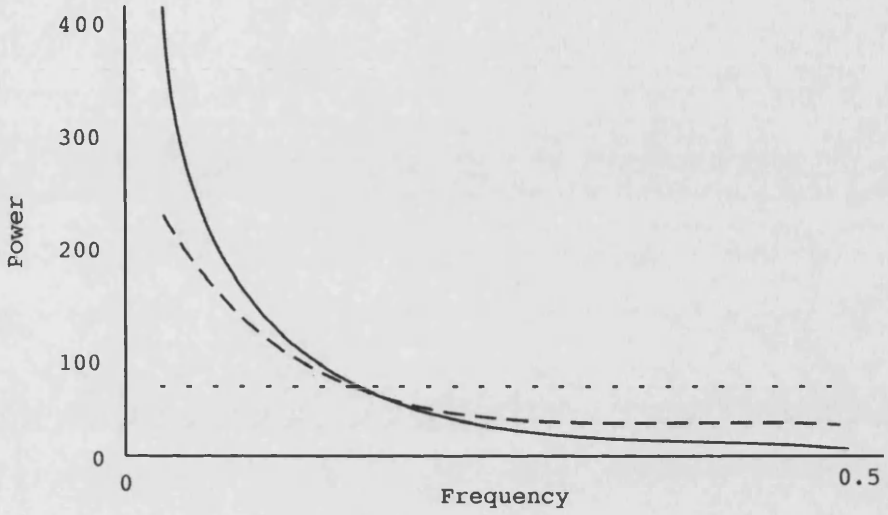

Figure A.5: Expected spectra of white noise (dotted), red noise (solid), and 1/f noise (dashes). Note that here the ordinates are plotted on a linear scale. Often when dealing with red noise and 1/f noise, a logarithmic scale is used so that high-frequency detail is not lost.

Between red noise and white noise, there is a type of spectrum called "pink noise" or "1/f noise", since the spectral density function is proportional to 1/f. Other types of noise also exist - blue noise, dominated by high frequencies, for example. These continuous spectra are significant because they often occur in nature: 1/f noise is especially common in this respect [34]. Such frequency spectra are an example of the wider phenomenon known as "self-similarity" or "scale invariance", exemplified by the shapes of coastlines, drainage networks, and many other natural features which exhibit similarity across time or length scales [34,35]. Mathematical models for such features include the famous Mandelbrot set and other "fractals", which exhibit self-similarity across all scales [34].

It is a matter of debate whether natural features can be genuine "fractals" since they can only exhibit self-similarity over a limited number of orders of magnitude [36], but complete or partial scale invariance of the frequency spectrum is common - variations in sea-level [37] and ocean current velocity [38] have been shown to resemble 1/f noise, for example. "Reddened" spectra in general - those dominated by low frequencies - are common for climatic data, because of autoregressive links between data points (as occurs with temperature change and snowmelt, for example, where the current state of the time-series is influenced by its past state), or (equivalently, in mathematical terms) because of white noise being filtered to remove

its higher frequencies. The thermal inertia of the oceans provides such a filter, for example, so that oceanic temperature variation is "redder" than atmospheric temperature variation [31].

Consider, then, the spectra of the various modes of climate variability summarised back in section 1.2. Some, such as Milankovitch cycles, may consist of isolated peaks, but many others have broader, noisier spectra, such as ENSO (which produces a broad increase in spectral power in the c. 2 to 10-year band) and the North Atlantic Oscillation, which varies across the spectrum in a manner not yet fully determined, possibly a combination of red noise and white noise [39,40]. One consequence of this is that to study such noisy, pseudoperiodic climate variability, it is necessary to consider the shape of the whole spectrum, not just isolated peaks in it. A problem arises here because of the nature of the periodogram. For white noise, the expected power at each frequency is $2\sigma^2$. However, real white noise spectra (see figure A.6) are "peaky" and unstable, and crucially do not flatten out as the time-series gets longer.

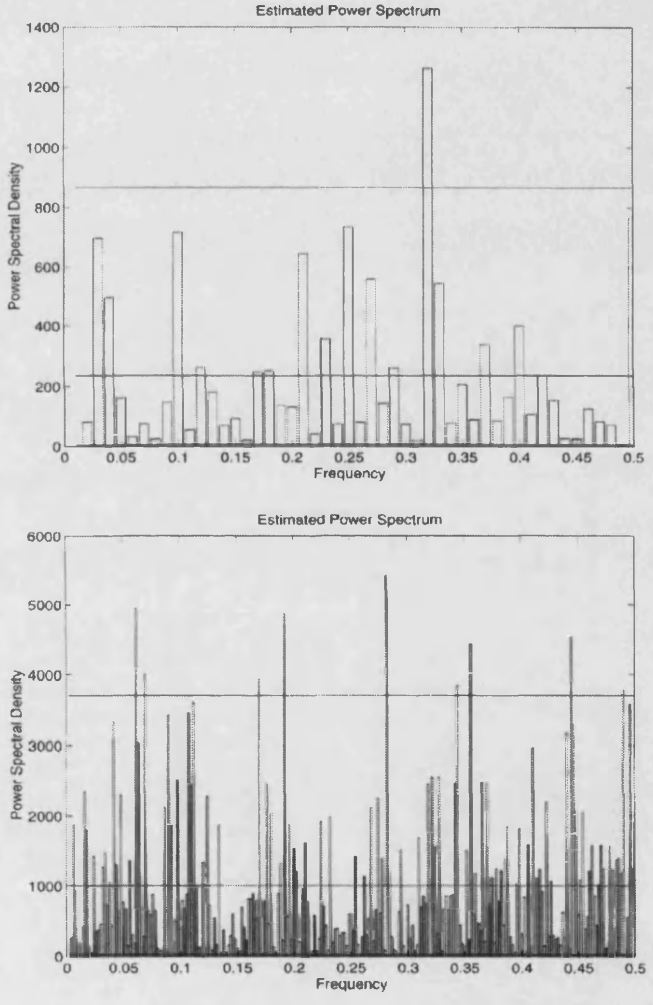

Figure A.6: Periodogram inconsistency. The upper periodogram is from a time-series of Gaussian white noise, of length T=100. The lower one is drawn from the same distribution, but is of length T=500. There is no tendency for the periodogram to become closer to the expected value (the lower horizontal line) as the length of the time-series increases. Note also the increased number of "significant" results at the 95% level (according to the Schuster test) in the lower periodogram, indicated by the upper horizontal line.

In most statistical procedures, when estimating a parameter of a data set, more confidence is gained in the estimate as the sample size gets larger. This is not the case for the periodogram: for a time-series with T values, the variance of I(f) does not decrease as T increases.

The explanation for this is that T independent Fourier coefficients are always being estimated from T values, such that however long the time-series is, the estimate of any one of these values never improves. (The improvement that *is* obtained by increasing T is a finer frequency grid, i.e. more data points between f = 0 and f = 0.5, which allows more precise location of peaks on the frequency axis, but not more confidence in their amplitudes). In order to reduce the wild fluctuations that characterise the periodogram, it needs to be modified such that the variance of I(f) decreases as T increases. This will produce a "consistent" estimator of the true spectrum.

Judgements of the unmodified periodogram as "worthless" usually assess it as a means of estimating a smooth spectrum, for which it is not suited. For sharp peaks, the unmodified periodogram is still worthwhile [41]. For smooth spectra, the periodogram needs to be modified or *filtered*.

A.6.2 The Daniell and Bartlett 1 filters

The variance of the periodogram ordinates can be reduced by applying a symmetrical moving average to them. This is the Daniell filter. It can only operate over an odd number of ordinates, because it is symmetrical. It averages m ordinates each time. For example, for m = 5, the moving average for frequency f(1) would cover f(-1), f(0), f(1), f(2), and f(3). The mean of these 5 ordinates is calculated, and this becomes the new value for f(1). This filter, or "spectral window", is a moving average. So after recalculating f(1), the new value for f(2) would be calculated by averaging f(0), f(1), f(2), f(3), and f(4). Note that the old, non-filtered value of f(1) is used. The filter moves across the whole periodogram in this way, producing a set of new, smoothed ordinates. The variance of the new set of ordinates equals the variance of the old set of ordinates divided by m, so it will get lower as m increases.

For a fixed set of periodogram ordinates, increasing m will result in a progressively smoother periodogram until all the peaks are subsumed into a smooth, slowly-changing spectrum. The "bandwidth" of the Daniell filter is most simply defined as m, the number of data points it averages each time. The bandwidth m can range from 1, which leaves the periodogram unchanged, up to a significant fraction of the number of ordinates. This is a compromise situation: to get more confidence in the ordinates, a wider bandwidth is needed, which makes individual peaks blur together. So, there is a trade-off between confidence and frequency resolution.

Now, time-series data can be studied in the time domain, by calculating the autocovariance series. This shows the "memory" of the time-series: how the data covary at different lags. Unusual as it may seem, the periodogram can be indirectly smoothed by filtering the autocovariance series. Recall that the frequency domain and the time domain are different representations of the same information. Any action in the time

domain has a corresponding action in the frequency domain, and vice versa. The Fourier transform is the "shuttle" used to travel back and forth between the two domains.

So, the Daniell filter is a rectangular or "boxcar"-shaped moving average applied in the frequency domain. But what effect does this filter have in the time domain? Its time-domain equivalent, obtained using the Fourier transform, is a filter applied to the autocovariance series: a set of weights that vary as lag increases. This is a "lag window"; recall that the original filter in the frequency domain is a "spectral window". The lag window is not a moving average; it is applied only once to the autocovariance series.

Because the Daniell filter has a rectangular shape in the frequency domain, it forms a sinusoidal curve in the time domain, with weightings falling from 1 at a lag of zero, to zero at some "truncation point" denoted by M. At lags above M, the weightings are all zero, i.e. all lags beyond M are ignored. This makes some intuitive sense for smoothing the periodogram, since the weightings reduce (or remove entirely) the influence of longer lags, which are calculated from fewer data points and are therefore more likely to be "noisy".

However, using the Daniell filter, the transition from large weights to small weights with increasing lag is irregular. The oscillating weighting curve even goes negative in some places, which makes little sense for smoothing the periodogram: why should any lag take on a negative value? So the Daniell filter makes sense in the frequency domain but not in the time domain.

Now consider the time-domain equivalent of the Daniell filter. This would be a lag window where all the weightings are one, up to a lag of M, beyond which all the weightings are zero, applied to the autocovariance series. So the smoothed periodogram is calculated from M unmodified lags but none of the remainder. The shape of this filter, like the Daniell filter in the frequency domain, is a rectangle or boxcar. This is called the Bartlett 1 filter [29] or just the Rectangular filter. Recall that lag windows such as this are only applied in a single position, unlike spectral windows, which are moving averages and which are applied across the whole periodogram.

M can be used to denote the number of lags that the Bartlett 1 filter covers. The length of the autocovariance series is the same as the length of the original time-series, N, since the lags range from 0 to N - 1. So, given N lags in total, applying a Bartlett 1 filter with M = N will include all of them, leaving the periodogram unchanged. So, for a lag window such as the Bartlett 1 filter, progressively reducing M results in a smoother and smoother periodogram. The parameter M in this sense works in the opposite direction to the parameter m that was defined as the bandwidth of the Daniell filter.

Again, there is a problem when the effects of filtering in both the frequency and the time domains are considered. The Bartlett 1 filter makes sense in the time domain, since it weights the lags it uses in a logical way. But in the frequency domain, it takes on a wiggly shape, just as the Daniell filter did in the time domain. This wiggly moving average has some undesirable effects on the periodogram ordinates. For

example, some of the weightings of the moving average are negative, so it can potentially produce negative periodogram ordinates, which are nonsensical. Similarly, positive "side lobes" each side of the main peak can produce "ghost peaks" in the smoothed spectrum which should not be there. Essentially, some of the new estimates of spectral power will be contaminated by "leakage" of power from other frequencies because of the shape of the filter. This is undesirable.

So, both the Daniell and Bartlett 1 filters look suitable in one domain but introduce problems in the opposite domain. This occurs because of their rectangular shapes. The Fourier transform approximates sharp corners by using many sinusoids in the opposite domain; this conversion of sharp corners into "ringing" sinusoids is known as the Gibbs phenomenon. A filter is needed which looks sensible in both domains, i.e. as both a spectral window and a lag window. This filter will not have sharp corners in either domain. Many different filters have been suggested to solve this problem of acceptability in both frequency and time domains [41]. "There really is no limit to the number of different windows which we could construct; in fact, virtually any even function $\lambda(s)$ which is such that $\lambda(0) = 1$ and $\lambda(s)$ decays smoothly to zero and involves a parameter which controls the rate of decay, will provide a 'reasonable' [lag] window" [41]. The filter used here is the Blackman-Tukey filter.

A.6.3 The Blackman-Tukey filter

This has a shape which looks reasonable in both the frequency and the time domains; in neither does it have sharp corners which would cause "ringing" in the other domain. It is defined in the time domain, i.e. as a lag window applied to the autocovariance series. For historical reasons, the nomenclature is confusing here [5]. The Blackman-Tukey *filter* is a lag window. It is not the same as the Blackman-Tukey *method*, which is the method of truncating the autocovariance series using any lag window. There are several versions of the Blackman-Tukey filter, of which the simplest is described here, since their effects are very similar.

Beyond a selected truncation point, M, the lags will be weighted at zero: they will not be "visible through the spectral window". M is the "number of lags" of the Blackman-Tukey filter. For lags from zero up to M, the autocovariance series is multiplied by a decreasing set of weights. It seems reasonable that the longer lags should be less important in calculating the smoothed periodogram, since they are calculated from less information.

As with other lag windows, the filter only needs to be applied once, to the autocovariance series, instead of multiple times across the whole periodogram, which is the case for spectral windows. Historically, this made lag windows, i.e. the Blackman-Tukey *method*, more popular than spectral windows, and by association, the Blackman-Tukey *filter* became the "standard" for smoothed periodograms in many fields, including palaeoclimatology. Because of this past familiarity, it remains the unofficial standard filter in palaeoclimatology today [10], as used by, for example, Chapman and Shackleton [42], and Bianchi and McCave [43].

The autocovariance weights for the Blackman-Tukey filter are defined as:

$$\lambda(k), \text{ for } k = 0 \text{ up to } k = M,$$

$$\text{where } \lambda(k) = {}^{1}/_{2} \, (1 + \cos (\pi \times (k / M)).$$

This works as follows. k runs from 0 up to M, so (k / M) runs from 0 up to 1. Consider the cosine term. This runs from cos (0), when k = 0, up to cos (π) when k = M. So, the value of $\lambda(k)$ at k = 0 is ${}^{1}/_{2}$ (1 + cos (π)), which equals 1. At k = ${}^{M}/_{2}$, $\lambda(k)$ is ${}^{1}/_{2}$ (1 + cos (π / 2)), which equals ${}^{1}/_{2}$. At k = M, $\lambda(k)$ equals ${}^{1}/_{2}$ (1 + cos (-π)), and since cos (-π) = -1, $\lambda(M)$ = 0. So $\lambda(k)$ decreases smoothly from 1 to 0 over the interval of 0 to M lags. The shape of the Blackman-Tukey filter in the time domain is similar to its shape in the frequency domain, although it does contain some small negative weightings for the moving average. These are not important, since in practice they do not produce negative ordinates unless M is unreasonably small. This can be clarified by reference to a diagram.

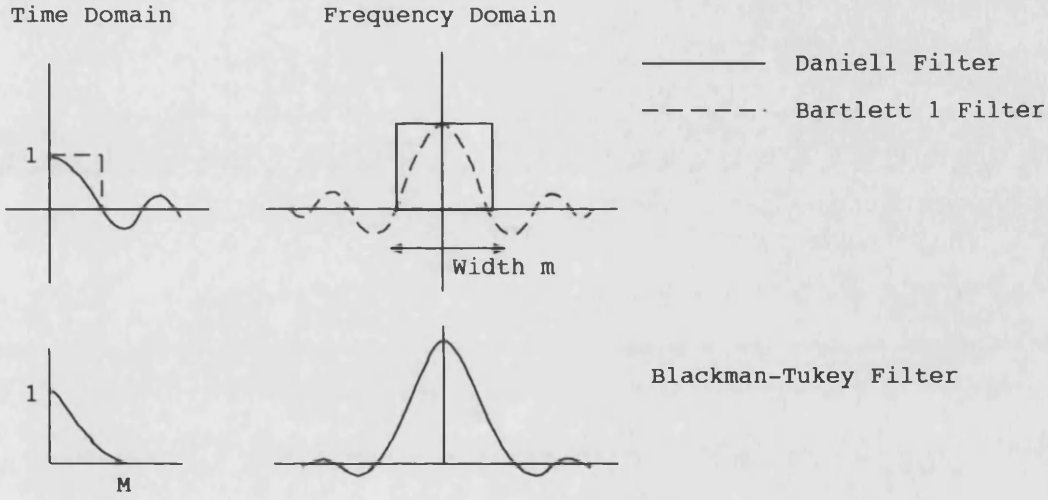

Figure A.7: Shapes of Daniell and Bartlett 1 filters (compared at top) and Blackman-Tukey filter (at bottom) in both the frequency and time domains. The Blackman-Tukey filter is the most suitable of the three, when its shape in both domains is considered.

The ordinates of a filtered spectrum still follow, approximately, a chi-squared distribution. This will have more than two degrees of freedom, hence the variance of the estimate will be lower. Calculating the exact degrees of freedom is difficult; usually, an "equivalent degrees of freedom" (EDF) is quoted for a given filter, in terms of the bandwidth used. For the Daniell filter, the EDF is just 2 × m, since m independent variables are being added each time, each of which is distributed as a chi-squared distribution with 2 degrees of freedom. The ordinates of a spectrum smoothed by applying the Blackman-Tukey filter approximately follow a chi-squared distribution with 8N / 3M degrees of freedom, where N is the total number of lags (or data points), and M is the truncation point [44].

After a filter has been applied, ordinates which are within one bandwidth of each other will no longer be independent, because they will have influenced each other's values. In general, then, the wider the bandwidth, the lower the independence of the

smoothed ordinates, as well as the greater the degrees of freedom. Choosing an appropriate bandwidth is an "art" [29]; there is no general solution. Bandwidths which are too low will not remove spurious "noise" peaks; bandwidths which are too high will omit important detail from the spectrum. Choosing a suitable truncation point for a lag window is analogous to choosing a suitable bandwidth for a spectral window. There is no general solution, and again a compromise must be sought between resolving separate peaks and smoothing out unwanted variance. Chatfield [5] suggests a value for M of $2 \times \sqrt{N}$ as a starting point.

For the Blackman-Tukey filter, as M gets smaller, as the autocovariance series is truncated to a greater degree, as the spectrum gets smoother, the EDF gets larger, so the threshold for a significant peak falls. This applies to all lag windows: the EDF is some function of N / M. Instead of specifying a number of lags, it is possible to use the "Blackman-Tukey parameter" (= N / M). This is advantageous because it gives the same amount of smoothing regardless of the length of the time-series; in comparing time-series of different lengths, a Blackman-Tukey parameter of 1/3, for example, could be fixed.

This value of 1/3 has entered time-series analysis "folklore" as the best value to start with, without any real justification [10]. Since the choice of bandwidth is more influential than the choice of filter on the shape of the periodogram, it is sensible to use a more sophisticated method than trial-and-error, or use of a "conventional" value, to find a suitable bandwidth.

The technique of "window closing", used here, involves starting with a very highly smoothed spectrum, then gradually increasing the bandwidth so that the spectrum becomes peakier. The analogy is with a spectral window which is being "closed" such that the bandwidth becomes progressively smaller. The behaviour of the spectrum as the bandwidth decreases is observed, the desired result being an optimum bandwidth which brings out any major peaks but is large enough to smooth out any noise [41]. In essence, a subjective decision is made as to when the spectrum is neither too smooth nor too peaky, implying that the observer somehow knows *a priori* the expected degree of smoothness of the optimally-filtered spectrum. This judgement depends strongly on previous experience with spectral analysis.

A.6.4 The outcome of filtering

What insight can be gained from a filtered spectrum? A spectrum that has been greatly smoothed can be compared with expected spectral density functions from the different processes mentioned in section A.6.1: red noise, for example. Such scale invariance in a smoothed spectrum can be linked to physical mechanisms such as "self-organised criticality" [45], which may underlie some forms of sedimentary deposition [46], though this research concentrates on periodic and pseudoperiodic signals which are better established as descriptors of climate variability. Such signals appear on filtered spectra as broad increases in power within appropriate frequency bands.

This sounds suspiciously vague. Can significance tests be applied to these broad increases? Yes, as long as the effects of the filtering are taken into account. The

EDF for the Blackman-Tukey filter is 8N / 3M, where N is the total number of lags (or data points) and M is the truncation point. Using a Blackman-Tukey parameter of 1/3, i.e. including 1/3 of the lags in the weighted autocovariance function, makes M / N equal to 1/3, so makes N / M equal to 3. So the EDF is (8 / 3) × 3, which equals 24 / 3, which equals 8. From a statistical table, the 0.95 quantile is 15.51. So the one-sided 95% confidence interval threshold for a white noise null hypothesis is (15.51 / 8) × 2 × σ^2 × N, which equals 3.8775 × σ^2 × N.

As the EDF increases, the confidence threshold gets lower, since although the table values get bigger, the division by the increased EDF more than compensates for this. As desired, greater smoothing results in a narrower confidence interval. However, there is a problem in applying the confidence interval threshold across the whole spectrum, since this implies that the ordinates are all independent. This is true for the unmodified spectrum, but not for the smoothed spectrum. Recall that filters in the frequency domain - spectral windows - act as weighted moving averages. Ordinates which contribute to each other's new, averaged values are no longer independent, so their significance cannot be tested simultaneously. In contrast, ordinates which are far enough apart that they are not averaged together at some point will remain independent. So, the independence of two points on the filtered spectrum depends on the bandwidth. Only if they are further apart than the bandwidth can they be tested simultaneously.

This can be visualised using what happens to an isolated peak on a flat background spectrum following filtering. The peak adopts the shape of the spectral window that was used. The raised values to either side of the peak are a consequence of the averaging; their new power values may be unusually large, but they are not independent from the original frequency, so there is no justification for claiming that the frequencies to either side of the peak are also now significant. In practice, the filtered spectrum is kept "honest" by quoting the bandwidth on the spectrum itself, as a horizontal bar, for example. Significance tests *are* applied to the whole spectrum simultaneously, but it is kept in mind that only peaks further apart than the bandwidth can have separate significance.

So, the filtered spectrum is an improvement because the variance of the ordinates is reduced. Simultaneously, the frequency resolution is reduced: sharp peaks become lower and broader. The price paid for decreased *variance* is increased *bias*. Generally, for Holocene climatic variability, this is a profitable exchange: confirmation of significant peaks on the spectrum is more important than their precise frequency values. However, problems remain with the interpretation of significance tests, as were mentioned briefly at the start of section A.5. Uncertainty in the interpretation of spectra showing palaeoclimate variability arises not just from the compromises inherent in filtering the spectrum, but also from the nature of significance testing itself. There is no need for further exhaustive coverage of spectral analysis: the methods to be used have already been covered, and the need for caution in interpretation which concludes this appendix is better justified at this point by noting the uncertainty of interpreting significant features in the data.

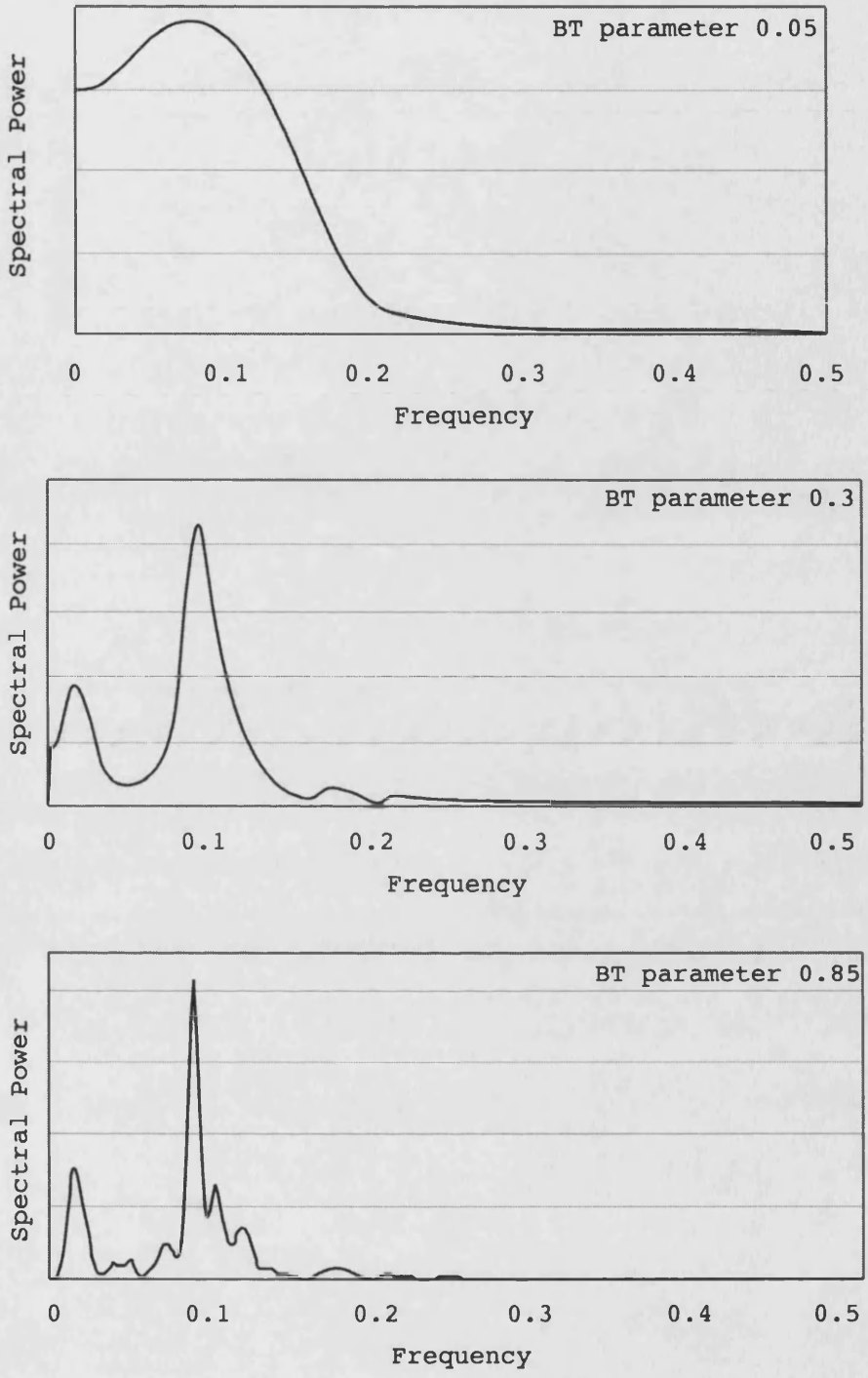

Figure A.8: The technique of "window closing", progressively making the spectrum less smooth until a subjective decision can be made that all the significant peaks are visible, without the structure being too confused by noise, which would emerge if the process were continued further. This example uses the Blackman-Tukey filter on the Wolfer sunspot data, with parameters of 0.05, 0.3, and 0.85 respectively. The structure of the spectrum gradually emerges, initially only showing the 11-year peak, then with more detail becoming apparent.

A.7 Spectral interpretation

A.7.1 Significance testing and statistical conservatism

The null hypothesis for a spectrum, whether white noise or anything else, cannot be disproven. Even the most highly-structured or unusual spectrum could conceivably result from a time-series of random values, since by definition, random values can take any values at all. So, significance testing of the spectrum, whether filtered or unfiltered, is a matter of rhetoric [47]: of convincing the reader that the results are significant, rather than proving that they are such.

The conventional probability level below which the null hypothesis is rejected is 5%: that is, there is a 5% chance of a type I error, which occurs when the null hypothesis is true but is falsely rejected. Its counterpart is a type II error, where the null hypothesis really is false, but the probability level is greater than 5%, so the null hypothesis is not rejected. (Strictly, this is not an "error", just a refusal to commit to a definite interpretation of the results.)

Is the conventional level of 5% adequate for all purposes? Problems naturally arise when the probability level just falls short of this. Bearing in mind the arbitrary nature of the 5% level, it is possible to claim that the results are "significant at the 7% level", say. Alternatively, a "p-value" can simply be stated, such as p=0.07, leaving its interpretation to the reader, though this is perhaps unacceptably non-committal. Is a "liberal" or a "conservative" style of interpretation preferable? This depends on the situation [19]. Medical safety testing, for example, may require absolute certainty that a significant result has not been accidentally missed: a type II error. For cyclicity in varve data, on the other hand, it is probably better to be cautious about any peak in the spectrum, even if apparently significant, in order to avoid a type I error. On what basis is this conservatism justified?

Firstly, peaks in the spectrum, even after smoothing, are not unusual. The "peaky" nature of pure noise spectra may not be well known to earth scientists, whose experience of spectral analysis is often confined to Milankovitch cyclicity, which is an unusual case. Finding peaks on a spectrum should not be a surprising result, but this unfamiliarity might make it so, in which case the "significance" of the result, in a Bayesian sense, is high: the data appear to challenge (erroneous) prior beliefs. Not only the presence of spectral peaks but their height, too, may appear significant simply because of the greater positive skewness of the exponential distribution, compared to that of the more familiar normal distribution [10]. Subsequent significance testing of these peaks may be regarded as superfluous by those who are unduly impressed by peaks on the spectrum. Prior experience is important in this case. *Not every peak must have an explanation.*

One way around this could be to consider only peaks found at pre-specified frequencies. In the author's opinion, this methodological argument is unconvincing. Palaeoclimatology, in its current state of infancy, is dominated by creative inference rather than confirmation: it works *from* the data, *towards* explanatory mechanisms such as solar variability and ice sheet surges, not the other way around. Thus, the time at

which evidence becomes known is not relevant to its status in support of a hypothesis [48]. Peaks in the spectrum, even at "characteristic" frequencies, must still be significance-tested if their interpretation is to be convincing.

Secondly, processing of the time-series data, even if well-intentioned, can produce falsely-significant spectral peaks. This ranges from obvious problems such as "fishing" for significant results from many spectra without adjusting the significance levels appropriately, to bias in the removal of outliers or certain frequencies from the data. As Hernandez [49] writes:

"Arbitrary changes to the character and magnitude of the sample variance lead to unpredictable results, which cannot be statistically supported ... it is simply invalid to assign to the original data the results of significance tests performed on data whose power spectrum has been arbitrarily manipulated. In fewer words, the tests for statistical significance are no longer being made on the original data and therefore are not relevant to them."

Thirdly, even if the data have not been tampered with, there is still the need to avoid type I errors as mentioned earlier. There are a number of reasons why type I errors should make it into the literature as "significant" results. Bias in publication is the most important. Consider a group of separate studies on cyclicity in varves; in many cases the decision to publish, and the success of such a decision, will be influenced by the presence or absence of a significant result, meaning that the nominal 5% chance of a type I error in the literature is an underestimate [50]. This is especially a problem for varve studies, because the field consists of many small, separate investigations with little meta-analysis [47]. Three examples of varve-based cyclicity testing are now discussed.

A.7.2 Examples of varve-based analysis

Ripepe *et al.* [51] claim to have found ENSO and sunspot cycles in Eocene varved oil shale. But they do no significance testing on their spectra; this would, in any case, have been complicated by the filtering and averaging that they used. It appears from their spectra that their chosen "peaks" are little different from the ones that they disregard, in terms of their height, although without significance testing it is impossible to say (see figure A.9).

Similarly, Schaaf and Thurow [52] do no significance testing on their spectra, simply assigning climatic influences to some peaks and disregarding others as insignificant or unexplained. Without significance testing, it seems unconvincing to describe their greyvalue-based spectra as in any way significantly different from red noise (see figure A.10).

Finally, Livingstone and Hajdas [53] claim to have found cyclicity in lake varves from Switzerland. They, at least, do significance testing on their spectra, but find that their chosen peaks are only barely significant even at a 90% level of confidence (see figure A.11). They excuse this weak level of significance by reference to Anderson and Koopmans [54], who argue opaquely that the presence of noise in varve data causes real peaks to be labelled as insignificant. In their original study, Anderson and Koopmans

[54] note only "general frequency areas of increased power". This tactic results in sixteen pages of detailed description of the random peaks in noise spectra.

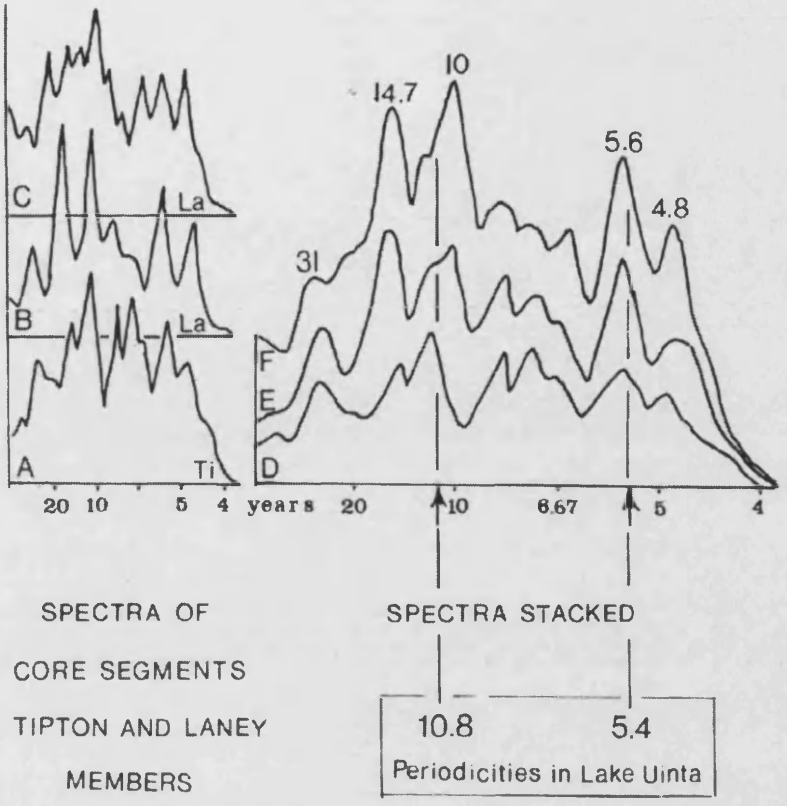

Figure A.9: Spectra of varve thicknesses from various records of Eocene oil shales, from Ripepe *et al.* [51]. The 10.8- and 5.4-year "guidelines" emphasise spectral peaks which are not obviously significant in isolation.

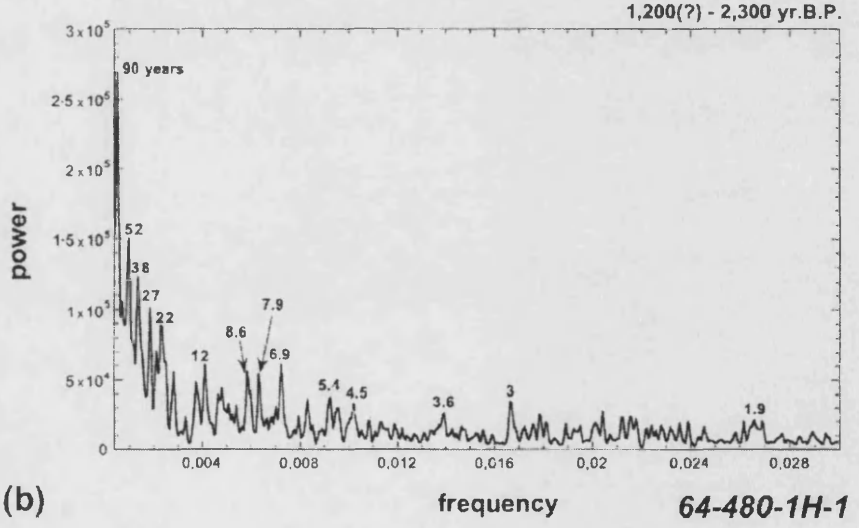

Figure A.10: Spectrum of a sediment greyvalue linescan from Schaaf and Thurow [52]. It is unclear which, if any, of the many labelled peaks are significant.

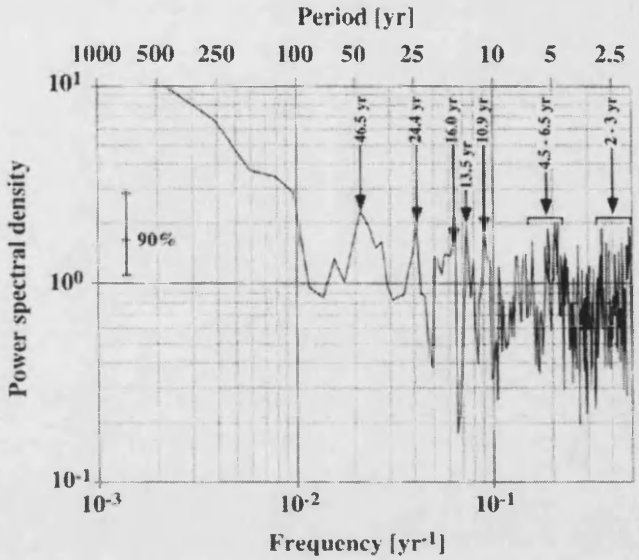

Figure A.11: Varve thickness spectrum from Livingstone and Hajdas [53]. Both spectral power and frequency are plotted on logarithmic scales, allowing a wide range of frequencies to be compared on the same spectrum. The bar indicates the excess height of a significant peak when compared to a smoothed version of the spectrum (the null hypothesis).

Evidently, research methodology has come full circle since Anderson and Koopmans [54], in 1963, argued for less strictness in identifying peaks in varve spectra. The general trend in varve-based spectral analysis seems to be to interpret climatically any spectral peaks that appear at desired frequencies, and to disregard all the rest, without taking much notice of significance testing. This approach is unsatisfactory because it leads to the imposition of a "conventional" view of palaeoclimate variability on each record, even if this fails to fit very well, and the casting aside of "inexplicable" variability in the data which could turn out to be important.

A.7.3 More complex spectral techniques

Numerous more complex techniques are available which may improve the spectral interpretation of palaeoclimate data, and these are described below, though in all cases an improvement in the ability to detect a given spectral peak is accompanied by a decrease in the confidence that the peak is meaningful. This, together with the need to use a more complex approach, explains why many investigations continue to use the basic periodogram as described above.

Firstly, a null hypothesis that is different to white noise can be chosen: a parametric approach, where one or more additional parameters are specified in the data model before the significance testing is done. The expected significance threshold values for a non-white-noise null hypothesis are simple to calculate because of the property of the exponential distribution that its standard deviation is equal to its mean. The significance threshold will no longer be uniform across the whole spectrum, of course. For example, a red noise spectrum, where power is proportional to $1/f^2$, could be used as a null hypothesis, or an autoregressive time-domain model could be fitted to the data, then the spectrum of this model used as a null hypothesis, or more

simply a very smoothed version of the spectrum of the data could be used as a null hypothesis to find peaks in the unmodified spectrum.

One problem with this latter approach is that pseudoperiodic climate variability does not generally produce sharp peaks in the spectrum anyway, unlike astronomically-driven cycles; in this way, parametric null hypotheses can potentially focus attention on noise - meaningless sharp peaks - rather than real spectral features. Another problem is that although this approach may seem more conservative than using white noise as a null hypothesis, producing results of greater significance, it is less parsimonious because more assumptions have been made about the data before the testing is done. Red noise and 1/f noise, as mentioned in section A.6.1, are common forms of climatic background noise, but only if there is good reason to believe that the background noise follows a non-white spectrum, should such a non-white null hypothesis be used.

Secondly, *evolutionary power spectra* can be constructed by splitting up a time-series into many subseries, say x_1 to x_{10}, x_{11} to x_{20}, and x_{21} to x_{30}, then calculating the spectrum for each subseries, then plotting the results in three dimensions, usually as a contour plot, i.e. with time on the x-axis, frequency on the y-axis, and power on a colour or shaded scale. This technique originated as a method of dealing with strongly non-stationary time-series which could be separated into stationary, or near-stationary, subseries, allowing cyclicity within the data to be studied without the spectra being distorted by the non-stationarity.

For strictly stationary time-series, the spectra of all the subseries should be identical, such that an evolutionary spectrum just shows minor random variation between one subseries and the next. However, for real, but noisy, climate data, short sections of the original time-series may show significant cyclicity whose lack of persistence means that it does not show up on the spectrum of the whole, for example, the influence of decadal and centennial-scale variability over the Holocene [12]. However, care must be taken to ensure that all the spectra are filtered to the same degree, and that significance levels are consistent, otherwise there is a risk that the "changing patterns of variability" seen only in the evolutionary spectrum are simply noise, which cancels out in the overall spectrum.

Thirdly, Maximum Entropy Spectral Analysis (MESA) [55] has also been used to generate spectra from palaeoclimate data [e.g. 56,57]. Maximum entropy spectra are not like ordinary spectra in that they do not contain all the information in the data. They are constructed by fitting an autoregressive model to the data which has the same autocorrelation function, and which produces the most random (i.e. least predictable) time-series. This is the "maximum entropy" solution in the sense that it fits the autocorrelation function, but is maximally non-committal as to the structure of the time-series over and above this.

Recall the "poor man's spectral analysis" with which Fourier coefficients were introduced in section A.4.3.1. A simplified way to understand MESA is as this process of progressively fitting sinusoids to the residual of the time-series. The result is a spectrum with peaks which are not independent, since the subtraction of one dominant frequency from the data affects the determination of the subsequent ones. This means

that no significance testing can be carried out on the spectrum, but in return, the ordinates are no longer restricted to the Fourier frequencies, meaning that all the peaks are in the right place. The nature of MESA spectra is similar: no significance tests can be carried out, and the heights of the peaks are not reliable, but their frequency positioning is accurate [58]. As with the filtered periodogram, a "window-closing" method can be used with MESA. A coefficient M is gradually reduced whilst plotting the spectrum. The nature of MESA is such that beyond a certain point, many "noise" peaks will arise in the spectrum; the value of M needs to be chosen using prior experience, such that only an appropriate number of peaks appear.

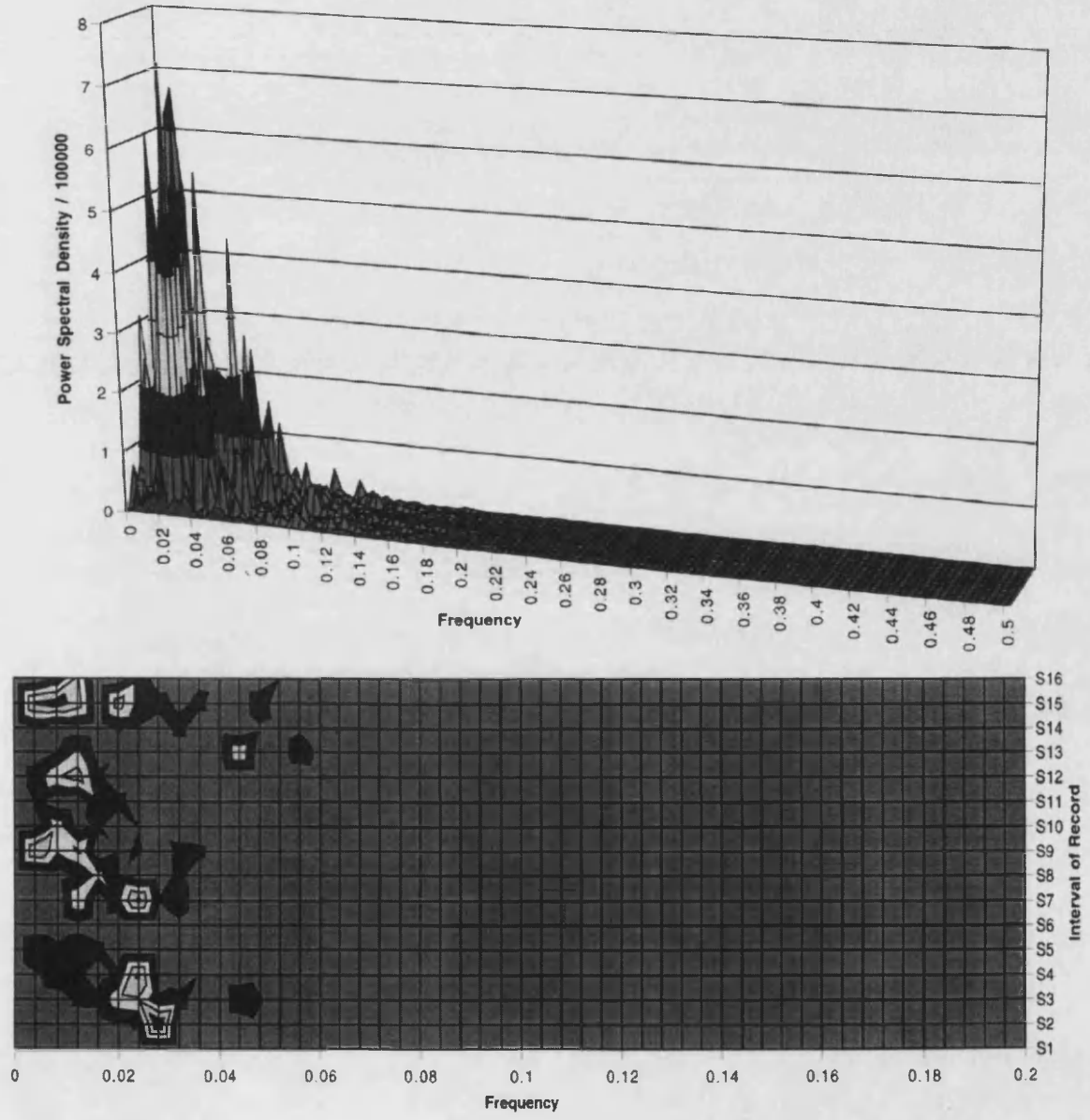

Fig A.12: A simple example of an evolutionary power spectrum, taken from Drammensfjord greyvalue data. The upper figure shows the true 3D representation. The lower figure shows the shaded contour plot: a simplified representation of the same data. Different greyvalues represent different levels of spectral power.

It is beyond the scope of this thesis to describe the many other varieties of spectral analysis that have been used on varve-based time-series, such as singular spectrum

analysis (SSA) [e.g. 11], and multitaper methods [e.g. 59]. To repeat a point made in section 6.1, it is better to use methods that are well-understood, as long as their weaknesses are acknowledged, than to produce apparently impressive results using a misapplied, complex technique. Of course, if multiple methods are used, which is often the best strategy [e.g. 60], then the results of all of them must be considered. It is not acceptable to choose only the method that gives the best results, and to ignore the rest.

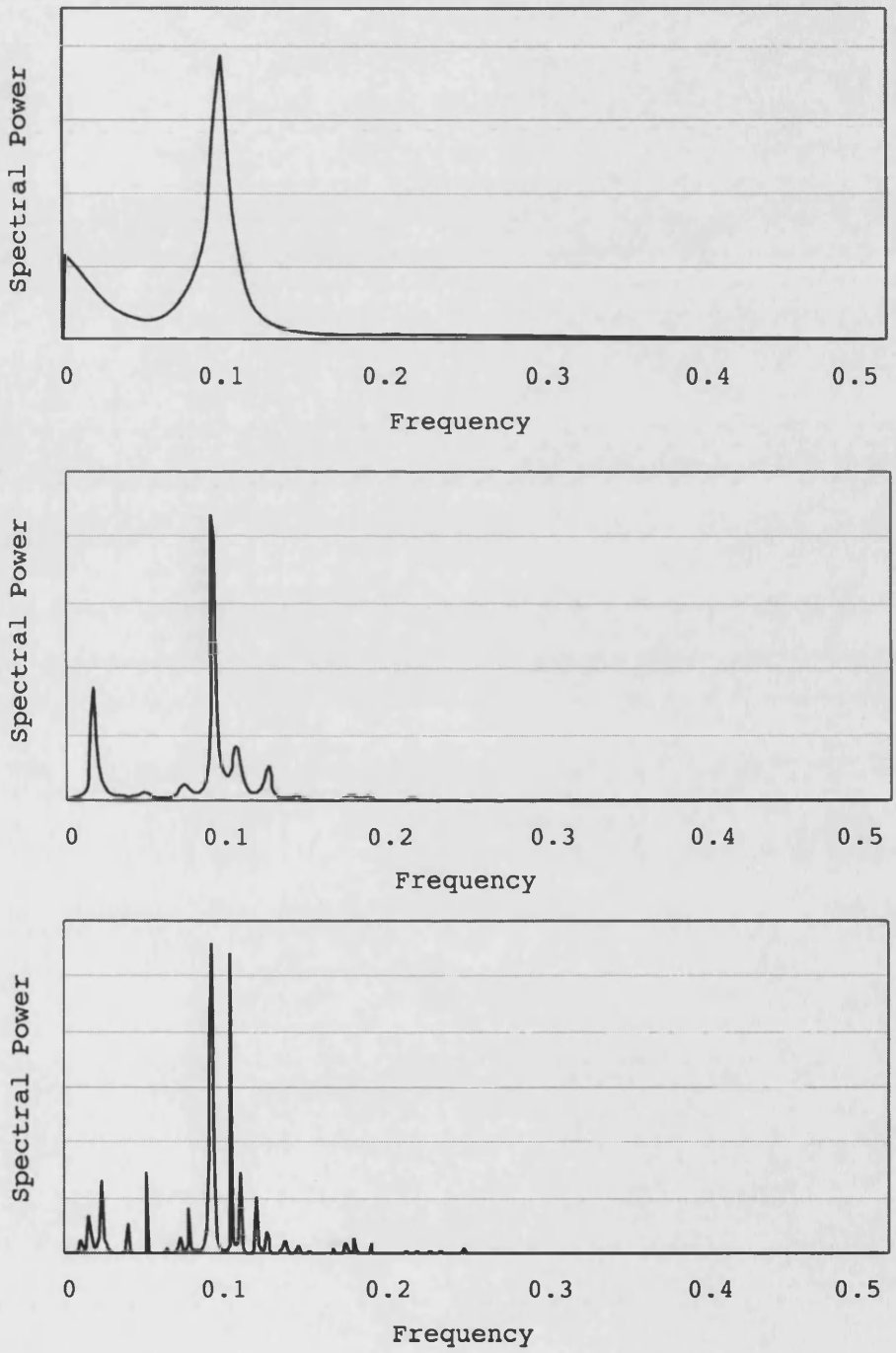

Figure A.13: MESA window-closing example using Wolfer sunspot data. The upper spectrum is too smoothed, the lower one is not smoothed enough. The middle spectrum shows an appropriate level of detail without being swamped by noise.

A.8 Conclusion: the need for caution in time-series analysis

This appendix has demonstrated how misunderstandings and poor practice can easily arise during time-series analysis because of its unfamiliar and difficult nature and because of the range of methods available.

"False" cyclicity, in particular, can arise from systematic distortion of the data, such as cyclicity introduced by uneven illumination of sediment core images: any frequency close to one cycle per image is suspect and should be ignored. More insidiously, cyclicity can arise out of noise by misguided attempts at filtering; the Slutsky-Yule Theorem demonstrates how a weighted moving average can introduce cyclicity into white noise: a result that may surprise the inexperienced [29].

Furthermore, significance testing of frequency spectra is not purely a mathematical exercise. The significance of a result cannot be *proven*; it can only be regarded as more, or less, convincing depending on the circumstances. This does not mean that frequency testing should be abandoned altogether, and that time-series should only be analysed in terms of a succession of "zones" as described in section A.2. But it does mean that as much experience as possible should be gained of spectral analysis - especially spectral analysis of *noise*, with all its apparently "significant" features - before real data are analysed, and that a cautious approach to the results of spectral analysis should be adopted, especially given the controversial nature of Holocene climate change.

Appendix A References

[1] Moore, P. D., 1986, Hydrological changes in mires, In: Berglund, B. E., (Ed.), Handbook of Holocene Palaeoecology and Palaeohydrology, John Wiley, p. 91-110.

[2] Lamb, H. H., 1995, Climate, History, and the Modern World, Second Edition, Routledge, 433 pp.

[3] Blackford, J., 1993, Peat bogs as sources of proxy climatic data: past approaches and future research, In: Chambers, F. M., (Ed.), Climate Change and Human Impact on the Landscape, Chapman and Hall, p. 47-56.

[4] Houghton, J. T., Ding, Y., Griggs, D. J., Noguer, M., van der Linden, P. J., and Xiaosu, D., (Eds.), 2001, Climate Change 2001: the Scientific Basis, Contribution of Working Group I to the Third Assessment Report of the Intergovernmental Panel on Climate Change (IPCC), Cambridge University Press, 944 pp.

[5] Chatfield, C., 1996, The Analysis of Time-series: An Introduction, Fifth Edition, Chapman and Hall / CRC, 283 pp.

[6] Fourier, J. B., 1822, La Théorie Analytique de la Chaleur, Paris.

[7] Cooley, J. W., and Tukey, J. W., 1965, An algorithm for the machine computation of complex Fourier series, Mathematical Computing, 19:297-301.

[8] T. A. Wheeler, personal communication, November 2001.

[9] Beveridge, W. H., 1922, Wheat prices and rainfall in western Europe, Journal of the Royal Statistical Society, 85:412-478.

[10] Muller, R. A., and MacDonald, G. J., 2000, Ice Ages and Astronomical Causes: Data, Spectral Analysis and Mechanisms, Springer Praxis, 318 pp.

[11] Schaaf, M., and Thurow, J., 1994, A fast and easy method to derive highest-resolution time-series datasets from drillcores and rock samples, Sedimentary Geology, 94:1-10.

[12] Schaaf, M., and Thurow, J., 1997, Tracing short cycles in long records: the study of inter-annual to inter-centennial climate change from long sediment records, examples from the Santa Barbara Basin, Journal of the Geological Society, London, 154:613-622.

[13] Rodbell, D. T., Seltzer, G. O., Anderson, D. M., Abbott, M. B., Enfield, D. B., and Newman, J. H., 1999, An ~15,000-year record of El Niño-driven alluviation in southwestern Ecuador, Science, 283:516-520.

[14] Jenkins, G. M., and Watts, D. G., 1968, Spectral Analysis and its Applications, Holden-Day, 525 pp.

[15] Janacek, G., 2001, Practical Time-series, Arnold Texts in Statistics, 156 pp.

[16] Schuster, A., 1898, On the investigation of hidden periodicities with application to a supposed 26-day period of meteorological phenomena, Terrestrial Magnetism and Atmospheric Electricity, 3:13-41.

[17] Fisher, R. A., 1929, Tests of significance in harmonic analysis, Proceedings of the Royal Society Series A, 125:54-59.

[18] Priestley, M. B., 1997, Chapter 5: Detection of periodicities, In: Subba Rao, T., Priestley, M. B., and Lessi, O., (Eds.), Applications of Time-series Analysis in Astronomy and Meteorology, Chapman and Hall, p. 65-88.

[19] Koen, C., 1990, Significance testing of periodogram ordinates, The Astrophysical Journal, 348:700-702.

[20] Whittle, P., 1952, The simultaneous estimation of time series harmonic components and covariance structure, Trabafos Estadistica, 3:43-57.

[21] Whittle, P., 1954, The statistical analysis of a seiche record, Journal of Marine Research, 13:76-100.

[22] Chiu, S. T., 1989, Detecting periodic components in a white noise Gaussian time series, Journal of the Royal Statistical Society B, 51:249-259.

[23] Hartley, H. O., 1949, Tests of significance in harmonic analysis, Biometrika, 36:194-201.

[24] Grenander, U., and Rosenblatt, M., 1957, Statistical Analysis of Stationary Time Series, John Wiley, 308 pp.

[25] Shimshoni, M., 1971, On Fisher's test of significance in harmonic analysis, Geophysical Journal of the Royal Astronomical Society, 23:373-377.

[26] Siegel, A. F., 1980, Testing for periodicity in a time-series, Journal of the American Statistical Association, 75:345-348.

[27] Bolviken, E., 1983, New tests of significance in periodogram analysis, Scandinavian Journal of Statistics, 10:1-9.

[28] Quinn, B. G., 1989, Estimating the number of terms in a sinusoidal regression, Journal of Time Series Analysis, 10:71-76.

[29] Gottman, J. M., 1981, Time-series Analysis: a Comprehensive Introduction for Social Scientists, Cambridge University Press, 400 pp.

[30] Granger, C. W. J., and Morgenstern, O., 1964, Spectral analysis of New York stock market prices, In: Cootner, P. H., (Ed.), The Random Character of Stock Market Prices, MIT Press, Ch. 8, p. 162-188.

[31] Burroughs, W. J., 1992, Weather Cycles: Real or Imaginary?, Cambridge University Press, 201 pp.

[32] Lorenz, E., 1963, Deterministic non-periodic flow, Journal of Atmospheric Sciences, 20:130-141.

[33] Yule, G. U., 1927, On a method of investigating periodicities in disturbed series with special reference to Wolfer's sunspot numbers, Philosophical Transactions of the Royal Society, London, A, 226:267-298.

[34] Mandelbrot, B. B., 1982, The Fractal Geometry of Nature, W. H. Freeman and Co., 468 pp.

[35] Turcotte, D. L., 1997, Fractals and Chaos in Geology and Geophysics, Second Edition, Cambridge University Press, 398 pp.

[36] Avnir, D., Biham, O., Lidar, D., and Malcai, O., 1998, Is the geometry of nature fractal?, Science, 279:39.

[37] Wunsch, C., 1972, Bermuda sea-level in relation to tides, weather, and baroclinic fluctuations, Reviews of Geophysics and Space Physics, 10:1-49.

[38] Taft, B. A., Hickey, B. M., Wunsch, C., and Baker Jr., D. J., 1974, Equatorial undercurrent and deeper flows in the central Pacific, Deep Sea Research, 21:403-430.

[39] Frankignoul, C., Muller, P., and Zorita, E., 1997, A simple model of the decadal response of the ocean to stochastic wind forcing, Journal of Physical Oceanography, 27:1,533-1,546.

[40] Stephenson, D. B., Pavan, V., and Bojariu, R., 2000, Is the North Atlantic Oscillation a random walk?, International Journal of Climatology, 20:1-18.

[41] Priestley, M. B., 1981, Spectral Analysis and Time Series, Academic Press, 925 pp.

[42] Chapman, M. R., and Shackleton, N. J., 2000, Evidence of 550-year and 1,000-year cyclicities in North Atlantic circulation patterns during the Holocene, The Holocene, 10:287-291.

[43] Bianchi, G. G., and McCave, I. N., 1999, Holocene periodicity in North Atlantic climate and deep-ocean flow south of Iceland, Nature, 397:515-517.

[44] Von Storch, H., and Zwiers, F. W., 2002, Statistical Analysis in Climate Research, Cambridge University Press, 528 pp.

[45] Jensen, H. J., 2000, Self-organized Criticality: Emergent Complex Behaviour in Physical and Biological Systems, Cambridge University Press, 168 pp.

[46] Gomez, B., Page, M., Bak, P., and Trustrum, N., 2002, Self-organised criticality in layered, lacustrine sediments formed by landsliding, Geology, 30:519-522.

[47] Abelson, R. P., 1995, Statistics as Principled Argument, Lawrence Erlbaum Associates, 221 pp.

[48] Snyder, L. J., 1998, Is evidence historical?, In: Curd, M., and Cover, J. A., (Eds.), Philosophy of Science: The Central Issues, W. W. Norton and Company, p. 460-480.

[49] Hernandez, G., 1999, Time series, periodograms, and significance, Journal of Geophysical Research, 140:10,355-10,368.

[50] Begg, C. B., 1994, Publication bias, In: Cooper, H., and Hedges, L. V., The Handbook of Research Synthesis, Russell Sage Foundation, p. 399-409.

[51] Ripepe, M., Roberts, L. T., and Fischer, A. G., 1991, ENSO and sunspot cycles in varved Eocene oil shales from image analysis, Journal of Sedimentary Petrology, 61:1,155-1,163.

[52] Schaaf, M., and Thurow, J., 1998, Two 30,000 year high-resolution greyvalue time series from the Santa Barbara Basin and the Guaymas Basin, in: Cramp, A., MacLeod, C. J., Lee, S. V., and Jones, E. J. W., (Eds.), Geological Evolution of the Ocean Basins:

Results from the Ocean Drilling Program, Geological Society Special Publication No. 131, p. 101-110.

[53] Livingstone, D. M., and Hajdas, I., 2001, Climatically relevant periodicities in the thicknesses of biogenic carbonate varves in Soppensee, Switzerland (9,740-6,870 calendar yr BP), Journal of Paleolimnology, 25:17-24.

[54] Anderson, R. Y., and Koopmans, L. H., 1963, Harmonic analysis of varve time-series, Journal of Geophysical Research, 68:877-893.

[55] Haykin, S., and Kesler, S., 1983, Prediction-error filtering and maximum-entropy spectral estimation, In: Haykin, S., (Ed.), Nonlinear Methods of Spectral Analysis, Topics in Applied Physics, v. 34, Springer Verlag, p. 9-72.

[56] Currie, R. G., 1994, Luni-solar 18.6-year and 10-11-year solar cycle signals in the Lamb, H. H., dust veil index, International Journal of Climatology, 14:215-226.

[57] Loewe, P., and Koslowski, G., 1998, The Western Baltic sea-ice season in terms of a mass-related severity index, 1879-1992, II: Spectral characteristics and associations with the NAO, QBO, and solar cycle, Tellus, A, 50:219-241.

[58] Ghil, M., Allen, M. R., Dettingerm M. D., Ide, K., Kondrashov, D., Mann, M. E., Robertson, A. W., Saunders, A., Tian, Y., Varadi, F., and Yiou, P., 2001, Advanced spectral methods for climatic time-series, Reviews of Geophysics, 40:1-41.

[59] Godsey, H. S., Moore, T. C., Rea, D. K., and Shane, L. C. K., 1999, Post-Younger Dryas seasonality in the North American midcontinent region as recorded in Lake Huron varved sediments, Canadian Journal of Earth Sciences, 36:533-547.

[60] Yiou, P., Fuhrer, K., Meeker, L. D., Jouzel, J., Johnsen, S., and Mayewski, P. A., 1997, Paleoclimatic variability inferred from the spectral analysis of Greenland and Antarctic ice-core data, Journal of Geophysical Research: Oceans, 102:26,441-26,454.

Appendix B: Supplementary Results

B.1 Drammensfjord varve data

The varves are numbered from the D1G core top downwards; these numbers are just identifiers and are not intended to represent any chronological information. Also given are the cumulative depth of the top of each varve, and the thickness and mean greyvalue of the black and pale grey sublayers. As noted in section 4.4.3, the automated measurement process treats the entire core sequence as a set of varves, such that grey event beds and other homogeneous intervals show up as abnormally thick varve sublayers. These are identified by numbered comments, which follow the results table.

Varve No	Total Thickness (mm)	Total Thickness (pixels)	Cumulative Thickness (mm)	Cumulative Thickness (pixels)	Black Sublayer Thickness (pixels)	Black Sublayer Greyval (0-255)	Pale Grey Sublayer Thickness (pixels)	Pale Grey Sublayer Greyval (0-255)	Comments
1	20.30	287	20.30	287	281	215	6	177	1
2	3.61	51	23.90	338	25	216	26	195	1
3	1.27	18	25.18	356	11	209	7	189	1
4	2.76	39	27.93	395	24	216	15	177	1
5	2.62	37	30.55	432	25	205	12	180	1
6	3.04	43	33.59	475	23	209	20	198	1
7	1.63	23	35.22	498	14	215	9	191	1
8	4.17	59	39.39	557	44	205	15	176	1
9	2.90	41	42.29	598	29	224	12	165	1
10	1.13	16	43.42	614	6	198	10	165	1
11	3.11	44	46.53	658	24	204	20	169	1
12	2.12	30	48.66	688	19	188	11	151	1
13	2.12	30	50.78	718	21	187	9	167	1
14	1.13	16	51.91	734	6	196	10	185	1
15	2.40	34	54.31	768	13	186	21	157	1
16	3.32	47	57.64	815	13	215	34	196	1
17	3.32	47	60.96	862	21	210	26	164	1
18	3.04	43	64.00	905	34	192	9	178	1
19	3.61	51	67.61	956	23	212	28	198	1
20	14.92	211	82.53	1167	174	216	37	186	1
21	24.40	345	106.93	1512	340	216	5	168	1
22	6.44	91	113.37	1603	76	199	15	154	1
23	6.29	89	119.66	1692	68	206	21	181	1
24	2.05	29	121.71	1721	23	216	6	195	1
25	2.69	38	124.40	1759	23	212	15	199	1
26	1.34	19	125.74	1778	12	226	7	211	1
27	1.34	19	127.09	1797	9	218	10	197	1
28	8.70	123	135.79	1920	111	217	12	181	1
29	4.31	61	140.10	1981	52	212	9	168	1
30	7.36	104	147.45	2085	74	213	30	159	1
31	1.13	16	148.59	2101	7	175	9	169	
32	1.41	20	150.00	2121	4	183	16	173	
33	2.48	35	152.48	2156	6	208	29	174	
34	1.84	26	154.31	2182	10	178	16	170	
35	1.41	20	155.73	2202	9	208	11	171	
36	2.62	37	158.35	2239	28	183	9	159	

Varve No	Total Thickness (mm)	Total Thickness (pixels)	Cumulative Thickness (mm)	Cumulative Thickness (pixels)	Black Sublayer Thickness (pixels)	Black Sublayer Greyval (0-255)	Pale Grey Sublayer Thickness (pixels)	Pale Grey Sublayer Greyval (0-255)	Comments
37	2.33	33	160.68	2272	13	203	20	180	
38	4.60	65	165.28	2337	3	217	62	202	
39	3.32	47	168.60	2384	19	214	28	183	
40	3.04	43	171.64	2427	24	216	19	202	
41	2.19	31	173.83	2458	13	224	18	206	
42	0.92	13	174.75	2471	8	220	5	214	
43	2.83	40	177.58	2511	19	209	21	198	
44	3.39	48	180.98	2559	33	218	15	180	
45	1.06	15	182.04	2574	7	216	8	207	
46	2.69	38	184.72	2612	27	214	11	194	
47	0.78	11	185.50	2623	4	213	7	196	
48	0.85	12	186.35	2635	7	211	5	195	
49	1.06	15	187.41	2650	9	224	6	205	
50	0.64	9	188.05	2659	4	211	5	184	
51	0.85	12	188.90	2671	6	206	6	181	
52	1.91	27	190.81	2698	14	217	13	209	
53	1.91	27	192.72	2725	20	228	7	219	
54	1.20	17	193.92	2742	9	228	8	221	
55	1.34	19	195.26	2761	13	219	6	208	
56	0.85	12	196.11	2773	6	223	6	204	
57	1.27	18	197.38	2791	11	208	7	188	
58	0.64	9	198.02	2800	4	211	5	201	
59	2.97	42	200.99	2842	35	223	7	215	
60	0.99	14	201.98	2856	10	217	4	200	
61	0.85	12	202.83	2868	7	206	5	199	
62	0.85	12	203.68	2880	5	205	7	191	
63	0.85	12	204.53	2892	8	218	4	218	
64	4.17	59	208.70	2951	10	228	49	173	
65	0.78	11	209.48	2962	5	206	6	187	
66	2.33	33	211.81	2995	25	211	8	201	
67	1.34	19	213.15	3014	7	217	12	183	
68	1.13	16	214.29	3030	10	202	6	171	
69	1.27	18	215.56	3048	5	213	13	199	
70	2.48	35	218.03	3083	31	199	4	135	
71	1.13	16	219.17	3099	11	197	5	144	
72	2.05	29	221.22	3128	16	202	13	186	
73	1.84	26	223.06	3154	17	209	9	185	
74	1.56	22	224.61	3176	7	218	15	182	
75	0.64	9	225.25	3185	5	213	4	194	
76	1.13	16	226.38	3201	8	218	8	206	
77	1.56	22	227.93	3223	7	220	15	200	
78	2.05	29	229.99	3252	7	201	22	187	
79	7.71	109	237.69	3361	13	221	96	191	
80	1.06	15	238.76	3376	13	218	2	168	
81	1.20	17	239.96	3393	14	202	3	191	
82	0.57	8	240.52	3401	4	209	4	180	
83	0.92	13	241.44	3414	5	218	8	212	
84	1.06	15	242.50	3429	5	214	10	192	
85	2.05	29	244.55	3458	7	193	22	192	

Varve No	Total Thickness (mm)	Total Thickness (pixels)	Cumulative Thickness (mm)	Cumulative Thickness (pixels)	Black Sublayer Thickness (pixels)	Black Sublayer Greyval (0-255)	Pale Grey Sublayer Thickness (pixels)	Pale Grey Sublayer Greyval (0-255)	Comments
86	1.98	28	246.53	3486	8	201	20	184	
87	3.82	54	250.35	3540	10	213	44	171	
88	4.10	58	254.46	3598	44	212	14	139	
89	4.31	61	258.77	3659	23	187	38	180	
90	1.49	21	260.25	3680	11	218	10	185	
91	1.20	17	261.46	3697	15	219	2	170	
92	4.31	61	265.77	3758	53	231	8	196	
93	1.49	21	267.26	3779	18	225	3	202	
94	3.82	54	271.07	3833	9	222	45	194	
95	1.27	18	272.35	3851	11	220	7	205	
96	0.78	11	273.13	3862	4	224	7	210	
97	0.71	10	273.83	3872	4	223	6	203	
98	0.57	8	274.40	3880	3	215	5	208	
99	1.70	24	276.10	3904	17	196	7	190	
100	2.40	34	278.50	3938	21	218	13	189	
101	1.27	18	279.77	3956	6	217	12	187	
102	2.40	34	282.18	3990	10	210	24	176	
103	2.69	38	284.87	4028	28	227	10	192	
104	3.11	44	287.98	4072	27	228	17	214	
105	1.20	17	289.18	4089	9	229	8	221	
106	2.05	29	291.23	4118	5	228	24	207	
107	2.40	34	293.64	4152	29	223	5	190	
108	2.40	34	296.04	4186	6	213	28	194	
109	4.03	57	300.07	4243	28	225	29	201	
110	7.00	99	307.07	4342	13	221	86	214	
111	0.99	14	308.06	4356	10	229	4	210	
112	1.27	18	309.34	4374	9	218	9	194	
113	5.16	73	314.50	4447	60	231	13	191	
114	1.27	18	315.77	4465	14	226	4	198	
115	2.48	35	318.25	4500	11	221	24	181	
116	0.50	7	318.74	4507	4	213	3	191	
117	0.64	9	319.38	4516	4	217	5	184	
118	0.42	6	319.80	4522	3	204	3	192	
119	2.05	29	321.85	4551	24	222	5	202	
120	0.78	11	322.63	4562	7	207	4	186	
121	0.50	7	323.13	4569	4	202	3	196	
122	0.71	10	323.83	4579	5	212	5	196	
123	0.50	7	324.33	4586	3	209	4	201	
124	1.06	15	325.39	4601	7	226	8	220	
125	2.40	34	327.79	4635	18	204	16	170	
126	1.20	17	329.00	4652	4	225	13	202	
127	1.20	17	330.20	4669	11	222	6	207	
128	1.13	16	331.33	4685	9	229	7	213	
129	0.78	11	332.11	4696	3	226	8	216	
130	0.99	14	333.10	4710	8	219	6	181	
131	1.27	18	334.37	4728	11	204	7	186	
132	1.56	22	335.93	4750	7	221	15	199	
133	0.92	13	336.85	4763	8	213	5	184	
134	19.66	278	356.51	5041	41	217	237	166	2

Varve No	Total Thickness (mm)	Total Thickness (pixels)	Cumulative Thickness (mm)	Cumulative Thickness (pixels)	Black Sublayer Thickness (pixels)	Black Sublayer Greyval (0-255)	Pale Grey Sublayer Thickness (pixels)	Pale Grey Sublayer Greyval (0-255)	Comments
135	1.56	22	358.06	5063	16	196	6	187	
136	0.78	11	358.84	5074	5	205	6	201	
137	1.06	15	359.90	5089	11	218	4	206	
138	1.41	20	361.32	5109	14	218	6	196	
139	1.49	21	362.80	5130	18	211	3	164	
140	1.91	27	364.71	5157	6	188	21	171	
141	0.64	9	365.35	5166	6	200	3	153	
142	2.19	31	367.54	5197	16	185	15	158	
143	1.20	17	368.74	5214	9	163	8	139	
144	0.71	10	369.45	5224	4	184	6	170	
145	1.06	15	370.51	5239	5	198	10	175	
146	1.20	17	371.71	5256	11	204	6	182	
147	0.71	10	372.42	5266	6	218	4	208	
148	0.85	12	373.27	5278	7	217	5	185	
149	1.98	28	375.25	5306	20	197	8	161	
150	0.64	9	375.88	5315	5	204	4	173	
151	0.50	7	376.38	5322	5	203	2	197	
152	0.85	12	377.23	5334	6	208	6	179	
153	0.85	12	378.08	5346	6	190	6	163	
154	3.11	44	381.19	5390	13	196	31	189	
155	0.92	13	382.11	5403	9	205	4	178	
156	2.40	34	384.51	5437	8	195	26	177	
157	1.77	25	386.28	5462	12	204	13	176	
158	1.77	25	388.05	5487	8	198	17	174	
159	1.56	22	389.60	5509	4	215	18	204	
160	1.63	23	391.23	5532	12	214	11	205	
161	1.06	15	392.29	5547	7	209	8	182	
162	1.34	19	393.64	5566	14	207	5	180	
163	1.34	19	394.98	5585	14	209	5	181	
164	0.64	9	395.62	5594	2	207	7	165	
165	1.20	17	396.82	5611	11	202	6	199	
166	0.99	14	397.81	5625	11	205	3	190	
167	0.92	13	398.73	5638	8	206	5	192	
168	0.71	10	399.43	5648	4	210	6	201	
169	0.99	14	400.42	5662	5	218	9	200	
170	1.27	18	401.70	5680	7	214	11	200	
171	0.64	9	402.33	5689	3	212	6	181	
172	1.84	26	404.17	5715	19	205	7	167	
173	0.64	9	404.81	5724	3	216	6	184	
174	1.06	15	405.87	5739	5	199	10	174	
175	1.13	16	407.00	5755	2	218	14	201	
176	5.52	78	412.52	5833	5	204	73	171	
177	0.71	10	413.22	5843	6	198	4	159	
178	0.85	12	414.07	5855	3	188	9	171	
179	1.84	26	415.91	5881	10	195	16	187	
180	0.99	14	416.90	5895	10	199	4	177	
181	0.85	12	417.75	5907	5	186	7	173	
182	0.57	8	418.32	5915	4	197	4	178	
183	0.78	11	419.09	5926	6	204	5	186	

Varve No	Total Thickness (mm)	Total Thickness (pixels)	Cumulative Thickness (mm)	Cumulative Thickness (pixels)	Black Sublayer Thickness (pixels)	Black Sublayer Greyval (0-255)	Pale Grey Sublayer Thickness (pixels)	Pale Grey Sublayer Greyval (0-255)	Comments
184	0.99	14	420.08	5940	9	198	5	195	
185	1.41	20	421.50	5960	5	207	15	195	
186	0.71	10	422.21	5970	4	215	6	197	
187	1.20	17	423.41	5987	8	196	9	175	
188	0.78	11	424.19	5998	5	215	6	201	
189	3.25	46	427.44	6044	39	221	7	175	
190	1.13	16	428.57	6060	4	223	12	203	
191	0.57	8	429.14	6068	6	223	2	205	
192	0.71	10	429.84	6078	5	218	5	190	
193	0.92	13	430.76	6091	3	200	10	199	
194	4.60	65	435.36	6156	59	223	6	193	
195	3.54	50	438.90	6206	42	214	8	158	
196	0.64	9	439.53	6215	5	199	4	171	
197	1.49	21	441.02	6236	13	213	8	207	
198	1.06	15	442.08	6251	4	215	11	183	
199	0.57	8	442.64	6259	5	214	3	204	
200	0.71	10	443.35	6269	6	220	4	217	
201	1.06	15	444.41	6284	10	227	5	216	
202	5.45	77	449.86	6361	5	215	72	197	
203	1.20	17	451.06	6378	14	211	3	206	
204	0.99	14	452.05	6392	5	219	9	183	
205	0.71	10	452.76	6402	6	199	4	189	
206	0.57	8	453.32	6410	3	213	5	184	
207	0.78	11	454.10	6421	6	201	5	191	
208	0.42	6	454.53	6427	2	202	4	199	
209	0.85	12	455.37	6439	5	207	7	187	
210	0.42	6	455.80	6445	3	205	3	197	
211	0.78	11	456.58	6456	6	211	5	183	
212	0.92	13	457.50	6469	4	214	9	199	
213	1.70	24	459.19	6493	12	209	12	168	
214	3.25	46	462.45	6539	21	211	25	182	
215	0.64	9	463.08	6548	5	206	4	198	
216	0.78	11	463.86	6559	4	214	7	206	
217	0.85	12	464.71	6571	8	219	4	210	
218	0.64	9	465.35	6580	5	219	4	210	
219	1.06	15	466.41	6595	12	224	3	215	
220	1.27	18	467.68	6613	13	223	5	196	
221	2.26	32	469.94	6645	28	226	4	176	
222	1.13	16	471.07	6661	7	220	9	201	
223	1.98	28	473.06	6689	24	224	4	179	
224	1.70	24	474.75	6713	5	212	19	202	
225	0.78	11	475.53	6724	6	226	5	219	
226	0.78	11	476.31	6735	7	225	4	202	
227	1.63	23	477.93	6758	9	220	14	206	
228	3.04	43	480.98	6801	10	217	33	179	
229	0.92	13	481.90	6814	5	201	8	194	
230	0.78	11	482.67	6825	4	201	7	187	
231	1.20	17	483.88	6842	4	196	13	183	
232	0.64	9	484.51	6851	2	203	7	184	

Varve No	Total Thickness (mm)	Total Thickness (pixels)	Cumulative Thickness (mm)	Cumulative Thickness (pixels)	Black Sublayer Thickness (pixels)	Black Sublayer Greyval (0-255)	Pale Grey Sublayer Thickness (pixels)	Pale Grey Sublayer Greyval (0-255)	Comments
233	0.85	12	485.36	6863	4	203	8	180	
234	0.50	7	485.86	6870	4	189	3	164	
235	1.27	18	487.13	6888	16	212	2	194	
236	0.42	6	487.55	6894	4	199	2	190	
237	0.85	12	488.40	6906	5	201	7	180	
238	0.71	10	489.11	6916	6	197	4	194	
239	0.64	9	489.75	6925	5	208	4	198	
240	0.78	11	490.52	6936	8	211	3	189	
241	1.98	28	492.50	6964	11	205	17	179	
242	0.78	11	493.28	6975	5	195	6	181	
243	2.40	34	495.69	7009	2	205	32	177	
244	4.24	60	499.93	7069	6	195	54	181	
245	0.57	8	500.50	7077	5	206	3	190	
246	0.57	8	501.06	7085	6	205	2	200	
247	0.50	7	501.56	7092	3	205	4	201	
248	1.27	18	502.83	7110	13	211	5	194	
249	0.57	8	503.39	7118	5	214	3	198	
250	0.92	13	504.31	7131	6	206	7	194	
251	3.39	48	507.71	7179	2	211	46	186	
252	2.12	30	509.83	7209	26	204	4	193	
253	0.71	10	510.54	7219	3	210	7	203	
254	0.78	11	511.32	7230	8	208	3	197	
255	0.71	10	512.02	7240	7	214	3	198	
256	0.57	8	512.59	7248	3	204	5	198	
257	0.42	6	513.01	7254	3	212	3	202	
258	1.49	21	514.50	7275	7	219	14	197	
259	0.85	12	515.35	7287	2	213	10	188	
260	1.13	16	516.48	7303	7	212	9	202	
261	0.64	9	517.11	7312	4	228	5	205	
262	0.57	8	517.68	7320	4	212	4	202	
263	0.50	7	518.18	7327	5	221	2	206	
264	0.71	10	518.88	7337	6	219	4	206	
265	0.42	6	519.31	7343	3	212	3	195	
266	0.57	8	519.87	7351	5	214	3	204	
267	0.35	5	520.23	7356	3	207	2	198	
268	1.27	18	521.50	7374	4	215	14	202	
269	0.92	13	522.42	7387	4	221	9	195	
270	0.42	6	522.84	7393	4	218	2	202	
271	0.85	12	523.69	7405	3	219	9	201	
272	0.28	4	523.97	7409	2	223	2	205	
273	0.71	10	524.68	7419	4	210	6	188	
274	0.85	12	525.53	7431	6	203	6	185	
275	0.78	11	526.31	7442	9	207	2	188	
276	0.50	7	526.80	7449	4	211	3	188	
277	0.92	13	527.72	7462	6	221	7	215	
278	1.06	15	528.78	7477	7	227	8	205	
279	0.28	4	529.07	7481	2	219	2	196	
280	1.34	19	530.41	7500	5	221	14	207	
281	0.42	6	530.83	7506	3	211	3	200	

Varve No	Total Thickness (mm)	Total Thickness (pixels)	Cumulative Thickness (mm)	Cumulative Thickness (pixels)	Black Sublayer Thickness (pixels)	Black Sublayer Greyval (0-255)	Pale Grey Sublayer Thickness (pixels)	Pale Grey Sublayer Greyval (0-255)	Comments
282	0.71	10	531.54	7516	7	225	3	206	
283	0.42	6	531.97	7522	2	211	4	205	
284	0.78	11	532.74	7533	7	230	4	215	
285	0.64	9	533.38	7542	6	226	3	215	
286	0.42	6	533.80	7548	4	226	2	222	
287	0.71	10	534.51	7558	7	221	3	207	
288	1.06	15	535.57	7573	11	214	4	179	
289	0.64	9	536.21	7582	5	208	4	198	
290	1.20	17	537.41	7599	5	220	12	192	
291	0.50	7	537.91	7606	3	211	4	196	
292	0.99	14	538.90	7620	10	197	4	172	
293	1.41	20	540.31	7640	13	204	7	192	
294	1.06	15	541.37	7655	11	211	4	201	
295	0.99	14	542.36	7669	7	205	7	193	
296	1.06	15	543.42	7684	9	209	6	192	
297	0.64	9	544.06	7693	4	198	5	184	
298	0.85	12	544.91	7705	6	199	6	185	
299	0.57	8	545.47	7713	5	199	3	196	
300	0.64	9	546.11	7722	6	207	3	197	
301	0.57	8	546.68	7730	3	208	5	202	
302	1.34	19	548.02	7749	5	220	14	197	
303	0.57	8	548.59	7757	4	200	4	200	
304	0.99	14	549.58	7771	3	218	11	210	
305	1.13	16	550.71	7787	3	221	13	206	
306	0.57	8	551.27	7795	3	218	5	204	
307	2.83	40	554.10	7835	25	227	15	214	
308	1.06	15	555.16	7850	6	209	9	205	
309	0.42	6	555.59	7856	3	225	3	219	
310	0.71	10	556.29	7866	4	227	6	210	
311	0.50	7	556.79	7873	3	218	4	216	
312	0.78	11	557.57	7884	7	222	4	197	
313	2.19	31	559.76	7915	13	207	18	173	
314	0.92	13	560.68	7928	4	209	9	185	
315	0.64	9	561.32	7937	4	218	5	202	
316	0.57	8	561.88	7945	5	219	3	213	
317	0.92	13	562.80	7958	4	223	9	218	
318	2.19	31	564.99	7989	20	230	11	212	
319	0.78	11	565.77	8000	8	218	3	205	
320	1.41	20	567.19	8020	17	232	3	197	
321	0.57	8	567.75	8028	4	215	4	204	
322	0.35	5	568.10	8033	3	224	2	220	
323	1.06	15	569.17	8048	5	231	10	205	
324	0.85	12	570.01	8060	7	220	5	213	
325	0.35	5	570.37	8065	3	212	2	208	
326	0.50	7	570.86	8072	2	219	5	205	
327	0.57	8	571.43	8080	3	207	5	199	
328	1.06	15	572.49	8095	12	222	3	215	
329	0.92	13	573.41	8108	10	228	3	206	
330	0.50	7	573.90	8115	3	206	4	201	

Varve No	Total Thickness (mm)	Total Thickness (pixels)	Cumulative Thickness (mm)	Cumulative Thickness (pixels)	Black Sublayer Thickness (pixels)	Black Sublayer Greyval (0-255)	Pale Grey Sublayer Thickness (pixels)	Pale Grey Sublayer Greyval (0-255)	Comments
331	0.42	6	574.33	8121	3	218	3	206	
332	0.85	12	575.18	8133	1	210	11	178	
333	0.50	7	575.67	8140	2	199	5	181	
334	0.78	11	576.45	8151	4	204	7	180	
335	1.27	18	577.72	8169	13	213	5	179	
336	0.78	11	578.50	8180	2	206	9	185	
337	0.64	9	579.14	8189	4	194	5	183	
338	0.42	6	579.56	8195	3	198	3	187	
339	0.57	8	580.13	8203	4	199	4	186	
340	0.50	7	580.62	8210	4	207	3	198	
341	0.57	8	581.19	8218	5	214	3	214	
342	0.42	6	581.61	8224	3	221	3	199	
343	0.42	6	582.04	8230	3	197	3	173	
344	0.42	6	582.46	8236	3	196	3	196	
345	0.42	6	582.89	8242	3	216	3	200	
346	0.57	8	583.45	8250	3	214	5	185	
347	0.71	10	584.16	8260	6	207	4	186	
348	0.57	8	584.72	8268	3	203	5	174	
349	1.41	20	586.14	8288	5	205	15	198	
350	0.42	6	586.56	8294	3	223	3	219	
351	0.57	8	587.13	8302	2	227	6	184	
352	0.35	5	587.48	8307	2	200	3	192	
353	0.78	11	588.26	8318	3	222	8	206	
354	0.64	9	588.90	8327	5	223	4	205	
355	0.64	9	589.53	8336	3	214	6	198	
356	0.99	14	590.52	8350	5	214	9	182	
357	1.13	16	591.65	8366	11	212	5	199	
358	0.99	14	592.64	8380	4	210	10	189	
359	0.71	10	593.35	8390	3	220	7	169	
360	0.78	11	594.13	8401	6	214	5	178	
361	0.57	8	594.70	8409	5	195	3	175	
362	0.35	5	595.05	8414	3	188	2	175	
363	0.71	10	595.76	8424	4	197	6	184	
364	0.50	7	596.25	8431	5	219	2	195	
365	0.57	8	596.82	8439	4	213	4	194	
366	0.71	10	597.52	8449	2	201	8	174	
367	0.85	12	598.37	8461	3	202	9	178	
368	0.64	9	599.01	8470	4	202	5	182	
369	1.06	15	600.07	8485	11	190	4	186	
370	1.20	17	601.27	8502	9	213	8	176	
371	0.64	9	601.91	8511	3	213	6	203	
372	0.50	7	602.40	8518	4	209	3	177	
373	0.92	13	603.32	8531	7	199	6	160	
374	1.20	17	604.53	8548	8	218	9	180	
375	0.50	7	605.02	8555	4	206	3	199	
376	0.35	5	605.37	8560	3	218	2	207	
377	0.42	6	605.80	8566	3	222	3	210	
378	0.57	8	606.36	8574	4	215	4	211	
379	0.42	6	606.79	8580	3	220	3	213	

Varve No	Total Thickness (mm)	Total Thickness (pixels)	Cumulative Thickness (mm)	Cumulative Thickness (pixels)	Black Sublayer Thickness (pixels)	Black Sublayer Greyval (0-255)	Pale Grey Sublayer Thickness (pixels)	Pale Grey Sublayer Greyval (0-255)	Comments
380	0.85	12	607.64	8592	6	219	6	194	
381	0.92	13	608.56	8605	4	215	9	191	
382	0.78	11	609.34	8616	8	207	3	166	
383	0.99	14	610.33	8630	6	204	8	169	
384	0.92	13	611.24	8643	9	184	4	122	
385	0.99	14	612.23	8657	8	187	6	162	
386	1.13	16	613.37	8673	10	196	6	143	
387	1.41	20	614.78	8693	16	193	4	149	
388	0.71	10	615.49	8703	6	192	4	143	
389	1.13	16	616.62	8719	10	181	6	157	
390	1.49	21	618.10	8740	11	207	10	175	
391	0.78	11	618.88	8751	6	183	5	143	
392	0.64	9	619.52	8760	4	194	5	182	
393	0.50	7	620.01	8767	3	195	4	191	
394	1.41	20	621.43	8787	13	211	7	181	
395	0.57	8	621.99	8795	6	205	2	188	
396	0.57	8	622.56	8803	4	209	4	213	
397	0.57	8	623.13	8811	4	224	4	222	
398	0.78	11	623.90	8822	5	222	6	200	
399	1.41	20	625.32	8842	17	225	3	221	
400	0.78	11	626.10	8853	7	229	4	218	
401	0.50	7	626.59	8860	4	226	3	217	
402	0.71	10	627.30	8870	5	225	5	215	
403	0.78	11	628.08	8881	9	225	2	214	
404	0.42	6	628.50	8887	2	216	4	211	
405	0.85	12	629.35	8899	7	219	5	185	
406	0.71	10	630.06	8909	7	211	3	190	
407	0.78	11	630.83	8920	5	205	6	192	
408	0.57	8	631.40	8928	5	216	3	208	
409	0.71	10	632.11	8938	5	211	5	176	
410	0.85	12	632.96	8950	7	216	5	175	
411	1.13	16	634.09	8966	5	200	11	170	
412	0.99	14	635.08	8980	5	194	9	189	
413	0.57	8	635.64	8988	4	207	4	179	
414	0.92	13	636.56	9001	4	195	9	169	
415	0.57	8	637.13	9009	3	181	5	158	
416	0.21	3	637.34	9012	1	179	2	178	
417	0.64	9	637.98	9021	5	203	4	177	
418	0.99	14	638.97	9035	8	206	6	185	
419	8.77	124	647.74	9159	10	214	114	149	
420	0.99	14	648.73	9173	10	201	4	194	
421	0.64	9	649.36	9182	6	223	3	217	
422	0.42	6	649.79	9188	4	219	2	203	
423	0.64	9	650.42	9197	4	210	5	209	
424	0.57	8	650.99	9205	4	220	4	201	
425	0.71	10	651.70	9215	6	221	4	193	
426	0.35	5	652.05	9220	3	211	2	195	
427	0.42	6	652.48	9226	2	203	4	191	
428	0.42	6	652.90	9232	3	204	3	199	

Varve No	Total Thickness (mm)	Total Thickness (pixels)	Cumulative Thickness (mm)	Cumulative Thickness (pixels)	Black Sublayer Thickness (pixels)	Black Sublayer Greyval (0-255)	Pale Grey Sublayer Thickness (pixels)	Pale Grey Sublayer Greyval (0-255)	Comments
429	0.57	8	653.47	9240	2	210	6	172	
430	0.64	9	654.10	9249	4	200	5	185	
431	0.71	10	654.81	9259	3	209	7	184	
432	0.85	12	655.66	9271	4	203	8	203	
433	0.64	9	656.29	9280	4	209	5	199	
434	0.57	8	656.86	9288	3	207	5	184	
435	1.49	21	658.35	9309	4	189	17	166	
436	0.78	11	659.12	9320	5	211	6	183	
437	0.57	8	659.69	9328	3	193	5	176	
438	2.69	38	662.38	9366	6	187	32	159	
439	0.78	11	663.15	9377	3	188	8	174	
440	0.57	8	663.72	9385	4	184	4	166	
441	0.92	13	664.64	9398	11	198	2	177	
442	0.64	9	665.28	9407	3	176	6	164	
443	1.56	22	666.83	9429	4	169	18	156	
444	0.78	11	667.61	9440	7	178	4	167	
445	1.70	24	669.31	9464	3	189	21	157	
446	0.57	8	669.87	9472	4	177	4	175	
447	0.50	7	670.37	9479	3	200	4	192	
448	0.78	11	671.15	9490	6	217	5	201	
449	0.99	14	672.14	9504	6	217	8	217	
450	1.13	16	673.27	9520	4	228	12	226	
451	0.99	14	674.26	9534	10	228	4	221	
452	1.27	18	675.53	9552	11	230	7	225	
453	0.35	5	675.88	9557	2	232	3	227	
454	0.50	7	676.38	9564	4	229	3	226	
455	0.35	5	676.73	9569	3	228	2	221	
456	0.71	10	677.44	9579	4	227	6	225	
457	0.71	10	678.15	9589	4	233	6	217	
458	0.35	5	678.50	9594	2	228	3	213	
459	0.50	7	679.00	9601	3	213	4	209	
460	0.35	5	679.35	9606	2	217	3	203	
461	0.50	7	679.84	9613	3	201	4	191	
462	1.13	16	680.98	9629	6	221	10	215	
463	0.64	9	681.61	9638	5	230	4	214	
464	0.71	10	682.32	9648	5	229	5	220	
465	0.99	14	683.31	9662	9	221	5	202	
466	0.78	11	684.09	9673	6	216	5	205	
467	0.57	8	684.65	9681	5	222	3	217	
468	0.50	7	685.15	9688	5	223	2	206	
469	0.57	8	685.71	9696	4	213	4	200	
470	0.64	9	686.35	9705	6	216	3	198	
471	0.78	11	687.13	9716	5	210	6	203	
472	0.85	12	687.98	9728	7	217	5	205	
473	0.50	7	688.47	9735	4	209	3	194	
474	0.35	5	688.83	9740	2	199	3	197	
475	0.57	8	689.39	9748	4	217	4	209	
476	1.06	15	690.45	9763	8	209	7	174	
477	0.85	12	691.30	9775	7	212	5	214	

Varve No	Total Thickness (mm)	Total Thickness (pixels)	Cumulative Thickness (mm)	Cumulative Thickness (pixels)	Black Sublayer Thickness (pixels)	Black Sublayer Greyval (0-255)	Pale Grey Sublayer Thickness (pixels)	Pale Grey Sublayer Greyval (0-255)	Comments
478	0.85	12	692.15	9787	5	225	7	205	
479	0.57	8	692.72	9795	5	208	3	190	
480	0.35	5	693.07	9800	3	207	2	205	
481	0.42	6	693.49	9806	4	213	2	202	
482	0.78	11	694.27	9817	7	202	4	186	
483	0.64	9	694.91	9826	4	205	5	189	
484	0.57	8	695.47	9834	4	200	4	171	
485	0.71	10	696.18	9844	6	170	4	148	
486	68.32	966	764.50	10810	4	176	962	145	3
487	0.35	5	764.85	10815	3	194	2	179	
488	0.57	8	765.42	10823	2	186	6	165	
489	0.42	6	765.84	10829	4	171	2	141	
490	3.04	43	768.88	10872	3	156	40	150	
491	0.35	5	769.24	10877	4	212	1	204	
492	0.28	4	769.52	10881	2	208	2	205	
493	0.85	12	770.37	10893	7	213	5	198	
494	0.99	14	771.36	10907	10	210	4	196	
495	0.42	6	771.78	10913	4	198	2	171	
496	0.64	9	772.42	10922	5	193	4	175	
497	0.42	6	772.84	10928	3	191	3	187	
498	0.92	13	773.76	10941	6	200	7	161	
499	0.57	8	774.33	10949	3	186	5	169	
500	8.98	127	783.31	11076	5	186	122	154	
501	0.42	6	783.73	11082	3	184	3	177	
502	0.64	9	784.37	11091	4	189	5	152	
503	1.20	17	785.57	11108	7	191	10	179	
504	0.50	7	786.07	11115	2	207	5	174	
505	0.42	6	786.49	11121	2	174	4	166	
506	0.35	5	786.85	11126	3	187	2	184	
507	0.57	8	787.41	11134	6	201	2	183	
508	0.85	12	788.26	11146	7	196	5	175	
509	0.57	8	788.83	11154	4	180	4	164	
510	0.99	14	789.82	11168	9	178	5	174	
511	0.50	7	790.31	11175	3	182	4	168	
512	0.57	8	790.88	11183	5	171	3	165	
513	0.42	6	791.30	11189	3	202	3	188	
514	0.42	6	791.73	11195	4	207	2	201	
515	0.71	10	792.43	11205	4	200	6	150	
516	0.85	12	793.28	11217	5	201	7	174	
517	0.71	10	793.99	11227	2	222	8	194	
518	0.50	7	794.48	11234	5	210	2	186	
519	0.64	9	795.12	11243	5	193	4	186	
520	0.92	13	796.04	11256	7	191	6	139	
521	0.71	10	796.75	11266	6	200	4	157	
522	0.64	9	797.38	11275	5	181	4	158	
523	0.85	12	798.23	11287	6	197	6	178	
524	0.92	13	799.15	11300	7	200	6	158	
525	0.64	9	799.79	11309	5	193	4	189	
526	0.50	7	800.28	11316	2	210	5	189	

Varve No	Total Thickness (mm)	Total Thickness (pixels)	Cumulative Thickness (mm)	Cumulative Thickness (pixels)	Black Sublayer Thickness (pixels)	Black Sublayer Greyval (0-255)	Pale Grey Sublayer Thickness (pixels)	Pale Grey Sublayer Greyval (0-255)	Comments
527	0.78	11	801.06	11327	8	206	3	176	
528	0.71	10	801.77	11337	3	182	7	153	
529	1.27	18	803.04	11355	6	203	12	154	
530	1.41	20	804.46	11375	3	187	17	142	
531	1.27	18	805.73	11393	11	208	7	165	
532	1.06	15	806.79	11408	5	211	10	160	
533	0.35	5	807.14	11413	2	192	3	192	
534	0.71	10	807.85	11423	5	223	5	202	
535	0.64	9	808.49	11432	6	216	3	184	
536	0.71	10	809.19	11442	4	218	6	192	
537	0.50	7	809.69	11449	2	201	5	187	
538	0.64	9	810.33	11458	6	198	3	192	
539	0.28	4	810.61	11462	2	216	2	215	
540	0.64	9	811.24	11471	5	207	4	154	
541	0.57	8	811.81	11479	3	199	5	184	
542	0.42	6	812.23	11485	2	200	4	166	
543	0.42	6	812.66	11491	2	184	4	173	
544	0.42	6	813.08	11497	3	203	3	193	
545	0.85	12	813.93	11509	7	208	5	170	
546	0.50	7	814.43	11516	5	184	2	165	
547	0.99	14	815.42	11530	4	190	10	163	
548	0.28	4	815.70	11534	2	209	2	206	
549	0.50	7	816.20	11541	3	216	4	179	
550	0.42	6	816.62	11547	4	205	2	186	
551	0.64	9	817.26	11556	5	200	4	172	
552	0.50	7	817.75	11563	4	201	3	195	
553	0.50	7	818.25	11570	5	208	2	180	
554	0.57	8	818.81	11578	6	198	2	169	
555	0.50	7	819.31	11585	5	191	2	157	
556	0.57	8	819.87	11593	3	194	5	170	
557	0.50	7	820.37	11600	2	179	5	158	
558	0.35	5	820.72	11605	3	193	2	190	
559	0.64	9	821.36	11614	5	193	4	179	
560	0.64	9	821.99	11623	5	212	4	165	
561	0.57	8	822.56	11631	4	206	4	178	
562	0.78	11	823.34	11642	7	207	4	167	
563	0.50	7	823.83	11649	3	204	4	182	
564	0.35	5	824.19	11654	2	195	3	170	
565	0.42	6	824.61	11660	2	182	4	153	
566	0.71	10	825.32	11670	4	200	6	191	
567	0.85	12	826.17	11682	6	203	6	185	
568	0.50	7	826.66	11689	3	202	4	180	
569	0.57	8	827.23	11697	3	190	5	144	
570	0.85	12	828.08	11709	4	197	8	186	
571	0.42	6	828.50	11715	3	180	3	166	
572	0.92	13	829.42	11728	9	172	4	153	
573	0.99	14	830.41	11742	4	183	10	153	
574	0.57	8	830.98	11750	5	196	3	183	
575	0.35	5	831.33	11755	2	204	3	193	

Varve No	Total Thickness (mm)	Total Thickness (pixels)	Cumulative Thickness (mm)	Cumulative Thickness (pixels)	Black Sublayer Thickness (pixels)	Black Sublayer Greyval (0-255)	Pale Grey Sublayer Thickness (pixels)	Pale Grey Sublayer Greyval (0-255)	Comments
576	0.28	4	831.61	11759	2	194	2	179	
577	0.28	4	831.90	11763	2	180	2	169	
578	0.28	4	832.18	11767	2	175	2	175	
579	0.42	6	832.60	11773	4	197	2	190	
580	0.42	6	833.03	11779	3	193	3	180	
581	0.50	7	833.52	11786	4	189	3	188	
582	0.57	8	834.09	11794	3	205	5	145	
583	0.42	6	834.51	11800	4	192	2	188	
584	0.35	5	834.87	11805	2	191	3	171	
585	0.42	6	835.29	11811	3	192	3	183	
586	0.64	9	835.93	11820	5	189	4	150	
587	0.57	8	836.49	11828	5	190	3	174	
588	0.50	7	836.99	11835	5	195	2	193	
589	0.42	6	837.41	11841	3	187	3	154	
590	0.71	10	838.12	11851	7	167	3	161	
591	0.57	8	838.68	11859	4	205	4	189	
592	0.50	7	839.18	11866	4	205	3	186	
593	0.50	7	839.67	11873	4	203	3	190	
594	0.35	5	840.03	11878	3	199	2	189	
595	0.42	6	840.45	11884	3	204	3	195	
596	0.35	5	840.81	11889	1	211	4	179	
597	0.50	7	841.30	11896	4	185	3	174	
598	0.35	5	841.65	11901	2	203	3	190	
599	0.42	6	842.08	11907	4	195	2	157	
600	0.42	6	842.50	11913	3	181	3	177	
601	0.50	7	843.00	11920	3	196	4	174	
602	0.28	4	843.28	11924	2	191	2	190	
603	0.35	5	843.64	11929	3	207	2	205	
604	0.42	6	844.06	11935	2	206	4	180	
605	0.42	6	844.48	11941	3	203	3	192	
606	0.64	9	845.12	11950	2	207	7	178	
607	0.78	11	845.90	11961	3	203	8	161	
608	0.99	14	846.89	11975	6	193	8	153	
609	0.42	6	847.31	11981	4	186	2	180	
610	0.99	14	848.30	11995	3	209	11	163	
611	0.42	6	848.73	12001	3	175	3	166	
612	0.78	11	849.50	12012	3	191	8	144	
613	1.27	18	850.78	12030	6	209	12	179	
614	0.78	11	851.56	12041	4	200	7	157	
615	0.85	12	852.40	12053	3	189	9	163	
616	0.42	6	852.83	12059	2	216	4	199	
617	0.57	8	853.39	12067	5	213	3	209	
618	0.57	8	853.96	12075	5	225	3	220	
619	0.57	8	854.53	12083	2	224	6	191	
620	0.50	7	855.02	12090	4	216	3	193	
621	0.42	6	855.45	12096	3	210	3	195	
622	0.57	8	856.01	12104	5	211	3	201	
623	0.35	5	856.36	12109	2	207	3	175	
624	0.50	7	856.86	12116	4	205	3	170	

Varve No	Total Thickness (mm)	Total Thickness (pixels)	Cumulative Thickness (mm)	Cumulative Thickness (pixels)	Black Sublayer Thickness (pixels)	Black Sublayer Greyval (0-255)	Pale Grey Sublayer Thickness (pixels)	Pale Grey Sublayer Greyval (0-255)	Comments
625	0.28	4	857.14	12120	2	190	2	189	
626	0.50	7	857.64	12127	2	196	5	185	
627	0.85	12	858.49	12139	4	219	8	204	
628	0.50	7	858.98	12146	2	216	5	191	
629	0.64	9	859.62	12155	6	219	3	198	
630	0.92	13	860.54	12168	9	221	4	210	
631	0.92	13	861.46	12181	5	208	8	183	
632	0.64	9	862.09	12190	6	212	3	192	
633	0.42	6	862.52	12196	4	216	2	199	
634	0.35	5	862.87	12201	2	204	3	193	
635	0.50	7	863.37	12208	3	202	4	188	
636	0.71	10	864.07	12218	4	198	6	186	
637	0.35	5	864.43	12223	1	211	4	180	
638	0.57	8	864.99	12231	3	195	5	193	
639	0.42	6	865.42	12237	4	213	2	200	
640	0.42	6	865.84	12243	3	206	3	200	
641	0.42	6	866.27	12249	3	202	3	197	
642	0.35	5	866.62	12254	3	203	2	186	
643	0.92	13	867.54	12267	6	201	7	176	
644	0.50	7	868.03	12274	3	198	4	190	
645	0.42	6	868.46	12280	3	211	3	211	
646	0.42	6	868.88	12286	2	214	4	206	
647	0.92	13	869.80	12299	6	215	7	172	
648	0.71	10	870.51	12309	3	180	7	147	
649	0.50	7	871.00	12316	3	177	4	168	
650	0.50	7	871.50	12323	3	206	4	171	
651	0.42	6	871.92	12329	2	172	4	171	
652	0.50	7	872.42	12336	4	209	3	197	
653	0.99	14	873.41	12350	3	198	11	169	
654	0.50	7	873.90	12357	4	199	3	197	
655	0.64	9	874.54	12366	5	209	4	199	
656	0.71	10	875.25	12376	7	223	3	204	
657	0.99	14	876.24	12390	8	227	6	210	
658	0.42	6	876.66	12396	3	212	3	211	
659	0.42	6	877.09	12402	4	218	2	212	
660	0.28	4	877.37	12406	2	212	2	201	
661	0.42	6	877.79	12412	3	206	3	198	
662	0.50	7	878.29	12419	3	203	4	184	
663	0.85	12	879.14	12431	4	213	8	200	
664	0.85	12	879.99	12443	3	212	9	201	
665	0.50	7	880.48	12450	4	217	3	200	
666	0.35	5	880.83	12455	2	211	3	205	
667	0.42	6	881.26	12461	4	218	2	209	
668	0.50	7	881.75	12468	3	215	4	198	
669	0.71	10	882.46	12478	6	203	4	168	
670	0.50	7	882.96	12485	4	207	3	172	
671	0.50	7	883.45	12492	3	187	4	164	
672	0.42	6	883.88	12498	2	206	4	154	
673	0.35	5	884.23	12503	2	185	3	170	

Varve No	Total Thickness (mm)	Total Thickness (pixels)	Cumulative Thickness (mm)	Cumulative Thickness (pixels)	Black Sublayer Thickness (pixels)	Black Sublayer Greyval (0-255)	Pale Grey Sublayer Thickness (pixels)	Pale Grey Sublayer Greyval (0-255)	Comments
674	0.71	10	884.94	12513	5	196	5	166	
675	0.42	6	885.36	12519	3	170	3	168	
676	0.64	9	886.00	12528	5	200	4	180	
677	0.57	8	886.56	12536	3	181	5	174	
678	0.57	8	887.13	12544	3	206	5	174	
679	1.41	20	888.54	12564	4	201	16	160	
680	0.99	14	889.53	12578	5	207	9	159	
681	1.06	15	890.59	12593	8	206	7	184	
682	0.50	7	891.09	12600	3	212	4	193	
683	1.20	17	892.29	12617	3	222	14	192	
684	0.35	5	892.64	12622	2	214	3	201	
685	0.57	8	893.21	12630	4	208	4	171	
686	0.99	14	894.20	12644	7	206	7	170	
687	0.50	7	894.70	12651	4	202	3	177	
688	0.50	7	895.19	12658	4	179	3	167	
689	0.42	6	895.62	12664	3	183	3	178	
690	1.34	19	896.96	12683	2	202	17	169	
691	0.99	14	897.95	12697	10	215	4	197	
692	0.50	7	898.44	12704	3	215	4	213	
693	0.57	8	899.01	12712	4	223	4	204	
694	1.06	15	900.07	12727	9	227	6	216	
695	0.42	6	900.50	12733	2	225	4	189	
696	0.42	6	900.92	12739	3	194	3	181	
697	0.85	12	901.77	12751	4	182	8	177	
698	0.50	7	902.26	12758	4	210	3	210	
699	0.42	6	902.69	12764	2	217	4	205	
700	0.42	6	903.11	12770	4	227	2	222	
701	0.78	11	903.89	12781	6	220	5	182	
702	1.20	17	905.09	12798	12	218	5	195	
703	0.42	6	905.52	12804	2	219	4	217	
704	0.42	6	905.94	12810	3	220	3	199	
705	0.42	6	906.36	12816	2	213	4	192	
706	0.50	7	906.86	12823	4	195	3	178	
707	0.57	8	907.43	12831	3	198	5	175	
708	0.28	4	907.71	12835	2	199	2	193	
709	1.70	24	909.41	12859	4	219	20	162	
710	0.50	7	909.90	12866	4	188	3	185	
711	0.78	11	910.68	12877	5	219	6	194	
712	0.35	5	911.03	12882	3	201	2	192	
713	1.77	25	912.80	12907	21	228	4	215	
714	0.50	7	913.30	12914	4	225	3	208	
715	0.28	4	913.58	12918	3	222	1	222	
716	0.50	7	914.07	12925	2	225	5	222	
717	0.57	8	914.64	12933	5	225	3	210	
718	0.64	9	915.28	12942	3	226	6	199	
719	0.42	6	915.70	12948	3	196	3	193	
720	0.57	8	916.27	12956	5	211	3	194	
721	0.92	13	917.19	12969	10	220	3	202	
722	0.50	7	917.68	12976	4	216	3	208	

Varve No	Total Thickness (mm)	Total Thickness (pixels)	Cumulative Thickness (mm)	Cumulative Thickness (pixels)	Black Sublayer Thickness (pixels)	Black Sublayer Greyval (0-255)	Pale Grey Sublayer Thickness (pixels)	Pale Grey Sublayer Greyval (0-255)	Comments
723	0.28	4	917.96	12980	2	218	2	215	
724	0.42	6	918.39	12986	3	219	3	198	
725	0.71	10	919.09	12996	6	222	4	215	
726	0.42	6	919.52	13002	3	214	3	207	
727	0.35	5	919.87	13007	3	210	2	203	
728	0.85	12	920.72	13019	6	215	6	165	
729	0.92	13	921.64	13032	5	170	8	169	
730	0.57	8	922.21	13040	4	193	4	188	
731	0.64	9	922.84	13049	5	214	4	196	
732	0.35	5	923.20	13054	2	213	3	193	
733	0.64	9	923.83	13063	6	202	3	197	
734	640.66	9059	1564.50	22122	2	203	9057	156	4
735	0.42	6	1564.92	22128	2	209	4	207	
736	0.35	5	1565.28	22133	2	217	3	208	
737	0.35	5	1565.63	22138	3	211	2	200	
738	0.35	5	1565.98	22143	3	207	2	199	
739	0.71	10	1566.69	22153	6	211	4	169	
740	0.50	7	1567.19	22160	2	189	5	187	
741	0.35	5	1567.54	22165	3	206	2	197	
742	0.42	6	1567.96	22171	3	206	3	191	
743	0.71	10	1568.67	22181	4	217	6	182	
744	0.35	5	1569.02	22186	3	190	2	165	
745	0.78	11	1569.80	22197	3	164	8	139	
746	0.42	6	1570.23	22203	3	181	3	179	
747	0.78	11	1571.00	22214	3	214	8	199	
748	0.50	7	1571.50	22221	3	220	4	200	
749	0.57	8	1572.07	22229	4	224	4	188	
750	0.57	8	1572.63	22237	4	207	4	177	
751	0.42	6	1573.06	22243	2	193	4	167	
752	0.57	8	1573.62	22251	3	189	5	162	
753	0.35	5	1573.97	22256	2	210	3	178	
754	0.64	9	1574.61	22265	6	204	3	194	
755	0.71	10	1575.32	22275	7	199	3	140	
756	0.42	6	1575.74	22281	4	191	2	185	
757	0.71	10	1576.45	22291	6	213	4	183	
758	0.50	7	1576.94	22298	2	205	5	188	
759	0.35	5	1577.30	22303	2	196	3	182	
760	0.57	8	1577.86	22311	3	207	5	200	
761	0.42	6	1578.29	22317	3	210	3	191	
762	0.35	5	1578.64	22322	3	202	2	190	
763	0.50	7	1579.14	22329	2	199	5	189	
764	0.42	6	1579.56	22335	4	217	2	213	
765	0.64	9	1580.20	22344	2	214	7	203	
766	0.57	8	1580.76	22352	5	213	3	165	
767	0.35	5	1581.12	22357	3	167	2	149	
768	0.64	9	1581.75	22366	6	194	3	168	
769	0.50	7	1582.25	22373	4	196	3	179	
770	0.99	14	1583.24	22387	9	210	5	192	
771	0.57	8	1583.80	22395	4	202	4	159	

Varve No	Total Thickness (mm)	Total Thickness (pixels)	Cumulative Thickness (mm)	Cumulative Thickness (pixels)	Black Sublayer Thickness (pixels)	Black Sublayer Greyval (0-255)	Pale Grey Sublayer Thickness (pixels)	Pale Grey Sublayer Greyval (0-255)	Comments
772	0.50	7	1584.30	22402	3	197	4	173	
773	84.79	1199	1669.09	23601	3	164	1196	141	5
774	0.78	11	1669.87	23612	7	159	4	136	
775	0.71	10	1670.58	23622	4	164	6	158	
776	0.64	9	1671.22	23631	5	169	4	158	
777	0.42	6	1671.64	23637	3	175	3	160	
778	0.35	5	1671.99	23642	2	170	3	164	
779	0.71	10	1672.70	23652	8	172	2	147	
780	0.78	11	1673.48	23663	4	176	7	163	
781	0.78	11	1674.26	23674	4	175	7	165	
782	0.99	14	1675.25	23688	3	180	11	174	
783	0.64	9	1675.88	23697	6	196	3	194	
784	0.42	6	1676.31	23703	2	202	4	183	
785	0.71	10	1677.02	23713	3	206	7	190	
786	0.42	6	1677.44	23719	3	207	3	188	
787	0.57	8	1678.01	23727	3	202	5	159	
788	0.50	7	1678.50	23734	4	210	3	199	
789	0.50	7	1679.00	23741	3	200	4	182	
790	0.57	8	1679.56	23749	3	195	5	184	
791	0.78	11	1680.34	23760	3	194	8	155	
792	0.42	6	1680.76	23766	4	201	2	175	
793	0.42	6	1681.19	23772	2	198	4	186	
794	0.42	6	1681.61	23778	2	194	4	177	
795	0.42	6	1682.04	23784	2	187	4	167	
796	0.64	9	1682.67	23793	5	188	4	174	
797	0.50	7	1683.17	23800	3	190	4	190	
798	0.42	6	1683.59	23806	3	208	3	190	
799	0.71	10	1684.30	23816	5	206	5	188	
800	0.92	13	1685.22	23829	8	185	5	156	
801	1.20	17	1686.42	23846	5	232	12	193	
802	0.64	9	1687.06	23855	4	191	5	154	
803	0.42	6	1687.48	23861	4	211	2	191	
804	0.78	11	1688.26	23872	4	195	7	173	
805	0.71	10	1688.97	23882	6	206	4	164	
806	0.64	9	1689.60	23891	7	196	2	189	
807	0.85	12	1690.45	23903	5	198	7	150	
808	0.50	7	1690.95	23910	4	193	3	171	
809	1.06	15	1692.01	23925	3	187	12	153	
810	0.50	7	1692.50	23932	4	189	3	184	
811	0.28	4	1692.79	23936	2	198	2	192	
812	0.35	5	1693.14	23941	3	190	2	158	
813	0.50	7	1693.64	23948	3	192	4	164	
814	0.71	10	1694.34	23958	3	193	7	145	
815	0.50	7	1694.84	23965	4	212	3	166	
816	0.71	10	1695.54	23975	6	210	4	176	
817	0.50	7	1696.04	23982	3	211	4	196	
818	0.35	5	1696.39	23987	2	199	3	183	
819	3.11	44	1699.50	24031	6	203	38	157	
820	0.64	9	1700.14	24040	7	205	2	174	

Varve No	Total Thickness (mm)	Total Thickness (pixels)	Cumulative Thickness (mm)	Cumulative Thickness (pixels)	Black Sublayer Thickness (pixels)	Black Sublayer Greyval (0-255)	Pale Grey Sublayer Thickness (pixels)	Pale Grey Sublayer Greyval (0-255)	Comments
821	0.35	5	1700.50	24045	3	203	2	196	
822	0.92	13	1701.41	24058	3	208	10	173	
823	0.57	8	1701.98	24066	4	180	4	170	
824	0.64	9	1702.62	24075	6	205	3	170	
825	0.64	9	1703.25	24084	6	210	3	199	
826	0.64	9	1703.89	24093	3	222	6	169	
827	0.50	7	1704.38	24100	3	180	4	171	
828	0.42	6	1704.81	24106	4	188	2	162	
829	0.99	14	1705.80	24120	6	175	8	126	
830	1.63	23	1707.43	24143	3	175	20	126	
831	0.57	8	1707.99	24151	5	207	3	172	
832	0.50	7	1708.49	24158	2	214	5	186	
833	0.57	8	1709.05	24166	4	210	4	189	
834	0.99	14	1710.04	24180	8	228	6	215	
835	0.57	8	1710.61	24188	4	226	4	214	
836	0.50	7	1711.10	24195	3	225	4	217	
837	0.78	11	1711.88	24206	8	204	3	167	
838	1.77	25	1713.65	24231	21	212	4	171	
839	0.78	11	1714.43	24242	8	218	3	212	
840	0.71	10	1715.13	24252	4	220	6	174	
841	1.20	17	1716.34	24269	13	216	4	182	
842	0.35	5	1716.69	24274	3	202	2	185	
843	1.06	15	1717.75	24289	11	211	4	188	
844	0.71	10	1718.46	24299	7	214	3	198	
845	0.78	11	1719.24	24310	6	209	5	159	
846	1.91	27	1721.15	24337	11	211	16	146	
847	0.71	10	1721.85	24347	4	196	6	165	
848	1.27	18	1723.13	24365	6	213	12	178	
849	0.50	7	1723.62	24372	4	186	3	178	
850	0.64	9	1724.26	24381	2	199	7	167	
851	0.78	11	1725.04	24392	7	214	4	176	
852	0.64	9	1725.67	24401	5	209	4	199	
853	0.42	6	1726.10	24407	2	199	4	184	
854	0.64	9	1726.73	24416	3	219	6	175	
855	0.71	10	1727.44	24426	4	209	6	171	
856	0.50	7	1727.93	24433	4	211	3	174	
857	0.35	5	1728.29	24438	3	196	2	171	
858	0.28	4	1728.57	24442	2	186	2	184	
859	0.50	7	1729.07	24449	3	197	4	177	
860	0.28	4	1729.35	24453	2	201	2	191	
861	0.35	5	1729.70	24458	2	196	3	193	
862	0.50	7	1730.20	24465	3	203	4	161	
863	0.64	9	1730.83	24474	5	195	4	182	
864	0.42	6	1731.26	24480	3	192	3	169	
865	0.35	5	1731.61	24485	3	167	2	147	
866	1.13	16	1732.74	24501	6	182	10	141	
867	1.56	22	1734.30	24523	8	181	14	141	
868	1.06	15	1735.36	24538	2	170	13	152	
869	0.85	12	1736.21	24550	7	189	5	121	

Varve No	Total Thickness (mm)	Total Thickness (pixels)	Cumulative Thickness (mm)	Cumulative Thickness (pixels)	Black Sublayer Thickness (pixels)	Black Sublayer Greyval (0-255)	Pale Grey Sublayer Thickness (pixels)	Pale Grey Sublayer Greyval (0-255)	Comments
870	1.56	22	1737.77	24572	12	197	10	175	
871	1.13	16	1738.90	24588	8	199	8	156	
872	0.50	7	1739.39	24595	3	205	4	190	
873	0.64	9	1740.03	24604	3	209	6	184	
874	0.35	5	1740.38	24609	2	182	3	173	
875	0.78	11	1741.16	24620	2	194	9	172	
876	0.42	6	1741.58	24626	3	187	3	179	
877	0.42	6	1742.01	24632	2	178	4	169	
878	0.28	4	1742.29	24636	1	196	3	191	
879	0.85	12	1743.14	24648	2	211	10	195	
880	0.85	12	1743.99	24660	7	207	5	187	
881	0.28	4	1744.27	24664	2	213	2	209	
882	0.42	6	1744.70	24670	2	213	4	192	
883	0.35	5	1745.05	24675	3	196	2	185	
884	0.64	9	1745.69	24684	5	196	4	156	
885	0.57	8	1746.25	24692	5	170	3	170	
886	1.06	15	1747.31	24707	3	180	12	154	
887	0.64	9	1747.95	24716	5	179	4	151	
888	0.42	6	1748.37	24722	3	172	3	155	
889	1.13	16	1749.50	24738	11	191	5	148	
890	1.56	22	1751.06	24760	5	201	17	149	
891	0.50	7	1751.56	24767	5	198	2	186	
892	1.63	23	1753.18	24790	8	198	15	163	
893	0.50	7	1753.68	24797	5	188	2	179	
894	0.92	13	1754.60	24810	4	183	9	161	
895	0.99	14	1755.59	24824	2	175	12	154	
896	701.20	9915	2456.79	34739	3	169	9912	142	6

Comments:

1. The topmost 15cm of core D1G does not contain well-preserved varves, and the varve count and thickness measurements from this interval are uncertain.
2. This is a 2cm-thick homogeneous pale grey event bed.
3. This is a 7cm-thick homogeneous pale grey event bed; it can also be seen in the BSEI image in figure 5.9.3.
4. This is a 64cm-thick homogeneous grey interval which contains no varves.
5. This is an 8cm-thick homogeneous pale grey event bed.
6. The bottom 70cm of the core is homogeneous and contains no varves.

B.2 Lake St Moritz sediment greyvalue data

B.2.1 5cm-resolution sediment greyvalue data

The depth indicates the *top* of each 5cm interval. To avoid disturbed areas of sediment at the ends of some of the core sections, not every interval corresponds to exactly 5cm according to the overall depth scale.

Depth (cm)	Mean Greyval	Depth (cm)	Mean Greyval	Depth (cm)	Mean Greyval
0	218.35	220	185.03	438	210.89
5	215.59	225	192.61	443	208.97
10	220.99	230	201.30	448	204.08
15	205.12	235	196.27	453	206.28
20	211.40	240	193.68	458	203.53
25	221.65	245	194.06	463	194.00
30	205.14	250	199.61	468	194.87
35	212.78	255	210.13	473	212.59
40	204.01	260	214.49	478	215.47
45	214.13	265	210.28	483	215.71
50	204.16	270	212.09	488	213.60
55	185.59	275	180.66	493	213.11
60	177.26	282	162.65	498	214.55
65	172.48	287	153.67	503	211.71
70	179.68	292	164.42	508	216.07
75	182.16	298	191.80	513	211.33
80	177.29	303	181.57	519	210.61
85	176.91	308	173.21	524	209.51
90	171.21	313	176.61	529	207.79
95	179.21	318	185.10	534	211.16
102	204.87	323	181.60	539	201.94
107	195.48	328	183.43	544	212.91
112	184.77	333	189.90	549	215.67
117	176.25	338	198.09	554	216.90
122	174.02	343	186.81	559	210.86
127	167.90	348	187.02	564	220.33
132	174.57	353	185.66	569	220.67
137	176.95	358	190.69	574	213.82
142	178.52	363	194.75	579	200.09
147	179.66	368	190.42	584	219.63
152	177.32	373	185.18	589	219.87
157	173.70	378	184.50	594	218.85
162	183.19	383	194.71	599	216.07
167	184.64	388	197.27	604	219.59
172	188.84	393	194.23	609	210.43
177	185.38	398	195.58	614	218.86
185	187.51	403	189.46	619	209.32
190	199.24	408	190.23	624	217.01
195	200.33	413	203.47	629	219.19
200	192.11	418	203.44	634	222.70
205	192.27	423	200.09	639	213.01
210	191.71	428	208.25	644	208.65
215	187.58	433	201.16	649	215.92

Depth (cm)	Mean Greyval	Depth (cm)	Mean Greyval	Depth (cm)	Mean Greyval
654	216.61	809	149.30	967	143.03
659	218.77	814	145.66	972	144.39
664	212.23	819	154.55	977	136.91
669	201.71	824	148.86	982	147.10
674	184.31	829	145.20	987	140.95
679	175.23	834	153.88	992	138.25
684	175.85	839	142.40	997	140.50
689	167.53	844	135.77	1002	141.85
694	166.59	849	143.44	1007	142.18
699	150.76	854	147.46	1012	135.54
704	141.71	859	158.85	1017	141.67
709	144.76	864	158.89	1022	140.35
714	156.78	869	148.04	1027	142.73
719	156.03	874	146.38	1032	133.23
724	150.48	879	150.13	1037	132.00
729	148.10	884	151.44	1042	132.62
734	152.55	889	142.97	1047	139.36
739	152.29	894	151.98	1052	137.47
744	145.15	902	152.30	1057	128.66
749	144.98	907	141.51	1062	136.50
754	152.09	912	146.45	1067	136.19
759	148.04	917	165.70	1072	134.18
764	146.87	922	147.94	1077	135.98
769	147.03	927	138.91	1082	140.27
774	145.85	932	140.02	1087	130.59
779	144.00	937	142.96	1092	125.18
784	143.57	942	140.99	1097	137.50
789	148.63	947	143.20	1102	138.79
794	151.32	952	137.23	1107	139.68
799	145.05	957	144.43	1112	134.69
804	150.27	962	140.37	1117	132.48
				1122	133.82

B.2.2 3cm-resolution sediment greyvalue data

For each 3cm interval, the mean and standard deviation of the sediment greyvalue were measured, using a modified version of the same NIH Image macro that was used to generate the 5cm-resolution greyvalue data. The data format is as for section B.2.1 above.

Depth (cm)	Mean Greyval	SD Greyval	Depth (cm)	Mean Greyval	SD Greyval
0	216.10	17.2	24	222.49	11.3
3	220.05	10.9	27	209.06	11.8
6	215.37	16.2	30	201.79	11.1
9	220.03	12.7	33	202.14	7.7
12	220.15	13.1	36	212.23	9.4
15	210.42	13.3	39	212.77	9.5
18	201.72	16.6	42	201.86	13.5
21	211.83	12.6	45	213.96	10.0

Depth (cm)	Mean Greyval	SD Greyval	Depth (cm)	Mean Greyval	SD Greyval
48	214.32	11.7	201	192.26	11.4
51	202.35	14.6	204	193.31	12.2
54	197.79	12.7	207	190.68	10.0
57	180.01	11.0	210	203.23	13.4
60	180.24	13.5	213	187.21	13.0
63	172.95	10.4	216	191.38	13.5
66	173.05	11.1	219	185.11	11.1
69	176.01	11.1	222	181.24	10.8
72	181.75	10.8	225	197.69	9.5
75	183.54	8.3	228	189.21	16.8
78	181.05	11.1	231	200.54	15.7
81	179.55	12.0	234	201.37	11.3
84	176.48	9.1	237	194.60	10.6
87	177.87	10.6	240	195.70	11.1
90	171.36	10.4	243	192.50	12.7
93	172.82	11.0	246	189.21	12.0
96	179.23	9.3	249	198.82	12.4
99	184.33	14.2	252	200.50	9.4
102	211.72	10.8	255	209.92	9.8
105	187.29	18.9	258	210.41	10.0
108	197.04	14.0	261	214.82	7.8
111	192.19	14.7	264	215.61	8.7
114	183.14	12.0	267	210.53	8.5
117	178.44	8.8	270	213.26	11.1
120	173.46	9.5	273	211.94	13.3
123	173.55	10.2	276	182.29	5.4
126	176.14	11.9	279	180.31	5.0
129	169.30	10.4	282	162.29	18.6
132	174.59	11.3	285	162.12	24.5
135	176.99	10.9	288	153.29	21.5
138	177.14	9.3	291	164.13	19.6
141	174.46	9.6	294	166.76	20.5
144	181.64	10.6	297	194.44	24.7
147	180.52	8.9	300	187.33	19.1
150	179.05	8.7	303	181.37	11.2
153	176.30	9.6	306	178.47	12.3
156	170.50	9.3	309	170.20	12.9
159	176.92	9.0	312	175.79	11.8
162	183.92	8.1	315	177.38	13.1
165	185.93	8.4	318	184.43	19.4
168	184.20	10.5	321	185.43	16.1
171	188.35	8.0	324	183.50	15.3
174	188.11	7.9	327	179.68	12.9
177	189.00	9.3	330	184.23	13.1
180	186.36	10.6	333	187.20	13.1
183	196.24	16.0	336	195.11	15.2
186	166.62	24.7	339	200.97	7.9
189	189.54	11.6	342	196.05	12.4
192	201.29	12.0	345	184.94	13.9
195	202.89	12.3	348	187.94	19.0
198	199.41	9.8	351	188.23	14.6

Depth (cm)	Mean Greyval	SD Greyval	Depth (cm)	Mean Greyval	SD Greyval
354	185.87	12.3	507	216.15	6.8
357	190.85	14.1	510	215.31	8.2
360	191.43	12.7	513	212.21	11.4
363	193.30	9.3	516	209.46	9.2
366	194.19	17.5	519	210.28	11.7
369	190.29	7.9	522	213.53	10.0
372	185.21	10.9	525	211.18	8.8
375	185.54	14.5	528	200.19	17.4
378	181.47	10.8	531	213.18	9.3
381	190.11	13.1	534	211.05	10.0
384	195.94	10.6	537	211.82	11.9
387	198.46	12.2	540	206.10	16.4
390	196.19	9.8	543	203.04	22.2
393	194.83	15.7	546	216.67	5.6
396	193.86	10.0	549	217.50	6.7
399	199.65	8.2	552	214.34	8.2
402	198.44	12.4	555	216.02	8.9
405	190.77	12.8	558	214.21	11.4
408	182.42	15.0	561	209.80	11.9
411	198.80	8.6	564	220.94	6.2
414	205.38	8.0	567	220.11	6.0
417	204.88	15.0	570	221.19	6.4
420	204.98	9.7	573	215.21	6.6
423	202.73	8.4	576	213.24	9.1
426	197.07	11.8	579	196.95	17.7
429	212.26	7.5	582	211.32	15.1
432	205.29	10.4	585	221.15	4.7
435	200.11	12.5	588	218.53	6.1
438	210.70	8.8	591	221.36	6.0
441	217.21	6.2	594	218.04	8.5
444	209.78	7.0	597	222.41	6.1
447	206.76	8.6	600	214.87	10.8
450	204.25	10.2	603	219.67	5.6
453	207.37	9.1	606	220.23	4.8
456	203.29	11.1	609	215.43	7.6
459	204.21	11.2	612	210.83	18.9
462	194.59	12.3	615	218.35	11.9
465	190.94	12.5	618	207.75	19.1
468	192.55	13.6	621	213.73	11.0
471	209.41	12.6	624	217.76	6.3
474	213.12	10.5	627	221.24	5.2
477	216.64	6.6	630	218.34	9.7
480	214.62	9.0	633	223.20	7.9
483	215.33	10.0	636	221.78	4.7
486	215.25	8.2	639	212.46	13.7
489	213.26	8.1	642	211.36	6.8
492	211.19	12.6	645	210.61	13.4
495	218.94	9.8	648	214.36	6.9
498	214.94	7.5	651	219.29	7.7
501	215.51	5.2	654	217.82	9.7
504	211.45	9.2	657	218.77	8.1

Depth (cm)	Mean Greyval	SD Greyval	Depth (cm)	Mean Greyval	SD Greyval
660	218.75	10.3	813	145.11	6.8
663	215.40	12.1	816	147.04	4.3
666	206.39	15.5	819	162.39	14.6
669	203.45	13.3	822	146.28	8.5
672	187.05	18.2	825	147.39	7.0
675	182.41	16.3	828	142.65	7.3
678	176.71	12.5	831	156.89	11.4
681	172.12	10.3	834	148.77	9.7
684	176.82	11.7	837	143.36	10.9
687	175.43	17.2	840	141.64	8.6
690	167.10	15.0	843	138.25	7.0
693	163.82	17.8	846	143.66	5.7
696	164.43	16.6	849	146.28	6.0
699	151.00	13.0	852	147.27	5.8
702	139.91	9.3	855	151.79	5.8
705	143.10	15.2	858	163.39	6.1
708	142.43	8.4	861	164.24	13.8
711	146.92	5.7	864	150.27	8.0
714	157.31	13.1	867	150.99	8.2
717	158.49	22.1	870	146.12	7.5
720	153.00	15.7	873	146.93	5.3
723	152.93	15.8	876	150.36	9.1
726	146.94	15.9	879	150.82	6.9
729	149.00	11.9	882	151.56	12.1
732	154.30	13.1	885	151.13	9.6
735	153.72	8.9	888	143.06	5.1
738	152.71	10.7	891	151.41	8.2
741	152.12	9.4	894	153.77	9.9
744	146.12	13.0	897	149.17	6.4
747	144.63	12.2	900	140.44	11.1
750	146.66	7.1	903	136.74	7.4
753	151.34	9.4	906	139.19	8.9
756	154.45	10.7	909	141.93	8.7
759	147.67	8.5	912	148.31	19.9
762	148.82	9.3	915	174.07	24.1
765	146.29	8.7	918	151.40	14.5
768	147.94	11.8	921	147.79	10.7
771	148.12	15.8	924	141.45	7.2
774	143.66	12.6	927	138.50	4.3
777	143.75	9.7	930	140.79	4.6
780	145.10	8.8	933	142.79	5.2
783	143.36	11.7	936	143.92	6.4
786	147.90	10.8	939	141.25	5.4
789	149.23	8.9	942	141.37	4.6
792	151.54	13.8	945	144.94	6.2
795	151.16	12.4	948	143.57	5.2
798	144.00	14.5	951	140.12	11.1
801	152.44	13.9	954	147.69	11.2
804	149.19	12.5	957	140.07	7.7
807	150.84	11.7	960	142.50	7.4
810	146.68	9.2	963	140.23	6.4

Depth (cm)	Mean Greyval	SD Greyval	Depth (cm)	Mean Greyval	SD Greyval
966	144.74	10.6	1047	139.76	12.6
969	144.31	6.3	1050	138.28	8.1
972	145.82	5.4	1053	139.48	9.1
975	147.70	5.5	1056	128.50	8.4
978	137.50	4.8	1059	134.55	8.4
981	154.80	22.2	1062	138.07	17.3
984	145.85	19.4	1065	136.63	11.9
987	139.29	6.5	1068	133.23	7.0
990	138.30	4.8	1071	134.12	10.1
993	140.80	7.6	1074	134.50	9.3
996	141.16	6.6	1077	137.28	8.1
999	141.58	6.6	1080	139.54	10.0
1002	131.79	8.9	1083	129.50	10.5
1005	149.23	22.1	1086	131.30	12.1
1008	135.43	9.1	1089	123.15	9.0
1011	136.59	6.2	1092	127.28	9.2
1014	138.37	5.2	1095	137.14	10.9
1017	145.30	6.7	1098	143.31	12.7
1020	140.66	5.6	1101	137.44	6.5
1023	140.59	5.6	1104	137.89	7.2
1026	144.75	6.7	1107	143.76	8.4
1029	136.18	11.8	1110	135.05	7.4
1032	130.86	8.7	1113	133.83	8.6
1035	132.68	8.8	1116	133.00	8.8
1038	133.05	8.4	1119	133.20	5.5
1041	132.65	7.8	1122	136.44	5.0
1044	138.23	10.4	1125	138.68	5.5

B.3 Lake St Moritz varve thickness data

B.3.1 Lake St Moritz varve thickness data for c. 0-100cm depth

Varve Number	Cumulative Thickness (mm)	Total Thickness (mm)	Pale Sublayer Thickness (mm)	Dark Sublayer Thickness (mm)	Comments
1	5.35	5.35	1.48	3.87	1
2	14.73	9.38	3.05	6.33	
3	24.09	9.36	3.21	6.15	
4	40.71	16.62	10.12	6.50	
5	50.99	10.28	3.79	6.50	
6	56.59	5.60	3.70	1.89	
7	59.48	2.88	1.65	1.24	
8	61.79	2.31	1.40	0.91	
9	64.01	2.23	0.91	1.32	
10	66.90	2.88	1.65	1.24	
11	70.69	3.79	1.73	2.06	
12	72.75	2.06	1.24	0.83	
13	76.13	3.38	1.81	1.57	
14	87.31	11.19	2.55	8.64	
15	90.12	2.80	1.89	0.91	
16	92.34	2.23	1.40	0.83	
17	97.12	4.78	1.81	2.96	
18	98.69	1.57	0.74	0.83	
19	100.34	1.65	0.83	0.83	
20	103.39	3.05	1.15	1.89	
21	123.13	19.74	0.99	18.75	2
22	146.49	23.36	1.07	22.29	
23	160.14	13.66	1.40	12.25	
24	174.29	14.15	3.70	10.45	
25	178.74	4.45	1.65	2.80	
26	185.49	6.75	2.22	4.53	
27	193.96	8.48	3.87	4.61	
28	202.52	8.56	4.28	4.28	
29	209.68	7.16	3.37	3.79	
30	216.59	6.91	2.31	4.61	
31	224.41	7.82	3.05	4.77	
32	229.27	4.86	1.89	2.96	
33	232.32	3.05	1.73	1.32	
34	235.86	3.54	1.81	1.73	
35	253.13	17.27	5.84	11.43	
36	257.25	4.12	1.81	2.31	
37	260.63	3.38	2.06	1.32	
38	264.83	4.20	1.98	2.22	
39	270.92	6.09	1.48	4.61	
40	283.34	12.42	2.72	9.71	
41	293.05	9.71	4.36	5.35	
42	304.32	11.27	3.54	7.73	
43	312.63	8.31	4.03	4.28	
44	316.50	3.87	1.57	2.31	
45	322.59	6.09	1.65	4.44	
46	327.04	4.45	1.48	2.96	
47	333.54	6.50	4.03	2.47	

Varve Number	Cumulative Thickness (mm)	Total Thickness (mm)	Pale Sublayer Thickness (mm)	Dark Sublayer Thickness (mm)	Comments
48	336.84	3.30	1.07	2.22	
49	342.03	5.19	2.55	2.63	
50	350.58	8.56	1.40	7.16	
51	372.79	22.21	7.07	15.13	
52	377.57	4.78	1.07	3.70	
53	381.35	3.79	1.98	1.81	
54	387.45	6.09	2.31	3.79	
55	391.73	4.28	2.63	1.65	
56	396.34	4.61	2.39	2.22	
57	402.27	5.93	4.20	1.73	
58	406.55	4.28	2.47	1.81	
59	410.61	4.06	1.99	2.07	
60	412.51	1.90	0.74	1.15	
61	414.90	2.39	1.15	1.24	
62	418.69	3.79	1.40	2.39	
63	425.85	7.16	1.57	5.59	
64	430.95	5.10	3.37	1.73	
65	435.48	4.53	1.48	3.05	
66	437.21	1.73	0.91	0.83	
67	451.78	14.56	8.88	5.68	
68	462.31	10.53	4.03	6.50	
69	464.37	2.06	0.74	1.32	
70	467.83	3.46	0.91	2.55	
71	470.47	2.64	1.57	1.07	
72	475.82	5.35	3.54	1.81	
73	480.35	4.53	3.13	1.40	
74	482.90	2.56	1.57	0.99	
75	487.27	4.36	2.39	1.98	
76	492.62	5.35	1.89	3.46	
77	495.25	2.64	1.24	1.40	
78	500.77	5.52	2.96	2.55	
79	506.12	5.35	2.31	3.05	
80	514.19	8.06	6.42	1.65	
81	518.30	4.12	3.29	0.83	
82	522.34	4.04	2.14	1.89	
83	524.73	2.39	1.07	1.32	
84	532.30	7.57	4.11	3.46	
85	544.23	11.93	5.51	6.42	
86	550.73	6.50	1.24	5.27	
87	565.46	14.72	8.23	6.50	3
88	574.59	9.13	4.36	4.77	
89	579.69	5.10	3.29	1.81	
90	587.60	7.90	6.50	1.40	
91	590.48	2.88	1.65	1.24	
92	593.94	3.46	2.22	1.24	
93	596.49	2.56	1.24	1.32	
94	599.38	2.88	1.81	1.07	
95	601.61	2.23	0.99	1.24	
96	606.05	4.45	2.14	2.31	
97	608.86	2.80	1.15	1.65	

Varve Number	Cumulative Thickness (mm)	Total Thickness (mm)	Pale Sublayer Thickness (mm)	Dark Sublayer Thickness (mm)	Comments
98	610.83	1.98	0.99	0.99	
99	613.64	2.80	1.73	1.07	
100	618.74	5.10	4.20	0.91	
101	620.39	1.65	0.83	0.83	
102	621.80	1.40	0.66	0.74	
103	624.76	2.97	2.22	0.74	
104	626.25	1.49	0.74	0.74	
105	628.81	2.56	1.65	0.91	
106	632.92	4.12	3.13	0.99	
107	635.97	3.05	2.22	0.83	
108	637.95	1.98	1.07	0.91	
109	641.00	3.05	1.98	1.07	
110	645.20	4.20	2.06	2.14	
111	647.92	2.72	1.57	1.15	
112	650.39	2.47	0.74	1.73	
113	657.14	6.75	4.03	2.72	
114	660.85	3.71	1.07	2.63	
115	663.65	2.80	2.06	0.74	
116	665.22	1.57	0.83	0.74	
117	667.86	2.64	1.73	0.91	
118	671.07	3.21	2.39	0.83	
119	674.12	3.05	1.65	1.40	
120	680.87	6.75	2.96	3.79	
121	683.02	2.14	1.40	0.74	
122	685.65	2.64	1.57	1.07	
123	687.30	1.65	0.99	0.66	
124	690.52	3.21	2.14	1.07	
125	696.36	5.84	4.36	1.48	
126	701.14	4.78	3.79	0.99	
127	704.76	3.62	2.55	1.07	
128	709.45	4.69	3.70	0.99	
129	713.16	3.71	1.15	2.55	
130	716.38	3.21	1.40	1.81	
131	718.68	2.31	0.91	1.40	
132	720.75	2.06	0.66	1.40	
133	735.64	14.89	6.91	7.98	
134	742.14	6.50	4.44	2.06	
135	745.93	3.79	1.98	1.81	
136	748.81	2.88	1.73	1.15	
137	752.11	3.30	1.81	1.48	
138	755.98	3.87	0.91	2.96	
139	758.94	2.97	1.81	1.15	
140	762.73	3.79	0.74	3.05	
141	764.38	1.65	0.74	0.91	
142	766.69	2.31	0.99	1.32	
143	773.03	6.34	3.21	3.13	
144	776.57	3.54	2.31	1.24	
145	780.44	3.87	2.31	1.57	
146	782.26	1.82	0.83	0.99	
147	784.49	2.23	1.32	0.91	

Varve Number	Cumulative Thickness (mm)	Total Thickness (mm)	Pale Sublayer Thickness (mm)	Dark Sublayer Thickness (mm)	Comments
148	787.54	3.05	1.81	1.24	
149	789.68	2.14	1.15	0.99	
150	793.14	3.46	2.14	1.32	
151	796.11	2.97	2.06	0.91	
152	799.90	3.79	1.57	2.22	
153	802.70	2.80	1.89	0.91	
154	804.59	1.90	0.66	1.24	
155	807.48	2.88	1.57	1.32	
156	809.54	2.06	1.15	0.91	
157	814.65	5.10	4.03	1.07	
158	816.22	1.57	0.74	0.83	
159	818.36	2.14	1.07	1.07	
160	820.67	2.31	1.40	0.91	
161	822.57	1.90	0.83	1.07	
162	824.55	1.98	0.91	1.07	
163	826.53	1.98	1.15	0.83	
164	828.75	2.23	1.32	0.91	
165	830.73	1.98	0.83	1.15	
166	834.28	3.54	2.47	1.07	
167	837.24	2.97	1.48	1.48	
168	839.96	2.72	1.81	0.91	
169	843.67	3.71	2.55	1.15	
170	845.89	2.23	1.48	0.74	
171	847.71	1.82	1.15	0.66	
172	849.44	1.73	0.91	0.83	
173	851.34	1.90	0.91	0.99	
174	854.31	2.97	1.98	0.99	
175	858.02	3.71	1.89	1.81	
176	863.37	5.35	3.13	2.22	
177	865.18	1.82	1.15	0.66	
178	868.23	3.05	1.48	1.57	
179	871.77	3.54	1.40	2.14	
180	873.09	1.32	0.58	0.74	
181	874.50	1.40	0.74	0.66	
182	878.21	3.71	1.07	2.63	
183	880.68	2.47	1.73	0.74	
184	882.41	1.73	0.91	0.83	
185	883.90	1.49	0.74	0.74	
186	887.19	3.30	0.99	2.31	
187	889.50	2.31	1.24	1.07	
188	893.79	4.28	0.00	1.81	
189	895.52	1.73	0.83	0.91	
190	898.49	2.97	1.32	1.65	
191	899.81	1.32	0.66	0.66	
192	902.04	2.23	0.99	1.24	
193	905.25	3.21	1.65	1.57	
194	908.79	3.54	2.55	0.99	
195	914.14	5.35	3.79	1.57	
196	919.00	4.86	3.95	0.91	
197	921.55	2.56	1.15	1.40	

Varve Number	Cumulative Thickness (mm)	Total Thickness (mm)	Pale Sublayer Thickness (mm)	Dark Sublayer Thickness (mm)	Comments
198	923.45	1.90	0.99	0.91	
199	925.52	2.06	0.99	1.07	
200	928.15	2.64	1.24	1.40	
201	931.53	3.38	1.65	1.73	
202	934.00	2.47	0.99	1.48	
203	935.49	1.49	0.91	0.58	
204	936.98	1.49	0.83	0.66	
205	939.45	2.47	1.15	1.32	
206	942.75	3.30	0.99	2.31	
207	944.97	2.23	1.07	1.15	
208	948.19	3.21	1.98	1.24	
209	949.51	1.32	0.83	0.50	
210	951.16	1.65	0.83	0.83	
211	955.44	4.28	3.05	1.24	
212	958.82	3.38	2.14	1.24	
213	961.13	2.31	1.48	0.83	
214	965.16	4.04	2.14	1.89	
215	968.62	3.46	1.32	2.14	
216	971.43	2.80	0.91	1.89	
217	973.41	1.98	1.07	0.91	
218	976.45	3.05	1.15	1.89	
219	981.31	4.86	1.48	3.37	
220	988.47	7.16	2.72	4.44	
221	990.86	2.39	0.91	1.48	
222	992.68	1.82	0.83	0.99	
223	995.48	2.80	1.73	1.07	
224	997.21	1.73	0.74	0.99	
225	999.28	2.06	1.32	0.74	
226	1000.60	1.32	0.58	0.74	
227	1002.58	1.98	0.99	0.99	
228	1005.14	2.56	1.57	0.99	
229	1007.77	2.64	1.32	1.32	
230	1010.58	2.80	1.81	0.99	
231	1014.53	3.95	3.05	0.91	
232	1016.18	1.65	0.83	0.83	
233	1018.65	2.47	1.57	0.91	
234	1021.46	2.80	1.73	1.07	
235	1024.67	3.21	2.22	0.99	
236	1026.65	1.98	1.32	0.66	
237	1029.29	2.64	1.32	1.32	
238	1033.16	3.87	2.22	1.65	
239	1035.88	2.72	1.32	1.40	

Comments:

1. The topmost few cm of PSM90.3 do not contain well-preserved varves, and the topmost few varve measurements from this interval are uncertain.
2. This 2cm-thick varve may correspond to the 1969 event bed (see section 5.3.5).
3. This varve may correspond to the 1911-1914 event bed (see section 5.3.5); it is not distinctly thick, but it is apparent in the digital images as an unusually pale layer.

B.3.2 Lake St Moritz varve thickness data for c. 200-275cm depth

These varves are numbered A1, A2, etc., to avoid any confusion with the data in section B.3.1. Three turbidites, which were deleted from the final time-series, are denoted by the letter 'T'.

Varve Number	Cumulative Thickness (mm)	Total Varve Thickness (mm)	Varve Number	Cumulative Thickness (mm)	Total Varve Thickness (mm)
A1	1.29	1.29	A44	62.62	1.67
A2	2.80	1.51	A45	64.66	2.04
A3	3.72	0.92	A46	65.72	1.06
A4	4.25	0.53	A47	67.07	1.35
A5	5.06	0.82	A48	67.91	0.84
A6	5.76	0.69	A49	68.97	1.06
A7	7.04	1.29	A50	70.03	1.06
A8	8.92	1.88	A51	73.05	3.02
A9	10.37	1.45	A52	74.48	1.43
A10	11.13	0.76	A53	75.93	1.45
A11	12.25	1.12	A54	77.44	1.51
A12	13.17	0.92	A55	79.18	1.74
A13	16.41	3.25	A56	80.38	1.20
A14	18.07	1.65	A57	81.07	0.69
A15	18.99	0.92	A58	81.75	0.67
A16	20.58	1.59	A59	82.58	0.84
A17	22.76	2.18	A60	83.40	0.82
A18	24.36	1.59	A61	84.32	0.92
A19	26.24	1.88	A62	84.85	0.53
A20	28.22	1.98	A63	85.61	0.76
A21	30.03	1.82	A64	86.28	0.67
A22	31.32	1.29	A65	87.04	0.76
A23	32.89	1.57	A66	87.73	0.69
A24	34.93	2.04	A67	88.24	0.51
A25	36.16	1.22	A68	88.93	0.69
A26	36.91	0.76	A69	89.91	0.98
A27	38.49	1.57	A70	90.98	1.06
A28	39.63	1.14	A71	91.57	0.59
A29	41.36	1.74	A72	92.26	0.69
A30	42.20	0.84	A73	92.85	0.59
A31	42.96	0.76	A74	93.55	0.69
A32	45.98	3.02	A75	94.00	0.45
A33	46.73	0.76	A76	94.83	0.84
A34	48.33	1.59	A77	95.43	0.59
A35	49.00	0.67	A78	95.90	0.47
A36	50.14	1.14	A79	96.65	0.76
A37	52.41	2.27	A80	97.47	0.82
A38	53.02	0.61	A81	98.45	0.98
A39	54.23	1.20	A82	99.90	1.45
A40	54.98	0.76	A83	100.80	0.90
A41	56.86	1.88	A84	101.86	1.06
A42	58.68	1.82	A85	103.53	1.67
A43	60.94	2.27	A86	105.19	1.65

Varve Number	Cumulative Thickness (mm)	Total Varve Thickness (mm)	Varve Number	Cumulative Thickness (mm)	Total Varve Thickness (mm)	
A87	106.17	0.98	A136	168.42	0.51	
A88	107.76	1.59	A137	169.06	0.64	
A89	110.02	2.27	A138	170.36	1.30	
A90	112.29	2.27	A139	171.17	0.82	
A91	113.43	1.14	A140	172.57	1.39	
A92	114.19	0.76	A141	194.57	22.00	T
A93	115.54	1.35	A142	195.96	1.39	
A94	116.76	1.22	A143	196.93	0.97	
A95	119.78	3.02	A144	197.59	0.66	
A96	120.54	0.76	A145	198.32	0.73	
A97	122.13	1.59	A146	199.14	0.82	
A98	124.62	2.49	A147	199.80	0.66	
A99	126.21	1.59	A148	201.10	1.30	
A100	127.56	1.35	A149	201.68	0.57	
A101	128.71	1.14	A150	202.34	0.66	
A102	129.99	1.29	A151	203.07	0.73	
A103	130.81	0.82	A152	203.55	0.49	
A104	131.63	0.82	A153	204.21	0.66	
A105	132.93	1.30	A154	205.03	0.82	
A106	134.89	1.96	A155	205.76	0.73	
A107	135.86	0.97	A156	206.82	1.06	
A108	137.19	1.32	A157	207.48	0.66	
A109	138.16	0.97	A158	208.14	0.66	
A110	140.36	2.21	A159	208.78	0.64	
A111	140.94	0.57	A160	209.20	0.42	
A112	141.67	0.73	A161	210.02	0.82	
A113	142.90	1.24	A162	210.66	0.64	
A114	144.87	1.96	A163	211.41	0.75	
A115	145.44	0.57	A164	212.14	0.73	
A116	146.08	0.64	A165	213.68	1.54	
A117	146.90	0.82	A166	215.07	1.39	
A118	147.23	0.33	A167	215.98	0.90	
A119	147.80	0.57	A168	216.71	0.73	
A120	149.04	1.24	A169	217.21	0.51	
A121	149.85	0.82	A170	218.67	1.46	
A122	150.43	0.57	A171	219.49	0.82	
A123	151.31	0.88	A172	220.81	1.32	
A124	152.46	1.15	A173	221.78	0.97	
A125	156.15	3.69	A174	222.84	1.06	
A126	157.93	1.79	A175	223.75	0.90	
A127	159.59	1.66	A176	225.14	1.39	
A128	160.65	1.06	A177	225.80	0.66	
A129	162.44	1.79	A178	226.68	0.88	
A130	163.58	1.15	A179	227.59	0.90	
A131	164.82	1.24	A180	228.40	0.82	
A132	165.88	1.06	A181	229.70	1.30	
A133	166.36	0.49	A182	231.67	1.96	
A134	167.27	0.90	A183	232.82	1.15	
A135	167.91	0.64	A184	234.69	1.88	

Varve Number	Cumulative Thickness (mm)	Total Varve Thickness (mm)		Varve Number	Cumulative Thickness (mm)	Total Varve Thickness (mm)	
A185	235.84	1.15		A234	282.43	0.64	
A186	237.08	1.24		A235	284.39	1.96	
A187	237.96	0.88		A236	285.63	1.24	
A188	239.35	1.39		A237	286.93	1.30	
A189	239.92	0.57		A238	288.08	1.15	
A190	241.56	1.63		A239	288.65	0.57	
A191	242.31	0.75		A240	289.47	0.82	
A192	242.88	0.57		A241	293.55	4.08	T
A193	243.61	0.73		A242	295.28	1.72	
A194	244.27	0.66		A243	296.82	1.54	
A195	245.57	1.30		A244	297.97	1.15	
A196	247.03	1.46		A245	299.51	1.54	
A197	248.18	1.15		A246	301.23	1.72	
A198	249.41	1.24		A247	306.31	5.08	
A199	250.89	1.48		A248	307.13	0.82	
A200	251.44	0.55		A249	307.86	0.73	
A201	252.19	0.75		A250	308.34	0.49	
A202	254.40	2.21		A251	314.08	5.74	T
A203	255.55	1.15		A252	314.90	0.82	
A204	256.12	0.57		A253	315.29	0.40	
A205	256.76	0.64		A254	315.71	0.42	
A206	258.24	1.48		A255	316.11	0.40	
A207	259.06	0.82		A256	316.84	0.73	
A208	260.27	1.21		A257	317.41	0.57	
A209	261.60	1.32		A258	317.83	0.42	
A210	262.57	0.97		A259	318.74	0.90	
A211	263.38	0.82		A260	319.31	0.57	
A212	264.44	1.06		A261	320.13	0.82	
A213	265.19	0.75		A262	320.85	0.73	
A214	266.16	0.97		A263	321.43	0.57	
A215	267.31	1.15		A264	322.16	0.73	
A216	267.89	0.57		A265	322.91	0.75	
A217	268.79	0.90		A266	323.64	0.73	
A218	270.82	2.03		A267	324.21	0.57	
A219	271.97	1.15		A268	324.85	0.64	
A220	273.45	1.48		A269	325.36	0.51	
A221	274.09	0.64		A270	326.24	0.88	
A222	274.84	0.75		A271	327.14	0.90	
A223	275.41	0.57		A272	327.81	0.66	
A224	276.05	0.64		A273	328.29	0.49	
A225	276.80	0.75		A274	328.95	0.66	
A226	277.77	0.97		A275	330.17	1.21	
A227	278.35	0.57		A276	330.83	0.66	
A228	279.01	0.66		A277	332.55	1.72	
A229	279.50	0.49		A278	333.04	0.49	
A230	280.07	0.57		A279	333.52	0.49	
A231	280.55	0.49		A280	334.19	0.66	
A232	281.37	0.82		A281	334.76	0.57	
A233	281.79	0.42		A282	335.49	0.73	

Varve Number	Cumulative Thickness (mm)	Total Varve Thickness (mm)	Varve Number	Cumulative Thickness (mm)	Total Varve Thickness (mm)
A283	336.30	0.82	A332	382.41	1.06
A284	337.21	0.90	A333	383.23	0.82
A285	338.36	1.15	A334	383.95	0.73
A286	339.24	0.88	A335	384.86	0.90
A287	339.99	0.75	A336	386.16	1.30
A288	340.72	0.73	A337	389.03	2.87
A289	341.29	0.57	A338	389.93	0.90
A290	342.20	0.90	A339	390.91	0.97
A291	343.26	1.06	A340	392.87	1.96
A292	344.14	0.88	A341	394.35	1.48
A293	345.13	0.99	A342	395.56	1.21
A294	347.25	2.12	A343	396.56	0.99
A295	348.31	1.06	A344	398.59	2.03
A296	349.21	0.90	A345	399.98	1.39
A297	350.12	0.90	A346	401.38	1.41
A298	350.76	0.64	A347	402.16	0.78
A299	351.27	0.51	A348	402.71	0.55
A300	351.91	0.64	A349	403.25	0.55
A301	352.66	0.75	A350	404.35	1.09
A302	353.54	0.88	A351	404.81	0.46
A303	353.87	0.33	A352	405.44	0.63
A304	354.62	0.75	A353	405.82	0.38
A305	356.01	1.39	A354	406.36	0.55
A306	356.83	0.82	A355	407.54	1.18
A307	358.37	1.54	A356	408.46	0.92
A308	359.19	0.82	A357	409.47	1.01
A309	360.16	0.97	A358	410.42	0.95
A310	361.24	1.08	A359	412.43	2.02
A311	361.97	0.73	A360	414.16	1.72
A312	362.70	0.73	A361	414.85	0.69
A313	363.85	1.15	A362	415.46	0.61
A314	364.84	0.99	A363	416.01	0.55
A315	365.90	1.06	A364	417.33	1.32
A316	366.63	0.73	A365	418.27	0.95
A317	367.29	0.66	A366	418.82	0.55
A318	368.02	0.73	A367	419.43	0.61
A319	368.75	0.73	A368	420.92	1.49
A320	369.98	1.24	A369	422.01	1.09
A321	371.20	1.21	A370	422.79	0.78
A322	372.19	0.99	A371	423.63	0.84
A323	373.01	0.82	A372	424.41	0.78
A324	374.22	1.21	A373	425.19	0.78
A325	375.46	1.24	A374	426.05	0.86
A326	376.18	0.73	A375	426.51	0.46
A327	377.42	1.24	A376	427.22	0.71
A328	378.24	0.82	A377	428.00	0.78
A329	378.97	0.73	A378	428.78	0.78
A330	380.69	1.72	A379	429.56	0.78
A331	381.35	0.66	A380	430.56	1.01

Varve Number	Cumulative Thickness (mm)	Total Varve Thickness (mm)	Varve Number	Cumulative Thickness (mm)	Total Varve Thickness (mm)
A381	432.12	1.55	A430	470.94	0.38
A382	432.58	0.46	A431	471.66	0.71
A383	433.13	0.55	A432	472.98	1.32
A384	433.84	0.71	A433	473.67	0.69
A385	435.17	1.32	A434	474.45	0.78
A386	435.94	0.78	A435	474.91	0.46
A387	436.95	1.01	A436	475.61	0.69
A388	437.73	0.78	A437	476.38	0.78
A389	438.51	0.78	A438	476.93	0.55
A390	439.05	0.55	A439	477.71	0.78
A391	439.89	0.84	A440	478.19	0.48
A392	440.44	0.55	A441	479.51	1.32
A393	441.22	0.78	A442	480.67	1.16
A394	441.99	0.78	A443	481.62	0.95
A395	442.54	0.55	A444	482.54	0.92
A396	443.25	0.71	A445	483.48	0.95
A397	444.03	0.78	A446	484.41	0.92
A398	445.19	1.16	A447	485.10	0.69
A399	446.19	1.01	A448	485.88	0.78
A400	447.37	1.18	A449	486.83	0.95
A401	448.00	0.63	A450	487.60	0.78
A402	448.55	0.55	A451	488.30	0.69
A403	450.02	1.47	A452	489.07	0.78
A404	450.80	0.78	A453	490.31	1.24
A405	452.27	1.47	A454	490.86	0.55
A406	452.98	0.71	A455	491.80	0.95
A407	453.44	0.46	A456	492.81	1.01
A408	454.14	0.69	A457	493.27	0.46
A409	454.60	0.46	A458	493.90	0.63
A410	455.08	0.48	A459	494.77	0.86
A411	455.92	0.84	A460	495.92	1.16
A412	456.64	0.71	A461	496.87	0.95
A413	457.96	1.32	A462	497.39	0.53
A414	459.05	1.09	A463	498.19	0.80
A415	459.83	0.78	A464	499.12	0.92
A416	460.29	0.46	A465	500.52	1.41
A417	461.30	1.01	A466	501.45	0.92
A418	461.76	0.46	A467	502.08	0.63
A419	462.31	0.55	A468	502.85	0.78
A420	463.00	0.69	A469	503.86	1.01
A421	464.26	1.26	A470	504.56	0.69
A422	464.87	0.61	A471	505.33	0.78
A423	465.50	0.63	A472	506.83	1.49
A424	466.05	0.55	A473	507.60	0.78
A425	467.06	1.01	A474	508.44	0.84
A426	468.23	1.18	A475	508.99	0.55
A427	469.07	0.84	A476	510.31	1.32
A428	470.08	1.01	A477	511.80	1.49
A429	470.56	0.48	A478	512.90	1.09

Varve Number	Cumulative Thickness (mm)	Total Varve Thickness (mm)	Varve Number	Cumulative Thickness (mm)	Total Varve Thickness (mm)
A479	513.74	0.84	A528	558.72	1.95
A480	514.68	0.95	A529	559.72	1.01
A481	515.29	0.61	A530	561.45	1.72
A482	516.38	1.09	A531	562.14	0.69
A483	517.33	0.95	A532	563.23	1.09
A484	518.17	0.84	A533	564.16	0.92
A485	518.80	0.63	A534	565.10	0.95
A486	519.98	1.18	A535	566.34	1.24
A487	521.68	1.70	A536	567.43	1.09
A488	522.60	0.92	A537	568.36	0.92
A489	523.09	0.48	A538	568.82	0.46
A490	523.78	0.69	A539	569.77	0.95
A491	524.18	0.40	A540	570.92	1.16
A492	524.79	0.61	A541	572.25	1.32
A493	525.42	0.63	A542	573.51	1.26
A494	526.19	0.78	A543	574.12	0.61
A495	527.52	1.32	A544	574.83	0.71
A496	528.53	1.01	A545	575.75	0.92
A497	529.62	1.09	A546	576.62	0.86
A498	530.54	0.92	A547	577.08	0.46
A499	531.09	0.55	A548	577.71	0.63
A500	531.72	0.63	A549	578.48	0.78
A501	532.33	0.61	A550	579.96	1.47
A502	532.88	0.55	A551	580.73	0.78
A503	533.82	0.95	A552	581.43	0.69
A504	534.75	0.92	A553	582.29	0.86
A505	535.69	0.95	A554	583.30	1.01
A506	537.01	1.32	A555	583.93	0.63
A507	537.71	0.69	A556	584.70	0.78
A508	538.57	0.86	A557	585.17	0.46
A509	539.26	0.69	A558	586.17	1.01
A510	539.72	0.46	A559	587.58	1.41
A511	540.90	1.18	A560	588.44	0.86
A512	541.59	0.69	A561	589.68	1.24
A513	542.22	0.63	A562	590.38	0.69
A514	543.55	1.32	A563	591.40	1.03
A515	544.41	0.86	A564	592.73	1.32
A516	545.25	0.84	A565	593.74	1.01
A517	546.19	0.95	A566	594.28	0.55
A518	548.21	2.02	A567	594.83	0.55
A519	550.23	2.02	A568	595.61	0.78
A520	550.94	0.71	A569	596.38	0.78
A521	551.64	0.69	A570	597.22	0.84
A522	552.56	0.92	A571	598.63	1.41
A523	553.34	0.78	A572	599.49	0.86
A524	554.12	0.78	A573	600.42	0.92
A525	554.75	0.63	A574	601.51	1.09
A526	555.84	1.09	A575	602.75	1.24
A527	556.76	0.92	A576	603.61	0.86

Varve Number	Cumulative Thickness (mm)	Total Varve Thickness (mm)	Varve Number	Cumulative Thickness (mm)	Total Varve Thickness (mm)
A577	604.16	0.55	A626	649.98	0.78
A578	605.25	1.09	A627	650.42	0.45
A579	605.86	0.61	A628	651.24	0.81
A580	606.72	0.86	A629	652.07	0.83
A581	607.81	1.09	A630	653.13	1.06
A582	608.74	0.92	A631	653.74	0.61
A583	609.28	0.55	A632	654.72	0.98
A584	610.23	0.95	A633	655.55	0.83
A585	611.15	0.92	A634	656.37	0.81
A586	611.87	0.71	A635	657.28	0.92
A587	612.64	0.78	A636	658.12	0.83
A588	613.42	0.78	A637	659.15	1.04
A589	614.20	0.78	A638	660.07	0.92
A590	614.81	0.61	A639	660.60	0.53
A591	615.21	0.40	A640	661.94	1.34
A592	616.07	0.86	A641	662.63	0.69
A593	617.39	1.32	A642	663.61	0.98
A594	618.40	1.01	A643	664.06	0.45
A595	619.72	1.32	A644	664.73	0.67
A596	621.83	2.10	A645	665.65	0.92
A597	622.98	1.16	A646	666.54	0.90
A598	623.84	0.86	A647	667.52	0.98
A599	624.93	1.09	A648	668.13	0.61
A600	626.03	1.09	A649	668.74	0.61
A601	627.04	1.01	A650	669.49	0.75
A602	628.36	1.32	A651	670.02	0.53
A603	629.45	1.09	A652	670.61	0.59
A604	630.54	1.09	A653	671.59	0.98
A605	630.92	0.38	A654	672.28	0.69
A606	631.55	0.63	A655	673.18	0.90
A607	632.79	1.24	A656	673.62	0.45
A608	633.34	0.55	A657	674.84	1.22
A609	634.49	1.16	A658	675.52	0.67
A610	635.82	1.32	A659	676.43	0.92
A611	636.53	0.71	A660	677.33	0.90
A612	637.37	0.84	A661	678.53	1.20
A613	638.23	0.86	A662	679.50	0.98
A614	638.95	0.71	A663	680.64	1.14
A615	639.72	0.78	A664	681.32	0.67
A616	640.56	0.84	A665	682.01	0.69
A617	641.74	1.18	A666	682.90	0.90
A618	642.83	1.09	A667	683.57	0.67
A619	643.53	0.69	A668	684.41	0.83
A620	644.07	0.55	A669	684.86	0.45
A621	645.40	1.32	A670	685.61	0.75
A622	646.26	0.86	A671	686.36	0.75
A623	647.04	0.78	A672	687.05	0.69
A624	648.42	1.39	A673	687.58	0.53
A625	649.20	0.78	A674	688.40	0.81

Varve Number	Cumulative Thickness (mm)	Total Varve Thickness (mm)
A675	689.31	0.92
A676	690.21	0.90
A677	690.90	0.69
A678	691.57	0.67
A679	692.32	0.75
A680	693.83	1.51
A681	694.81	0.98
A682	696.84	2.04
A683	698.35	1.51
A684	699.04	0.69
A685	700.24	1.20
A686	700.99	0.75
A687	701.67	0.67
A688	702.11	0.45
A689	702.81	0.69
A690	703.40	0.59
A691	703.92	0.53
A692	704.68	0.75
A693	705.43	0.75
A694	706.65	1.22
A695	707.18	0.53
A696	708.08	0.90
A697	709.22	1.14
A698	710.11	0.90
A699	710.72	0.61
A700	711.47	0.75
A701	712.23	0.75
A702	713.06	0.83
A703	714.40	1.34
A704	714.93	0.53
A705	716.22	1.28
A706	716.66	0.45
A707	717.50	0.83
A708	718.25	0.75
A709	719.23	0.98
A710	719.76	0.53
A711	720.37	0.61
A712	721.34	0.98
A713	721.71	0.37
A714	722.54	0.83
A715	723.24	0.69
A716	723.99	0.75
A717	724.58	0.59
A718	725.27	0.69
A719	725.86	0.59
A720	726.53	0.67
A721	727.37	0.83
A722	728.34	0.98
A723	729.93	1.59
A724	731.44	1.51
A725	732.27	0.83
A726	733.02	0.75
A727	733.78	0.75
A728	734.45	0.67
A729	734.92	0.47
A730	735.59	0.67
A731	736.20	0.61
A732	736.87	0.67
A733	737.62	0.75
A734	738.15	0.53
A735	738.52	0.37
A736	739.13	0.61
A737	740.03	0.90
A738	740.55	0.53
A739	741.31	0.75
A740	742.06	0.75
A741	742.98	0.92
A742	743.59	0.61
A743	744.79	1.20
A744	745.46	0.67
A745	746.21	0.75
A746	747.13	0.92
A747	748.86	1.73
A748	749.98	1.12

B.4 Lake St Moritz calibrated radiocarbon data

This section contains the output from the CALIB v. 4.4 program which was used to calibrate the 20 Lake St Moritz dates. The calibrated ages are given to the nearest year, although the real accuracy is more likely to be to the nearest 10 years, as indicated by the weighted average calibrated ages.

UtC-9871
Depth (cm): 142-144
Material: Needles
Radiocarbon age (^{14}C yrs BP): 1120 ± 30
95% (2σ) error age ranges (cal BP) and relative area under probability distribution:
952 - 1081 0.985
1112 - 1120 0.009
1162 - 1167 0.005
Weighted average calibrated age: 1020 BP

UtC-9870
Depth (cm): 226-228
Material: Needles
Radiocarbon age (^{14}C yrs BP): 1870 ± 40
95% (2σ) error age ranges (cal BP) and relative area under probability distribution:
1710 - 1890 0.997
1914 - 1916 0.003
Weighted average calibrated age: 1800 BP

UtC-9869
Depth (cm): 330-332
Material: Needles
Radiocarbon age (^{14}C yrs BP): 3140 ± 40
95% (2σ) error age ranges (cal BP) and relative area under probability distribution:
3264 - 3309 0.157
3317 - 3465 0.843
Weighted average calibrated age: 3370 BP

UtC-9868
Depth (cm): 382-384
Material: Needles
Radiocarbon age (^{14}C yrs BP): 3920 ± 60
95% (2σ) error age ranges (cal BP) and relative area under probability distribution:
4153 - 4172 0.024
4175 - 4205 0.040
4220 - 4450 0.846
4465 - 4520 0.090
Weighted average calibrated age: 4340 BP

UtC-9867
Depth (cm): 400-402
Material: Needles
Radiocarbon age (^{14}C yrs BP): 3950 ± 40
95% (2σ) error age ranges (cal BP) and relative area under probability distribution:
4257 - 4271 0.023
4279 - 4450 0.791
4465 - 4519 0.186
Weighted average calibrated age: 4390 BP

UtC-9865
Depth (cm): 436-438
Material: Needles
Radiocarbon age (^{14}C yrs BP): 4750 ± 50
95% (2σ) error age ranges (cal BP) and relative area under probability distribution:
5326 - 5407 0.263
5448 - 5591 0.737
Weighted average calibrated age: 5480 BP

UtC-9519
Depth (cm): 454-456
Material: Needles
Radiocarbon age (^{14}C yrs BP): 5300 ± 50
95% (2σ) error age ranges (cal BP) and relative area under probability distribution:
5933 - 6197 1.000
Weighted average calibrated age: 6070 BP

UtC-9864
Depth (cm): 462-464
Material: Needles
Radiocarbon age (^{14}C yrs BP): 5280 ± 50
95% (2σ) error age ranges (cal BP) and relative area under probability distribution:
5928 - 6180 1.000
Weighted average calibrated age: 6050 BP

UtC-9863
Depth (cm): 476-478
Material: Needles
Radiocarbon age (^{14}C yrs BP): 5880 ± 50
95% (2σ) error age ranges (cal BP) and relative area under probability distribution:
6552 - 6763 0.898
6765 - 6800 0.088
6823 - 6826 0.003
6840 - 6848 0.011
Weighted average calibrated age: 6670 BP

UtC-9862
Depth (cm): 500-502
Material: Needles, *Betula* fruit
Radiocarbon age (^{14}C yrs BP): 6400 ± 50
95% (2σ) error age ranges (cal BP) and relative area under probability distribution:
7253 - 7420 1.000
Weighted average calibrated age: 7340 BP

UtC-9861
Depth (cm): 522-524
Material: Needles
Radiocarbon age (^{14}C yrs BP): 6670 ± 50
95% (2σ) error age ranges (cal BP) and relative area under probability distribution:
7432 - 7452 0.051
7456 - 7613 0.943
7642 - 7647 0.007
Weighted average calibrated age: 7540 BP

UtC-9860

Depth (cm): 536-538
Material: Needles
Radiocarbon age (^{14}C yrs BP): 7700 ± 70
95% (2σ) error age ranges (cal BP) and relative area under probability distribution:

8374 - 8599	1.000

Weighted average calibrated age: 8490 BP

UtC-9859

Depth (cm): 548-550
Material: Needles
Radiocarbon age (^{14}C yrs BP): 8110 ± 60
95% (2σ) error age ranges (cal BP) and relative area under probability distribution:

8778 - 8830	0.050
8859 - 8882	0.018
8897 - 8917	0.016
8932 - 8940	0.004
8952 - 8965	0.005
8976 - 9272	0.907

Weighted average calibrated age: 9100 BP

UtC-9526

Depth (cm): 578-580
Material: Needles
Radiocarbon age (^{14}C yrs BP): 9070 ± 70
95% (2σ) error age ranges (cal BP) and relative area under probability distribution:

9920 - 9944	0.015
9958 - 9994	0.032
10011 - 10017	0.004
10031 - 10055	0.018
10068 - 10079	0.008
10112 - 10135	0.017
10146 - 10425	0.897
10457 - 10471	0.010

Weighted average calibrated age: 10270 BP

UtC-9525

Depth (cm): 584-586
Material: Fruits, needles, bark
Radiocarbon age (^{14}C yrs BP): 9340 ± 60
95% (2σ) error age ranges (cal BP) and relative area under probability distribution:

10287 - 10301	0.013
10307 - 10319	0.010
10330 - 10341	0.009
10362 - 10371	0.006
10378 - 10693	0.949
10712 - 10731	0.013

Weighted average calibrated age: 10530 BP

UtC-9524

Depth (cm): 596-598
Material: Anthers, needles
Radiocarbon age (^{14}C yrs BP): 9260 ± 130
95% (2σ) error age ranges (cal BP) and relative area under probability distribution:

10179 - 10763	0.975
10959 - 11004	0.013
11018 - 11058	0.012

Weighted average calibrated age: 10480 BP

UtC-9857

Depth (cm): 760-765
Material: Wood, leaves
Radiocarbon age (^{14}C yrs BP): 10200 ± 70
95% (2σ) error age ranges (cal BP) and relative area under probability distribution:

11364 - 11375	0.003
11439 - 11468	0.013
11490 - 11498	0.002
11552 - 12343	0.981

Weighted average calibrated age: 11930 BP

UtC-9522

Depth (cm): 795-800
Material: Leaves, wood, bark
Radiocarbon age (^{14}C yrs BP): 9660 ± 120
95% (2σ) error age ranges (cal BP) and relative area under probability distribution:

10599 - 10608	0.004
10640 - 10658	0.008
10669 - 11234	0.986
11251 - 11254	0.001

Weighted average calibrated age: 10940 BP

UtC-9521

Depth (cm): 895-900
Material: Wood
Radiocarbon age (^{14}C yrs BP): 10100 ± 100
95% (2σ) error age ranges (cal BP) and relative area under probability distribution:

11256 - 12134	0.974
12220 - 12290	0.026

Weighted average calibrated age: 11710 BP

UtC-9520

Depth (cm): 925-930
Material: Charcoal, leaves
Radiocarbon age (^{14}C yrs BP): 10050 ± 90
95% (2σ) error age ranges (cal BP) and relative area under probability distribution:

11228 - 11782	0.822
11786 - 11973	0.146
12015 - 12103	0.032

Weighted average calibrated age: 11580 BP

B.5 Lake St Moritz sediment greyvalue time-series data

This section presents the sediment greyvalue data from section B.2, resampled using the radiocarbon chronology to produce a time-series with a sampling interval of 30 years. Rounding errors in the "AnalySeries" program mean that the sampling interval is actually very slightly greater than 30 years, though this is not statistically significant.

Age (cal BP)	Mean Greyval	Age (cal BP)	Mean Greyval	Age (cal BP)	Mean Greyval
15	216	1276	188	2537	161
45	214	1306	188	2567	154
75	204	1336	188	2597	160
105	180	1366	187	2627	165
135	175	1396	195	2657	172
165	180	1426	169	2687	193
195	176	1456	184	2717	189
225	178	1486	197	2747	184
255	204	1516	202	2777	180
285	188	1546	201	2807	178
315	192	1576	196	2837	173
345	196	1606	192	2867	172
375	194	1636	192	2897	175
405	190	1666	192	2927	176
435	185	1696	202	2957	180
465	181	1726	187	2987	184
495	179	1756	190	3017	185
525	177	1786	186	3047	184
555	174	1816	182	3077	183
585	173	1846	192	3107	180
615	173	1876	192	3138	181
645	173	1906	195	3168	184
675	175	1936	200	3198	185
705	174	1966	198	3228	188
735	170	1996	194	3258	193
765	173	2026	194	3288	197
795	176	2056	191	3318	200
825	177	2087	190	3348	197
855	176	2117	198	3378	193
885	174	2147	200	3408	187
915	179	2177	208	3438	185
945	181	2207	210	3468	187
975	180	2237	213	3498	188
1005	179	2267	215	3528	188
1035	176	2297	213	3558	186
1066	172	2327	211	3588	186
1096	173	2357	213	3618	189
1126	178	2387	212	3648	190
1156	184	2417	188	3678	191
1186	185	2447	181	3708	191
1216	184	2477	172	3738	192
1246	186	2507	162	3768	193

Age (cal BP)	Mean Greyval	Age (cal BP)	Mean Greyval	Age (cal BP)	Mean Greyval
3798	193	5330	208	6861	215
3828	193	5360	206	6891	215
3858	191	5390	204	6921	215
3888	188	5420	202	6951	215
3918	186	5450	200	6981	215
3948	185	5480	203	7011	214
3978	185	5510	207	7041	213
4008	184	5540	211	7071	213
4038	182	5570	213	7101	212
4068	182	5600	215	7131	211
4098	186	5630	216	7161	211
4128	190	5660	213	7191	213
4158	193	5690	211	7221	215
4189	196	5720	209	7251	218
4219	197	5750	208	7282	217
4249	198	5780	207	7312	216
4279	197	5810	206	7342	215
4309	196	5840	205	7372	215
4339	195	5870	204	7402	215
4369	195	5900	205	7432	215
4399	194	5930	206	7462	215
4429	194	5960	207	7492	213
4459	193	5990	206	7522	212
4489	196	6020	204	7552	211
4519	198	6050	203	7582	213
4549	199	6080	203	7612	214
4579	198	6110	203	7642	216
4609	197	6140	204	7672	215
4639	194	6170	201	7702	215
4669	191	6200	198	7732	215
4699	187	6230	194	7762	214
4729	184	6261	193	7792	213
4759	185	6291	192	7822	212
4789	191	6321	191	7852	211
4819	198	6351	191	7882	210
4849	201	6381	191	7912	210
4879	203	6411	192	7942	209
4909	205	6441	197	7972	209
4939	205	6471	203	8002	210
4969	204	6501	208	8032	210
4999	204	6531	210	8062	211
5029	204	6561	211	8092	212
5059	204	6591	212	8122	213
5089	203	6621	214	8152	212
5119	202	6651	215	8182	212
5149	201	6681	216	8212	211
5179	199	6711	216	8242	209
5210	197	6741	215	8272	206
5240	202	6771	214	8302	202
5270	208	6801	214	8333	201
5300	211	6831	214	8363	205

Age (cal BP)	Mean Greyval	Age (cal BP)	Mean Greyval	Age (cal BP)	Mean Greyval
8393	209	9504	220	10615	219
8423	213	9534	220	10645	220
8453	212	9564	220	10675	219
8483	211	9594	220	10705	217
8513	211	9624	220	10735	215
8543	211	9654	220	10765	213
8573	211	9684	218	10795	211
8603	211	9714	216	10825	212
8633	210	9744	215	10855	215
8663	208	9774	214	10885	217
8693	207	9804	213	10915	213
8723	205	9834	211	10945	208
8753	204	9864	206	10975	209
8783	203	9894	200	11005	212
8813	203	9924	198	11035	214
8843	208	9954	203	11065	216
8873	212	9984	208	11095	218
8903	216	10014	212	11125	219
8933	216	10044	216	11155	221
8963	217	10074	219	11185	219
8993	217	10104	220	11215	218
9023	216	10134	219	11245	220
9053	215	10164	218	11275	222
9083	214	10194	219	11305	222
9113	214	10224	220	11335	221
9143	215	10254	221	11365	218
9173	215	10284	220	11396	213
9203	215	10314	219	11426	212
9233	215	10344	218	11456	211
9263	214	10375	219	11486	211
9293	213	10405	221	11516	210
9323	212	10435	221	11546	218
9353	210	10465	218	11576	183
9384	211	10495	215	11606	168
9414	214	10525	216	11636	142
9444	218	10555	218	11666	153
9474	220	10585	219	11696	153

B.6 Supplementary data on CD-ROM

- "LJoin.doc"

VBA code for the "LinescanJoiner" Excel macro which uses cross-correlation to align two overlapping sediment greyvalue linescans by finding the overlap position of maximum correlation. The data to be joined must be placed in columns A and B.

- "DF_Log.doc"

Detailed, 1cm-resolution lithological description of the three Drammensfjord cores, chiefly derived from the high-resolution digital images. Lithological intervals having a grey background contain laminated sediment of some kind; those with white backgrounds do not.

- "DF_Line.xls"

0.5mm-resolution master linescans for the nine Drammensfjord cores, as shown in figure 5.3. Normalised sediment greyvalue is given, aligned on a single common depth scale. These series were constructed using one linescan per image, and by using LinescanJoiner to join them via their overlapping margins. This is a large file (2.7MB) and may require additional memory to be made available for MS Excel to use.

- "DF_Pix.xls"

Comparison between measured depths in Drammensfjord core D1G (according to the tape measure visible in all the digital images) and the depth in pixels along the composite linescan used to derive the varve measurements. There is a near-constant linear relationship between the two (see section 5.2.5).

- "DF_Var.xls"

Drammensfjord varve thickness and sediment greyvalue data in Excel format, as tabulated in section B.1.

- "LSM_Dep.xls"

Record of sediment greyvalue changes with depth from Lake St Moritz core PSM90.3, measured at resolutions of 5cm and 3cm (on separate Excel worksheets), as tabulated in section B.2.

- "LSM_Var.xls"

Varve thickness data from Lake St Moritz core PSM90.3, for varves 1-239 (as tabulated in section B.3.1) and varves A1-A748 (as tabulated in section B.3.2) on separate Excel worksheets.

- "LSM_Tim.xls"

Age-depth data for Lake St Moritz core PSM90.3 at 3cm resolution, derived from the varve data and the smoothed calibrated-radiocarbon curve, and (on a separate Excel worksheet) 30-year resolution resampled sediment greyvalue time-series, as tabulated in section B.5, calculated from the data in B.2.